



HAL
open science

Specific properties of supercritical fluids for fast and exothermic reactive systems

Bruno Miguel da Silva Pinho

► **To cite this version:**

Bruno Miguel da Silva Pinho. Specific properties of supercritical fluids for fast and exothermic reactive systems. Material chemistry. Université de Bordeaux, 2015. English. NNT : 2015BORD0229 . tel-01683247

HAL Id: tel-01683247

<https://theses.hal.science/tel-01683247>

Submitted on 13 Jan 2018

HAL is a multi-disciplinary open access archive for the deposit and dissemination of scientific research documents, whether they are published or not. The documents may come from teaching and research institutions in France or abroad, or from public or private research centers.

L'archive ouverte pluridisciplinaire **HAL**, est destinée au dépôt et à la diffusion de documents scientifiques de niveau recherche, publiés ou non, émanant des établissements d'enseignement et de recherche français ou étrangers, des laboratoires publics ou privés.

THÈSE PRÉSENTÉE
POUR OBTENIR LE GRADE DE

**DOCTEUR DE
L'UNIVERSITÉ DE BORDEAUX**

ÉCOLE DOCTORALE DES SCIENCES CHIMIQUES
SPÉCIALITÉ : Génie des procédés

Par Bruno Miguel DA SILVA PINHO

**Specific properties of supercritical fluids for fast and
exothermic reactive systems**

Sous la direction de : Cyril AYMONIER et Samuel MARRE

Thèse IFPEN promue par Ghislain BERGEOT

Soutenue le 23 novembre 2015

Devant la commission d'examen formée de :

Mme BOUTROT, Catherine, Chef de projet, Axens

Présidente

M. JAUBERT, Jean-Noël, Professeur, LRGP, Université de Lorraine

Rapporteurs

M. MERCADIER, Jacques, Professeur, LATEP, Université de Pau et des Pays de l'Adour

M. P. MADEIRA, Luis M., Professeur, LEPABE, Faculdade de Engenharia da Un. do Porto

Examineurs

M. AYMONIER, Cyril, Directeur de recherche CNRS, ICMCB, Université de Bordeaux

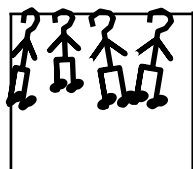
M. MARRE, Samuel, Chargé de recherche CNRS, ICMCB, Université de Bordeaux

M. BERGEOT, Ghislain, Ingénieur, IFP Energies Nouvelles

M. BAZER-BACHI, Frédéric, Ingénieur, IFP Energies Nouvelles

*“Eles não sabem que o sonho
é uma constante da vida
tão concreta e definida
como outra coisa qualquer” ...*

*“Ellos no saben que el sueño
es vino, es espuma, es levadura,
mascota alegre y sedienta,
con un hocico puntiagudo” ...*



*“Ils ne savent pas que le rêve
est la toile, est la couleur, est le pinceau,
base, fût, chapiteau,
ogive en lancette, vitrail,
pinacle d'une cathédrale,
contrepoint, symphonie” ...*

*“They neither know, nor dream,
that dreams command life.
That whenever a man dreams
the world bounces, advances,
as if it were a coloured ball
held by the hands of a child”*

Pedra Filosofal, António Gedão

Acknowledgements

This thesis would never be possible without the support of great and enthusiastic scientists and technicians. You are the soul of my work and the reason of my success. I deeply express my gratitude for these three wonderful years. The time spent on ICMCB and IFPEN was wonderful and friendly, demanding and dynamic, and above all, an international experience I will never forget. I would like to dedicate a music to all persons that had participated directly and indirectly (music performed with my friends after my thesis defense: <https://youtu.be/H0AG8v4mZb4>).

First, I would like to thank Mrs. Catherine Boutrot, project leader at Axens, to have agreed to chair the jury and to have perfectly orchestrated my defense. I also would like to express my gratitude to Prof. Jean-Noël Jaubert, professor at ENSIC (Univ. Lorraine), and to Prof. Jacques Mercadier, professor at ENSGTI (Univ. de Pau et des Pays de l'Adour), for giving me the honor and the pleasure to evaluate my work as “rapporteurs”. I present my appreciation to Prof. Luís M. P. Madeira, professor at FEUP (Univ. Porto), coming from Portugal to assist to my defense, and to evaluate my work and giving me the honor of having a compatriot in my jury.

I also would like to acknowledge Dominique Humeau, head of R15, and Herve Cauffriez, head of R151, for accepting me as a Ph.D. candidate at IFPEN, and for all the financial and human resources put at my disposition. I also would like to thank Mario Maglione, director of ICMCB, for approving my work at ICMCB. I also like to express my gratitude to Annie Borg, for all her kindness and hard working.

I would like to express my deeply and sincere gratitude to Cyril Aymonier and Samuel Marre for accepting guiding my thesis work with their vast experience and brilliance. Thank you for all the helpful discussions and the enthusiasm. In particular, I would like to thank Cyril Aymonier for his support, personality and for recognizing my capacities to accomplish the challenges proposed, even when I doubted. I would like to thank Samuel Marre for his advises, kindness, moral support, stress-free personality and enthusiasm in every moment during the challenging period at ICMCB. I remember that you always gave me nice words, even when I broke pricy materials in the laboratory.

I acknowledge the IFP engineers: Ghislain Bergeot, Frédéric Bazer-Bachi and Stéphane Girardon, which fully contributed to the success of this thesis from the first to the last day. I address my gratitude to Ghislain Bergeot for his availability, patience and scientific discussions. To Frédéric Bazer-Bachi, I express my gratitude for his constant attention and excellent ideas to achieve a valuable and interesting work in an industrial perspective. You always have a very tight schedule, but you always found time to encourage, advise and inspire me. To Stéphane Girardon for the valuable advises and rich scientific discussions, so useful for this work. I also would like to thank you for your stress-free personality and for all the jokes.

To Matthieu Rolland and Priscilla Avenier for the help given in carrying out this work. Thank you for all the discussions, and the expertise and knowledge shared. To Claudio Fonte and Vânia Santos-Moreau for the scientific discussions and moral support.

I also would like to thank all of IFPEN staff that contributed to this work: Noël Jurado, Sabri Kchaou, Carole Michon and Eric Volland, for all the motivational words and help offered since the moment I first step in the pilot plant.

I also would like to thank Bruno Sousa, who worked with me during his internship. Due to his perseverance and nice results, which helped me to better understand the reactive system.

Special thanks to my colleagues and friends:

Supercritical team: Fabien Palencia, Yves Garrabos, Baptiste Giroire, Liu Na, Ricardo Couto, Oana Pascu, Blanca Motos, Gilles Philippot, Lucile Henry, Sandy Morais, Suchithra Padmajan Sasikala, Cyril Quilfen, Patrick Rosa, Elena Prieto, ...

IFPEN: Léna Brunet-Errard, Isabelle Merdrignac, Mickael Rivallan, Nicolas Pannaci and Pascal Mouglin, Adrien, Matthieu, Rami, Charles, Anaïs, Mohammad, Amir, Juba, Sina, Julien, Diep, Luc, Leonel, Tiago, Luigi, Achir, Edouard, Rim, Teixeira, Ferdaous, Robin, Yoldes, Daniel, Laura, Florine, Marisa, Maria, Maïté, Mafalda, Sofia, Leonel, André, Bruno, Joana, Família Araujo, ...

Music group: Dominique Venka, Pauline, Sophie, Denis, Franck, Herve, Frédéric, Thierry, ...

My sincere gratitude to Fabien Palencia and the Araújo family, who supported me during a very difficult time.

Special thanks to those who wanted to be with me during this time, but, unfortunately, could not:

To my mom and dad, who allowed me to go abroad and follow my dream. To my brother for being close to me, even when I was physically distant. To my grandparents for motivating me to do my best, and for being proud of the person I have become.

To Marta for all your support during the difficult periods. She was my encouragement when work looked overwhelming... she always put a smile upon my face.

Les propriétés spécifiques des fluides supercritiques au service des systèmes réactifs contraignants

Introduction

La conception et le développement d'un nouveau catalyseur est un grand défi qui implique plusieurs années d'étude pour des équipes de chimistes et d'ingénieurs procédés. Le travail des chimistes est de créer plusieurs prototypes de catalyseurs et de comprendre ce qui se passe au niveau moléculaire. Leur travail est généralement réalisé à l'échelle du laboratoire (petites quantités). Le travail des ingénieurs procédés est d'évaluer les prototypes et de décider quel est le plus compétitif pour une mise en œuvre à l'échelle industrielle (Figure 1). Les performances des catalyseurs sont alors généralement testées dans des unités pilotes (taille intermédiaire entre les échelles « laboratoire » et « industrielle ») car, pour des raisons économiques, les prototypes ne peuvent pas être testés directement au niveau industriel (risque pour l'industriel, quantité de catalyseur prototype disponible,...). En effet, une unité industrielle a souvent un volume compris entre 1 et 100 m³ tandis qu'une unité pilote est plutôt de l'ordre de grandeur de quelques dizaine de cm³. Puisque les installations pilotes sont de plus petites tailles, il est difficile de tester les performances du catalyseur dans les conditions réelles d'utilisation. Par conséquent, le défi est de réaliser une mise à celles de l'échelle rentable qui reproduit des performances (activités initiales et /ou vieillissement) similaires à l'échelle industrielle.

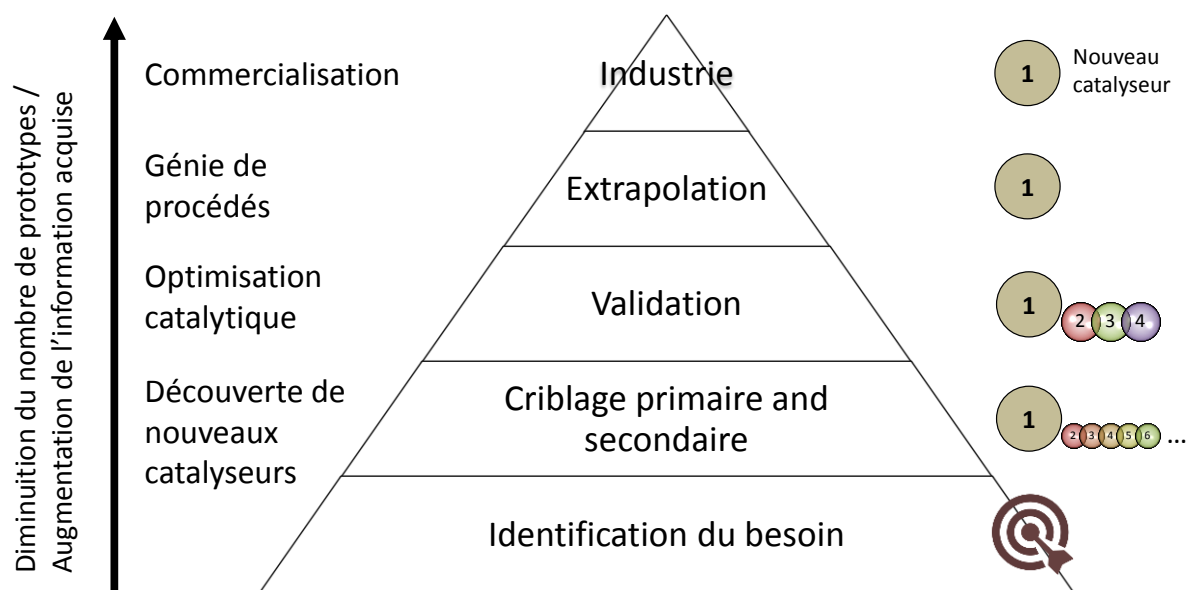


Figure 1 : Différentes étapes du développement d'un catalyseur (adapté de Jandeleit et al. 1999).

Il y a une volonté claire et croissante d'augmenter la représentativité des unités pilotes pour se rapprocher du fonctionnement industriel tout en limitant les volumes mis en jeu. Normalement, les données obtenues dans de petits réacteurs sont modélisées pour obtenir les informations nécessaires à l'extrapolation à l'échelle industrielle. Les modèles peuvent prendre en compte l'hydrodynamique, la morphologie du catalyseur, l'équilibre chimique, le schéma réactionnel et la cinétique. Néanmoins,

dans de nombreux cas, la complexité de la charge, du régime de réaction ou la non-existence de données cinétiques peuvent sérieusement entraver ou même empêcher la modélisation.

Aujourd'hui, la performance de nouveaux catalyseurs devient de plus en plus difficile à prédire pour certaines applications, notamment du fait d'une activité très importante des catalyseurs de dernière génération (Figure 2). Le transfert de masse est parfois responsable de la réduction de la vitesse de réaction à l'échelle pilote, conduisant à des résultats ambigus lors de la comparaison des catalyseurs (car les transferts sont différents à l'échelle industrielle). Par exemple, dans des réactions gaz-liquide-solide rapides, l'étape limitant est souvent le transfert de masse des espèces gazeuses réactives. Les espèces gazeuses doivent diffuser et se mélanger dans la phase liquide, puis s'adsorber et réagir sur la surface du catalyseur. Toutes ces résistances au transfert de masse réduisent le taux de réaction global. Le transfert de masse entre le gaz et le liquide peut, par exemple, limiter la réactivité de procédés tels que les hydrogénations et les oxydations sélectives.

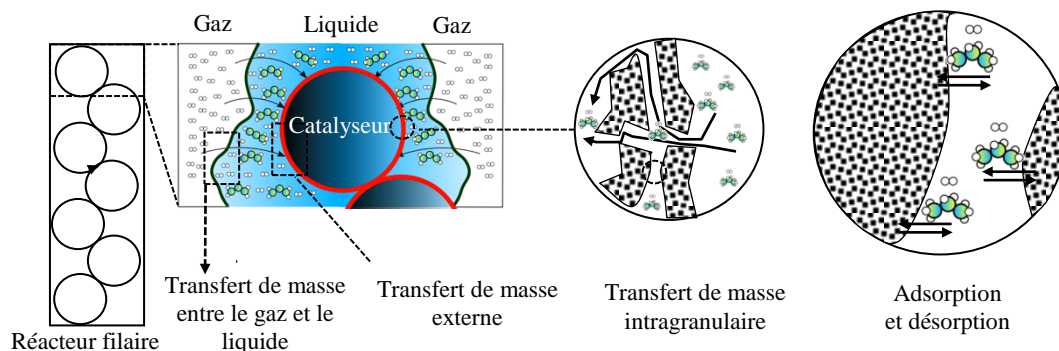


Figure 2 : Schéma des étapes successives d'une réaction multiphasique.

Lorsque les réactions catalytiques sont faites en conditions non conventionnelles, par exemple à haute pression ou en conditions supercritiques, il est possible (i) d'éliminer la résistance au transfert de masse entre le gaz et le liquide (Flores et al., 2003; Hyde et al., 2001; Keybl, 2011; Selva Pereda et al., 2002) en passant d'un système triphasique à un système biphasique, (ii) d'améliorer la diffusion des réactifs à l'intérieur de la particule (Cherayil, 2002; Drozdov and Tucker, 2001) et (iii) d'avoir des propriétés physiques modulables (Figure I.15). Il est également mentionné dans la littérature (Hassan et al., 2012) que le dépôt de coke peut être limité, ce qui augmente la cyclabilité du catalyseur (et donc sa durée de vie). Ainsi, les réactions en milieux fluides homogènes pourraient être d'excellentes options pour la catalyse (Hassan, 2011).

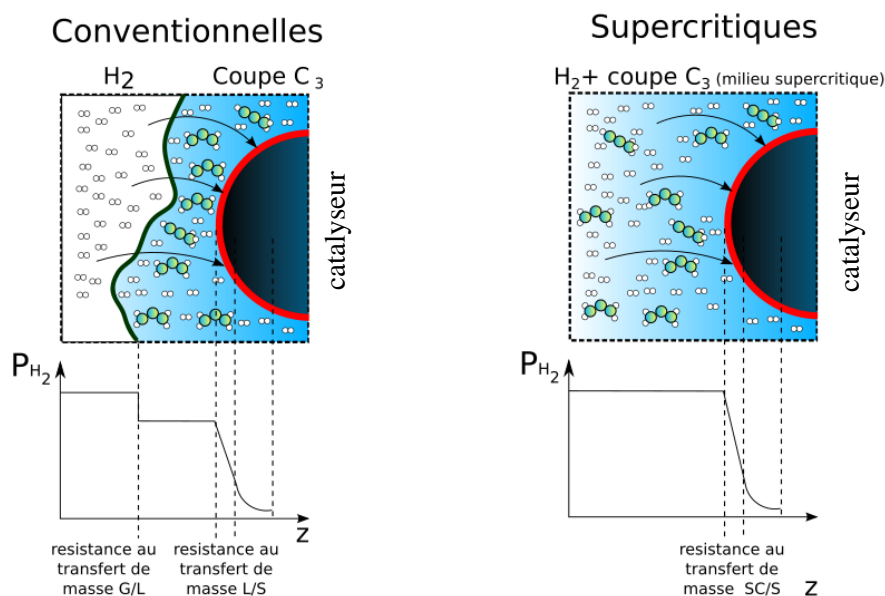


Figure 3 : Comparaison d'une hydrogénation sélective en conditions conventionnelles et d'une hydrogénation réalisée en conditions supercritiques (suppression des transferts de matière gaz-liquide).

Dans ce contexte, cette thèse propose une approche innovante pour réaliser le criblage des catalyseurs pour des réactions rapides multiphasiques à l'échelle pilote. La réaction modèle considérée pour cette étude est l'hydrogénation sélective de la coupe C3 (propane + [méthyl-acétylène (MA) + propadiène (PD)] = MAPD+propylène), qui conduit à la formation de propylène. Afin de minimiser les effets des transferts de masse sur la cinétique de la réaction, des expériences ont été réalisées en utilisant des conditions non conventionnelles (liquides homogènes ou supercritiques). Ces conditions permettent de tester des catalyseurs dans un système biphasique (une phase fluide et une phase solide), en limitant les résistances de transfert de masse aux résistances fluide-solide (internes/externes).

Les principaux objectifs de cette thèse ont été de développer et d'appliquer une méthodologie pour améliorer le criblage des catalyseurs et accéder à leurs performances intrinsèques. Pour atteindre ces objectifs, la thèse est divisée en cinq chapitres:

- I. Etat de l'art
- II. Etude thermodynamique (pour déterminer les conditions opératoires)
- III. Etude de modélisation en CFD (pour caractériser le réacteur : hydrodynamique et transfert de masse fluide-solide)
- IV. Etude expérimentale en conditions classiques et non conventionnelles
- V. Modélisation de la réaction

Deuxième chapitre:

Pour effectuer l'hydrogénation de la coupe C₃, il est nécessaire de définir les conditions opératoires, en particulier, le choix du solvant, des températures et des pressions pour atteindre les conditions non conventionnelles (haute pression et supercritiques). Ainsi, le présent chapitre est consacré :

- A. A la vérification du modèle thermodynamique le plus fiable pour prédire les points critiques pour des mélanges d'hydrocarbures contenant des composés légers (hydrogène, azote, CO₂, ...);
- B. Au développement d'une méthodologie pour planifier des expériences basées sur le comportement thermodynamique des mélanges et l'interpolation de ces résultats;
- C. A la mise en place d'une approche microfluidique pour étudier les diagrammes de phase P-T;
- D. A l'évaluation des points critiques pour la coupe C₃ et la définition des conditions opératoires à appliquer dans l'unité pilote.

Les données expérimentales (coordonnées critiques) sont généralement obtenues via l'utilisation de cellules optiques haute pression (HPOC), en utilisant des méthodes isochores ou dynamiques (Juntarachat et al., 2012). Bien que ces méthodes puissent conduire à des données thermodynamiques précises et fiables, elles prennent un temps non-négligeable. Cette limitation est principalement due aux temps requis pour atteindre l'équilibre thermodynamique dans des cellules ayant des volumes conséquents (généralement > 10 cm³). Pour cette raison, une nouvelle méthodologie a été développée sur la base d'un outil expérimental microfluidique (Figure 4) couplée à une approche de type « plan d'expérience ».

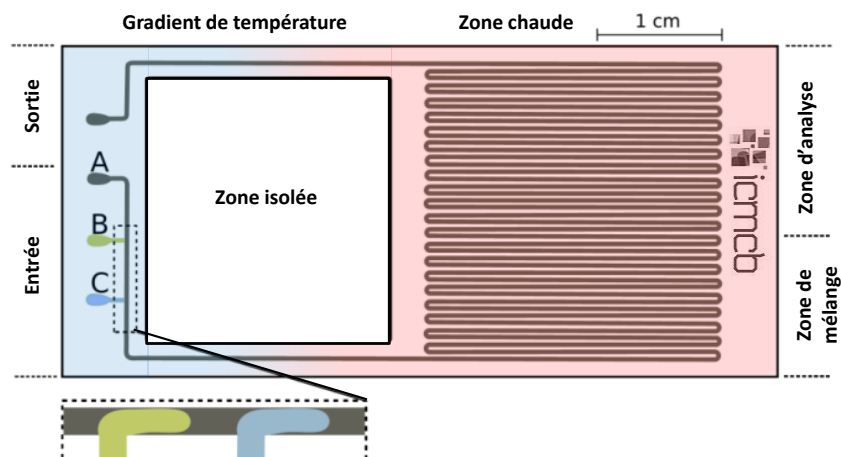


Figure 4 : Schéma du dispositif microfluidique développé pour cette étude.

Cet outil expérimental (microfluidique) permet de déterminer les coordonnées critiques de mélanges complexes via la détermination des points de bulle et des points de rosée. Les résultats ont été obtenus *via* un mode dynamique d'arrêt d'écoulement, qui permet le criblage rapide des paramètres opératoires (température, pression et composition). Le régime d'écoulement dynamique a été réalisé en utilisant une ligne de « bypass », ce qui permet de maintenir une pression constante à l'intérieur du système tout en variant la température.

Comme présenté dans la Figure 5, les résultats obtenus avec l'approche microfluidique sont en très bon accord avec ceux de la littérature, l'écart-type relatif moyen étant de 2%. La principale raison à cet écart est la variation de composition à l'entrée du système. Les légères déviations des résultats obtenus (la température et la pression critique) s'expliquent par les faibles variations du débit de la pompe qui peuvent changer la composition globale du système. Le modèle PPR78 prouve aussi que cette approche peut être utilisée pour obtenir des données expérimentales, qui sont essentielles pour la modélisation des procédés, avec des acquisitions jusqu'à 5 fois plus rapides que les méthodes classiques en HPOC pour des mélanges binaires. Cette stratégie peut aussi fournir des données

thermodynamiques expérimentales précises pour les mélanges plus complexes incluant plusieurs espèces chimiques.

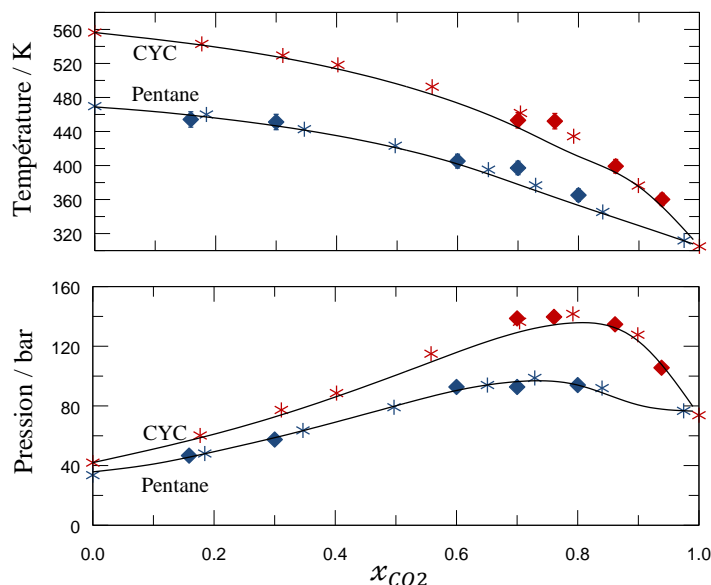


Figure 5 : Points critiques pour les binaires **cyclohexane (CYC)+CO₂** et **pentane+CO₂**. ♦ Résultats expérimentaux sur puce (approche microfluidique); * Données de la littérature: **CYC+CO₂** (Zhang et al., 2005); **pentane+CO₂** (Cheng et al., 1989); et — résultats calculés avec l'équation d'état PPR78, en utilisant l'algorithme de Heidemann et Khalil (1980) (**CYC+CO₂**; **pentane+CO₂**).

Pour utiliser la coupe C₃ en conditions supercritiques, il est nécessaire d'ajouter un solvant inerte de façon à réduire les coordonnées critiques du mélange (pression et température) pour les rendre compatibles avec les capacités de l'unité pilote et s'éloigner le moins possible des conditions industrielles. Plusieurs diagrammes ont été construits avec cet outil expérimental, parmi lesquels des mélanges incluant la coupe C₃. A partir des résultats obtenus, il a été possible de définir que le mélange avec le solvant CH₄ présente les conditions les plus douces de fonctionnement (température). Le CH₄ a aussi une plage de travail plus grande, ce qui signifie qu'il y a plus de flexibilité dans le choix de la composition du milieu réactionnel.

Troisième chapitre:

Afin d'identifier les avantages des conditions non conventionnelles (haute pression et supercritiques), il est important de bien maîtriser la technologie du réacteur pilote. En effet, le réacteur doit présenter : (i) un bon taux de transfert de masse pour des conditions classiques (G/L/S à 20 bar et 300K) et non conventionnelles (L/S ou SC/S à 120 bar et 300 K) et (ii) il doit permettre de fournir des résultats reproductibles, clairs et facilement compréhensibles.

Pour cela, l'hydrogénation de la coupe C₃ a été réalisée dans un réacteur filaire cylindrique immergé dans un bain thermostatique (permettant de s'approcher des conditions d'un réacteur isotherme). La forme cylindrique a été choisie afin de limiter de possibles zones hydrodynamiques mortes. Le réacteur utilisé a été défini en fonction du diamètre moyen du catalyseur ($d_{reactor} > d_{cat.} \approx 2.45 \text{ mm}$) et du poids du catalyseur nécessaire pour balayer la gamme de *vitesse* spatiale horaire en

pois étudiée (« Weight Hourly Space Velocity » - WHSV) qui est une des principales variables du procédé, entre 150 et 1500 h⁻¹.

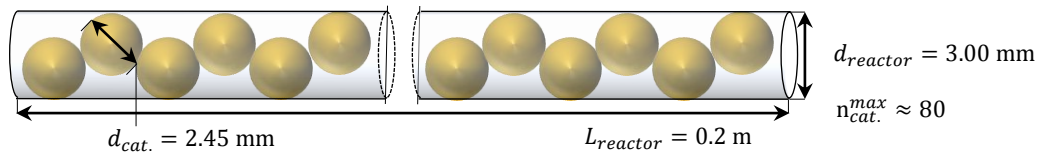


Figure 6 : Schéma simplifié d'un réacteur filaire cylindrique utilisé dans l'unité pilote.

Comme le réacteur filaire est une technologie simplifiée, l'hydrodynamique et le transfert de masse devraient être, a priori, plus faciles à caractériser avec des outils numériques (CFD) en comparaison des technologies plus traditionnelles (réacteur à lit fixe). L'utilisation d'un modèle CFD permet de gagner du temps par rapport à la validation expérimentale de l'installation.

Une étude numérique a été effectuée pour simuler l'hydrodynamique et le transfert de masse fluide-solide en utilisant un milieu réactionnel fluide homogène. L'influence du nombre de Reynolds des écoulements a été évaluée. Concernant l'hydrodynamique, les résultats de la distribution de temps de séjour montrent que l'écoulement peut être traité par un modèle d'écoulement piston avec une faible dispersion axiale. Au niveau du transfert de masse, il a été montré que la théorie du film pouvait être appliquée. Par conséquent, un coefficient de transfert de masse peut être utilisé pour la modélisation. À cet effet, une corrélation a été obtenue *via* l'étude CFD. Ces résultats sont très proches de la corrélation de Ranz et Marshall (1952).

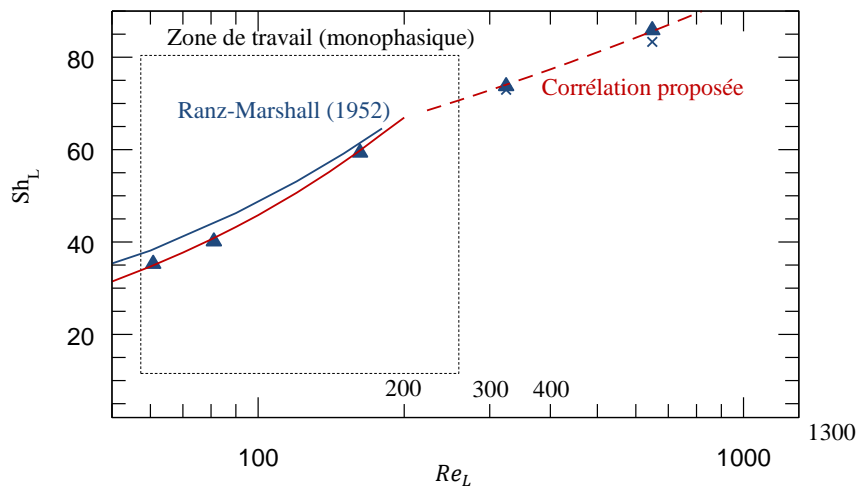


Figure 7 : Nombre adimensionnel de Sherwood (liquide/solide) en fonction du nombre de Reynolds (phase liquide). Les lignes représentent différentes corrélations pour le transfert de masse. Les lignes en rouge (continues et en pointillés) correspondent à la corrélation proposée par ce travail. Les points ont été obtenus à partir d'un modèle CFD pour des régimes d'écoulement laminaires (▲) et turbulents (×).

Quatrième chapitre:

Stratégie

Pour comprendre et quantifier l'impact du transfert de masse sur le rendement de la réaction, une série de tests d'hydrogénation du MAPD a été réalisée dans des conditions classiques et non conventionnelles. Le principal objectif de ce chapitre est d'étudier l'influence des conditions haute pression et des conditions supercritiques (SC) sur l'hydrogénation sélective de la coupe C₃. Pour être capable de comparer les différentes conditions, il est important de comprendre les effets de plusieurs paramètres, tels que: la WHSV (h⁻¹), la concentration en MAPD, le ratio H₂/MAPD, la température, la pression, le type de solvant et son état physique (Figure 8).

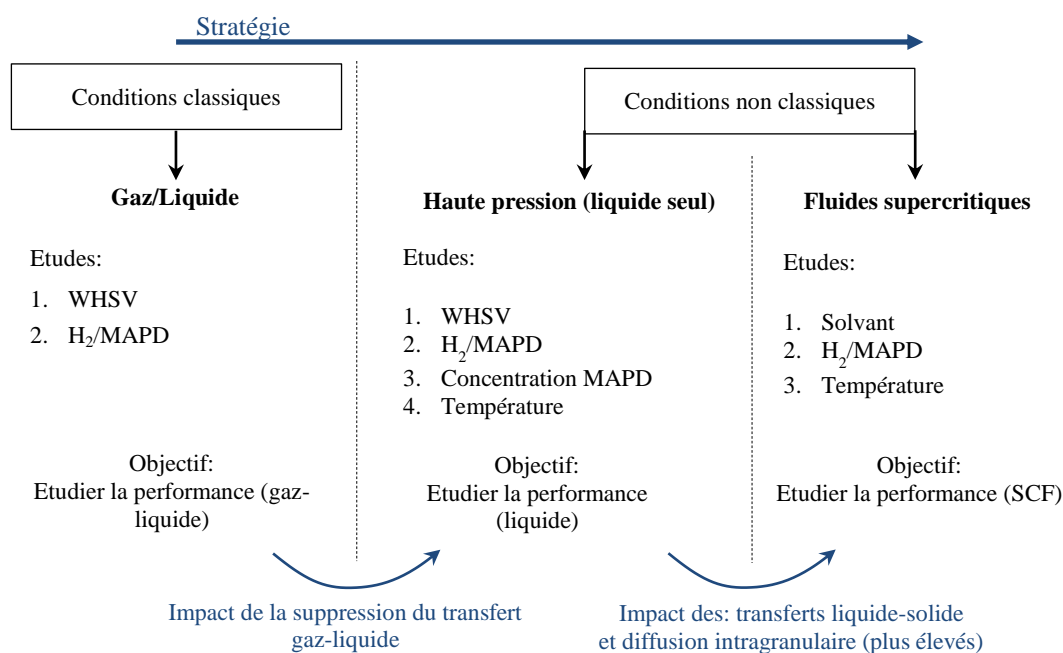


Figure 8 : Stratégie proposée pour étudier chaque condition de réaction.

Le changement de WHSV, de la concentration de MAPD, du ratio H₂/MAPD et de la température permet de caractériser la réaction pour chaque condition testée. Par ailleurs, le changement de la pression, de l'état physique et de l'addition d'un solvant aide à comprendre les limitations liées au transfert de masse pour les conditions testées.

Pour les conditions classiques, deux paramètres ont été étudiés afin de définir les zones dans lesquelles la réaction a les meilleures et les moins bonnes performances (conversion et sélectivité). En considérant des conditions non conventionnelles, l'interface gaz-liquide a été supprimée. L'impact de cette suppression a été étudié en utilisant plusieurs paramètres. L'impact le plus marqué est dû à la variation du coefficient de diffusion, qui conduit à un changement du taux de transfert de masse.

Résultats

Conditions classiques: Comme on peut le voir sur la Figure 9, les conditions classiques possèdent trois zones définies: (1) $\psi_{GL} < 1$ (le temps de séjour est trop court pour réaliser un transfert de masse gaz-

liquide total → la réaction est ralentie), (2) $Da^{mod.} < 1$ (le temps de séjour est trop court → la réaction est ralentie) et (3) une zone où la sélectivité est contrôlée par le flux molaire de H_2 .

Il a été montré que dans notre réacteur filaire le flux molaire d' H_2 était inférieur à un celui d'un réacteur industriel travaillant dans les régimes de hautes et de basses interactions (écoulement à bulle et ruisselant, respectivement). Néanmoins, les conditions classiques sont proches d'un réacteur industriel dans le régime d'interactions moyennes (écoulement pulsé), lorsque que $WHSV \sim 200 \text{ h}^{-1}$.

- En conclusion, ces conditions ne sont pas adaptées pour effectuer le criblage de catalyseurs, car la sélectivité est trop dépendante du flux molaire entre le gaz et le liquide.

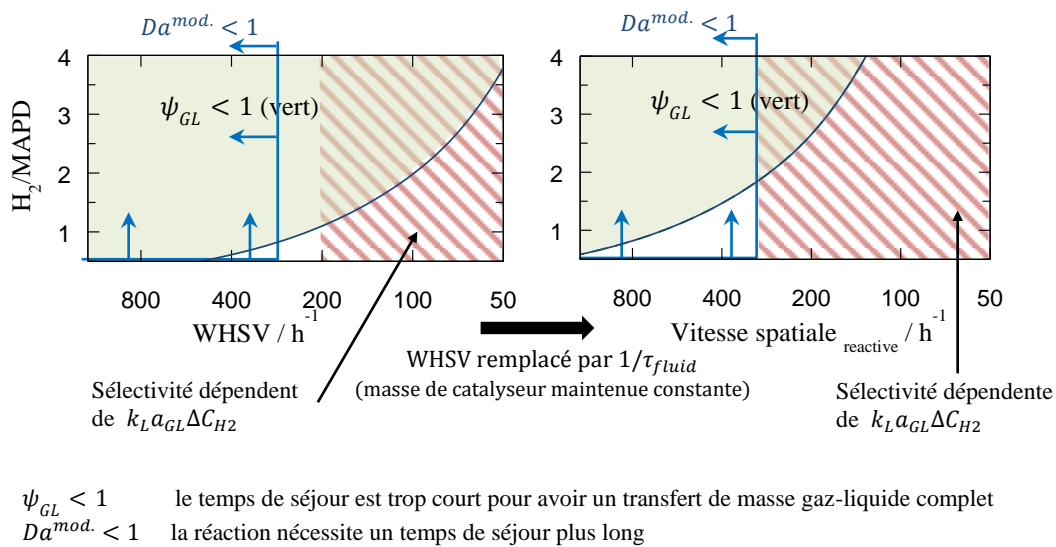
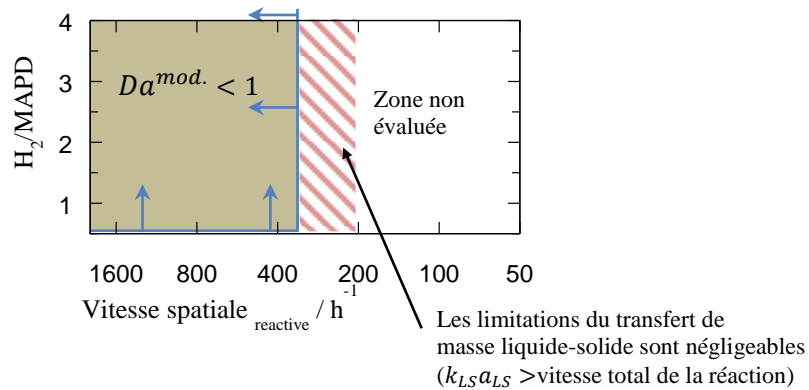


Figure 9 : Différentes zones définies avec la WHSV et la vitesse spatiale (« space velocity ») pour des conditions classiques (303K et 20 bar).

Conditions de haute pression: Comme on peut le voir sur la Figure 10, deux zones ont pu être définies : (1) $Da^{mod.} < 1$ (le temps de séjour est trop court → la réaction est ralentie) et (2) $Da^{mod.} > 1$. Pour ces conditions, le flux molaire de MAPD est proche de celui observé dans un réacteur industriel avec un régime d'interactions moyennes (écoulement à pulse) ou un régime d'interactions hautes (écoulement à bulles). Les deux régimes dépendent de la vitesse spatiale horaire (« space velocity ») utilisée. Dans les conditions de haute pression, il n'y a pas de transferts gaz-liquide (par définition) et les limitations au transfert de masse entre le liquide et le solide sont négligeables.

- En conclusion, ces conditions sont adaptées pour effectuer le criblage de catalyseurs, car la sélectivité ne change pas avec la vitesse spatiale horaire (« space velocity ») utilisée et les limitations du transfert de masse externe sont négligeables.

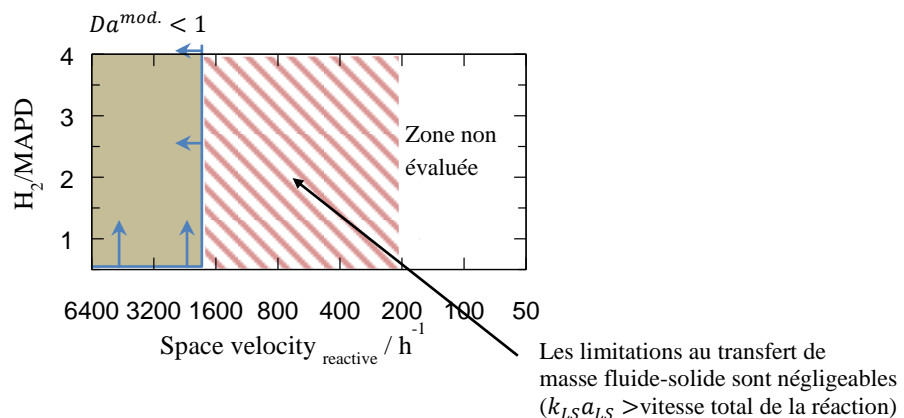


$Da^{mod.} < 1$ la réaction a besoin d'un temps de séjour plus long

Figure 10 : Schéma des différentes zones pour des conditions haute pression (303K et 120 bar).

Conditions supercritiques: Comme on peut le voir sur la Figure 11, les tests en conditions supercritiques présentent également deux zones: (1) la zone $Da^{mod.} < 1$ et (2) une zone dans laquelle le transfert de masse entre le fluide et le solide est négligeable. Pour ces conditions, la vitesse de réaction est plus élevée (4,8 fois) qu'en conditions haute pression, sans avoir de changements notables sur les taux de conversion du MAPD et du propane. Cela est dû à la diffusivité élevée en milieu supercritique. En résumé pour les conditions supercritiques :

- Ces conditions sont adaptées pour effectuer le criblage de catalyseurs et pour étudier les limitations intragranulaires du transfert de masse (grâce à une meilleure diffusivité). Par conséquent, elles permettent également d'accéder à des données expérimentales plus proches de la cinétique intrinsèque ($\eta_{SC} > 4,8 \eta_{HP}$).
- Les données expérimentales en conditions supercritiques - couplées avec les données en conditions haute pression - peuvent donner plus d'informations sur le système. Cela permet en effet d'évaluer la cinétique intrinsèque par modélisation.



$Da^{mod.} < 1$ La réaction a besoin d'un temps de séjour plus long

Figure 11 : Schéma des différentes zones pour des conditions supercritiques (303K et 120 bar).

Cinquième chapitre:

Dans la dernière partie de ce travail de thèse, nous avons travaillé sur le développement d'un modèle pour vérifier les interprétations proposées et pour estimer les paramètres cinétiques intrinsèques. L'hydrodynamique, le transfert de masse et les résultats obtenus concernant les études liées à la réaction d'hydrogénation ont été couplés pour obtenir un aperçu par modélisation de la réaction globale au niveau du procédé, mais également au niveau du catalyseur.

Les coefficients de diffusivité et les facteurs d'efficacité étant différents entre les conditions HP et SC (Tableau 1 ; Figure 12), la concentration en réactifs à l'intérieur de la particule sera donc plus élevée pour les conditions supercritiques. Si la réaction est modélisée en conditions haute pression et en conditions supercritiques, il devrait être possible de mieux appréhender les paramètres cinétiques intrinsèques.

Tableau 1 : Principales caractéristiques du transfert de masse et principales propriétés des conditions HP et SC.

Conditions	Limitations du transfert de masse		Propriétés	
	Gaz-liquide	Liquide-solide	$D_{MAPD} / \text{m}^2 \cdot \text{s}^{-1}$	η_{SC} / η_{HP}
Haute pression (HP)	Non	Négligeable	1.22×10^{-8}	1.0
Supercritique (SC)	Non	Négligeable	5.49×10^{-8}	>4.8

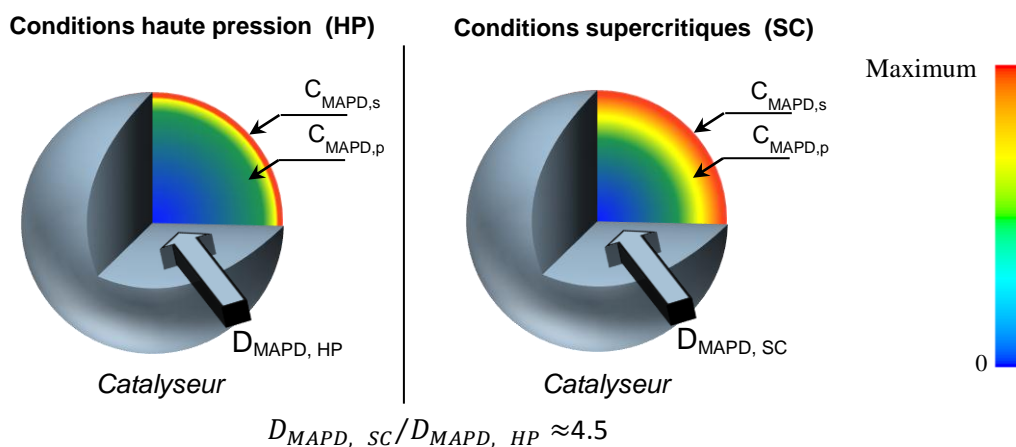


Figure 12 : Schéma présentant l'impact possible de la diffusivité du MAPD à l'intérieur d'une particule de catalyseur. $C_{MAPD,s}$ est la concentration de MAPD à la surface du catalyseur et $C_{MAPD,p}$ est la concentration de MAPD à l'intérieur du catalyseur.

Pour étudier les différents mécanismes réactionnels, le réacteur a été modélisé avec un modèle « réacteur piston » avec dispersion axiale et diffusion intragranulaire, en utilisant un solveur numérique (Comsol® V5). L'objectif est d'utiliser les données expérimentales obtenues (HP et SC) avec différentes diffusivités de façon à obtenir plus d'informations. La fonction « objectif » a été minimisée en utilisant la fonction « fminsearch » du logiciel Matlab® V2014a (optimisation). La Figure 13 décrit brièvement la méthodologie d'optimisation.

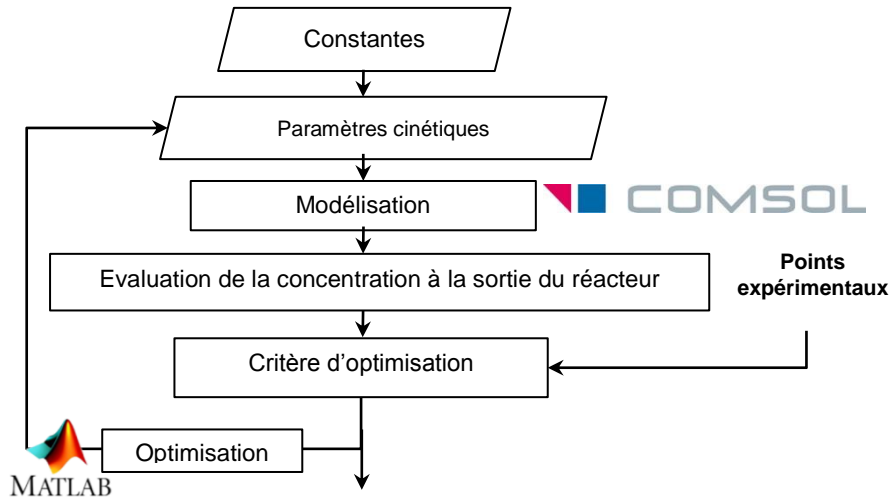


Figure 13 : Méthodologie adoptée pour étudier les paramètres cinétiques de l'hydrogénation du MAPD et du propylène.

Différents mécanismes cinétiques ont été testés, tels que des « mécanismes d'ordre » et des mécanismes basés sur le LH-HW. Le mécanisme d'ordre avec deux variables de décision (constantes cinétiques) a permis d'obtenir les meilleurs résultats. Pour cette raison, il a été choisi pour simuler l'hydrogénation sélective du MAPD. Les résultats obtenus avec ce modèle corroborent les interprétations/conclusions obtenues expérimentalement en conditions haute pression (liquide homogène à 120 bar) et en conditions supercritiques.

Les résultats de modélisation montrent que les données expérimentales HP et SC combinées sont intéressantes pour étudier la cinétique intrinsèque, donnant des estimations fiables, qui ne pourraient pas être obtenues autrement. Pour cette raison, les fluides supercritiques pourraient être utilisés avec d'autres systèmes réactionnels pour explorer et comprendre les cinétiques dans les systèmes réactifs rapides.

Conclusion:

Ce travail a permis d'évaluer les performances intrinsèque d'un catalyseur d'hydrogénation sélective de la coupe C₃. Les conditions HP et SC apportent des informations supplémentaires sur les catalyseurs et sur la compréhension du système en conditions de fluides denses (HP et SC). De plus, cela nous a permis d'accéder aux paramètres aux paramètres cinétiques intrinsèques de l'hydrogénation sélective du MAPD, en couplant des études expérimentales et de modélisation concernant les mécanismes thermodynamiques, hydrodynamiques et de réactivité chimique au sein d'un réacteur pilote filaire.

Index

GENERAL INTRODUCTION	31
BIBLIOGRAPHIC STUDY	33
I.1 INTRODUCTION	33
I.2 REACTIONS IN PILOT PLANTS	34
I.2.1 <i>Catalyst screening: tools to understand complex reactions</i>	34
I.2.2 <i>Some example of pilot reactor technologies</i>	35
I.2.3 <i>Conclusions</i>	37
I.3 MULTIPHASIC REACTIONS.....	38
I.3.1 <i>Interphase mass transfer</i>	39
I.3.2 <i>External mass transfer</i>	42
I.3.3 <i>Internal mass transfer</i>	43
I.3.4 <i>Catalyst performance</i>	44
I.3.5 <i>Adsorption/desorption</i>	46
I.3.6 <i>Pilot plants uncertainties and limitations</i>	48
I.3.7 <i>Conclusions</i>	48
I.4 C ₃ CUT HYDROGENATION	49
I.4.1 <i>Overview of C₃ cut hydrogenation</i>	49
I.4.2 <i>Process Description</i>	51
I.4.3 <i>Catalyst characteristics</i>	53
I.4.4 <i>Kinetics</i>	54
I.4.5 <i>Hydrogenation at pilot-scale state</i>	59
I.4.6 <i>Conclusion</i>	60
I.5 HIGH-PRESSURE REACTION CONDITIONS.....	61
I.5.1 <i>Pressure effect</i>	61
I.5.2 <i>Pressure effect on kinetics</i>	62
I.5.3 <i>Pressure effect on mass transfer</i>	62
I.5.4 <i>Interphase equilibrium</i>	64
I.5.5 <i>Conclusion</i>	68
I.6 REACTION IN SUPERCRITICAL CONDITIONS.....	68
I.6.1 <i>Introduction</i>	68
I.6.2 <i>Heterogeneous catalysis in SCFs</i>	69
I.6.3 <i>Example of hydrogenation in supercritical media</i>	76
I.6.4 <i>Phase behavior</i>	77
I.6.5 <i>Conclusions</i>	80
I.7 CONCLUSION	80
STUDY OF UNCONVENTIONAL REACTIVE CONDITIONS	83
II.1 INTRODUCTION	84
II.2 SUPERCRITICAL SOLVENTS FOR C ₃ CUT	84
II.3 ALGORITHM AND APPROACH FOR “DESIGN OF EXPERIMENTS”	86
II.3.1 <i>Introduction</i>	86
II.3.2 <i>Methodology</i>	87
II.3.3 <i>Critical point determination for multicomponent mixtures: state of the art</i>	88

Index

II.3.4	Algorithm	89
II.3.5	Results.....	90
II.3.6	Discussion	99
II.3.7	Conclusions	101
II.4	ESTIMATION OF C ₃ CUT CRITICAL POINTS BY MODELING	102
II.4.1	Binaries for propane and hydrogen containing mixtures	102
II.4.2	Binary combinations of C ₃ cut + solvents and H ₂	103
II.4.3	Ternary combinations of C ₃ cut + solvents + H ₂	104
II.4.4	Conclusions	109
II.5	EXPERIMENTAL APPROACH (HT/HP MICROFLUIDICS)	109
II.5.1	Introduction	109
II.5.2	HP/HT microfluidic tool.....	110
II.5.3	Microfluidic strategy to build P-T phase diagrams	113
II.5.4	Results and discussion	116
II.5.5	Conclusions	119
II.6	APPLICATION TO C ₃ CUT HYDROGENATION	120
II.6.1	Miscibility diagrams.....	120
II.6.2	C ₃ cut - ternary combination (direct interpretation).....	121
II.6.3	C ₃ cut - ternary combination (with interpolation)	122
II.6.4	C ₃ cut hydrogenation working zone.....	125
II.6.5	Conclusion.....	127
II.7	GLOBAL CONCLUSIONS	127
PILOT PLANT: PRESENTATION AND CHARACTERIZATION		129
III.1	INTRODUCTION	130
III.2	EXPERIMENTAL SECTION	131
III.2.1	Chemicals	131
III.2.2	Experimental set-up	131
III.2.3	Catalyst characterization	135
III.2.4	Packing characterization	136
III.3	HYDRODYNAMICS AND MASS TRANSFER IN THE SINGLE PELLETT STRING REACTOR	137
III.3.1	Introduction.....	137
III.3.2	CFD modeling	138
III.3.3	Mesh sensitivity analysis	141
III.3.4	Hydrodynamic simulations.....	143
III.3.5	Mass transfer simulations.....	148
III.3.6	Mass transfer coefficients for pilot and industrial reactors	159
III.4	CONCLUSIONS	169
C₃ CUT HYDROGENATION IN CONVENTIONAL AND UNCONVENTIONAL CONDITIONS.....		171
IV.1	INTRODUCTION.....	172
IV.2	METHODOLOGY	172
IV.2.1	Experimental conditions.....	174
IV.2.2	Studied parameters and strategy.....	176
IV.3	CONVENTIONAL CONDITIONS.....	178
IV.3.1	WHSV effect	178
IV.3.2	H ₂ /MAPD ratio effect	180
IV.3.3	Determination of the zone $\psi_{GL} < 1$	183

Index

IV.3.4	Conclusions (conventional conditions)	188
IV.4	HIGH-PRESSURE CONDITIONS	189
IV.4.1	High-pressure properties	190
IV.4.2	Pressure and WHSV effect	191
IV.4.3	H ₂ /MAPD ratio effect	194
IV.4.4	MAPD concentration effect	198
IV.4.5	Temperature effect	200
IV.4.6	Conclusion (high-pressure conditions)	203
IV.5	SUPERCRITICAL CONDITIONS	205
IV.5.1	Diffusion in supercritical fluids	206
IV.5.2	Solvents	208
IV.5.3	Planning of experiments	211
IV.5.4	Solvent effect (<i>iso</i> : space velocity and MAPD concentration)	212
IV.5.5	Supercritical vs high-pressure conditions	215
IV.5.6	Space velocity effect	217
IV.5.7	H ₂ /MAPD ratio effect	219
IV.5.8	Supercritical conditions with different solvents	221
IV.5.9	Conclusion (supercritical conditions)	223
IV.6	CONCLUSIONS	224
	MODELING MAPD HYDROGENATION	229
V.1	INTRODUCTION	230
V.2	MODEL	231
V.2.1	Constants	231
V.2.2	Kinetic parameters and reaction mechanisms	232
V.2.3	Model the pilot reactor	234
V.2.4	Optimization criteria	237
V.3	RESULTS	238
V.3.1	Interest of supercritical fluids in modeling	238
V.3.2	Liquid-solid mass transfer correlation verification (in the zone of low impact)	240
V.3.3	Determination of the initial guesses	241
V.3.4	Optimization of kinetic models	242
V.3.5	Model vs experiments: space velocity and H ₂ /MAPD ratio (HP)	243
V.3.6	Model vs experiments: high-pressure and supercritical conditions	247
V.4	CONCLUSIONS	249
	GENERAL CONCLUSION AND PERSPECTIVES	251
	NOTATION AND GLOSSARY	255
	REFERENCES	263
	APPENDIX	275
I.	CHAPTER I	275
I.1	Catalysis in stationary catalytic basket reactors	275
I.2	Interphase mass transfer: boundary conditions and equations	275
I.3	Empirical isotherm adsorption models	277
I.4	Pilot scale uncertainties	277
I.5	Reaction rates (schemes)	280

Index

I.6	Activation volume (pressure effect)	281
II.	CHAPTER II.....	284
II.1	Algorithm formulation.....	284
II.2	Algorithm detailed.....	288
II.3	Interaction parameters.....	290
II.4	From binary to quaternary diagrams	291
II.5	C ₃ cut - ternary combination (direct interpretation).....	292
III.	CHAPTER III.....	293
III.1	Intragranular diffusion.....	293
III.2	Catalyst reduction.....	295
III.3	Packing characterization	295
III.4	Single string pellet reactor: hydrodynamic regime	299
IV.	CHAPTER IV	300
IV.1	Derivation of ψ	300
IV.2	Choice of liquid hold-up correlation (Eq. IV.5)	302
IV.3	High-pressure: MAPD concentration effect and H ₂ /MAPD ratio	302
IV.4	Supercritical vs high-pressure: 2 H ₂ /MAPD ratio	304
IV.5	Diffusion correlations.....	305
V.	CHAPTER V	308
V.1	Main function (Matlab+Comsol).....	308
V.2	Minimization function (Matlab+Comsol).....	309

General Introduction

In today's chemical plants, the need to reduce the costs and to increase productivity make the difference between success and failure. To be competitive, a chemical company is expected to keep or increase the annual production with lower cost and reduced environmental impact. A way to reduce costs consists in changing the catalyst with a new generation, which has higher efficiency towards the desired product. Research companies are interested in the development of innovative catalysts to answer the market demand.

Designing a new catalyst represents a big challenge and involves years of development. Teams of chemists and engineers have to work together to innovate. The chemists' job is to create several catalyst prototypes and to understand what is going on at the molecular level. Their job occurs at lab-scale (small quantities). The engineers' job is to evaluate the prototypes and to decide which one is better for industrial conditions. Their activity occurs at pilot or/and industrial scale. Unfortunately for economical reason, the prototypes cannot be tested at the industrial level. They have to be tested on small-scale industrial plants. An industrial unit has often a volume between 1 and 100 m³ and a pilot plant often between 10 to 100 cm³. Since pilot plants are small, it is difficult to test the catalyst performance in a real case scenario. Therefore, **the challenge is to achieve a cost-effective scale-up that ensures performances (initial activities and/or aging) similar to the industrial scale.**

There is a clear and growing desire to bridge the gap between pilot and industrial scale technologies. **The target is to have pilot plants that are representative of the industrial ones.** Normally, the data obtained in small reactors is modeled to provide suitable information to extrapolate results to larger scales. The models can take into account hydrodynamics, catalyst morphology, chemical equilibrium, reaction scheme and kinetics. However, in many cases, **the complexity of the feedstock, of the reaction scheme or the non-existence of kinetic data can seriously impede or even prevent modeling.**

Nowadays, it is becoming more difficult to predict the performance of new catalysts for certain applications. Some of the new generations of catalysts are increasingly more active than previous ones. Unfortunately, mass transfer can put the brake on the reaction rate at pilot-scale, leading to ambiguous results between catalysts. For instance, **in fast gas-liquid-solid reactions, the limiting step is often the mass transfer of reactant gas species.** Indeed, the gas species have to dissolve, diffuse/mix with the liquid, and then to adsorb and react on the catalyst surface. All these mass transfer resistances reduce the overall reaction rate. **Thus, the mass transfer of the gas species may limit the overall reactivity in processes such as selective hydrogenations, selective oxidations or steam reforming.**

In this context, this thesis proposes an innovative approach to perform catalyst screening for fast multiphasic reactions at pilot-scale. The selected reaction was methyl-acetylene (MA) and propadiene (PD) hydrogenation, which leads to propylene production (chemical industry uses ~90 million tons per year). To minimize the effects of mass transfer rates on reaction

kinetics, experiments were adapted by using **high-pressure** and **supercritical** conditions (fluid properties between gas and liquid). **These conditions make possible to test the catalyst in a homogeneous fluid phase and to reduce mass transfer resistances (external/internal).**

The main goals of this thesis are to develop and apply a methodology to improve catalyst screening and to access the catalyst intrinsic kinetics at pilot scale. This methodology will be applied for the MA+PD reaction (fast reaction) (C_3 cut hydrogenation). To achieve these goals, the thesis is divided into five chapters.

The first chapter aims to present the state-of-art key points. In this chapter, the main concepts related to pilot plants will be detailed, going from macroscopic (e.g. reactor design) to catalyst level (e.g. kinetic mechanisms). A special attention will be paid to C_3 cut hydrogenation and to operating with unconventional conditions, such as high-pressure and supercritical.

Before performing C_3 cut hydrogenation, it is necessary to define the operating conditions, in particular, the choice of the solvent, temperatures and pressures to reach supercritical conditions. The second chapter aims to access the C_3 cut in supercritical conditions by experimental and model means. Here, a new methodology will be presented, based on an on-chip experimental tool coupled with a thermodynamic model. This may aid us having a widespread thermodynamic analysis of the studied mixtures.

After acquiring the operating conditions, the pilot plant has to be characterized before performing the hydrogenation reaction, since the literature is scarce for the reactor used. Therefore, the third chapter aims to characterize the reactor for hydrodynamic and liquid-solid mass transfer by numerical means. This study will give us essential information to interpret future experimental results and to construct a reactor model. The hydrodynamic will be investigated with a residence time distribution, and the mass transfer will be investigated between the fluid and a particle.

Once the working conditions and the pilot plant are characterized, the experimental tests will be performed. The fourth chapter focuses on studying experiments at conventional (gas-liquid-solid) and unconventional (fluid-solid) conditions. The intention is to understand conventional conditions, before going to unconventional ones. At the end, the results obtained under different conditions are compared. This analysis may fill the primary goal of this thesis.

Finally, a model is interesting to verify the explanations proposed and to estimate the intrinsic kinetics parameters. Thus, chapter five aims to model experiments in unconventional conditions (high-pressure and supercritical). The hydrodynamic, mass transfer and hydrogenation study will be now used to give insights about the reactor and catalyst crust. This may allow us to fill the secondary goal of this thesis.

Chapter I

Bibliographic study

Abstract

The primary goal of this thesis is to study new methods to perform catalyst screening for fast multiphasic reactions at pilot-scale (applied to the C₃ cut hydrogenation). These reactions have a high level of complexity, because they are fast and the reaction kinetics are often limited by interphase, external and/or internal mass-transfer rates. Understanding the influence of each mass-transfer rate is necessary to differentiate and create new generations of catalysts. To minimize the influence of mass transfer rates over reaction kinetics, high-pressure and supercritical conditions were investigated in a single pellet string reactor, making possible to have a homogeneous phase and to improve reactant diffusion. To this end, in the first subchapter, the heterogeneous catalysis in industrial and research reactors is detailed. This part is followed by a literature review of the heterogeneous catalysis of methylacetylene and propadiene. In the last subchapter, the state of the art for unconventional operating conditions (high-pressure and supercritical) applied to heterogeneous catalysis will be discussed.

I.1 Introduction

In fast gas-liquid-solid reactions, the limiting step is often the mass transfer of reactant gas species. Indeed, the gas species are forced to dissolve, diffuse/mix with the liquid, and then to adsorb and react on the catalyst surface. All these mass transfer resistances reduce the overall reaction rate (Adagiri et al., 2012; Frouws et al., 1976). Typically, the mass transfer of the gas species limits the overall reactivity in processes such as selective hydrogenations (Wu and Li, 2011), selective oxidations (Theyssen et al., 2006) and steam reforming (Lee et al., 2004).

Before addressing the limitations of heterogeneous catalysis for pilot and industrial plants, it is necessary to clarify the stages of catalyst screening and the currently used reactor technology.

This chapter is divided in 4 sections: (i) reactions in pilot plants, (ii) multiphasic reactions, (iii) C₃ cut hydrogenation and (iv) unconventional media reaction.

I.2 Reactions in pilot plants

I.2.1 Catalyst screening: tools to understand complex reactions

The catalysts selection is an important milestone in process development because all the catalysts conception relies on catalysts screening (Jandeleit et al., 1999). By definition, the catalysts screening compares catalysts performance at the same experimental conditions: temperature, pressure, feed composition, residence time, catalyst mass, etc. Catalyst screening allows research and development teams to select the best prototypes.

From a lab environment to an industrial chemical plant there are several stages in catalyst screening. These stages are, in chronological order, primary and secondary screenings, validation and extrapolation.

Primary and secondary screenings: Normally, the primary and secondary catalyst screenings are done in laboratory batch reactors with stationary catalytic baskets (Braga et al., 2014; Jenzer et al., 2001). This is a simple and yet powerful selection stage because the prototype comparison takes less than a week, and the prototype concept can be quickly switched (Jandeleit et al., 1999). The goal is to evaluate, in a fast way, different catalyst prototypes. Also, it is very cost-efficient, meaning that many samples can be tested without significant funding restrictions. The difference between primary and secondary screenings are in the test time and the used feed composition. In a primary screening, tests often last only one day and the feed has a defined composition (model feedstock). In comparison, in a secondary screening, the tests last one week and a real feed is used, which means complex mixtures with composition variations.

Validation: Advancing from secondary catalyst screening into validation involves moving from standard laboratory equipment to pilot plants (cm^3 to m^3). The biggest advantage of the pilot plant approach is to have a catalytic process easier to interpret and model (physical phenomena and system response were already widely studied in literature) (Hill et al., 2014). From this point onwards, the data obtained enables scale-up and process optimization (Edgar et al., 2001; Jandeleit et al., 1999; Wu and Li, 2011). While in primary/secondary catalyst screenings, one hundred catalyst prototypes could be tested, in the validation stage only the 3 to 5 best prototypes are subjected to be evaluated. About the cost, validation requires high-throughput techniques, experimental planning and costly equipment.

Extrapolation: The validation stage is the first step to scale-up, and it brings many problems (Gianetto and Specchia, 1992). To study heterogeneous catalysis in a pilot plant, several challenges should be addressed to avoid introducing variability in the system, such as: (i) multiphase mixture (Fonte et al., 2014; Hipolito et al., 2010; Lane et al., 2002; Musko et al., 2012), and (ii) catalyst packing (Dorai et al., 2012; Shi and Zhang, 2008). Given the difficulty to understand some phenomena, it is wisely moving to a scale close to the real one (displaying similar mass transfer limitations) before the commercialization of a new catalyst. This stage is characterized by costly and long-term tests.

The reactors technologies applied (on those steps) are important to select the best prototype.

1.2.2 Some example of pilot reactor technologies

Today, the activities of catalysis research centers are more focused on improving and developing pilot technologies towards a better understanding of catalytic processes. This involves (i) the design, (ii) the scale-up or scale-down operations, (iii) the control and (iv) the optimization of processes, ranging from reactors at pilot scale (Pitault et al., 2004) down to micro scale (Claus et al., 2001). Today research's emphasis is focused on the development of innovative technologies that can provide reproducibility and reliability results at low cost (Dixon and Nijemeisland, 2001; Dorai et al., 2012; Zimmermann and Taghipour, 2005), which can be extrapolated to the industrial scale.

In this subchapter, we will discuss general considerations and state of the art linked to technologies used for catalyst screening: packed bed, stationary catalytic basket and single pellet string.

Packed bed reactor

Packed bed reactors are the most conventional tools used for catalyst screening at pilot scale, because of their simple geometry, which is close to a large number of industrial applications. For instance, they are employed in cyclohexene hydrogenation (Arunajatesan et al., 2001) and ammonia oxidation (Mulder et al., 1995). In its basis, a packed bed reactor consists of a cylindrical tube filled with catalyst pellets (see Figure I.1).

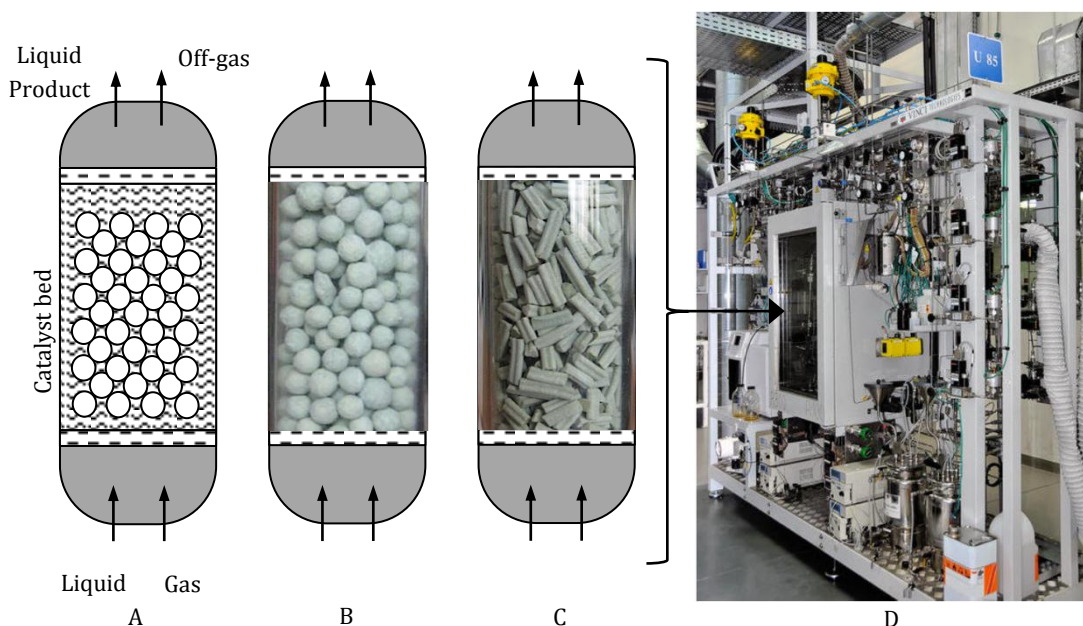


Figure I.1: A: Scheme of a pilot plant working in upflow mode. B: Spherical catalyst packing. C: Extruded catalyst packing. D: Packed bed reactor pilot plant with 4 parallel reactors (10 ml), adapted from Rolland (2014).

The packed bed reactors have many **advantages** compared to other reactors types. They have a (i) simple form, thus (ii) low fabrication, operation and maintenance costs, and they require (iii) little auxiliary equipment. Another important attribute is the (iv) flexibility to change operating conditions, going to extremely high temperatures or pressures without being very costly and involving significant investments (Guo Jun-Wang et al., 1998).

There are also **disadvantages** with the packed bed technology. The (i) heat is not always well transferred to the surrounds, leading to zones with different temperature profiles (Larachi et al., 2003; Zabaleta et al., 2007). They often represent a significant problem in catalytic interpretation, because there are zones with (ii) different catalytic activities. The appearance of (iii) preferential flow paths within the catalyst bed and (iv) eventual poor wetting of the catalyst particles can also be a problem (Dorai et al., 2012).

The LHSV (liquid hourly space velocity) (h^{-1}) is a process parameter that connects the performance between industrial and pilot plants (Satterfield, 1975). It is defined as:

$$LHSV = \frac{Q}{(1 - \varepsilon)V_{reactor}} \quad \text{Eq. I.1}$$

where Q ($\text{m}^3 \cdot \text{h}^{-1}$) is the liquid volumetric flow-rate, ε is the bed porosity and $V_{reactor}$ (m^3) is the reactor volume [$(1 - \varepsilon)V_{reactor} \rightarrow$ volume of catalyst]. In certain processes, instead of the LHSV (h^{-1}), the WHSV (weight hourly space velocity) (h^{-1}) can be used (for the cases where the reactor is not characterized).

$$WHSV = \frac{W}{m_{cat.}} \quad \text{Eq. I.2}$$

where W ($\text{kg} \cdot \text{h}^{-1}$) is the liquid mass flow-rate and $m_{cat.}$ (kg) is the mass of the catalyst bed.

The LHSV and WHSV can be maintained with different flow-rates, but with substantial variations in mass transfer rates (Mederos et al., 2009). For instance, a slow flow-rate has a lower mass transfer in a small catalyst bed than a fast flow-rate in a large catalyst bed, despite having the same LHSV.

Catalysis in pilot packed bed reactors: When designing a packed bed reactor for a pilot plant several parameters have to be considered, such as: (i) the length of the catalyst bed, (ii) the type of catalyst morphology and (iii) catalyst packing. The catalyst can have different morphologies depending on the process (Buffham, 2000). To be specific, the catalyst can have spherical, cylindrical or other shaped pellets. A spherical catalytic structure usually has a diameter between 1 to 5 mm (Rolland, 2014). The choice of the particle diameter is a key variable in the process. It will affect the overall performance: yield, catalytic aging, hydrodynamics and mass transfer (Buffham, 2000).

Extrapolation: To extrapolate the performance of packed bed reactors, iso *LHSV* values use to be considered (Satterfield, 1975). This approach should be only used when the pilot plant and the industrial unit have exactly the same reactor design and operating conditions (to maintain hydro and mass transfer conditions). It means that both reactors must have the same temperature, pressure, catalyst configuration and hydrodynamic regime, which is hardly the case, so a model (with correlations) is used.

Single pellet string reactor

The single pellet string reactor is also a **downsized packed bed reactor**. The reactor diameter has nearly the same size as the catalyst pellets (Figure I.2) This means that the catalyst packing can be easily reproduced (Hipolito et al., 2010).

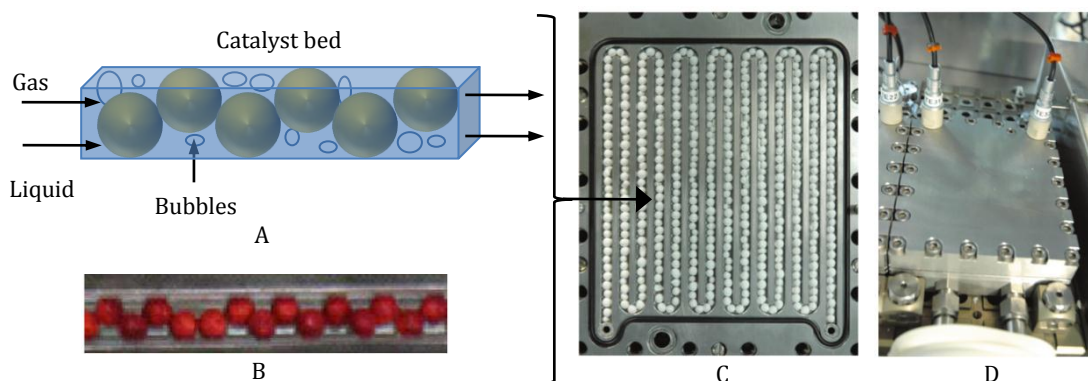


Figure I.2: A and B: Scheme and photography of a channel for a single pellet string reactor, respectively. C: Reactor module filled with catalyst pellets. D: Top view of the reactor module adapted from Hipolito et al. (2010).

In conventional pilot packed bed reactors, the packing is completely random, and the results tend to change between experiments. Another advantage of pellet string reactors is the velocities profiles around the catalyst pellets, which are easier to predict/obtain than in classical packed bed or basket reactors. They are therefore suitable for rapid and exothermic reactions, such as hydrogenation, where the limitations in mass and heat transfers mask the grain kinetics. According to Hipolito et al. (2010), the gas-liquid mass transfer coefficient ($k_L a_{GL}$) is in the same range of the stationary basket reactors, from 0.15 to 0.35 s⁻¹, and is often ten times higher than in conventional pilot packed bed reactors.

Extrapolation: Similar to packed bed reactors, the extrapolation is based on iso *LHSV* values (Hipolito et al., 2010). Although the pilot plant design seems to be easier to manipulate than a classical packed bed reactor, the concept is quite new. Thus the extrapolation is not completely understood (Rolland, 2014).

Stationary catalytic basket reactor

Despite widespread use of the packed bed reactor in industry, their utilization at laboratory scale has often some limitations due to the gas/liquid segregation (Braga et al., 2014; Laranjeira et al., 2009; Yang et al., 2005). Unfortunately, the stationary batch reactors are not as flexible as packed bed reactors and the partial pressure of the gas reactant changes during the reactions, which impedes understanding. Also, the duration of the test is limited to the feedstock put at the beginning of the reaction, which is not compatible with long-term trials. For more information, see Appendix §I.1.

1.2.3 Conclusions

Several types of reactor technologies can thus be applied in catalyst screening tests (Pitault et al., 2004), such as **packed bed reactors**, **stationary basket reactors** or **string pellet**

reactors. The technological choice depends on the complexity of the reaction scheme and reaction rate. **For processes where the reaction rate is slow, the selection of the reactor does not have a significant role when comparing catalysts.** Therefore, a packed bed reactor is typically used. The mass transfer rate has a small impact on the chemical performance, and the obtained data can be easily extrapolated from pilot to industrial-scale (Speccia et al., 1978). **However, for some processes where the reaction occurs in a matter of seconds, the selected process has a significant role in the reaction performance.** For these reactions, the overall reaction rate can greatly depend on the mass transfer rate (Pérez-Ramírez et al., 2000).

In the recent years, IFPEN has developed **single pellet string reactors to better understand and improve catalysts for fast reactions** (Hipolito et al., 2010). This reactor technology helps to reduce the variability of the results, due to the reduction of catalyst random packing. By having the small random packing, it contributes to understand better hydrodynamics in the liquid phase near the grains (Burghardt and Kubaczka, 1996; Guedes De Carvalho et al., 2004). **Despite these improvements, fast reactions in multiphasic systems may still have mass transfer limitations. They may lead to an inaccurate comparison between catalysts** (Ancheyta et al., 2002; Rolland, 2014; Samanta and Richert, 2014). In other words, it is difficult to evaluate the intrinsic kinetics. These limitations will be discussed in the next chapter.

I.3 Multiphasic reactions

Although using single pellet string reactors to study multiphasic gas-liquid-solid reactions, it is still complex to fully understand the reaction systems in pilot plants (Gianetto and Specchia, 1992; Rolland, 2014). When looking at gas-liquid-solid systems, the reaction takes place only if these steps are followed: (i) diffusion of the gas species into the liquid (*G/L mass transfer*), (ii) diffusion of the reactant species through the solid particles boundary layer (*external mass transfer*), (iii) diffusion in the porous solid (*internal mass transfer*), (iv) *adsorption* of the reactants, (v) *reaction* of the adsorbed species, (vi) *desorption* and (vii) *diffusion* of the product. Once the surface of the catalyst desorbs the product, the active catalyst sites can adsorb new molecules of the reactants (see Figure I.3).

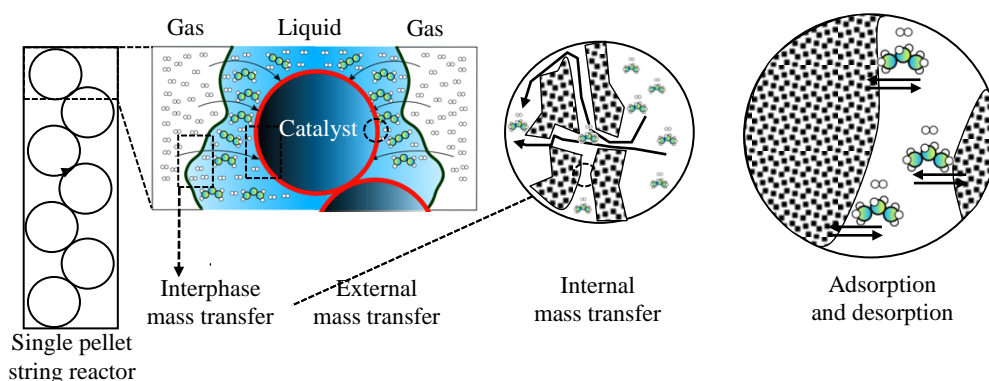


Figure I.3: Scheme of the essential steps in multiphasic reactions. The reactants go from the diluted mixture to the catalyst surface, where they are adsorbed.

In highly reactive systems, the steps that often drive the reaction rate are the interphase and external mass transfer (Devetta et al., 1999). If the external and/or internal mass transfer rate is not superior to the reaction rate (constrained systems), the gas or liquid reactants will not be continuously available on the catalyst surface. Their disponibility limits the whole potential of the catalyst.

In the next subchapters, a brief description of interphase, external and internal mass transfers will be discussed before presenting typical kinetics for the studied reaction (C_3 cut hydrogenation).

1.3.1 Interphase mass transfer

Rigorous model

The interphase mass transfer is a non-equilibrium process where a local concentration gradient drives the molecular motion between two phases. This mass transfer occurs when distinct phases are in contact, and the fluid velocity is significantly decreased near the phase interface (Mangers and Ponter, 1980). At this point, molecular diffusion drives the mass transfer rate. The most generalize equation to estimate mass transfer is the Fick's second law:

$$\frac{\partial(x_i C_{total})}{\partial t} = D_i \frac{\partial^2(x_i C_{total})}{\partial z^2} \quad 0 \leq z \leq \mathcal{L} \quad , \quad 0 \leq t \leq \infty \quad \text{Eq. I.3}$$

where, C_{total} (mol.m^{-3}) is total molar concentration in the liquid phase, x_i is the molar fraction, t (s) is the time, D_i ($\text{m}^2.\text{s}^{-1}$) is the diffusion coefficient of the species i in the liquid phase, z (m) is the position in the liquid phase and \mathcal{L} (m) is the characteristic dimension.

The Fick's second law has an only analytical solution for very simple cases, and for more complex ones the solution is only obtained numerically. Of course, if the variables are coupled with the reaction system model, the solution will become even less straightforward. For more information see Appendix §I.2.

Approximate model

To keep the mass transfer simple, it is advised to relate the molar concentration flow with a mass transfer coefficients (k in m.s^{-1}) (Gut et al., 1986; Larachi et al., 2003; Mena et al., 2011). Thus, knowing that the gas/liquid resistance is often located in the liquid phase, because the gas is normally pure or sparingly soluble, the mass transfer resistance of the gas phase can be neglected. So, the molar concentration flow (\mathcal{N}_i) ($\text{mol.m}^{-3}.\text{s}^{-1}$) can be defined as:

$$\mathcal{N}_i = k_L a_{GL} C_{Total} (x_i^* - x_i) = k_{GL} a_{GL} C_{Total} (f_i/H_i - x_i) \quad \text{Eq. I.4}$$

where k_L (m.s^{-1}) is the mass transfer coefficient between gas and liquid (liquid side), x_i is the molar fraction, x_i^* is the molar fraction far from the zone, a_{GL} (m^{-1}) is the specific area between gas and liquid, C_{Total} (mol.m^{-3}) is the total concentration, f (bar) is the fugacity and H (bar) is the Henry's contant. The subscript i is related to the species.

The solution is much more straightforward than for the previous equation system because it exhibits analytical solutions (Appendix §I.2). The main limitation is that the mass transfer

coefficients have to be experimentally determined. They are dependent on the species properties, the reactor technology and the flow conditions on both sides of the phase interface (Maćkowiak et al., 2011). Furthermore, the overall transfer coefficients should be only employed in the same conditions and reactor design. Therefore, one complicated exercise is to select the correct mass transfer coefficient for each application (at least to model the reactor).

The most widely used equations to determine liquid-film mass transfer coefficients are those of Sherwood and Holloway (1940). In the same line, several authors have conducted studies on the gas-liquid (liquid phase) mass transfer coefficient. The goal is to correlate the mass transfer coefficient with different geometries, using dimensionless numbers (Bragaet al., 2014; Burghardt et al., 1995; Hipolito et al., 2010; Iliuta et al., 1999; Larachi et al., 2003; Losey et al., 2001; Pitault et al., 2005). From their works, a generalized correlation can be written as:

$$Sh_L = c Re_G^\alpha Re_L^\beta Sc_L^\gamma Ga_L^\theta We_L^\phi \chi^\omega \quad \text{Eq. I.5}$$

where α , β , γ , θ , ϕ and ω are exponents and c is a constant. Sh is the Sherwood number (of the liquid phase). The subscripts concern the gas or the liquid phase. The dimensionless groups previously used are presented in Table I.1.

Table I.1: Dimensionless numbers.

Reynolds number	$Re = \frac{\mathcal{L}u\rho}{\mu}$	Ratio of inertial to viscous forces
Schmidt number	$Sc = \frac{\mu}{\rho D}$	Ratio of momentum to mass diffusivities
Sherwood number	$Sh = \frac{k\mathcal{L}}{D}$	Ratio of mass transfer rate to diffusion rate
Galilei number	$Ga = \frac{g\mathcal{L}^3}{u^2}$	Ratio of gravity to viscous forces
Weber number	$We = \frac{\rho u^2 \mathcal{L}}{\sigma}$	Ratio of inertial forces to surface tensions
Lockhart-Martinelli number	$\chi = \frac{u_L}{u_G} \sqrt{\frac{\rho_G}{\rho_L}}$	Ratio of liquid to gas mass

where \mathcal{L} (m) is the characteristic length dimension (diameter or length), D ($\text{m}^2.\text{s}^{-1}$) is the diffusivity, u ($\text{m}.\text{s}^{-1}$) is the average velocity, ρ ($\text{kg}.\text{m}^{-3}$) is the fluid density, μ ($\text{Pa}.\text{s}$) is the dynamic fluid viscosity, σ ($\text{N}.\text{m}^{-1}$) is the surface tension and k ($\text{m}.\text{s}^{-1}$) is the mass transfer coefficient between phases. The subscript L and G are related to liquid and gas.

For any given set of conditions, the $k_L a_{GL}$ coefficient will be different according to the changes on those dimensionless numbers. According to literature, some trends can be observed when changing fluid velocities, fluid properties and particle sizes.

Velocity effect: An increase in the gas or liquid fluid velocity will enhance turbulence near the particle pellets, leading to a more favorable mass transfer coefficient. Moreover, when increasing the gas velocity, the gas holdup and the number of bubbles are higher (Bouaifi et al., 2001; Torab-Mostaedi and Safdari, 2009). This leads to an increase of interfacial area,

which enhances k_L . The dimensionless numbers affected by velocity are Re_L , Re_G , Ga_L and We_L .

Particle dimensions effect: The mass transfer coefficients are affected by the volume fraction of solids and their size distribution (Junmei et al., 2006). By adding a solid, the mass transfer can be enhanced with the increase of eddy generation and bubbles breaking, which leads to a greater interfacial area. Mena et al. (2011) studied the effect of adding particles in gas-liquid systems and the respective physical mechanisms for hydrophobic and hydrophilic particles. The authors concluded that $k_L a_{GL}$ is improved when the solid load is in certain ranges, normally with fine particles with a diameter above 9.6 μm . The dimensionless numbers (more) affected by particle diameter are Re_L , Ga_L and We_L .

Viscosity effect: To study the viscosity effect, the common procedure is to add a more viscous fluid, as glycerol, to the liquid bulk. According to Mangers (1980) and Song (2014), the liquid-film mass transfer coefficients ($k_L a_{GL}$) may increase when adding a certain quantity of a viscous solvent; usually below 20 wt% of the mixture. The increase can be attributed to a higher interfacial area between gas and liquid (Hipolito et al., 2010; Pitault et al., 2004). Above 20 wt% of solvent in the mixture, the $k_L a_{GL}$ is greatly reduced due to the smaller degree of mixing occurring in the liquid phase. For viscous effects, the dimensionless numbers (more) affected are Re_L and Sc_L .

Wettability effect: The wettability may also have an impact on gas-liquid mass transfer. Normally, the effect is small and difficult to dissociate from others. The dimensionless number affected by wettability is We_L .

A brief survey of the main correlations used for pilot plants (discussed in §I.2.2) are presented in Table I.2.

Table I.2: Overview of the liquid-film mass transfer correlations found in the literature for pilot plants. In gray is the correlation we are interested in. The Sh is related to k_L .

Pilot reactor technology	Correlations	References
Low interaction between fluids (trickle flow):		
<u>Industrial reactors</u>	$Sh = 2.8 \times 10^{-4} \left[\chi_G^{0.5} Re_L^{0.8} We_L^{0.2} Sc_L^{0.5} \left(\frac{a_s d_h}{1 - \varepsilon} \right)^{0.25} \right]^{3.4}$	
Particle diameter (cm): $5.4 \times 10^{-2} < d_p < 2.64$	Transition (pulse flow);	
Particle shape: spherical, cylindrical, extrudates, Raschig and Pall rings, Intalox, Berl saddles	$Sh = 0.091 \left[\chi_G^{0.25} Re_L^{0.2} We_L^{0.2} Sc_L^{0.3} \left(\frac{a_s d_h}{1 - \varepsilon} \right)^{0.25} \right]^{3.8}$	Wild G. et al. (1992)
Reactor shape: cylindrical	High interaction (bubble and dispersed bubble flows):	
	$Sh = 0.45 \left[\chi_G^{0.5} Re_L^{0.8} We_L^{0.2} Sc_L^{0.5} \left(\frac{a_s d_h}{1 - \varepsilon} \right)^{0.25} \right]^{1.3}$	
<u>Stationary basket reactors with auto-inducing impeller</u>	$Sh = 3.15 Re_L^{0.95} We_L^{1.55} Sc_L^{0.8}$	Pitault et al. (2004)
<u>Single pellet string reactors</u>		
Particle diameter (cm): $0.2 < d_p < 0.4$	$Sh = 21 Re_L^{0.3} Re_G^{3/25}$	Hipolito (2010)
Particle shape: spherical		
Reactor shape: rectangular		

where a_s (m^{-1}) is the catalyst specific area and d_h (m) is the hydraulic diameter.

1.3.2 External mass transfer

The liquid-solid transfer is also a key step for the global catalyst performance. Since the reaction is carried out in the solid phase, the species in the liquid bulk have to travel through a thin film to reach the catalyst pellet. The rigorous approach typically involves the resolution of the Navier-Stokes equations coupled with Fick's or Maxwell-Stefan's laws at the particle scale with a *CFD* solver (Cornelissen et al., 2007; Eberl et al., 2000; Krishna and Wesselingh, 1997). For the approximate models, the scientific approach is similar to the interphase mass transfer. Thus, the molar concentration flow rate (\mathcal{N}_i) can be written as a function of a mass transfer coefficient:

$$\mathcal{N}_i = k_{LS} a_{LS} (C_{i,L} - C_{i,S}) \quad \text{Eq. I.6}$$

where C (mol.m^{-3}) is the concentration. The subscript L means liquid and S solid.

Approximate model

The correlations proposed in literature to estimate external mass transfer coefficients contain, principally, Sc and Re numbers. The general correlation can be written as:

$$Sh = c Re_L^\alpha Sc^\beta \quad \text{Eq. I.7}$$

where α and β are exponents and c is a constant. Before going into details about the correlations proposed in literature for pilot plants, we will first start observing k_{LS} trends depending on velocity and particle size.

Velocity effect: Several authors described enhancements of k_{LS} with the increase of liquid velocity in single or two-phase flow, due to a higher convection in the liquid film around the particles. It leads to better wetting, greater turbulence and lower fluid retention (Eberl et al., 2000; Hipolito, 2010; Lakota and Levec, 1990a). For two-phases flows, Speccia et al. (1978) observed that when increasing the gas flow-rate at the same liquid flow-rate, the $k_{LS} a_{LS}$ increases firstly markedly and then slowly. The author's justification is that small gas hold-up increases wettability of solid particles and changes the liquid hydrodynamics, so $k_{LS} a_{LS}$ will increase. For high gas hold-up, the authors supposed that there is almost a complete wetting of solid particles (no a_{LS} variations) and the $k_{LS} a_{LS}$ will only increase with turbulences. For velocity effects, the dimensionless number affected is the Re_L .

Particle size effect: Particle size may influence the $k_{LS} a_{LS}$ coefficient. Its contribution is not clear, because both a_{LS} and k_{LS} vary with particles size. Goto et al. (1975) tested different particle size and noticed that k_{LS} was affected. Indeed, several studies have been conducted in the same regime as Goto et al. (1975) with the same measurement method and they arrived at contradicting conclusions (Lakota and Levec, 1990a; Speccia et al., 1978). The dimensionless number affected by different particle size is the Re_L .

An example of correlations used for pilot plants (discussed in §I.2.2) is presented in Table I.3.

Table I.3: Overview of the liquid-solid mass transfer correlations found in the literature. In gray is the correlation that we are interested in. The Sh is related to k_{LS} .

Pilot reactor technology	Correlations	References
<u>Packed reactors</u> with monophasic flow ($0 < Re_L < 200$) Reactor shape: cylindrical	$Sh = 2 + 1.8Re_L^{0.5}Sc^{0.33}$	Ranz and Marshall (1952)
<u>Stationary basket reactors</u> with auto-inducing impeller	No correlation was found, but there are experimental data available in the literature.	Braga (2014)
<u>Single pellet string reactors</u> ($0 < Re_L < 350$) Reactor shape: rectangular	$Sh = 2 + 0.7Re_L^{0.5}Sc^{0.33}$ (monophasic flow) $Sh = 0.24(Re_L/\varepsilon_L)Re_G^{0.5}$ (biphasic flow)	Hipolito (2010)

where ε_L is the liquid hold-up.

1.3.3 Internal mass transfer

Once the reactant species have passed through the liquid film around the solid particle, they diffuse from the external surface into and through the porous surface of the catalyst, in which the reaction occurs. In the catalyst pores, the flow of the species involves convective-diffusive mass transport mechanisms within the porous media (Yiotis et al., 2007), namely:

- flow through liquid films formed at the pore walls;
- vapor diffusion through the dry pores.

To describe the convective-diffusive mass transport inside the catalyst pellets, several authors used Maxwell-Stefan equations for multicomponent mixtures (Datta and Vilekar, 2010; Krishna and Wesselingh, 1997; Liu et al., 2011). For simple cases, like diffusion in infinitely diluted systems, Fick's first law can model the mass transfer (simplified law for mass transfer). Thus, the internal diffusion molar flux φ_{dif} ($\text{mol}\cdot\text{m}^{-2}\cdot\text{s}^{-1}$) is generically defined as:

$$\varphi_{i,dif} = D_{i,e} \frac{\partial x_i C_{total}}{\partial z} \quad \text{Eq. I.8}$$

where x_i is the molar composition, C_{total} ($\text{mol}\cdot\text{m}^{-3}$) is the total concentration, z (m) is the axial position and $D_{i,e}$ ($\text{m}^2\cdot\text{s}^{-1}$) is the effective diffusion coefficient which depends on the porous material. The pore-network in the pellet is not straight or cylindrical, but is rather tortuous, having interconnected paths and variations in pore cross-sectional areas. Consequently, the pore surfaces have different local concentrations. Therefore, the rate of reaction profile will differ with the pellet location: it should be higher in the pore "mouth" than in the pore. To avoid describing individually the diffusion within every tortuous pathway, the effective diffusion coefficient for a species i is given by:

$$\frac{1}{D_{i,e}} = \frac{1}{D_{i,be}} + \frac{1}{D_{i,ke}} \quad \text{Eq. I.9}$$

where $D_{i,be}$ and $D_{i,ke}$ ($\text{m}^2\cdot\text{s}^{-1}$) are the effective diffusion coefficients for bulk and Knudsen diffusions for a species i , respectively.

$D_{i,b}$ and $D_{i,ke}$ can be calculated as (Satterfield, 1970):

$$D_{i,be} = \frac{D_{i,b}\varepsilon}{\tau^*} \quad \text{Eq. I.10}$$

$$D_{i,ke} = \frac{\varepsilon d_{porous}}{\tau^*} \frac{1}{3} \sqrt{\frac{8RT}{\pi M_i}} \quad \text{Eq. I.11}$$

where $D_{i,b}$ ($\text{m}^2.\text{s}^{-1}$) is the bulk diffusion, ε is the catalyst porosity, τ^* is the tortuosity factor of the pores, d_{porous} (m) is the mean porous diameter (catalyst), T (K) is the reaction temperature and M_i ($\text{g}.\text{mol}^{-1}$) is the molecular weight of the species i .

Eq. I.11 is usually applied when a molecule has more probability to hit with the walls than with another molecule (mean free path length \approx mean porous diameter).

The Knudsen diffusion is only meaningful at low pressure (gas state) and small pore diameter. So it is not likely to be required in liquid and high-pressure processes. For dense fluids, Eq. I.10 can be written as (Bertuccio and Vetter, 2001; Smith, 1970):

$$D_{i,be} = \frac{D_{i,b}\varepsilon + \rho_s K'_{i,s} D_{i,s}}{\tau^*} \quad \text{Eq. I.12}$$

where ρ_s ($\text{kg}.\text{m}^{-3}$) is the solid density, $K'_{i,s}$ ($\text{m}^3.\text{kg}^{-1}$) is the linear equilibrium adsorption constant at the solid surface and $D_{i,s}$ ($\text{m}^2.\text{s}^{-1}$) is the surface diffusion.

Intraparticle diffusion models can be used to describe how the diffusion and reaction occur in a catalytic pellet. A typical model is called homogeneous surface diffusion model (HSDM), which represents mass transport in an amorphous and homogeneous sphere combined with reaction.

The HSDM equation is written as:

$$\frac{\partial(rF_{i,dif})}{\partial r} = r^2 R'(C_{i,p}, T) \quad \text{Eq. I.13}$$

where $C_{i,p}$ ($\text{mol}.\text{m}^{-3}$) is the concentration of a species i inside the particle and R' ($\text{mol}.\text{m}^{-2}.\text{s}^{-1}$) is the observed reaction rate per surface area, which is function of $C_{i,p}$ and T (temperature).

1.3.4 Catalyst performance

For a catalyst that is limited by mass transfer, the reaction rate observed is not the real reaction of the catalyst (intrinsic rate), but rather the rate with all the mass limitations (global rate). So, to measure the efficiency of a catalyst and to characterize its full potential, the effectiveness factor is widely used. The effectiveness factor represents the ratio of the pellet production rate to the rate that should be observed in the absence of any diffusional and thermal resistance (Aris, 1957):

$$\eta_i = \frac{\text{global rate}}{\text{intrinsic rate}} = \frac{1}{V_p} \frac{\iiint_{V_p} R(C_{i,p}, T) dV_p}{R(C_{i,s}, T_s)} \quad \text{Eq. I.14}$$

where V_p (m^3) is the particle volume, $C_{i,s}$ ($\text{mol}\cdot\text{m}^{-3}$) is the concentration at the catalyst surface, η is the effectiveness factor and R ($\text{mol}\cdot\text{m}^{-3}\cdot\text{s}^{-1}$) is the reaction rate. The subscript i correspond to the species.

In general, the effectiveness factor varies between 0 and 1 in reactions without competition for the active sites. For systems where the reactants inhibit reaction by adsorbing and blocking active sites, the η can be larger than the unity, *e.g.*, the reaction mechanism follows a Langmuir-Hinshelwood type of expression (later discussed). This expression will be discussed in the next subchapter, which is dedicated to adsorption and desorption. Looking beyond the competition, the intra-particle heat limitations can also overweight the intrinsic rate, leading to $\eta > 1$ (Weisz and Hicks, 1962).

Before detailing the adsorption/desorption process, an overview of the literature survey will be presented for η variations with different pore sizes and catalytic shapes.

Pore size effect: The influence of the pore structure in the catalyst performance has been studied extensively in the past. For instance, Fan et al. (1992) studied the effect of two pore sizes with light and heavy hydrocarbons for the Fischer-Tropsch reaction. The authors observed that for light carbons, from C_1 to C_{10} , there is only a slight difference in conversion between both pores (11.4 and 33.5 nm). However, from C_{10} to C_{20} (bigger molecules), with a pore of 33.5 nm the performance decreases but is still high. When going with a pore of 11.4 nm, the catalyst performance decreases remarkably with the increase of carbon number, reaching zero with C_{20} . Also, Wernert et al. (2010) studied the influence of the molecule size on its transport properties through a porous medium.

Catalyst shape effect: The design of the catalyst shape defines the intensity of mass transport within the pellet. On one hand if a pellet is designed to have a low internal transfer, it will have a higher surface in upper layers than in lower layers (*e.g.* inert support + active metal crust). On the other hand, if a pellet is designed to have a non-uniform pore distribution, it will take advantage of upper and lower layers surface. For an isothermal first-order reaction, Burghardt and Kubaczka (1996) reported that the effectiveness factor can be expressed by a modified Bessel function for any catalyst shape (the effectiveness factor was related to the shape factor). In addition to this initial work, Mariani et al. (2009) developed a one-dimensional model to estimate effectiveness factors in catalyst pellets with different shapes and nonlinear kinetics.

To understand the effect of the catalyst shape on the effectiveness factor, Thiele in 1939 proposed a relation between the activity and the particle size based on a parameter, so-called Thiele modulus ($\phi_{i,gen} = \frac{\text{reaction rate}}{\text{diffusion rate}}$). In Thiele's work, it was observed that if the reaction rate is much greater than the diffusion rate, the diffusion forces are the rate-limiting of the process, and therefore, η is inferior to 0.1. This system is often called diffusion-controlled. In the opposite case, when the diffusion rate is greater than the reaction rate, η should be near 1. This system is often called chemical-controlled pores. The previous observations are presented in Figure I.4.

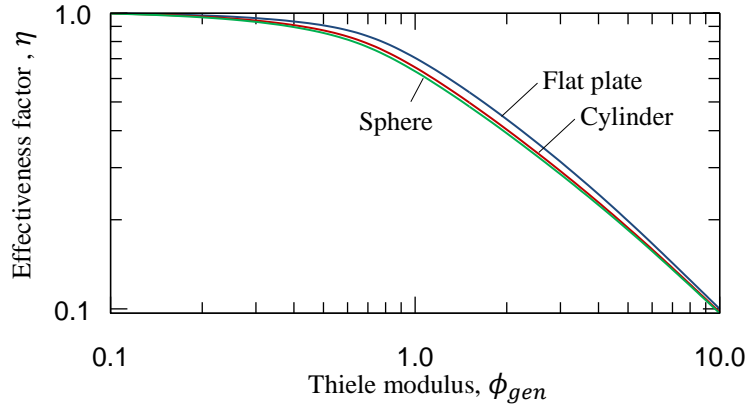


Figure I.4: Effectiveness factor as a function of the Thiele modulus for different pellets shapes in a first order, isothermal, isobaric reaction. Image from (Kashid et al., 2014).

Later, Aris (1957) suggested a generalized relationship based on the Thiele modulus for arbitrary pellet shape. The expression was accomplished by making the ratio of a pellet volume to its external surface area as characteristic diffusion length. Petersen (1965) proposed a further correction to a n^{th} order reaction:

$$\phi_{i,gen} = \frac{\text{reaction rate}}{\text{diffusion rate}} = \frac{V_p}{A_p} \sqrt{\frac{k^*_r C_{i,s}^{(n-1)}}{D_{i,e}}} \sqrt{\frac{n+1}{2}} \quad \text{Eq. I.15}$$

Where ϕ_{gen} is the Thiele modulus, k^*_r ($\text{m}^{3(n-3)} \cdot \text{mol}^{-n+1} \cdot \text{s}^{-1}$) is the reaction kinetics for a n^{th} order reaction.

The Eq. I.15 was defined for a n^{th} order reaction, but in the majority of the reactions the kinetics can not be fully understood by a power law kinetic model. Therefore, it is necessary to go further and study the adsorption/desorption to understand the reaction kinetics.

1.3.5 Adsorption/desorption

One of the key factors to evaluate and characterize the catalyst intrinsic kinetics and reaction mechanism is to understand how the adsorption and desorption happen in the catalyst pellets (Dabrowski, 2001). Depending on the level of details needed, the adsorption can be described by empirical or chemical models. Despite the simplifications in the empirical models, they are still often used in process design. The most used empirical approach to describe adsorption and desorption is the Langmuir model (Brandao et al., 2007), and the simplest application is the adsorption of a single species. In this model, the adsorption equilibrium can be written as:



where A is the considered species, $k_{A,ads}$ (s^{-1}) is the adsorption rate, $k_{A,des}$ (s^{-1}) is the desorption rate, s is the active site and As is the species A adsorbed on the s active site.

The adsorption rate is defined as:

$$\left\{ \begin{array}{l} R_{ads}^A = k_{A,ads}C_A(1 - \theta_{A,cat.}) - k_{A,des}\theta_{A,cat.} \\ \theta_{A,cat.} = \frac{K_A C_A}{1 + K_A C_A} \\ K_A = \frac{k_{A,des}}{k_{A,ads}} \\ \theta_A = \frac{q_A}{q_m} \end{array} \right. \quad \text{Eq. I.17}$$

where K_A is the adsorption equilibrium constant of the isotherm, q_A (mg.g^{-1}) is the amount of solute adsorbed per weight unit of adsorbent. R_{ads} ($\text{mol.m}^{-3}.\text{s}^{-1}$) is the adsorption rate.

In Table I.4, two formulations of the Langmuir isotherm are presented (for competition between two or more species for the same active site and for multi-surface adsorption by a single specie).

Table I.4: Formulations of the Langmuir isotherm.

Competition of two or more species:	Multi-surface adsorption
$A + s \xrightleftharpoons[k_{A,des}]{k_{A,ads}} As \quad ; \quad B + s \xrightleftharpoons[k_{B,des}]{k_{B,ads}} Bs \quad \dots$	$A + s \xrightleftharpoons[k_{A1,des}]{k_{A1,ads}} As \quad ; \quad A + z \xrightleftharpoons[k_{A2,des}]{k_{A2,ads}} Az \quad \dots$
$\left\{ \begin{array}{l} R_{ads}^A = k_{A,ads}C_A \left(1 - \sum_i \theta_i \right) - k_{A,des}\theta_A \\ R_{ads}^B = k_{B,ads}C_B \left(1 - \sum_i \theta_i \right) - k_{B,des}\theta_B \\ \theta_A = \frac{K_A C_A}{1 + \sum_i K_i C_i} \\ \theta_B = \frac{K_B C_B}{1 + \sum_i K_i C_i} \\ \dots \end{array} \right.$	$\left\{ \begin{array}{l} R_{ads}^A = \sum_{Ai} \left[k_{Ai,ads}C_A \left(1 - \sum_{Ai} \theta_{Ai} \right) - k_{Ai,des}\theta_{Ai} \right] \\ \theta_{Ai} = \frac{K_{Ai} C_A}{1 + \sum_i K_i C_i} \end{array} \right.$

The Langmuir adsorption isotherm has significant flaws because it ignores the adsorbents surface roughness and the direct and indirect interactions between adsorbate and adsorbent. It also ignores the possibility to have multilayer coverage of the adsorbent, which means that each active site holds only one molecule of A. For this reason, it is important to briefly summarize the main models for adsorption, which would be a great asset to better understand chemical kinetics.

General adsorption models: There are two types of adsorption models: empirical or chemical. The most common used empirical models are: Freundlich, Elovich, Temkin, Langmuir and Toth. These models usually give excellent results, because the isotherm parameters used are obtained by a curve-fitting procedure. Therefore, they are only valid for the chemical conditions under which the experiment was conducted. The chemical models, on the other hand, provide a molecular description using an equilibrium approach. The most common chemical adsorption models are: constant capacitance (CCM by Stumm et al. 1980), the diffuse layer (DLM by Schindler et al. 1976) and triple layer (TLM by Davis and Leckie 1978).

In the present manuscript, empirical adsorption models will be considered. Table 1 summarizes in Appendix §I.3 the main characteristics of several empirical models previously introduced.

Based on those adsorption models, Hinshelwood the typical reaction rate equation can be given by:

$$R = k^* \prod_i \theta_i \quad \text{Eq. I.18}$$

where R ($\text{mol.m}^{-3}.\text{s}^{-1}$) is the reaction rate and k^* is the kinetic constant.

The Langmuir-Hinshelwood kinetic model (LH) is considered by the scientific community as a “standard” to describe heterogeneous catalytic reactions. Indeed, according to Zamostny and Belohlav (2002) there are new and more detailed mathematical models. However, they are not yet widely used because they can call into question the validity or the adequacy of many empirical rules and established approaches. The Langmuir-Hinshelwood approach can connect ordinary empirical rules (Kumar et al., 2008). For example, when $C_i \gg K_i$ the reaction model will become an order mechanism.

At this point, the subjects related to the steps present in a heterogeneous catalytic reaction were discussed. The next step will be to discuss how they affect results in pilot plants.

I.3.6 Pilot plants uncertainties and limitations

Even using the knowledge available in the literature for mass transfer phenomena (interphase, external and internal), there are still many doubts about the overall reaction. The adsorption/desorption mechanisms and intrinsic kinetics are still not completely known. Thus, it is not always possible to model and to extrapolate the results obtained. To understand why the pilot plants data are hard to interpret, the experimental uncertainties are discussed on Appendix §I.4

I.3.7 Conclusions

The experimental evaluation and understanding of a catalyst is a complex procedure. It involves a significant number of physical and chemical phenomena. To determine the **intrinsic kinetics**, the **mass transfer** and **adsorption/desorption** were discussed. For **mass transfer phenomena**, the state-of-art for interphase and external **mass transfers was detailed** (e.g., main empirical correlations for the pilot plants technologies commonly used). The **concept of effectiveness factor** was also discussed. These concepts will be later used to interpret and model our experimental results.

For **pilot plants with three-phases** systems, it was estimated that the **maximum conversion uncertainty can go up to 19%**, taking into account feedstock, packing and hydrodynamic regime variations.

In the next subchapter, the heterogeneous reaction will be discussed, particularly the hydrogenation of dienes and alkynes in the raw C_3 cut.

I.4 C₃ cut hydrogenation

In pilot scale catalyst screening, the typical mass transfer controlled reactions are hydrogenation, oxidation and steam reforming. For these reactions, there are only a few studies about the intrinsic kinetics and reactions mechanisms, which is not sufficient to uncover and clear up any doubtful or problematic results (Marshall et al., 2005). To have deeper understanding on the influence of mass transfer limitations, the hydrogenation of dienes and alkynes in the raw C₃ cut was selected as a model reaction. This reaction was chosen because there is an economic interest to understand C₃ cut hydrogenation.

Despite this interest, there is only one literature reference that investigates the reaction intrinsic kinetics (Godinez et al., 1996). More recently in 2007, Brandao et al. (2007) discussed that the (impact of the mass transfer on) the intrinsic kinetics is still not totally clear, even if it is a widely used reaction system. Therefore, the state-of-art for this reaction will be presented in this subchapter. It will be divided in (i) overview of C₃ cut hydrogenation, (ii) industrial process description and (iii) state-of-art for laboratory and pilot scale.

I.4.1 Overview of C₃ cut hydrogenation

Propylene is a key chemical in industry [~90 million tonnes produced per year], being used as raw material for propylene oxide, propylene glycol, acrylic acid, acrylonitrile, butyraldehyde and polypropylene (~70% of the global usage of propylene). The primary source of propylene is oil refining (Derrien, 1986), more precisely the steam cracking of naphtha, but it also can be obtained from natural gas processing. In oil refining, the propylene (PR) produced by steam cracking is isolated and subjected to hydrogenation catalysis to remove impurities as dienes and alkynes, so-called methylacetylene (MA) and propadiene (PD) (see Figure I.6). This helps obtaining the required chemical grade of propylene to maximize the productivity in downstream processes, *e.g.*, petrochemical industry.

The hydrogenation reactions of C₃ cut are highly exothermic ($\Delta H \approx -170 \text{ kJ} \cdot \text{mol}^{-1}$ for $\text{MAPD} + \text{H}_2$) and it happens in a matter of minutes, $LHSV \approx 50 \text{ h}^{-1} \rightarrow \tau \approx 1.2 \text{ min}$, using a catalyst based on palladium supported on an alumina carrier (Thomazeau and Boyer, 2004).

The C₃ cut hydrogenation can be performed in a gas-solid or gas-liquid-solid phase. When selecting the approach to be used, there is a commitment between the two reactive media. Although a gas-solid phase reaction exhibits a direct contact between the reactants and the active centers, it has a lower heat transfer than the gas-liquid reactions (Derrien, 1986). It leads to several hot spots in the catalyst level and reducing the selectivity. The C₃ cut liquid phase helps eliminate the reaction heat excess by convection and liquid evaporation. The concept of liquid evaporation suppress the reactor internal cooling module, making the hydrogenation of the C₃ cut more economical (Derrien, 1986).

The reaction is typically done in gas-liquid-solid phase (Figure I.5) to promote good thermal exchange between the catalyst and the reactive medium. The interphase mass transfer restricts the reaction rate and masks the kinetic effect, which prevents fine catalyst screening. According to Gut et al. (1986) the catalyst has limited access to the gas species, due to the low solubility of the hydrogen in the liquid phase.

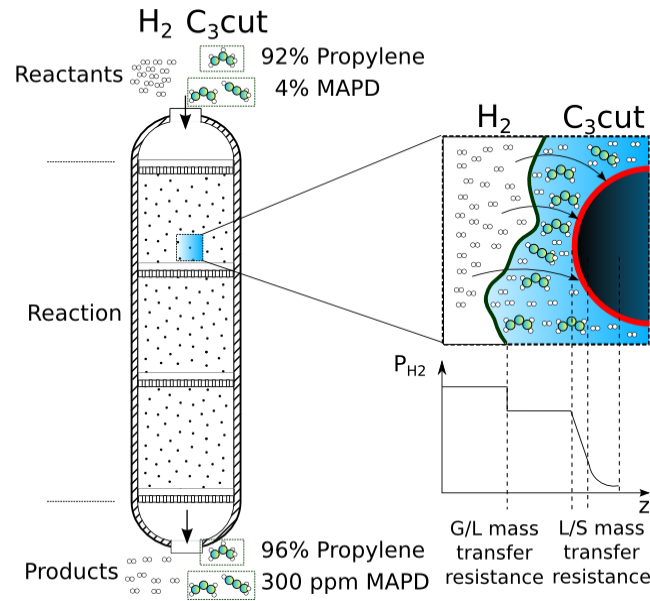


Figure I.5: Scheme of an industrial packed bed reactor for the C_3 cut selective hydrogenation. In the right side of the reactor, the mass transfer limitations that occur during the reaction are detailed (% in mol).

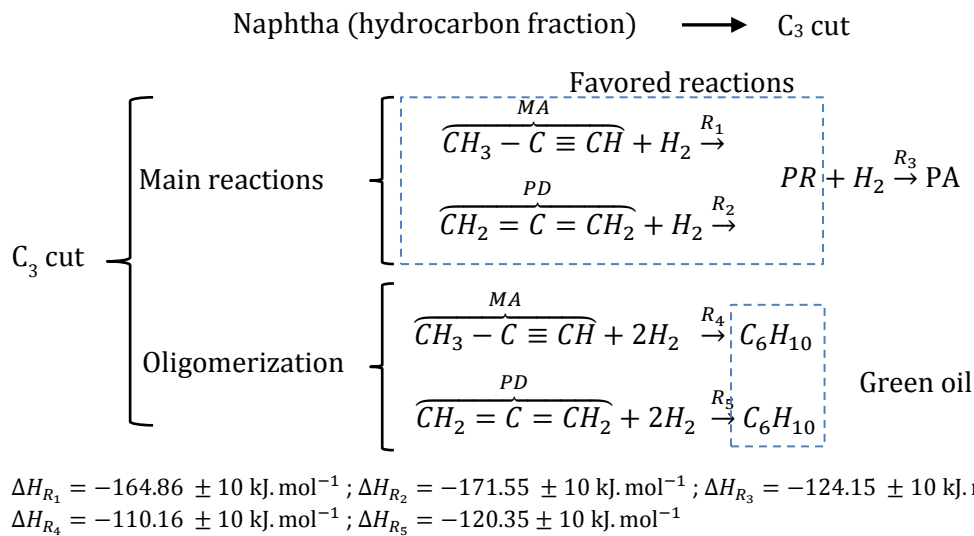


Figure I.6: Main proposed reaction network for the MAPD (MA + PD mixture) selective hydrogenation. PR is propylene and PA is propane. Adapted from Samimi et al. (2015) and Wu et al. (2011). For additional information see Appendix §I.5. ΔH is the enthalpy variation and R is the reaction rate.

About the active metal, the catalyst is often palladium-based, and it should be stable and highly selective towards the hydrogenation of methylacetylene (MA) and propadiene (PD). Fajardo et al. (1996) pointed out an easy way to increase selectivity: reducing the palladium content on the catalyst surface, which implies lower reaction rate, thus less impact of the mass transfer. Furthermore, decreasing temperature, from 300 down to 280 K, and varying the hydrogen partial pressure may favor the catalyst selectivity towards propylene production. Brandao et al. (2007) measure the impact of the hydrogen partial pressure on the reaction rate for a gas-solid close reactor. When increasing the hydrogen pressure from 1 to 10 bar, the

overall reaction rates (initial) had a linear behavior with the catalytic conversion. For the selectivity, it is usually degraded when increasing the hydrogen partial pressure (Hamilton et al., 2002; Kennedy et al., 2004).

1.4.2 Process Description

Feedstock

The primary source of propylene comes from the steam cracking of light naphtha, but also from steam cracking of ethane, propane, butane and gas-oil (Wang and Froment, 2005). In the outlet of naphtha-processing plants, the propylene obtained is still a mixture of hydrocarbons called C₃ cut. It contains about 90 wt% of propylene (PR), 6 wt% propane (PA) and 4 wt% methylacetylene (MA) and propadiene (PD). This composition can vary, depending on the feed cracked as we can see in the Table I.5.

Table I.5: Composition of the C₃ cut for different steam cracking units. (Derrien, 1986)

Type of feed cracked	Ethane	Propane	Butane	Naphtha	Gas-oil
Propylene yield (wt%)	2	16	15	13.2	13.1
Composition of C ₃ cut (wt%)					
MAPD	1.6	3.2	4.2	3.6	-
Propylene	64	94	92	93	-
Propane	34.4	2.8	3.8	3.4	-

Specifications required for propylene after C₃ cut hydrogenation

For the polymerization of propylene, the mixture may contain a maximum of 10 ppm of MAPD, which puts the raw C₃ cut out of the specifications. For MAPD concentration above 30 ppm, the mixture will block the continuous chain polymerization of propylene (Hageman and Van, 2005). Table I.6 summarizes the specifications for polymer and chemical propylene grade in comparison with the raw C₃ cut.

Table I.6: C₃ cuts and commercial propylene grade (Derrien, 1986).

	C ₃ cuts		Propylene grade	
	Steam cracker	Fluid catalytic cracking	Chemical grade	Polymerization grade
Propylene (% wt)	92	65	92-94	95-99.9
MA+PD	4 wt%	0.01wt%	20-30 ppm	10 ppm
C4 (wt ppm)	2000	2000	200	50
C6 (wt ppm)	-	-	1000	10

To reach the product specifications for chemical or polymer industries, two approaches can be chosen: a primary and finishing reactor or a separator (C₃ splitter) [to purify propylene by removing MAPD and propane (Hanika and Staněk, 1986)]. The catalytic reaction process is the most interesting option for years, mainly due to the splitter cost. Nowadays, primary reactor followed by a C₃ cut splitter is a more cost-efficient solution. In the frame of this

thesis, we will focus on the main reactor used in C_3 selective hydrogenation process, which usually contains 3 to 4 mol% of MAPD.

Industrial process

For multiphase hydrogenation, the bubble flow reactor technology is widely used, due to its simple design and good heat exchange, operating in adiabatic conditions (Hwang et al., 2004). The C_3 cut hydrogenation has two-stages: a reactor with separator drum and a finishing reactor. Figure I.7 shows a schematic view and a photo of a MAPD hydrogenation industrial plant.

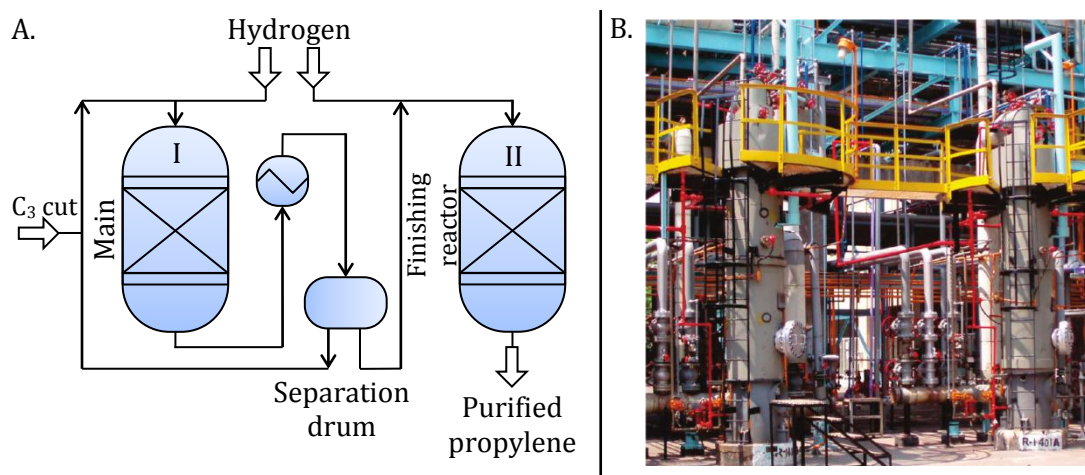


Figure I.7: A) Historical scheme of an industrial MAPD process for hydrorefining of the propylene-rich cut (C_3 cut). B) MAPD hydrogenation unit (Wu et al., 2011).

The C_3 cut feed comes from the top of a depropanizer (C_3 - C_4^+ separation) and is mixed with an intermediate recycling line with hydrogen. It helps decreasing the C_3 activity by reducing temperature and concentration of unsaturated species and increasing the $LHSV$ (Wu et al., 2011). Then the mixture enters in the main reactor [objectives: $x_{MAPD} \sim 2.5$ mol%, $\bar{u}_L \sim 2$ -3 $\text{cm}\cdot\text{s}^{-1}$ [bubble flow] [superficial velocity of the liquid phase]). During the reaction, the heat generated causes a slight temperature rise, controlled by a partial vaporization of the C_3 mixture. The outlet flows from the main reactor (I) (500-3000 ppm of MAPD), then the effluent is sent to the separator drum. There the pressure is maintained by a second H_2 make up, avoiding hydrocarbons losses or the need for gas recycling to the cracked gas compressor.

Typically, the main reactor (I) operates in a bubble regime, assured by co-flow of liquid with higher liquid velocities. Inside the reactor, the pressure range varies between 20 and 30 bar and the temperature from 300 to 330 K, with a molar ratio slightly superior to 1:1 (H_2 /MAPD). The classical operating conditions used in industry are summarized in Table I.7, and the typical weight fraction in the reactor streams are presented in Table I.8.

Table I.7: Example of historical industrial operating conditions. Adapted from Wu et al. (2011).

Operating conditions	
pressure (bar)	2.4-2.6 (gas-solid) 20-30 (gas-liquid-solid)
H ₂ /MAPD (mol/mol)	1.5-2.0
recycle ratio	1-5
T_I^{ref} (K)	300-350
T_{II}^{ref} (K)	300-325
porosity (ε)	0.2-0.5
solid density (ρ_s)	1100-1200 kg.m ⁻³
bulk density (ρ_b)	650-1100 kg.m ⁻³

Table I.8: Typical weight fractions in an industrial plant for MAPD hydrogenation.

wt %	Process Feed (in of I)	Intermediate product (out of I)	End-product (out of II)
methylacetylene (MA)	2.2	0.05	1 ppm
propadiene (PD)	1.8	0.25	10 ppm
propylene (PR)	92.0	95.30	94.40
propane (PA)	4.0	4.10	5.50
n-butyl acetylene	0.0	0.30	0.30

1.4.3 Catalyst characteristics

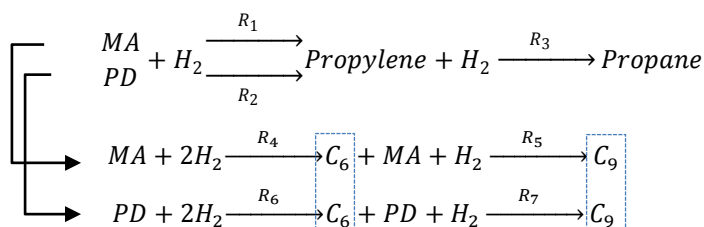
To design a catalyst for diffusion-controlled reactions, the activity, the support structure and the influence of pellet size have to be studied (Vayenas and Pavlou, 1987). Common catalysts for selective hydrogenation consist in metallic palladium (metal sites) deposited with an eggshell distribution into the porous material (acidic sites), generally alumina. The metal sites catalyze the hydrogenation and the alumina often catalyzes the oligomerization, producing the green oil (Wang and Froment, 2005).

The catalytic activity is known to be in strong relation with the thickness of the palladium crust (Cabiac et al., 2013). According to Thomazeau et al. (2004), small pellets are often used to limit the internal diffusion, often having an equivalent diameter between 2 and 5 mm (processed by a granulator). For smaller diameters, there are problems with the catalytic shaping process and with the pressure drop inside the reactor.

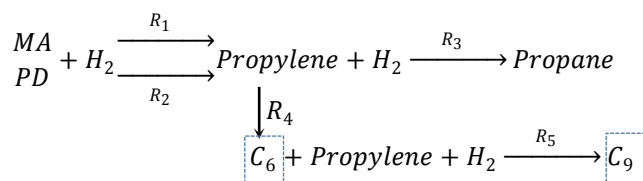
1.4.4 Kinetics

Figure I.6 shows a simplified reaction scheme from the literature, for C₃ cut hydrogenation (Samimi et al., 2015). Wang and Froment (2005) proposed three possible reaction schemes, which differ only in the mechanism of oligomerization (Figure I.8).

Scheme 1



Scheme 2



Scheme 3

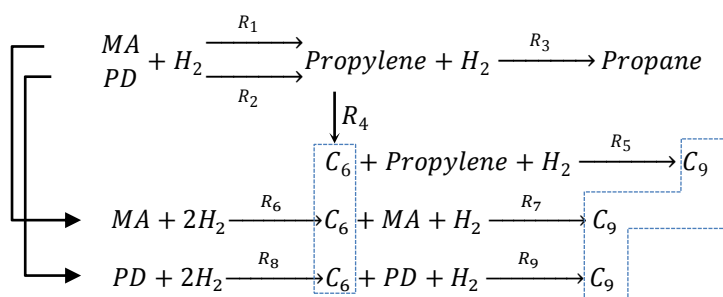


Figure I.8: Reaction schemes for the formation of oligomers (C₆ and C₉). Adapted from Wang and Froment (2005). *R* is the reaction rate.

Despite the information about different possible reaction schemes, the oligomerization reaction is still not fully understood. The most commonly proposed scheme is Scheme 1 because it provides better interpretation and parameters estimation (Wang and Froment, 2005), *i.e.*, it fits better the experimental data.

After identifying the main reaction scheme, the reaction mechanisms will be discussed.

Reactions Mechanisms

Reactions mechanisms involve the adsorption and breakdown of the molecules that are connected to the metal or the acidic sites. In hydrogenation, the presence of a metal catalyst often breaks the H-H bond in H₂ cleaves. After breaking, the hydrogen atom is transferred to unsaturated carbon atoms available in alkenes or alkynes species. These two species are present in consecutive parallel reactions, MAPD and propylene hydrogenation (previously shown in Figure I.8). They will compete for the hydrogen adsorbed on a finite number of active sites. This competition may suggest that kinetics models are only dependent on the surface reaction, which may not be true. Indeed, there are many systems where the kinetic is strongly affected by the rate of the adsorption phenomena.

Nowadays, there is no consensus on the key reaction mechanism and, depending on the author, the rate models are sometimes conflicting, having different assessments for the rate limiting step and adsorption mechanism.

In 1996, Fajardo et al. studied the hydrogenation of MAPD and propylene in the gas phase. The authors compared reaction rate equations based on LH-HW (Langmuir-Hinshelwood-Hougen-Watson) and equations based on power-law models for the reaction Scheme 1 (Figure I.8). They conclude that the power-laws were favored to LH-HW for the C₃ cut hydrogenation because they offered the best data fit. Despite the proposed power-law equation, the optimization results are physically meaningless, since the model did not take into account the intrinsic kinetics and the different reaction schemes.

Wang and Froment (2005) investigated three different schemes (Figure I.8) for a gas-phase reaction. They proposed similar LH-HW model for each scheme, and they concluded that Scheme 1 had the best data fitting results.

In 2007, Brandao *et al.* studied kinetics in gas-phase for palladium nanoclusters in an isothermal batch reactor. In their study, they were only interested in the MAPD hydrogenation step; so only the initial reaction rates were analyzed with LH-HW. They found that the experimental data agrees with LH-HW mechanism without competition between propylene and hydrogen for the catalyst surface, and the hydrogen addition to surface reactions was the limiting step.

More recently, in 2015, Samimi et al. proposed an approach to estimate kinetic parameters also based on LH-HW model for Scheme 1. Their approach aims at modeling each step in an industrial gas-liquid-solid hydrogenation, going from the gas phase to the solid phase. They took into account the interphase mass transfer, the external mass transfer and the catalyst effectiveness factor.

The key factor is to identify the optimal mechanism from all the suggestions. To identify the best approach, the strategy was to consider different kinetics mechanism for carrying out MAPD and propylene hydrogenation individually. At the end, both mechanisms will be combined to have the global mechanism. To clarify the different mechanisms for MAPD and propylene hydrogenation, a brief overview of the main approaches is presented in Table I.9 and Table I.10 based on LH-HW models for gas-solid. Since the diffusion coefficients in gases are relatively high, and it is in single-phase condition, it is expected to have enough hydrogen at the catalyst surface, therefore, no mass transfer limitations to impede the reaction mechanism evaluation.

Table I.9: LH-HW models for MAPD hydrogenation. Since the fit quality varies with each publication, a • system was applied in this table. The • is related to each author best fitting (e.g. ●●●● - best fitting). To know respective residual values, see references.

Mechanistic scheme	N°	Controlling step	Rate expression	Reference	Fit quality
A: $H_2 + Z \rightleftharpoons H_2Z$ B: $C_3H_4 + H_2Z \rightleftharpoons C_3H_6Z$ C: $C_3H_6Z \rightleftharpoons C_3H_6 + Z$	A1	H ₂ adsorption (A)	$R_{MAPD} = \frac{k^*_A P_H}{1 + K_C P_{PR}}$	(Fajardo et al. 1996)	●●
	A2	Surface reaction (B)	$R_{MAPD} = \frac{k^*_B K_B [P_{MAPD} P_H - P_{PR}/K]}{1 + K_A P_H + K_C P_{PR}}$	(Fajardo et al. 1996)	●
	A3	Propylene desorption (C)	$R_{MAPD} = \frac{k^*_C K_C P_{MAPD} P_H}{1 + K_A P_H + K_C P_{PR}}$	(Fajardo et al. 1996)	●●
A: $H_2 + 2Z \rightleftharpoons 2HZ$ B: $C_3H_4 + 2HZ \rightleftharpoons C_3H_6 + 2Z$	A4	H ₂ adsorption (A)	$R_{MAPD} = k^*_A K_A P_H$	(Fajardo et al. 1996)	●●●●
	A5	Surface reaction (B)	$R_{MAPD} = \frac{k^*_B K_A [P_{MAPD} P_H - P_{PR}/K]}{(1 + K_A P_H)^2}$	(Fajardo et al. 1996)	●
A: $H_2 + Z \rightleftharpoons H_2Z$ B: $C_3H_4 + Z \rightleftharpoons C_3H_4Z$ C: $C_3H_4Z + H_2Z \rightleftharpoons C_3H_6Z + Z$ D: $C_3H_6Z \rightleftharpoons C_3H_6 + Z$	A6	MAPD adsorption (B)	$R_{MAPD} = \frac{k^*_B P_{MAPD}}{1 + K_A P_H + K_C P_{PR}}$	(Fajardo et al. 1996)	●●●
	A7	Surface reaction (C)	$R_{MAPD} = \frac{k^*_C K_A K_B P_H P_{MAPD}}{1 + K_A P_H + K_B P_{MAPD} + K_C P_{PR}}$	(Fajardo et al. 1996)	●●●
A: $H_2 + 2Z \rightleftharpoons 2HZ$ B: $C_3H_4 + Z \rightleftharpoons C_3H_4Z$ C: $C_3H_4Z + HZ \rightarrow C_3H_5Z + Z$ D: $C_3H_5Z + HZ \rightarrow C_3H_6Z + Z$ E: $C_3H_5Z \rightleftharpoons C_3H_6 + Z$	A8	Surface reaction (C)	$R_{MAPD} = \frac{k^*_C K_A K_B \sqrt{P_H} P_{MAPD}}{(1 + K_B P_{MAPD} + \sqrt{K_A P_H})^2}$	(Brandao et al. 2007)	●●●
	A9	Surface reaction (D)	$R_{MAPD} = \frac{k^*_D K_A K_B P_H P_{MAPD}}{(1 + K_B P_{MAPD} + \sqrt{K_A P_H})^2}$	(Brandao et al. 2007)	●●●
A: $H_2 + 2Z \rightleftharpoons 2HZ$ B: $C_3H_4 + Z \rightleftharpoons C_3H_4Z$ C: $C_3H_4Z + 2HZ \rightarrow C_3H_6Z + 2Z$ E: $C_3H_5Z \rightleftharpoons C_3H_6 + Z$	A10	H ₂ adsorption (A)	$R_{MAPD} = \frac{k^*_A K_A P_H P_{MAPD}}{(1 + K_B P_{MAPD} + K_A P_H)^2}$	(Brandao et al. 2007)	●●●
	A11	Surface reaction (C)	$R_{MAPD} = \frac{k^*_C K_A P_H K_B P_{MAPD}}{(1 + K_B P_{MAPD} + \sqrt{K_A P_H})^3}$	(Brandao et al. 2007)	●●●●
A: $H_2 + 2Z \rightleftharpoons 2HZ$ B: $C_3H_4 + S \rightleftharpoons C_3H_4S$ C: $C_3H_4S + 2HZ \rightarrow C_3H_6S + 2Z$ E: $C_3H_6S \rightleftharpoons C_3H_6 + S$	A12	Surface reaction (C)	$R_{MAPD} = \frac{k^*_C K_A K_B P_H P_{MAPD}}{(1 + K_B P_{MAPD})(1 + \sqrt{K_A P_H})^2}$	(Brandao et al. 2007)	●●
	A13	H ₂ adsorption (A)	$R_{MAPD} = \frac{k^*_A K_A P_H}{(1 + K_B P_{MAPD})^2}$	(Brandao et al. 2007)	●●
A: $H_2 + 2Z \rightleftharpoons 2HZ$ B: $C_3H_4 + S \rightleftharpoons C_3H_4S$ C: $C_3H_4S + HZ \rightarrow C_3H_5S + Z$ D: $C_3H_5S + HZ \rightarrow C_3H_6S + Z$ E: $C_3H_6S \rightleftharpoons C_3H_6 + S$	A14	Surface reaction (C)	$R_{MAPD} = \frac{k^*_C K_A K_B \sqrt{P_H} P_{MAPD}}{(1 + K_B P_{MAPD})(1 + \sqrt{K_A P_H})^2}$	(Brandao et al. 2007)	●●●●●

According to Table I.9, there are three mechanisms that can provide proper data fitting: A4, A11 and A14. The mechanism A4 is based on the hydrogen dissociative adsorption and reaction with MAPD without being adsorbed. The limitation step is the hydrogen adsorption. The mechanism A11 is also based on the hydrogen dissociative adsorption and reaction with the MAPD adsorbed, being limited by the surface reaction. In mechanism A14, two different

active sites are necessary, one for the hydrogen and another for the MAPD adsorption. In the authors approach, the limitation step is the first hydrogen addition to the surface reaction.

Table I.10: LH-HW models for propylene hydrogenation. Since the fit quality varies with each publication, a • system was applied in this table. The • is related to each best fitting (e.g. ●●●● - best fit). To know respective residual values, see references.

Mechanistic scheme	N°	Controlling step	Rate expression	Reference	Fit quality
A: $H_2 + Z \rightleftharpoons H_2Z$ B: $C_3H_6 + H_2Z \rightleftharpoons C_3H_8Z$ C: $C_3H_8Z \rightleftharpoons C_3H_8 + Z$	B1	H ₂ adsorption (A)	$R_{PR} = \frac{k^*_A[P_H - P_{PA}/(KP_{PR})]}{1 + K_B P_{PR}/(KP_{PA}) + K_C P_{PA}}$	(Fajardo et al. 1996)	•
	B2	Surface reaction (B)	$R_{PR} = \frac{k^*_B K_B [P_{PR} P_H - P_{PA}/K]}{1 + K_A P_H + K_C P_{PA}}$	(Fajardo et al. 1996)	••
A: $H_2 + 2Z \rightleftharpoons 2HZ$ B: $C_3H_6 + 2HZ \rightleftharpoons C_3H_8 + 2Z$	B3	H ₂ adsorption (A)	$R_{PR} = k^*_A K_A P_H$	(Fajardo et al. 1996)	••••
	B4	Surface reaction (B)	$R_{PR} = \frac{k^*_B K_A P_{PR} P_H}{(1 + \sqrt{K_A P_H})^2}$	(Fajardo et al. 1996)	••••
A: $H_2 + Z \rightleftharpoons H_2Z$ B: $C_3H_6 + Z \rightleftharpoons C_3H_6Z$ C: $C_3H_6Z + H_2Z \rightleftharpoons C_3H_8Z + Z$ D: $C_3H_8Z \rightleftharpoons C_3H_8 + Z$	B5	Surface reaction (C)	$R_{PR} = \frac{k^*_C K_A K_B (P_H P_{PR} - P_{PA}/K)}{1 + K_A P_H + K_B P_{PR} + K_D P_{PA}}$	(Fajardo et al. 1996)	••••
A: $H_2 + 2Z \rightleftharpoons 2HZ$ B: $C_3H_6 + Z \rightleftharpoons C_3H_6Z$ C: $C_3H_6Z + 2HZ \rightarrow C_3H_8Z + 2Z$ D: $C_3H_8Z \rightarrow C_3H_8 + Z$	B6	H ₂ adsorption (A)	$R_{PR} = \frac{k^*_A P_H}{(1 + K_B P_{PR} + K_D P_{PA})^2}$	(Fajardo et al. 1996)	•••••
	B7	Surface reaction (C)	$R_{PR} = \frac{k^*_C K_A K_B P_{PR}}{(1 + \sqrt{K_A P_H} + K_B P_{PR} + K_D P_{PA})^3}$	(Fajardo et al. 1996)	•••••

According to Table I.10, there are two mechanisms with good data fitting: B6 and B7. Both mechanisms are based on the hydrogen dissociative adsorption and reaction with the MAPD adsorbed. For the mechanisms B6 and B7, the rate control stages are the hydrogen adsorption and the surface reaction, respectively.

From the previous tables, it is now possible to combine both hydrogenation mechanisms. Firstly, we know that the MAPD reaction is faster than the propylene one. Therefore, we may say that if the hydrogen adsorption does not limit the MAPD species, the propylene reaction should not be limited either. The possibilities are: A4 + B6 or A11 + B7 or A14 + B7.

A4 + B6 mechanisms are not entirely compatible, because the propylene (product from MAPD reaction) is not adsorbed on the catalyst surface for A4 mechanism (i.e. the MAPD and propylene are not adsorbed during the reaction), but it should be adsorbed for B6. Therefore, this combination was discarded.

A14 + B7 proposition was also discarded, because the A14 mechanism suggested that the propylene was adsorbed in a different active site than the hydrogen, and the B7 mechanism suggested the contrary (i.e. propylene adsorption in the same site as hydrogen). Finally, the last combination A11 + B7 is more reasonable, because both reactions have similar mechanisms and the rate-controlled step is the same. The final mechanism expression for

MAPD and propyne hydrogenation is presented in Table I.11. The reaction scheme for the rate models will be based on (previously presented) Scheme 1:

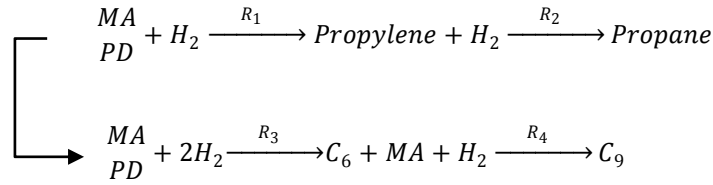


Figure I.9: Suggested scheme for the reaction (hydrogenation and oligomerization).

The most interesting reaction mechanism and equations for MAPD and propylene are the following ones (which will be used in this thesis):

Table I.11: More likely mechanism for MAPD and propylene hydrogenation (in the gas state).

Mechanistic scheme	
A: $H_2 + 2Z \rightleftharpoons 2HZ$	
B: $C_3H_4 + Z \rightleftharpoons C_3H_4Z$	
C: $C_3H_4Z + 2HZ \rightarrow C_3H_6Z + 2Z$	
E: $C_3H_5Z \rightleftharpoons C_3H_6 + Z$	
F: $C_3H_6 + Z \rightleftharpoons C_3H_6Z$	
G: $C_3H_6Z + 2HZ \rightarrow C_3H_8Z + 2Z$	
H: $C_3H_8Z \rightarrow C_3H_8 + Z$	
Reaction rate	
$R_1 = \frac{k^*_C K_A P_H K_B P_{MAPD}}{(1 + \sqrt{K_A P_H} + K_B P_{MAPD} + K_F P_{PR} + K_H P_{PA})^3}$	Eq. I.19
$R_2 = \frac{k^*_G K_A K_F P_H P_{PR}}{(1 + \sqrt{K_A P_H} + K_B P_{MAPD} + K_F P_{PR} + K_H P_{PA})^3}$	Eq. I.20

where R_1 and R_2 are the reaction rates for the propylene and propane formation, respectively.

In fact, several authors agree with the previous LH-HW reaction rate model (Brandao et al., 2007; Wang and Froment, 2005; Wu et al., 2011). An application of this reaction model is in Wu et al. (2011) work, where the authors managed to apply the kinetic model to on-site plant data. Regarding the oligomerization reactions, the reaction rate equations are similar to MAPD and propylene rate models (Wu et al. 2011):

$$R_3 = \frac{k^*_{MAPD-C_6} P_H^2 P_{MAPD}^2}{(1 + \sqrt{K_A P_H} + K_B P_{MAPD} + K_{C_6} P_{C_6} + K_{C_9} P_{C_9})^3} \quad \text{Eq. I.21}$$

$$R_4 = \frac{k^*_{MAPD-9} P_H P_{MAPD} P_{C_6}}{(1 + \sqrt{K_A P_H} + K_B P_{MAPD} + K_{C_6} P_{C_6} + K_{C_9} P_{C_9})^3} \quad \text{Eq. I.22}$$

where R_3 and R_4 are the reaction rate for the C_6 and C_9 formation, respectively.

The previous reaction rates (R_1 , R_2 , R_3 and R_4) were obtained in gas medium, which may be different from the kinetics obtained in gas/liquid medium, because the reactant species will have higher concentration and the mean free path between species is lower. The molecules may shock more often between themselves, which can change the kinetics mechanism.

Catalyst deactivation

Although studying the overall reaction rate is essential to understand catalyst screening, knowing the deactivation of the metal sites is also crucial.

The catalyst deactivation is a complex phenomenon, and it can be defined as the loss of catalytic activity and/or selectivity over time. For palladium and platinum catalysts, the deactivation is caused by coke formation or metal site poisoning by an external agent. Wang and Froment (2005) investigated the deactivation of a Pd/alumina catalyst for MAPD gas-phase hydrogenation. The experiments were done in a packed bed reactor at 350K. The deactivation was evaluated for seven runs, and each run took from 10 to 20 hours. For the catalyst tested, the conversion of MAPD decreased by a 10-20% for each run covered. The authors were able to analyze oligomers until 12 carbons with a GC-FID. From the results observed, the deactivation was attributed to the heavy oligomers formed, exceeding 12 carbons. Quoting the authors, “these higher oligomers would not elute from the reactor”, and so they were irreversibly adsorbed on the catalyst sites, acting as a deactivating agent.

I.4.5 Hydrogenation at pilot-scale state

As mentioned before, §I.3.6, changes in hydrodynamic regimes, random packing and so on, can easily affect the pilot scale uncertainty for diffusion-controlled reactions. The catalyst performance is influenced by several factors as: type of catalyst, mass of catalyst, feed concentration, substrate purity, solvent, temperature and pressure. Therefore, the selection and extrapolation of the multiple parameters is a meticulous step. In most of the literature studies for MAPD hydrogenation, the reaction is studied in gas-solid medium, despite the extensive use of gas-liquid-solid medium at the industrial level. The objective is to avoid interphase mass transfer limitations (Brandao et al., 2007; Marshall et al., 2005; Wu and Li, 2010). Consequently it is easier to access to kinetics closer to intrinsic kinetics. However, making the hydrogenation in the gas phase is very different from the liquid phase, due to different chemisorption, effective diffusion and kinetic behavior. According to Marshall et al. (2005), the reaction exhibits a kinetic discontinuity for a catalyst with 1 wt % Pd/C. Depending on the reactant concentration, sudden changes in conversion and selectivity are expected. Some typical operating conditions are presented in Table I.12.

Table I.12: Pilot plant operating conditions. Adapted from Fajardo et al. (1996).

Operating conditions	
temperature (K)	294-350
pressure (bar)	1.0-2.6 (gas-solid) 20-30 (gas-liquid-solid)
H ₂ /MAPD (mol/mol)	0.25-4.0
porosity (ϵ)	0.2-0.6
catalyst weight (g)	0.5-1
particle size (mm)	0.05-4
LHSV	1000-3000 h ⁻¹ (gas-solid) 10-150 h ⁻¹ (gas-liquid-solid)

1.4.6 Conclusion

The operating conditions, process description and kinetics for C₃ cut hydrogenation were reviewed with a particular emphasis on industrial and pilot scales. This reaction is **controlled by mass transfer** [external and internal (in liquid-phase)] and can be easily **influenced by** factors such as **variations of the hydrodynamic regime and catalyst packing**, which hinders catalytic activity.

To better understand the MAPD hydrogenation, the **reaction scheme and mechanisms were investigated** from kinetic studies **in the gas-phase medium**. Indeed, gas-phase is much easier to perform kinetic studies, due to **high diffusion coefficients** and **single-phase conditions**. **However**, according to the literature there are **local hot spots** on the **catalyst surface** and **low concentration** of the reactants, *i.e.*, only small molecules can be transferred to a gas phase at reasonable pressures and temperatures. **These characteristics are not ideal for the pilot scale studies** and are far from gas-liquid-phase industrial conditions. Therefore, the excellent reaction properties of the gas-phase (high diffusion) can only be used for small, volatile molecules.

At this point, **several reactions mechanisms were reviewed, and the best one was detailed**, being the hydrogen dissociation and reaction with reactants adsorbed in the same active center.

As we see, performing catalyst screening in pilot scale in gas-liquid-phase is very complex, due to the uncertainties of the hydrodynamic regime for triphasic systems. Furthermore, the fluid mixture reacts almost immediately in contact with the organometallic active centers (Yermakov and Arzamaskova, 1986). So, the next subchapter will present development paths to reduce and to study reaction resistances. The high-pressure technology will be discussed in the next subchapter, and the supercritical technology will be discussed in the last subchapter.

I.5 High-pressure reaction conditions

As detailed in the previous subchapter, analyzing, interpreting and modeling catalytic data can be challenging. The catalyst screening for C₃ hydrogenations requires careful selection of multiple parameters beyond the catalysts composition (Godinez et al., 1996), such as temperature, pressure, solvent and substrate-to-catalyst ratio (LHSV or WHSV). It is well known that the catalytic conversion, the selectivity and the deactivation will be influenced by the operating conditions (Hodnett and Delmon, 1986; Marshall et al., 2005). The modeling of gas-liquid hydrogenation is not straightforward and requires different assumptions about the mass transfer. Therefore, a shift from conventional to unconventional reaction medium may be a feasible solution to simplify the model (S. Pereda et al., 2002; Rovetto et al., 2003) (high-pressure means > 50 bar).

Today, new hydrogenation technologies are being developed to resolve key issues associated with mass transfer (Girgis and Gates, 1991; Grunwaldt et al., 2003a; Martins and Aranda, 2000; Thomson et al., 2001). The future technologies may be based on the reduction of interphases, external and internal mass transfers by increasing pressure and/or adding a co-solvent (Muthanna H Al-Dahhan and Duduković, 1995; Girgis and Gates, 1991; Grunwaldt et al., 2003b).

After discussing in §I.3 the influence of the interphase, external and internal mass transfers in the catalytic performance, in this subchapter, it will be covered the impact of the pressure on kinetics and mass transfer. The first part of the subchapter is devoted to the effect of pressure in reaction kinetics. The second part is related to the effect of pressure on mass transfer. In this section, the diffusion in dense gases will be discussed.

I.5.1 Pressure effect

Pressure variations may affect the reaction rate (Thomson et al., 2001). Therefore, the question is: how pressure affects the reaction rate in C₃ cut hydrogenation?

So, if we consider the reaction rate for $MAPD + H_2 \xrightarrow{R_1} Propylene (PR)$.

$$R_1 = \frac{k^*_C K_A P_H K_B P_{MAPD}}{(1 + \sqrt{K_A P_H + K_B P_{MAPD} + K_F P_{PR} + K_H P_{PA}})^3} \quad \text{§Eq. I.19}$$

On the one hand, the pressure will act on the amount of species available in the catalytic sites, *e.g.*, P_H , P_{MAPD} , P_{PR} and P_{PA} (bar). On the other hand, the pressure will act on the rate constants (k^*_C , ...) as well as on the adsorption equilibrium (K_A , K_B , K_F , K_H , ...), increasing or decreasing the overall reaction rate. The pressure effect is more significant in gas-solid than in gas-liquid-solid hydrogenation, because the liquid phase has lower compressibility (Gut et al., 1986; S. Pereda et al., 2002). In other words, pressure variations in gas-phase lead to more important variations in reactant concentrations on catalytic surface than in the liquid-phase.

According to Girgis and Gates (1991), pressure effects are analogous to temperature effects (ΔP can be interpreted as an exponential equation). In applications at high-pressure, the reaction yield and selectivity can be improved.

The overall reaction rate does not depend only on the kinetics and adsorption parameters, but also on the rate of mass transfers. For example, for a generic reaction rate R_i , a function can be written as:

$$R_i = f(k_i^*, P_i, D_i, k_L a_{GL}, k_{LS} a_{LS}, \eta_i) \quad \text{Eq. I.23}$$

where k_i^* (the units depend on the kinetic model) is the kinetics constant, P_i (bar) is the partial pressure, D_i ($\text{m}^2 \cdot \text{s}^{-1}$) is the diffusion coefficient, η_i the effectiveness factor and $k_L a_{GL}$ and $k_{LS} a_{LS}$ ($\text{m}^3 \cdot \text{s}^{-1}$), the gas-liquid and liquid-solid mass transfer coefficients, respectively.

1.5.2 Pressure effect on kinetics

As previously seen in §I.4.4, much emphasis is placed on understanding reaction mechanisms. Normally, the activation energy is estimated for each reaction as a way to investigate the chemical system at the molecular level. The goal is to combine activation energy (Avrami, 1939; Drljaca et al., 1998; Eldik et al., 1989), reaction rates and molar volume data variations at several positions inside the reactor (the reaction coordinate is normally z-axis). This information may contribute to elucidate the reaction mechanism, thus adding comprehension to the reaction kinetics and assists the catalyst screening (Avrami, 1939).

Similar to temperature-dependence studies, which tell us about the energies involved in the system, pressure-dependence studies reveal valuable information about the process, particularly about the transitory species ($X^\#$). For more information see Appendix §I.6.

1.5.3 Pressure effect on mass transfer

In heterogeneous reactions governed by diffusion, the pressure variations influence not only the kinetic parameters but also the mass transport, such as interphase equilibrium and diffusion coefficients. In gas-phase, the mass transport is extremely sensitive to pressure changes and the diffusion coefficients have to be carefully regarded (Bertucco and Vetter, 2001; Girgis and Gates, 1991). In liquid-phase, the mass transport is relatively insensitive to pressure variations, therefore interphase equilibrium and diffusion coefficients are usually disregarded (Rovetto et al., 2003). For the C_3 cut hydrogenation, we are concerned about the gas-liquid-solid hydrogenation (gas: hydrogen; liquid: propylene). Therefore, diffusion coefficients and interphase equilibria have to be individually regarded.

Diffusion coefficients

In heterogeneous catalysis, diffusion coefficients are required to estimate transfer rates between fluid phases and exterior/interior of catalytic pellets. In more details, diffusion coefficients are present in the Sc (Schmidt) numbers and in the D_e , from which $k_L a_{GL}$, $k_{LS} a_{LS}$ and η are estimated. Although there are a vast number of publications about diffusion, in unconventional high-pressure applications the data are still scarce or non-existent. To complement literature, correlations are necessary to estimate self and binary or multiphase diffusion coefficients where data are scarce. This is the case for diffusion of *MAPD* in propylene at high pressure. There are several approaches for correlating diffusion coefficients, depending on the theory adopted to describe molecule interaction and collision. The

correlations are based on hydrodynamic theory, kinetic theory, absolute-rate theory of Eyring, free volume theory and idealized fluids (Liu et al., 1997a).

The approaches based on hydrodynamic theory (Stokes-Einstein equation) require value of viscosity (μ) at the operating pressure and temperature. They are defined as:

$$D_{AB}^{HS} = \frac{\kappa_B T}{6\pi\mu r_B} \quad \text{Eq. I.24}$$

where κ_B (J.K^{-1}) is the Boltzmann's constant, μ (Pa.s) is the average viscosity of the fluid, r_B (m) is the effective radius of one solute molecule, the superscript stands for the theory applied (hard spheres), and A is the solvent and B is the solute.

Stokes-Einstein was derived assuming circulation of a liquid solvent around large hard spherical molecule (HS) of solute ($r_B \gg r_A$) under infinitely dilution. Stokes-Einstein modified equations, in which Wilke and Chang (1955) is grouped, have been extended to high-pressure conditions and even to supercritical domain. Nonetheless, these approaches can be only applied to fluid with densities superior than critical density, otherwise the diffusion coefficients may be overestimated (Liong et al., 1991).

The approaches based on kinetic theory with contact correlation (Enskog-Thorne equation with Chapman and Cowling formalism):

$$\left\{ \begin{array}{l} (n^* D_{AB}^E)_{Ref} = \frac{3}{8\sigma_{AB}^{*2}} \sqrt{\frac{\kappa_B T}{2\pi m_{AB}}} \quad \text{Binary mixture at low pressure from kinetic theory} \\ (n^* D_{AB}^E)_P = \frac{(n^* D_{AB}^E)_{Ref}}{g_{AB}} \quad \text{Low pressure to high-pressure correlation} \end{array} \right. \quad \text{Eq. I.25}$$

where n^* is the density number ($n^* = \rho_A N_A / M_A$), σ_{AB}^* (m) is a characteristic length which depends on the intermolecular force law, m_{AB} is the reduced molar mass ($m_{AB} = M_A M_B / [M_A + M_B]$), g_{AB} is the contact correlation, N_A (mol^{-1}) is the Avogadro's number, M (g.mol^{-1}) is the molar mass, ρ_A (kg.mol^{-1}) is the solvent density, the subscript *Ref* denotes ideal gases and superscript *E* denotes Enskog-Thorne theory.

Several functions can be added to Chapman-Enskog equations to improve accuracy. The Lennard-Jones potential function is often added to take into account attractive forces, which can play a significant role at low temperatures. As examples, different correlations are proposed in the literature as Catchpole and King (1994), Liu-Silva-Macedo (1997) and Lito-Magalhães-Gomes-Silva (2013).

Lito et al. (2013) suggested Eq. I.26 to infinite diluted gas, liquid and supercritical polar and non-polar solvents.

$$D_{AB} = \frac{3}{8n^* \sigma_{AB}^{*2}} \sqrt{\frac{\kappa_B T}{2\pi m_{AB}}} \frac{F_{AB}}{g_{AB}} e^{-\frac{E_D}{RT}} \quad \text{Eq. I.26}$$

where F_{AB} is a correction factor of hard sphere system and E_D ($\text{J}\cdot\text{mol}^{-1}$) is the activation energy of the diffusion process.

Their model was validated for 487 systems with 8293 data points, covering a wide temperature and pressure range, having AARD (average absolute relative deviation) of only 2.74%. This is a big improvement in relation to the hydrodynamic correlations (AARD=[20.74; 56.28]%, depending on the correlation) and a slight improvement in relation to Liu-Silva-Macedo (1997), so-called TLSM equation (AARD around 16.88% for supercritical mixtures).

The diffusion coefficients for the MAPD in propylene are not available in literature and the database of Lito-Magalhães-Gomes-Silva (2013). Consequently, a similar system was suggested as an example of the application of their correlation, namely propane and 1-octene (AARD=1.64%, Figure I.10).

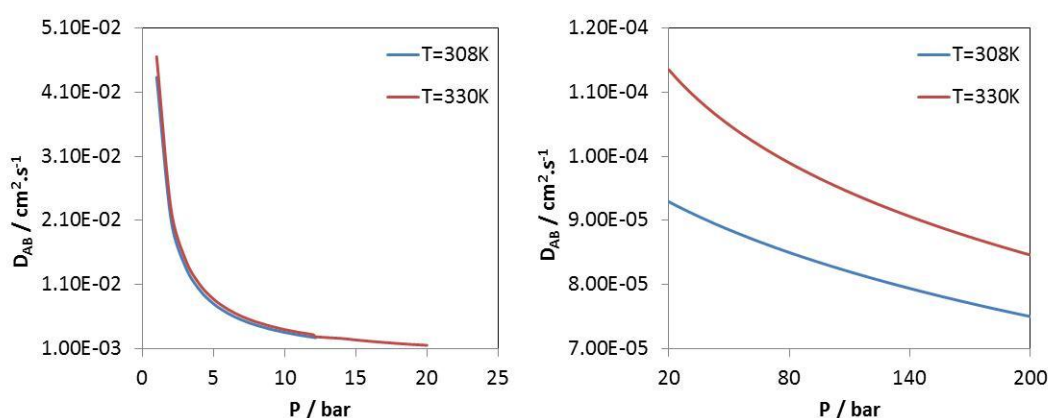


Figure I.10: Estimated tracer diffusion coefficients for propane (A: solvent) and 1-octene (B: solute) in gas and liquid phases, using Lito-Magalhães-Gomes-Silva (2013) equation. The example was extracted from Lito et al. (2013) database.

For the system propane/1-octane the diffusion coefficient in the liquid phase can be 30 times lower than in the gas-phase, which may be unfavorable to mass transport, since Sh depends on Sc . For liquid-phase, when increasing pressure, the loss of diffusivity was merely 1.3 times, which can mean that in liquid-phase the reduction in diffusivity may be bearable in relation to the gains in kinetics and equilibrium (Vapor-Liquid-Equilibrium: VLE). In other words, the solubility in the liquid should increase with the pressure (later discussed).

In the next subchapter, the phase equilibrium will be discussed.

1.5.4 Interphase equilibrium

Experimental data

The phase behavior of any system depends on temperature, pressure and molar composition of the species (set by the feedstock mixture). For gas-phase systems, it is only interesting to play with the pressure, in order to raise the molar concentration. For vapor-liquid systems, changing the temperature and/or the pressure can help increasing the solubility of the gas species in the liquid-phase (Maniquet and Girardon, 2012) [internal report]. Unfortunately, light hydrocarbon-systems show reverse-order solubility over a considerable range of

temperatures. Figure I.11 contains experimental data for hydrogen solubility in C_3 liquid systems. From the graphic, propane and C_3 mixture have reverse-order solubility.

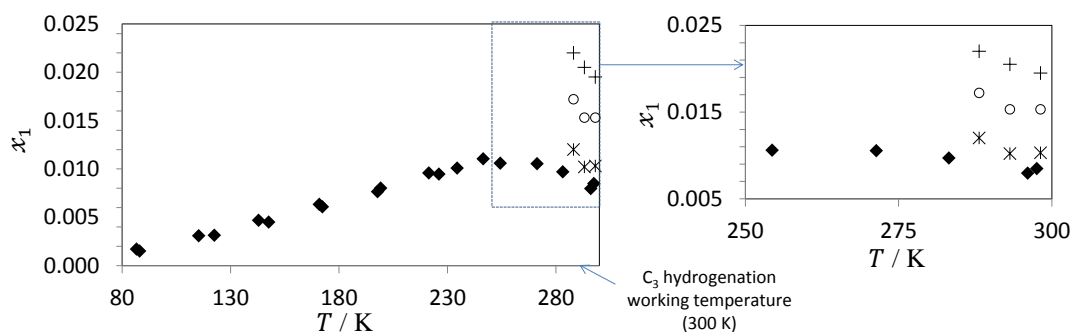


Figure I.11: Temperature-composition diagram for the hydrogen composition (x_1) in the C_3 liquid phase (pure propane and or C_3 cut mixture). \blacklozenge : 17.5 bar; $*$: 20 bar; \circ : 25 bar; $+$: 30 bar. (Benham et al., 1957; Maniquet and Girardon, 2012; Trust and Kurata, 1971)

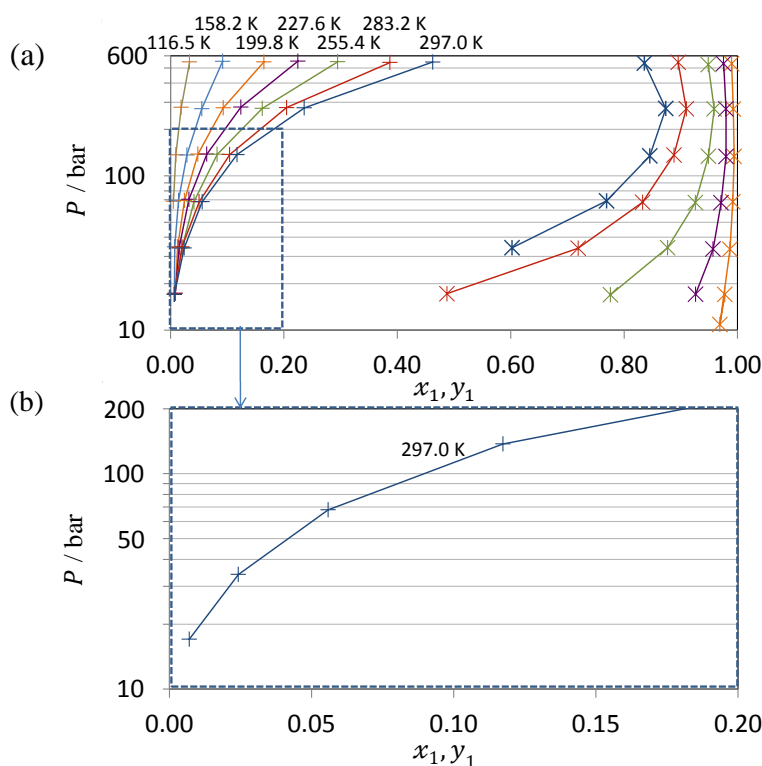


Figure I.12: (a) Experimental data for dew and bubble curves for hydrogen (1) with propylene (2) mixture. (b) Closer zoom for dew point at $T=297.0$ K. $+$: experimental bubble points; $*$: experimental dew points. Solid lines: interpolation. x_1 and y_1 are the hydrogen mole fraction in the liquid and vapor phase, respectively. Obtained from Williams & Katz (1954).

Since the hydrogen solubility decreases with the increase of the temperature (see Figure I.12), temperature variations are not a good solution to perform hydrogenation. Moreover, increasing the temperature results in a loss of catalytic selectivity, because the rates of secondary reactions can increase (Fajardo et al., 1996). So, to improve the solubility, it is

mandatory to increase the pressure. In that line in literature, Williams & Katz (1954) obtained experimentally vapor-liquid equilibrium data for the hydrogen-propylene different iso-temperature lines (Figure I.12a). Looking more specifically at data for MAPD at 297 K (Figure I.12b), when the pressure increases, the hydrogen quantity solubilized in the liquid phase (x_1) increases. At 297 K, from 15 to 50 bar the H_2 solubility increases by 2 mol%, and from 15 to 200 bar, it increases by 10 mol%. This increase is not negligible, because the main problem in gas-liquid-solid hydrogenation is the lack of hydrogen on the catalyst's surface. Achieving a higher solubility can help improving the system's performance. High-pressure conditions also allow having single-phase C_3 cut hydrogenation (liquid) (H_2 /MAPD feed needed < H_2 /MAPD soluble).

As a conclusion, experiments at high pressure can lead to the higher solubility of hydrogen in the liquid phase. This will help to meet the objective of having higher hydrogen concentration on the catalyst's surface.

Modeling

Although there is some experimental data for hydrogen solubility, the industrial feedstock is rarely identical (Rolland, 2014). Since industrial mixtures are complex, modeling is an interesting and necessary tool to follow solubility in the C_3 cut. To better understand hydrogen-hydrocarbon systems, Benham et al. (1957) proposed a correlation for binary mixtures based on Williams & Katz (1954) experimental results. The modified Henry constant and hydrogen molar fraction in the liquid phase are:

$$\log_{10}(fy/x)_1 = \log_{10}H + \bar{v}_1 P / (0.1587 \mathfrak{R}T) \quad \text{Eq. I.27}$$

$$H \propto \left(\frac{5T}{3\sqrt{5T_B}} \left[1 + \frac{1458}{(T_C - T)^2} \right] \right) \quad \text{Eq. I.28}$$

Where y_1 and x_1 are the molar fractions of hydrogen in gas and liquid phase, respectively. f_1 (bar) is the fugacity of hydrogen at T (K) and P (bar), H (bar) is the Henry's constant at T , v_1 ($m^3 \cdot mol^{-1}$) is the molar volume of hydrogen in liquid phase, T_B and T_C (K) are the boiling point and critical temperature of the solvent, respectively.

This correlation is restricted to low pressures (up to 30 bar) and when applied to high pressures the values obtained are overestimated. Moreover, it is not a predictive method, because it needs experimental knowledge of the mixture.

In thermodynamic, the most common equations of state used to model the hydrocarbon mixtures are based on the van der Waals equation of state (cubic type). In the cubic type of equations, the Peng-Robinson78 is frequently used:

$$P = \frac{\mathfrak{R}T}{v_m - b} - \frac{a\alpha}{v_m^2 + 2bv_m - b^2} \quad \text{Eq. I.29}$$

where \mathfrak{R} ($m^3 \cdot bar \cdot mol^{-1} \cdot K^{-1}$) is the ideal gas constant, T (K) is the temperature, v_m ($m^3 \cdot mol^{-1}$) is the molar volume, a ($bar \cdot m^3 \cdot mol^{-2}$) is the attraction parameter, b ($m^3 \cdot mol^{-1}$) is the effective parameter and α is a dimensionless parameter.

This equation Eq. I.29 is only suitable to be used with pure compounds. To be applied to mixtures, it is necessary to couple with mixing rules, such as the van der Waals mixing rule. In the mixing rule formulation, there are always parameters corresponding to binary interactions between compounds that need to be known. The others parameters, a_{ii} and b_{ii} , can be easily calculated from the properties of each pure compound.

$$a = \sum_{i=1}^{n_c} \sum_{j=1}^{n_c} x_i x_j a_{ij} \quad b = \sum_{i=1}^{n_c} \sum_{j=1}^{n_c} x_i x_j b_{ij} \quad \text{Eq. I.30 \& Eq. I.31}$$

$$b_{ij} = \frac{b_{ii} + b_{jj}}{2} \quad a_{ij} = (1 - k_{ij}) \sqrt{a_{ii} a_{jj}} \quad \text{Eq. I.32 \& Eq. I.33}$$

where i and j are an index of pure components. When $i=j$, a_{ij} and b_{ij} are parameters for mixture components, and when $i \neq j$, a_{ij} and b_{ij} are the unlike-interaction parameters.

The most important parameter in these equations is the k_{ij} parameter, which is the interaction parameter between binary compounds and is usually obtained by fitting. In a vast number of publications k_{ij} is constant and not temperature dependent for hydrocarbons-hydrogen mixtures, which is not the case (Nishiumi and Gotoh, 1990). To predict the evolution of k_{ij} with temperature for hydrogen containing binary mixtures, Qian et al. (2012) developed the group contribution method to improve the accuracy of the PPR78 for binary hydrogen-containing mixtures. The authors evaluated the VLE behavior for 39 binary mixtures (8100 experimental points) over a broad range of pressures and temperatures. In their database, the closer species compared to C_3 cut is propylene. For the binary mixture hydrogen-propane, when comparing to literature results, the PPR78 model gave excellent results up to 500 bar (Figure I.13). This is consistent with the type of phase behavior [type III, according to Konynenburg & Scott (1980) classification system (later explained, §I.6.4)].

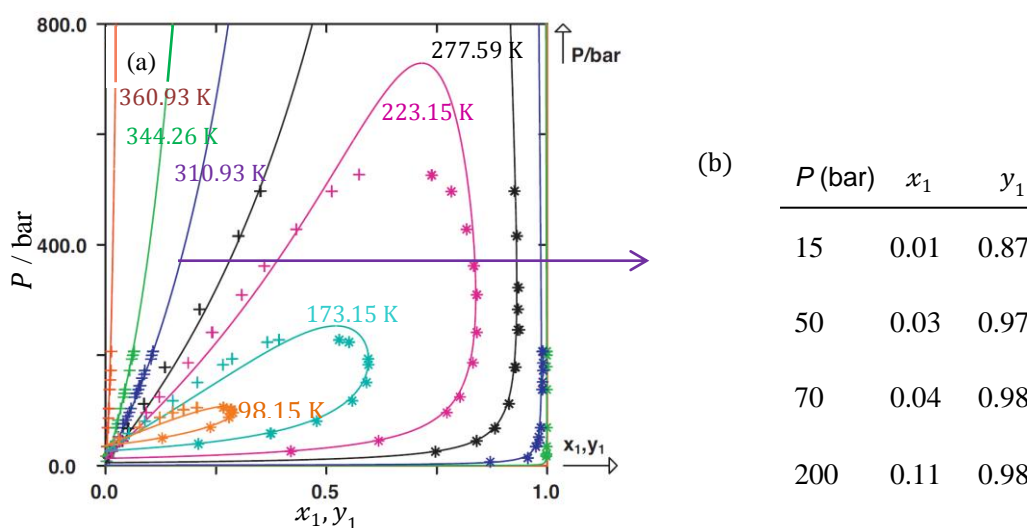


Figure I.13: Plot from Qian et al. (2012) (a) Prediction of dew and bubble curves for hydrogen (1) with propane (2) mixture for 7 sets of temperatures.

(b) Table with experimental points at $T=310.93$ K. +: experimental bubble points; *: experimental dew points (Bol'shakov and Linshits, 1953; Burriss et al., 1953a; J.-W. W. Qian et al.,

2013; Trust and Kurata, 1971; Williams and Katz, 1954b). **Solid lines: PPR78 model. x_1 and y_1 are the hydrogen mole fraction in the liquid and vapor phase, respectively.**

As a conclusion, using the knowledge obtained with the equations of state, it is possible to model the H_2 solubility for diverse industrial feedstock.

1.5.5 Conclusion

It is **interesting to reach high pressures for hydrogen-hydrocarbon systems**, because the overall **reaction rate will be enhanced** (Girgis and Gates, 1991; Hitzler et al., 1998; Musko et al., 2012). For certain systems, such as the hydrogenation of the C_3 cut, **the single-phase domain can be achieved at relatively low pressures**, which means no interphase mass transfer resistance. The majority of the systems (with more carbons than C_3) used in hydrogenation cannot be fully solubilized even when increasing the pressure (Ronze et al., 2002; Yin and Tan, 2006). Beyond liquid-solid, another type of conditions can be used (Grunwaldt et al., 2003b). These conditions are supercritical, and it will be discussed in the next subchapter.

1.6 Reaction in supercritical conditions

1.6.1 Introduction

To address the complexity of catalytic reactions, it is possible to move from conventional (or classical) to supercritical conditions. The objective is to have a homogeneous phase and improve mass transfer rates (Carlès, 2010a; Grunwaldt et al., 2003b). A supercritical fluid is defined as a substance above its critical point, for pressure and temperature (Savage et al., 1995a). At the critical point, the liquid is similar to the one of vapor, featuring a unique behavior for isothermal compressibility ($\uparrow \infty$), heat capacity ($\uparrow \infty$), refraction factor ($\uparrow \infty$) and sound velocity ($\downarrow 0$) (Grunwaldt et al., 2003b; Ke et al., 2010, 2001). Figure I.14b shows a simple diagram for a pure fluid.

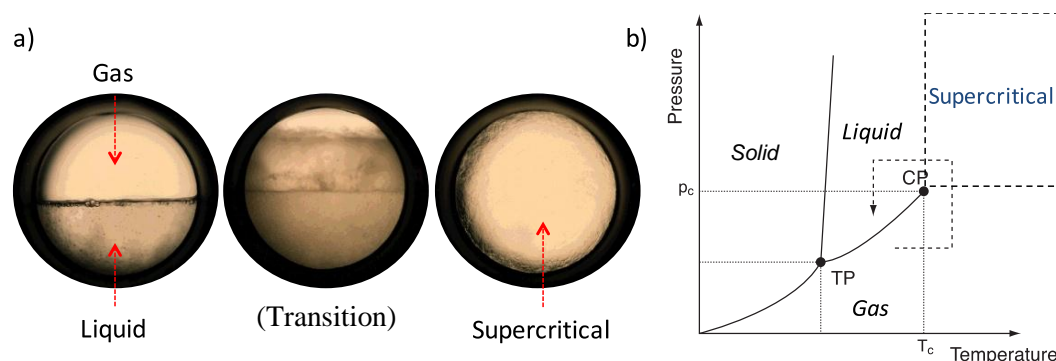


Figure I.14: (a) The carbon dioxide vapor/liquid phase merge into a supercritical domain by increasing of temperature and pressure (left to right) (Nasa, 2013); (b) Schematic phase diagram of a pure substance (Ke et al., 2001): CP is the critical point and TP is the triple point.

The physical properties, such as density, viscosity and diffusion, will be intermediate between those of liquids or gases (Carlès, 2010b). If temperature and pressure are slightly changed in the supercritical domain, the physical properties can go from liquid-like to gas-like

(Gourgouillon et al., 1998; Toda et al., 2011). Table I.13 shows the order of magnitude values for some SCFs properties. As gas-like and liquid-like properties are combined, it is expected (roughly) to have diffusivities being close to gas-like and to have densities/dissolving power/heat capacity being liquid-like (Grunwaldt et al., 2003b) [this can be different, depending on the applied conditions]. These contributions of physical and transport properties will result in very interesting enhancements in reactions controlled by mass transfer (Rovetto et al., 2003). According to Savage et al. (1995), increases of conversions can be anticipated (for reactions in gas-liquid-solid phase).

Table I.13: Comparison of gases, supercritical fluids and liquids.

	<i>Density</i> (kg.m ⁻³)	<i>Viscosity</i> (μPa.s)	<i>Diffusivity</i> (m ² .s ⁻¹)
Gases	1	10	10 ⁻⁶ -10 ⁻⁵
Supercritical fluids	100-1000	10-100	10 ⁻⁸ -10 ⁻⁷
Liquids	1000	500-1000	10 ⁻⁹

In the first part of this subchapter, the advantages of the supercritical medium will be highlighted with a particular focus on supercritical hydrogenation. In the second part, the different phase behaviors for binary mixtures will be detailed.

I.6.2 Heterogeneous catalysis in SCFs

Supercritical fluids are a well-established technology in reaction engineering, being extensively used in laboratory and industry scale. A large number of reactions have been studied at lab-scale, such as hydrogenation (Härröd et al., 2001), oxidation (Shah et al., 2000), isomerization (Bogdan et al., 2004), hydration (Anikeev et al., 2004) and Fischer-Tropsch synthesis (Malek Abbaslou et al., 2009). Although there are a great potential to perform reactions in the near critical or supercritical domain (Hitzler and Poliakoff, 1997), only a hand full of classical reactions are nowadays performed at supercritical conditions in industry (Perrut, 2000), probably due to higher investment costs. In this manuscript, only the hydrogenation reactions will be covered in supercritical fluids.

Catalytic heterogeneous hydrogenations generally have three distinct phases: solid, liquid and gas, which are responsible for mass transfer limitations (Arunajatesan et al., 2001; Selva Pereda et al., 2002; Wandeler, 2001). The use of supercritical fluids can offer promising solutions to improve mass transfer limits (Figure I.15).

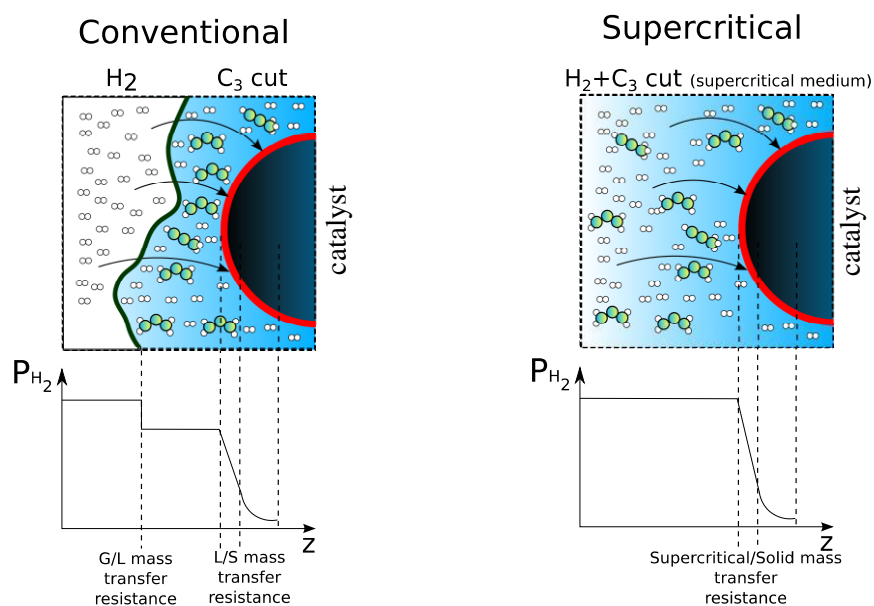


Figure I.15: Comparison of a conventional selective hydrogenation versus supercritical hydrogenation (suppression of the gas-liquid resistance).

When carrying out catalytic reactions in SFCs, it is expected to (i) eliminate gas/liquid mass transfer resistance (Flores et al., 2003; Hyde et al., 2001; Keybl, 2011; Selva Pereda et al., 2002), (ii) enhance reactant diffusion in the bulk and inside the particle (Cherayil, 2002; Drozdov and Tucker, 2001) and (iii) have adjustable physical properties (slight changes in P and T can suit the process needs: viscosity, density and heat capacity). There is also the potential suppression of coke deposition, which increases the catalyst lifetime cycle (Hassan et al., 2012). Thus, fluid-solid reactions with a homogeneous fluid medium could be an excellent option for catalysis [to measure (pilot scale) and to enhance (industrial)] (Hassan, 2011). Thereby, the importance of each feature will be detailed individually.

i. Single-phase mass transfer

The suppression of the interface between fluid phases can happen at high pressure or supercritical conditions (Zimm, 1950). Normally in high-pressure hydrogenation, it is not common to have homogenous reactions. In supercritical fluids, on the other hand, it is common (Ke et al., 2001).

Hydrogenations with single-phase fluids may possibly lead to improvements in (i) process intensification and selectivity control (Zhao et al., 2003). It is easy to imagine a reaction with no gas-liquid interface; therefore $k_L a_{GL}$ is no longer needed. Therefore, (ii) the uncertainties related to the empirical $k_L a_{GL}$ correlations no longer exist in pilot scale [hydro §I.4].

Another advantage is the (iii) control of the hydrogen and substrate concentration on the catalyst surface (Selva Pereda et al., 2002). So, the accurate stoichiometric ratio hydrogen/substrate (in the bulk) can be easily achieved. Pillai & Sahle-Demessie (2003) studied the hydrogenation of 4-oxoisophorone over a 1 wt% Pd/Al₂O₃ catalyst from 313 to 398 K at 193 bar. For the same reaction at stoichiometric conditions, they reported higher conversions (classical: 32%; supercritical CO₂ medium: 70 to 100%), selectivity variations and lower catalytic deactivation in the supercritical media than in conventional multiphase

medium. The higher conversions are related to a high concentration of substrat on the catalytic surface. The selectivity variations are possible, since the amount of hydrogen in the fluid can be controlled, which is not feasible in a gas-liquid fluid media.

We expect that a similar behavior (for conversion, selectivity and deactivation) may happen to C₃ cut hydrogenation, since the hydrogen used could be in the optimal stoichiometric conditions.

ii. Enhancement of reactant diffusion in the bulk and inside the particle

In the majority of supercritical applications, the use of supercritical conditions relies on the combination with a solvent (Burgener et al., 2005b). The addition of a solvent will allow an (i) increase of molecular diffusion and (ii) soft operating pressure and temperature (Wu et al., 1991). The right supercritical solvent has to achieve complete (iii) miscibility at moderate pressures, be (iv) inert with the reactants and products and has to respect reaction, environment and economic conditions.

According to Medina (2012), the diffusion coefficient is inversely proportional to the molar volume of the solute. A solute with larger molar volume tends to diffuse more slowly. The association of a solvent to a solute can decrease or increase the diffusion coefficient. It also can change the miscibility in certain T-P ranges. An empirical rule is to choose a solvent with a critical temperature below the reaction temperature.

For hydrogenation of the C₃ cut, we identified three potential solvents: methane, ethane and CO₂. It is expected that the higher solute diffusivity and Reynolds number will enhance the external ($k_{LS}a_{LS}$) and internal mass transfer (related to D_e), improving the effectiveness factor (Cherayil, 2002; Drozdov and Tucker, 2001). Since the literature is scarce for C₃ cut + solvent mixtures, the diffusion coefficients in supercritical medium have to be calculated by predictive equations. In the majority of publications, the binary diffusion coefficients have been studied in systems with supercritical CO₂.

There are several models to predict fluid diffusion coefficients (Table I.14). Medina (2012) published a comparative study of the main correlations for 40 systems (600 points) in supercritical CO₂. He pointed out that for supercritical fluids, the Rough-Hard-Sphere expressions are better than the Stokes-Einstein models to estimate diffusion. Later, Magalhães et al. (2013) analyzed two-parameter correlations, Stokes-Einstein and Rough-Hard-Sphere based expressions for supercritical fluids over a broad range of experimental data. The total average relative deviation (AARD) proposed was inferior about 3.05% for correlations and 4.21% for predictable expressions. They remarked that Wilke-Chang's equation (Stokes-Einstein based) should be avoided because the AARD can vary between 1.2 and 300%. The foremost used equations and their respective AARD for supercritical fluids are detailed in Table I.14.

Table I.14: Average absolute relative deviation for Stokes-Einstein and Rough-Hard-Sphere based equations. * 40 systems with 600 experimental supercritical data points (Medina, 2012); ** 487 systems with 8293 experimental data points [liquid, gas and supercritical] (Lito et al., 2013 and Magalhães et al., 2013). The gray are the most interesting equations for this manuscript.

Equation authors	Equation	Based model	AARD %
Wilke and Chang (1955)	$D_{AB} = \frac{5.88 \times 10^{-17} T \sqrt{M_B}}{\mu_B v_{boil,A}^{0.6}}$	Stokes-Einstein	10.3* 26.5**
Tyn and Calus (1975)	$D_{AB} = 8.93 \times 10^{-16} \frac{T}{\mu_B} \left(\frac{v_{boil,A}^{\frac{1}{6}}}{v_{boil,B}^{\frac{1}{6}}} \right) \left(\frac{\Gamma_B}{\Gamma_A} \right)$	Stokes-Einstein	9.4*
Eaton and Akgerman (1997)	$D_{AB} = 1.42 \times 10^{-21} \sqrt{T} \left(\frac{\sigma_A^{*eff}}{\sigma_B^{*eff}} \right)^{1.7538} \times \left(\frac{M_A + M_B}{M_A} \right)^{\frac{1}{2}} \left(\frac{(v_B)_0}{(\sigma_B^{*eff})^2} \right) \left[\left(\frac{v_B}{(v_B)_0} \right)^e - \frac{b_{AB}}{(v_B)_0} \right]$ $e = \frac{\sigma_B^{*eff}}{\sigma_A^{*eff}} - \frac{1}{3}$	Rough-Hard-Sphere	8.1*
He and Yu (1998)	$D_{AB} = 10 \times 10^{-10} \alpha \sqrt{\frac{T}{10^3 M_A}} e^{\left(\frac{0.3887 v_{cB}}{v_B - 0.23 v_{cB}} \right)}$ α is a function [see Medina (2012)]	Rough-Hard-Sphere	6.6*
Liu-Silva-Macedo (1997)	$D_{AB} = \frac{\kappa_B T}{\frac{8}{3} \mu_B (\sigma_{AB}^{*eff})^2 (\pi m_{AB} \kappa_B T)^{\frac{1}{2}}} e^{\left(-\frac{0.75 n_B^*}{1.2588 - n_B^*} - \frac{0.27862}{T_{AB}^*} \right)}$	Rough-Hard-Sphere	10.3* 3.6**
Funazuki-Kong-Kagai	$\ln \left(\frac{Sc - Sc^0}{Sc^0} \right) = -4.9252 + 54.5529 \left(\frac{(v_B)_0}{v_B} \right) - 245.2314 \left(\frac{(v_B)_0}{v_B} \right)^2 + 607.8939 \left(\frac{(v_B)_0}{v_B} \right)^3 - 708.8840 \left(\frac{(v_B)_0}{v_B} \right)^4 + 329.6114 \left(\frac{(v_B)_0}{v_B} \right)^5$	Rough-Hard-Sphere	8.3*
Lito-Magalhaes-Gomes-Silva (2013)	$D_{AB} = \frac{3}{8 n^* \sigma_{AB}^{*2}} \sqrt{\frac{\kappa_B T}{2 \pi m_{AB}}} \frac{F_{AB}}{g_{AB}} e^{-\frac{E_D}{RT}}$ F_{AB} and g_{AB} proposed functions (see publication)	Rough-Hard-Sphere	2.74**

The previous expressions (Table I.14) will help to determine the impact of diffusion variations in the overall reaction rate.

iii. Adjustment of physical properties

The supercritical fluids allow adjusting easily dimensionless numbers (Pillai and Sahle-Demessie, 2003b; Seki et al., 2008). The principal dimensionless number is the Re number, because it takes part in hydrodynamic, mass transfer and heat transfer. It is dependent on two thermophysical properties: **density** and **viscosity**.

The **density** can be estimated by equations of state as PR78 (Heidemann and Khalil, 1980; Stockfleth and Dohrn, 1998), PPR78 (Jaubert and Mutelet, 2004; Mutelet et al., 2005; Privat et al., 2008), SPHCT (García-Sánchez and Ruiz-Cortina, 1992) and PC-SAFT (Justo-García

et al., 2008). Justo-García et al. (2008) applied PR78, PSRK, SPHCT and PC-SAFT to 45 non-polar and polar binary systems, being composed of N_2 , CO_2 , and methane to n-decane. They obtained satisfactory results for all the equations of state proposed; AARD from 1.08 to 3.48% and 2.58 to 4.03% for P_C and T_C , respectively. They indirectly showed that cubic equations of state could have similar or better results compared to PC-SAFT and SPHCT for hydrocarbons mixed with polar and non-polar substances. The state-of-art of the equations of state and their performance in the critical region is shown in Table I.15.

For the hydrogenation of C_3 cut, the EOS that best assess for hydrogen containing systems in the critical region is the PPR78 (Table I.15) [next page]. This equation can be used for pressure system below 500 bar with minor error [§I.5.4].

The other important thermophysical property is the **viscosity**. Some prediction methods have been proposed for the viscosity of pure fluids and mixtures from medium to high pressures. Vesovic et al. (1998) proposed a method to predict viscosity in binary mixtures based on Vesovic and Wakeham (1989) methodology. According to the authors, the method proposed does not require the knowledge of mixture properties at high pressures. The viscosity of each pure component should be described by a universal density function (independent of temperature). In other words, their method only requires as input the viscosity data of the pure components in the dilute-gas limit.

For methane-containing systems (rich in methane) the viscosity of supercritical multicomponent fluid mixtures is within $\pm 5\%$ for AARD. As an example of comparison between experimental and calculate data, the authors presented the binary methane-hydrogen (Figure I.16).

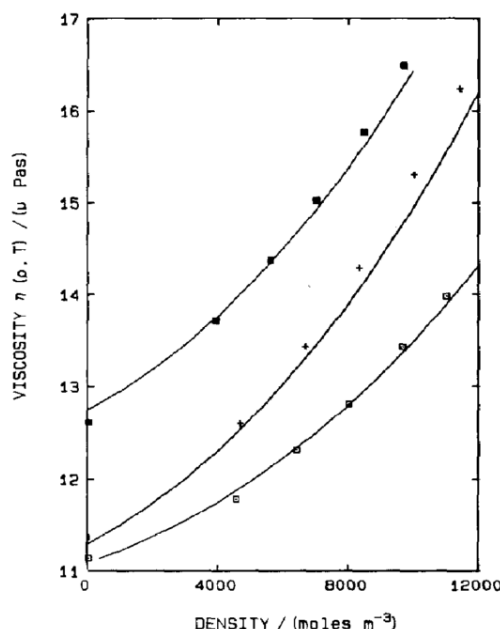


Figure I.16: Viscosity of CH_4 - H_2 mixture versus molar concentration (“density”). The lines are calculated values; (+) $T = 298.15$ K and $x_{CH_4} = 0.552$; (□) $T = 298.15$ K and $x_{CH_4} = 0.359$; (■) $T = 348.15$ K and $x_{CH_4} = 0.552$. Obtained from Vesovic & Wakeham (1989).

Table I.15: Brief characteristics of the main used equations of state to predict properties in the critical region (critical pressure, critical temperature and critical molar volume). For more detailed see Jaubert et al. (2005), Justo-García et al. (2008) and Valderrama (2003). The multicomponent phase behavior presented involves classical *Van der Waals* mixing rules.

Authors	Year	Group of EOS	Equation	Characteristics
Van der Waals	1873	1) Base cubic equation	$P = \frac{\mathfrak{R}T}{\underbrace{v_m - b}_{\text{repulsive term}}} - \frac{a}{\underbrace{v_m^2}_{\text{attractive term}}}$	<ul style="list-style-type: none"> • Rarely accurate for critical properties and phase equilibrium (e.g. the AARD can be 60% for critical pressure and temperature)(Chen and Kreglewski, 1977);
Redlich-Kwong (RK)	1949	1.1) Modified attractive term	$P = \frac{\mathfrak{R}T}{v_m - b} - \frac{a}{T^{0.5}v_m(v_m + b)}$	$a = 0.4278\mathfrak{R}^2T_c^{2.5}/P_c \quad b = 0.0867\mathfrak{R}T_c/P_c$ <ul style="list-style-type: none"> • Substantial improvement from van der Waals equation for polar and/or non-polar substances, but has problems for complex fluids with non-zero acentric factor (ω);
Soave-Redlich-Kwong (SRK)	1972	1.2) Modified attractive term	$P = \frac{\mathfrak{R}T}{v_m - b} - \frac{a(T)}{v_m(v_m + b)}$	$a(T) = 0.4274(\mathfrak{R}^2T_c^2/P_c)\{1 + m[1 - (T/T_c)^{0.5}]\}^2 \quad m = 0.480 + 1.57\omega - 0.176\omega^2$ <ul style="list-style-type: none"> • Improved accuracy for phase behavior near the critical region for mixtures (e.g. methane + hydrocarbon the AARD are 4.94, 6.57 and 19.56% for T_c, P_c and v_c)(Elliott and Daubert, 1987a); • The critical compressibility factor is overestimated (AARD can be 22%) (Elliott and Daubert, 1987b);
Peng-Robinson (PR78)	1978	1.3) Modified attractive term	$P = \frac{\mathfrak{R}T}{v_m - b} - \frac{a(T)}{v_m^2 + 2bv_m - b^2}$	$a(T) = 0.45724(\mathfrak{R}^2T_c^2/P_c)\{1 + m[1 - (T/T_c)^{0.5}]\}^2$ $m = 0.37464 + 1.5422\omega - 0.26922\omega^2 \quad b = 0.07780\mathfrak{R}T_c/P_c$ <ul style="list-style-type: none"> • Can be used to predict well vapor pressure and volumetric behavior for single and multicomponent mixtures; • In a system hydrocarbon + non-hydrocarbon (35 multicomponent mixtures), the critical properties have an AARD of 1.40 and 2.58 % for T_c and P_c (Justo-García et al., 2008);
Peng-Robinson-Stryjek-Vera 2 (PRSV-2)	1986	1.4) Modified attractive term	$P = \frac{\mathfrak{R}T}{v_m - b} - \frac{a(T)}{v_m^2 + 2bv_m - b^2}$	$m = [m_0 + m_1(m_2 - T_R)(1 - T_R^{0.5})](1 + T_R^{0.5})(0.7 - T_R)$ $m_0 = 0.378893 + 1.4897153\omega - 0.17131848\omega^2 + 0.01965554\omega^3$ <ul style="list-style-type: none"> • For polar mixtures has an AARD of 0.33, 1.95 and 20.35 (8 binary mixtures) for T_c, P_c and v_c. For non-polar mixtures, it has an AARD of 0.56, 2.21 and 3.03 for T_c, P_c and v_c (8 binary mixtures)(Abu-Eishah, 1999).
Volume-translated Peng-Robinson (VTPR)	1998	1.5) Modified attractive and repulsive term	$P = \frac{\mathfrak{R}T}{v_{exp} - b} - \frac{a(T)}{v_{exp}^2 + 2bv_{exp} - b^2}$ $v_{exp} = v_m + v_t$	$a(T) = [1 + M(1 - T_R) + N(1 - T_R)(0.7 - T_R)]^2 \quad v_t = \mathfrak{R}T_c/P_c [k_1 + k_2(1 + T_R^{2/3}) + k_3(1 + T_R^{2/3})^2]$ $M = 0.20473 + 0.83548\omega - 0.18470\omega^2 + 0.16675\omega^3 - 0.09881\omega^4$ <ul style="list-style-type: none"> • Overall AARD of 0.83 and 0.93% for pressure and liquid molar volume (Tsai and Chen, 1998). Better results than PRSV-2 for molar volume (7.61% at PRSV-2);

Table I.16: (cont. Table I.15)

Authors	Year	Group of EOS	Equation	Characteristics
Predictive Peng-Robinson (PPR78)	2004	1.6) Modified attractive and repulsive term	$P = \frac{\mathcal{R}T}{v_m - b} - \frac{a(T)}{v_m^2 + 2bv_m - b^2}$	<p>$a(T)$ and b is the same as PR78, but $\begin{cases} m = 0.37464 + 1.5422\omega - 0.26922\omega^2 & \omega \leq 0.491 \\ m = 0.379642 + 1.48503\omega - 0.164423\omega^2 + 0.016666\omega^3 & \omega > 0.491 \end{cases}$</p> <ul style="list-style-type: none"> • Better estimation of interaction parameter for classical Van der Waals mixing rules: $k_{ij}(T) = \frac{-\frac{1}{2} \left[\sum_{k=1}^{N_g} \sum_{l=1}^{N_g} (\alpha_{ik} - \alpha_{jk})(\alpha_{il} - \alpha_{jl}) A_{kl} (298.15/T)^{B_{kl}/A_{kl} - 1} \right] - \left[\sqrt{a_i(T)/b_i} - \sqrt{a_j(T)/b_j} \right]^2}{2\sqrt{a_i(T)a_j(T)/(b_i b_j)}}$ <ul style="list-style-type: none"> • Accurate results for sub- and critical region in a vast number of experimental data. Overall AARD of 3.79 and 9.33% for P_c and x_c for alkenes + alkanes [160 critical points (J.-W. Qian et al., 2013)]. Overall AARD of 14.08 and 9.3% for P_c and x_c for hydrogen binary systems [75 critical points (J.-W. W. Qian et al., 2013)].
Simplified Perturbed Hard Chain Theory (SPHCT)	1986	2) EOS for chain molecules	$P = \frac{\mathcal{R}T}{v_m} - \frac{c\mathcal{R}T}{v_m} \frac{4\eta - 2\eta^2}{(1 - \eta)^3} - \frac{\mathcal{R}T}{v_m} \frac{Z_m v_m^* Y}{v + v_m^* Y}$	<ul style="list-style-type: none"> • Cover repulsive and attractive, providing good results for polymer behavior and a wide variety of compounds, from hydrogen to polyethylene; • Accurate predict the solubility of light gas in a polymer solvent or light component in a supercritical solvent; • Possibility to estimate phase behavior diagrams in accordance to Konynenburg & Scott (1980) classification system, (Van Pelt et al., 1991)[AARD is 1.48 and 4.34 for T_c and P_c (Justo-García et al., 2008)];
Statistical Associating Fluid Theory (SAFT)	1990	3) EOS for associating fluids	$A = A^{ideal} + A^{seg} + A^{chain} + A^{assoc}$ <p>where A is the Helmholtz energy</p>	<ul style="list-style-type: none"> • Can be applied to correlate vapor-liquid equilibrium for small, large, polydisperse and associating molecules over a whole density range; • Provides reasonable critical point prediction [AARD is 1.07 and 4.03 for T_c and P_c (Justo-García et al., 2008)];

I.6.3 Example of hydrogenation in supercritical media

To understand the impact of supercritical fluids on reactive systems, Hitzler et al. 1998 studied the hydrogenation of alkenes, alkynes, aliphatic hydrocarbons, aromatic ketones, aldehydes, epoxides, phenols, oxides and nitrobenzene in supercritical media. The authors reported that depending on the experimental conditions, the hydrogenation process could be mild and selective or extreme with full hydrogenation of the carbon double bond.

Hitzler & Poliakoff (1997) detailed temperature, pressure and solvent influence on the hydrogenation of cyclohexene. The reaction is highly boosted using supercritical media, the reaction yield was superior to 96% for CO₂ and propane as solvents. The reaction was performed at pressure conditions above 60, 80 and 120 bar. The authors claim that experiments with a cyclohexene mixture (~derived mixture) indicate better selectivity in scCO₂ than in gas-phase and higher reaction rates than in liquid-phase, which leads to the use of 35 times less catalyst. Table I.17 shows other types of hydrogenations performed in supercritical media.

Table I.17: Experimental studies (with a supercritical solvent performed) in a continuous set-up (Hitzler & Poliakoff, 1997).

Solvent	Reagents	Working P & T	$V_{reactor}$	\bar{t}_{res}	Catalyst
CO ₂	m-Cresol, H ₂	120 bar/250°C	5 and 10 mL	<5 min	5% Pd APII Deloxan catalyst (0.3-0.8 mm)
CO ₂	Benzaldehyde, H ₂	120 bar/95°C	5 mL	<10 min	5% Pd APII Deloxan catalyst (0.3-0.8 mm)
CO ₂	Propionaldehyde, H ₂	120 bar/150°C	5 mL	<10 min	5% Ru APII Deloxan (<0.2 mm)
CO ₂	Furan, H ₂	120 bar/300-350°C	5 mL	<5 min	5% Pd APII Deloxan catalyst (0.3-0.8 mm)
C ₃ H ₈	Nitrobenzene, H ₂	80 bar/150-200°C	5 mL	-	1% Pd APII Deloxan catalyst (0.2-0.5 mm)
C ₃ H ₈	<i>N</i> -benzylidenemethylamine, H ₂	120 bar/40-50°C	5 mL	-	5% Pd APII Deloxan catalyst (0.3-0.8 mm)
C ₃ H ₈	2-Butanone oxime, H ₂	80 bar/150-200°C	5 mL	-	5% Pd APII Deloxan catalyst (0.3-0.8 mm)
CO ₂	1-octyne, H ₂	120 bar/40°C	5 mL	-	5% Pd APII Deloxan catalyst (0.3-0.8 mm)
CO ₂	Cyclohexene, H ₂	120-140 bar/>40°C	5 mL	-	5% Pd on Deloxan
CO ₂	Isophorone, H ₂	120 bar/<200°C	5 mL	-	5% Pd APII Deloxan catalyst (0.3-0.8 mm)

From an industrial point of view, the reactions in supercritical medium (supercritical media are always single-phase) are only interesting if there is an improvement in the ratio productivity/cost from the conventional process. In general, the main drawback of the process feasibility is the cost of the compressor, which can be expensive (Härröd et al., 2001; S. Pereda et al., 2002).

As far as we know, there is no literature about C_3 cut hydrogenation in supercritical media. Also, there is no information about the conditions to achieve the system critical region. To understand C_3 cut in supercritical media, it is mandatory to study multicomponent systems phase behavior. To start understanding multicomponent systems phase behavior, the binary systems phase behavior will be discussed.

I.6.4 Phase behavior

The critical conditions for supercritical hydrogenations can be quite a challenge to obtain, due to the complexity of the phase behavior diagrams for mixtures (Benham et al., 1957; Burriss et al., 1953b; Schneider, 2004). The phase diagram for mixtures is different than for pure fluids. A pure fluid has a single critical point. Mixtures have several critical points depending on the composition. The critical point is neither the maximum point for pressure and temperature, nor the minimum point (Grunwaldt et al., 2003a). The highest point in temperature (for a curve V/L) is called maxcondentherm point and the highest point in pressure is called maxcondenbar point. Since the critical point does not coincide with the maxcondentherm or the maxcondenbar point, there is a retrograde condensation. In other words, a single-phase mixture separates into two phases upon variations in conditions: isothermal expansion or isobaric heating (Ke et al., 2010). Depending on the relative location of the critical point in relation to the maxcondenbar and maxcondentherm point, retrograde dew formation or bubble formation at constant temperature or pressure can happen (Figure I.17).

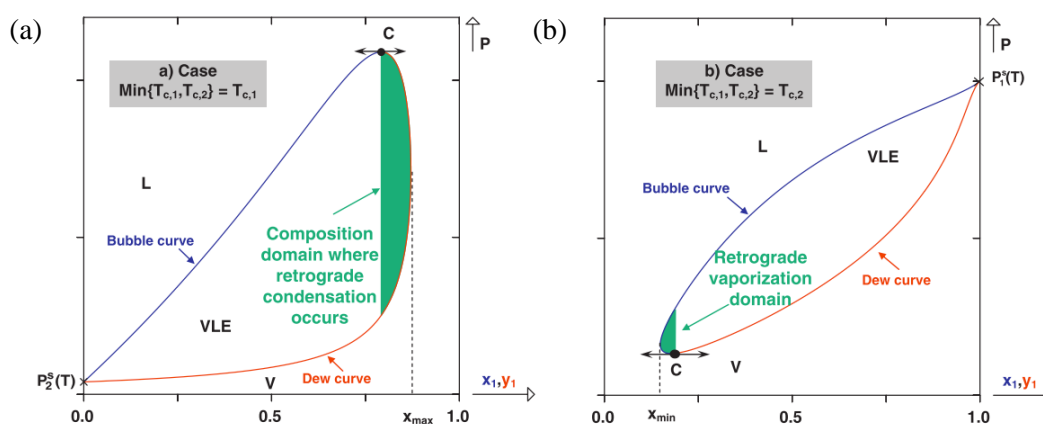


Figure I.17: Representation of phase behavior and illustration of retrograde vaporization and condensation by Privat and Jaubert (2013). The authors refer: (a) pure component 1 is supercritical whereas pure component 2 is subcritical; (b) pure component 2 is supercritical whereas pure component 1 is subcritical. VLE: Vapor-liquid equilibrium; V: vapor phase; L: liquid phase C: Mixture critical point.

The mixture critical points are difficult to obtain because there is no clear boundary in the critical phase transition as for pure species. Therefore, particular attention has to be paid when detecting the critical point, because of fluid-fluid immiscibility, gas-gas immiscibility, retrograde condensation and discontinuities of critical lines (Grunwaldt et al., 2003b).

To better understand their critical complexity, Konynenburg & Scott 1980 proposed a classification system for binary mixtures. The exhaustive classification of binary systems can be found in Privat and Jaubert (2013).

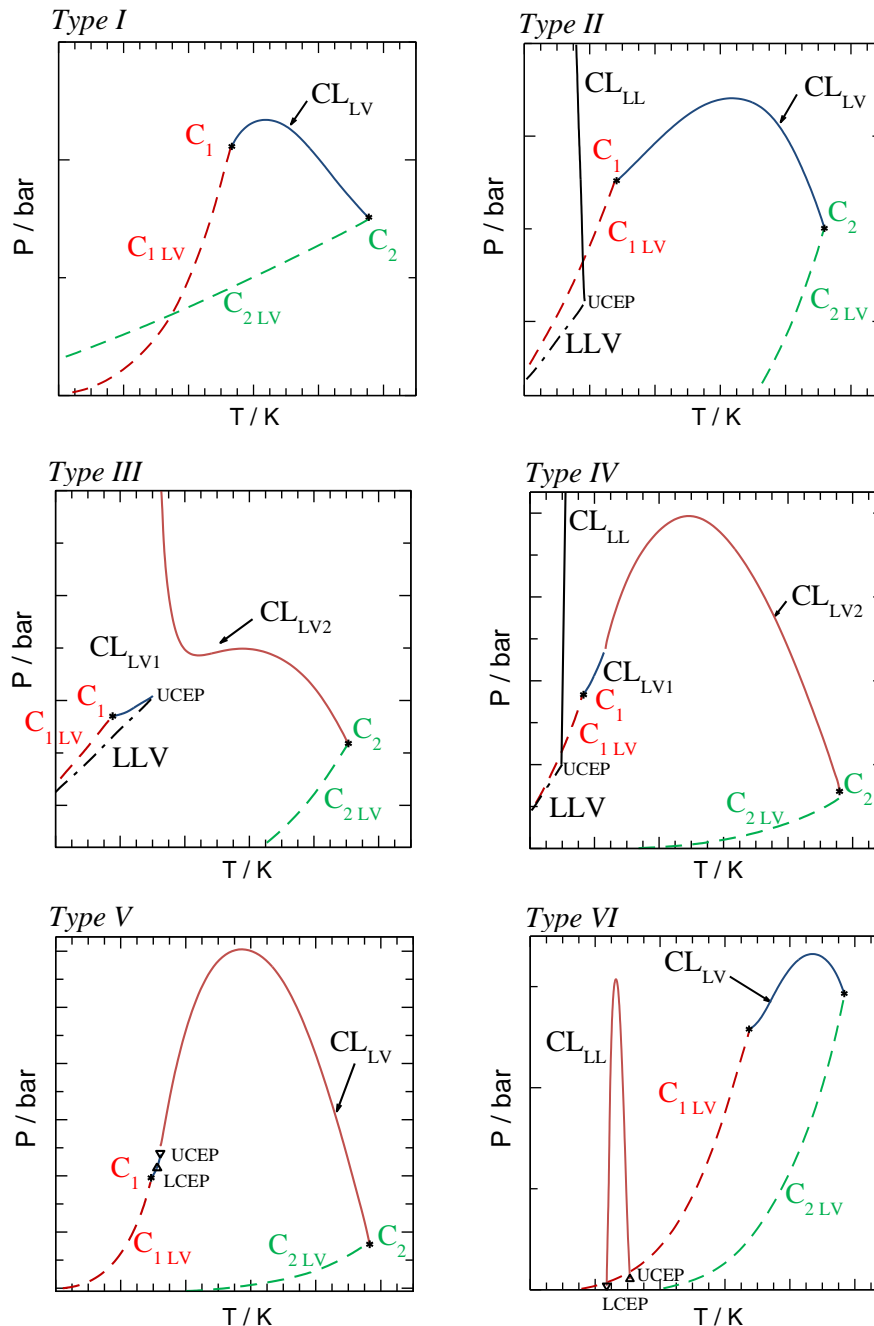


Figure I.18: Classification schemes of binary systems according to Konynenburg and Scott (1980) based on the PPR78 equation of state [adapted from Privat and Jaubert (2013)]. C: critical point; CL: critical line; UCEP: upper critical end point; LCEP: lower critical end point; Az: azeotropic point.

Type I: Mixtures are characterized to have complete miscibility in the liquid phases at all the compositions and temperatures (Figure I.18). It typically appears when two components are chemically very similar: molecular size, interaction strength and/or critical properties (Privat, 2008). For type I, the critical locus curve (series of critical points for a mixture plotted on pressure versus temperature) is a continuous critical line joining the pure component critical points. According to Grunwaldt et al. (2003a) review, the type I is expected from: methane + C_1 to n- C_5 , ethane + C_1 to n- C_{19} , propane + long chain hydrocarbon (from n- C_{40} to n- C_{50}),

CO₂ + ethane, etc. Depending on the shape of the critical curve, 5 subtypes can be distinguished. For detailed information about subtypes, we propose the readers to view “opportunities for reactions in supercritical fluids” by Grunwaldt et al. (2003a).

Type II: The critical locus is similar to type I: continuous liquid-vapor critical line. The only difference is in the phase behavior (Konynenburg and Scott, 1980). The mixtures have the liquid-liquid immiscibility at low temperature, and it extends from low to high pressures. Phase behavior diagram increases the complexity by to the presence of azeotropes (not shown in the figure). According to Grunwaldt et al. (2003a), the systems that usually show this behavior are CO₂ + n-octane, CO₂ + ethane, CO₂ + n-pentane, **CO₂ + propane** (potential solvent), H₂O + phenol, etc.

Type III: Mixtures are characterized to have immiscibility ranged from low temperatures up to the critical region. If the liquid–liquid immiscible region moves to higher temperatures, the UCST (upper critical solution temperature) of the liquid may interact with the liquid-vapor critical curve, resulting in discontinuities (vertical tangent in $P - T$ phase diagram). In other words, the type II is converted to type III. Thus, there are two liquid-vapor curves. The first gas–liquid critical line (LV1) extends from the critical point of the more volatile compound to the UCEP (upper critical end point). The second gas-liquid critical line (LV2) starts in the UCEP and goes until the critical point of the less volatile compound, having a smooth transition after the critical line after the discontinuity (UCEP). Roughly, the type III diagram can be seen as two envelops regions separated at the temperature of the UCEP. For more information, see Privat and Jaubert (2013).

The appearance of type III depends on the degree of the mutual immiscibility of the two components, happening for components with very different critical properties, molecule size, etc. This type of systems occur in methane + toluene, n-ethane + methanol, **H₂ + n-propane** (close to our study case), etc (Quiñones-Cisneros, 1997).

Type IV: Mixtures have two separate regions of liquid-liquid immiscibility: one at low temperatures and another one at higher temperatures (intersection with the liquid-vapor critical curve). At the intermediate temperature, the mixture is in the homogeneous state. It is an intermediary type of diagram between type II and type III (Figure I.18). As the type III, there are two liquid-vapor curves. The first gas–liquid critical line (LV1) extends from the critical point of the most volatile compound to the UCEP. The second gas-liquid critical line (LV2) starts in the LCEP (lower critical point) and goes until the critical point of the less volatile compound. Roughly, the type III diagram can be seen as two envelops regions separated at a temperature of the UCEP. An example of type IV is mixture methane + 1-hexene.

Type V: It is very similar to type IV without the liquid–liquid immiscibility at low temperatures. Thus, the UCEP for the liquid-liquid immiscibility is suppressed. This behavior happens for alkanes mixture with larger molecules, such as methane + n-hexane (Privat, 2008).

Type VI: Mixtures have liquid–liquid immiscibility at intermediate temperatures, and the UCST does not interfere with the gas–liquid critical. Type VI occurs for strong intermolecular bonding, such as hydrogen bonding (e.g. water + 2-Butoxyethanol).

It is important to keep in mind that this classification is brief, which nevertheless does not take into account the possible subtypes. For a detailed explanation about the Konynenburg & Scott 1980 classification system, see Mostowfi et al. 2012 and Privat and Jaubert (2013).

Experimentally, the critical point can be obtained using a high-pressure optical cell (HPOC), fused silica capillary capsule (FSCC), etc. These approaches can be coupled with techniques that allow the characterization of the transition between subcritical regions to the supercritical domain. The characterization techniques often used are “optical visualization of cloud point transition and soundwave velocity propagation” (Khammar and Shaw, 2011).

To calculate the critical point, Heidemann et al. 1980 algorithm is generally used (Castier and Sandler, 1997; Hoteit et al., 2006; Justo-García et al., 2008; Stockfleth and Dohrn, 1998; Stradi et al., 2004). It is based on Gibbs theory for a critical phase coupled with an equation of state (Peng-Robinson78, PC-SAFT, etc).

Those two points will be extensively detailed in chapter II.

Phase behavior during reaction (methodology)

J. Ke et al. (2001) studied the change of the critical point during the hydroformylation of propene in supercritical CO₂. Their reaction system involves six species: H₂, CO, CO₂, C₃H₆, n-butyraldehyde and isobutyraldehyde. This number of species easily spans a wide range of critical parameters, because it is necessary to quantify all the binary interactions between compounds. In total, there are 15 possible binary interactions. The strategy was to measure the critical curve with all the binary mixtures containing CO₂, and then to measure mixtures with three, four and six compounds. With experimental information, they took the conditions to the feed, and they analyzed the intermediate products and the outlet composition to know if the single-phase state has changed.

1.6.5 Conclusions

The state-of-art shows that supercritical fluids may **help reactions governed by the mass transfer rate**, e.g., **increasing diffusivity**. The main advantage of supercritical fluid technology is to reduce the mass transfer resistances. The most exciting features of supercritical fluids are **the higher diffusivities, the suppression of gas-liquid interface and the adjusting of fluid physical properties**. These features will be detailed for C₃ cut in the next chapter.

Several authors prove that **hydrogenation in supercritical fluids** can boost a lot the reaction conversion, but **there is no hydrogenation information about C₃ cut, neither thermodynamic data about C₃ cut critical points**. Based on other literature, it is expected that the C₃ cut hydrogenation could also be boosted for MAPD conversion.

1.7 Conclusion

Fast multiphasic reactions are **limited by mass transport**, such as interphase (gas to liquid), external (liquid to solid) and internal (inside the catalyst). To solve this, two ways can be

followed: (i) **increase the pressure**, and (ii) **change the reaction's conditions to supercritical**. Increasing the pressure can lead to a single-phase medium in some particular cases. Supercritical medium will further increase the diffusivity and will always give a single-phase medium.

The majority of publications claim that supercritical hydrogenation can improve reaction conversion. The precise influence of supercritical fluid for fast reaction has not been analyzed in the literature. **The gain in the elimination of gas-liquid interface as well as the gain with the diffusion coefficient (D_e) is unknown for C_3 cut hydrogenation.** We must therefore seek to determine if supercritical fluids are a better way to achieve better catalyst screening (or performance).

The main goal of this thesis is to develop and apply a methodology to access the catalyst intrinsic kinetics. In order to achieve this goal several steps are required:

1. Determine the critical coordinates for C_3 cut hydrogenation mixture

The phase behavior is expected to be difficult to model since the feedstock used comes from the oil industry. For this reason, the study of the critical coordinates will be conducted in microfluidics apparatus (new methodology proposed), which should be faster than the classical methods.

❖ Discussed on chapter II

2. Propose the best conditions to perform catalyst screening

The reactor and the C_3 cut hydrogenation will be study to achieve this goal. The reactor (single pellet string reactor) will be characterized for hydrodynamic and mass transfer, which will give the information required to interpret reaction data. The hydrogenation will be done at conventional (for understanding) and unconventional conditions (high-pressure and supercritical) [obtained from phase behavior study].

❖ Discussed on chapter III and IV

3. Propose a novel methodology to estimate the catalyst intrinsic kinetics parameters

The methodology will be based on a reactor model with intragranular diffusion. The experimental data will be used to obtain the kinetic parameters. It will allow us to have an idea how the catalyst is working (in an intragranular way) for the first time.

❖ Discussed on chapter V

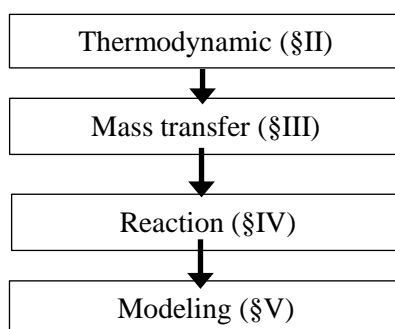


Figure I.19: Manuscript's guideline.

Chapter II

Study of unconventional reactive conditions

Abstract

To show the potential of hydrogenation in unconventional conditions (high pressure and/or supercritical), phase behavior diagrams have to be obtained, in order to determine hydrogen solubility and mixture critical point. These conditions will be later used in pilot plant experiments. Looking at industrial mixtures (feedstock), the composition is not often known or is very complex, having an impact on phase behavior. Therefore, it is necessary to perform experimental studies to determine the most feasible conditions.

In this chapter, a methodology was developed to characterize the mixture critical locus.

Firstly, a “design of experiments” was defined using the concept of the optimal number of points necessary to characterize by model the critical behavior. This allows us planning the experiments and reducing the experimental time consumed per each multicomponent system. To ensure the accuracy of the algorithm, several EOS were studied, such as PR78 and PPR78. The algorithm was validated through the studies of (model) binary CO₂ / alkanes mixtures (literature).

Secondly, the strategy was to acquire P-T diagrams and critical coordinates experimentally. With this in mind, a microfluidic-based approach was developed for investigating complex systems, allowing faster and cheaper screening of the operating conditions than classical systems. The obtained results were successfully compared to PPR78 EOS-calculated and literature data. This strategy was then applied for determining critical coordinates for the mixture C₃ cut + H₂ + solvent (CO₂ or CH₄ or ethane) [ternary and quaternary mixtures].

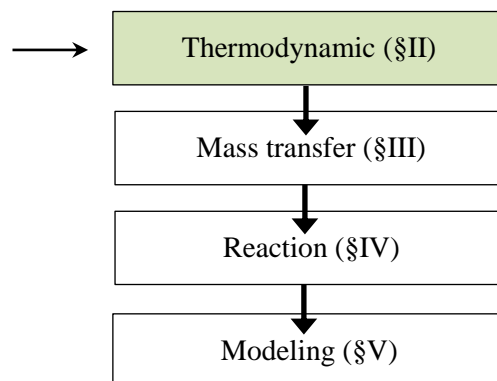


Figure II.1: Manuscript’s guideline.

II.1 Introduction

In general, the processes shifted to unconventional conditions (high-pressure and/or supercritical) involves the study of complex mixtures [often more than six components (Gendrineau et al., 2012; Phiong et al., 2003)]. The determination of the LV and critical data for these mixtures is not always an easy task (Juntarachat et al., 2013, 2012). A possible way to overcome the lack of data is to predict the phase behavior by calculations (Heidemann and Khalil, 1980; Henderson et al., 2010; Jaubert and Mutelet, 2004; Justo-García et al., 2008; J.-W. W. Qian et al., 2013). The EOS can reasonably predict phase behavior for synthetic mixtures (Jaubert et al., 2011; J.-W. W. Qian et al., 2013), because compositions are known and there are no chemical impurities. In industrial mixtures, this is not always the case (Rolland, 2014). The mixtures, such as C₃ cut, have a wide number of compounds, which are difficult to identify and quantify. Since unknown compounds can have an impact on the fluid behavior and properties, it is necessary to perform experimental studies to check phase behavior.

To be able to understand multicomponent industrial mixtures (such as C₃ cut) in supercritical medium, perhaps there is no need to conduct a vast number of experiments. If the experiments are planned (“design of experiments”^a), the total experimental runtime required for each multicomponent system can be significantly reduced. Moreover, if new phase behavior technologies based on microfluidics (micro-scale tools) can be used, the experimental time can be further reduced. Thus, the present chapter is devoted to:

- a) Verify the most reliable thermodynamic model to predict critical points for hydrocarbons mixtures containing light compounds (hydrogen, nitrogen, CO₂ and H₂S). **Keywords:** EOS; critical points; Heidemann and Khalil
- b) Develop a methodology to plan experiments based on thermodynamics and cubic interpolation (§II.3). **Keywords:** critical points; ternary diagrams
- c) Develop a microfluidic approach for thermodynamic studies (§II.5). **Keywords:** microfluidics; high-pressure; high-temperature; dew point; bubble point
- d) Evaluate the critical points for industrial C₃ cut mixtures. Define the pilot plant operating conditions (§II.6). **Keywords:** critical points C₃ cut; supercritical operating conditions

II.2 Supercritical solvents for C₃ cut

As previously detailed (§I.4.2), the C₃ cut is a multicomponent mixture mainly composed by: propylene (~92 mol%), propane (~4.0 mol%), methyl-acetylene (~2.2 mol%) and propadiene (~1.8 mol%). In reaction conditions, the C₃ cut is mixed with hydrogen (>3 mol%) and only

^a optimal number of points necessary to understand the critical behavior.

less than 1 mol% of hydrogen is solubilized at 20 bar (§I.5.4). Some authors reported that it is possible to have a single-phase medium for propylene + hydrogen at high pressure (Williams and Katz, 1954b). Besides this information, as far as we know, there is no additional experimental data available in the literature for C_3 - H_2 based mixtures at high-pressure conditions. For supercritical conditions, the only data found is related with propylene + hydrogen critical points (Burriss et al., 1953a). According to their results, high temperatures are required to achieve supercritical conditions for the composition necessary in hydrogenation ($x_{H_2} < 10$ mol%). These temperatures are out of the admissible operating ranges ($280 < T$ (K) < 350) (Wu and Li, 2011). In order to achieve supercritical conditions with softer temperatures (Hitzler et al., 1998; Savage et al., 1995a), the C_3 cut + hydrogen mixture could be combined with a solvent, knowing that it will increase the final mixture complexity (from 4 to 6 species). Different solvents may be suggested to mix with C_3 cut + H_2 , such as non-polar solvents (e.g. CH_4 , CO_2 , ethane, butane, pentane, hexane and octane). Since there is no critical data available for C_3 cut + hydrogen + solvent, the earlier choice of the solvents was based on literature experimental data for binary mixtures containing propane (Figure II.2). From the previous range of solvents, only a few solvents fit the necessary working range ($273 < T$ (K) < 333) and, therefore, only a few can be applied.

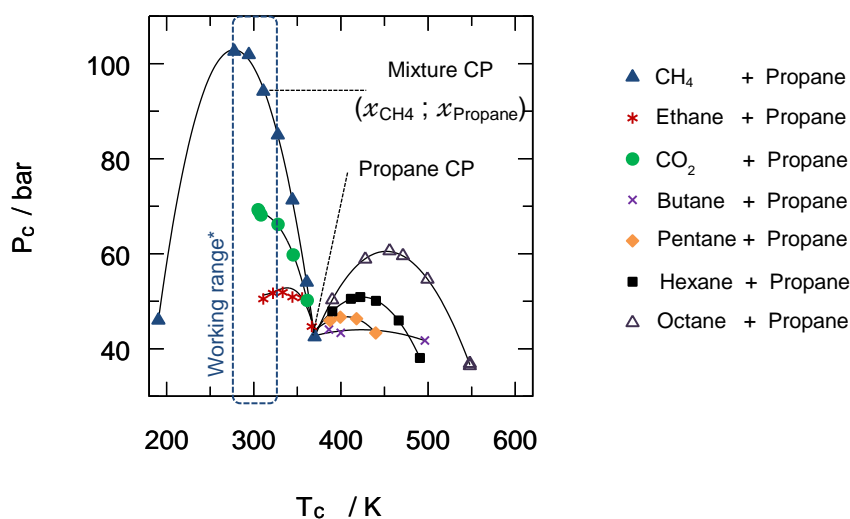


Figure II.2: Critical locus curve for propane containing binary mixtures [from Ortiz (2001) database]. The points presented are experimental points and the lines are fitted curves (to clarify the critical curve behavior). CP: critical point. *Expected temperature-working zone for hydrogenation.

According to the critical locus (Figure II.2), the solvents with admissible operating ranges are CH_4 , ethane and CO_2 . From Konynenburg and Scott (1980) classification system (§I.6.4):

- propane + CH_4 is type V (liquid-liquid immiscibility at high temperatures with the intersection of liquid-vapor curves).
- propane + ethane is type I (complete miscibility of the liquid phase and continuous critical curves).
- propane + CO_2 is type II (liquid-liquid immiscibility from low temperatures to high temperatures).

Regarding propane + CH₄ closely, the mixture critical pressures are higher than the actual critical pressures for the pure species, which is typical for (example) type V. Since the catalyst activity is normally more sensitive to temperature than to pressure, the solvents with higher critical pressures are not rejected (pressure is not a problem for the set-up up to 200 bar).

For hydrogen + solvent and hydrogen + propylene (dominant species in the C₃ cut), it is anticipated to have binaries of type III. This means that the system has a discontinuity in the critical locus. Moreover, the critical pressure near the discontinuity will be significantly increased (Grunwaldt et al., 2003b; Privat and Jaubert, 2013). Burriss et al. (1953) and Ke et al. (2001) reported that the discontinuity for hydrogen mixture is localized beyond 20 mol%. Figure II.3 shows that the addition of hydrogen to a solvent or propylene only has an impact on the critical pressure. In this way, the choice of the solvent should only be based on the interaction between solvent and C₃ cut. Therefore, it was decided to evaluate firstly the critical behavior of the C₃ cut with CH₄, ethane and CO₂.

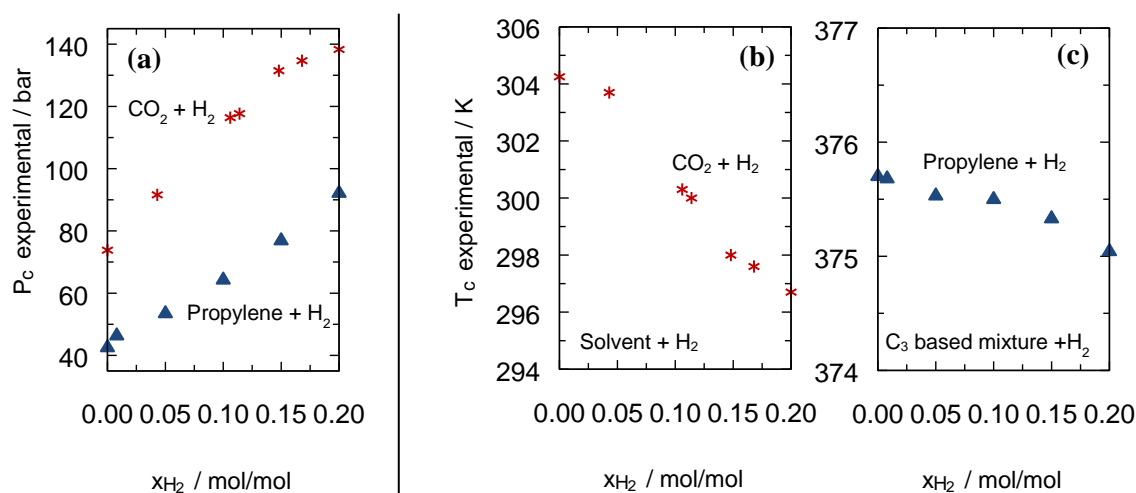


Figure II.3: Experimental critical pressure (a) and temperature (b, c) for hydrogen containing binary mixtures: $CO_2 + H_2$ [* (Ke et al., 2001)] and propylene + H_2 [▲ (Burriss et al., 1953a)].

The Figure II.2 and Figure II.3 give hints about the solvents to choose, but they cannot provide the operating conditions to perform the reaction. To have it, it is necessary to evaluate the critical locus for all the known species present in it (industrial multicomponent mixture: C₃ cut). So, firstly the critical locus was evaluated using thermodynamic models (§II.3) and then by experiments (§II.5). The thermodynamic model will help to define the tests required.

II.3 Algorithm and approach for “design of experiments”

II.3.1 Introduction

For industrial mixtures, it is often required to acquire experimental critical data to enhance phase behavior studies and to improve the thermodynamic model (estimate model parameters) (Horstmann et al., 2001). The model parameters are mainly obtained by optimization of binary mixtures, *e.g.*, estimation of k_{ij} parameters (§I.6.4 and Appendix

§II.3). Indeed, models such as PPR78, which has been developed by Jaubert and co-authors (Jaubert et al., 2005; Juntarachat et al., 2013; Qian et al., 2012; J.-W. W. Qian et al., 2013), is based on this methodology.

Figure II.4 shows the approach adopted to study critical data.

Steps 1 and 2: Experimental input (binary, ternary, ...) and model. When studying binary mixtures, it is possible to notice the critical trends, being possible to anticipate experiments with or without a model. In contrast, multicomponent mixtures trends are difficult to foresee, even with the help of a model.

Step 3: A thermodynamic methodology was developed to predict the optimal number of critical points necessary to experimentally characterize the critical locus (Figure II.4: step 3). This methodology will save experimental time when investigating complex (industrial) mixtures.

Step 4: Validate the approach by checking if the industrial mixture is well represented by the ternary diagram proposed (with the optimal number of points).

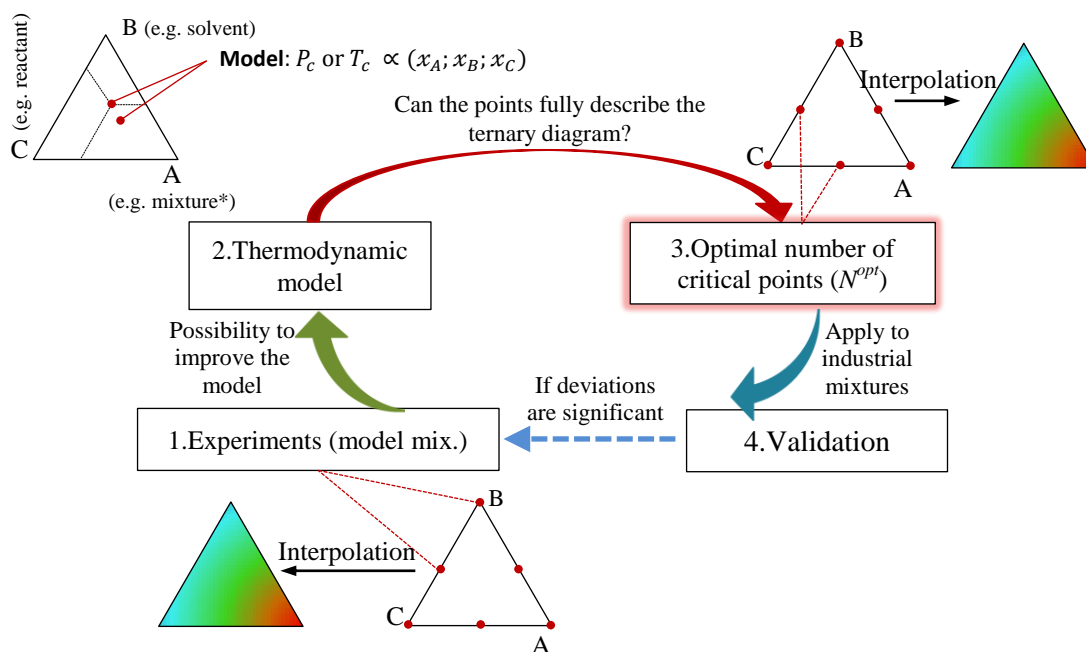


Figure II.4: Approach suggested based on the ternary diagram. * studied mixture

In this subchapter, we will focus on the steps 2 and 3.

II.3.2 Methodology

The aim of this subchapter is to propose a thermodynamic method to evaluate the optimal number of critical points necessary to experimentally characterize the critical locus. This will

save experimental time when investigating industrial mixtures (see strategy scheme: Figure II.5).

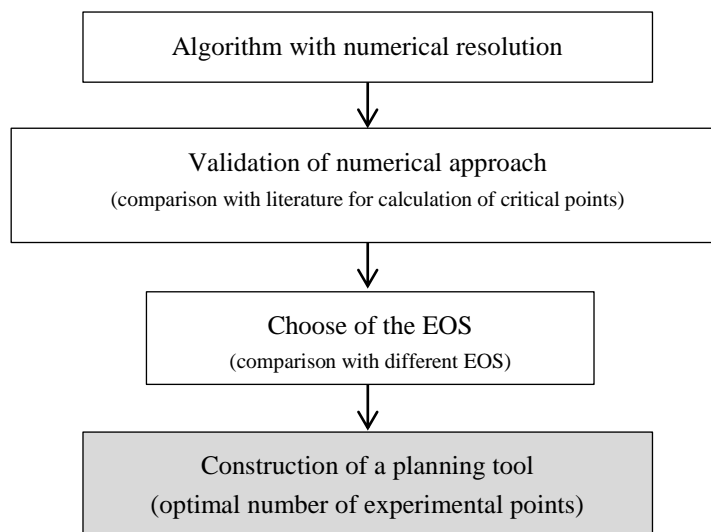


Figure II.5: Strategy adopted to acquire the (theoretical) minimum number of experimental points (gray).

The tool is based on ternary diagrams constructed by interpolation of calculated critical points for multicomponent mixtures. To calculate the critical points, an algorithm was built based on (i) Heidemann and Khalil (1980) formulation, (ii) Stockfleth & Dohrn (1998) numerical derivatives and (iii) Hoteit et al. (2006) efficient and robust algorithm proposition. The knowledge introduced by those authors was coupled with the algorithm. The main advantages are the small time-consumed and the flexibility (possibility to rapidly change the equation of state). For instance, it is easy to implement the PPR78 EOS (Jaubert et al., 2005), which extends the PR78 range of applicability. [More precisely, the PPR78 takes into account the temperature dependence of the k_{ij} (binary interaction parameter)].

In this work, PPR78 and several equations of state based on the cubic type were compared: PR78, PRSV-2 and VTPR. According to Justo-García et al. (2008) study, these kind of equations can provide feasible results, depending on the mixture system. For mixtures with hydrocarbons, they obtained results with equal or better accuracy than advanced molecular equations of state as PC-SAFT. Their explanation was that the fitting parameter (k_{ij}) puts the cubic equations closer to the experimental results.

II.3.3 Critical point determination for multicomponent mixtures: state of the art

Heidemann and Khalil (1980) proposed an algorithm based on Gibbs theory for critical phase, in which the critical point must lie on the stability limit. The authors created an algorithm with two constraint equations deduced from the critical stability. When a system is stable, shifting from near thermodynamic states lead to small variations in thermodynamic parameters (e.g. ρ and μ). When a system is unstable, shifting from near thermodynamic states lead to important variations (§I.6). These important variations define the critical coordinates (P_c and T_c).

From a thermodynamic point of view, the Helmholtz energy can be expressed by a derivative of the fugacity, which can be analytically or numerically determined. Several equations of state (EOS) were used to calculate the fugacity: (i) PR78 (Heidemann and Khalil, 1980; Stockfleth and Dohrn, 1998), (ii) SPHCT (García-Sánchez and Ruiz-Cortina, 1992) and (iii) PC-SAFT (Justo-García et al., 2008). However, changing the EOS is not an easy task because it requires huge modifications in the algorithm resolution. For instance, each time the EOS is changed it is mandatory to derivate analytically all the equations and to change a huge part of the source code. So, to solve this problem, a specific approach developed by Stockfleth & Dohrn (1998) was proposed: they have proposed to numerically derivate fugacity by constructing matrices based on four-point derivative scheme.

In the Heidemann and Khalil (1980) article, the algorithm convergence was assured by 1D Newton-Raphson method. However, this method is not sufficiently robust and computationally time-efficient for mixtures with a large number of components (Hoteit et al., 2006; Stradi et al., 2004). To correct these problems, Hoteit et al. (2006) proposed modifications to the algorithm searching process, using a better initial guess search and Brent hybrid method (Brent, 1973; Zhang, 2011). The Brent method combines three different approaches: bisection method, secant method and inverse quadratic method. This methodology was chosen to ensure the convergence of our general algorithm.

II.3.4 Algorithm

This subchapter is divided into three main parts:

- **Algorithm formulation** (Figure II.6), with the description of several EOS.
- **Results section**, where the validation of the algorithm, the study of the influence of cubic equations of state and the creation of ternary diagram tools are presented.
- **Discussion section**, which aims to analyze in details the ternary diagram tool.

The algorithm formulation is divided in:

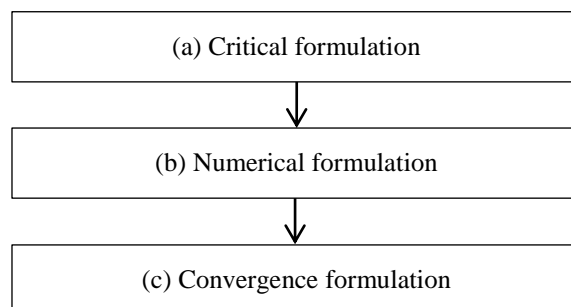


Figure II.6: Algorithm formulations. For more detailed information about the algorithm, please see the appendix.

The details of each formation are presented in Appendix §II.1 and §II.2.

II.3.5 Results

In this subsection, the results will be presented, being divided in: (a) algorithm validation, (b) comparison of cubic EOS and (c) experimental planning tool.

a) Algorithm validation

The algorithm was created in Matlab[®] V8.0. Its validation was made by comparison between results with PR78 EOS and literature data for several mixtures: hydrocarbon mixtures (from methane to heptane) + N₂ (Henderson et al., 2010), CH₄ + H₂S (Stradi et al., 2004), H₂ + CO₂ (Ke et al., 2001) and cyclohexane (CYC) + CO₂ (Zhang et al., 2005). Thus, the algorithm was subjected to binary, ternary, quaternary and quinary mixture systems to check the reliability of results with multicomponent systems. Indeed, even if the methodology proposed later in this subchapter is based on ternary system diagrams, our goal is to study critical points in a distinct type of mixtures (similar to C₃ cut mixture). The pure component data used for the calculations (the acentric factors, the critical points and interaction parameters) was obtained directly from literature (Table II.1 and Table 3 [Appendix §II.3]). The comparison between literature experimental critical points and numerically calculated ones is shown in Figure II.7.

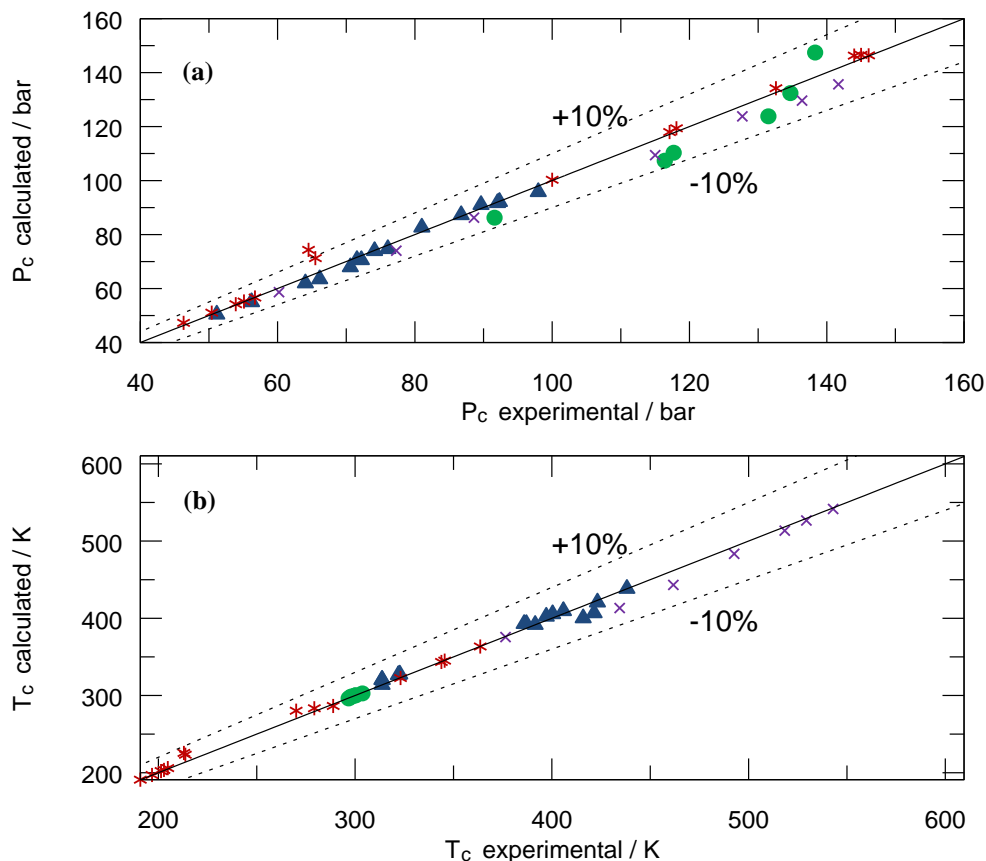


Figure II.7: Comparison of critical pressures (a) and temperatures (b) calculated using PR78 and Van der Waals mixing rules with literature experimental data (42 critical points): (▲) C₁ to n-C₇ and N₂ mixtures by Henderson et al. (2010); (*) CH₄ and H₂S mixtures by Stradi et al. (2004); (●) H₂+CO₂ mixture by R. Zhang et al. (2005); (×) CYC+CO₂ mixtures by Ke et al. (2001).

Figure II.7 shows that the algorithm is good enough to be used to predict the experimental critical point, being capable of providing feasible critical point values even for

multicomponent mixtures. For type I-II mixtures (mostly hydrocarbons mixtures), the maximum relative error is around 3% for critical pressure and temperature. For more complex types of systems (type III), such as H₂+CO₂, the maximal relative deviation is 6% for pressure and 0.1% for temperature. Until a H₂ molar fraction of 0.20, the mixture has small deviations from the calculated value, but when increasing the quantity of H₂, the deviation rises. The algorithm quality is not affected by this deviation because it is punctual, and it is caused by the large size difference between CO₂ and H₂ molecules (Ke et al., 2001).

For the 42 critical points analyzed, the average relative deviation (ARD) is 2.9% in pressure and 1.8% in temperature. Justo-García et al. (2008) obtained similar deviations when using PC-SAFT EOS for hydrocarbons. Their results endorse the choice of a cubic EOS, such as PR78. The PR78 EOS will be compared with other equations of state to check if the average deviations can be reduced.

Table II.1: Critical properties of pure compound.

<i>N</i> ^o	<i>Component</i>	<i>T_c /K</i>	<i>P_c /bar</i>	<i>w</i>	<i>Reference</i>
1	Methane	190.6	47.0	0.008	Henderson et al. (2010)
2	Ethane	305.3	48.8	0.099	Henderson et al. (2010)
3	Propane	369.8	42.4	0.152	Henderson et al. (2010)
4	Butane	425.2	38.0	0.199	Henderson et al. (2010)
5	Pentane	469.6	31.7	0.251	Henderson et al. (2010)
6	Hexane	507.3	29.7	0.293	Pro/II [®] database
7	Heptane	540.2	27.4	0.350	Henderson et al. (2010)
8	Nitrogen	126.2	33.9	0.040	Henderson et al. (2010)
9	Carbon Dioxide	304.2	73.8	0.177	Pro/II [®] database
10	Hydrogen	33.2	18.0	-0.220	Pro/II [®] database
11	Cyclohexane	556.4	42.0	0.205	Pro/II [®] database
12	Hydrogen sulfide	373.5	90.1	0.087	Pro/II [®] database

The interaction parameters are presented in Appendix §II.3.

b) Comparison of cubic EOS

Potential models

There is a huge number of models that can be used with the previous formulation. In general, EOS as NTRL, UNIQUAC, UNIFAC and SAFT are interesting due to their reliability when predicting equilibrium for a large number of mixtures. Although these are very reliable EOS, the critical point can also be successfully calculated with cubic EOS, which provides good predictions for T_c and P_c in short times (Jaubert et al., 2005).

Cubic EOS were selected to calculate the critical points due to their reliability and small inputs. Four cubic EOS were tested: (i) PR78 (Robinson et al., 1977), (ii) PRSV-2 (Abu-

Eishah, 1999), (iii) VTPR (Tsai and Chen, 1998) and (iv) PPR78 (Jaubert et al., 2005), see §I.6.4 and Table I.15. Even if an EOS is not suitable for one type of liquid-vapor system, it can be better for other systems. Therefore, different equations of state should be tested.

As we are mostly interested in hydrocarbon mixtures, EOS were compared for such systems. About hydrogen-based mixtures, Qian et al. 2013 presented numerous equilibrium liquid-vapor comparisons of PR78 with experimental results. In their work, they have generated k_{ij} parameters depending on the temperature and the type of molecules (group contributions). The results have good agreement with literature data at low fractions of hydrogen.

For middle/high molar fraction of H_2 (> 0.3) the critical pressure becomes quickly too high (>300 bar) with small molar variations of H_2 . Thus, the model has difficulties in predicting the critical point. Despite this minor limitation, these molar fractions are rarely used. At a low molar fraction of H_2 , the results are accurate, which is our case (< 0.3).

Choice of EOS

All the EOS have similar deviations (predicted vs experimental), with the exception of the VTPR correlation (Figure II.8a). This means that the modified parameters of the cubic equation do not have a huge impact on the results for the critical point (in the mixtures analyzed).

Among these equations, the selection criterion was to limit the required parameters, which have to be easily found in the literature. The PRSV-2 EOS parameters are hard to find in literature. Therefore, it is not very suitable to be used. Between the two remaining EOS [Figure II.8(b) and (c)], the PR78 and PPR78 were confronted with 255 hydrocarbons (experimental) binary mixtures [database collected by Ortiz (2001)]. Based on those results, the PPR78 was chosen, because it has less deviation than PR78. In addition, the interaction parameters (k_{ij}) are determined by group contributions, and it takes into account temperature variations. Since k_{ij} varies with temperature, the results can be more accurate than with constant k_{ij} values (used in PR78), even if in the validation cases, these differences are not straightforward. Moreover, when the PPR78 EOS is employed in the algorithm, the initial guess ($T_{c,0}$ and $P_{c,0}$) needs to be close to the final result to assure the convergence of the system.

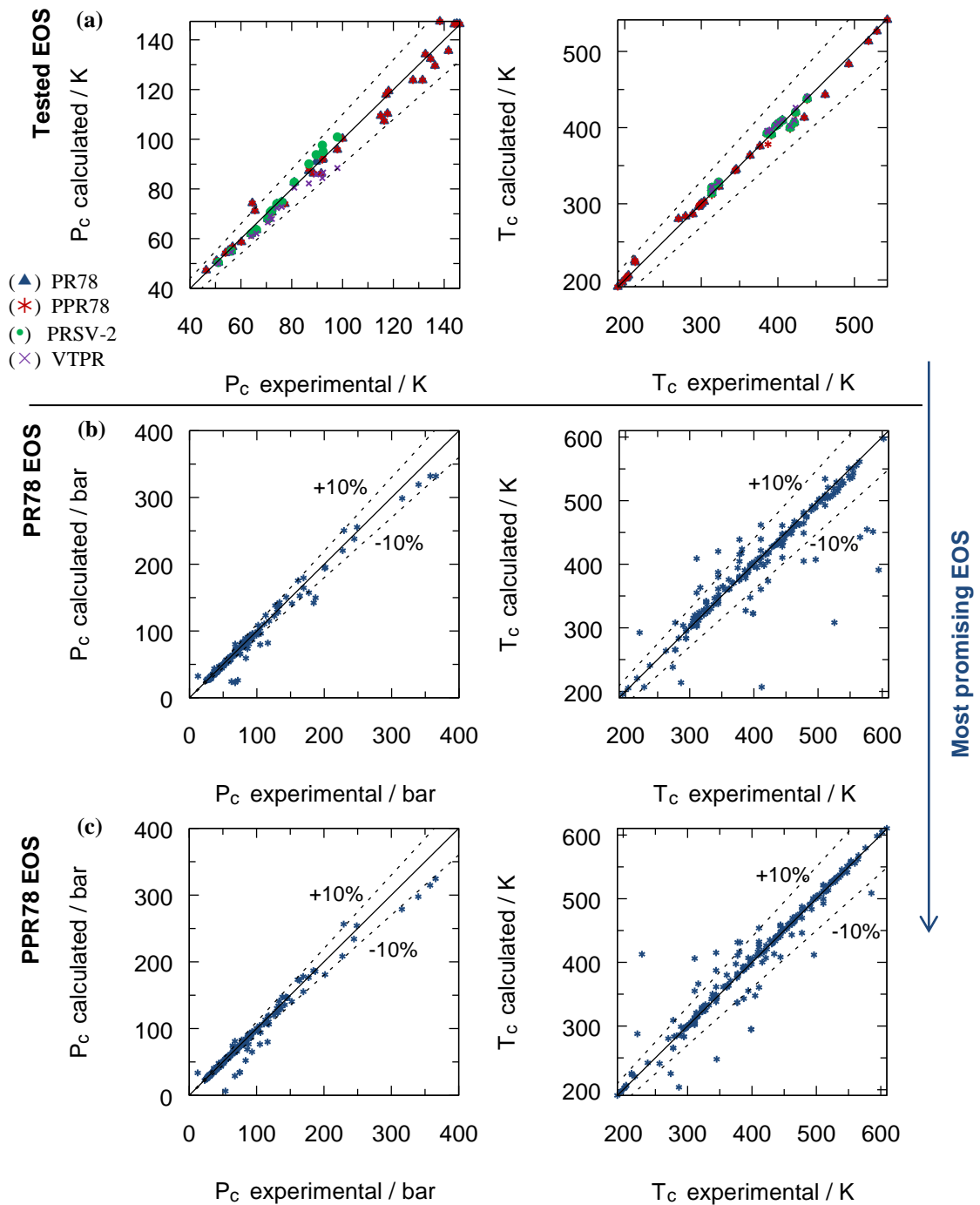


Figure II.8: (a) Comparison of critical P and T calculated using 4 EOS and Van der Waals mixing rules with literature experimental data (Henderson et al., 2010; Stradi et al., 2004; Tsai and Chen, 1998) – best results for PR78 and PPR78 [parameters Table II.1 and Table 3]. Comp. of PR78 (b) and PPR78 (c) calculated data with experimental data [255 binary hydrocarbon containing mixtures from Ortiz (2001) database and sources presented in (a)].

c) Experimental planning tool

A ternary diagram can be used to simplify the data interpretation for multicomponent mixtures. It is constructed with fluid compositions (three coordinates) and mixture critical pressure or critical temperature (isolines). For mixtures with more than 3 compounds, it is

often possible to split them into three representative mixtures (studied mixture=A+B+C), upon which it is intended to vary compositions. Therefore, for reactions with solvent, the ternary diagram will be characterized as industrial mixture (A) + solvent (B) + main reactant (C). Looking closely to Figure II.9, at each corner of the triangle there are critical pressures and temperatures for each fluid studied (A, B and C). In the triangle sides, there are binary diagrams (P_c or T_c for binary combinations: A+B, B+C and C+A). Finally, the delimited area has values for P_c or T_c for the ternary combination, A+B+C.

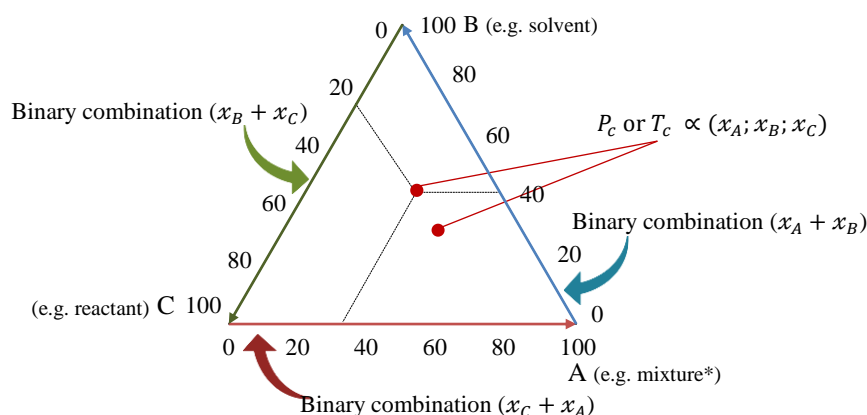


Figure II.9: Schemate of a ternary diagram to evaluate critical pressure or critical temperature.

If a minimal of points is placed in this area, it should be possible to evaluate P_c or T_c values for all the area by interpolation. The objective is to identify the thermodynamic optimal number of points to have a good picture of the diagram, as to precise the number of experiments needed and thus to reduce the experimental work.

Interpolation

To obtain an acceptable ternary diagram, our strategy was to create a data set of N points and guess intermediate points with interpolation methods via Matlab[®] (*scatteredInterpolant* function). The quality of the interpolation (fit) analysis is highly dependent on the data set applied, which is characterized by a set of positions and the total number of points. The generated diagram typically has higher quality for large data sets than for small. Additionally, the data set has to be carefully chosen, depending on the type of binary systems studied (Konynenburg and Scott, 1980). For instance, a ternary diagram with type I binary combinations needs fewer points than a diagram with type III + type III + type I binary combinations. This is related to the surroundings of discontinuities regions (sudden increase of pressure), which renders difficult to interpolate/extrapolate.

Two different methodologies were considered to find the optimal number of points (N^{opt}) based on a data set proposed. In the first one, the ternary diagram is divided into several equilateral triangles (Table II.2-Method I). In the second one, the data set points are obtained based on pressure and temperature gradients (Table II.2-Method II). To quantify the quality of the interpolation method, the relative deviation between fitted and non-fitted points (both outside the data set) was quantified. In other words, at each query point specified ($x_A; x_B; x_C$) outside the data set (N points), there should be a fitted value and a value obtained by

calculation of critical coordinates. The average deviation of critical temperature and pressure is defined as:

$$AARD_{T,i} (\%) = \frac{1}{\mathcal{M}} \sum_{i=1}^{\mathcal{M}} |T_{c \text{ fitted},i} - T_{c \text{ non-fitted},i}| / T_{c \text{ non-fitted},i} \times 100 \quad \text{Eq. II.1}$$

$$AARD_{P,i} (\%) = \frac{1}{\mathcal{M}} \sum_{i=1}^{\mathcal{M}} |P_{c \text{ fitted},i} - P_{c \text{ non-fitted},i}| / P_{c \text{ non-fitted},i} \times 100 \quad \text{Eq. II.2}$$

where the subscript *fitted* and *non-fitted* represent fitted and non-fitted points. For the total points compared (\mathcal{M}), we considered that 351 equally distant points (n=26 divisions) are enough to discretize the ternary diagram (Figure II.10 c). The global strategy adopted was:

- A. Discretize the ternary diagram in 351 points (\mathcal{M}) and evaluate their critical coordinates with an equation of state (*e.g.* PPR78);
- B. Guess a number of points (N) required to represent the ternary diagram;
- C. Evaluate the proposed N points with an equation of state;
- D. Make the interpolation of the N points using Matlab[®] (Figure II.10 d);
- E. Compare the values interpolated values with the 351 values previously calculated;
- F. If N points cannot give acceptable deviations, the number of points guessed in step B should be increased.

To obtain the optimal number of points, the methodologies I and II were adopted:

Table II.2: Methodologies taken to estimate the optimal number of points.

Method I (Figure II.10 a)	Method II (Figure II.10 b)
<p>Guess points according to the sum of n natural numbers:</p> $N = \sum_{i=1}^n i = \frac{n(n+1)}{2} \quad \text{Eq. II.3}$ <p>where n is the number of divisions for each binary combination.</p>	<ol style="list-style-type: none"> I. Construct a distance matrix \mathbf{d} between points. The distance for each point (i) to all the data set (j) is presented by $d_{i,j}$; II. At each point, calculate $\nabla \mathbf{P}_C$ and $\nabla \mathbf{T}_C$ for the full ternary diagram (∇ is the first derivative related to the total distance [d]); III. From the 351 points, a point is eliminated if $d_{ij} < 2\% \min \mathbf{d} \wedge \nabla \mathbf{P}_C < \min \nabla \mathbf{P}_C \wedge \nabla \mathbf{T}_C < \min \nabla \mathbf{T}_C$.

The proposed methodologies are presented in the next figure.

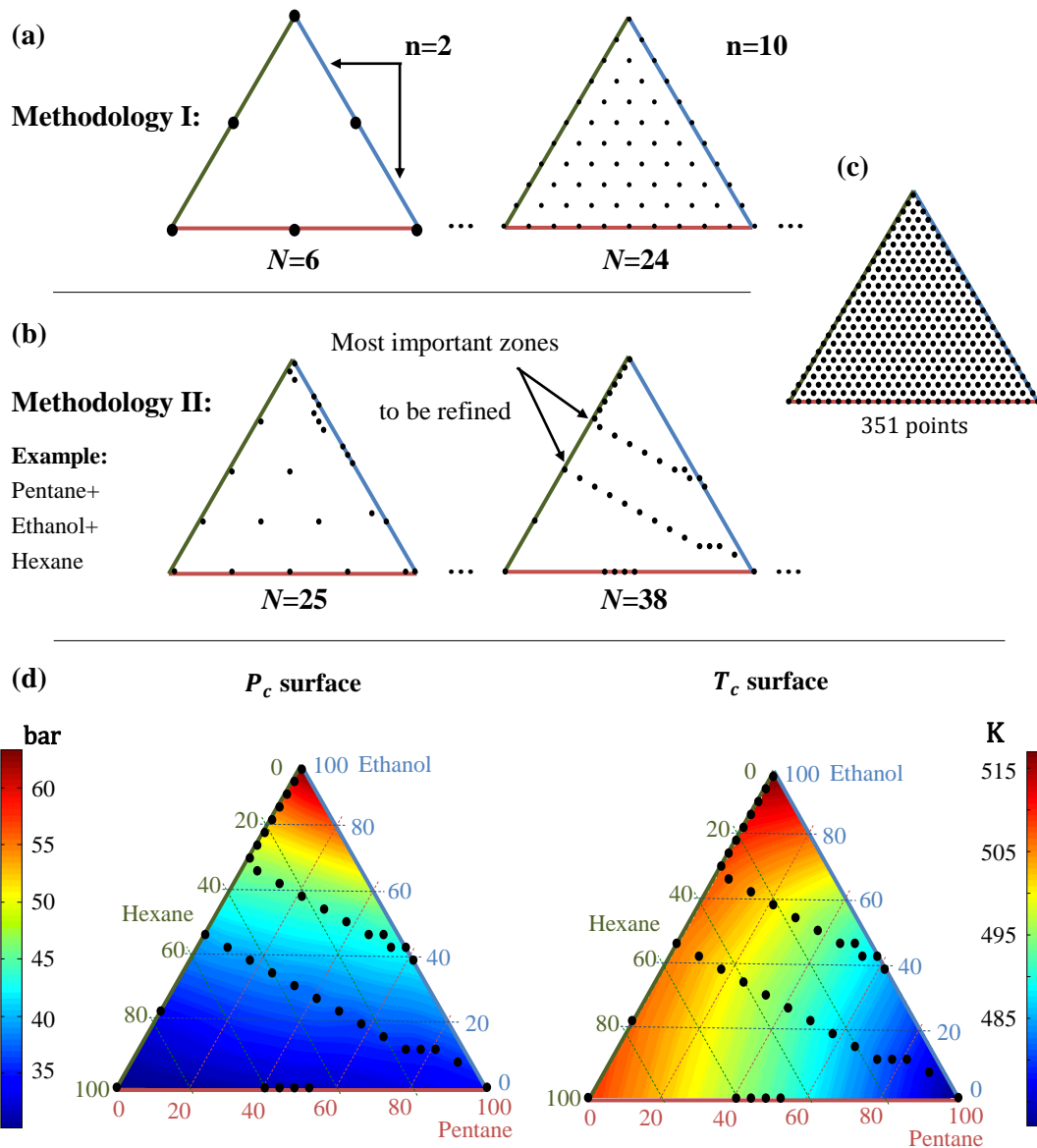


Figure II.10: (a) Division of the ternary diagram in N equally distributed points (methodology I); (b) Division of the ternary diagram in N points obtained by gradient methodology (II); (c) Maximum discretization of the ternary diagram, 351 points; (d) Strategy applied to obtain the interpolated points. The ternary contours are based on $N=38$ points for the mixture Pentane + Ethanol + Hexane.

Several ternaries with known binary combinations types were tested to understand the variation of the number of optimal points (N^{opt}) with the type of ternary combinations. The mixtures tested are composed of hydrocarbons, H_2S and CO_2 (listed in Table II.3). For the systems type with discontinuities, only the continuity zones were quantified.

Table II.3: Type of ternary mixtures systems analyzed. The binary mixtures types are according to Konynenburg & Scott classification system.

Types				System components		
A/B	B/C	C/A	A/B/C	A	B	C
I (c)	I (c)	I (a)	I	Pentane	Ethanol	Hexane
I (c)	I (a)	I (e)	I	Propane	H ₂ S	CO ₂
I (c)	I (c)	I (a)	I	Ethane	Toluene	Propane
II (b)	I (c)	II (b)	II	CO ₂	Ethane	Benzene
III (a)	III (a)	I (a)	III	Ethane	Methanol	Propane
I (a)	III (c)	III (c)	III	Ethane	Methane	NH ₃
II (b)	II (a)	V	V	Ethane	CO ₂	Octane

The optimal number of points is reached when the average relative deviation is achieved. In this case, it was considered being acceptable at 5%, because it seems sufficient for most applications. According to Figure II.11 – methodology I, for systems analyzed based on combinations of types I, II, III and V it is necessary to have $N=10$, $N=36$, $N=66$ and $N=21$, respectively. In the case of type I ternary, $N=10$ is an unexpected result, because there is only a need to have one value of the ternary mixture. The N increases from type I to type III, due to the increase in system complexity. In the particular case of type III, there are discontinuities (for more information §I.6.4).

Regarding Figure II.11, between the methodologies I and II, there is not a striking difference for N^{opt} . The choice of the methodology depends on the region of interest. If the region is close to a discontinuity, the methodology II should be adapted rather than methodology I, because the discontinuity surrounded region will be well refined.

Occasionally, the increase of the number of points leads to a punctual increase of the average relative error, more prominently for the methodology I with type III based ternaries. This difference is because the data set coordinates can fall in the zone immediately before the discontinuity, so the interpolation values will be affected.

The N values proposed can be only for systems where the sides of the ternary diagram are binary combinations (each corner is a pure fluid). For more complex systems, the N values can be predicted by applying the algorithm previously detailed (at least one corner is a mixture). For example, propane (in a corner) can be replaced by C₃ cut.

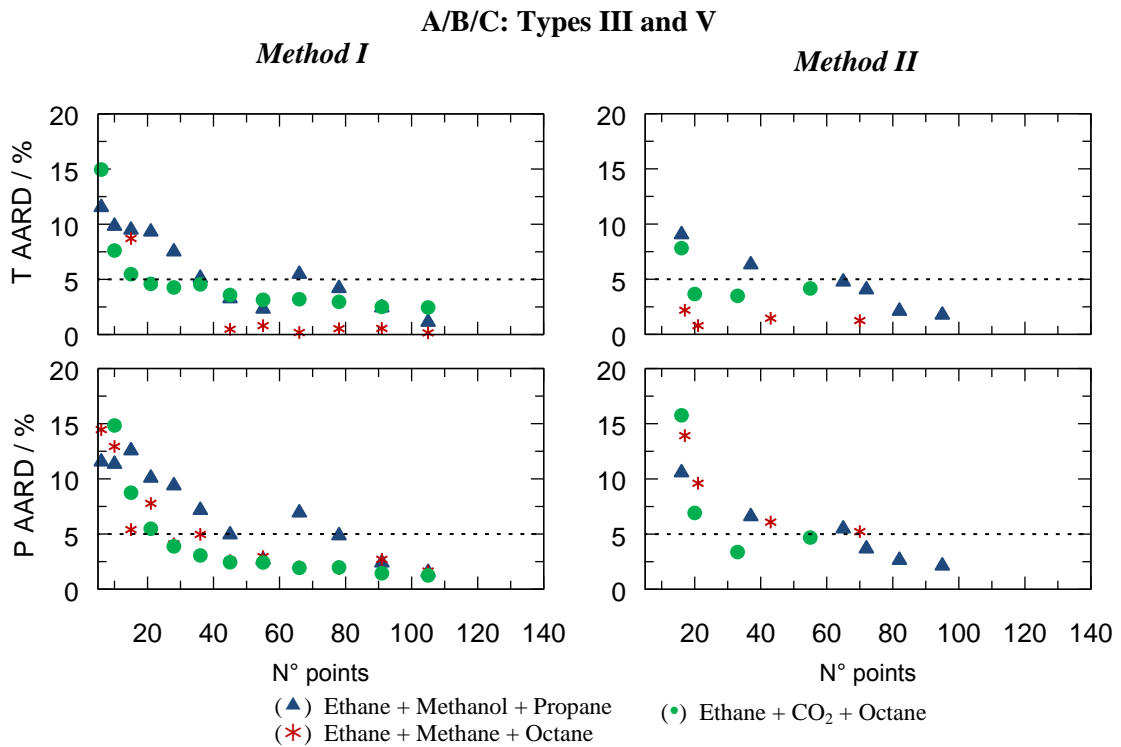
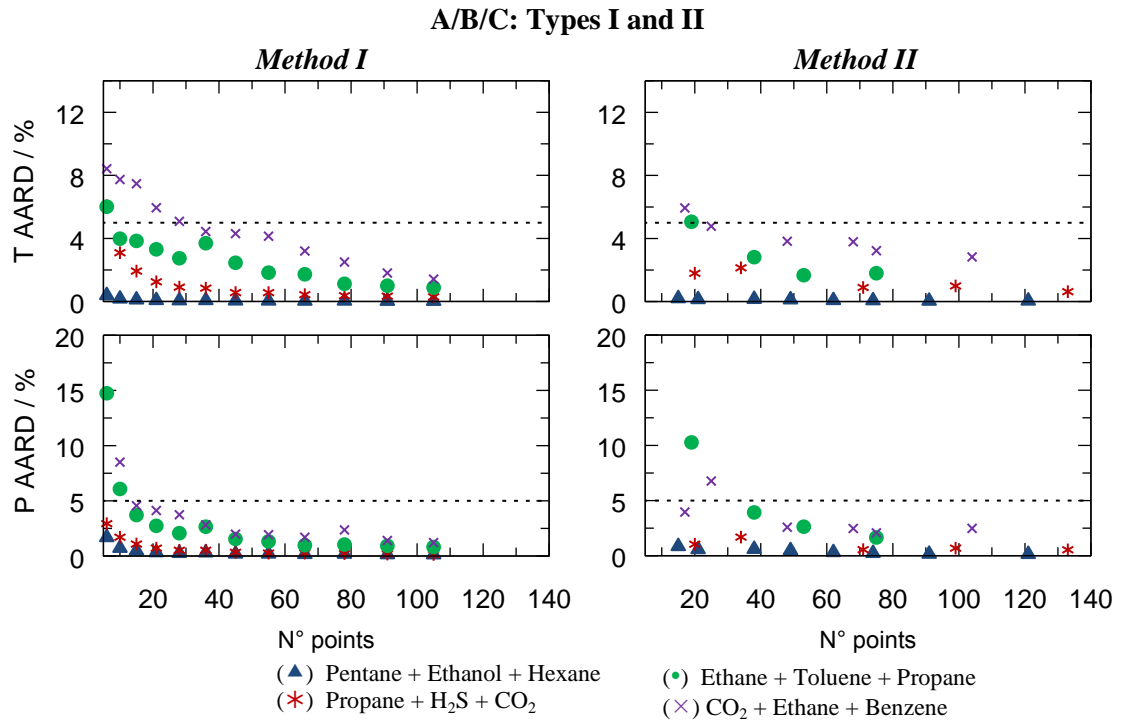


Figure II.11: Comparison of different types of ternary systems in terms of relative deviation. The dashed line indicates the maximum deviation of 5%. The results were obtained for a full ternary diagram.

II.3.6 Discussion

In this section, the strategy presented to determine the optimal number of experimental points (N^{opt}) is put into practice. Firstly, a case where the fitted ternary helps to save experimental time is presented. Then, we will go further by applying the construction of ternary diagrams to obtain the working zone.

Experimental application

As an example of application, ternary mixtures (with literature critical experimental data) was studied (Pentane + Hexane + Ethanol). This system is based on type I binary combinations. Therefore, there is no need to have more than 10 points evaluated to ensure a proper fitted ternary diagram (AARD below 5%). Therefore, an interpolated ternary diagram has been constructed based on 10 experimental points obtained from Soo et al. (2010). After construction, the fitted ternary diagram was then compared to additional experimental points (33 points more, Soo et al. (2010)). The comparison of the binary critical locus is shown in Figure II.12a. For the ternary mixture points, the critical temperature and pressure are illustrated in Figure II.12b-c and Table II.4.

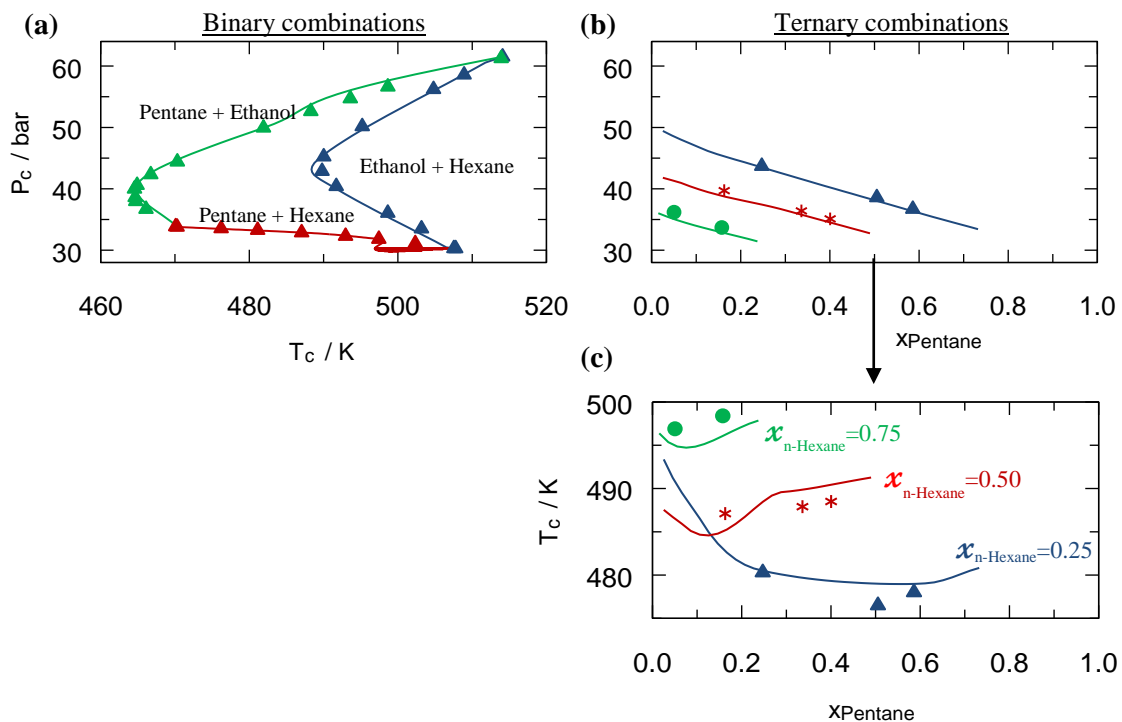


Figure II.12: (a) Binary critical locus for comparison between fitted points (base $N=10$) and experimental data (Soo et al., 2010). (b/c) Critical pressure and critical temperature for ternary mixtures with constant n-Hexane fraction (\blacktriangle $x_{n-hexane}=0.25$; $*$ $x_{n-hexane}=0.50$; \bullet $x_{n-hexane}=0.75$). The lines are the values evaluated by ternary interpolation, and the dots are literature experimental data (Soo et al., 2010).

Table II.4: Overview of some experimental and fitted critical points for ternary pentane + ethanol + n-hexane. The x_1 and x_2 are the composition of pentane and ethanol, respectively.

		Interpolation		Literature(Soo et al., 2010)		ARD (%)	
x_1	x_2	T_c (K)	P_c (bar)	T_c (K)	P_c (bar)	T_c	P_c
0.14	0.59	483.5	45.3	485.0	45.7	0.3	0.9
0.14	0.86	491.1	54.8	498.7	56.6	1.5	3.3
0.33	0.67	481.2	49.2	481.9	49.9	0.2	1.4
0.34	0.16	490.1	35.7	487.9	36.4	0.4	1.9
0.58	0.42	466.9	42.6	466.7	42.3	0.0	0.5
0.59	0.16	479.6	36.2	478.0	36.7	0.3	1.3
0.87	0.00	475.4	33.7	476.2	33.5	0.2	0.5
0.87	0.13	467.6	36.4	466.1	36.7	0.3	0.8

Figure II.12 and Table II.4 suggest that the fitted ternary values are close to experimental data. The AARD is 1.5% and 0.5% for the pressure and temperature. Thus, the behavior of the ternary system was successfully characterized with only 10 points rather than with 43 [experimentally obtained by Soo et al. (2010)]. With this application case, it is possible to understand the advantage of the approach developed towards reducing the experimental time-consumption.

Working zone

Besides the critical points, a critical ternary diagram can also give information about the supercritical working zone (according to the range of temperature and/or pressure and/or stoichiometry desired in the process). For instance, the ternary diagrams were limited to a working zone:

Table II.5: Two possible restricted operating conditions scenarios.

Cases	Zone 1	Zone 2
A	$\max T_c=493$ K	$\max P_c=40$ bar
B	$\max T_c=498$ K	$\max P_c=50$ bar

The zones limited by constant pressure and temperature were highlighted in the ternary diagram (Figure II.13). The intersection with these zones gives information about the conditions required to be in the supercritical domain. It is also possible to know the maximum composition of each component to be within the supercritical working zone. The great advantage of this type of representation is a fast construction and data interpretation. In this way, the compositions and operating conditions can be easily adjusted to the process needs.

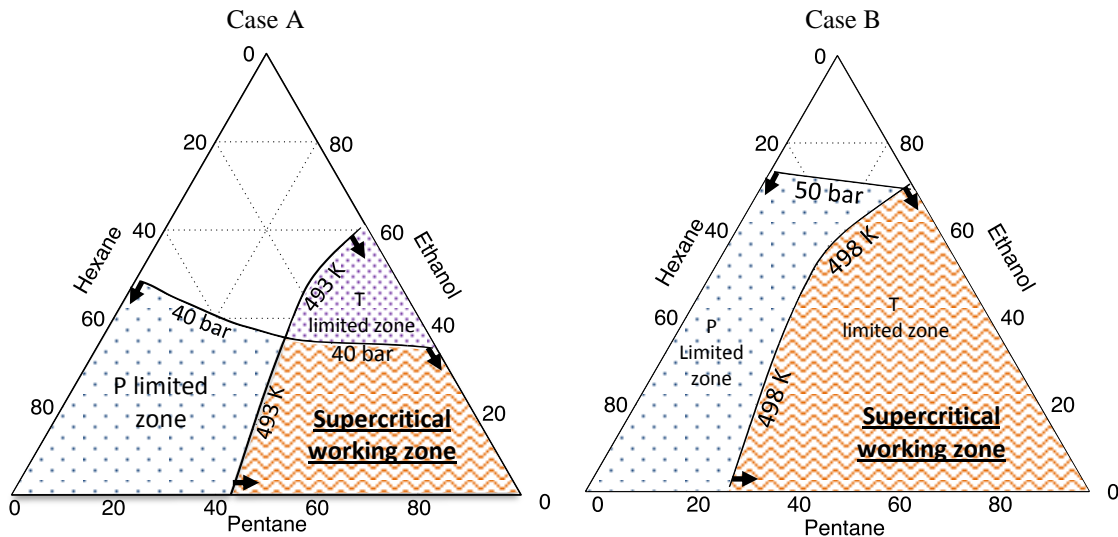


Figure II.13: Identification of the supercritical working zone. Case A: Ternary diagram restricted to 493 K and 40 bar. Case B: Ternary diagram limited to 498 K and 50 bar.

II.3.7 Conclusions

The strategy adopted makes possible to **locate and determine the optimal number of points to construct ternary diagrams for critical pressure and temperature**. The construction and validation of the ternary tool were based on the **PPR78** equation of state. To prove its accuracy, this equation was previously tested for 255 hydrocarbon multicomponent mixtures, providing more reliable results than other EOS. Our approach is simple and can be **applied** to complex types of **ternary and multicomponent systems**.

The influence of the number of points in the fitted surface was discussed. The innovative side is the **capability to relate predicted and experimental values** for mixture system where the access to the overall **composition is not available**. The tool proposed in this subchapter can help experimental and decision procedures. It can also be applied as “**design of experiments**”, in order to know the minimum number of experimental points required.

Furthermore, the fitted values obtained can give sufficient information to identify the operating conditions for restricted chemical processes.

Perspective: The method developed will be used to estimate the number of experimental points needed to characterize the ternary combinations for C_3 cut (C_3 cut + CH_4 + H_2 ; C_3 cut + Ethane + H_2 ; C_3 cut + CO_2 + H_2). The results/model will be described in the next subchapter.

II.4 Estimation of C₃ cut critical points by modeling

As it was explained before (§I.4.2), the C₃ cut is a multicomponent mixture composed by: propylene (PR), propane (PA), methyl-acetylene (MA) and propadiene (PD). The C₃ cut will be combined with hydrogen and a solvent (ternary combination with our methodology), which increases mixture complexity, going from 4 to 6 components (at least). To understand and validate the mixture critical behavior, the following strategy was adopted:

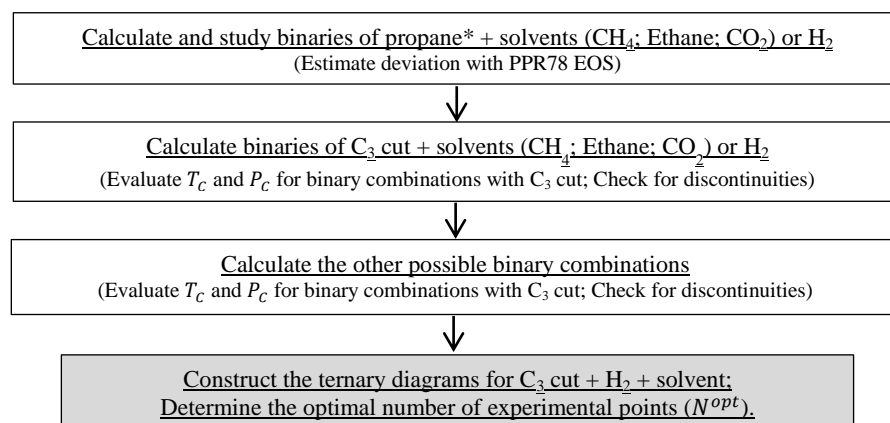


Figure II.14: Strategy applied to determine the optimal number of points for C₃ cut mixture. * the propane is used instead of propylene, because there is more data available in literature

By starting with binary combinations and increasing the complexity in small steps forward, the previous strategy ensures that the ternary diagrams have reliable results. About the hydrogenation of C₃ cut, the H₂ content should be less than 20 mol% [~10 H₂/MAPD ratio (§I.4.2)]. So, instead of having the totality of the ternary diagram evaluated, only a small part was estimated. All the studies proposed were done using the PPR78 equation of state.

II.4.1 Binaries for propane and hydrogen containing mixtures

The results obtained for propane + solvents and propylene + H₂ have an excellent agreement with experimental data (Figure II.15a). The maximum relative error is 0.7% and 1.1% for T_C and P_C, respectively. For hydrogen-containing mixtures, it was expected to have discontinuities because they are classified as type III. But, despite this, there are no discontinuities found for H₂ below 20 mol% (Figure II.15b) and the agreement is still good between experimental and simulated data.

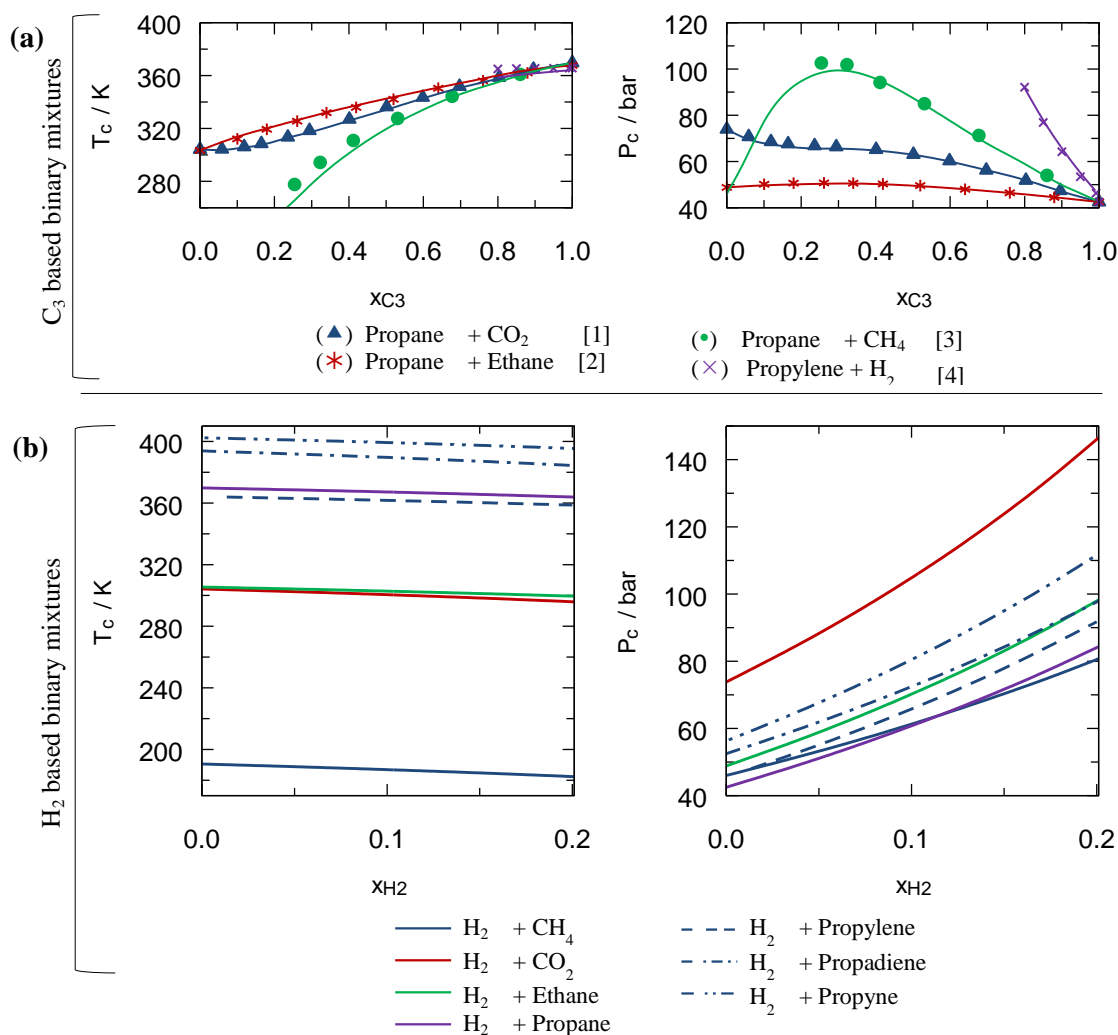


Figure II.15: (a) Comparison between experimental and calculated data for propane + solvent (CO₂, CH₄, C₂H₆) and propylene + H₂. (b) Calculated critical coordinates (PPR78 EOS) for hydrogen containing binary mixtures (CO₂, CH₄, C₂H₆). [1] S. Horstmann (1999); [2] Sven Horstmann et al. (2001); [3] Ortiz (2001) database; [4] Burriss et al. (1953).

II.4.2 Binary combinations of C₃ cut + solvents and H₂

When replacing propane with a C₃ cut mixture (6 mol% MAPD), the results between mixtures are still very close (Figure II.16 vs Figure II.15a), which proves that k_{ij} values proposed by PPR78 are still reliable. The major difference is at 100% of C₃ cut, due to the different critical point between the propane and the C₃ cut (Propane: $T_c = 367.7$ K and $P_c = 42.5$ bar; C₃ cut: $T_c = 366.2$ K and $P_c = 46.7$ bar;). In addition, two matrix with MAPD, propane and propylene content variation were evaluated (Table II.6). The results (Figure II.16) show that there is almost no difference when the mixture has distinct MAPD composition, due to the large quantity of propylene in the C₃ cut. In conclusion, these two-steps (§II.4.1 and II.4.2) validate the k_{ij} values (obtained by PPR78) that will be used to construct calculated ternary diagrams for C₃ cut + H₂ + solvent.

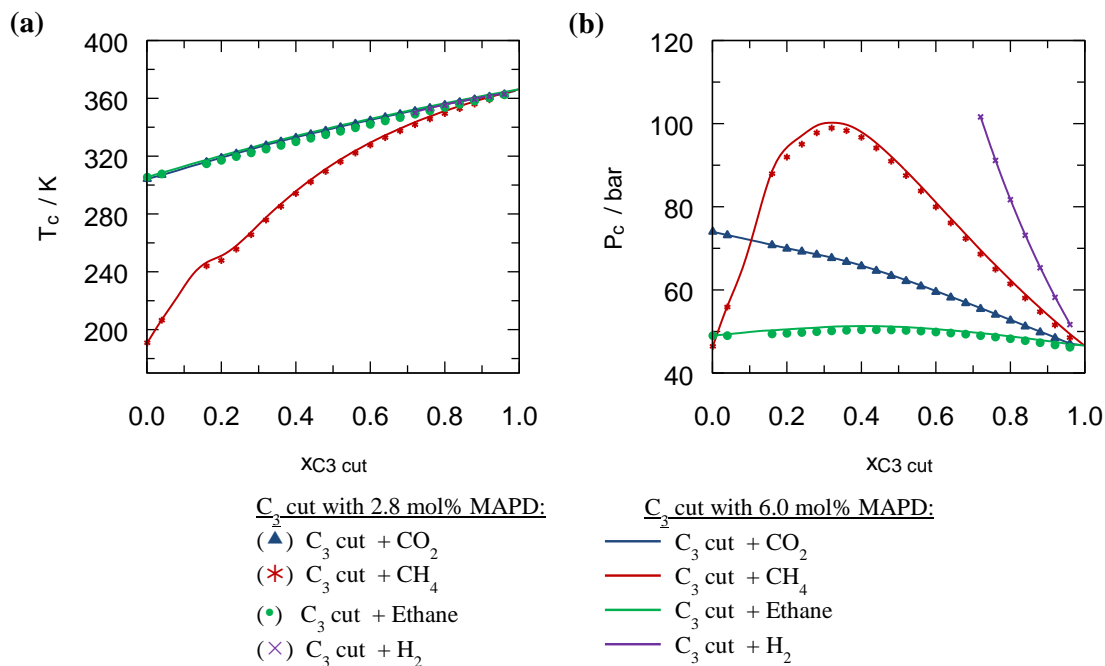


Figure II.16: Calculated critical data for two composition-matrix of C_3 cut (2.8 mol% and 6.0 mol% MAPD). (a) Critical temperature. (b) Critical pressure. The lines (2.8 mol% MAPD) and the dots (6.0 mol% MAPD) were calculated with PPR78 EOS.

Table II.6: C_3 cut mixture composition.

Components	$x_{C_3 \text{ cut}}$ (2.8 mol% MAPD)	$x_{C_3 \text{ cut}}$ (6.0 mol% MAPD)
Propane	3.27	4.00
Propylene	93.83	90.02
Propadiene	1.72	3.45
Methyl-acetylene	1.18	2.53

II.4.3 Ternary combinations of C_3 cut + solvents + H_2

Optimal number of points

By knowing that ternary diagrams are based on binary combinations of type III (H_2 containing) + type III + type IV (CH_4 containing) or type I (CO_2 and ethane containing), the optimal number of points is below 20 (Figure II-17). These points are located in the region of interest (from 0 to 20 mol% of H_2). For the solvents CO_2 and C_2H_6 , Figure II-17 shows that having 10 points can lead to reliable ternary diagrams. Nevertheless, due to the different critical behavior of mixtures containing CH_4 (Figure II.16), a bigger number of experiments is necessary to have a picture of the ternary diagram, $N^{opt} \approx 21$ (methodology I). This is due to the interactions of CH_4 with liquid hydrocarbons [very different volatilities (Valyashko, 2002)] which often have gas-liquid immiscibility at high pressures, affecting the critical locus curves.

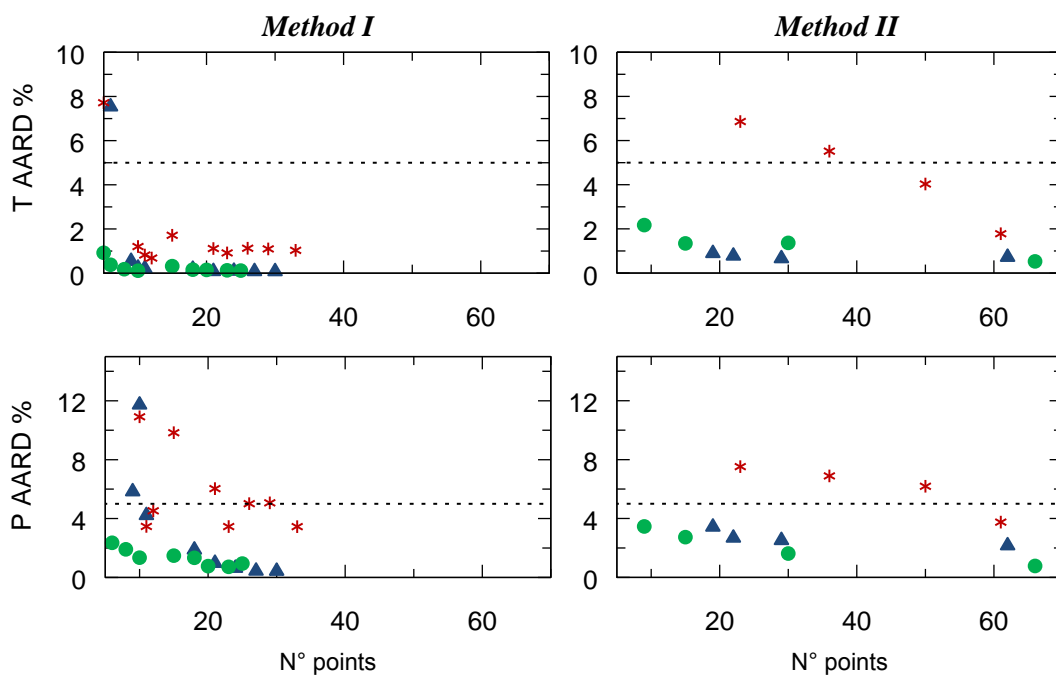


Figure II-17: Optimal number of experimental points needed for C_3 cut + H_2 + solvent ternary systems. T [AARD] and P [AARD] is the average deviation in critical temperature and critical pressure. The dashed line indicates the maximum deviation of 5%. (\blacktriangle) C_3 cut + H_2 + CO_2 ; ($*$) C_3 cut + H_2 + CH_4 ; (\bullet) C_3 cut + H_2 + Ethane.

Based on the optimal number of points, several ternary diagrams were created for mixtures with C_3 cut + H_2 + solvent (CO_2 or CH_4 or ethane) (Figure II-18, Figure II-20 and Figure II-19). The diagrams with the full data set were also constructed. The goal is to compare the fitted diagrams for a big data set and a small one.

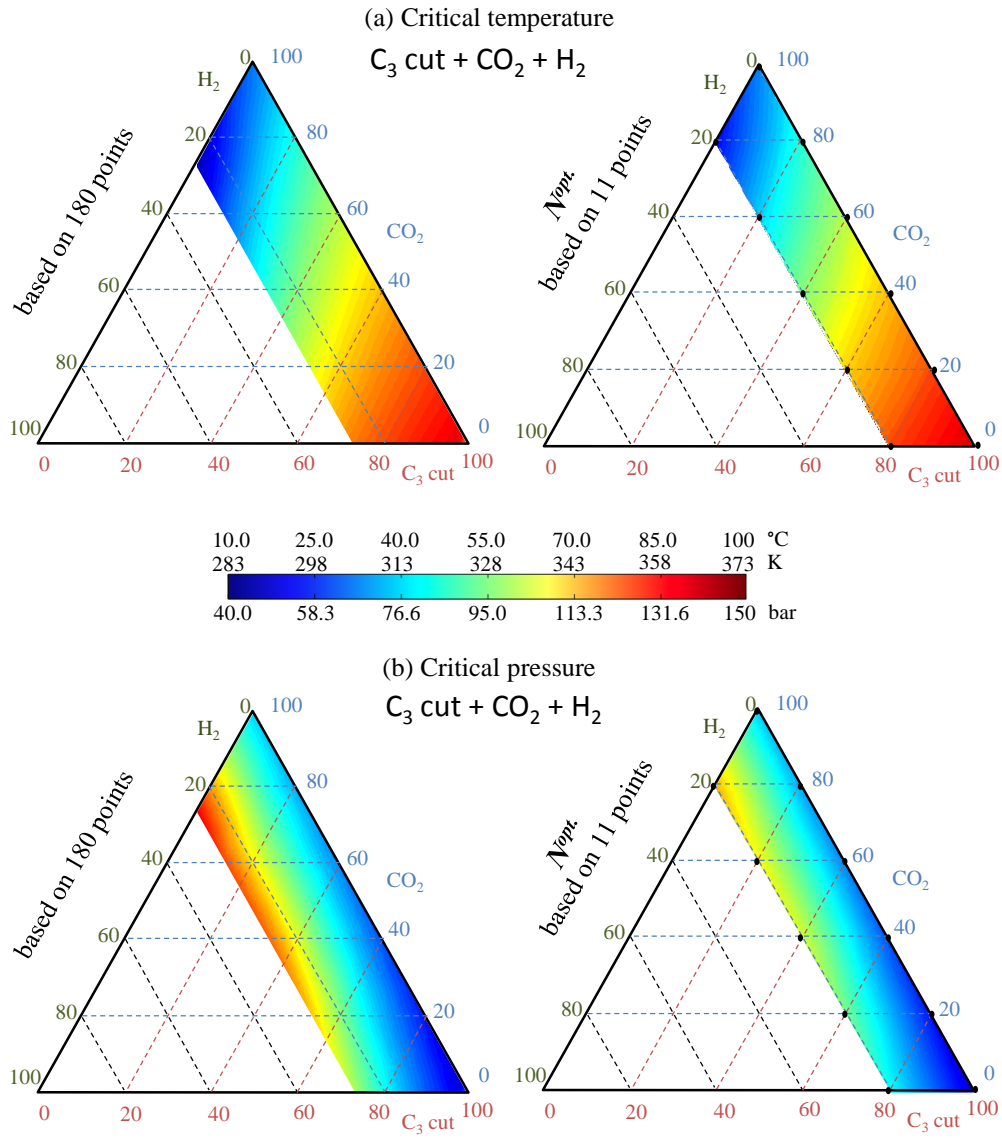


Figure II-18: Comparison between fitted points, 180 and N^{opt} , for C_3 cut (6% MAPD) + CO_2 + H_2 . The values were calculated using PPR78 EOS. (a) Critical temperature. (b) Critical pressure. The dots are the data set to be experimentally evaluated.

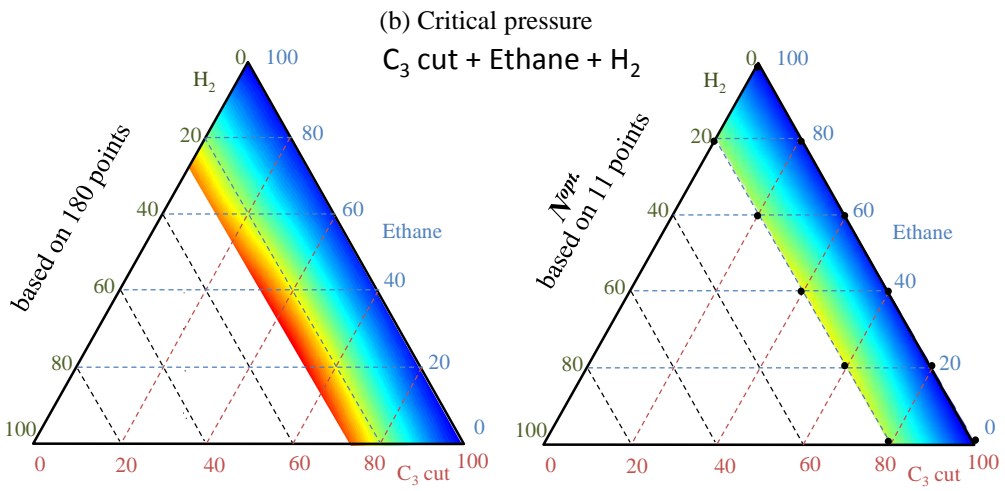
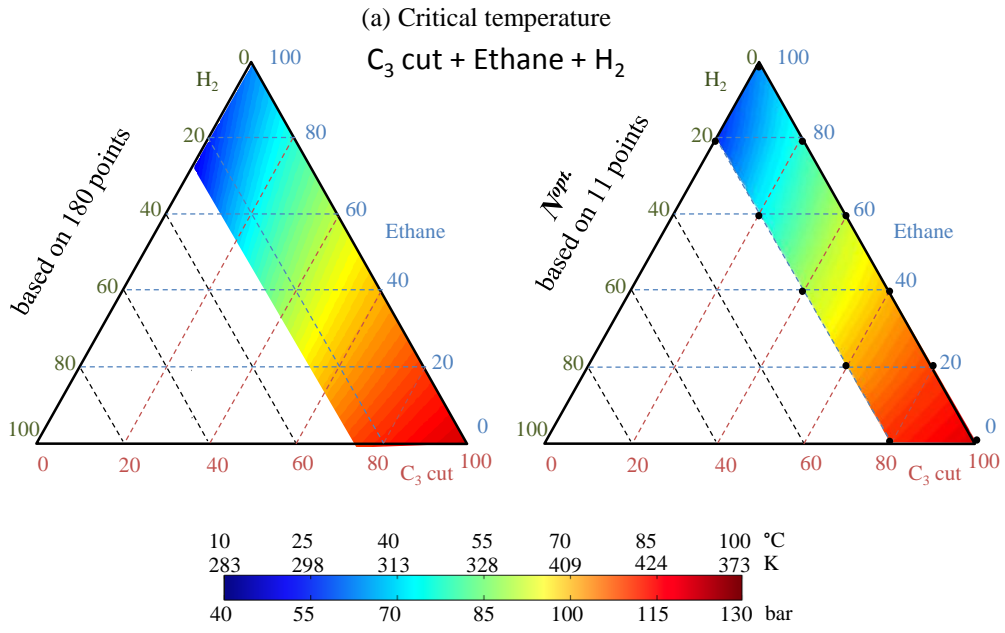


Figure II-19: Comparison between fitted points, 180 and N^{opt} , for C₃ cut (6% MAPD) + Ethane + H₂. The values were calculated using PPR78 EOS. (a) Critical temperature. (b) Critical pressure. The dots are the data set to be experimentally evaluated.

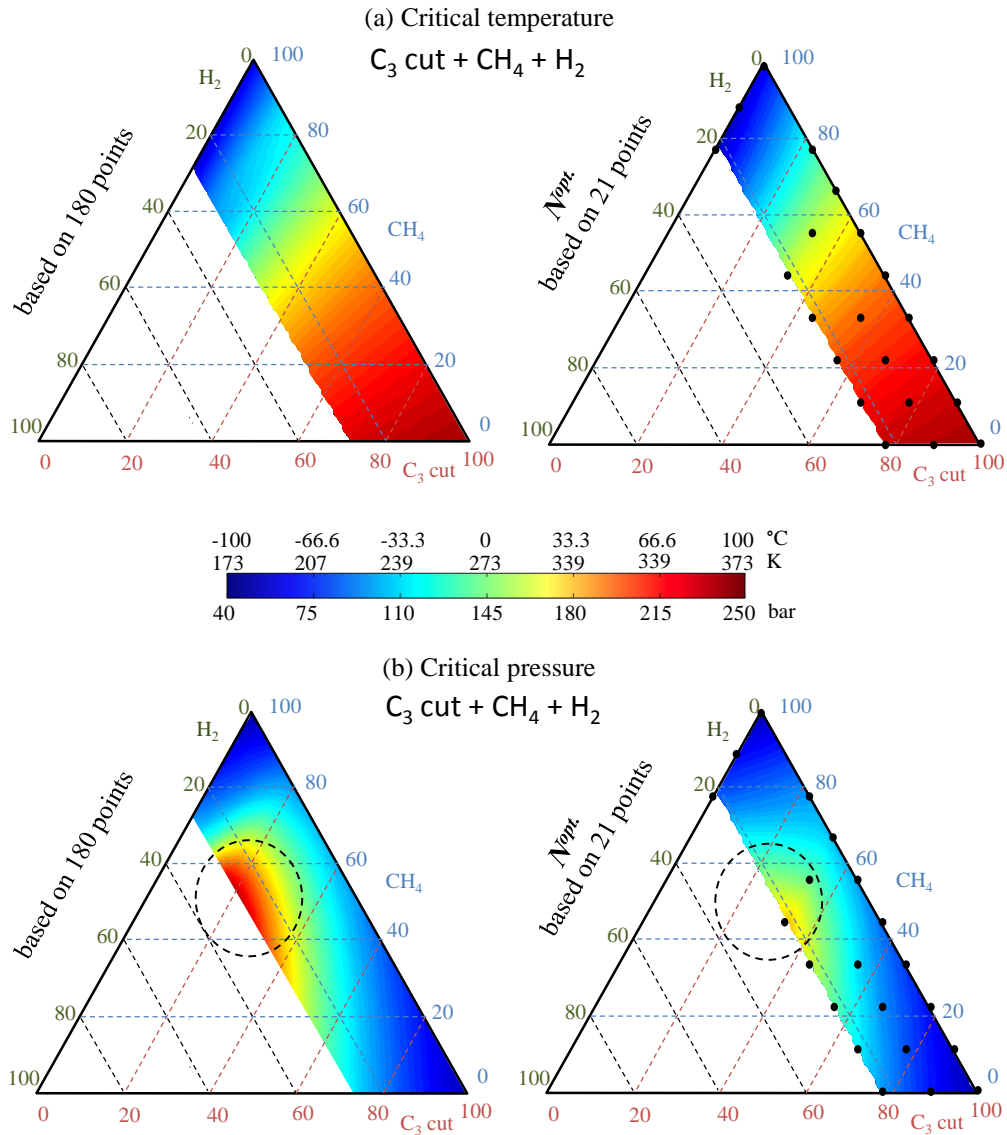


Figure II-20: Comparison between fitted points, 180 and N^{opt} , for C_3 cut (6% MAPD) + CH_4 + H_2 . The values were calculated using PPR78 EOS. (a) Critical temperature. (b) Critical pressure. The dots are the data set needed to evaluate experimentally. The circular dashed zone defines the region where the N^{opt} data set cannot fit well the data.

Regarding the previous figures, the minimum number of points used can well describe the ternary diagram used (the interpolation is reliable). It is possible to conclude that C_3 cut + H_2 + CH_4 has the highest critical pressure (up to 250 bar) and the lowest critical temperature (173 K). The influence in the range of critical coordinates is more pronounced for ternary combinations with CH_4 (Figure II-20) than for other solvents.

Although, having the predicted critical coordinates for mixtures, they cannot replace the experimental measurements, which are always time-consuming and difficult to analyze (Horstmann, 1999; Juntarachat et al., 2013, 2012; Konyneburg and Scott, 1980). For the previous C_3 cut mixture, hypothetical compositions were assumed (6% MAPD), which may be different for the industrial feedstock. Usually, the C_3 cut mixture has more than 6

components before the reaction (Hoteit et al., 2006). Since a supercritical medium is used, more than two components should be added to the mixture. In total we are dealing with more than 8 components. Therefore, it is interesting to check the mixture critical behavior experimentally.

II.4.4 Conclusions

Critical coordinates for **binary mixtures containing propane** (properties close to the C₃ cut) **were calculated and compared with experimental results** to check the reliability of the algorithm. A **good agreement** was achieved between them. After, the **critical coordinates and the “design of experiments”** were evaluated for the mixture of interest: **C₃ cut + H₂ + solvent** (CO₂, CH₄ and ethane) via PPR78 EOS. The optimal number of experimental points was evaluated for all the cases (all the solvents). It was shown **that 10 points** can reliably describe ternary combinations with **CO₂** and **ethane**. For **CH₄**, **21** points are necessary to have a good picture of a ternary diagram.

The strategy adopted (model + “design of experiments”) seems reliable for C₃ cut (industrial mixture). To validate the model towards critical studies, the **next step is to determine experimentally the critical point of the C₃ cut** (industrial mixture) and to compare it with the model predictions (PPR78). To achieve this, an experimental approach based on high-pressure and high-temperature microfluidics was developed.

II.5 Experimental approach (HT/HP microfluidics)

II.5.1 Introduction

Traditionally, phase diagrams and critical coordinates are obtained with chromatography techniques (Hou et al., 2013) and/or high-pressure optical cell (HPOC) measurement methods (Ke et al., 2001; Stradi et al., 2001) using isochoric or dynamic methods (Juntarachat et al., 2012). Although these methods can lead to very precise and reliable thermodynamic data, they are time-consuming. This limitation is mainly due to the macro scale volumes. Performing phase behavior analysis in microfluidic devices is emerging and aims to develop alternative methods to the traditional ones. Nowadays, phase microscale behavior analyses at high pressures and temperatures are possible because of:

- the development of supercritical microfluidics (Marre et al., 2010);
- the modeling of supercritical microflows (Mostowfi et al., 2012).

All this knowledge opened space for conducting on-chip phase behavior studies, which require advanced control of the operating parameters (pressure, temperature and composition). Compared to conventional techniques, the microfluidic approaches can add huge benefits. It provides low reagent consumption, fast screening, low operating times [97% time reduction compared to conventional pressure-volume-temperature (PVT) techniques (Mostowfi et al., 2012)] and the ability to implement *in situ* analysis techniques (Gervais et al., 2006; Urakawa et al., 2008). Furthermore, the ability to work in continuous flow modes allows solving hydro/mass transfer/thermodynamic problems simultaneously through on-chip

μ PIV (Shinohara et al., 2004), mass transfer analysis (Fisher et al., 2013; Gervais and Jensen, 2006) and PVT construction (Mostowfi et al., 2012).

The first published approach to study on-chip phase behavior was proposed by Mostowfi et al. (2012). In their work, the authors successfully developed a microdevice equipped with fluidic restrictions inside the microchannel, which is responsible for droplet nucleation. This ensures a fast equilibrium after the fluid restriction. It was used to investigate binary phases PVT diagrams, using integrated membrane-based optical sensors for *in situ* pressure measurements. The fluid phase behavior was analyzed at equilibrium using flow visualization to determine the gas-liquid volume fractions, depending on temperature and pressure. These data provide sufficient information to construct binary phase diagrams. More recently, Fisher et al. (2013) used the same principle to investigate hydrocarbons equilibrium in oil. Good agreements were obtained when compared to pycnometer flash experiments. In both cases, the pressure inside the microsystem was maintained thanks to the pressure drop at the microsystem outlet, meaning that the pressure was flow-rate dependent. To some extent, this could potentially affect the time to reach phase equilibrium [gas-liquid mass transfer is high, (Gervais and Jensen, 2006)], reducing the contact time between phases at high flow rates. The authors proposed to use microchannels with small hydraulic diameter, allowing screening an acceptable range of pressures by minor changes of flow-rates.

In this general context, this subchapter presents an innovative strategy to conduct on chip multicomponent phase behavior studies at high pressures ($1 < P$ (bar) < 200) and temperatures ($300 < T$ (K) < 500). The developed method is primarily based on (i) bubbles and dew points detection through optical characterization and (ii) the use of a so-called “dynamic stop-flow” measurement mode, for fast screening of the operating parameters. The proof of concept will be demonstrated through the determination of phase diagrams and critical locus curves for benchmark binary (alkanes + CO₂) and ternary (alkanes + CO₂ + H₂) mixtures. These mixtures were chosen as model ternary combinations because they are commonly used in industry. They are relatively stable at high-pressure and high-temperature conditions (no reactivity between components), and there is literature data available for comparison.

The first section of the thesis briefly discusses the microsystem design, set-up and the general strategy. After the experimental results are presented, being later compared with literature and numerical data calculated with the PPR78 EOS.

II.5.2 HP/HT microfluidic tool

Chemicals

Cyclohexane and pentane (both 99.5% purity) were purchased from Sigma-Aldrich[®] and used as received. Carbon dioxide, hydrogen and propylene were purchased from AirLiquid[®].

Microsystem design

We developed a silicon/Pyrex microsystem fabricated using standard lithography/dry etching techniques (Marre et al., 2010). The microsystem exhibits rectangular channels with dimensions of 200 μm and 100 μm , for width and depth, respectively (*i.e.* hydraulic diameter of 133 μm). The microchannel has a total length of 1 m with rounded edges. The overall design leads for instance to a pressure drop of 0.8 bar when considering pure cyclohexane flowing at 50 $\mu\text{L}\cdot\text{min}^{-1}$, which was roughly estimated using a Hagen–Poiseuille-based equation (note that the pressure drops calculated assuming laminar flow in the cylindrical configuration are in good agreement with the experimental measurements):

$$\Delta P = -128 \frac{\mu Q}{\pi d_h^4} L \quad \text{Eq. II.4}$$

where ΔP is the pressure drop (Pa), L the channel length (m), μ the fluid viscosity (Pa.s), Q the volumetric flow-rate ($\text{m}^3\cdot\text{s}^{-1}$) and d_h the hydraulic diameter (m).

To guarantee the mixing quality and fluid temperature, the microsystem has three different zones: inlet/outlet zones, mixing zone and analysis zone (Figure II-21).

The fluids enter at room temperature (in the inlet/outlet zones) and are later allowed to mix while temperature increases, from room temperature to the working temperature. Finally, the fluid mixture reaches the operating conditions before entering the analysis zone, where it is characterized.

To study binary and ternary mixtures, the microsystem includes three inlets and two T-junction mixing points (Figure II-21). The fluid inlets are kept with mitered 90° elbows with sharp bends in order to enhance fluid mixture by generating vortex at the corners. To study binary mixtures, one of the inlets is plugged. This approach allows the validation of the experimental set-up for binary and ternary mixtures, separately. The microsystem was connected to the external set-up using a compression module described elsewhere (Marre et al., 2010).

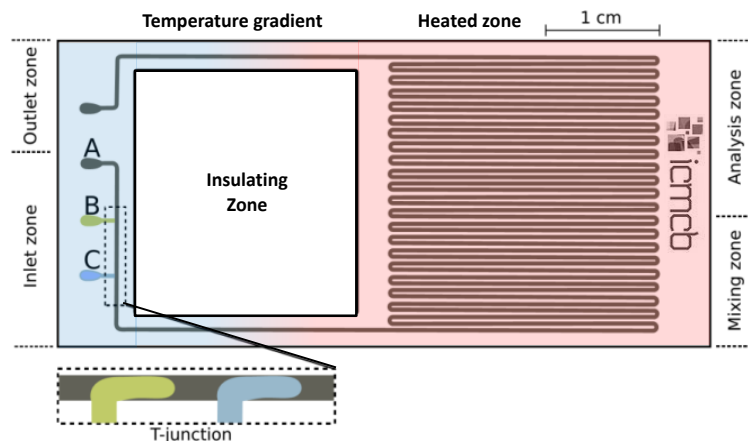


Figure II-21: Schematic of the microfluidic device with the three different zones: A, B and C.

Experimental set-up

The general set-up is described in Figure II-22. Briefly, the flow rates are controlled by three high-pressure piston pumps (ISCO[®] 100DM), while a back pressure regulator (Equilibar[®] ULF) placed downstream is used to maintain a constant pressure in the microsystem. Finally, the temperature is controlled within a ± 0.1 K interval by a EuroTherm[®] 3200. The microdevice is heated with an electrical resistance of 200 W, contacting the silicon backside to guarantee a constant heat transfer at temperatures above 380 K, compensating the convective heat losses. To monitor the temperature within the set-up, two K-type thermocouples are used. They will monitor the fluid temperature (i) in the piston pumps (thermostat with a recirculating cooling fluid - T_1), and (ii) the microsystem operational part (in direct contact with the backside of the microsystem - T_2). To monitor the pressure, two pressure transducers are placed upstream and downstream the microsystem. To guarantee the exact same measurement conditions, both pressure sensors were immersed in a constant temperature bath (50/50 wt% ethylene glycol/water) at 300 K. Analyses were conducted within a temperature range from 300 to 500 K, and a pressure range of 60 to 150 bar.

A bypass line was also added to run the set-up in a dynamic stop-flow mode (see details below).

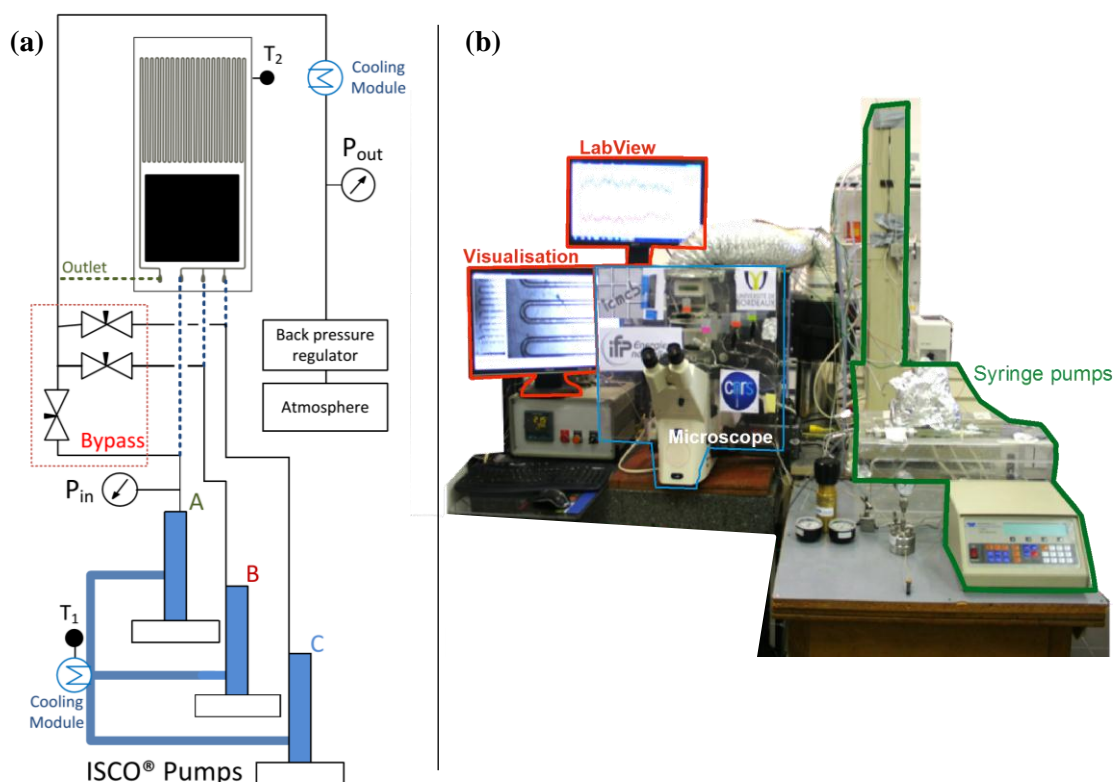


Figure II-22: (a) Schematic diagram of the developed set-up to investigate complex mixtures (with a bypass line). (b) Picture of the installation.

To construct the thermodynamic diagrams, several movies were recorded with Phantom[®] Version 9.1 at different capturing velocities. For bubble formation and nucleation, movies

were captured at 300 fps (1632×1200). For visualizing equilibrium evolutions, movies were captured between 4 and 40 fps (1632×1200). The high-speed camera is coupled with a Zeiss Axiovert 200 M inverted microscope equipped with a $5\times$ objective.

II.5.3 Microfluidic strategy to build P-T phase diagrams

Principle: bubble and dew point detection

To construct a multicomponent P-T diagram, our approach is based on bubble and dew point (on-chip optical) detection to access the phase envelope. Initially, a fluid mixture with a given composition is introduced at equilibrium state in the microsystem, displaying multiphasic liquid–vapor, i.e., droplets/bubbles are formed inside the microchannel and can be easily observed (Figure II-23a-C*).

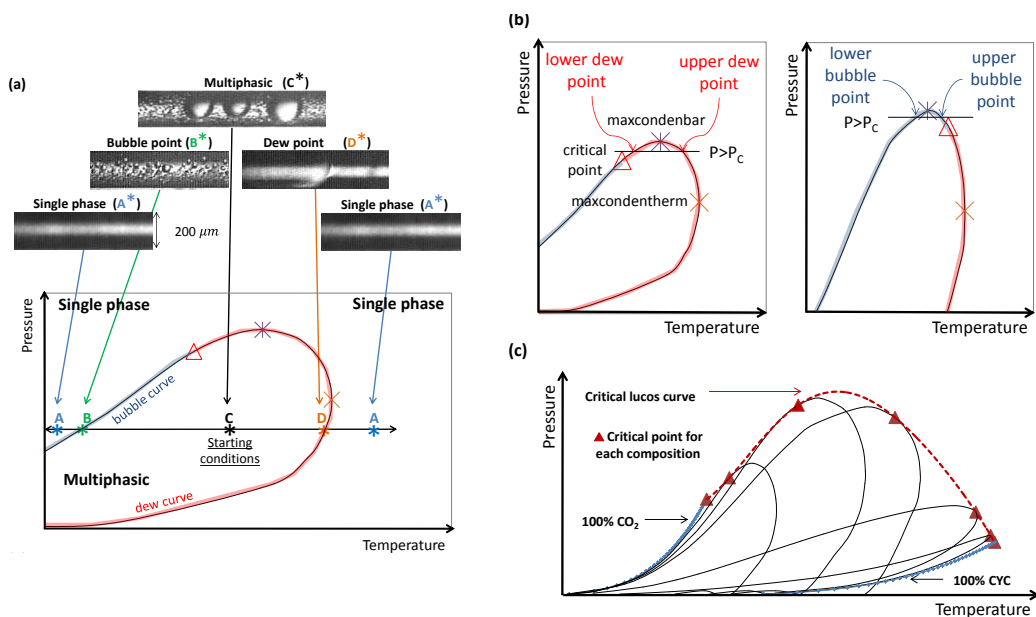


Figure II-23: (a) General loop method for building a P-T phase diagram through the bubble and dew points detection and plotting the phase envelope. The instabilities were generated by increasing or decreasing the temperature under isobaric conditions. The images were captured at 4 fps for a mixture of CO₂ + cyclohexane (CYC). (b) Critical point location after and before the maxcondenbar. (c) General description of a binary mixture critical locus [CO₂/ CYC: type I-a mixture (Zhang et al., 2005)].

Starting from these initial conditions, the temperature was subjected to variations under isobaric conditions, in order to find the bubble and dew points. This means that the mixture becomes fully miscible (Figure II-23a-A*) by crossing the phase envelope in the (P,T) projection of the phase diagram. This process can be viewed as the transition from the 2-phase to the 1-phase region. The bubble point (Figure II-23a-B*) corresponds to a temperature value (at a given pressure) where the first bubble starts forming in the fluid medium. Similarly, the dew point (Figure II-23a-D*) corresponds to the temperature (at a given pressure) where the last bubble disappears. After finding these points, the pressure was increased and the process was repeated. This loop method was carried out until the maxcondenbar (MCB) point is found, which is located at the maximum pressure of a P-T envelope (Figure II-23b). After finding the MCB, the loop method was carried out until the maxcondentherm (MCT) is found, which is the maximum temperature of a P-T envelope

(Figure II-23b). Then, to determine the critical point, it is worth noting that the critical pressure (Figure II-23b, left) is located between the MCT and the MCB pressures ($P_{MCT} < P_C < P_{MCB}$) (Privat and Jaubert, 2013). By definition, the critical point is the junction between bubble and dew curves (Figure II-23b). This means that if $P < P_C$ there is a dew point and a bubble point; however, for $P > P_C$, we will have either two dew points (lower and upper) or two bubble points (lower and upper). The lower and upper bubble points and dew points are easy to spot in microfluidics, as exemplified in Figure II-24.

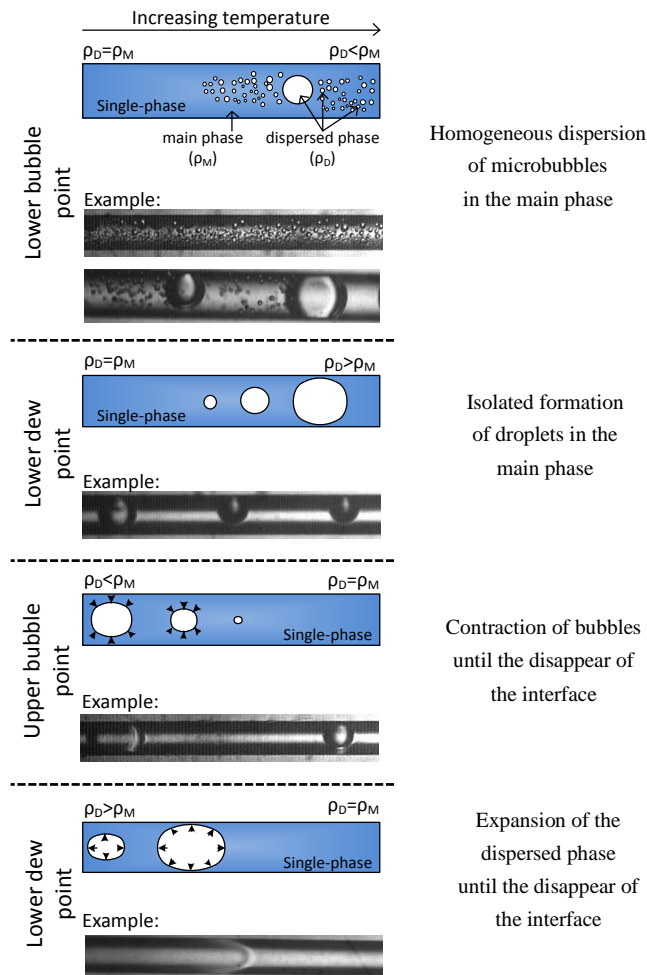


Figure II-24: Schematic of the point detection of the different behavior of the medium at $P > P_C$. The variable ρ represents the density of the fluid.

Repeating the proposed method for several compositions and linking the critical points, the mixture critical locus curve was determined, as exemplified in Figure II-23c for a binary CO_2 + cyclohexane (CYC) mixture. The microsystem can be operated in stop-flow (isochoric) or continuous flow mode.

In isochoric systems, the pressure is directly controlled by temperature variations (Wang *et al.*, 2011), *e.g.* increasing temperature leads to an increase on the fluid pressure. These approaches could lack of flexibility when targeting a fast screening of phase behavior. On the contrary, continuous microflow mode allows for fast screening of the operating conditions (temperature, pressure and composition), but leads to poor precision over the system

operating pressure due to the induced pressure drop inside the microchannels. To overcome these limitations, our strategy is to operate the microsystem in a proposed dynamic stop-flow mode (see next section) [methodology developed in this thesis]. In this regime, the fluid is completely stopped (no induced pressure drop), but is not confined to a specific volume, which means that P-T parameters can be changed independently. This ensures an improved precision over the operating conditions, making it ideal to do precise and fast phase behavior studies.

The dynamic stop-flow concept for fast screening

The dynamic stop-flow approach takes advantage of an open system, similar to continuous flow regime, but the fluid is in a no motion status. The concept developed behind this method is based on hydrodynamic resistance. Flowing through small hydraulic diameter (d_h) tubes leads to higher hydrodynamic resistance than flowing through a tube with larger hydraulic diameter (the fluidic resistance varies as d_h^4 , see Eq. II.4). Therefore, bypassing the microsystem with a large hydraulic diameter (Figure II-25) forces the fluid to select the line with lower hydrodynamic resistance.

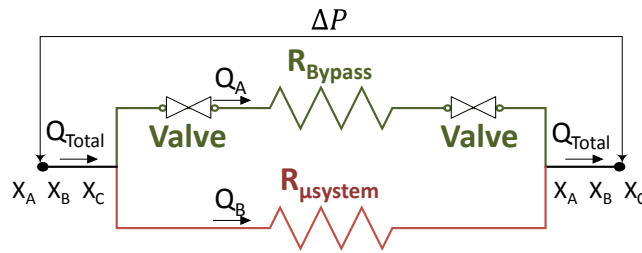


Figure II-25: Flow resistance circuit that one fluid undergoes in the dynamic stop-flow mode.

Indeed, by considering the Hagen-Poiseuille equation (Eq. II.4) for equal tubing length, we can express the flow-rate ratio between two lines as the inverse of the fluidic resistance ratio and as the hydraulic diameter ratio to the power 4:

$$\frac{Q_A}{Q_B} = \frac{\mathcal{R}_{\mu system}}{\mathcal{R}_{Bypass}} \approx \left(\frac{d_{h Bypass}}{d_{h \mu system}} \right)^4 \quad \text{Eq. II.5}$$

where Q_A and Q_B are the volumetric flow rates in each section (microsystem and bypass), respectively, \mathcal{R} is the fluidic resistance and d_h the hydraulic diameter.

Considering our set-up, the hydraulic diameters are 133 and 750 μm for the microsystem and the bypass, respectively. The flow-rate ratio between the bypass and the microsystem line is $\sim 10^3$. In other words, at the T-junction, the fluid will always largely flow preferentially into the bypass line ($Q_A \gg Q_B$), thus flowing around the microsystem without disturbing the fluid mixture inside it. In a typical experiment, pure fluids are firstly mix in the desired proportions while flowing through the microsystem until the upstream pressure is stable ($Q_{total} = 50 \mu\text{L}\cdot\text{min}^{-1}$, bypass valves are closed, meaning $Q_A = 0 \mu\text{L}\cdot\text{min}^{-1}$). This step lasts from 1 to 10 min depending on the overall compressibility of the considered fluid mixture. When the bypass valves are opened, the mixture inside the microsystem is kept in a quasi no-motion state ($Q_A \sim 50 \mu\text{L}\cdot\text{min}^{-1}$, $Q_B \sim 0.05 \mu\text{L}\cdot\text{min}^{-1}$).

To prove the concept, a flow of $\text{CO}_2 + \text{CYC}$ was introduced into the microsystem at a velocity of $\sim 8 \times 10^{-2} \text{ m.s}^{-1}$. Then, the bypass valves were opened, which led to a small decrease of the upstream pressure sensor. Since the pressure drop is smaller in the bypass line, the fluid starts to be in a quasi no-motion state.

In continuous mode, to observe fluid flow inside the microchannel it is necessary to capture movies with a minimum of 300 fps (Figure II-26a). On the contrary, in the case of a quasi no-motion flow (such as $\text{CO}_2 + \text{CYC}$), 4 fps is enough and it becomes possible to visualize in detail the size of each bubble (Figure II-26b). Therefore, the dynamic stop-flow works as expected (no pressure drop).

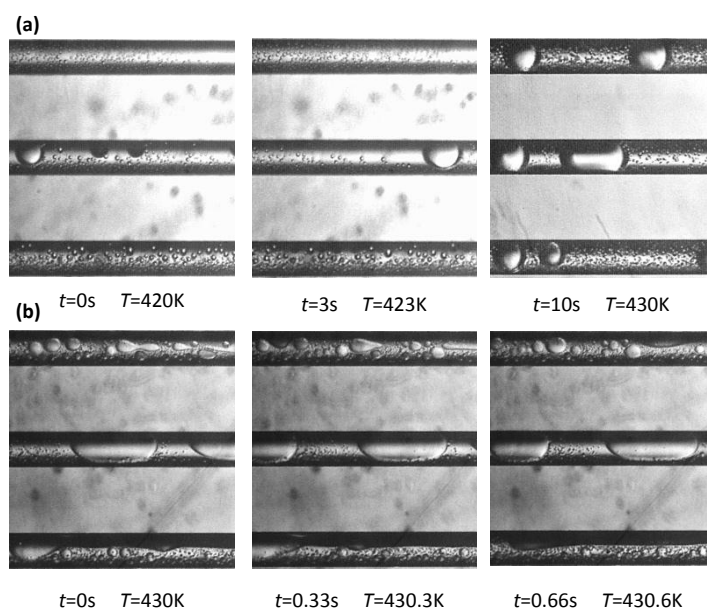


Figure II-26: Volume variation of the bubbles during a temperature increase. The bubbles are trapped into the microsystem, having a molar composition of 24 mol% cyclohexane and 76 mol% CO_2 at $P = 138 \text{ bar}$. (a) Images captured at 300 fps using a continuous flow mode, (b) images captured at 4 fps using the dynamic stop-flow mode.

Each isobaric set of experiments covers the full range of temperatures in typically less than 5 minutes (*i.e.* temperature variation is almost instantaneous). When the temperature rises inside the system, the fluid will expand and the volume variation will be expelled into the bypass line, avoiding pressure variations inside the microsystem. Changing P–T conditions destabilizes the stationary regime of the system, inducing slight movements in the fluid until a new stationary regime is reached. Between stationary states, the bubbles' appearance, growth and disappearance can be easily investigated (Figure II-26). In the transition between stationary states the bubbles/droplets increase or decrease in size, giving the opportunity to extend the concept proposed in this paper to study PVT diagrams.

II.5.4 Results and discussion

Set-up reliability and PT diagrams for binary CO_2 / alkanes mixtures

To check the reliability of our approach, two benchmark binary mixtures were considered: $\text{CO}_2 + \text{cyclohexane}$ and $\text{CO}_2 + \text{pentane}$, for which literature data are available, allowing

evaluation of the set-up performance. Furthermore, the critical locus curve in mixtures of hydrocarbons and CO₂ is commonly of type II (Konynenburg and Scott, 1980; Vitu et al., 2008) [§I.6.4]. In other words, these binary fluid mixtures only have a heterogeneous liquid–gas equilibrium and a liquid–gas critical locus curve between the critical points of each pure component. Note, however, that it is also possible to have a liquid–liquid heterogeneous equilibrium (Privat and Jaubert, 2013).

To obtain a P–T phase envelope, the system was first placed under equilibrium conditions. Then, the procedure described previously was followed in order to determine the bubble and dew points (varying temperature, then pressure). Figure II.27 presents P–T miscibility diagrams obtained for some selected CO₂ + pentane and CO₂ + cyclohexane compositions. The critical point for each composition can be found using the procedure earlier described. The evolution of the critical pressure and temperature (as a function of mixture composition) was then determined based on the critical points obtained from the P–T diagrams; this curve was directly compared with literature and PPR78 EOS calculated data (Figure II.28).

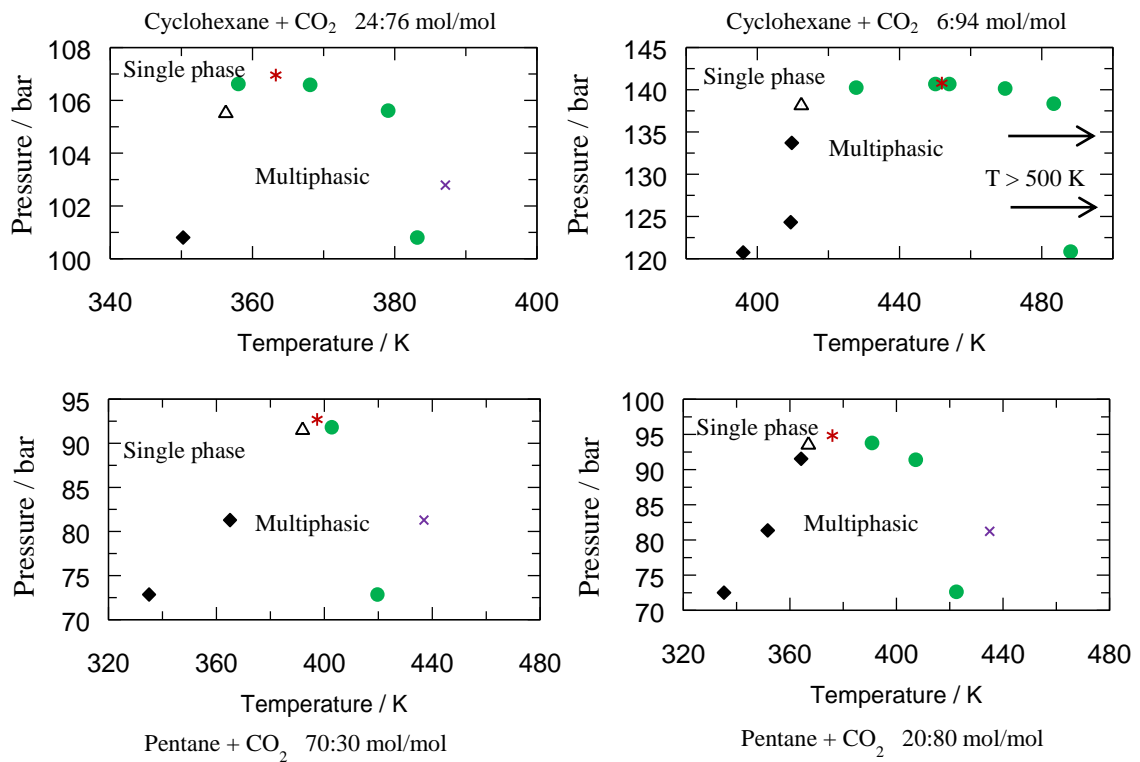


Figure II.27: P-T miscibility diagrams for binary mixtures CO₂+cyclohexane and CO₂+pentane obtained through the microfluidics approach. ♦ Bubble points; ● Dew points; * Maxcondenbar; × Maxcondentherm; △ Mixture critical points.

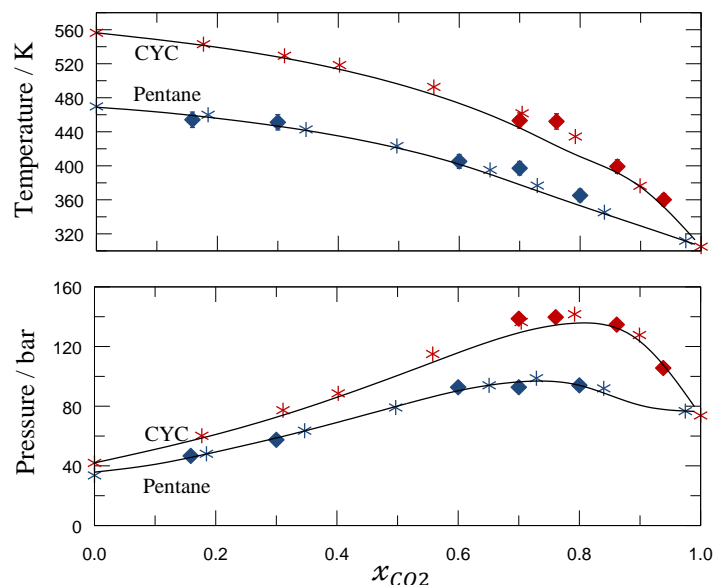


Figure II.28: Critical points for the binaries **CYC+CO₂** and **pentane+CO₂**. **♦ On-chip experimental results; *Literature data: CO₂+CYC** (Zhang et al., 2005) ; **CO₂+pentane** (Cheng et al., 1989); and **— PPR78 EOS results, using Heidemann *et al.* algorithm** (Heidemann and Khalil, 1980) (**CYC+CO₂**; **pentane+CO₂**).

Compared to the literature data, the obtained values have an average relative deviation of 2%. The main contribution to the deviation value is the composition variation at the system inlet, *i.e.*, small pump flow rate variations change the overall system composition, making it possible to have slight deviations in the critical temperature and pressure. However, the excellent overall agreement of the results with the literature and the PPR78 model proves that our approach can be used to obtain critical data for binary mixtures.

From binary to ternary diagrams

To verify that the concept can be used for more complex mixtures, a quaternary mixture, CO₂ + propylene + propane + CO₂ was chosen as a model mixture. Such a system is representative of a hydrogenation reaction of propylene in CO₂, generating propane. The addition of hydrogen dramatically complicates the system, since this compressible fluid can interact with all three other species. To simplify the system, we fixed the propylene/propane molar ratio to 93:7. We first determine the CO₂ + propylene + propane ternary critical locus curve to obtain a pre-validation step before investigating the quaternary system including hydrogen. The obtained experimental results were later compared with the numerical results obtained through the Predictive Peng-Robinson cubic equation of state (Figure II.29).

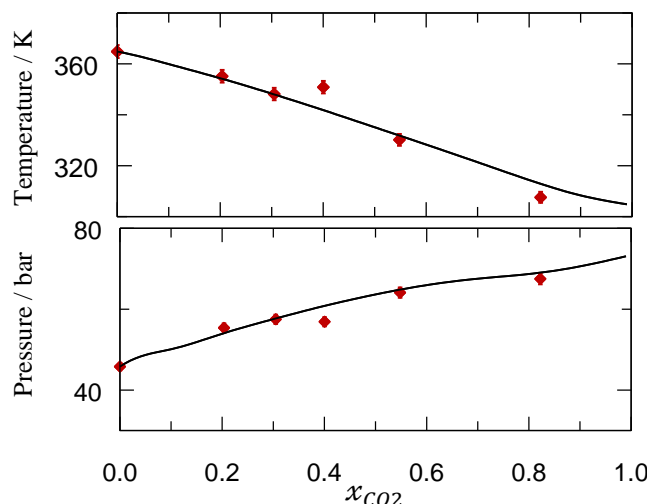


Figure II.29: Critical points for the ternary mixture CO_2 + propylene + propane (propylene/propane molar ratio fixed at 93:7). \blacklozenge On-chip experimental results; — PPR78 EOS results for CO_2 +propylene+propane (CO_2 + propylene; propylene + propane; propane + CO_2).

The results are in excellent agreement with the calculated data, having an average relative deviation of 2% for critical temperature and pressure.

The set-up was also applied to quaternary mixtures, please see Appendix §II.4. Perspectives: Use this new experimental tool to evaluate the C_3 cut.

II.5.5 Conclusions

A microfluidic-based approach was presented to **determine the P–T phase diagrams of multicomponent mixtures**. This **method** couples an on-chip optical detection of both **bubble and dew points** with a so-proposed **dynamic stop-flow mode**, for fast screening of the operating parameters (temperature, pressure and composition). The dynamic stop-flow regime was created using a bypass line, making it possible to maintain a constant pressure inside the system while tuning the temperature.

We demonstrate that this strategy can provide accurate experimental thermodynamic data for multicomponent mixtures, which were successfully compared to PPR78 EOS-calculated and literature data (for several cases). Additionally, this microfluidic approach works very efficiently (**typically 5 times faster than conventional HPOC methods**), taking advantage of:

- the fast heat and mass transfer;
- the easy control of all the set-up operating parameters;
- the use of a dynamic stop-flow mode, which can provide all of the advantages of a quasi no-motion fluid in an open system.

This ease of operation allows accessing data that can later feed EOS modeling, in particular through the back calculation of binary interaction coefficients (k_{ij}). Although the presented method was only used to investigate P-T diagrams, **it is also possible to envision building PVT diagrams, taking into account the void fraction**, as previously reported (Mostowfi et al., 2012).

The next step is to apply this new technology to C_3 cut (industrial mixture) + solvent + H_2 . Also, the optimal number of points (“design of experiments”) [§II.4] will be used.

II.6 Application to C_3 cut hydrogenation

This subchapter focuses on the evaluation of critical data for C_3 cut mixtures with the tools previously developed: determination of optimal number of points [§II.3] and on-chip critical point detection [§II.5]. For the optimal number of points, it was shown that a data set with 10 points can provide good accuracy. In this chapter, the number of experiments goes from 20 to 25 points per ternary combination. The number of experimental points is higher than the required one to ensure the results (conservative approach). All the values were obtained using on-chip experimental approach [§II.5.2], based on dew/bubble point detection [§II.5.3]. The goal is to find the critical coordinates by studying the expansion and compression of the fluid.

II.6.1 Miscibility diagrams

Figure II.30 exemplifies the envelopes obtained in microfluidics systems for C_3 cut + CO_2 , C_3 cut + H_2 and C_3 cut + CO_2 + H_2 .

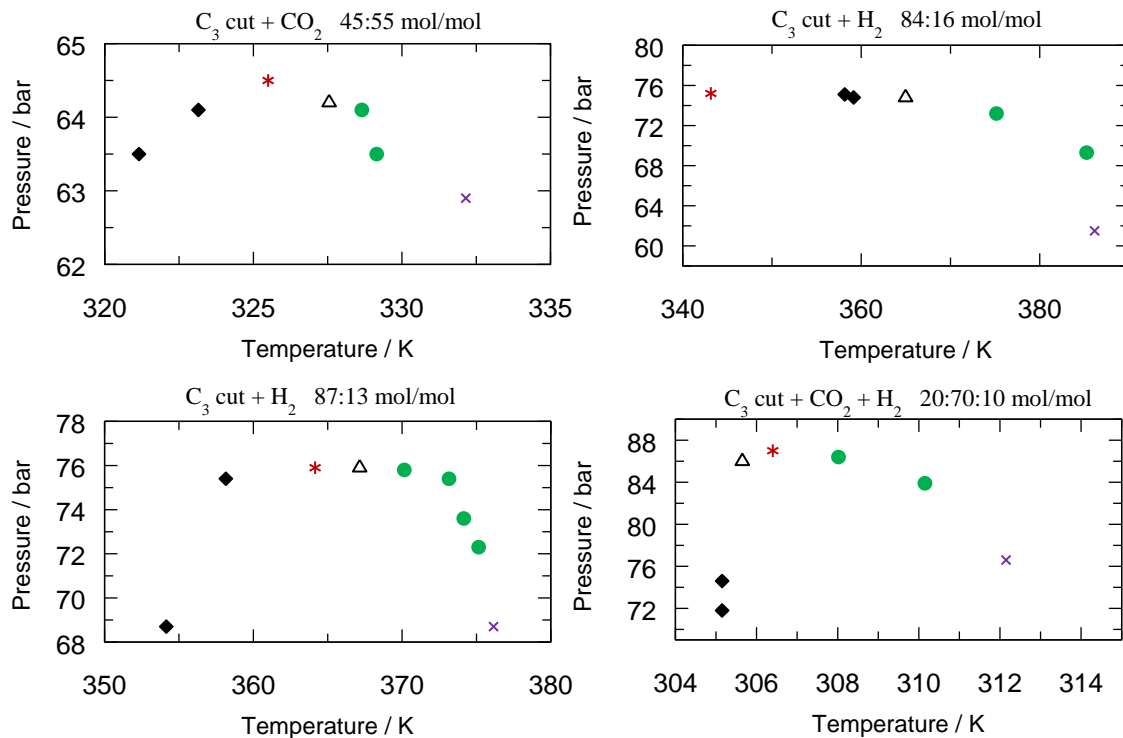


Figure II.30: P-T miscibility diagrams for binary mixtures (C_3 cut + CO_2 and C_3 cut + H_2) and C_3 cut + CO_2 + H_2 obtained through the microfluidics approach. \blacklozenge Bubble points; \bullet Dew points; $*$ Maxcondensar; \times Pseudo-maxcondensar; \triangle Mixture critical points.

C_3 cut binary combination

As previously seen in §II.4, the PPR78 EOS coupled with the algorithm provides reliable results for the binaries: propane + solvent (CO_2 , Ethane and CH_4) and propylene + H_2 .

Therefore the C_3 cut mixture (3 mol% MAPD [composition in §II.4]) on-chip critical data was compared with estimated data.

Figure II.31 shows temperature and pressure values as a function of the mole fraction of C_3 cut. It is possible to conclude that the binaries C_3 cut + CO_2 , C_3 cut + Ethane and C_3 cut + H_2 are close to the estimated values provided by PPR78, having an average relative deviation of 2%. For the case of C_3 cut + CH_4 , the average deviation is around 2%. Only a small range was analysed because the set-up was not adapted to achieve the low temperatures required (for C_3 cut + CH_4). To solve this experimental limitations, PPR78 EOS was used. Since it gives reliable results for literature binary mixtures, propane + CH_4 , and for the other C_3 cut binary mixtures, it should give also for C_3 cut + CH_4 .

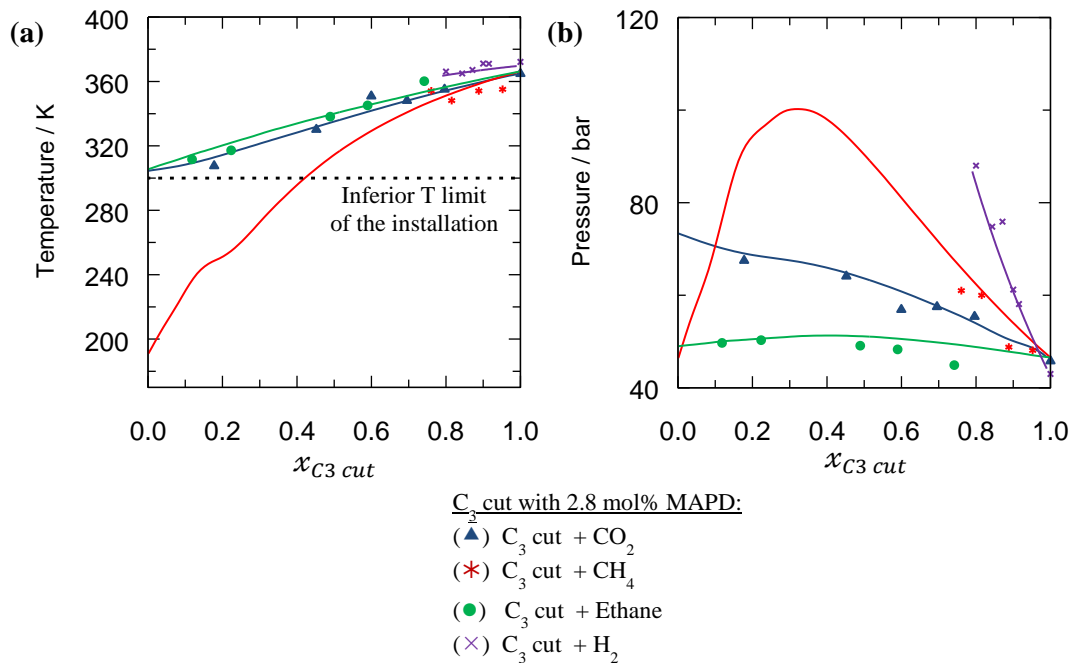


Figure II.31: Critical data for the binary combination of C_3 cut (2.8 mol% MAPD) + solvent and hydrogen. (a) Critical temperature. (b) Critical pressure. The dots are values experimentally obtained with on-chip technology, and the lines were estimated with PPR78 EOS. The critical points of the pure fluids [CO_2 , CH_4 and Ethane] were obtained from literature.

Based on these results, it is expected that the interaction parameters (k_{ij}) proposed by PPR78 EOS are good enough to be applied to the industrial mixture of C_3 cut.

II.6.2 C_3 cut - ternary combination (direct interpretation)

It was previously seen [§II.5.4] that the experimental approach can handle ternary and quaternary mixtures. Therefore, the following step was to study C_3 cut + solvent (CO_2 , Ethane and CH_4) + H_2 for critical data. Experiments with around 10 mol% and 20 mol% of H_2 were compared with predicted data (PPR78). See Appendix §0 and §II.5.

The results cannot be easily interpreted without interpolation. Therefore, the next step was to interpolate the results, using the ternary diagram tool.

II.6.3 C₃ cut - ternary combination (with interpolation)

As previously discussed (for Figure II.31 and Appendix §0 and §II.5), plotting experimental values and comparing them with estimated iso-H₂ lines can be a challenge. The experimental H₂ content can vary from the one expected, *i.e.*, instead of having 20 mol% of H₂, we can have rather 24 mol%. It happens, because the variations of the density with the pressure were not corrected in real-time on the piston pumps (only in post-treatment). To compare all the values, it is necessary to represent ternary combination (C₃ cut + solvent + H₂) with the help of a ternary diagram. This way, several diagrams based on experimental points were created and compared with the ones obtained with PPR78 (Figure II-32, Figure II-33 and Figure II-34).

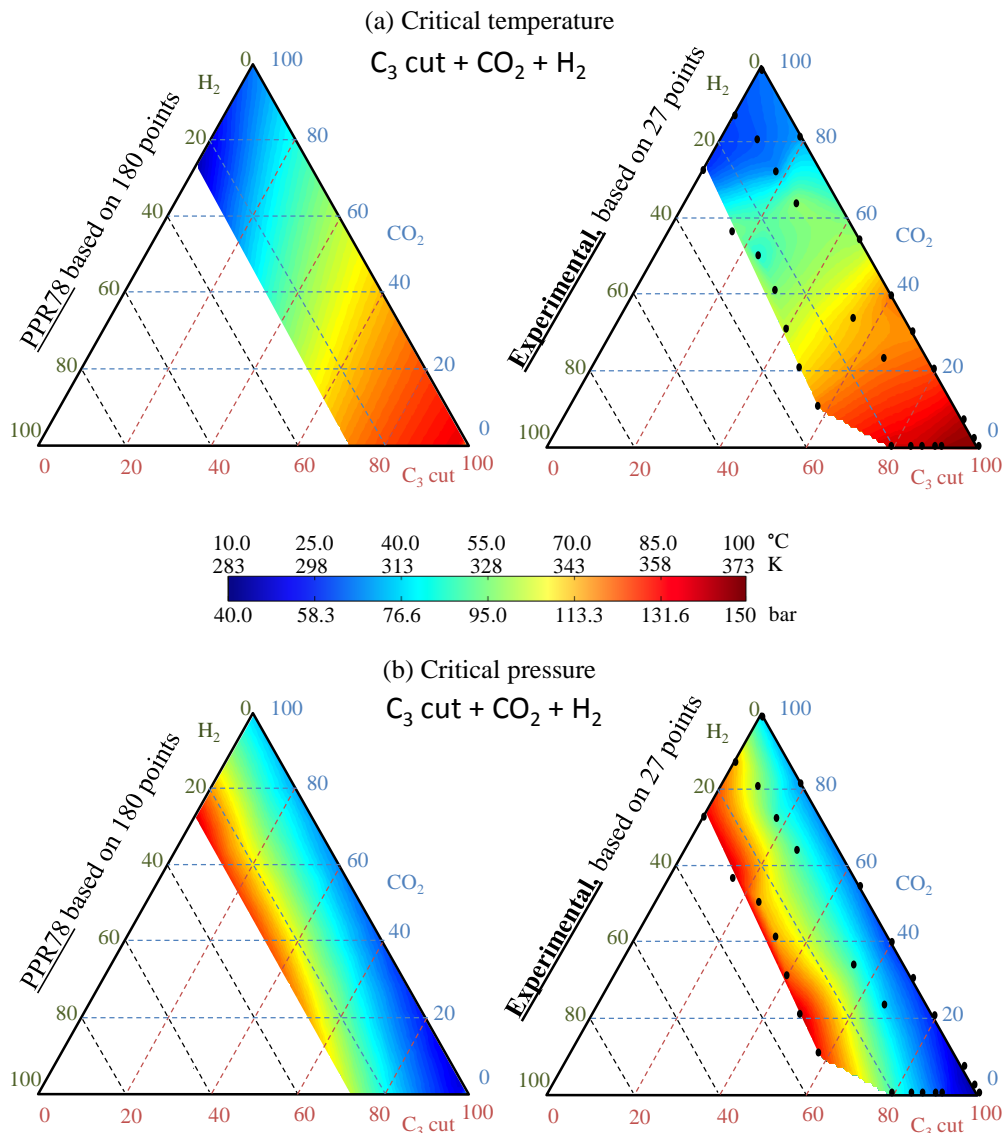


Figure II-32: Comparison between PPR78 EOS and experimental based ternary diagrams, for C₃ cut (2.8 mol% MAPD) + CO₂ + H₂. (a) Critical temperature. (b) Critical pressure. The dots are the data set experimentally evaluated.

Regarding the previous diagram, for the ternary combination C_3 cut (2.8 mol% MAPD) + CO_2 + H_2 , the contours are similar between experiments and PPR78 model. From this, it is possible to conclude that PPR78 and experiments have good agreement, which is satisfactory, proving the quality of the experiments and the model.

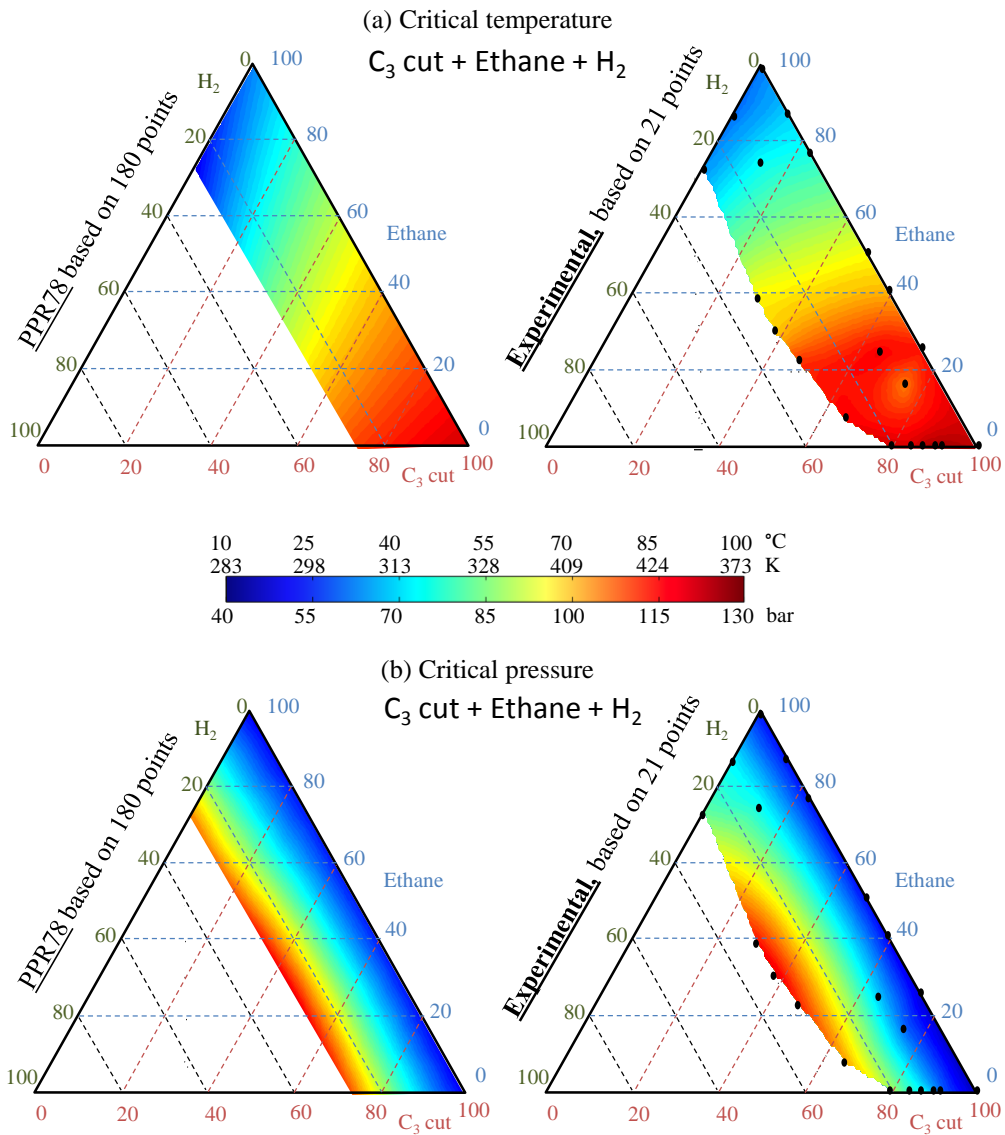


Figure II-33: Comparison between PPR78 EOS and experimental based ternary diagrams, for C_3 cut (2.8 mol% MAPD) + Ethane + H_2 . (a) Critical temperature. (b) Critical pressure. The dots are the data set experimentally evaluated.

For the ternary combination C_3 cut (2.8 mol% MAPD) + Ethane + H_2 , the contours are similar between experiments and PPR78 model, proving again the quality of the experiments and the model.

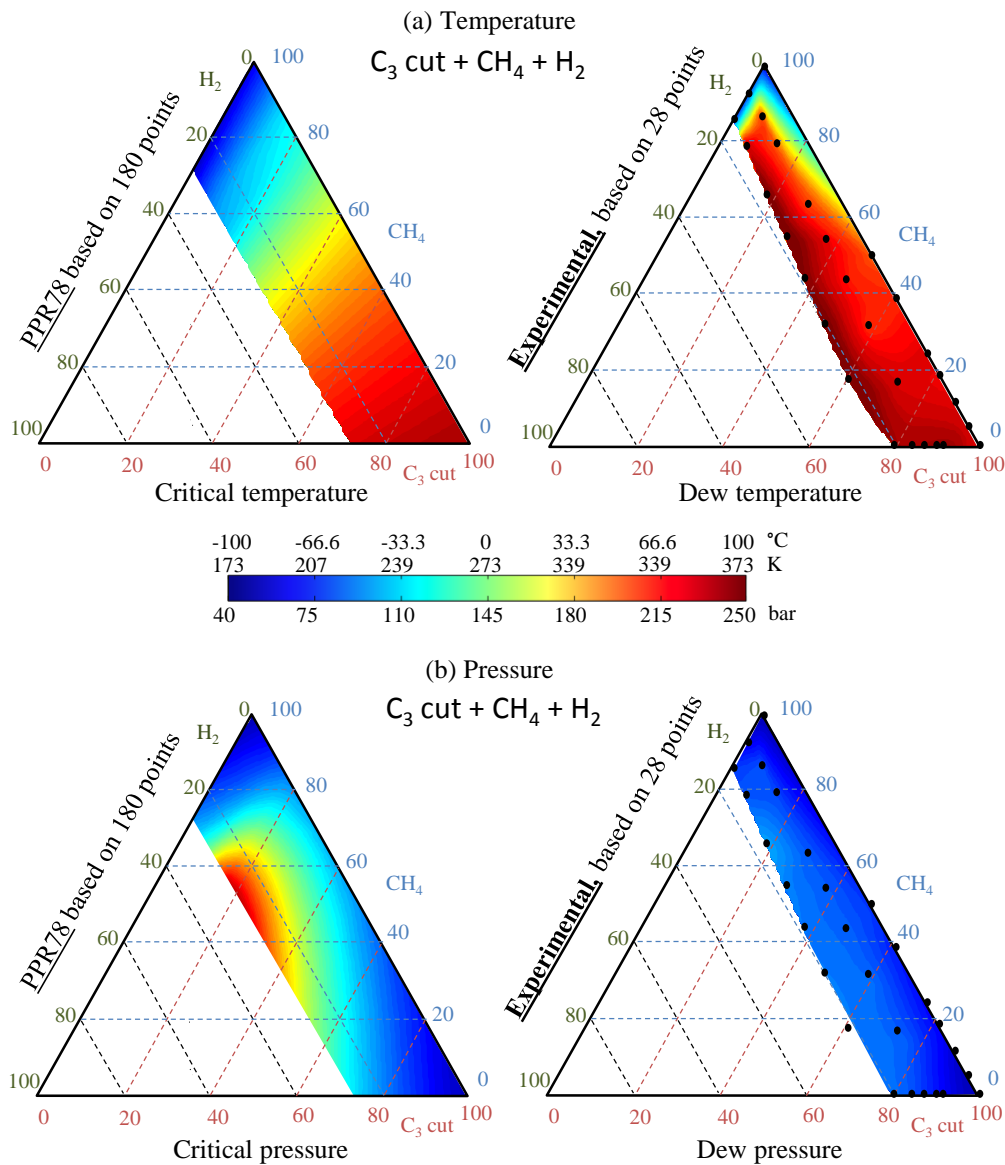


Figure II-34: Comparison between PPR78 EOS (critical points) and experimental (dew points) based ternary diagrams, for C_3 cut (2.8 mol% MAPD) + CH_4 + H_2 . (a) Temperature. (b) Pressure. The dots are the data set experimentally evaluated. The critical point for pure CH_4 was obtained in literature.

As previously discussed, the ternary combination C_3 cut (2.8 mol% MAPD) + CH_4 + H_2 was impossible to obtain experimentally because the installation was not adapted to go below 300K. So, only the dew point results are presented (Figure II-34 – right side). They will be used as a guideline to outline the working zone. Nevertheless, since the previous ternary diagrams and the binary C_3 cut (2.8 mol% MAPD) + CH_4 have good agreement with PPR78 results, we assume that the critical ternary diagram obtained with PPR78 also has reliable results.

The next step is to define the working zones that will be used on the pilot plant.

II.6.4 C₃ cut hydrogenation working zone

From the previous data, several graphics were constructed based on slices of the ternary diagrams [e.g. line from 100% solvent to 97.2% for 1 MAPD:H₂ ratio]. These slices focus on the working zone for several MAPD:H₂ stoichiometry ratio (for hydrogenation), solvent composition and pilot plant & process limitations (180 bar [pilot plant maximum pressure] and 330 K [to preserve the catalytic activity (Cabiac et al., 2013)]), see Figure II-35.

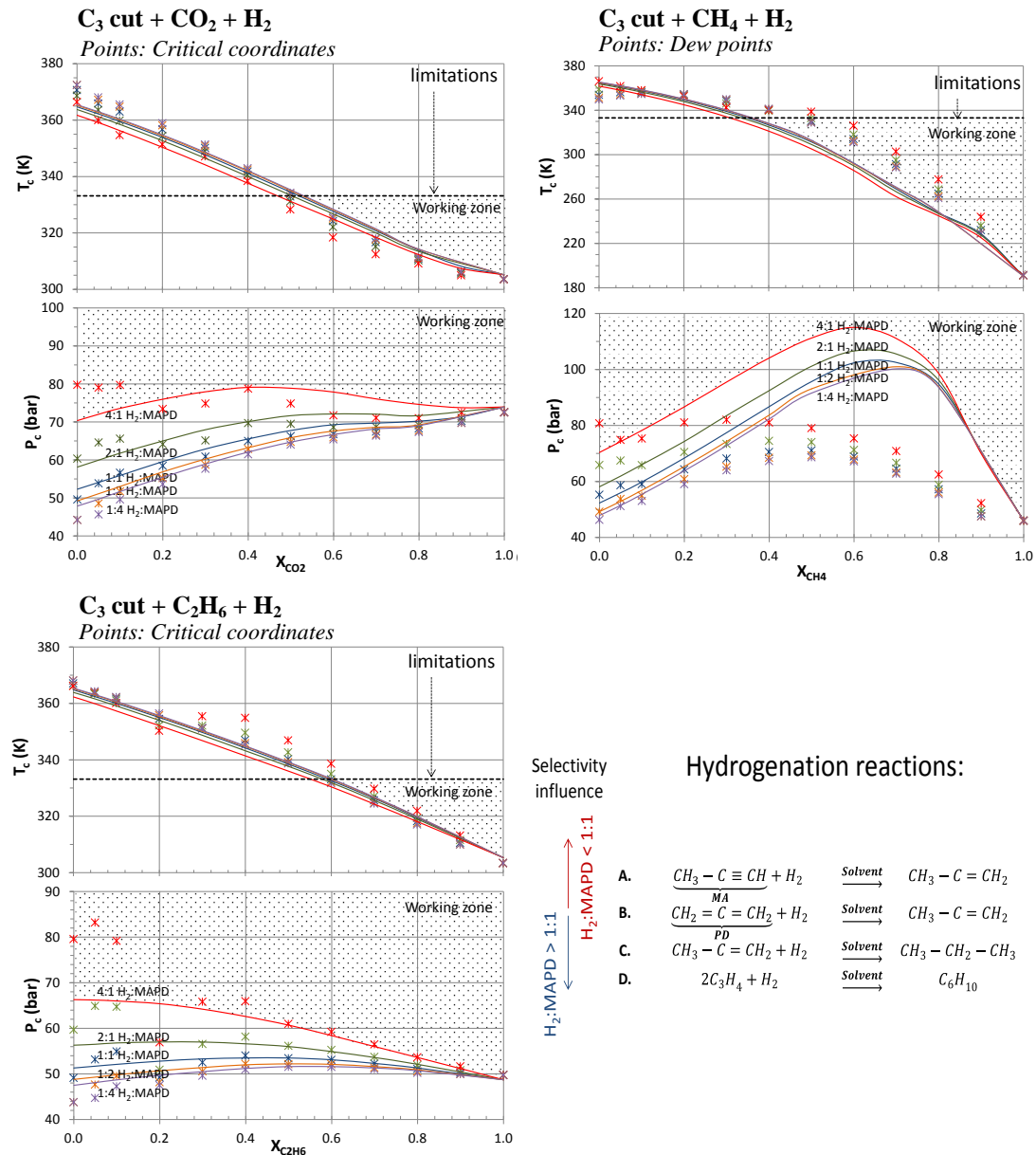


Figure II-35: Pressure and temperature conditions to be in the supercritical domain, depending on the stoichiometry ratio and solvent composition. The lines are related to the model results, and the points are related to experimental values.

These graphics are very useful because they give information about the conditions required to be in supercritical conditions within process-restricted conditions. Regarding each one in detail:

CO₂ as solvent: the model has excellent agreement with the experimental data for the temperature (Average Relative Deviation=1%). For the pressure, there is a small deviation of 4% (ARD), which is acceptable.

Ethane as solvent: there are some deviations that are related to low composition of ethane (experimental problems). Even so, the model has also an excellent agreement with the experimental data, having an ARD of 1% for the temperature and 4% for the pressure.

CH₄ as solvent: Inside the measurable zone ($T > 300\text{K}$), the results have a good agreement. The ARD for critical temperature is 1% and for critical pressure is 7%. The only problem of this diagram is in the zone below 300K, where we could not have the access to the critical points. This is due to a limitation in the experimental set-up used (not able to work below 300 K), rather than a problem in the experimental methodology.

For the pilot plant required conditions, it is now possible to say that the mixture with the solvent CH₄ has the softer conditions (temperature) and the less quantity of solvent required. In the other hand, it has the highest working pressures, but it is not a problem for the pilot plant. Thus, CH₄ proves to be the best solvent for working with the C₃ cut at supercritical conditions, because of the larger working range. This means that we will have a higher composition of solvent to parameterize, giving more working flexibility. However, this is not an eliminatory condition because the different solvents have different chemical properties (e.g. diffusivity), which can be interesting for the reaction.

Our choice: (1) CH₄ → (2) ethane → (3) CO₂ (last one because it might interact with the catalyst).

In terms of the reactions experiments, we may raise the question: **is the supercritical medium conserved during the reactions?** Two elements should be considered to answer this question:

Heat generated during the reaction: can be easily transferred, but even so, the temperature will rise with the exothermic reaction, which goes in the right sense. The supercritical conditions will be maintained.

Reactant consumption: it was proved that MAPD variation has only a minimal impact on critical conditions [§II.4.2], which leave us with the H₂ consumption. During reaction H₂ will decrease, which will reduce the critical pressure required to maintain supercritical conditions. For instance, if we look at 4:1 H₂:MAPD and 1:4 H₂:MAPD (Figure II-35). It is possible to realize that the reducing H₂:MAPD ratio leads to the reduction of the critical pressure required. In other words, this also goes in the right sense to keep supercritical domain during the reaction.

Answer: If supercritical at the beginning, it should be supercritical at the end.

II.6.5 Conclusion

The **experimental and predicted points** for the C₃ cut were obtained with **excellent agreement between both approaches**, following the strategy previously developed.

The thermodynamic model is validated, and it can be used for C₃ cut + solvent +H₂. **The model will allow planning experiments in the pilot plant** for the supercritical domain and to obtain data related to fluid density.

The **CH₄ proves to be the best solvent** for working with the C₃ cut at supercritical conditions, because of the larger working range.

The next step is to apply the right conditions to the pilot plant and perform catalytic reactions in supercritical medium. This should allow to accessing intrinsic kinetics constants at different temperatures and pressures.

II.7 Global conclusions

This chapter was focused on the determination of the critical coordinates for the C₃ cut hydrogenation. The strategy and conclusions are:

1. Development and validation (literature) of an **algorithm to predict critical points** for multicomponent systems.
 - a. Good agreement between algorithm and literature. The average relative deviation is 2.9% for pressure and 1.8% for temperature;
 - b. From the EOS studied, the PPR78 seems to be the best one.
2. “**Design of experiments**” for multicomponent systems.
 - a. A ternary diagram tool was developed. It allows to estimate the optimal number of points required to fully describe the multicomponent systems (for critical coordinates);
 - b. It is easy to apply and can reduce the number of experiments needed (less time-consuming).
3. **Development and validation of experimental set-up** to determine critical points.
 - a. A microfluidic device was designed to have access to multicomponent mixtures in no motion regime (new technique developed called “dynamic stopflow”);
 - b. It was shown that set-up can provide accurate data for multicomponent mixtures (compared to PPR78 EOS-calculated and literature data) and fast screening.
4. **Application** of the experimental set-up and “design of experiments” **to C₃ cut**.
 - a. The experimental and predicted points for the C₃ cut were obtained with excellent agreement (Figure II-35).
 - b. The working zone with several solvents (CH₄; Ethane; CO₂) was defined. The choice of solvents is: CH₄, then ethane, then CO₂.

With the strategy adopted it was possible to evaluate critical points. It allowed a fast experimental screening (of the experimental conditions) and lower costs, with no loss of quality.

The **next step** is to **apply the conditions previously obtained (working zone) to the pilot plant**. The goal is to perform catalytic reactions in supercritical medium. It allows approaching the reactions intrinsic kinetics and conversions with different temperatures and pressures (which is difficult with the current operating conditions [§I.4]). The effect of the solvent on the intrinsic kinetics will be evaluated for CO₂, CH₄ and ethane.

Chapter III

Pilot plant: presentation and characterization

Abstract

This chapter is devoted to the presentation of the experimental set-up and to the characterization of the selected reactor, particularly the single pellet string reactor. To characterize it, the random packing, the hydrodynamics and the mass transfer were studied using photo analysis (for particle arrangement) and computational fluid dynamics (CFD). The hydrodynamic study shows that the reactor adopted can be modeled as a plug flow reactor with low axial dispersion ($Pe > 70$). For the mass transfer, a liquid-solid correlation is proposed from CFD simulations and compared with the Ranz and Marshall (1952) correlation for packed bed reactors in monophasic system. The results obtained are close to a Ranz and Marshall (1952) correlation.

To study the difference between the reactors at the pilot and industrial scale, the mass transfer rates of the reactor studied was compared with industrial reactors for different flow regimes (bubble, trickle and pulse). The selected reactor can be adapted to have equal mass transfer rates for industrial reactors working at the bubble or pulse flow regimes.

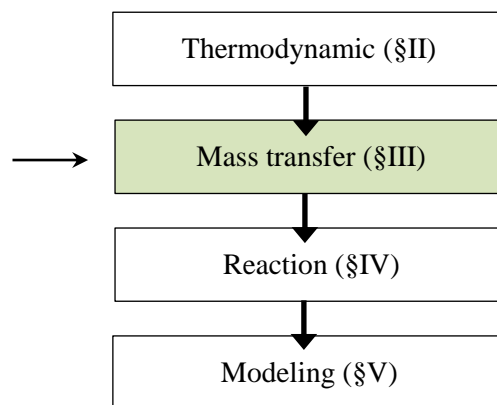


Figure III.1: Manuscript's guideline.

III.1 Introduction

To be able to **identify the benefits of unconventional conditions** (high pressure and supercritical fluids) **in hydrogenation reactions**, the pilot reactor technology must be carefully designed. The **choice of the reactor is not easy**, because the reactor should have **good mass transfer rates** (G/L and L/S) **for classical** (G/L/S at 20 bar and 300K for the MAPD hydrogenation) **and unconventional conditions** (L/S or SC/S at 120 bar and 300K). Moreover, it should provide repeatable results (almost no dead zones and random packing effects) and, at the same time, it should be offer clear and easily understandable data.

Regarding classical conditions for MAPD hydrogenation (gas-liquid-solid) (Samimi et al., 2015), if a **catalytic basket reactor technology** (batch or semi-continuous) is used, the gas and liquid flows are forced to pass through a basket filled with catalyst pellets (Magnico and Fongarland, 2006). In this technology, the **interstitial velocity and the gas hold-up inside a catalytic basket are difficult to quantify**, experimentally or by computational means (Braga, 2014; Magnico and Fongarland, 2006). Basket reactors require an extensive experimental set study, such as impeller rotation and porosity inside the basket (Magnico and Fongarland, 2006). As a consequence of complex velocity fields, the overall mass transfer evaluated may be inaccurate or inadequate for the necessary conditions. Since one of the goals is to quantify the mass transfer gains between classical and unconventional conditions, **the basket reactor is not a suitable option for the present study**.

An excellent way to quantify mass transfer is to perform reactions in a simplified packed bed technology called **single pellet string reactor**, which was firstly introduced by Satterfield et al. (1969). This technology operates in continuous mode, and the catalyst bed is arranged in a line, which reduces random packing effects (Hipolito et al., 2010). It usually operates in plug flow (good mixing due to a stationary mixing zone) or stratified regime for gas-liquid-solid systems. For these regimes, the catalyst in classical conditions is usually covered by a liquid film (surface wetted from 70 to 100%) (Hipolito, 2010; Schweitzer et al., 2010).

Before performing C₃ cut hydrogenation in unconventional conditions, **the single pellet string reactor and the catalyst packing should be characterized** (*e.g.* particle diameter distribution, hydrodynamics, interphase and external mass transfer). This reactor has been investigated in terms of hydrodynamic and mass transfer by experimental and numerical means (Haase et al., 2013; Hipolito et al., 2010; Müller et al., 2012). In the recent years, the most extensive study was accomplished by Hipolito et al. (2010). They characterized a square reactor and proposed correlations for gas-liquid and liquid-solid mass transfer. When injecting a tracer in liquid-solid experiments, the authors observed deviations from a dispersive plug flow reactor. **With regards to this problematic, a single pellet string reactor with circular section was selected instead of one with a square section**. The goal is to avoid, as much as possible, dispersion effects (monophasic only) by reducing low-velocity locations and dead zones. Regarding Müller et al. (2012) results (CFD experiments), better results should be expected for a cylindrical reactor than for a square reactor.

Before characterizing the pilot reactor, the first subchapter details the **experimental set-up**. It is followed by a **description of the single pellet string reactor selected**, placing the primary

focus on the packing of the catalyst. Then, the **catalyst characterization**, the catalyst reduction process, the analysis method and the data processing are also discussed.

In the second subchapter, the **CFD methodology** adopted (Computational Fluid Dynamics) to characterize the reactor is detailed. Finally, the results obtained for **RTD** (Residence Time Distribution) and **liquid-solid mass transfer** are presented.

III.2 Experimental section

III.2.1 Chemicals

The fluids used were C₃ cut (composition 2.8 mol% MAPD, see Table III.1), H₂, CO₂, CH₄, ethane and n-heptane. The C₃ cut mixture was obtained at a refinery from the outlet of the steam cracker after separation. The H₂, CO₂, CH₄ and ethane (N45 purity) were purchased from AirLiquid[®]. The n-heptane (99.5 mol%) was purchased from Sigma-Aldrich[®].

Table III.1: C₃ cut mixture composition.

Components	$x_{C_3\text{ cut}}$ (2.8 mol% MAPD)
Propane	3.27
Propylene	93.93
Propadiene	1.62
Methyl-acetylene	1.18

III.2.2 Experimental set-up

The hydrogenation of the C₃ cut was performed in a cylindrical single pellet string reactor immersed in a thermostatic bath to maintain conditions close to an ideal isothermal reactor. The circular section was chosen to avoid dead zones. The reactor used was defined according to the catalyst mean diameter ($d_{reactor} > d_{cat.} \approx 2.45\text{ mm}$) and the catalyst weight required for the WHSV studied (150 and 1500 h⁻¹). In this way, the reactor selected has an inner diameter of 3 mm and 0.2 m of total length ($n_{cat.}^{max} \approx 80 \Rightarrow$ max. number of pellets inside the reactor) (**Figure III.2**). It was mounted horizontally, in order to fit inside the thermostatic controlled bath (**Figure III.3**). This is not the most conventional reactor position, but since it has a well-packed bed (maximum packing during the filling) and it will be mostly used for monophasic flow (the impact of gravity forces are low), the flow regime should be not too different from an upflow vertical position.

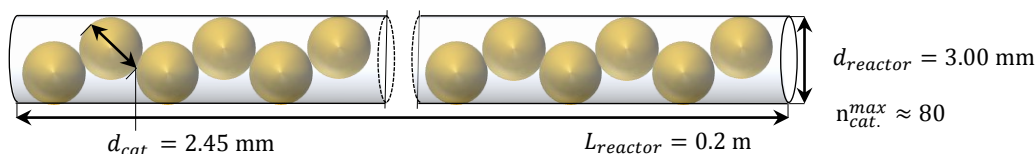


Figure III.2: Simplified scheme of a cylindrical single pellet string reactor used in the pilot plant (codename: U856). The real catalyst packing may be different.

The fluids are driven by three technologies: HPLC pumps (Gilson[®] 305), a Coriolis mass-flow controller (mini CORI-FLOW[®] device) and a thermal mass flow controller (Brooks Instrument's[®]) (see **Figure III.3**).

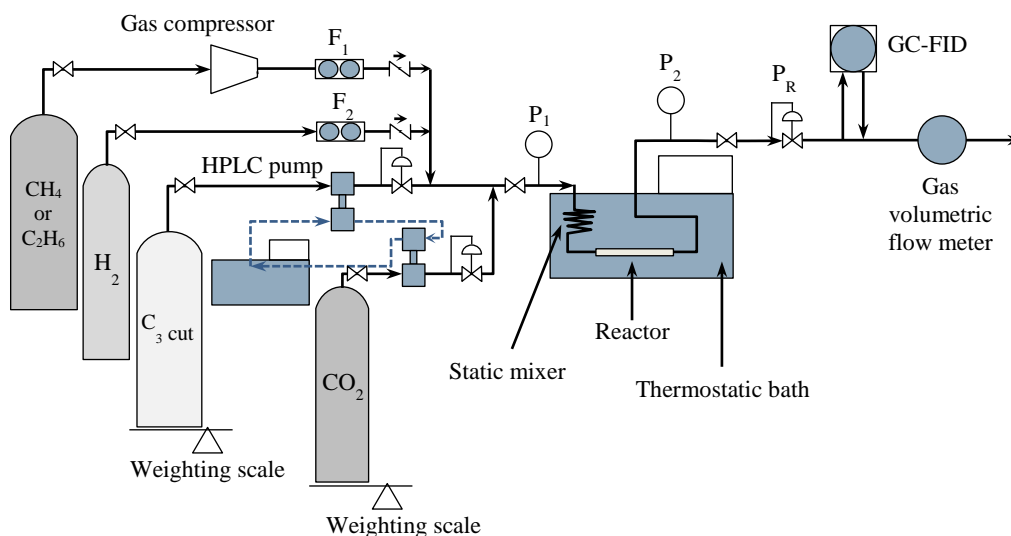


Figure III.3: Simplified scheme of the experimental set-up. F_1 is the Coriolis mass-flow controller; F_2 is the thermal mass flow controller; P_1 is the reactor downstream pressure transducer; P_2 is the reactor upstream pressure transducer; P_R is the back pressure regulator.

In the experimental set-up, two high-pressure piston pumps are used to feed the reactor with liquefied C_3 cut, CO_2 and/or n-heptane. The pumps' heads are maintained at 263K with a cooling fluid (ethylene glycol) to achieve liquefaction. Both fluids are always pressurized at 140 bar (back pressure regulators) to avoid density fluctuations and backflows during experiments. After the pumps and shortly before the static mixers, the fluids are depressurized to the process pressure. To measure the mass flow rate, in the upstream of each pump, the bottles (C_3 cut and CO_2) are connected to a weighting scale (mass variations).

For CH_4 or ethane, a Coriolis mass-flow controller sets the mass flow-rate (see **Figure III.3-F₁**). They are pressurized at 150 bar with the help of a pressure booster, then depressurized to the operating pressure with the aid of the flow controller. The check valves are placed in the downstream line before the static mixer to avoid backflow. Similar to CH_4 or ethane, the H_2 is subjected to the same procedure, being controlled by a thermal mass flow controller.

Monitoring and controlling the operating conditions

The pressure is controlled downstream of the reactor with a control valve connected to a gauge pressure transducer, with a sensitivity of 0.1 bar. The pressure drop through the reactor is monitored with two gauge pressure transducers placed in the downstream and upstream lines, having each a resolution of 2 mbar. All pressures reported are relative to the atmosphere. The temperature inside the reactor is controlled by an agitated thermostatic bath with a sensitivity of 0.2K and a working range from 273 to 423K.

Set-up reliability

For each experiment, the mass balance is checked with a gas volumetric flow meter (at NTP conditions) placed at the end of the set-up (see **Figure III.3**) to ensure reliable results. The working range goes from 40 to 4000 dm³h⁻¹. If any significant irregularity is detected [relative mass deviation (g) > 3 %], the set-up is checked for leakages and the experimental points are repeated. Standard procedures were adopted to detect leakages in the tubing network.

The inlet and outlet fluids are analyzed using gas chromatography (Agilent GC[®]) with flame ionization detector (FID) based on the combustion of H₂/air. Therefore, the H₂ content feed to the chromatograph cannot be detected. To quantify the H₂ content at the outlet, a carbon mass balance is evaluated in relation to the MAPD consumption and the propane production (later discussed). To separate the main species (propadiene, propyne, propane and propylene), a chromatography column of Al₂O₃ (Agilent[®]) is used. Each chromatography analysis takes 20 minutes. During the analysis period, the oven goes from 323 to 493K in 15 minutes, and then in the remaining 5 minutes, the temperature goes from 493 to 323K. For the analysis, the mobile phase selected is helium.

C₃ cut feedstock analysis

To check the accuracy and reliability of the gas chromatography and set-up, the C₃ cut feedstock was analyzed without reaction (bypassing the reactor) during 2 hours (~6 chromatograms) (Figure III.4 and Figure III.5), which is the usual time of an experiment. Furthermore, the C₃ cut feedstock was analyzed at the beginning of each day of tests to follow the evolution of the composition inside the bottle. The tests were performed with the same feedstock.

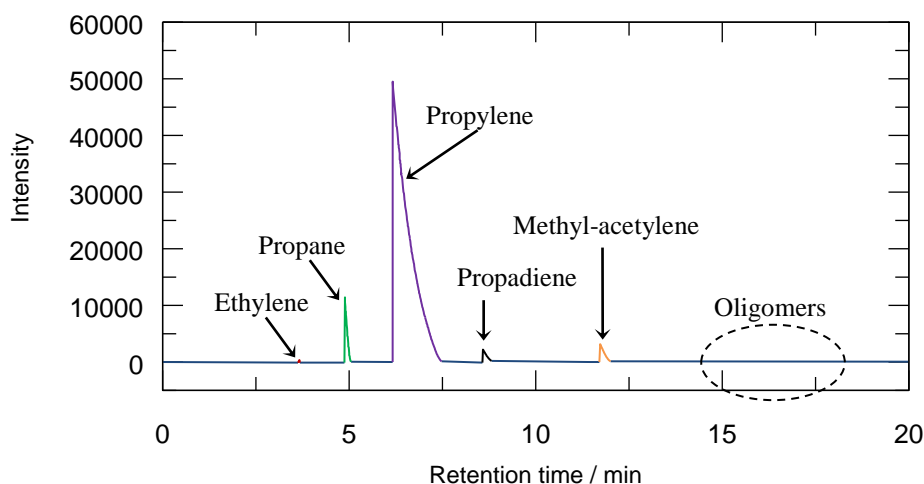


Figure III.4: Chromatogram (GC-FID) of the C₃ cut feedstock. The molar composition is obtained by normalization of peaks (area) without including the produced oligomers (not possible to identify the species). The dashed circle represents the retention time zone for oligomers (C₄ to C₈).

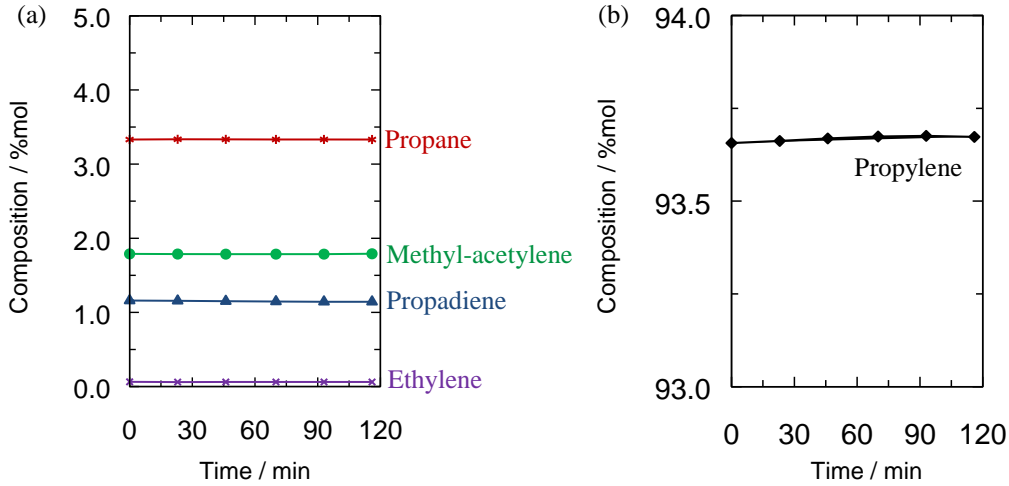


Figure III.5: Analysis of the C₃ cut feedstock by GC-FID. (a) Compounds (propane, MAPD and ethylene) with low mole fraction; (b) Compound (propylene) with high mole fraction.

Regarding Figure III.5, the average absolute deviation between feedstock analysis is almost negligible (less than 0.5%). The feedstock is monitored daily. The feedstock composition is stable during an extended period (weeks and months).

With the analytic methodology adopted (GC-FID), it is impossible to quantify the content of H₂ and oligomers, since the FID flame is generated by H₂ combustion and the separation/identification of oligomers is problematic. More research has to be done to optimize the GC analysis. Additional improvements are possible to enhance H₂ and oligomer detection, specifically adding a second detection sensor and a second separation column. However, to support this thesis, the MAPD consumption and propane production should be enough to quantify the impact of unconventional conditions (high-pressure and supercritical). The oligomers were considered as a single compound and were quantified by relative area (later discussed, §IV.2). This will help understanding the effect of the new conditions on the oligomerization reaction.

Experimental data processing

The *WHSV* is calculated with the total mass flow rate (W_{total} : solvent and C₃ cut). The *LHSV* (§I.2) definition was not adopted, in order to avoid uncertainties related to density variations during reaction (normally few, according to the PPR78 EOS). The superficial velocities are calculated based on the total volume flow-rate (Q_{total} : solvent, C₃ cut and H₂). The equations used are written below

$$\text{Weight hourly space velocity (h}^{-1}\text{)} \quad WHSV = W_{total}/m_{cat.} \quad \text{Eq. III.1}$$

$$\text{Interstitial average velocity (m.s}^{-1}\text{)} \quad \bar{u}_{int} = Q_{total}/(\varepsilon A_{reactor}) \quad \text{Eq. III.2}$$

$$\text{Section area (m}^2\text{)} \quad A_{reactor} = \pi d_{reactor}^2/4 \quad \text{Eq. III.3}$$

$$\text{Molar concentration flow-rate variation for a species } i \text{ (mol.m}^{-3}\text{.s}^{-1}\text{)} \quad \Delta \mathcal{N}_i = \mathcal{N}_{total,inlet} x_{i,inlet} - \mathcal{N}_{total,outlet} x_{i,outlet} \quad \text{Eq. III.4}$$

$$\text{Molar fraction of a species } i \quad \mathcal{N}_i = \frac{\mathcal{N}_{total} x_i}{\mathcal{N}_{total}} \quad \text{Eq. III.5}$$

Total molar concentration flow-rate (mol.m⁻³.s⁻¹)
$$\mathcal{N}_{total} = \sum_{C_1}^{C_3} \mathcal{N}_i + \mathcal{N}_{H_2} \quad \text{Eq. III.6}$$

Mass balance for H₂ (g.m⁻³.s⁻¹)
(*assumption*: no oligomers produced)
$$\Delta \mathcal{N}_{H_2} M_{H_2} = \Delta \mathcal{N}_{MAPD} M_{MAPD} + \Delta \mathcal{N}_{PA} M_{PA} \quad \text{Eq. III.7}$$

Conversion of a species *i*
$$X_i = \frac{\Delta \mathcal{N}_i}{\mathcal{N}_{total,inlet} x_{i,inlet}} \quad \text{Eq. III.8}$$

Selectivity for PR (propylene)
$$S_{PR} = - \frac{\Delta \mathcal{N}_{PR}}{\Delta \mathcal{N}_{MAPD}} \quad \text{Eq. III.9}$$

where W_{total} (kg.h⁻¹) is the total mass flow-rate, $m_{cat.}$ (kg) is the mass of the catalyst, Q_{total} (m³.s⁻¹) is the volume flow-rate, ε is the reactor porosity and \mathcal{N}_i (mol.m⁻³.s⁻¹) is the molar concentration flow-rate of a species *i*.

III.2.3 Catalyst characterization

To perform C₃ cut hydrogenation, a catalyst (named W in this report) developed at the IFPEN was selected. The catalyst has a spherical shape. It has an average diameter of 2.45±0.07 mm and a normal particle mass distribution of $8.4 \times 10^{-3} \pm 1.1 \times 10^{-3}$ g/particle (Figure III.6). It is based on Al₂O₃ with an < 1000 μm palladium crust. The catalyst porosity (ε_p) was determined using mercury intrusion porosimetry (MIP), being about 0.65.

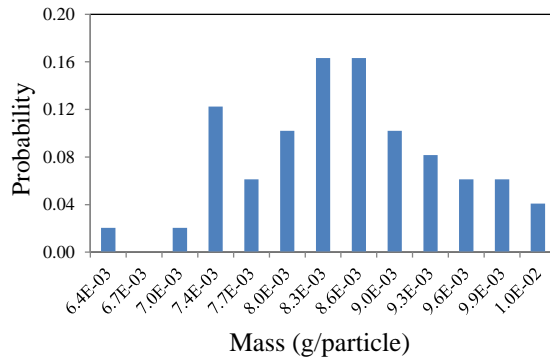


Figure III.6: Particle mass distribution for the catalyst W. For this catalyst, the particles have a diameter between 2.38 and 2.50 mm.

To inspect the catalyst effective diffusion (intragranular), H-1 DOSY-NMR (diffusion-ordered spectroscopy – nuclear magnetic resonance) measurements with PFG (pulse gradient field gradient) were done at the IFPEN (by Mickael Rivallan from dept. of material characterization). The results and discussion are in Appendix §III.1.

The results show that the free self-diffusion ($D_{Tot,b}$) and particle diffusion ($D_{Tot,e}$) are identical. To fully understand the DOSY-NMR results, more studies, and an enhanced model might be required. Our goal was to draft some guidelines to analyze the obtained data, in order to have hints about the diffusion of species presented in C₃ cut hydrogenation. Concerning the effective diffusion of MA, PD, and other species in C₃ cut, it is assumed that their value might be equal to their diffusion in the bulk.

The catalyst activation (reduction) is discussed in Appendix §III.2.

III.2.4 Packing characterization

After characterizing catalyst and describing the reduction process, the next step is to characterize the installation. In this topic, the catalyst packing will be firstly described.

The most interesting advantage of the single string pellet reactor technology is to reduce catalyst-packing effects. There are almost no preferential paths and random packing, which are significantly present in fixed bed reactors (Dorai et al., 2012). Although particle packing is compact and confined, random packing may still exist (Haase et al., 2013), varying from the densest packing form to the lightest packing form (perfect pellet string). It may introduce uncertainties in the reaction results because the porosity, superficial velocity, and hydrodynamic behavior can change.

Hipolito et al. (2010) suggested that there are three types of particle arrangements inside a square single pellet string reactor. The authors compared the pressure drop with these arrangements and observed that the pressure drop could vary up to 5 times for liquid flows. For liquid-gas systems, the same order of magnitude is anticipated. Unfortunately, the impact of the particle arrangements in the catalytic conversion was not discussed in their publication. Since pressure drop varies with different particle arrangements, we might think that it can also have an impact on the reactor performance (*e.g.* conversion).

This way, two strategies were followed to address particles arrangement:

1. A small particle diameter range selected (from 2.38 to 2.50 mm);
2. The reactor diameter was designed to be close to the particle diameter ($d_{reactor} - d_{cat.} \approx 0.46$ mm). Therefore, particles have small space available;
3. The particle arrangement with catalyst particles inside the reactor was characterized.

This study may give future clues about performance variations for young catalysts, operating with identical conditions and coming from the same production batch. The purpose of the next development is to identify the preferential arrangements (*i.e.* angle that characterize the position between pellets). They will be later used in hydrodynamic and mass transfer simulation, using CFD tools (Fluent). The study is presented in Appendix §III.3. The preferential arrangements are shown on Figure III.7.

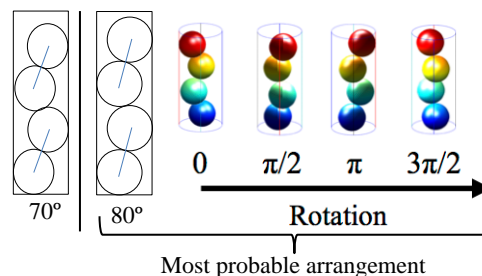


Figure III.7: Most probable particle arrangements and 3D view of a 80° particle arrangement reconstruction.

The particle packing characterization shows that with the reactor designed and the catalyst distribution, it is possible to have small random packing, since **72% of the particle follows 70° and 80° arrangements**. To favor the 80° particle arrangement, it is suggested to have a more homogeneous spherical shape distribution at the pilot scale. Nevertheless, since the catalyst pellet size distribution is small, improving the spherical shape distribution could be a challenge. **For this thesis purposes, 72% of certainty about the particle arrangement is enough to move to the next step:** characterize the single pellet string reactor for hydrodynamic and mass transfer.

III.3 Hydrodynamics and mass transfer in the single pellet string reactor

III.3.1 Introduction

Single pellet string reactors are used in research and development to perform catalyst screening for fast multiphasic reactions (§I.2.2), such as C₃ cut hydrogenation (Schweitzer et al., 2010). Their unique design with **single pellet string bed has benefits and limitations**.

The main **benefits** are the **reduced random packing** [previously detailed on Appendix §III.3], the **mass transfer enhancements** (Hipolito, 2010) and the **reduced macroscopic back mixing** (Haase et al., 2013). A considerable **drawback** is that the **mass transfer coefficients** ($k_L a_{GL}$ and $k_{LS} a_{LS}$) are **more sensitive** to the reactor diameter, reactor shape and particle size than in a packed bed reactor. Modifications of these key physical parameters lead to changes in the hydrodynamic regime and the superficial velocities. For instance, two authors proposed significant difference in mass transfer correlations for square pellet reactors (Haase et al., 2013; Hipolito, 2010), due to the square section and the particle size. Hipolito (2010) used a $4 \times 4 \text{ mm}^2$ reactor with particle diameter from 2 to 3 mm. Haase et al. (2013) used a $1 \times 1 \text{ mm}^2$ reactor with 0.8 mm particle diameter. Thus, for the reactor ($d_{reactor}=3$ mm, cylindrical shape) and catalyst selected ($d_{cat.} \approx 2.45$ mm), the mass transfer correlations should be reevaluated.

To characterize **mass transfer and hydrodynamics**, two approaches can be followed: experiments and/or **CFD (numerical)**.

Brief state of the art

To characterize the reactor's **hydrodynamics**, the typical techniques are tracer experiments (RTD) and particle image velocimetry (PIV). In Hipolito's (2010) work, it was shown by RTD experiments that the flow in a square single pellet string reactor ($4 \times 4 \text{ mm}^2$) follows a plug flow-dispersion model for gas-liquid flows ($Pe > 50$, depending on the pellet size and flow-rates). For single-phase (liquid only), the flow differs significantly from the plug flow-dispersion model, due to the dead volumes, which are potentially caused by the channel geometry.

To experimentally evaluate the **mass transfer coefficients**, particles of β -naphthol, with similar size to the catalyst pellets, can be dissolved in a fluid (Hipolito, 2010). This fluid

should have well-known physical properties, such as diffusivity, density, and viscosity. Afterward, by monitoring the β -naphthol concentration in the bulk and applying mass balances (to liquid film around a particle and the reactor), it is possible to obtain mass transfer coefficients. The reactor mass balance equation should be modeled according to the reactor's hydrodynamics. For more information see Appendix §III.4.

Objectives

Since the **single pellet string reactor** is a **simplified technology**, it should be, *a priori*, **easier to describe hydrodynamics and mass transfer with numerical tools** (CFD) in comparison to traditional technologies, such as packed bed reactor. A CFD model allows **saving time by avoiding the construction and the validation of an experimental set-up**. Furthermore, in CFD it is possible to characterize the reactor with the working fluid at the experimental conditions (C_3 cut at 120 bar and 303K). These conditions are a challenge to the experimental set-up because the optical sensors (tracer detection) must support high pressures.

In a previous chapter §II.6 (thermodynamic chapter), it was shown that single-phase flows are present at **high-pressure and supercritical conditions**. **Using single-phase fluids avoids liquid-gas behavior and complex simulations** (no Euler-Euler multiphase approaches are required, *e.g.* VOD model). Moreover, the flow may have a laminar regime in the working range ($10 < Re_L < 600$) (later discussed), which simplifies the CFD model.

Since the CFD model to characterize the reactor is very simplified for single-phase fluid (the major parameter is the mesh refinement), the CFD methodology was adopted rather than the experimental one. **For conventional conditions (G/L/S), the simulations were not performed, since the liquid-gas behavior is complex and the simulations are long**. These simulations are not a limitation since the goal of the thesis is to have a single-phase fluid.

To calculate the liquid-solid mass transfer coefficient (k_{LS} in single-phase), the infinite reaction condition was set on the catalyst surface, then the bulk concentration and ∇C in the film was acquired.

III.3.2 CFD modeling

CFD simulations were performed in a 3D single-phase model with liquid propene at high-pressure conditions (120 bar). The geometry and grid were generated with DesignModeler[®] and Meshing[®] from Ansys 14 package. The hydrodynamic in the reactor and the quantification of mass transfer were solved with the commercial CFD solver Fluent 14.

Methodology

The single pellet reactor used in this study has a cylindrical shape ($d_{reactor}=3$ mm) and the particles have a spherical shape ($d_{cat.}=2.45$ mm). When packing, the particle arrangement typically follows a 3D helical shape (preferential particle arrangement). In the previous subsection (§III.2.4), it was shown that it is possible to simplify the 3D helical shape to a 3D zigzag shape. This was accomplished by using a characteristic angle between particles, instead of the two angles normally required. In the created geometry, the contact points (between spheres and sphere-wall) were replaced by a gap of 30 μm (almost no impact in the

superficial area distribution). This treatment is typically used in literature (Dixon et al., 2012) and the overall impact in mass transfer is kept at the minimum. The goal is to avoid numerical difficulties when solving the problem (this hypothesis will be later checked for mass transfer, since it is expected to have zero mass flux between the particles and the fluid at the contact points).

To characterize the single pellet string reactor, different geometries were adopted depending on the number of spheres studied (fully represented): 3 (basic block; Figure III.8), 7 and 80. To construct the different geometries, a basic 3-sphere block was repeated. There are two main advantages of a basic block. The first one is related to the mesh sensitivity analysis. The basic block can be tested with different meshes and the sensitivity results can be extended for a larger block (more spheres), since the basic block mesh characteristics will be maintained (basic 3-sphere block mesh is repeated). The second advantage is the capacity to easily change the number of spheres studied. The basic block was created to take into account, at each fully represented particle, the fluid behavior imposed by the particle before and after (Figure III.8). It was constructed based on the preferential particle arrangement of 80° (γ) between spheres (§III.2.4). This atypical geometry will be later important for the mass transfer studies.

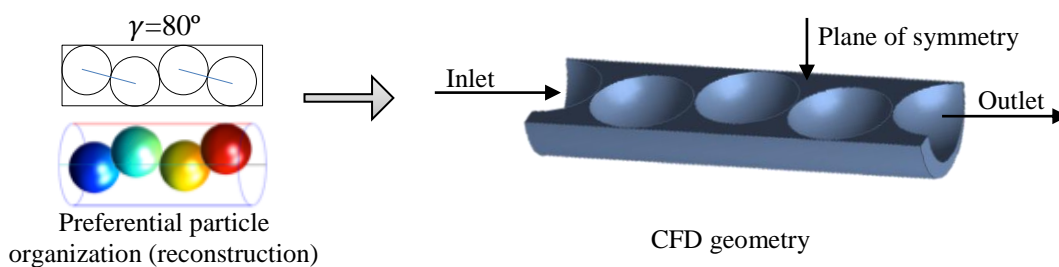


Figure III.8: Construction of the CFD geometry based on preferential particle arrangement. At each fully represented particle, the behavior before and after is taken into account (half spheres at the inlet and outlet of the channel).

Computational strategy adopted:

The calculations were performed for hydrodynamics and liquid-solid mass transfer, using single-phase fluids (unconventional conditions). Since the calculations are long, a representative block (basic block: 3-spheres) was used, and its mesh was subjected to sensitivity analysis for hydrodynamics and mass transfer. The basic block was duplicated (7 spheres) to check if its hydrodynamics and mass transfer are representative (minimum number of spheres).

After knowing the minimum number of spheres and mesh elements necessary to describe hydrodynamics and mass transfer, two different meshes were created: one for the hydrodynamics (full reactor, 80 spheres with an intermediate refined mesh [max.]) and another for the species transfer (3 spheres, highly refined mesh) (Figure III.9). At the end, a liquid-solid mass transfer correlation and the residence time distribution were obtained and compared with Ranz and Marshall (1952) correlation.

Finally, a 1D model will be deduced and will be later applied to model the reactor (§V.2).

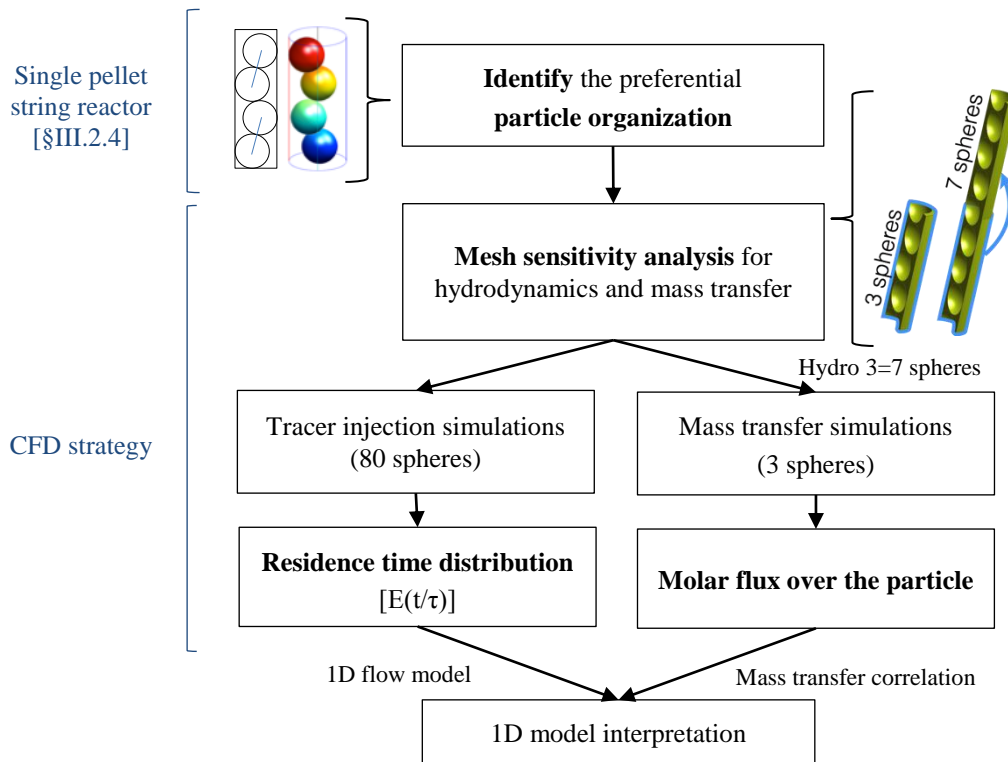


Figure III.9: CFD methodology adopted in the present study.

Global specifications

The current approach (Figure III.9) involves three numerical studies:

- i. mesh sensitivity analysis (goal: verify the mesh quality);
- ii. RTD (goal: 1D flow model);
- iii. liquid-solid mass transfer simulations (goal: liquid-mass transfer correlation).

The main CFD specifications are presented below. For hydrodynamics and mass transfer, the individual specifications will be later described in each simulation.

Solver properties: For hydrodynamic simulations (ii), the convective terms of the flow equations were discretized with a second order upwind scheme, and the pressure spatial derivatives with the SIMPLE scheme. For species transport (iii), a second order upwind scheme was used. The simulations were carried out in a stationary state (for hydrodynamics and mass transfer) and non-stationary state (for RTD simulations). All simulations were done in steady state regime, and the solutions were accepted for residuals lower than 10^{-6} .

Boundary conditions: Regarding the CFD geometry, only half of the 3-spheres block was simulated (Figure III.8). To simulate the missing half, the symmetry condition was activated. The 3-sphere block was used rather than a smaller block since the periodic inlet-outlet condition can be only adapted for hydrodynamics (not to mass transfer). Therefore, the inlet velocity was defined as uniform. Consequently, the fluid after the inlet has to have enough time to develop until stationary velocity profiles. It is expected that after 2 spheres the

hydrodynamic should be stationary [based on the interpretation of velocity fields shown by Müller et al. (2012)]. The reactor and catalyst pellets have stationary walls with no slip condition (velocity at the surface walls is zero). The outlet was defined as a pressure outlet, zero gauge pressure.

Fluid properties: The fluid was defined as incompressible propylene (~94 mol% of C₃ cut; in liquid state) at 120 bar and 303K ($\rho_L=526.83 \text{ kg.m}^{-3}$ and $\mu_L=1.07\times 10^{-4} \text{ Pa.s}$). For RTD and mass transfer simulations, a second fluid was used with propylene physical properties. The molecular self-diffusion (propylene-propylene) was defined as $1.1\times 10^{-8} \text{ m}^2.\text{s}^{-1}$ at 120 bar and 303 K [based on NIST webbook of physical properties (Lemmon et al., 2015) and Wilke and Chang (1955) correlation]. This approach was chosen to avoid adding mixing rules to determine local diffusivity coefficients, which can introduce uncertainties. Furthermore, the propylene diffusivity is very close to MAPD diffusivity (propylene: $1.1\times 10^{-8} \text{ m}^2.\text{s}^{-1}$ vs MAPD: $1.17\times 10^{-8} \text{ m}^2.\text{s}^{-1}$), which is the main reactive component.

Hydrodynamic regime: The (particle) Reynolds (Re_L) adopted for flow and mass transfer simulations is calculated based on the particle diameter and superficial velocity, rather than on the reactor diameter (normal Reynolds definition). It is often used in mass transfer studies.

$$Re_L = \frac{\rho_L \bar{u}_L d_{cat.}}{\mu_L} = \frac{\rho_L \bar{u}_L d_p}{\mu_L} \quad \text{Eq. III.10}$$

$$Re_{int} = Re_L / \varepsilon \quad \text{Eq. III.11}$$

$$\bar{u}_L = \frac{W_L}{\rho_L A_{reactor}} \rightarrow \bar{u}_L = \frac{u_{inlet \ surface} A_{inlet}}{A_{reactor}} \quad \text{Eq. III.12}$$

where ρ_L (kg.m^{-3}) is the liquid density, \bar{u}_L (m.s^{-1}) is the liquid average superficial velocity, $d_{cat.}$ (m) is the catalyst diameter, d_p (m) is the particle diameter, μ_L (Pa.s) is the liquid viscosity, W_L (kg.s^{-1}) is the mass flow-rate and $A_{reactor}$ (m^2) is the channel section area.

According to the literature experimental results (for packed and single pellet string reactors) (Appendix §III.4), laminar and turbulent models (k- ε model) were adopted from $10 < Re_L < 400$ and from $Re_L > 400$, respectively. To compare the influence of the regime model, for $Re_L > 400$ the laminar model was compared with the turbulent model. For the experiments performed in the next chapter (§IV), the Re_L will vary between 50 and 700, for high-pressure conditions (liquid), and it will be above 1700, for supercritical conditions.

III.3.3 Mesh sensitivity analysis

In mass transfer simulations, the mesh refinement is a critical parameter to avoid numerical diffusion. To validate the mesh structure, a study of hydrodynamics and species concentration should be performed varying the mesh density. At the end, the solutions of velocity and concentration profiles should be independent of the mesh density.

Two 3D geometries with different reactor lengths were created: 10 mm (3-spheres block) and 20 mm (7 spheres block). The basic block geometry was discretized with 4 mesh types with tetrahedral elements [500 000, 1 500 000, 4 200 000 and 6 600 000 (Figure III.10)]. The difference between the meshes is in the refinement near the particle and the wall. For the

boundary layer adjoining the reactor wall, the maximum thickness was calculated using Eq. III.13 (Blasius, 1908).

$$\delta_{max} \approx 4.91 d_p / (2Re_{Int, max}) \approx 4.91 \frac{2.45 \text{ mm}}{2 \times 1500} \Rightarrow 4 \mu\text{m} \quad \text{Eq. III.13}$$

where δ_{max} (μm) is the maximum thickness expected for the first layer counting from the reactor wall. The d_p (mm) is the diameter of the particle in study (catalyst).

To construct the mesh, it was necessary to add gaps ($30 \mu\text{m}$) in place of contact points between particles. The impact of the gaps will be later discussed (III.3.4). The mesh refinement was studied for hydrodynamic and mass transfer for the basic block (3 spheres). An example of mesh for the basic block is shown in Figure III.10 for the 6 600 000 elements.

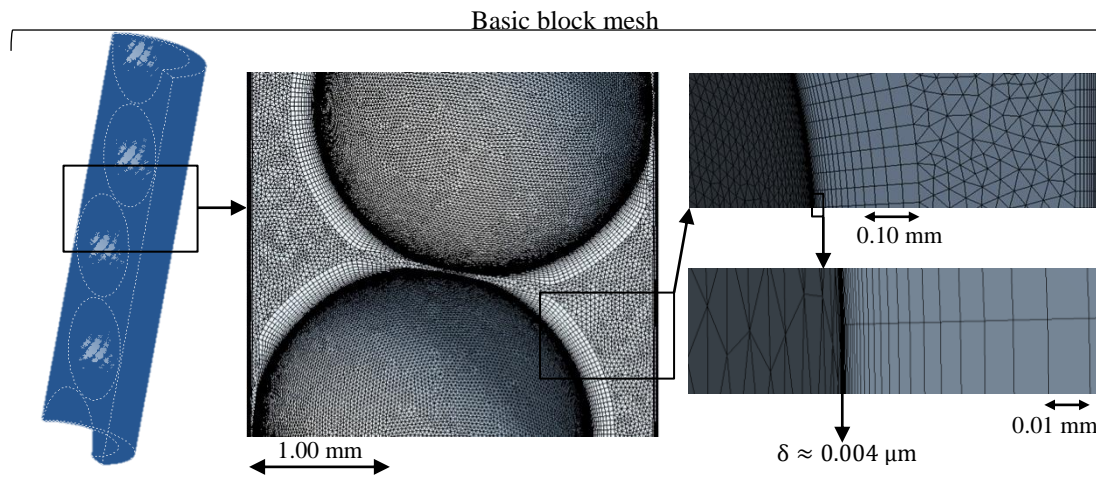


Figure III.10: Basic block mesh constructed for mass transfer simulations (max. 6 600 000 elements). The wall boundary layer was created with a thickness of $0.004 \mu\text{m}$ (over meshed conservative approach to avoid numerical diffusion). δ (μm) is the thickness.

For hydrodynamic, velocity profiles were evaluated in three zones: outlet, front and middle of the last fully represented particle (third particle). After 1 500 000 elements the results remained similar ($\sim 375\ 000$ elements/particle). For the mesh with fewer elements, the results have an average velocity deviation of 0.5% in relation to the other meshes. For mass transfer, the infinite reaction was set on the particle surface, and the average concentration profile in the reactor was evaluated. After 1 500 000 elements, the results remained similar.

To check if the hydrodynamic model in the basic block (3 spheres) is representative of a longer reactor, several velocity profiles were compared between 3 and 7 spheres block: reactor outlet, front and middle of the last fully represented sphere (Figure III.11a). The geometries used were over meshed (conservative approach), having 6 600 000 (3 spheres block) and 20 000 000 elements (7 spheres block). The approach logic is: if 3 and 7 spheres block have similar velocity profiles, also 3 and 80 spheres block will have (80 is the max. number of spheres inside the reactor).

Regarding Figure III.11b, identical profiles seem to be obtained from different geometries. For this reason, the hydrodynamic around the last fully represented sphere of the basic block

can be considered representative of an infinite single pellet string reactor in steady state. In other words, the basic block meshing can be assumed transposable to other lengths.

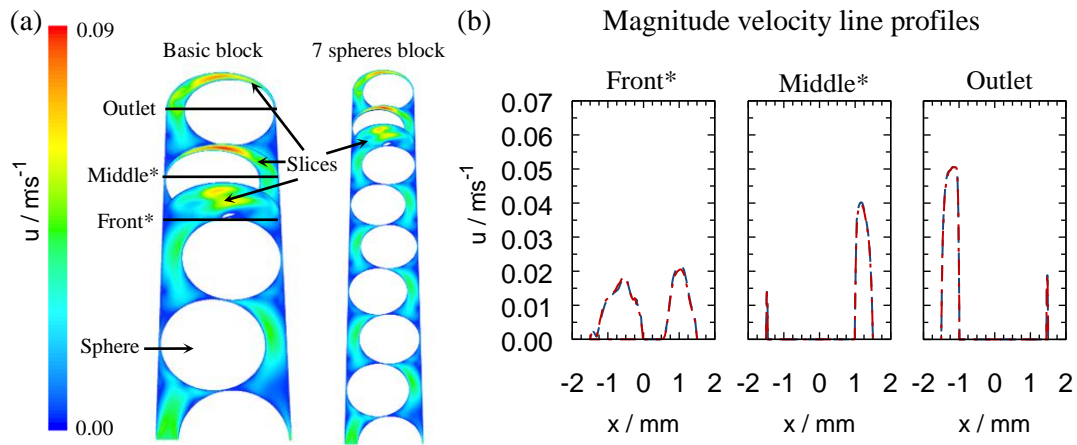


Figure III.11: (a) CFD hydrodynamic simulations for 3 and 7 spheres blocks. (b) Velocity profiles at reactor outlet and at the front and middle of the last fully represented particle*. The blue lines and red lines (side-by-side on the graphic) represent the 3 and 7 spheres block. In this example, the average velocity in the inlet was 0.04 m.s^{-1} .

III.3.4 Hydrodynamic simulations

Before analysing the mass transfer simulations, the understanding of the flow patterns in a single pellet string bed reactor is necessary. So, the hydrodynamic simulations will be firstly detailed before dealing with RTD. The objectives are to understand flow streamlines and to measure dispersion in the bed, which is defined by a Peclet number.

After this subchapter, the liquid-solid mass transfer will be detailed.

CFD specifications

Residence time distribution (RTD) mesh

To estimate the axial Peclet number, it is crucial to simulate the flow in the full reactor (80 spheres). Consequently, the mesh is computationally intense and time-consuming. Unfortunately, since the basic block has to be repeated to achieve 80 spheres, the mesh density will be too computationally intensive (~ 37 million of elements) and time-consuming. The strategy was to proceed with a less dense mesh, even knowing that results can be affected. They occur especially due to effects near the walls because they are not finely refined (reactor and particle). However, this model should provide close results for RTD, giving us information about the flow pattern and the existence of dead zones and/or preferential paths.

In conclusion, for the residence time distributions (RTD) simulations, a basic block with 500 000 elements was used and repeated 23 times (reactor with 80 spheres). At the end, the mesh used has around 12 million elements (Figure III.12).

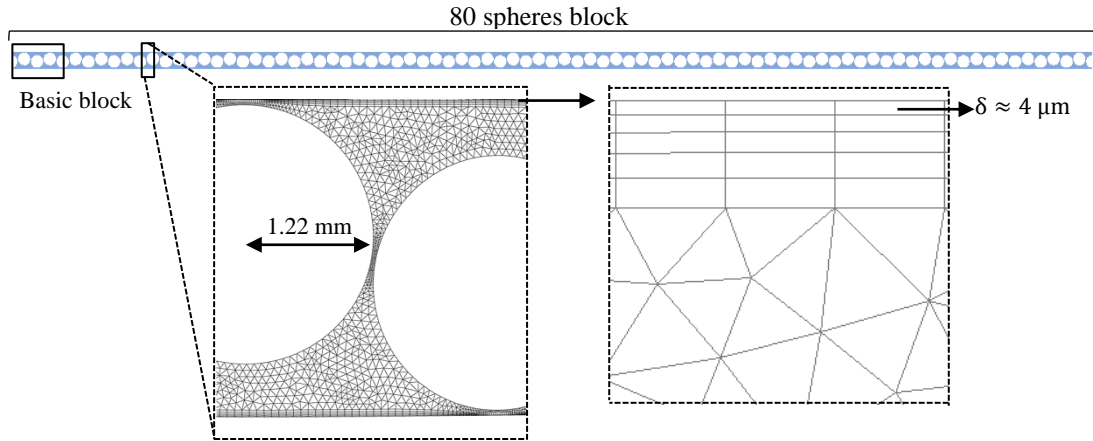


Figure III.12: Symmetric plane (2D) representation of the (3D) 80 spheres block mesh for the RTD simulations (12 500 000 elements). The wall boundary layer has a thickness of 4 μm .

Tracer injection: The residence time distributions (RTD) were accomplished by injecting an infinitesimal volume of tracer (mole fraction of 1) at the reactor inlet. The dispersion of the tracer mole fraction was monitored with several slices at different reactor length positions. Regarding the CFD model, the hydrodynamic was simulated in steady-state with mass transport equations disabled. The results were accepted when the steady-state residuals were below 10^{-6} . After having the flow pattern simulated and converged, the tracer transport was solved. The steady-state solver was modified to transient-state, the species transport equation was activated and the hydrodynamic equation was disabled. A conservative time step of $\tau_{reactor}/1800$ (s) was adopted for a total simulation time of $2\tau_{reactor}$ (s). At each time step, the continuity equations residuals were accepted below 10^{-5} . The quantity (total) of the tracer injected was obtained at the outlet for the simulations performed.

Results: hydrodynamic phenomena

Flow pattern and velocity contours

To understand the flow pattern inside the reactor, the velocity (magnitude) streamlines were evaluated for different Reynolds (Re_L), varying from 40 to 650. Similar flow patterns were founded in CFD simulations for the Reynolds evaluated. Also, similar results were obtained for 3 and 80 spheres block. For this reason, a dimensionless illustration of the streamlines is presented in Figure III.13 for the basic block to better illustrate the streamlines. In Figure III.13, it is also presented an example of the dimensionless contours.

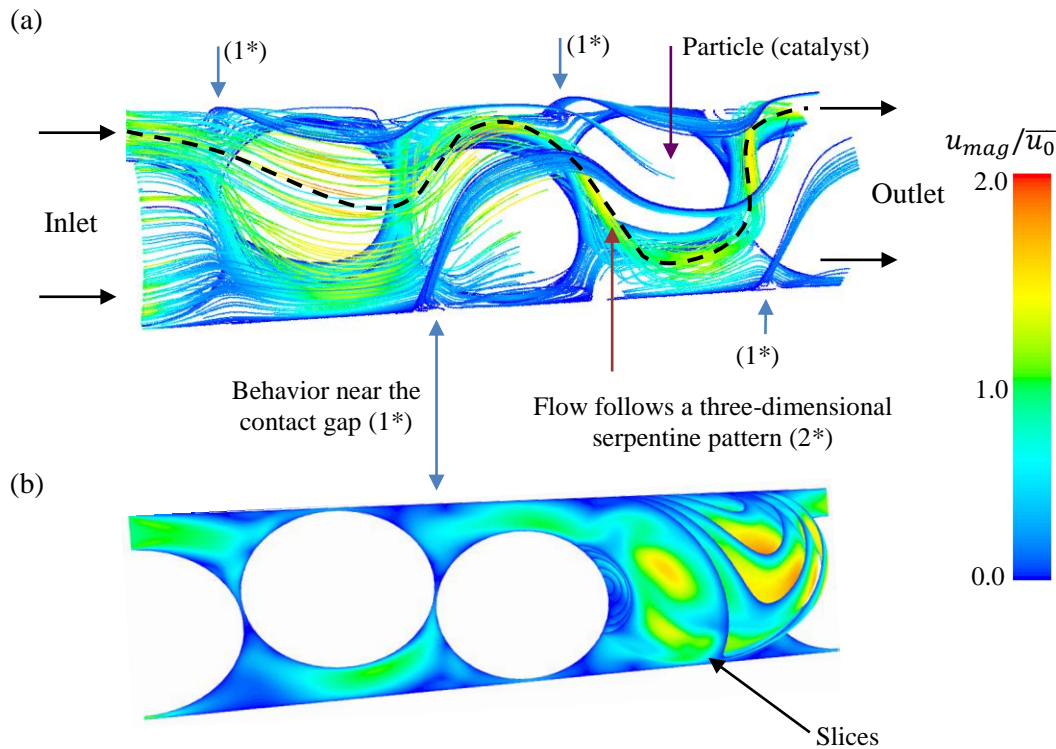


Figure III.13: (a) Typical dimensionless velocity magnitude (u_{mag}/\bar{u}_0) streamlines developed in the basic block (3-spheres block) [\bar{u}_0 is located at the inlet]. (b) Example of velocity contours for $Re_L = 160$ (laminar regime) in the plane of symmetry. The results were simulated in a 6 600 000 elements mesh (Figure III.10). Same behavior was observed in the 80 particle mesh (Figure III.12).

In Figure III.13, the streamlines indicate that the majority of the fluid has a 3D serpentine flow pattern (2*), which is caused by the zigzag particle arrangement adopted. For the real case scenario, it is expected a helical flow pattern, because the particles have a helical arrangement inside the channel. At this point the hypothesis that both particle arrangements have the 3D serpentine flow pattern was adopted (2*).

The velocity variations are generated by local changes in the superficial area, *i.e.*, different local porosities inside the reactor. As expected, the fluid is accelerated inside the gaps between particles (Figure III.16a, yellow color). It is noticeable that in the vicinity (1*) and inside the contact gaps (30 μm), the velocity magnitude is virtually zero, since the fluid tends to flow through the zones with less flow resistance (serpentine flow pattern). In other words, the majority of the flow tends to cross-channel in another position (Figure III.13 1*) to avoid losing energy. This also occurs experimentally, because the contact gap does not exist, therefore there are zones with no flow circulation (contact points; $u_{mag} = 0 \text{ m}\cdot\text{s}^{-1}$) or stagnant fluid ($u_{mag} \approx 0 \text{ m}\cdot\text{s}^{-1}$).

Figure III.13 suggests that having a contact gap ($u_{mag} \approx 0 \text{ m}\cdot\text{s}^{-1}$) should be well-representative for mass transfer simulations ($Re_L \approx 0 \Rightarrow Sh \approx 2 \Rightarrow$ almost no molar flux in the particle surface).

Residence time distributions (RTD) simulations

Having access to information about residence time distribution [E(t)] and average value ($\overline{t_{res}}$) allows to characterizing and constructing a reactor model, which will be later applied to the C₃ cut hydrogenation in a single fluid-phase. For the tracer concentration, the RTD is defined by:

$$E(t/\tau) = \frac{C_{tracer}}{\int_0^{\infty} C_{tracer} d(t/\tau)} \quad \text{Eq. III.14}$$

where C_{tracer} (mol.m⁻³) is the concentration of tracer, t (s) is the time and τ (s) is $V_{reactor}/Q_{total}$.

The residence time distribution was calculated in three different reactor positions: end of the 1st (3.7 mm), 30th (70.8 mm) and 80th (190 mm) fully represented particle. The goal is to access the tracer dispersion along the reactor in a single-phase. The $E(t/\tau)$ will be later used to construct a model of the reactor (§V).

The tracer pulse injection was similar to a Dirac to avoid adjusting time distributions. The simulations were performed on the full particle represented bed (mesh Figure III.12) for three different Reynolds (Re_L): 20 ($\bar{u}_0 = 0.005$ m.s⁻¹), 40 ($\bar{u}_0 = 0.01$ m.s⁻¹) and 160 ($\bar{u}_0 = 0.04$ m.s⁻¹). The inlet area is 2.39×10^{-6} m². The Reynolds 20 was chosen to increase the range of the reactor characterization, since the dispersion is higher for lower Reynolds. The results obtained were compared with a plug flow model with axial dispersion. For the present study, the radial dispersion was not evaluated, since it can be considered negligible, because the reactor diameter is small (3 mm).

Plug flow model with axial dispersion:

$$E(t/\tau)^{model} = \frac{1}{2} \sqrt{\frac{Pe_{ax}}{\pi t/\tau}} e^{-\frac{Pe_{ax}(1-t/\tau)^2}{4t/\tau}} \quad \text{Eq. III.15}$$

$$Pe_{ax} = \frac{\bar{u}_{int}.L}{D_{ax,PE}} \quad \text{Eq. III.16}$$

where Pe_{ax} is the Peclet number for axial dispersion, \bar{u}_L (m.s⁻¹) is the i velocity, L (m) is the reactor length and $D_{ax,PE}$ (m².s⁻¹) is the axial dispersion of propylene (tracer).

The Pe_{ax} was estimated by minimization the difference between the two residence time distributions: CFD and model.

$$F_{obj.} = [E(t/\tau)^{CFD} - E(t/\tau)^{model}]^2 \quad \text{Eq. III.17}$$

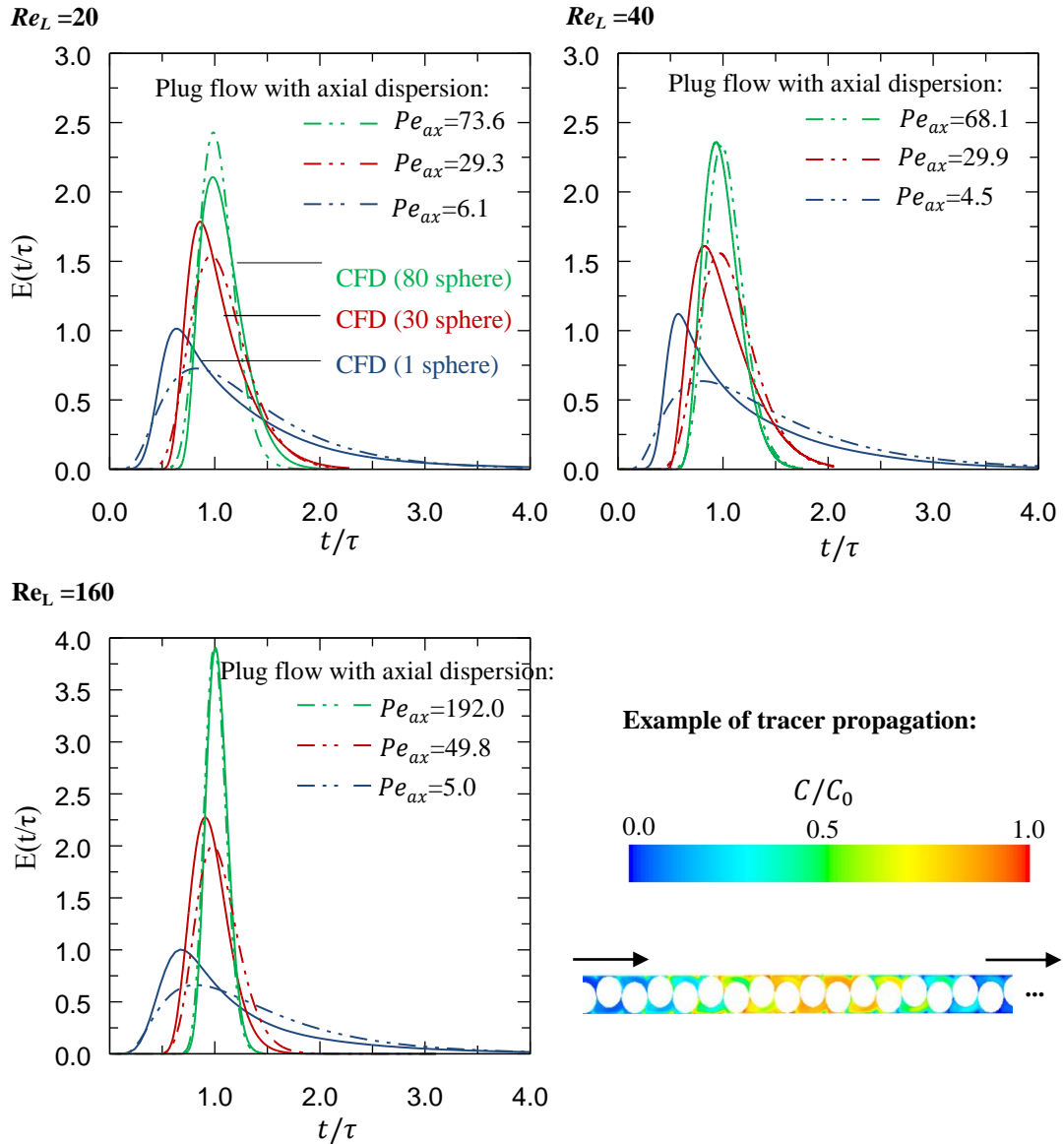


Figure III.14: Residence time distributions for three different Reynolds numbers at several positions: end of 1st sphere (3.7 mm), end of 30th sphere (70.8 mm) and end of 80th sphere (190 mm). The full lines are the CFD results for single-phase flow. The dashed lines are the plug flow model results (Eq. III.15).

As the Reynolds number increases, the residence time distribution trends to have higher Peclet numbers in the zones monitored. After 80 spheres, the CFD residence time distribution is close to a plug flow model with axial dispersion (low dispersion), having a $Pe_{ax} > 50$ (Figure III.14). For the Reynolds of 160, the axial dispersion is negligible ($Pe_{ax} > 190$) and the reactor flow may be considered as plug flow. The classification used is based on Rolland (2014).

For the experiments that will be performed in high-pressure conditions (liquid) [next chapter (§IV)], the Re_L will vary between 50 and 700. For points with $Re_L \approx 50$ the $Pe_{ax} > 68$. For the majority of the experiments $Re_L > 100$, so it is expected to have $Pe_{ax} > 100$.

For supercritical conditions, the $Re_L > 1700$ (34 times superior to $Re_L = 50$) and the diffusivity ($D_{ax,PE}$) is in maximum 10 times higher (§IV.5.1). Since the relative increase of Re_L is higher than the relative increase of diffusivity, it should be expected to have $Pe_{ax} > 68$ (plug flow with low axial dispersion).

The simulations will allow the construction of a model of the reactor (hydrodynamics), by using $E(t/\tau)$ for the experiments in a single phase (liquid et supercritical). The $E(t/\tau)$ can be replaced by a plug flow model with axial dispersion.

Conclusions

A **numerical hydrodynamic study** was performed to **investigate the flow inside a single string pellet reactor**. The influence of several Reynolds numbers was tested for the **residence time distribution**. It was indicated that the fluid has a serpentine flow pattern for the zigzag particle arrangement used. It was also shown that the velocity is virtually zero for the contact gaps adopted, which is verified experimentally (the velocity in the contact points between particles is zero). This verification should be enough to have confidence in hydrodynamic simulations before proceeding to liquid-solid mass transfer simulations. For the residence time distribution studied, it was considered acceptable to model the reactor as: **plug flow with low axial dispersion for $20 < Re_L < 160$ ($Pe_{ax} \gtrsim 70$) and plug flow for $Re_L > 160$ ($Pe_{ax} \gtrsim 190$)**. This will be the basis of the model, later discussed in §V.

The liquid-solid (or fluid-solid) mass transfer rates are still unknown for liquid and supercritical. To understand their impact, they should be quantified before performing the experimental work (§IV).

III.3.5 Mass transfer simulations

External mass transfer coefficients can be correlated with physical and process variables (§I.3.2). The correlations proposed in the literature are dependent of dimensionless numbers, such as Sc , Sh and Re numbers. In literature (Haase et al., 2013; Highfill and Al-Dahhan, 2001), the Sh_L (liquid-solid) for a particle bed with a single-phase fluid can be written as:

$$Sh_L = 2 + c Re_L^\alpha Sc_L^\beta \Rightarrow \frac{k_{LS} L}{D_i} = 2 + c \left(\frac{d_{cat} \bar{u}_S \rho}{\mu} \right)^\alpha \left(\frac{\mu}{\rho D_i} \right)^\beta \quad \text{Eq. III.18}$$

where α and β are exponents, c is a dimensionless constant, k_{LS} ($m s^{-1}$) is the mass transfer coefficient, L (m) is the reactor length, D_i ($m^2 s^{-1}$) is the diffusivity coefficient of the species i in the liquid, \bar{u}_L ($m s^{-1}$) is the superficial velocity and μ (Pa's) is the fluid average viscosity. The Schmidt number (Sc) is a ratio of the effectiveness external momentum transfer to external diffusional transfer (Smith, 2007). The Sherwood number (Sh) represents the ratio between mass transfer rate and diffusivity (Smith, 2007).

According to literature, β is equal to 1/3 for spherical particles (Cussler and Cussler, 2009; Dessimoz et al., 2008; Hipolito et al., 2010). Therefore, it is only required to vary the Reynolds number in order to estimate the mass transfer correlation for the studied reactor. In total, 6 Reynolds were studied for mass transfer: 40, 60, 80, 160, 320 and 650.

CFD specifications

It was previously discussed in §III.3.3, that the hydrodynamics in the basic block (at the last fully represented particle) is similar to a bigger single pellet reactor. Therefore, the basic block (3 spheres block) was applied to study mass transfer between the liquid phase (propylene) and the particle. The study was done in the last fully represented particle.

Mass transfer mesh: In this study, a conservative over meshed was used to avoid numerical diffusion, having 6.6 millions of elements (~1 600 000 elements/particle) (Figure III.10) rather than 1.5 millions (minimum required according to sensitivity studies).

Boundary conditions:

The particles used are defined as walls (no intraparticle diffusion) with infinite reaction. To evaluate the molar flux [φ (mol.m⁻².s⁻¹)] between the fluid and the particles, a common method is to set infinite reaction conditions at the particle surface. This way, the concentration at the catalyst surface is null ($C_{i,S} = 0$ mol.m⁻³) and the concentration far from the particle surface is non-null ($C_{i,av. \infty} \neq 0$ mol.m⁻³).



The molar flux can be computed directly in Fluent[®] or calculated. In the present work, the molar flux was calculated using 16 surfaces around the spherical particle (equal divided surfaces [Figure III.15]) to identify the zones with different fluxes (presented in the result section).

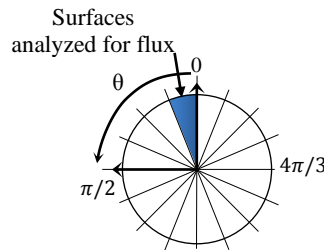


Figure III.15: Schemes of the surfaces analyzed to calculate molar flux (Eq. III.19).

The equation used to estimate the molar flux (normal to the sphere surface) is:

$$\varphi_{i,\theta} = -D_i \left. \frac{\partial C_i^*}{\partial r} \right|_{r=0,\theta} = -D_i \nabla C_{i,\theta}^* \quad \text{Eq. III.19}$$

where φ (mol.m⁻².s⁻¹) is the molar flux, D (m².s⁻¹) is the solute diffusivity, C^* (mol.m⁻³) is the flux concentration (so-called) and r (m) is the radial position to the particle center. The index θ (rad) represents the range of angle analyzed. For the concentrations used in the molar flux equation, the term flux concentration was introduced, which defines the methodology used to acquire the concentration (Figure III.16). The $\nabla C_{i,\theta}^*$ was estimated by using a linear regression model for three (flux) concentrations near the particle surface.

Reactive species properties: The fluids used were propylene and MAPD (very diluted; 0.03 mol%, close to the C₃ cut composition). The physical properties of MAPD were based on the methyl-acetylene (also known as propyne) properties, acquired from NIST Webbook (Lemmon et al., 2015) and Wilke and Chang (1955) correlation. The NIST was used for fluid density, and the Wilke and Chang correlation was used for diffusivity. As there are no data available in the literature for viscosity, the propylene's viscosity was used.

Results (mass transfer)

To estimate mass transfer coefficients, the liquid-solid molar flux and the bulk concentration should be related. To relate them, a thin diffusional film should exist around the particle. In the literature, the concentration profiles around the particle were not yet studied for the designed reactor. For this reason, the (flux) concentration, the diffusion film and bulk vs (flux) concentration will be studied. The goal is to check whether and how the mass transfer coefficients can be used.

Flux concentration

Regarding Figure III.16, at 60 μm from the particle surface, the local (flux) concentration is close to the (flux) concentration far from the surface. From the figure, it appears that the concentration can be described almost linearly between the particle surface ($C_{i,S}^*$) and the fluid (bulk, $C_{i,b}^*$). This suggests that there is a thin liquid film around the particles at the angle evaluated $[0; \pi/8]$ and the (flux) concentration has a constant and stable value.

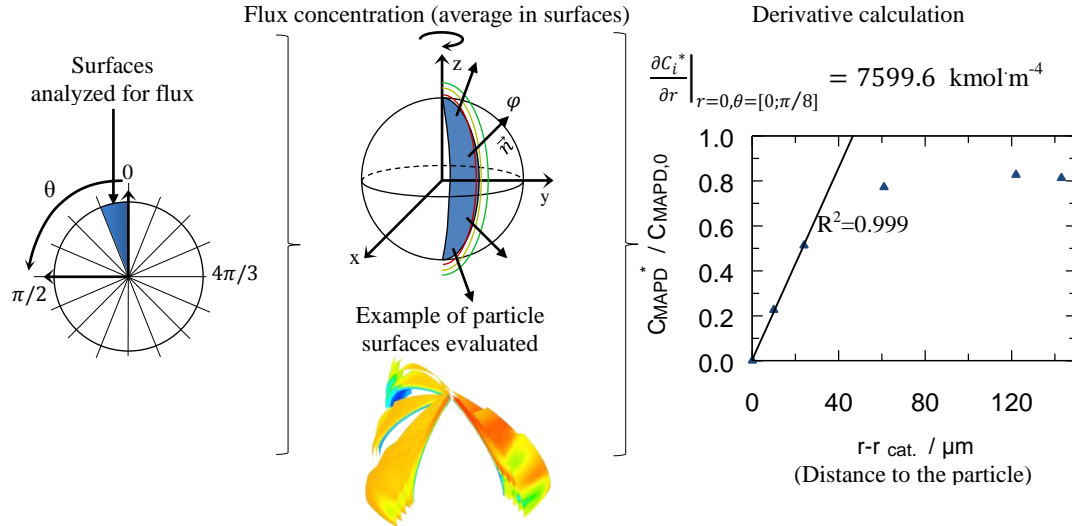


Figure III.16: Schemes of the surfaces analyzed to calculate molar flux (normal to the sphere surface) by using the concentration average at each surface (above the particle in steady-state) (Eq. III.19). The lines represent radial translations of the blue surface and the $C_{MAPD,0}$ is the concentration at the reactor inlet. The graphic was obtained in the first slide $[0; \pi/8]$, having $Re=160$ and $\bar{u}_0=0.04 \text{ m}\cdot\text{s}^{-1}$.

Consequently, the film theory might be considered, and thus the mass transfer coefficient ($k_{i,LS} [\text{m}\cdot\text{s}^{-1}]$) can be expressed by one-film model for the liquid side:

$$k_{i,LS} = \left(\frac{1}{k_{i,L}} + \frac{1}{k_{i,S}} \right)^{-1} = \frac{D_i}{\delta_{film}} = \left(\overbrace{C_{i,S}^*}^0 - C_{i,b}^* \right) / \varphi_i \quad \text{Eq. III.20}$$

where $k_{i,LS}$ ($\text{m}\cdot\text{s}^{-1}$) is the overall mass transfer coefficient around the particle, $C_{i,b}^*$ ($\text{mol}\cdot\text{m}^{-3}$) is the bulk (flux) concentration, δ_{film} (m) is the film thickness and φ_i ($\text{mol}\cdot\text{m}^{-2}\cdot\text{s}^{-1}$) is the molar flux in the particle surface. The Eq. III.20 can be considered as a resistance to the species transportation between the liquid and the solid surface. Since an infinite reaction assumption was adopted, the resistance in the particle (so called $1/k_{i,s}$) can be neglected.

In the film theory, one of the hypothesis generally made (Eq. III.20) is that the reactant fluid concentration is uniform around the particle surface ($C_{i,b}^* \approx C_{i,average}$), so-called stagnant model. This model is reasonable under well-mixed conditions, which for single pellet string beds is a non-verified hypothesis (Satterfield et al., 1969). For more complex beds, such as packed beds, it is known that in certain conditions the concentration around the particle is not uniform (Perez-Tello et al., 1999). Therefore, it is of interest to investigate the gradient concentration around a pellet, since the mass transfer is very sensitive to the concentration. In the present study, the mass transfer coefficients were investigated under 16 surfaces (16 θ angle ranges) around the particle (Figure III.16).

The overall mass transfer coefficient can be written as:

$$k_{i,LS} = \frac{\sum_{\theta=1}^{16} k_{i,\theta,LS}}{16} = \frac{\sum_{\theta=1}^{16} \left(\overbrace{C_{i,\theta,S}^*}^0 - C_{i,\theta,b}^* \right) / \varphi_{i,\theta}}{16} \quad \text{Eq. III.21}$$

where $k_{i,\theta,LS}$ ($\text{m}\cdot\text{s}^{-1}$) is a local mass transfer coefficient for the angle range investigated, $C_{i,\theta}^*$ ($\text{mol}\cdot\text{m}^{-3}$) is the local (flux) concentration and $\varphi_{i,\theta}$ ($\text{mol}\cdot\text{m}^{-2}\cdot\text{s}^{-1}$) is the local molar flux.

The Eq. III.21 can only be used if the film theory is applied. This means that particles should have diffusional films and that bulk (flux) concentrations should be close to the average fluid concentration ($C_{i,\theta,b}^* \approx C_{i,\theta,average}$). The goal of this study is to understand mass transfer in a single pellet string reactor and check if a simplified 1D model (film model) can provide reasonable results. These two goals will allow to better understand liquid-solid mass transfer when performing a reaction (§IV and §V).

The next two steps are to:

1. check if there are diffusional films around the particles;
2. check if bulk (flux) concentrations ($C_{i,\theta,b}^*$) are close to the fluid average concentration ($C_{i,\theta,average}$).

Diffusional film

To investigate if the stagnant layer is present in the single pellet string reactor selected (§III.2.4), the diffusion film thickness around the last particle of the basic block was evaluated for 6 Reynolds (numbers) values (min.: 40; max.: 650) and 16 angle ranges. The results obtained in laminar regime are shown in Figure III.17, namely the concentration for

different Reynolds and angle ranges (θ_i). The comparison between laminar and turbulent results will be later presented.

It can be noticed that a thin-film exists surrounding the particle studied, having a thickness below 100 μm for the three considered Reynolds (Re_L): 40, 160 and 650. To give an order of magnitude, a 100 μm thickness represents 1/5 of the width available (500 μm) in the channel (reactor). Analyzing the fluid diffusion zone, the concentration dependency between the particle surface ($C_{i,s}^*$) and the fluid (bulk, $C_{i,b}^*$) can be represented linearly. Moreover, it is possible to conclude that (flux) concentrations far from the particle ($>100\mu\text{m}$) are more dispersed at Reynolds 40 (Figure III.17a) than at Reynolds 650 (Figure III.17c). The dimensionless (flux) concentration varies between 0.2 and 0.9 for $Re_L=40$, and 0.85 and 0.9 for $Re_L=650$. These variations indicate that the bulk (flux) concentration is not uniform, being lower at the contact points (e.g. $-\pi/8$). This is presumably close to the reality, since the back of the contact points are regions with stagnant flow (Satterfield et al., 1969). Therefore, the mass transfer is not so efficient at every location (Figure III.17b).

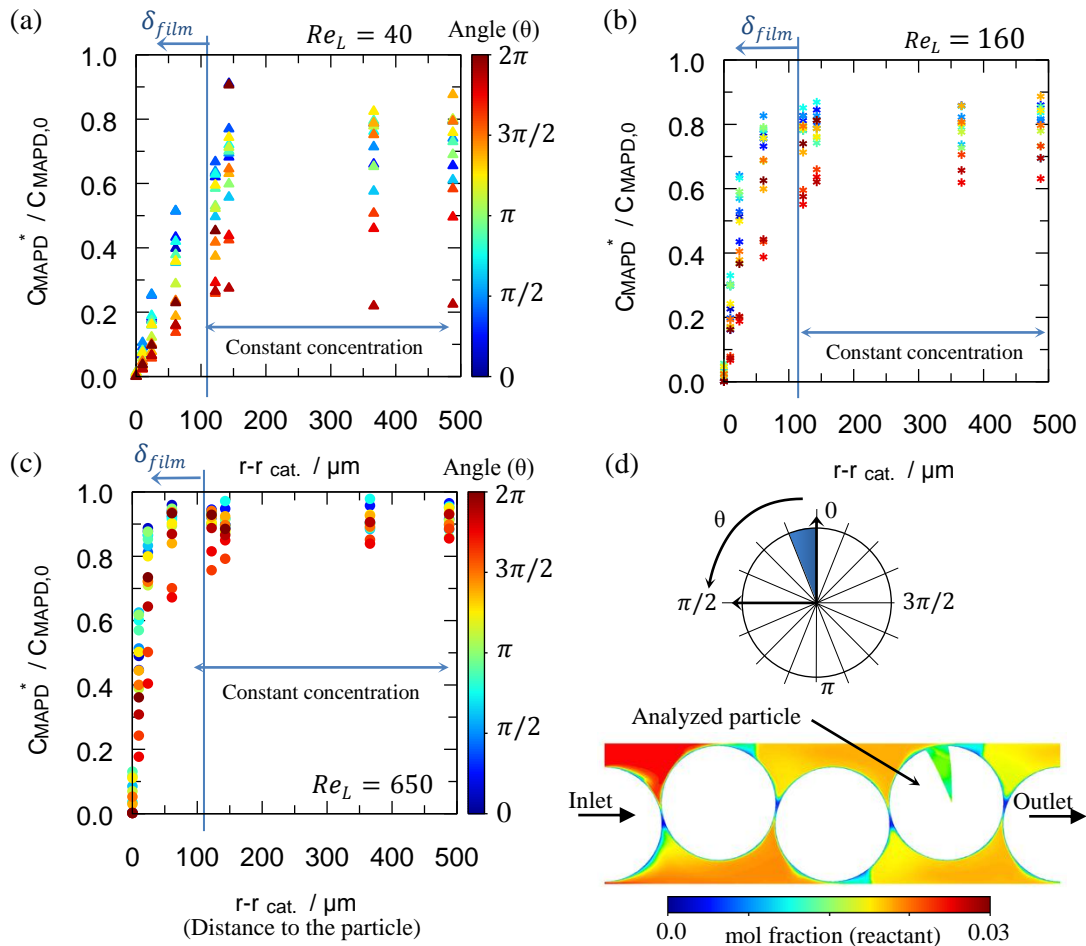


Figure III.17: MAPD dimensionless (flux) concentration as a function of the distance to the particle and angle analyzed (θ_i) (e.g. θ_i represents the range $[\theta_i-\pi/8; \theta_i]$). The film thicknesses are identified for 3 out of 6 Reynolds: (a) $Re_L=40$; (b) $Re_L=160$; (c) $Re_L=650$. (d) Schematic of the zones analyzed (angles) and mole fraction results for infinite reaction in CFD (inlet composition of the reactant is 0.03 and $Re_L=160$).

Having a non-uniform bulk concentration in a single pellet string bed was expected since the fluid has different velocities depending on the reactor section available. For a single pellet string bed, the effect of velocity distribution is typically more pronounced than in a packed bed reactor. Even if the bulk concentration is not uniform, the Eq. III.21 is still valid because it takes into account different mass transfer coefficients at the different locations of the particles surface.

The same behavior for the laminar and turbulent model was spotted. For the single pellet string reactor selected [§III.2.4], it was shown that the diffusional film hypothesis might be applied. These results, allow to apply (in our system) the film hypothesis as a simplified model to represent mass transfer.

The next step is to check if the bulk (flux) concentration is similar to the average fluid concentration far from the particle surface. The mass transfer coefficients ($k_{i,\theta,LS}$) can be only estimated (Eq. III.21 – simplified model), if the bulk (flux) concentration is close to the average concentration. This will be checked in the next subsection.

Bulk (flux) concentration vs Fluid average concentration (planes)

The difference between the two definitions is how the concentration is obtained. The bulk (flux) concentration is examined on a surface at the beginning of the diffusional film (surface at $150\ \mu\text{m}$ far from the particle). The average concentration is examined at several planes that slice the particle from 0 to $1000\ \mu\text{m}$ (the surface accounts different distances to the particle). For the average concentration, the particle was divided into 160 planes (angle increment: $\pi/80$) normal to the sphere surface. For each plane surface, one overall concentration was obtained. Figure III.18 shows the different methodologies used.

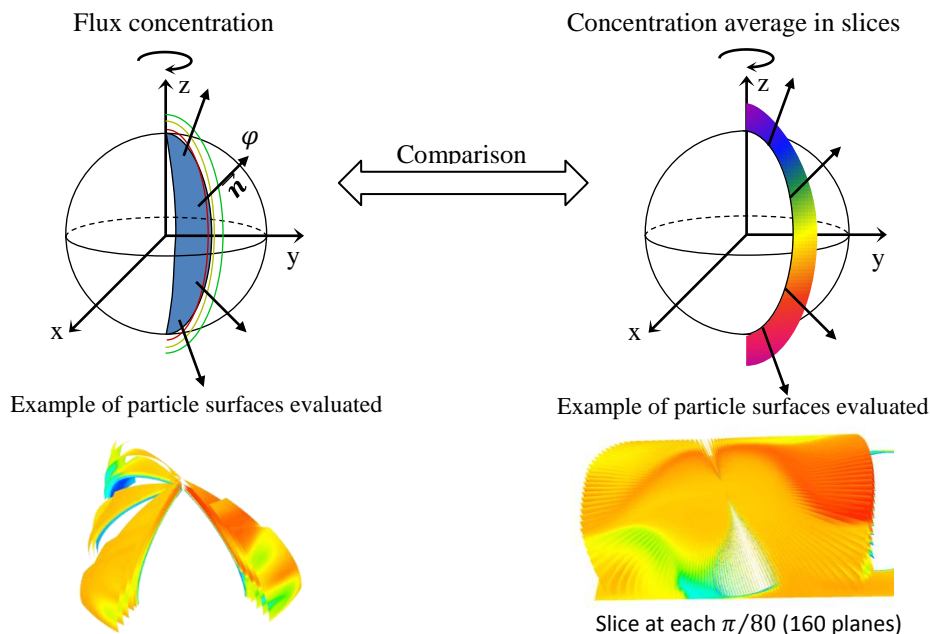


Figure III.18: Schematics of the zones examined for (flux) concentration and concentration average in the slices.

To understand if the bulk (flux) concentration is close to the average fluid concentration, 6 Reynolds were evaluated (min.: 40; max.: 650). Only 3 out of 6 Reynolds numbers are present in Figure III.19: minimum ($Re_L=40$), intermediary ($Re_L=160$) and the maximum ($Re_L=650$).

Figure III.19 shows that for Reynolds of 160 and 650, both concentrations evaluated with different methodologies have similar results, having an average relative deviation (between concentrations) of 3.1% and 4.5%, respectively. Looking more specifically at Reynolds 650 (with a laminar and turbulent model), the particle seems to be surrounded by a uniform concentration. Decreasing the Reynolds, from 650 to 40, the hypothesis of uniform concentration around the particle begins to fail. Indeed, there are fluid zones around the particle, in which the concentration is lower than the rest, particularly at Reynolds of 40. Even so, for these Reynolds, if the bulk (flux) concentration is compared with the average concentration (planes), the average relative deviation is still small, having 4.5%.

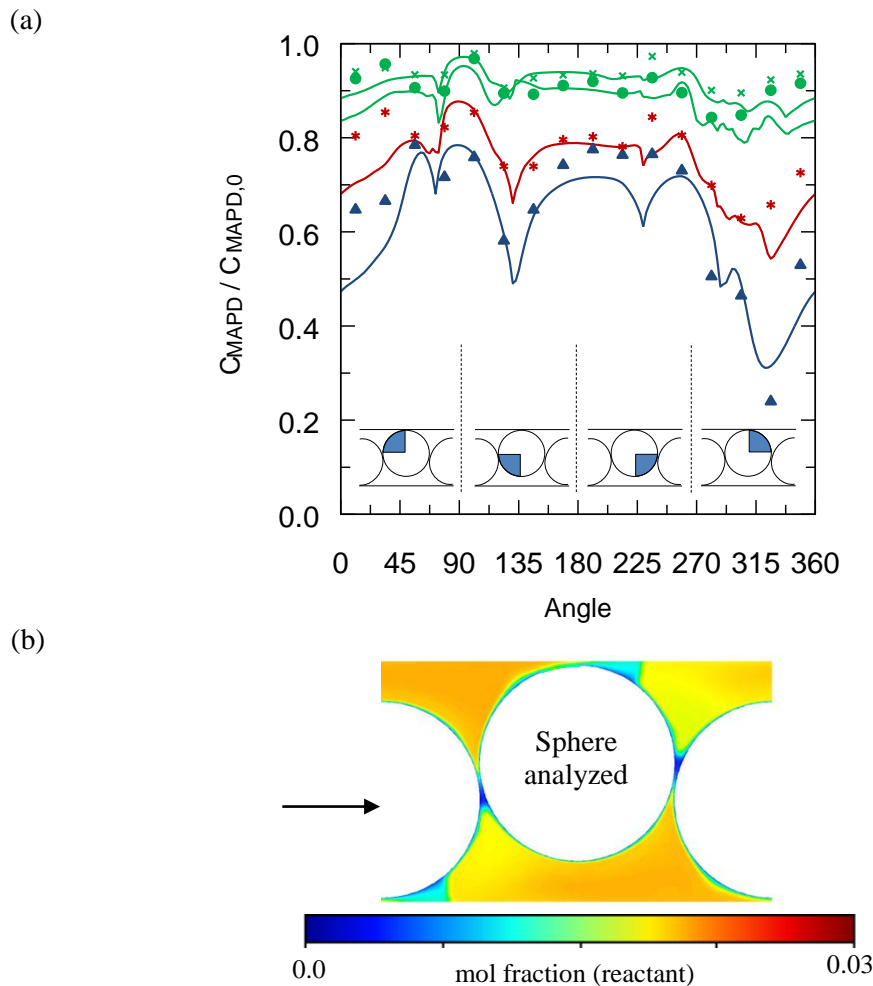


Figure III.19: (a) Bulk (flux) concentration (points) versus fluid average concentration (lines) with laminar model: $Re_L=40$ (\blacktriangle), $Re_L=160$ ($*$) and $Re_L=650$ (\bullet), and with turbulent model $Re_L=650$ (\times). (b) Mole fraction results for infinite reaction in CFD (inlet composition of the reactant 0.03 and $Re_L=160$).

Since the average relative deviation is inferior to 5%:

$$C_{i,\theta,b}^* \approx C_{i,\theta,average} \quad \text{Eq. III.22}$$

This conclusion makes it possible to simplify the 3D CFD mass transfer model into a 1D model (if consider overall $k_{i,LS}$), which is more flexible, less time consuming and, above all, can be easily coupled with the MAPD hydrogenation model for the full reactor (later developed, §V).

After checking that the 3D model can be simplified into a 1D model, the next step is to propose an external mass transfer correlations [§I.3.2].

External mass transfer coefficients and mass transfer correlation

To propose an external mass transfer correlation, the molar flux and the k_{LS} must be quantified for the reactor ($d_{reactor} = 3$ mm; $d_{cat.} \approx 2.45$ mm). As previously described, the film theory was a representative assumption. This hypothesis was verified for a monophasic system only, since our primary goal is to understand the kinetics and mass transfer in unconventional conditions (high pressure and SCF → single phase).

Retaking the proposed equations (Eq. III.18 to Eq. III.22), the following equation system can be specified.

$$\left\{ \begin{array}{l} Sh = 2 + cRe_L^\alpha Sc^\beta \Rightarrow \frac{k_{LS}L}{D_{i,L}} = 2 + c \left(\frac{d_{cat.}\bar{u}_L\rho_L}{\mu_L} \right)^\alpha \left(\frac{\mu_L}{\rho_L D_{i,L}} \right)^\beta \quad \text{mass transfer correlation} \\ k_{i,LS} = \frac{\sum_{\theta=1}^{16} k_{i,\theta,LS}}{16} = \frac{\sum_{\theta=1}^{16} (0 - C_{i,\theta,average}) / \varphi_{i,\theta}}{16} \quad \text{mass transfer coefficients} \\ \varphi_{i,\theta} = -D_{i,L} \left. \frac{\partial C_{i,\theta}^*}{\partial r} \right|_{r=0,\theta} = -D_{i,L} \nabla C_{i,\theta}^* \quad \text{molar flux} \end{array} \right. \quad \text{Eq. III.23}$$

To identify mass transfer correlation, it is necessary to solve the previous system by using the following sequence:

$$Sh \rightarrow k_{i,LS} \rightarrow k_{i,\theta,LS} \rightarrow \varphi_{i,\theta} \Rightarrow Re_L$$

The MAPD molar flux ($\varphi_{i,\theta}$) and mass transfer coefficients ($k_{i,\theta,LS}$ and $k_{i,LS}$) between the liquid and the solid, for different Reynolds, are shown in Figure III.20. The MAPD molar flux ($\varphi_{i,\theta}$) was obtained from CFD and $k_{i,\theta,LS}$ was obtained fro Eq. III.23.

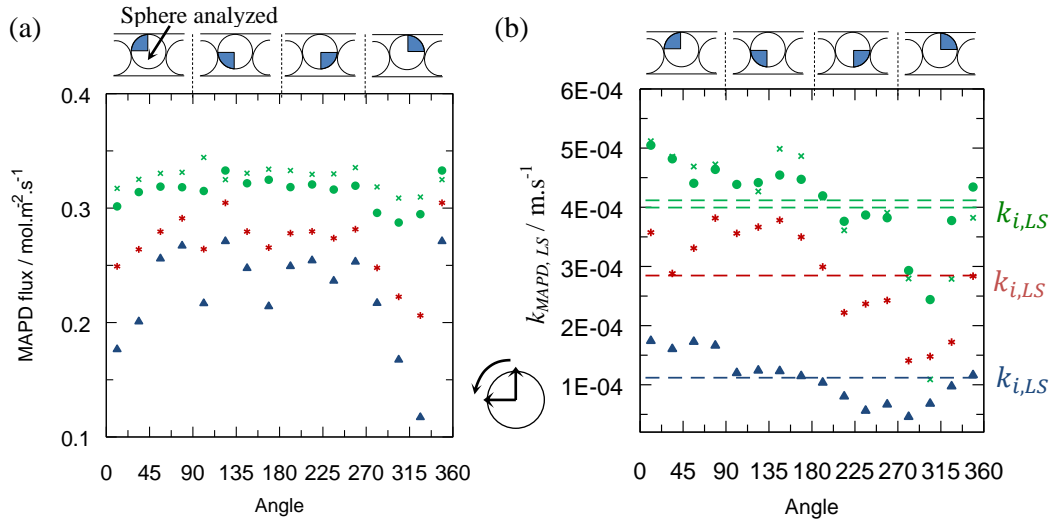
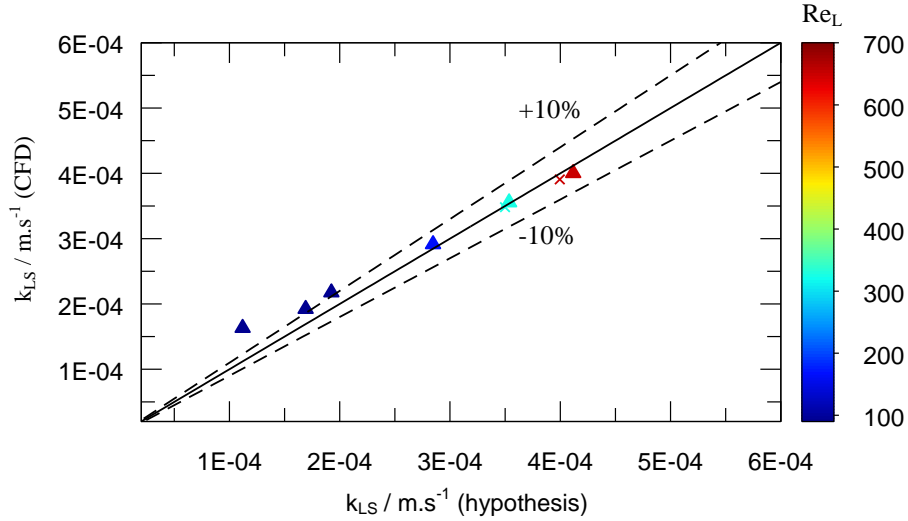


Figure III.20: (a) MAPD molar flux ($\varphi_{i,\theta}$) for different zones and Reynolds. (b) $k_{i,\theta,LS}$ and $k_{i,LS}$ for different zones and Reynolds. In the graphic with laminar model: $Re_L=40$ (\blacktriangle), $Re_L=160$ (\blackstar) and $Re_L=650$ (\bullet). For turbulent model $Re_L=650$ (\times). The dashed lines (blue, red and green) are the $k_{i,LS}$ (average value for 16 zones).

As expected, the MAPD molar fluxes and mass transfer coefficients (local and average) increase with Re . Comparing both graphics, the molar flux (directly from CFD) has a slight different behavior than the mass transfer coefficient plot (obtained by calculation). It can be explained by the approximation used for the concentration, $C_{i,\theta,b}^* \approx C_{i,\theta,average}$.

To better understand this hypothesis, a comparison between $k_{i,LS}$ with hypothesis ($C_{i,\theta,b}^* \approx C_{i,\theta,average}$) and $k_{i,LS}$ without hypothesis (direct CFD) was done. As previously explained, the $k_{i,LS}$ with hypothesis is the one that can be actually used in the reactor model, because the bulk (flux) concentration cannot be estimated without using computational tools, such as CFD.



$$k_{i,LS} (\text{hypothesis}) = \frac{\sum_{\theta=1}^{16} k_{i,\theta,LS}}{16} = \frac{\sum_{\theta=1}^{16} \varphi_{i,\theta} / (0 - C_{i,\theta,average})}{16}$$

$$k_{i,LS} (\text{CFD}) = \frac{\sum_{\theta=1}^{16} k_{i,\theta,LS}}{16} = \frac{\sum_{\theta=1}^{16} \varphi_{i,\theta} / (0 - C_{i,\theta,b}^*)}{16}$$

Figure III.21: Parity graphic comparing the $k_{MAPD,LS}$ calculated with $C_{MAPD,\theta,b}^*$ (CFD) and $C_{MAPD,\theta,b} \approx C_{MAPD,\theta,average}$ (hypothesis). The points were obtained in CFD for laminar model (▲) and for turbulent model (×).

According to Figure III.21, the point with lower Reynolds has a relative deviation of 18%. For the other points, they have deviation equal or inferior to 10%. In our case, the Reynolds number of the experiments will be around 160. Therefore, it should be close to the one without a hypothesis, obtained in CFD.

After estimating $k_{i,LS}$ average values, a mass transfer correlation was proposed, being based on Eq. III.23. The K and α parameter were fitted using CFD values. Then, the values obtained with Fluent were compared with literature for a packed bed and for a single pellet string reactors with square section (Figure III.22 and Table III.2).

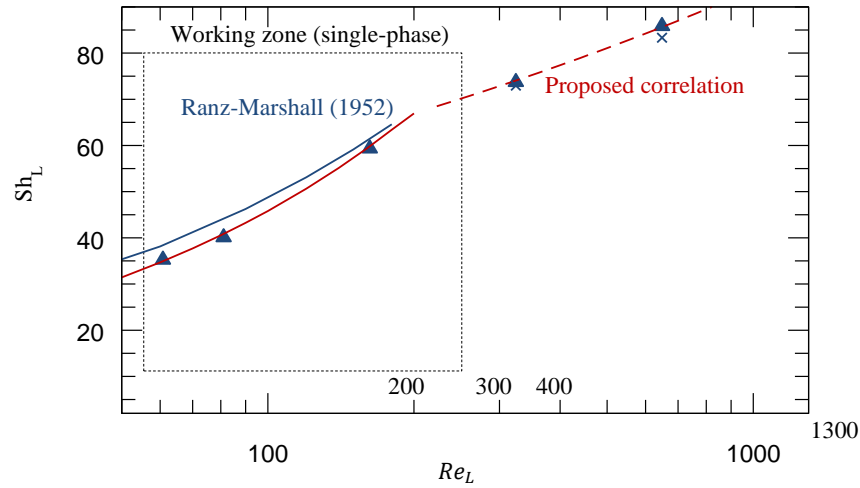


Figure III.22: Dimensionless Sherwood number (liquid/solid) as a function of the Reynolds number (liquid phase). The lines represent different correlations for mass transfer. The red lines (filled and dashed) is the correlation proposed by this work. The points were obtained with CFD for the laminar model (▲) and turbulent model (×).

Table III.2: Comparison between parameters for the correlations proposed in the literature and the one proposed in this work for monophasic fluids (liquid only). Based on $Sh = 2 + cRe_L^\alpha Sc^\beta$.

Authors	Reynolds	c	α	β	Description	Study type
Ranz and Marshall (1952) (cylindrical)	$0 < Re_L < 200$	1.8	1/2	1/3	Cylindrical packed bed reactor with spherical particles	Experimental study
Hipolito (2010) (square)	$0 < Re_L < 350$	0.7	1/2	1/3	Square single pellet string reactor with (spherical particles; $2.0 < d_{cat} < 2.8$ mm; 4×4 mm ² reactor)	Experimental study
This work (cylindrical)	$0 < Re_L < 200$ $200 < Re_L < 700$	1.202 8.023	0.574 0.214	1/3 1/3	Cylindrical single pellet string reactor (spherical particles; $2.38 < d_{cat} < 2.50$ mm; $d_{reactor} = 3.0$ mm)	CFD study

Regarding Figure III.22 and Table III.2, the constant c , which multiplies $Re_L^\alpha Sc^{1/3}$ (Eq. III.23), is inferior than Ranz and Marshall (1952) correlation for a packed bed reactor.

According to Hipolito et al. (2010), this can be explained by a higher porosity for single pellet string reactors than for classical packed bed reactors.

For the single pellet string reactor selected (cylindrical), the mass transfer is improved in relation to the reactor with square section used by Hipolito (2010). Since the porosity is lower and the majority of the fluid has a serpentine flow pattern in the cylindrical reactor, there are less dead zones and preferential passages.

Conclusions

A **numerical study** was performed to **investigate the mass transfer in the single pellet reactor** used. The effects of the Reynolds number in the liquid-solid mass transfer were studied. It was shown that the film theory might be assumed, and an average mass transfer coefficient could be used. **A mass transfer correlation was proposed for the working zone.** Since this correlation was obtained by CFD, it should be used carefully, even if the results are very close to the Ranz and Marshall (1952) correlation. **This correlation will be mostly used in §V to model the MAPD hydrogenation system (pilot scale).**

III.3.6 Mass transfer coefficients for pilot and industrial reactors

Before addressing the reaction (§IV) and the model (§V), it will be interesting to evaluate the mass transfer for pilot and industrial reactors. This step helps comparing the overall mass transfer limitations between scales and to have knowledge on the pilot that might be closer to the industrial scale. To perform the comparison, an industrial reactor present in literature was used (Samimi et al., 2015). This reactor is not representative of all the industrial reactors available, but it will give a first order of magnitude.

Pilot and industrial correlations

To predict and understand pilot and industrial scale mass transfer rates, the mass transfer coefficient (k_{GLS}) can be approximated for a single units as (Haase et al., 2013):

$$k_{GLS}a_{GLS} = k_{GS}a_{GS} + \left(\frac{1}{k_L a_{GL}} + \frac{1}{k_{LS} a_{LS}} \right)^{-1} \approx \left(\frac{1}{k_L a_{GL}} + \frac{1}{k_{LS} a_{LS}} \right)^{-1} \quad \text{Eq. III.24}$$

where k_{GS} , k_L and k_{LS} ($\text{m}\cdot\text{s}^{-1}$) are the mass transfer coefficients and a_{GS} , a_{GL} and a_{LS} are the interfacial areas. The subscript GLS means gas-to-liquid-to-solid, the GS means gas-to-solid, the GL means gas-to-liquid and the LS means liquid-to-solid. In the present approach, it is considered that the catalyst is always covered by a liquid film (100% wettability), therefore $k_{GS}a_{GS}$ is negligible.

To difference mass transfer resistances for the pilot and the industrial scale, the mass transfer coefficients were calculated and compared. For the pilot scale the reactors compared were: the cylindrical single pellet reactor selected for this thesis and the Hipolito et al. (2010) square reactor. The comparison was based on the same particle diameter (2.45 mm), the actual catalyst mass used in industry and in pilot scale, and a range of weight hourly space velocities (WHSV) (0.1 to 1500 h^{-1}). For the calculations, the mass transfer general correlations were

used based on Sherwood. The data used in the comparison are presented in Table III.3. The diffusivity were calculated based on the Wilke and Chang (1955) correlation (for liquid) [first approach to model diffusivity]. The thermodynamic data, viscosity and density were obtained in Nist webbook (Lemmon et al., 2015).

Regarding Table III.3, the selected reactor has different operating conditions than other reactors, which can give different results due to different interactions liquid-solid (e.g. adsorption equilibrium). For the moment, only the mass transfer will be compared assuming that the operating conditions do not affect the reaction kinetics. Later the influence of unconventional conditions will be discussed (§IV).

Table III.3: Physical parameters used to compare reactors. The industrial unit conditions were obtained from Samimi et al. (2015). *the gas and liquid are in a homogeneous phase; # maximum for the actual pilot reactor (due to the length of the reactor used).

	Selected single pellet string reactor	Hipolito et al. (2010) – catalyst screening	Industrial reactor
Medium phase	Liquid phase	Liquid/Gas phase	Liquid/Gas phase
L / m	0.2	1.7	3.65
$d_{reactor}$	3 mm	4 mm (square)	1.1 m
$m_{cat.}$	0.6 g (max) [#] and 5 g	0.6 and 5 g (max.)	2 625 kg
$d_{cat.}$ / mm	2.45	2.45	2.45
D_{H_2} in propylene (m ² .s ⁻¹)	2.14×10^{-8}	2.41×10^{-8}	2.41×10^{-8}
D_{MAPD} in propylene (m ² .s ⁻¹)	1.17×10^{-8}	1.34×10^{-8}	1.34×10^{-8}
Pressure (bar) / temperature (K)	120 bar / 303 K	24.5 bar / 303 K	24.5 bar / 296 K
Mass flow rate (liquid)	~[10 : 1000] g.h ⁻¹	~ [10 : 500] g.h ⁻¹	~ 91 000 kg.h ⁻¹
Mass flow rate (gas)	*	~[0.55 : 2.20] g.h ⁻¹	~ 126 kg.h ⁻¹
Porosity (ϵ)	0.55	0.5	0.4
Sh equation	On Table III.2	Eq. III.25 + Eq. III.26	Eq. III.28 to Eq. III.37
H ₂ /MAPD mol/mol	1	1	1

From the data present on Table III.3, the Sh will be evaluated with the following correlations.

Single pellet string reactor (cylindrical) for single phase (liquid) only:

See equation present in Table III.2.

Single pellet string reactor (square section) (Hipolito et al., 2010):

For gas-liquid mass transfer (pulse regime):

$$Sh = \frac{k_L a_{GL} d_{cat.}^2}{D_{i,L}} = 21 \left(\frac{d_{cat.} \bar{u}_L \rho_L}{\mu_L} \right)^{1/3} \left(\frac{d_{at.} \bar{u}_G \rho_G}{\mu_G} \right)^{3/25} \frac{Sc_L^{1/3}}{45.6^{1/3}} \quad \text{Term added} \quad \text{Eq. III.25}$$

where $Sc_L = \mu_L/(\rho_L D_{i,L})$ and \bar{u}_G (m.s⁻¹) is the superficial velocity of the gas. This correlation was proposed without the Schmidt number, because only one fluid mixture (one diffusivity) was studied for mass transfer, namely, hydrogen in alpha-methyl styrene. In order to apply this correlation to hydrogen in propylene, the term $Sc_L^{1/3}/45.6^{1/3}$ was added. The first value ($Sc_L^{1/3}$) is widely used in this type of correlations for spherical particles (Haase et al., 2013). The constant $45.6^{1/3}$ ($Sc_L^{1/3}$ at the authors conditions) was added to respect the correlation proposed by Hipolito et al. (2010) for the hydrogen in alpha-methyl styrene.

For liquid-solid mass transfer (biphasic):

$$Sh = \frac{k_{LS}d_{cat.}}{D_{i,L}} = \frac{0.24}{\varepsilon_L} \underbrace{\left(\frac{d_{cat.}\bar{u}_L\rho_L}{\mu_L}\right)}_{Re_L} \underbrace{\left(\frac{d_{cat.}\bar{u}_G\rho_G}{\mu_G}\right)^{3/25}}_{Re_G} \underbrace{\frac{Sc_L^{1/3}}{45.6^{1/3}}}_{\text{Term added}} \quad \text{Eq. III.26}$$

$$\varepsilon_L = 1 - (1 - \varepsilon) * 0.725 \frac{\bar{u}_G}{\bar{u}_G + \bar{u}_L} - \varepsilon \quad \text{Eq. III.27}$$

where ε_L is the liquid hold-up and ε is the bed porosity. The \bar{u}_L (m.s⁻¹) and \bar{u}_G (m.s⁻¹) was defined as the superficial velocities ($\bar{u}_L = \frac{W_L}{\rho_L \pi R_{reactor}^2}$ m.s⁻¹ and $\bar{u}_G = \frac{W_G}{\rho_G \pi R_{reactor}^2}$ m.s⁻¹).

Industrial reactor:

According to Samimi et al. (2015), the industrial reactor regime can be considered as a trickle flow for the conditions presented in Table III.3. Despite this information, when regarding industrial working conditions, it is expected to have a flow regime between pulse and bubble flow (Muthanna H Al-Dahhan and Duduković, 1995) (Figure III.23). Consequently, the Wild and Larachi F (1992) gas-liquid mass transfer correlations were used. These correlations allow estimating mass transfer coefficients for the trickle (low interaction), pulse (medium interaction) and bubble flow (high interaction) regime.

From the industrial reactor selected from the literature, the working regime is not well defined, because it is located in a transition zone. It can be a pulse or dispersed, or even trickle regime (red point in Figure III.23). Therefore, the correlations for different regimes will be presented.

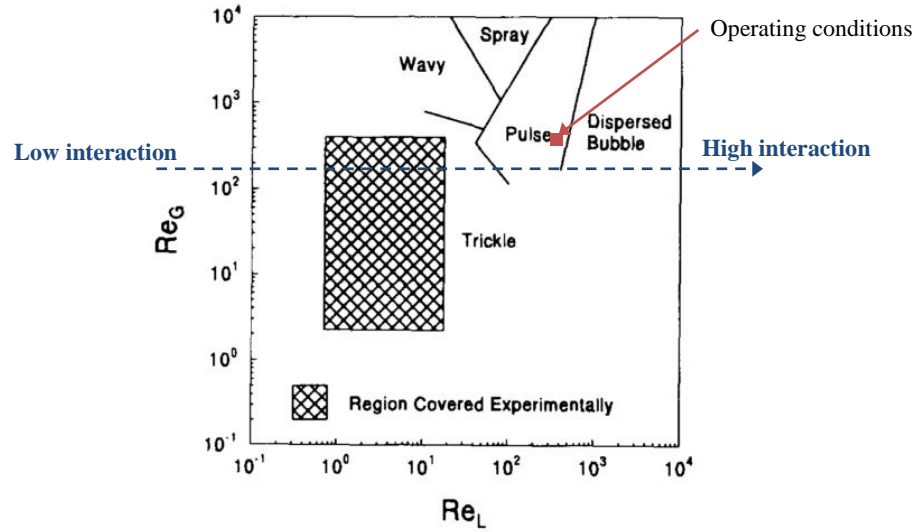


Figure III.23: Different flow regimes as a function of Re_L and Re_G . Adapted from Muthanna H. Al-Dahhan and Duduković (1995).

Gas-liquid mass transfer correlations:

$$\text{Low interaction} \quad Sh = \frac{k_L a_{GL} d_h^2}{D_{i,L}} = 2.8 \times 10^{-4} \left(\chi_G^{0.5} Re_L^{0.8} We_L^{0.2} Sc_L^{0.5} \left(\frac{a_s d_h}{1 - \varepsilon} \right)^{0.25} \right)^{3.4} \quad \text{Eq. III.28}$$

$$\text{Medium interaction} \quad Sh = \frac{k_L a_{GL} d_h^2}{D_{i,L}} = 0.091 \left(\chi_G^{0.25} Re_L^{0.2} We_L^{0.2} Sc_L^{0.3} \left(\frac{a_s d_h}{1 - \varepsilon} \right)^{0.25} \right)^{3.8} \quad \text{Eq. III.29}$$

$$\text{High interaction} \quad Sh = \frac{k_L a_{GL} d_h^2}{D_{i,L}} = 0.45 \left(\chi_G^{0.5} Re_L^{0.8} We_L^{0.2} Sc_L^{0.5} \left(\frac{a_s d_h}{1 - \varepsilon} \right)^{0.25} \right)^{1.3} \quad \text{Eq. III.30}$$

$$\chi_G = (\bar{u}_G \sqrt{\rho_G}) / (\bar{u}_L \sqrt{\rho_L}) \quad \text{Eq. III.31}$$

$$We_L = \bar{u}_L^2 d_{cat} \rho_L / \sigma_L \quad \text{Eq. III.32}$$

$$d_h = d_{cat} \sqrt[3]{16\varepsilon^3 / (9\pi(1 - \varepsilon)^2)} \quad \text{Eq. III.33}$$

$$a_s = \frac{6(1 - \varepsilon)}{\delta d_{cat}} + \frac{4}{d_{reactor}} \quad \text{Eq. III.34}$$

where χ_G is the Lockhart-Martinelli number, We_L is the liquid-phase Weber number, d_h (m) is the Krischer and Kast hydraulic diameter, σ_L (N.m⁻¹) is the surface tension, a_s (m⁻¹) is the particle external area per reactor volume and δ is the sphericity factor.

For the liquid-solid mass transfer (biphasic), three mass transfer correlations were used for the three types of flow regimes:

1. Low interaction (trickle);
2. Medium interaction (pulse);
3. High interaction (bubble).

The Van Krevelen and Krekels (1948) correlation was used for low interaction regimes. The Jadhav and Pangarkar (1990) correlation was used for medium interactions and the Lakota and Levec (1990) correlation was used for a high interaction system.

Liquid-solid mass transfer correlations:

$$\text{Low interaction} \quad Sh = \frac{k_{LS}d_{cat.}}{D_{i,L}} = 1.8 \left(\frac{d_{cat.}\bar{u}_L\rho_L}{\mu_L} \right)^{0.5} Sc_L^{1/3} \quad \text{Eq. III.35}$$

$$\text{Medium interaction} \quad Sh = \frac{k_{LS}d_{cat.}}{D_{i,L}} = \frac{0.487}{\epsilon_L^{0.495}} \left(\frac{d_{cat.}\bar{u}_L\rho_L}{\mu_L} \right)^{0.495} Sc_L^{1/3} \quad \text{Eq. III.36}$$

$$\text{High interaction} \quad Sh = \frac{k_{LS}d_{cat.}}{D_{i,L}} = 0.221 \left(\frac{d_{cat.}\bar{u}_L\rho_L}{\mu_L} \right)^{0.64} Sc_L^{1/2} \quad \text{Eq. III.37}$$

Pilot scale and industrial reactor (comparison)

To compare the mass transfer rates for different pilot reactors, the same weight of catalyst were used: 0.6 g and 5 g. In pilot scale, the catalyst mass allows to improve the external mass transfer by increasing the mass flow rate (higher Reynolds), keeping the same LHSV or WSHV (contact time). For an industrial reactor, a total of 2.6 ton of catalyst was used (Samimi et al., 2015). Since there is no clear boundary between flow regimes and they have a significant impact on mass transfer rate, the strategy adopted was to estimate the mass transfer for all the regimes present at the industrial scale: trickle, pulse and bubble. Therefore, the mass transfer rates of three hypothetical industrial reactors were compared with pilot reactors. Each industrial reactor is in a single flow regime, independent of the physical accuracy (*e.g.* Re_G vs Re_L). The goal is to understand, by using orders of magnitude, how far the pilot plants are performing in relation to the industrial ones. In total, 7 cases were compared for mass transfer coefficients, being presented in **Figure III.24**. The industrial process is divided into 3 reactors, each one for each regime studied.

Briefly, 7 calculations were done with 5 geometries:

- 3 industrial reactors: 1 catalyst mass and 3 different regimes;
- 2 Hipolito et al. (2010) reactors: 2 catalyst weights;
- 2 selected reactors: 2 catalyst weights.

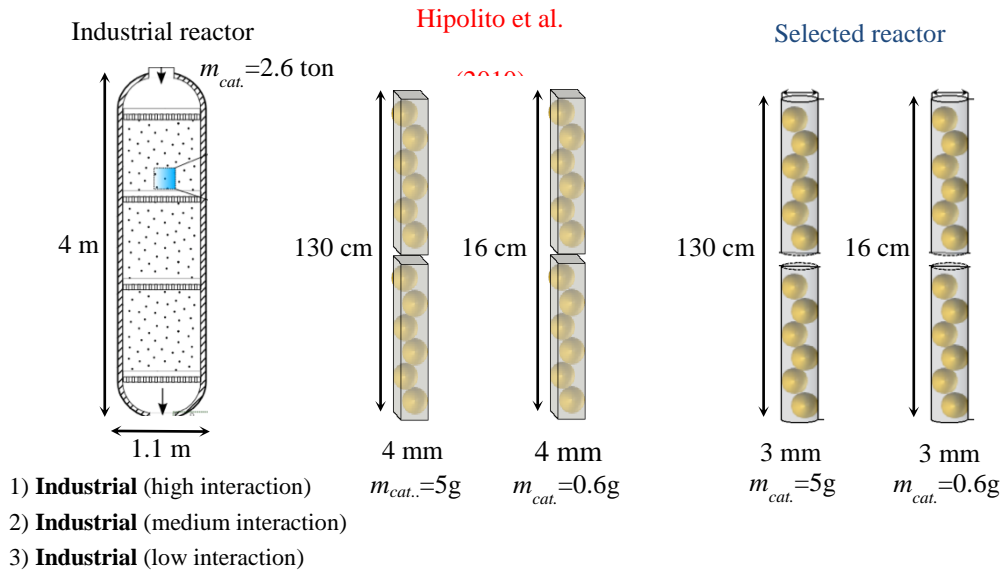


Figure III.24: Reactors at pilot and industrial scale, for which the mass transfer coefficients were compared. The 16 cm is based on a reactor fill with 70 particles (defined by us).

Gas-liquid mass transfer (hydrogen)

For the gas-liquid mass transfer coefficients, only the pilot reactor from Hipolito (2010) was compared with industrial reactors (in three hypothetical regimes). The selected reactor of this thesis is not presented, because it is in a single-phase, which means that $k_L a_{GL}$ (s^{-1}) does not exist.

Regarding Figure III.25, the industrial reactor with pulse regime (medium interaction) has the closest $k_L a_{GL}$ to Hipolito's reactor at WHSV of 35 h^{-1} (operating conditions of the industrial reactor), 0.69 s^{-1} (industrial) in comparison with 0.28 s^{-1} . This means that a pilot reactor ($Re_L = 79.83$; $Re_G = 32.57$; $\bar{u}_L = 6.0 \text{ mm.s}^{-1}$; $\bar{u}_G = 3.7 \text{ mm.s}^{-1}$) has at least 2.5 times less gas-liquid mass transfer than an industrial reactor. When comparing the pilot to other regimes, such as the bubble regime, the differences go up to 28 times less [9.23 s^{-1} (industrial) compared to 0.28 s^{-1}].

The reactors studied can be placed in the following order for gas-liquid mass transfer:

Hipolito ($m_{cat.} = 0.6 \text{ g}$) < Hipolito ($m_{cat.} = 5.0 \text{ g}$) < Industrial (medium) < Industrial (high) < Industrial (low)

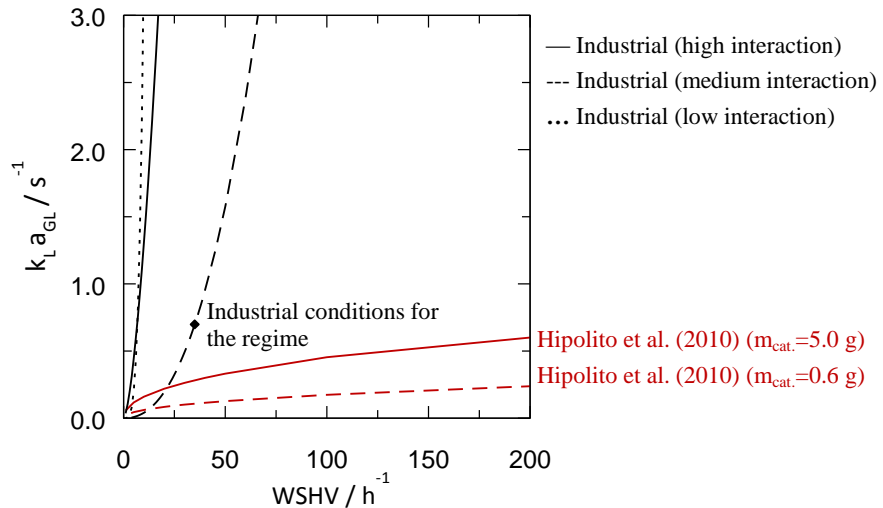


Figure III.25: Comparison between hydrogen gas-liquid mass transfer coefficients for pilot and industrial reactors as a function of WSHV (h^{-1}) of the C3 cut. The selected reactor has infinite gas-liquid mass transfer (liquid only at high-pressure). The industrial WSHV is about 35 h^{-1} .

Liquid-solid mass transfer (hydrogen)

Between hypothetical industrial reactors, the pulse (medium interaction) and the bubble (high interactions) regimes have similar k_{LS} values for the operating conditions, around $3.6 \times 10^{-4} \text{ m s}^{-1}$. This performance is similar to the one of pilot reactors with 5.0 g. If a trickle bed (low interaction) is considered, k_{LS} is around $8.2 \times 10^{-4} \text{ m s}^{-1}$. The performance of the 5.0 g single pellet string reactor (liquid only) is similar to the 5.0 g Hipolito's reactor (liquid-gas) for WSHV below 40 h^{-1} . After, both mass transfer coefficients have a different behavior. This behavior can be explained by an extrapolation of the correlations proposed by Hipolito et al. (2010).

The reactors studied can be placed in the following order for liquid-solid mass transfer (at $\text{WSHV}=35 \text{ h}^{-1}$):

Hipolito ($m_{cat}=0.6\text{g}$) < Selected reactor ($m_{cat}=0.6\text{g}$) < Selected reactor ($m_{cat}=5.0\text{g}$) \approx Industrial (medium and high interaction) \approx Hipolito ($m_{cat}=5.0\text{g}$) < Industrial (low interaction)

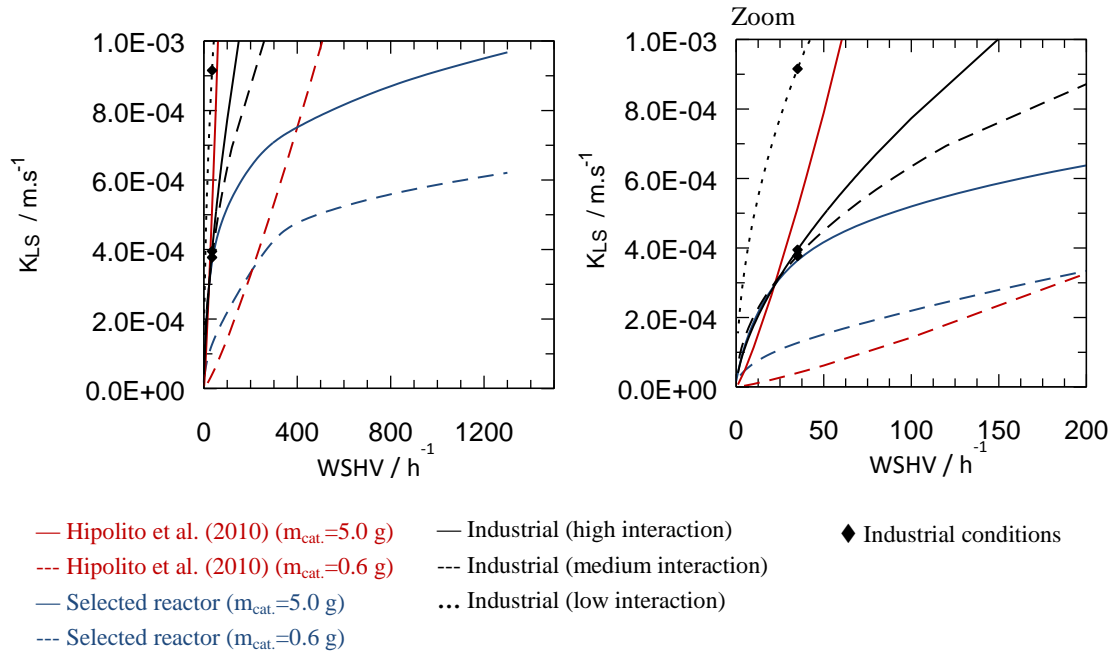


Figure III.26: Comparison between hydrogen liquid-solid mass transfer coefficients for pilot and industrial reactors in function of WSHV (h^{-1}) of the C_3 cut. The industrial WSHV is about 35 h^{-1} .

Global mass transfer

The global mass transfer was evaluated by:

$$k_{GLS}a_{GLS} \approx \left(\frac{1}{k_L a_{GL}} + \frac{1}{k_{LS} a_{LS}} \right)^{-1} \quad \text{Eq. III.38}$$

It was previously discussed that the difference between an industrial reactor and the Hipolito's pilot reactor is at the gas-liquid mass transfer rate, $k_L a_{GL}$. This problem does not exist for the selected single pellet string reactor, since it is always completely monophasic during the reaction. Thus, it is expected that the selected reactor has an improved mass transfer in relation to the Hipolito's pilot reactor.

Hydrogen analysis

Regarding Figure III.27, the trickle, pulse and bubble flow regimes [low (1.34 s^{-1}), medium (0.30 s^{-1}) and high (0.55 s^{-1}), respectively] have higher (hydrogen) mass transfer than Hipolito reactor (5.0 g). For the selected reactor (5.0 g), only the trickle flow regime (low interaction) has a higher value.

Comparing the bubble (high interaction) industrial reactor with the pilot reactors, it is 0.6 times lower than the selected reactor and 2.3 times greater than the Hipolito's reactor, both with 5.0 g of catalyst (see Figure III.27).

If the industrial reactor is in a pulse regime (medium interaction), the selected reactor (5.0 g) is better (2.6) than the industrial reactor. If the selected reactor has 0.6 g, the performance is

the similar to the industrial. In relation to Hipolito's reactor (5.0 g), it has lower hydrogen mass transfer than the industrial reactor.

The reactors studied can be placed in the following order for hydrogen global mass transfer (at $WHSV=35 \text{ h}^{-1}$):

Hipolito ($m_{cat.}=0.6\text{g}$) < Hipolito ($m_{cat.}=5.0\text{g}$) < Industrial (medium) < Selected reactor ($m_{cat.}=0.6\text{g}$) < Industrial (high) < Selected reactor ($m_{cat.}=5.0\text{g}$) < Industrial (low interaction)

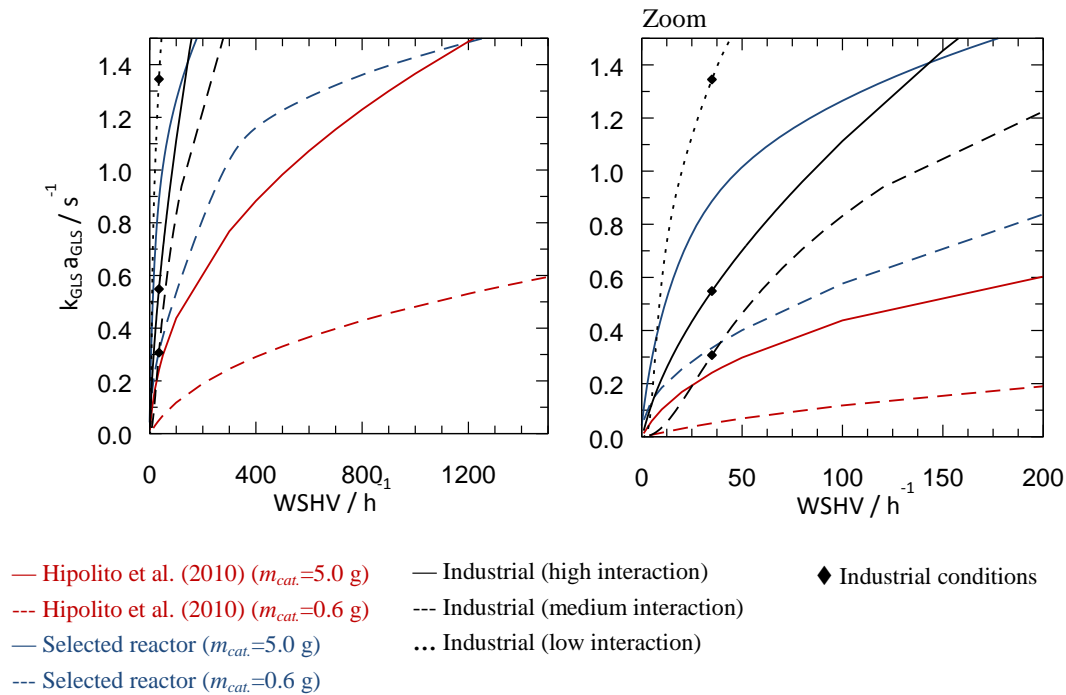


Figure III.27: Comparison between global hydrogen mass transfer coefficients for pilot and industrial reactors in function of WSHV (h^{-1}) of the C_3 cut. The industrial WSHV is about 35 h^{-1} .

MAPD analysis

Regarding Figure III.28, the trickle, pulse and bubble flow regimes [low (0.95 s^{-1}), medium (0.34 s^{-1}) and high (0.41 s^{-1}), respectively] have higher (MAPD) mass transfer than pilot reactors with 0.6 g.

The pilot reactors with 5.0 g have higher mass transfer than industrial reactors in high and medium interaction regimes. If the industrial reactor is in a trickle regime (low interaction), both pilot reactors (5.0 g) have lower performance than the industrial reactor.

The reactors studied can be placed in the following order for MAPD global mass transfer (at $WHSV=35 \text{ h}^{-1}$):

Hipolito ($m_{cat.}=0.6\text{g}$) < Selected reactor ($m_{cat.}=0.6\text{g}$) < Industrial (medium) < Industrial (high) < Selected reactor ($m_{cat.}=5.0\text{g}$) < Hipolito ($m_{cat.}=5.0\text{g}$) < Industrial (low interaction)

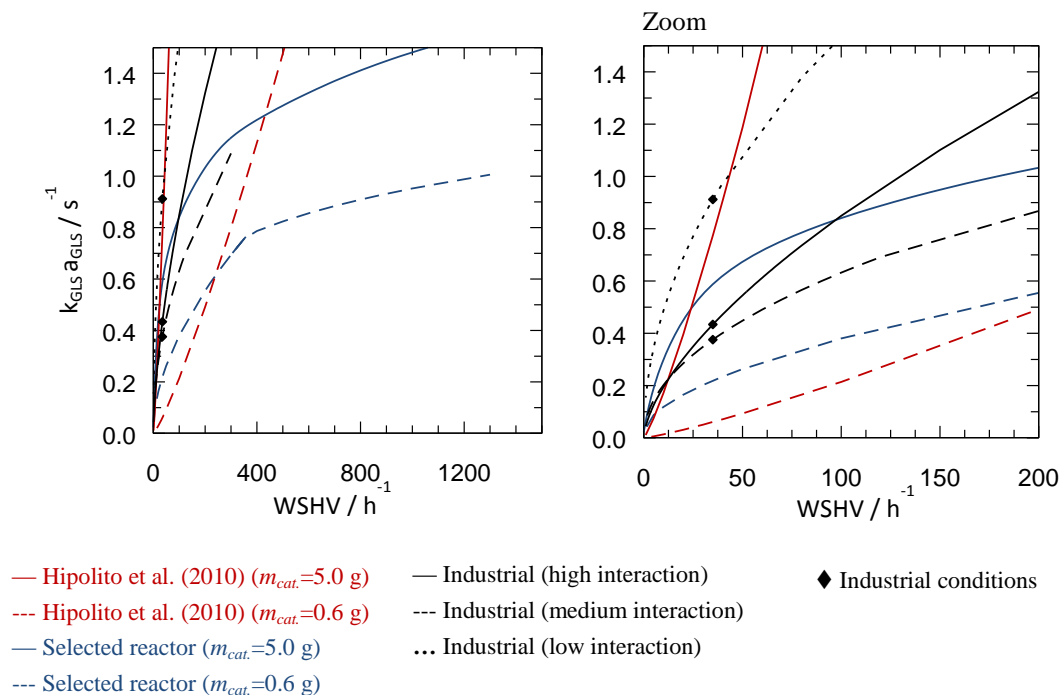


Figure III.28: Comparison between global MAPD mass transfer coefficients for pilot and industrial reactors in function of WSHV (h^{-1}) of the C_3 cut. The industrial WSHV is about 35 h^{-1} .

(a) Conclusions

From Table III.4, the H_2 global mass transfer rate is lower than MAPD for gas-liquid-solid systems (Hipolito and industrial reactors, excepting the one with medium interactions). However, for liquid-solid systems (selected reactor), the MAPD mass transfer rate is lower than H_2 . Therefore, when performing hydrogenation in liquid-solid conditions, the MAPD mass transfer should be preferentially analyzed rather than H_2 .

Table III.4: Mass transfer rates for H_2 and MAPD. The gray color indicates which species has lower mass transfer rate.

Operating condition		WHSV	35 h^{-1}	35 h^{-1}
Reactor type			$\text{H}_2 \text{ } k_{\text{GLS}} a_{\text{GLS}} / \text{s}^{-1}$	MAPD $k_{\text{GLS}} a_{\text{GLS}} / \text{s}^{-1}$
Pilot scale	Hipolito 0.6g		0.04	0.06
	Selected reactor 0.6g		0.30	0.23
	Hipolito 5.0g		0.24	0.77
	Selected reactor 5.0g		0.87	0.60
Industrial scale	Low interaction		1.31	0.91
	Medium interaction		0.31	0.37
	High interaction		0.55	0.43

In conclusion, **if the industrial reaction is performed in a pulse (medium) or bubble (high) regime, it should be better to use the selected reactor** (cylindrical string pellet reactor at high pressure), in order to have the same catalyst **screening conditions as in industry**. Since, this reactor is not affected by $k_L a_{GL}$, the overall H_2 mass transfer rate should be closer to the industrial reactor, independent the pulse and bubble regimes at industry. For the Hipolito's reactor, since it is has a big difference of $k_L a_{GL}$, from 2.5 up to more than 13.3 (if considered pulse or bubble regimes at industry), it should be difficult to extrapolate the results to an industrial level.

Looking back to the main goals of this thesis: (1) improve catalyst screening (with no $k_L a_{GL}$) and (2) get access to intrinsic reaction kinetics. Although, **not having limitations in gas-liquid mass transfer for the selected string pellet reactor**, does not mean that it is possible to access the intrinsic reaction kinetics. **It is still possible to be limited by liquid-solid (external) and intragranular mass transfer**. Thereby, it is interesting to improve these transfer rates, this can be achieved by going to supercritical conditions. By changing physical "state", it is possible to have higher Re_L (lower viscosity) and Sc (higher diffusivity), which improves the mass transfer rate ($\underbrace{k_{GLS} a_{GLS}}_{\text{Supercritical fluids}} > \underbrace{k_{GLS} a_{GLS}}_{\text{High-pressure}}$).

Going to supercritical conditions may lead to an increase of mass transfer rates. Consequently, the results may be far from the industrial reactor, but even so, SCFs will help us to have a better understanding about the catalyst.

III.4 Conclusions

The goal of this chapter was to **characterize the experimental set-up and the reactor for hydrodynamics and liquid-solid mass transfer**.

In relation to the experimental set-up, **a single pellet string reactor with cylindrical section was chosen**. The **experimental set-up proves to be reliable** to perform MAPD hydrogenation, since the analysis equipment (GC-FID) has an average absolute deviation of 0.5% for the C_3 cut feedstock (reactant). Several experiments were performed to determine the effective diffusivity inside the catalyst, being close to the self-diffusion.

To construct a CFD model of a single string pellet reactor, **the particle arrangement** was experimentally studied. It was shown that **72% of the particle follows 70° and 80° arrangements**.

A **CFD hydrodynamic** study was performed to investigate the flow inside the reactor. It was shown that the fluid has a serpentine flow pattern for the zigzag particle arrangement used. For the residence time distribution studied, it was considered acceptable to model the reactor as: **a plug flow with low axial dispersion ($Re_L=20$; $Pe_{ax}\approx 70$) and a plug flow ($Re_L=160$; $Pe_{ax}\approx 190$)**. This will allow to build a simplified reactor model (§V).

Then, a **CFD study** was performed to **investigate the liquid-solid mass transfer**. A **mass transfer correlation was proposed** for the working zone. Since this correlation was obtained by CFD, and the results were not validated experimentally, it should be used with caution. Even so, the results have **good agreement with the Ranz and Marshall (1952) correlation**, which gives confidence in the obtained results.

Finally, to have an idea of **the performance of the pilot reactors in relation to industry**, the **mass transfer rates were compared with an industrial reactor in three hypothetical regimes**: trickle (low interaction), pulse (medium interaction) and bubble (high interaction). If the industrial reaction is performed in a pulse (medium) or bubble (high) regime, it should be better to use the selected reactor for catalyst screening (cylindrical string pellet reactor at high pressure).

The Hipolito's reactor and the industrial reactors are controlled by the H_2 global mass transfer. The selected reactor is controlled by global MAPD mass transfer. For the **Hipolito's reactor**, since it has a big difference of $k_{GLS}a_{GLS}$, from 1.2 up to more than 4 (depending on the flow regime of the industrial reactor), **it should be difficult to extrapolate the results to an industrial level**.

To conclude, the single pellet string reactor selected is characterized for hydrodynamics and mass transfer in a single-phase flow. **The CFD data obtained will be used to analyze directly experimental results and to build a reaction model**. The selected reactor seems to be appropriated to conduct experimental studies.

Chapter IV

C₃ cut hydrogenation in conventional and unconventional conditions

Abstract

The purpose of this chapter is to evaluate the impact of unconventional conditions on the hydrogenation of unsaturated hydrocarbons, in particular, the methylacetylene (MA) and the propadiene (PD). This reaction was chosen due to its fast kinetics, being controlled by mass transfer at conventional pilot scale conditions. The mass transfer restrictions go from interphase (gas-liquid) to the catalyst pellet, having superior limitations in the interphase mass transfer (§I.3.1). Therefore, it is difficult to acquire intrinsic kinetics and to be able to extrapolate the results. By operating the process at unconventional conditions (homogeneous fluid), the interphase mass transfers (gas-liquid) do not exist, and the external and intragranular mass transfers are enhanced.

To understand the gain in catalytic performance (yield and selectivity), conventional (G/L phase), high-pressure (L phase) and supercritical (SC phase) conditions are compared for equal residence time and mass of catalyst. The effects of several parameters are evaluated, such as the WHSV (catalyst mass), the stoichiometry (expressed as H₂/MAPD ratio), the pressure and the type of solvent.

In the experiments, a fresh catalyst (symbolically called W) based on Pd/ α -Al₂O₃ was employed. Consequently, the data acquired will be related with the initial kinetics without catalyst deactivation. It is shown that high-pressure and supercritical conditions are not controlled by liquid-solid mass transfer. Additionally, the supercritical medium has higher reaction rate (~5 times) than high-pressure conditions.

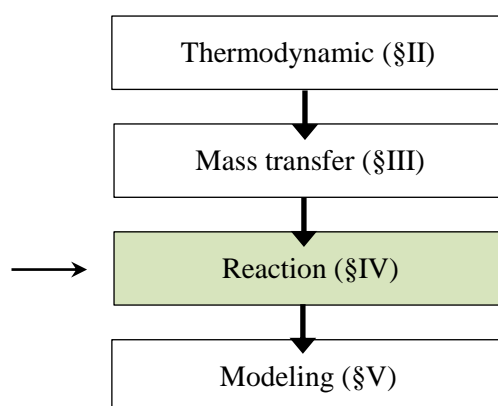


Figure IV.1: Manuscript's guideline.

IV.1 Introduction

The selective hydrogenation of unsaturated hydrocarbons is a fundamental process in the petrochemical industry (Brandao et al., 2007). This reaction involves the conversion of alkynes and dienes into alkenes, such as propylene [**~90 million tons produced per year**] (§I.4). The propylene is mostly produced by steam cracking, which contains impurities: methyl-acetylene (MA) and propadiene (PD) (Table II.6). As previously mentioned (I.4), the reaction scheme of MAPD hydrogenation can be presented as in Figure IV.2. The oligomers produced have 6 carbons or more. Since they are difficult to quantify, they will be treated as 6 carbons.

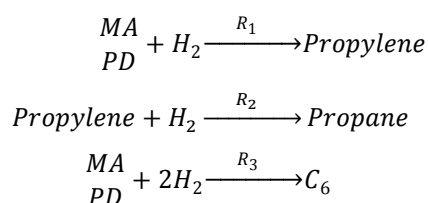


Figure IV.2: Simplified reaction scheme (§I.4.4).

To better understand and quantify the impact of mass transfer on the reaction yield, **the MAPD hydrogenation was subjected to a series of tests in conventional and unconventional conditions. The main goal of this chapter is to study the influence of high-pressure and supercritical conditions (SC) in fast selective hydrogenation of the C₃ cut.** The SCFs conditions were **chosen**, because they can help to **enhance the reaction performance by simplifying phase behavior and improving (external and internal) mass transfer.**

To hydrogenate the C₃ cut at supercritical conditions, it is necessary to add an inert solvent to reduce the critical pressure and temperature. The inert solvents selected were: CH₄, C₂H₆ and CO₂ (§II.6). The CH₄ leads to softer temperature conditions (supercritical medium) than the others, which make it a more reliable fluid. It allows performing reactions at the same temperature as conventional conditions ($T=303$ K). Higher temperatures are required ($T>333$ K) to achieve the supercritical conditions when other solvents, ethane or CO₂, are used.

In this chapter, the methodology, the parameters and the conditions studied will be first described. Then, the experimental results will be presented and discussed.

IV.2 Methodology

The experimental set-up and data processing were already presented in §III.2. It should be noticed that the hydrogen composition is not detected by the chromatography system adopted. Thus, the hydrogen was obtained by a mass balance of the MAPD consumed and propane produced (Eq. IV.1).

Hydrogen quantification

Mass balance for H_2 ($\text{g}\cdot\text{m}^{-3}\cdot\text{s}^{-1}$)

(*Assumption*: no oligomers produced)

$$\Delta\mathcal{N}_{H_2}M_{H_2} = \Delta\mathcal{N}_{MAPD}M_{MAPD} + \Delta\mathcal{N}_{PA}M_{PA} \quad \text{Eq. IV.1}$$

where M ($\text{g}\cdot\text{mol}^{-1}$) is the molar mass and \mathcal{N} ($\text{mol}\cdot\text{m}^3\cdot\text{s}^{-1}$) is the molar concentration flow.

The hydrogen consumed to produce oligomers should be integrated into this equation. Unfortunately, the oligomers cannot be quantified in mole fraction due to problems in peak separation and identification (GC-FID). Therefore in Eq. IV.1, it was assumed that the oligomers quantities are negligible (for more information see §III.2.2).

Oligomers relative quantification

To verify the previous assumption, the oligomers produced are monitored in GC-FID for the relative area, which is quantified to a defined condition:

$$A_{i, \text{relative}} = \frac{\overbrace{\int A_{i, \text{peaks}} dt_r}^{\text{oligomers}}}{\underbrace{\int A_{\text{peaks}} dt_r}_{\text{oligomers}} \Big|_{\text{conventional conditions}}} \quad \text{Eq. IV.2}$$

where $A_{i, \text{relative}}$ is the relative area of oligomers, A_{peaks} is the area of all the chromatogram peaks with more than C_3 carbons, and t_r (s) is the retention time. The conventional conditions are $P=20$ bar and $T=303$ K. The $\int A_{\text{peaks}} dt_r$ was obtained by averaging of the values analyzed for conventional conditions.

According to Figure IV.3, the oligomers produced in different experimental conditions have a similar relative area (from 0 to 2). Also, the area of the peaks is small. For these reasons, the oligomers quantity can be neglected when studying and comparing different experimental conditions.

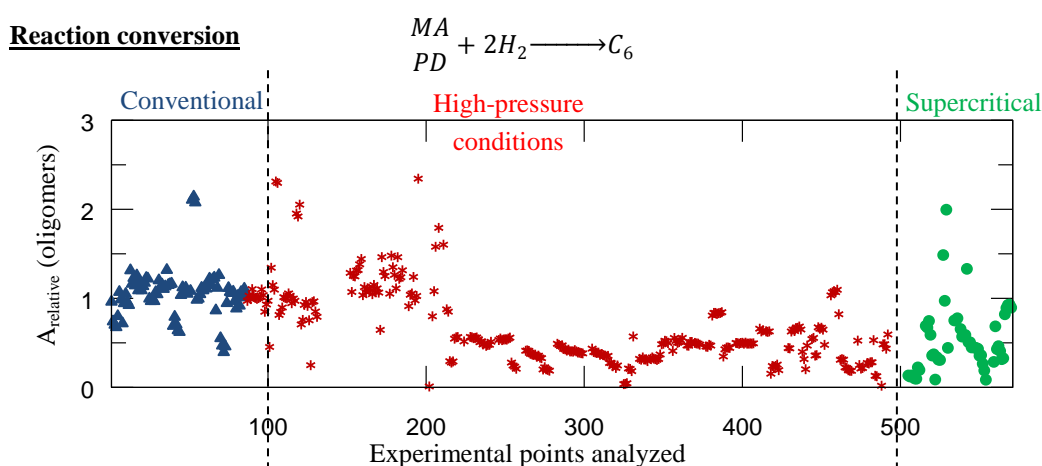


Figure IV.3: Experimental points related to the oligomerization in the conditions used: conventional, high-pressure and supercritical conditions (Table IV.1).

Dimensionless numbers

To interpret the experimental results, a dimensionless number (ψ) was proposed. This number determines if a fluid has sufficient time to have full mass transfer between phases. The deduction of this expression is explained in the Appendix §IV.1.

$$\psi = \frac{\text{flow time to full transfer}}{\text{transfer time}} \Rightarrow \begin{cases} \psi_{GL} = \frac{\overbrace{k_L a_{GL}}^{\text{transfer time}}}{\underbrace{\tau_G}_{\text{residence time}}} / 2 \\ \psi_{LS} = \frac{\overbrace{k_{LS} a_{LS}}^{\text{transfer time}}}{\underbrace{\tau_L}_{\text{residence time}}} / 2 \end{cases} \quad \text{Eq. IV.3}$$

If $\psi < 1$, the fluid stays less time than what is required to perform full mass transfer between two phases (the reaction is limited).

If $\psi > 1$, the fluid has sufficient time to perform full mass transfer, but the reaction can still be controlled by molar concentration flow (gas to liquid or liquid to solid). In other words, the ψ only specifies if the gas or liquid is totally transferred to another phase. The quantity transfer will still influence the reaction rate.

The ψ_{GL} parameters (gas-liquid) are expressed as:

$$\tau_G = \frac{V_{reactor}(\varepsilon - \varepsilon_L)}{\frac{Q_G}{\bar{u}_L}} \quad \text{Eq. IV.4}$$

$$\varepsilon_L = \frac{\bar{u}_L}{\bar{u}_G + \bar{u}_L} \varepsilon \quad \text{Eq. IV.5}$$

where $V_{reactor}$ (m^3) is the reactor volume, ε is the bed porosity, ε_L is the liquid hold-up, \bar{u}_G (m.s^{-1}) is the gas superficial velocity and \bar{u}_L (m.s^{-1}) is the liquid superficial velocity. The choice and source of Eq. IV.5 is detailed in the Appendix §IV.2.

IV.2.1 Experimental conditions

The conventional and unconventional conditions are presented in Table IV.1. For high-pressure and supercritical fluids, these conditions were detailed in §I.5.4 and §II.6, respectively.

The set-up solvent maximum capacity is 60 mol%. Consequently, it is only possible to have the supercritical region for CO_2 and CH_4 at the temperature ($T=303$ K) (Figure IV.4 ●) (§II.6). For ethane, it is not possible to reach supercritical conditions at this temperature required. Conserving the conventional temperature is interesting since the goal is to compare the conventional with unconventional conditions without changing the intrinsic reaction rate.

Table IV.1: Pilot-scale operating conditions for C₃ cut hydrogenation (2.8 mol% MAPD).

	Conventional	High-pressure	Supercritical
Pressure (bar)	20	120	120
Temperature (K)	303	303	[303 to 353]
Physical state	liquid-gas	liquid	supercritical
Solvent (mol%)	0	0	~60
H ₂ /MAPD ratio	1 to 2	1 to 4	1 to 2
Mass transfer rate	$k_L a_{GL}$ $k_{LS} a_{LS}$	$k_{LS} a_{LS}$	$k_{LS} a_{LS}$
Thiele modulus	Standard	Standard	Lower (higher effectiveness factor)
Catalyst mass (g)	0.6 (70 pellets)	0.6 (70 pellets)	0.6 (70 pellets)

The strategy adopted was:

1. to use the CH₄ as the solvent and to compare the results with conventional conditions;
2. the CO₂ was not used since it can have a negative impact on the reaction (Burgener et al., 2005a);
3. to increase the temperature and compare the performance of the other solvents at supercritical conditions (T=353 K; Figure IV.4 ●).

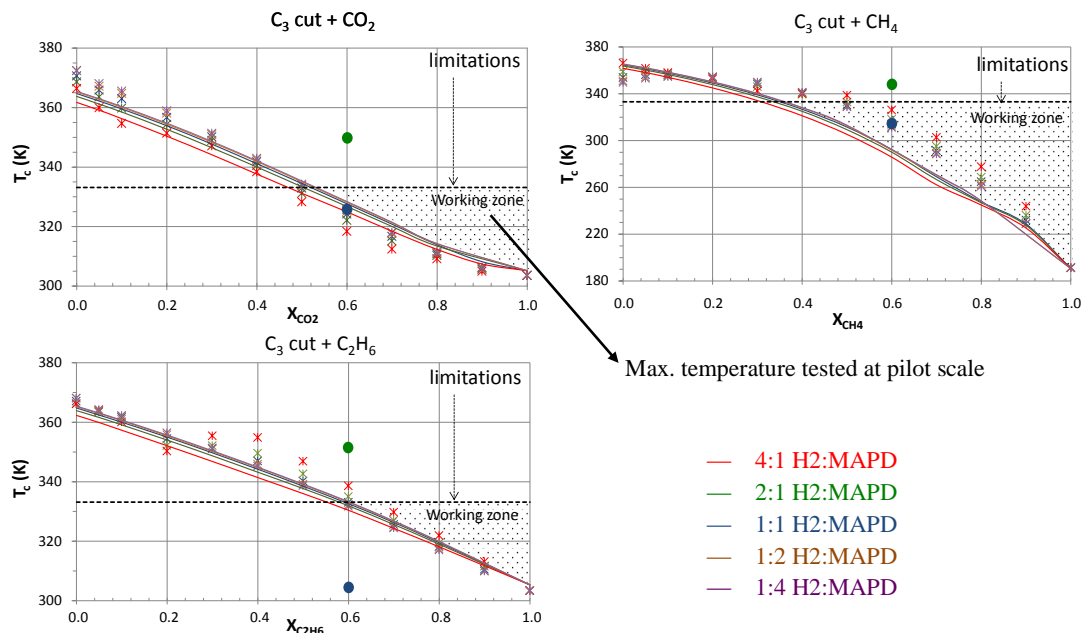


Figure IV.4: Temperature conditions for the supercritical domain, depending on the stoichiometry ratio and solvent composition. The pressure is not shown since the pilot plant is not limited by it (P can go above 120 bar). The lines are related to the model results and the crosses (X) are experimental values. The point ● 303 K is linked with the working conditions studied. The point ● 353 K is related to the conditions to achieve supercritical domain with all the solvents studied.

IV.2.2 Studied parameters and strategy

Parameters

To be able to compare unconventional and conventional conditions (Table IV.1), it is important to understand individually the effects of several parameters, such as: WHSV (h^{-1}), MAPD concentration, H_2 /MAPD ratio, temperature, pressure, solvent type and phase state.

On one hand, changing WHSV, MAPD concentration, H_2 /MAPD ratio and temperature helps characterizing the reaction for each condition (Table IV.2). On the other hand, changing pressure, phase state and adding a solvent help comparing conditions for mass transfer limitations (Table IV.2). However, some of these parameters are coupled and cannot be individualized. For this reason, Table IV.2 was created to detail the main physico-chemical properties modified with each parameter.

Table IV.2: Pairs of effects analyzed/main properties changed during the reaction. (*number of parameters changed)

	Effects analyzed	Main properties changed	Complexity*
Characterize reaction (conventional and unconventional)	WHSV	Residence time (h)	2
		Mass transfer ($k_L a_{GL}$ and $k_{LS} a_{LS}$) (s^{-1})	
	MAPD concentration	Molar conc. flow ($k_{LS} a_{LS} \Delta C_{MAPD}$) ($\text{mol.m}^{-3}.\text{s}^{-1}$)	1
	H_2 /MAPD ratio	Molar conc. flow ($k_L a_{GL} \Delta C_{H_2}$ and $k_{LS} a_{LS} \Delta C_{H_2}$) ($\text{mol.m}^{-3}.\text{s}^{-1}$)	1
	Temperature	Density (kg.m^{-3})	5
Viscosity (Pa.s)			
Diffusivity ($\text{m}^2.\text{s}^{-1}$)			
Mass transfer ($k_L a_{GL}$ and $k_{LS} a_{LS}$) (s^{-1}) Reaction rate ($\text{mol.m}^3.\text{s}^{-1}.\text{kg}^{-1}$)			
Pressure	Density (kg.m^{-3})	4	
	Viscosity (Pa.s)		
	Diffusivity ($\text{m}^2.\text{s}^{-1}$)		
	Mass transfer ($k_L a_{GL}$ and $k_{LS} a_{LS}$) (s^{-1})		
Unconventional conditions	Solvent type	Density (kg.m^{-3})	7
		Viscosity (Pa.s)	
		Residence time (h)	
		Diffusivity ($\text{m}^2.\text{s}^{-1}$)	
		Mass transfer ($k_L a_{GL}$ and $k_{LS} a_{LS}$) (s^{-1})	
		Adsorption equilibrium Reaction rate ($\text{mol.m}^3.\text{s}^{-1}.\text{kg}^{-1}$)	
Phase state	Density (kg.m^{-3})	6	
	Viscosity (Pa.s)		
	Residence time (h)		
	Diffusivity ($\text{m}^2.\text{s}^{-1}$)		
	Mass transfer ($k_L a_{GL}$ and $k_{LS} a_{LS}$) (s^{-1}) Adsorption equilibrium		

Table notes

From WHSV to pressure effects (see Table IV.2), the properties are weakly correlated. The main properties that change are thermodynamic properties, diffusivity and mass transfer. The thermodynamic properties can be estimated using an equation of state (PR78 or PPR78), providing satisfactory results (Ke et al., 2001; Qian et al., 2012). The diffusivity can be estimated by a diffusion correlation (Liu et al., 1997b). The mass transfer can be estimated by Sh correlations (*e.g.*, liquid only). In relation to the pressure, the density variations are negligible for liquids. However, for gases and supercritical fluids, the density variations are important, and they can influence the residence time and the mass transfer coefficients ($k_L a_{GL}$ and $k_{LS} a_{LS}$).

For solvent and phase effects (see Table IV.2), properties are difficult to isolate and study, such as catalytic adsorption, diffusivity and reaction time. This increases the difficulty in comparing and understanding unconventional with conventional conditions. To study and characterize the reaction, our strategy is detailed in Figure IV.5.

Strategy

Starting from conventional conditions, two parameters were studied to define the zone where the reaction has better and worst performance (reaction and selectivity). By changing to unconventional conditions (high-pressure), the gas-liquid was suppressed. This impact was studied using several parameters. Then going to supercritical conditions, the impact of an improved fluid-solid mass transfer and diffusivity coefficient will be explored.

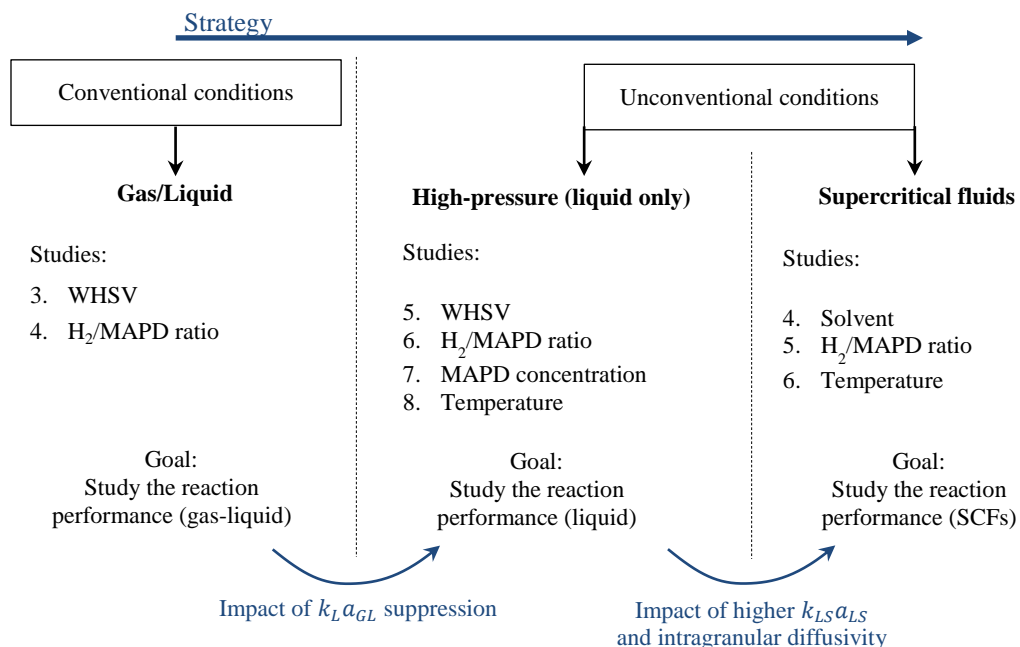


Figure IV.5: Strategy proposed to study each reaction technology.

IV.3 Conventional conditions

The reaction in conventional conditions is performed in two phases: one vapor phase (hydrogen-rich phase) and one liquid phase (propylene-rich phase with hydrogen solubilized). Studying conventional conditions help estimating the reaction time and identifying zones where the reaction is limited by mass transfer (gas-liquid and/or liquid-solid).

During the experiments, the oligomers could not be quantified (see §III.2.2 and IV.2). Consequently, the H_2 consumed for their production was also not quantified (by calculations), which explains that sometimes 95% of H_2 is converted instead of 100%.

Studies performed: variation of (i) WHSV and (ii) H_2 /MAPD ratio.

Feedstock: MAPD (3.02 mol% [375 mol.m⁻³]) and Propane (3.29 mol% [408 mol.m⁻³]).

IV.3.1 WHSV effect

Conditions: 1 H_2 /MAPD ratio, 303 K, 20 bar and catalyst mass of 0.6 g (catalyst W).

Main properties changed: reaction time (h) and mass transfer ($k_L a_{GL}$ and $k_{LS} a_{LS}$).

Observations

Figure IV.6 shows the influence of the WHSV on the species conversion.

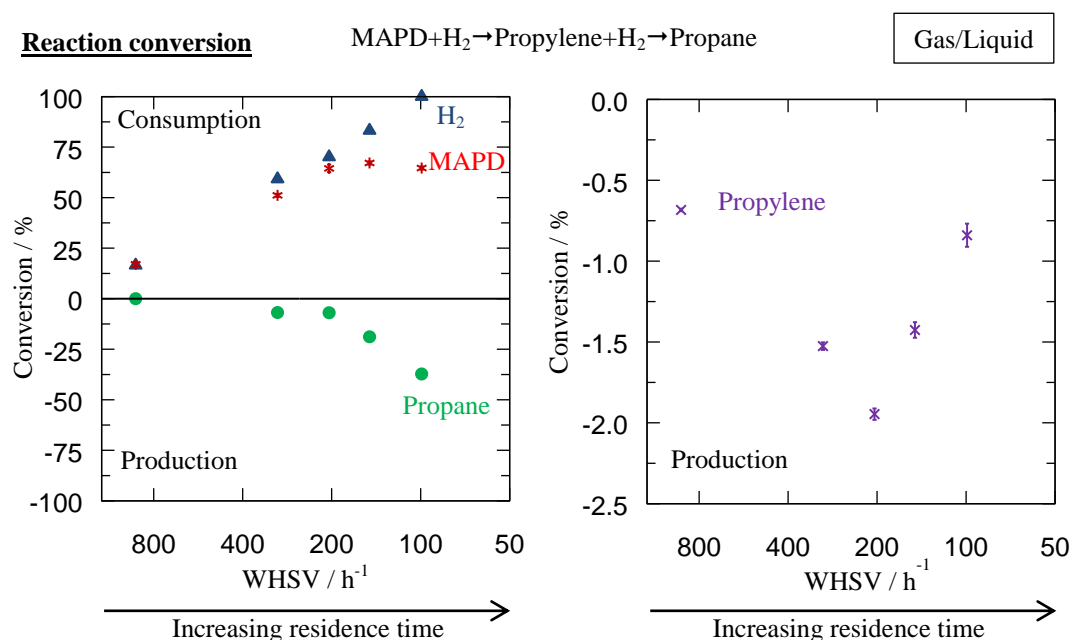


Figure IV.6: Selective hydrogenation at 1 H_2 /MAPD ratio, 303K and 20 bar. Conversions of MAPD (*), Propane (●), Hydrogen (▲) and Propylene (×).

Hydrogen: Regarding the H_2 (▲ Figure IV.6), when the WHSV decreases, the H_2 conversion increases linearly (log scale). At low WHSV (100 h⁻¹), the system might have enough time to react and perform the gas-liquid and liquid-solid mass transfer ($\psi_{GL} > 1$ and $\psi_{LS} > 1$; Figure IV.7). At 100 h⁻¹, the hydrogen is fully converted (1.0 H_2 /MAPD ratio).

MAPD: Regarding * Figure IV.6, the MAPD conversion increases from 900 to 200 h⁻¹, having a linear behavior (similar to H₂). Two possible explanations are possible:

- a) Regarding ψ_{GL} values (Figure IV.7), in this range, there might not be sufficient residence time to guarantee all the gas-liquid transfer, $\psi_{GL} < 1$.
- b) There might be insufficient residence time for the reaction (chemical part).

From 200 to 100 h⁻¹ the conversion is stable (65%). Therefore, the MAPD reaction rate is greater at high WHSV than at low WHSV. This is a curious result because in this range there is still H₂ available and enough time to have transfer ($\psi_{GL} > 1$) (Figure IV.7).

Propane: Regarding ● Figure IV.6, the propane production (negative conversion) suddenly increases from 200 to 100 h⁻¹. This might be related to mass transfer (global molar conc. flow $k_{GLS}a_{GLS}\Delta C_{H_2}$ or $k_{GLS}a_{GLS}\Delta C_{MAPD}$) and/or reaction rate. In addition, it might be possible to have a competition for the catalyst active sites.

Propylene: The propylene production decreases from 900 to 200 h⁻¹ and increases from 200 to 100 h⁻¹. The explanations for this change are the same as for the propane. Since propylene is a consequence of other species, for now on it will not be discussed, but the graphics will be shown as additional information.

The gas-liquid and liquid-solid mass transfer coefficients (Figure IV.7 a,c) decrease from 900 to 100 h⁻¹. Both coefficients are directly proportional to the Reynolds numbers for gas (Re_G) and liquid (Re_L), which decrease with the decrease of the WHSV (lower velocity inside the reactor).

The ψ_{GL} and ψ_{LS} are present in Figure IV.7 (b,d). These figures should be read as zones: if there is sufficient time to have full mass transfer (>1) or not (<1). More information about ψ can be found in the Appendix §IV.1.

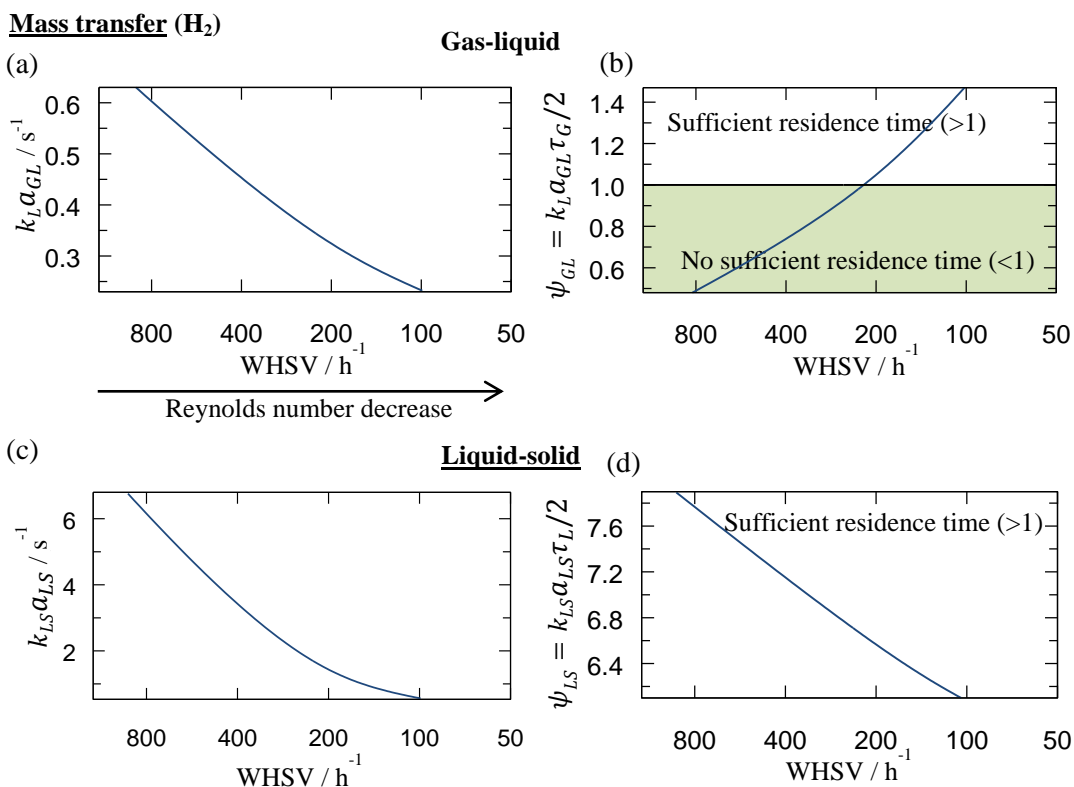


Figure IV.7: Selective hydrogenation at 1 H₂/MAPD ratio, 303K and 20 bar. (a, b) Hydrogen mass transfer coefficient (gas-liquid) and ψ_{GL} were calculated based on Hipolito (2010) correlation for $k_L a_{GL}$ (hydrogen). (b, d) Hydrogen mass transfer coefficient (liquid-solid) and ψ_{LS} were calculated based on Hipolito et al. (2010) correlation for $k_{LS} a_{LS}$ (hydrogen).

Summary

From the results presented, it is possible to conclude that:

1. 900 to 200 h⁻¹: This range might be limited by gas-liquid mass transfer ($\psi_{GL} < 1$) or by reaction rate. But, since the kinetics is unknown, no more explanations can be addressed.
2. 200 to 100 h⁻¹: The performance might be explained by: (i) mass transfer limitations (take liquid-solid), (ii) molar conc. flow variations and/or (iii) competition between reactant species for the active sites.

If mass transfer limitations are considered, we may think the calculated gas-liquid transfer coefficients are overestimated (the Hipolito et al. (2010) gas-liquid correlation may not be adapted for the selected reactor geometry). This can be related to changes in the flow regime and preferential paths. Consequently, at 200 h⁻¹, the reaction can still be limited by mass transfer ($\psi_{GL} < 1$ - no time to have full mass transfer), which does not occur at 100 h⁻¹ (full conversion of hydrogen).

IV.3.2 H₂/MAPD ratio effect

In the previous point, the impact of the WHSV was studied at 1.0 H₂/MAPD ratio. In this subsection, a range of H₂/MAPD ratio is evaluated and the influence of H₂ molar

concentration flow ($k_L a_{GL} \Delta C_{H_2}$ and $k_{LS} a_{LS} \Delta C_{H_2}$) is studied. Changing the H₂/MAPD ratio has an impact in $k_{LS} a_{LS}$, τ_G and ΔC_{H_2} . So going from 1 to 2 in H₂/MAPD ratio, does not mean twice the molar concentration flow, since the gas inside the reactor has a different residence time.

Apart from H₂/MAPD ratio, two WHSV were also studied: 200 and 100 h⁻¹. From 200 to 100 h⁻¹ there might be mass transfer limitations and/or competition between reactants.

Main properties changed: molar concentration flow ($k_L a_{GL} \Delta C_{H_2}$ and $k_{LS} a_{LS} \Delta C_{H_2}$).

Observations

Figure IV.8 shows the influence of the H₂/MAPD ratio on the species conversion for two WHSV.

MAPD: The MAPD conversion increases linearly with H₂/MAPD ratio for the majority of the points studied (Figure IV.8a). It is an expected result because there is an increase of the reactant (H₂) that is potentially limiting the reaction rate. Between 0.8 and 1.3 H₂/MAPD ratios, the conversion is almost independent of the WHSV studied. However for H₂/MAPD ratio superior to 1.3, the conversion depends on the WHSV studied. The exception is at 1.8 H₂/MAPD ratio (200 h⁻¹), where the MAPD conversion goes from 69.6±1.8% (previous point) to 62.5±0.9%.

Propane: From 0.8 to 2.1 H₂/MAPD ratio, the produced propane increases (negative propane conversions) (Figure IV.8b). Comparing 100 to 200 h⁻¹, the produced propane is higher for 100 h⁻¹. The point at 1.8 H₂/MAPD ratio (200 h⁻¹) has similar conversion as the previous point (1.3 H₂/MAPD ratio). At 1.8 H₂/MAPD ratio (200 h⁻¹), it was expected higher propane production since the MAPD is lower.

Hydrogen: When H₂/MAPD ratio increases (Figure IV.8c), the H₂ conversion decreases almost linearly for 200 and 100 h⁻¹, even if reactants, such as MAPD and propylene, are still available. For both WHSV values, there is still H₂ available at the reactor outlet above 1.2 H₂/MAPD ratio.

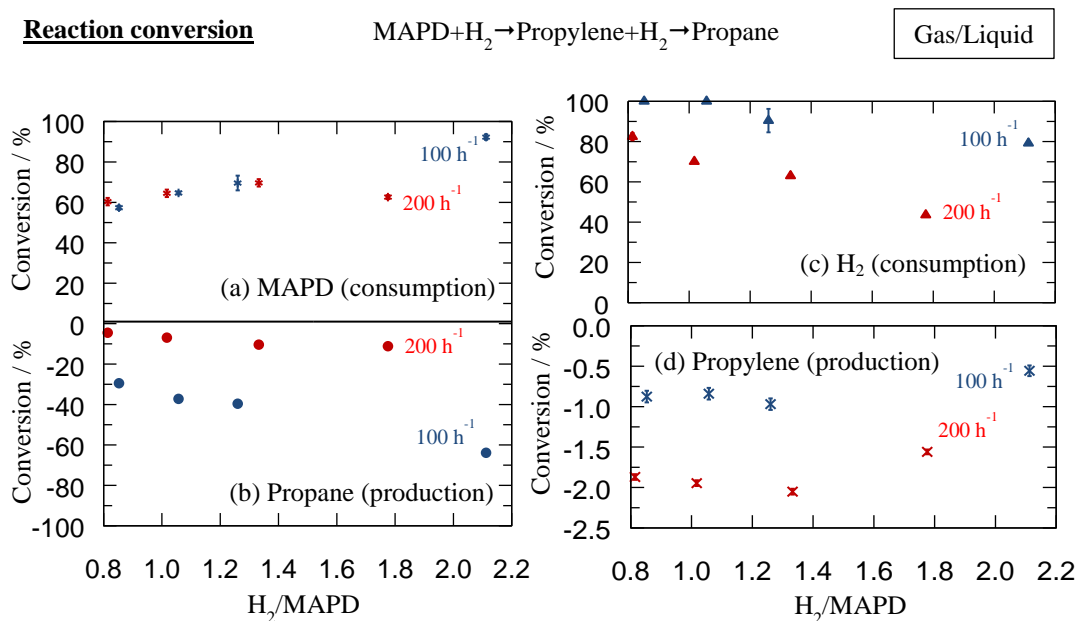


Figure IV.8: Selective hydrogenation at 200 h⁻¹ (red) and 100 h⁻¹ (blue) [303K and 20 bar]. Conversions of MAPD (a), Propane (b), Hydrogen (c) and Propylene (d).

The gas-liquid and liquid-solid mass transfer coefficients (Figure IV.9a) increase from 0.8 to 2.2 H₂/MAPD ratio for the WHSV studied (100 and 200 h⁻¹). This is related to the increase of gas and liquid velocities by the addition of more gas (\Rightarrow higher Re_G and Re_L). Figure IV.9b has the ψ_{GL} zones defined. Only for H₂/MAPD ratio superior than 1.2 (200 h⁻¹), there is not sufficient time to have full gas-liquid mass transfer.

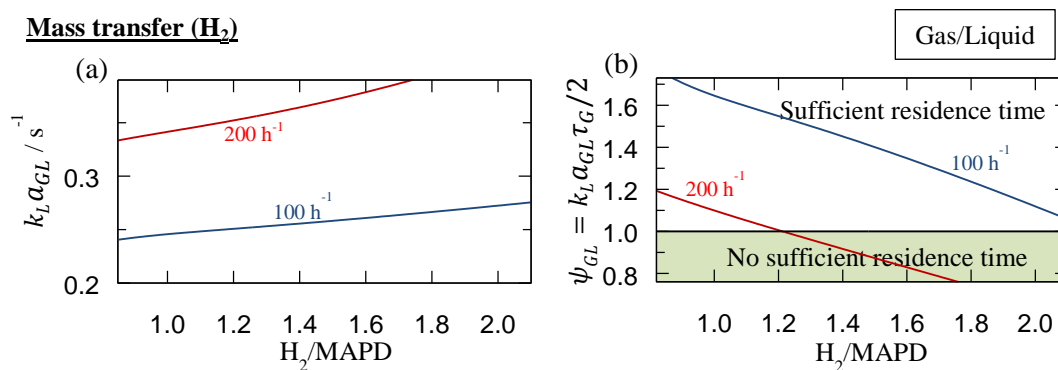


Figure IV.9: Selective hydrogenation at 200 h⁻¹ (red) and 100 h⁻¹ (blue) [303K and 20 bar]. (a, b) Hydrogen mass transfer coefficients (gas-liquid) and ψ_{GL} as a function of H₂/MAPD ratio. Both were calculated based on Hipolito et al. (2010) correlation for $k_L a_{GL}$ (hydrogen).

Results discussion

From 0.8 to 1.3 H₂/MAPD ratio at 100 h⁻¹, the MAPD and propane conversion can be explained by the lack of H₂. After 1.3 H₂/MAPD ratio, there is sufficient H₂ to perform the reaction.

The point at 1.8 H₂/MAPD ratio at 200 h⁻¹ has a strange behavior since the MAPD and propane conversion are virtually stable. It was expected to have higher values, because the

reaction rate increases (more H₂), and the gas-liquid (Figure IV.9a) and liquid-solid (not shown) mass transfer coefficients are slightly higher. A possible justification is that there is not enough time to perform full gas-liquid mass transfer ($\psi_{GL} < 1$; Figure IV.9b). For 100 h⁻¹ there is enough time ($\psi_{GL} > 1$; Figure IV.8b), which might explain the higher conversion.

In Figure IV.8 (a,b), it seems that there is a linear dependency of the MAPD and propane conversion with the H₂/MAPD ratio (for $\psi_{GL} > 1$). Therefore, the reaction order for hydrogen concentration might be one. This value should be later verified in a reactive system without gas-liquid mass transfer, namely unconventional conditions (§IV.4 and IV.5).

Summary

From the previous WHSV experiments (§IV.3.1), three explanations were proposed for the stability of MAPD conversion (200 to 100 h⁻¹): (option I) mass transfer, (option II) molar concentration flow is controlling the reaction and/or (option III) competitions between species for the active sites. After these results:

Option I: it seems a possible explanation. The experiments with different H₂/MAPD ratios can be explained by ψ_{GL} although the uncertainty of the liquid-gas mass transfers and gas hold-up correlations.

Option II: it may be present in a part of the results.

Option III: it is still not clear. More results are needed.

To summarize:

1. 200 h⁻¹: not enough time to perform full hydrogen mass transfer;
2. 100 h⁻¹: enough time to perform full hydrogen mass transfer;
3. The hydrogen reaction order might be one;
4. ψ_{GL} can help understand MAPD hydrogenation.

IV.3.3 Determination of the zone $\psi_{GL} < 1$

Before studying the impact of the $k_L a_{GL}$ on the reaction performance using unconventional conditions at high-pressure (no $k_L a_{GL}$), it is interesting to delimit and to verify the zone where the reaction should be limited by mass transfer ($\psi_{GL} < 1$). Figure IV.10 shows a first diagram of this zone.

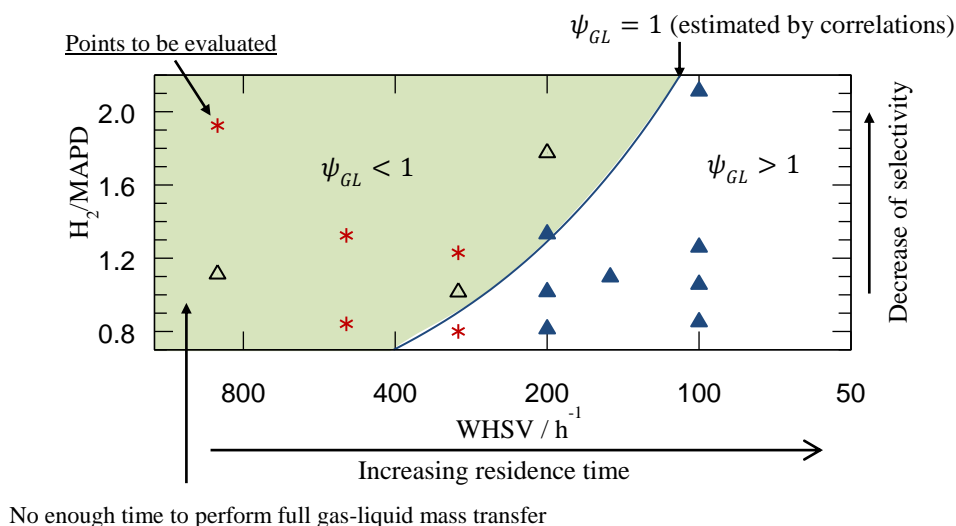


Figure IV.10: Zone with $k_L a_{GL}$ (hydrogen) limitations for the selected reactor ($\psi_{GL} < 1$): H_2 /MAPD ratio versus WHSV (303 K and 20 bar). (▲) Experimental points with $\psi_{GL} > 1$; (△) experimental points with $\psi_{GL} < 1$; (*) untested points.

Although the uncertainties in τ_G (s) and in $k_L a_{GL}$ (s^{-1}), the zones defined by ψ_{GL} are in agreement with the experimental results. To check if they are well defined, 5 new points (*) were added (close to $\psi_{GL} = 1$ and in the middle of $\psi_{GL} < 1$ zone). The next step is to define the zones of the red points by experiments.

Conditions: 303 K, 20 bar and catalyst mass of 0.6 g (catalyst W).

Main properties changed: reaction time (h), mass transfer ($k_L a_{GL}$ and $k_{LS} a_{LS}$) and molar conc. flow ($k_L a_{GL} \Delta C_{H_2}$ and $k_{LS} a_{LS} \Delta C_{H_2}$).

Observations

Figure IV.11 shows the influence of the H_2 /MAPD ratio and WHSV for all the points evaluated (Figure IV.10). The goal is to delimit the zone with $\psi_{GL} < 1$.

MAPD: The MAPD (Figure IV.11a) has two different zones for the majority of points: linear increase (900 to 200 h^{-1}) and stability (200 to 100 h^{-1}). The only exception is the point at 2.0 H_2 /MAPD ratio and 100 h^{-1} (previously discussed in §IV.3.2), for which the conversion increased from 200 to 100 h^{-1} .

Propane: From 900 to 100 h^{-1} , the propane production increases for all the H_2 /MAPD ratios studied (Figure IV.11b). Regarding each WHSV, increasing H_2 /MAPD ratio leads to a higher propane production. From 100 to 200 h^{-1} , the produced propane is higher. Regarding Figure IV.12 (selectivity), this zones has the lower selectivity, going from 80% to 20%.

Hydrogen: The hydrogen conversion (Figure IV.11c) increases almost linearly from 900 to 100 h^{-1} (similar behavior as in §IV.3.1). The new points [900 h^{-1} ; 500 h^{-1} ; 300 h^{-1} ; (*) Figure IV.10] follow the main trend.

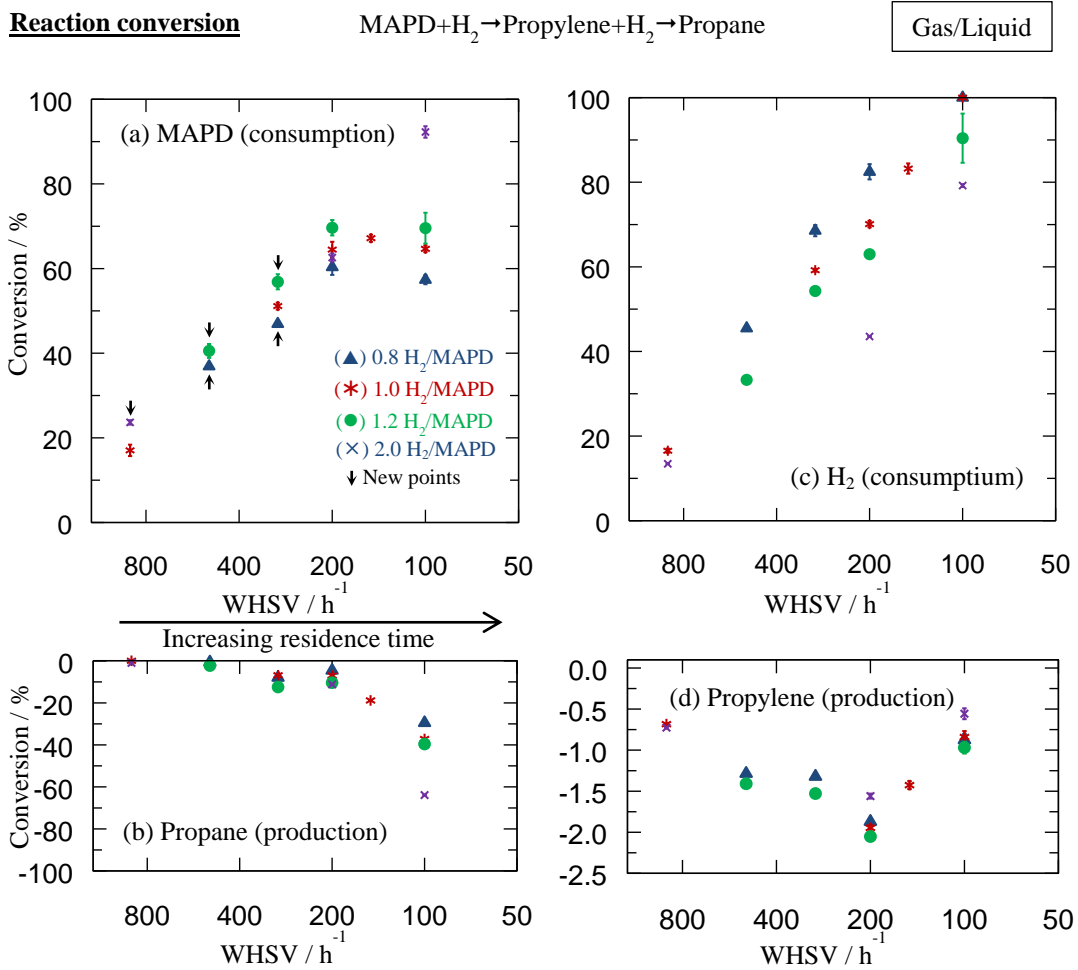


Figure IV.11: Selective hydrogenation at 303 K and 20 bar for a wide range of WHSV and H₂/MAPD ratio. Conversions of MAPD (a), Propane (b), Hydrogen (c) and Propylene (d).

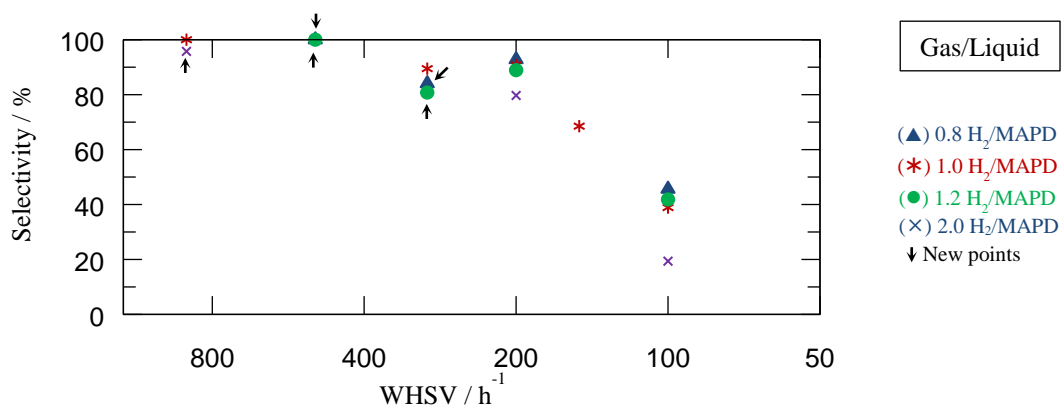


Figure IV.12: Reaction selectivity to MAPD at 303 K and 20 bar for a wide range of WHSV and H₂/MAPD ratio (information figure).

The gas-liquid mass transfer coefficients (Figure IV.13a) decreases from 900 to 50 h⁻¹. This is related to the decrease of gas and liquid velocities. Figure IV.13b has the ψ_{GL} zones defined. For 0.8 to 1.2 H₂/MAPD ratio, there is sufficient time to perform full gas-liquid mass transfer below 350 h⁻¹. At 2.0 H₂/MAPD ratio, the WHSV required is lower, below 150 h⁻¹. This is due to higher $k_L a_{GL}$ values.

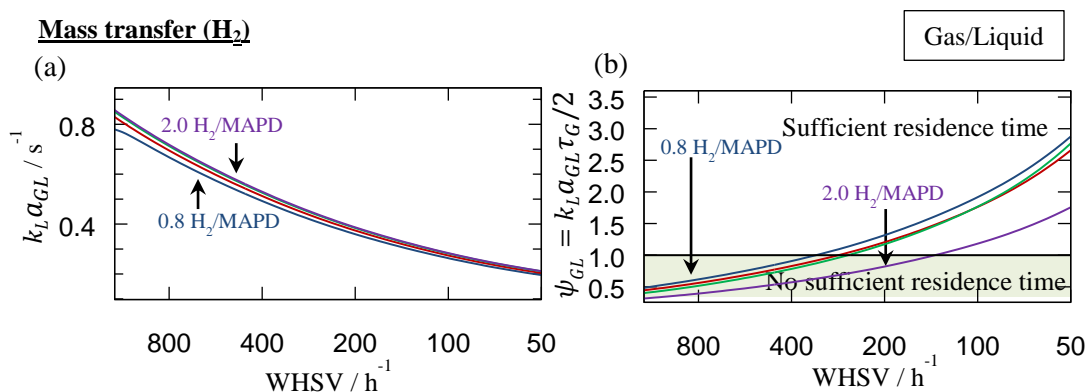


Figure IV.13: Selective hydrogenation at 303 K and 20 bar for a wide range of WHSV and H₂/MAPD ratio. (a) Hydrogen gas-liquid mass transfer coefficients and (b) ψ_{GL} for hydrogen mass transfer.

Results discussion

The additional experimental points [900 h⁻¹; 500 h⁻¹; 300 h⁻¹ (†) Figure IV.11] follow the main trend for the different species. Based on these results, the conversions plot can still be divided into two distinct zones: 900 to 200 h⁻¹ and 200 to 100 h⁻¹. The first zone is limited by gas-liquid mass transfer ($\psi_{GL} < 1$) and/or residence time. The other zone has enough time to have full gas-liquid mass transfer and reaction, but the selectivity might change with the molar concentration flow ($k_L a_{GL} \Delta C_{H_2}$) and there is a possible competition for the catalyst sites.

The previous justifications will be later investigated in unconventional conditions. Nevertheless, there is a strong assumption that in the first zone (900 to 200 h⁻¹) there are gas-liquid mass transfer problems. Although there are uncertainties concerning ψ_{GL} , the two zones estimated can be coupled with the experimental results.

Thanks to the experimental results, the zone where the reaction is limited by mass transfer ($\psi_{GL} < 1$) is now defined (Figure IV.14). The line $\psi_{GL} = 1$ was estimated using Hipolito et al. (2010) gas-liquid mass transfer correlation. This line has a deviation of ~10% for $k_L a_{GL} \tau_G$ in relation to the experimental results obtained (Figure IV.14). This means that either Hipolito et al. (2010) correlation or τ_G are overestimated. This uncertainty might be related with the correlation, since it was constructed with ~10% average relative deviation. In addition, it was proposed for a different reactor geometry (square reactor). Therefore, it seems a better option to use a modified $k_L a_{GL}$ correlation (Eq. IV.6) to characterize the reactor. The modification was achieved by adding a correction parameter (0.9 factor; see Eq. IV.6).

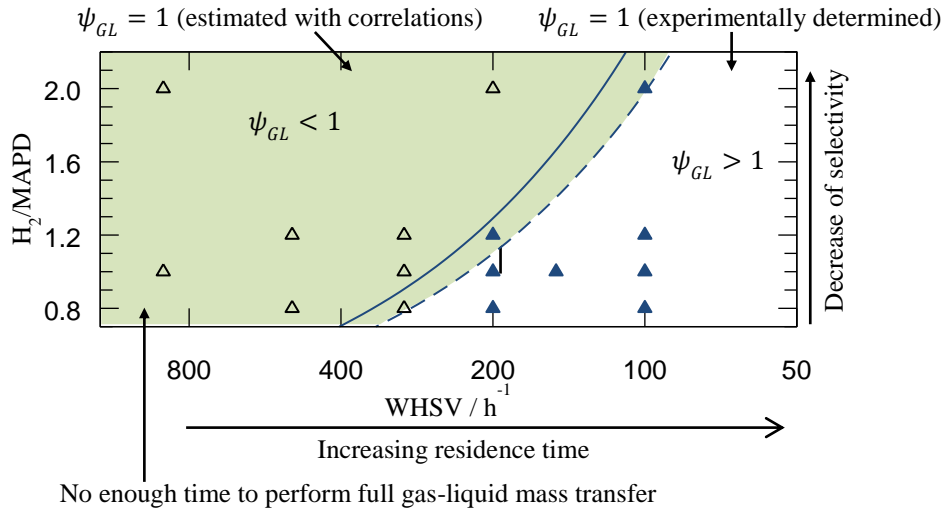


Figure IV.14: Zone with $k_L a_{GL}$ (hydrogen) limitations for the selected reactor ($\psi_{GL} < 1$): H_2 /MAPD ratio versus WHSV (303 K and 20 bar). (▲) Experimental points with $\psi_{GL} > 1$; (△) experimental points with $\psi_{GL} < 1$.

Correction of the Hipolito et al. (2010) correlation (to obtain the experimentally defined zone):

For gas-liquid mass transfer (based on pulse regime):

$$Sh = \frac{k_L a_{GL} d_{cat.}^2}{D_{i,L}} = \underbrace{0.9}_{\text{Correction}} \times 21 \left(\frac{d_{cat.} \bar{u}_L \rho_L}{\mu_L} \right)^{1/3} \left(\frac{d_{cat.} \bar{u}_G \rho_G}{\mu_G} \right)^{3/25} \frac{Sc_L^{1/3}}{45.6^{1/3}} \quad \text{Eq. IV.6}$$

Term added

where $Sc_L = \mu_L / (\rho_L D_{i,L})$ and \bar{u}_G (m.s⁻¹) is the superficial velocity of the gas.

This correlation will be used for now on.

Summary

1. The additional points follow the main trend;
2. Based on experimental results, the estimated ψ_{GL} zones were corrected;
3. Increasing H_2 /MAPD leads to lower selectivity;
4. From 900 to 200 h⁻¹: limited by gas-liquid mass transfer ($\psi_{GL} < 1$) and/or residence time;
5. From 200 to 100 h⁻¹: there is enough time to have full gas-liquid mass transfer ($\psi_{GL} > 1$) and reaction. The selectivity might change with the molar concentration flow ($k_L a_{GL} \Delta C_{H_2}$) and there is a possible competition for the catalyst sites.

IV.3.4 Conclusions (conventional conditions)

Pilot reactor

Thanks to the experimental results, two zones can be defined:

From 900 to 200 h^{-1} (WHSV), there is not enough time to have full G/L mass transfer and/or reaction.

From 200 to 100 h^{-1} (WHSV), there is enough time to have full G/L mass transfer and reaction. It seems that the reaction selectivity is controlled by the H_2 molar conc. flow and/or a competition for the active sites.

H_2 : The selectivity seems degraded by the increase of H_2/MAPD ratio and reaction/residence time. Comparing 100 and 200 h^{-1} (Figure IV.15b), the reaction has higher selectivity (>80%) at 200 h^{-1} than at 100 h^{-1} (>39%). This is related to the higher H_2 molar conc. flow and/or less residence time to produce secondary products (propane).

Figure IV.15 summarizes the results acquired in this subchapter (303 K; 20 bar), based on two zones for gas-liquid mass transfer.

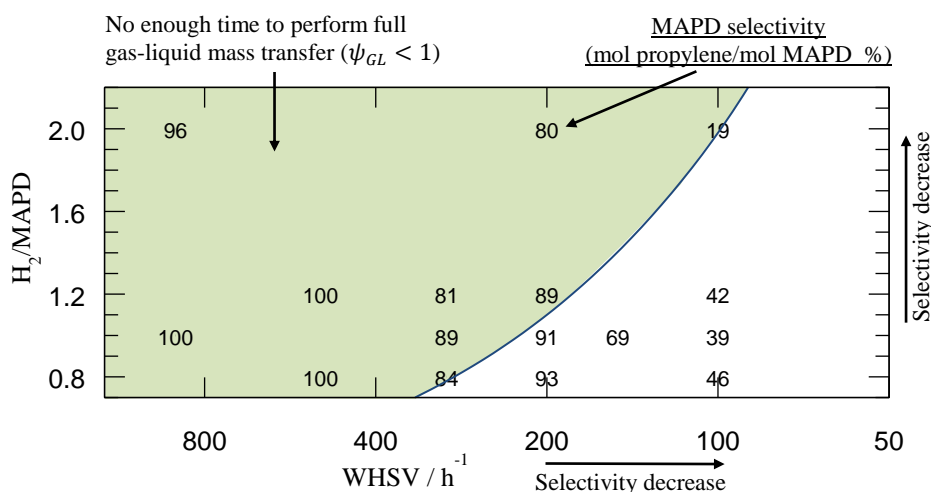


Figure IV.15: Zone with $k_L a_{GL}$ (hydrogen) limitations for the selected reactor ($\psi_{GL} < 1$) (303 K and 20 bar). In the graphic, the zone with MAPD selectivity is identified (values in the graphic for the selected reactor).

It can be noticed that when $\psi_{GL} < 1$, the selectivity has slight changes with the H_2/MAPD ratio. In the zone $\psi_{GL} > 1$, the selectivity decreases significantly from 200 to 100 h^{-1} WHSV and from 0.8 to 2.0 H_2/MAPD ratio. It is related to the lower molar conc. flow at lower WHSV (lower $k_L a_{GL}$).

Pilot reactor vs industrial reactor

Figure IV.16 compares the selected reactor (pilot scale; 0.6 g catalyst) with three hypothetical industrial reactors [at 35 h⁻¹ (WHSV)], showing H₂ molar conc. flow vs H₂/MAPD ratio. To recall, there are three hypothetical industrial reactors because the flow regime is unknown [different regimes; see §III.3.6].

The pulse flow regime (medium interaction) has the closer molar conc. flow conditions between the pilot scale at 200 h⁻¹ and industrial scale. The other industrial reactors have higher molar conc. flows (industrial > pilot scale). If the selectivity is influenced by the increase of the H₂ molar conc. flow, different results should be expected between pilot and industrial scale. Therefore, it is interesting to have pilot reactors with similar H₂ molar conc. flow.

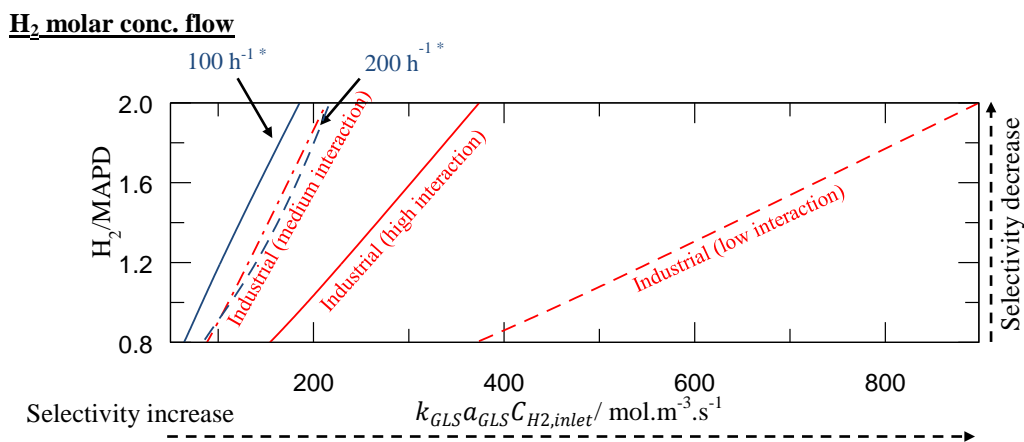


Figure IV.16: H₂ molar conc. flow in function of H₂/MAPD ratio and WHSV (h⁻¹) for the selected reactor (blue lines*) and the industrial reactor (red lines).

The blue lines were estimated using Eq. IV.6 and Hipolito et al. (2010) correlation for liquid-solid mass transfer. The red lines were estimated using Wild G et al. (1992) correlations (§III.3.6).

IV.4 High-pressure conditions

The previous experiments were done under conventional conditions (303K and 20 bar). For these conditions, it is difficult to estimate the reaction kinetics mainly due to gas-liquid transfer limitations or residence time limitations. Moreover, the hydrogen molar conc. flow (from gas to liquid) may have an impact on the selectivity for $\psi_{GL} > 1$. In order to understand the effect of mass transfer limitations, two different operating conditions will be used in order to suppress and/or reduce these limitations: high-pressure (no $k_L a_{GL}$) [this chapter] and supercritical (no $k_L a_{GL}$ and improved $k_{LS} a_{LS}$) [§IV.5].

Feedstock: MAPD (3.02 mol% [375 mol.m⁻³]) and Propane (3.29 mol% [408 mol.m⁻³]).

Studies performed: (i) WHSV, (ii) H₂/MAPD ratio, (iii) MAPD concentration and (iv) temperature.

Conditions: 303-353 K, 60-120 bar and catalyst mass of 0.6 g (catalyst W).

IV.4.1 High-pressure properties

Going to high-pressure leads to changes in the different properties, such as: density ($\text{kg}\cdot\text{m}^{-3}$), viscosity ($\text{Pa}\cdot\text{s}$), residence time (h), reaction rate ($\text{mol}\cdot\text{m}^{-3}\cdot\text{s}^{-1}$), diffusivity ($\text{m}^2\cdot\text{h}^{-1}$), mass transfer rate (s^{-1}) and adsorption equilibrium. The solubility (boundary condition of mass transfer) and the diffusivity will be detailed, because they are the most interesting properties when going from conventional to high-pressure conditions.

Solubility of H_2

Increasing pressure for the C_3+H_2 mixtures leads to higher solubility (§I.5.4). Figure IV.17 shows the influence of pressure and temperature on the solubility of H_2 in C_3 hydrocarbons, such as propane, propylene and C_3 cut.

Based on (experimental) literature points:

- at 60 bar and 310 K, it is only possible to solubilize 3.5 mol% of H_2 ($\sim 1.5 \text{ H}_2/\text{MAPD}$ ratio);
- at 120 bar and 310 K, it is possible to solubilize up to 7 mol% of H_2 ($\sim 3 \text{ H}_2/\text{MAPD}$ ratio).

For high H_2/MAPD ratio ($>3 \text{ H}_2/\text{MAPD}$), the temperature has to be decreased to have a single-phase mixture at the reactor inlet.

At 360K, it is expected to solubilize only 1 mol% of H_2 at 120 bar. Only in the supercritical medium it will be possible to have a single-phase mixture (the addition of a solvent will lead to a homogeneous medium).

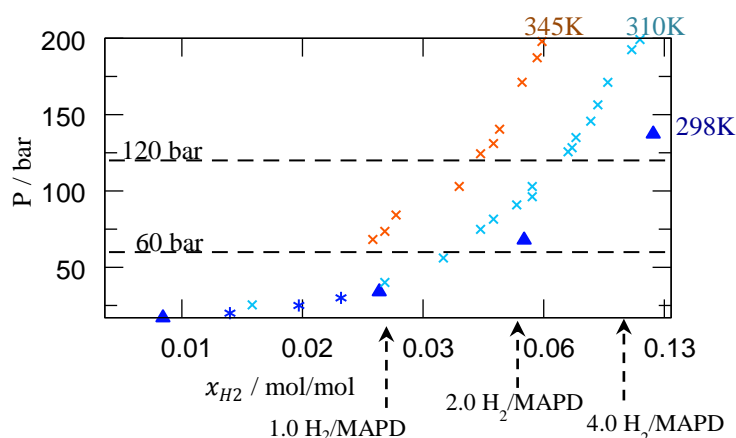


Figure IV.17: Pressure-composition diagram for the hydrogen composition (x_1) in the C_3 liquid phase (pure propane, pure propylene or C_3 cut mixture). **▲: Propylene+ H_2 (Williams and Katz, 1954a); *****: C_3 cut+ H_2 (Maniquet and Girardon, 2012); **×**: Propane+ H_2 (Bol'shakov and Linshits, 1953; Burriss et al., 1953a; J.-W. W. Qian et al., 2013; Trust and Kurata, 1971; Williams and Katz, 1954b).**

Diffusivity of MAPD

The diffusivity impacts the mass transfer coefficients ($k_L a_{GL}$ and $k_{LS} a_{LS}$) by changing Sh and Sc . Thus, it is interesting to determine the diffusion coefficients at high-pressure. The correlation selected was the Liu-Silva-Macedo (1997), and it can be applied for gases, liquids and supercritical fluids (Medina, 2012). For the selection of the correlation see Appendix §IV.5.

For high-pressure conditions, because of the single-phase medium, MAPD has lower liquid-solid mass transfer coefficients (lower diffusion than H_2); therefore its diffusion should be studied instead of H_2 . Figure IV.18 shows the variation of MAPD diffusion coefficients with pressure (20 to 150 bar) and temperature (303K and 353K). The diffusion decreases with the pressure (0.86 from 20 to 120 bar at 303K) and increases with temperature (1.67 from 303 to 353K at 120 bar). For H_2 , a similar behavior is expected.

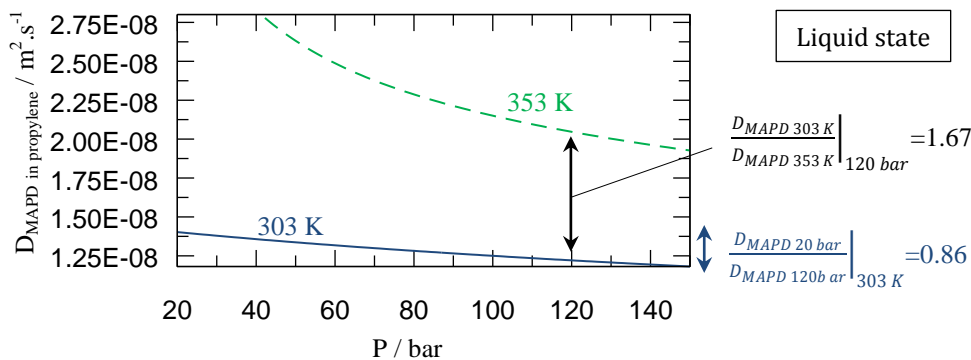


Figure IV.18: Predicted diffusion coefficients for MAPD infinitely diluted in propylene. Based on the Liu-Silva-Macedo (1997) correlation.

IV.4.2 Pressure and WHSV effect

To understand the impact of high-pressure conditions, in a first stage, the WHSV at 1 H_2 /MAPD ratio will be studied. The temperature of 303K was used to have single-phase medium (liquid) for 60 and 120 bar.

Objective 1: Investigate the differences in conversion between 20 (G/L), 60 (L) and 120 bar (L).

Objective 2: See if the changes in the physical properties from 60 to 120 bar are sufficient to have differences in catalytic performance.

Main properties changed: reaction time (h), density ($kg.m^{-3}$), viscosity (Pa.s), diffusivity ($m^2.s^{-1}$) and mass transfer ($k_{LS} a_{LS}$).

Observations

Figure IV.19 shows the influence of the WHSV and the pressure on the conversion of each species.

MAPD: The MAPD conversion slightly increases from 900 to 100 h⁻¹ for 60 and 120 bar (liquid) (Figure IV.19a), having a difference of 13% for both pressures. For high-pressure conditions (60 and 120 bar – liquid state) at ~900 h⁻¹, the conversion is 58%. In contrast, for 20 bar (gas-liquid) and 900 h⁻¹, the conversion is below 20%. From 200 to 100 h⁻¹, the MAPD conversion is similar for all the pressures (20, 60 and 120 bar). The H₂ conversion is around 100%.

Propane: The propane conversion slightly increases from 900 to 100 h⁻¹ for 60 and 120 bar (Figure IV.19b). Comparing high-pressure (60 and 120 bar) to conventional pressure (20 bar), the propane is less produced from 200 to 100 h⁻¹. For higher WHSV (900 to 200 h⁻¹), the propane is more produced at high-pressure conditions.

Hydrogen: For the WHSV range studied, the hydrogen conversion slightly increases from 900 to 100 h⁻¹ (Figure IV.19c), having similar values between 60 and 120 bar. The only exception is at 100 h⁻¹, where the point at 60 bar has less ~30% hydrogen conversion than at 120 bar. For high-pressure conditions (liquid), the H₂ conversion is ~73% at high WHSV (~900 h⁻¹). For 20 bar (gas-liquid), the H₂ conversion is ~19% at ~900 h⁻¹.

The H₂ is more consumed in high-pressure experiments than at 20 bar.

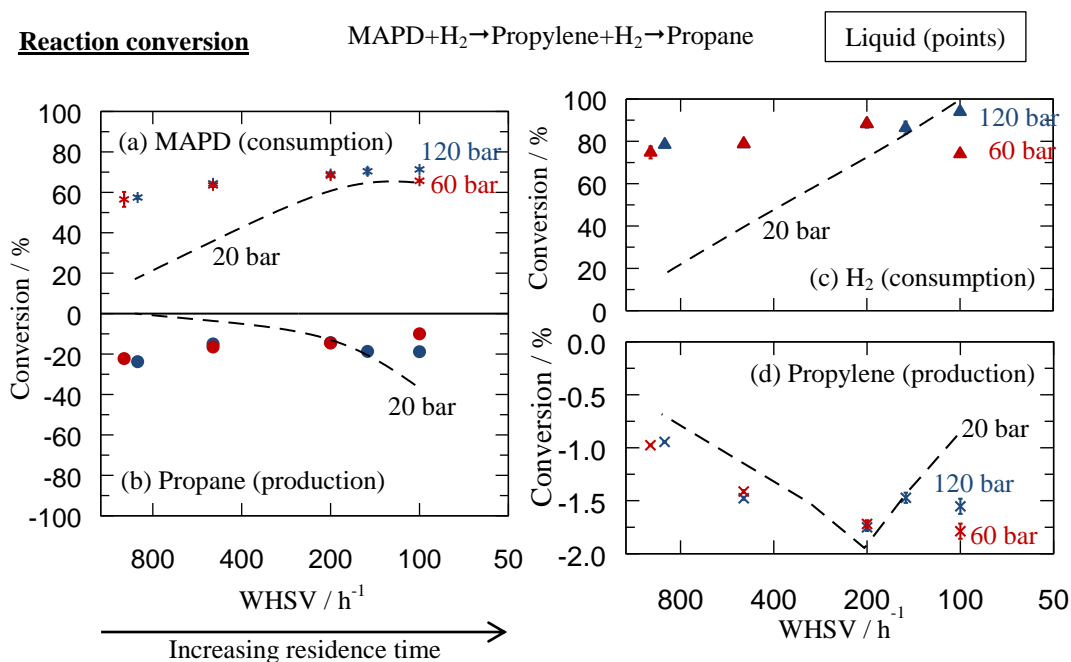


Figure IV.19: Selective hydrogenation at 1 H₂/MAPD ratio and 303 K. The plots are in function of pressure (20, 60 and 120 bar) and WHSV. (a) Conversions of MAPD (*), (b) Propane (□), (c) Hydrogen (▲) and (d) Propylene (×). The lines are fitted curves of the experimental results at 20 bar.

The liquid-solid mass transfer coefficients (Figure IV.20a) decreases from 900 to 100 h⁻¹ for 60 and 120 bar. This is related to the decrease of the liquid velocities. Figure IV.20b has the ψ_{LS} zones defined, being superior to 1.5 in all the WHSV range studied. Therefore, there is sufficient residence time to perform full liquid-solid mass transfer.

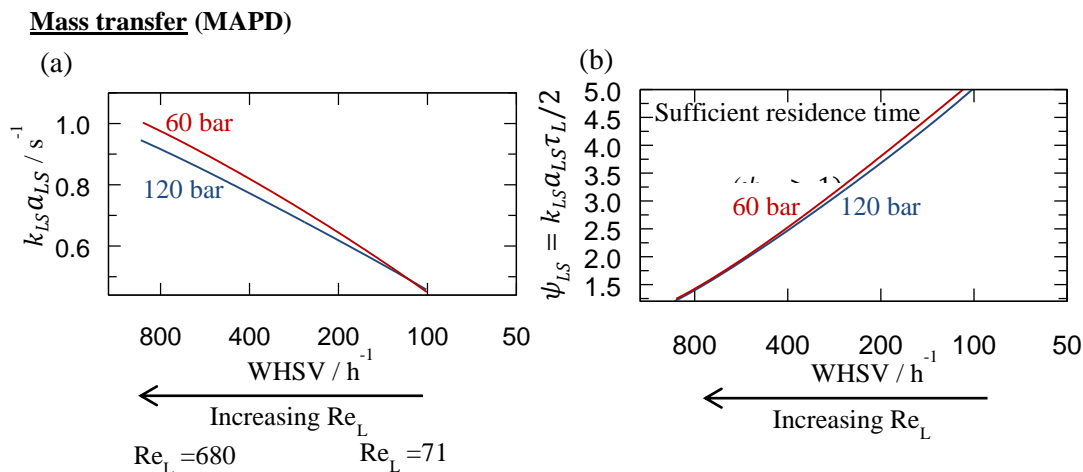


Figure IV.20: (a) MAPD mass transfer coefficients (liquid-solid) and (b) ψ_{LS} for 60 and 120 bar. The values were calculated based on the developed correlation (Eq. III.36) for $k_{LS}a_{LS}$ (MAPD).

Results discussion

Between 60 and 120 bar, there are almost no differences in conversion for the studied WHSV range. The impact of a pressure variation is practically negligible for a single-phase fluid mixture, but there is a significant difference compared to the conventional conditions (20 bar: gas-liquid). Visually, there are no problems with the residence time (one of the possible explanations proposed). Therefore, the proposition based on ψ_{GL} seems to explain conventional conditions (WHSV: 900 to 200 h^{-1}).

For high-pressure conditions, it is now possible to understand the influence of gas-liquid mass transfer on the MAPD hydrogenation (2.8 mol% MAPD). From the previous studies at 20 bar (lines Figure IV.19a), two zones were defined: 900 to 200 h^{-1} and 200 to 100 h^{-1} .

1. From 900 to 200 h^{-1} (20 bar), there is not enough time to perform a full gas-liquid mass transfer ($\psi_{GL} < 1$). Therefore, the reaction kinetics was hidden behind the mass transfer.

From 900 to 200 h^{-1} (120 bar), there is only a slight impact on the MAPD conversion (13 %). This means that the reaction time has a low impact on the conversions (MAPD, propane and propylene), which is related to high catalyst activity. Also, there is time to have full liquid-solid mass transfer, since $\psi_{LS} > 1$ (Figure IV.19b).

2. From 200 to 100 h^{-1} (20 bar), the $\psi_{GL} > 1$ (§IV.3.4). Despite these values, it was suggested that the overall molar concentration flow rate (controlled by $k_L a_{GL} \Delta C_{H_2}$) and the competition between species might have an impact on the reaction kinetics.

From 200 to 100 h^{-1} (120 bar), the species conversions are practically equal (liquid only). This shows that the H_2 molar concentration flow rate at 20 bar has an impact on the reaction selectivity. At 120 bar (100 h^{-1}), the reaction is more selective than at 20 bar (100 h^{-1}) (later quantified).

There is more propane produced at high WHSV (900 h^{-1}) than at low WHSV (100 h^{-1}) at 120 bar. This will be later explained with the help of a model (§V).

Summary

1. Similar performance obtained for 60 and 120 bar;
2. Difference between conventional (G/L) and high-pressure conditions (L):
 - a. At 120 bar from 200 to 100 h^{-1} , the reaction seems more selective than at 20 bar;
 - b. At 120 bar, the reaction seems more active than at 20 bar, which is related to higher H_2 molar conc. flow rate.
3. At 20 bar, the reaction selectivity and activity are controlled by the H_2 molar conc. flow rate. The residence time cannot explain low conversion from 900 to 200 h^{-1} . However, it can be explained by gas-liquid mass transfer (ψ_{GL}).

The next step is to understand the impact of H_2/MAPD concentration.

IV.4.3 H_2/MAPD ratio effect

Main properties changed: molar conc. flow ($k_{LS}a_{LS}\Delta C_{\text{H}_2}$), reaction rate and residence time.

Observations

Figure IV.21 shows the reactant conversions as a function of H_2/MAPD ratio (inlet). Two WHSV (lowest and highest) are studied.

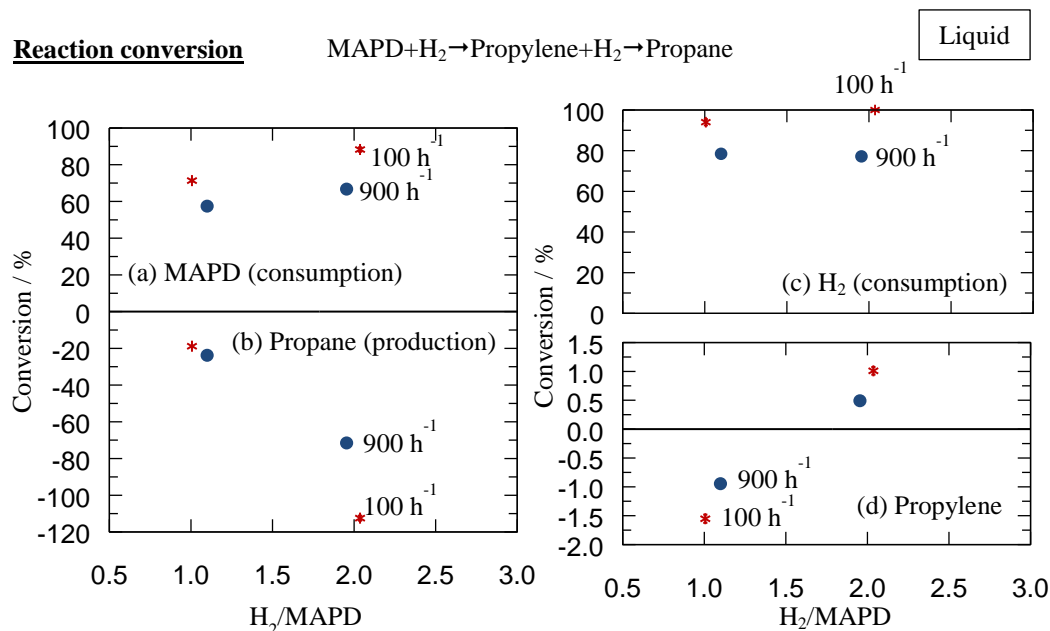


Figure IV.21: Selective hydrogenation at 120bar and 303 K. Curves plotted as a function of the H_2/MAPD ratio (1 and 2) and WHSV (100 and 900 h^{-1}). Conversions of MAPD (a), Propane (b), Hydrogen (c) and Propylene (d).

MAPD: From 1 to 2 H₂/MAPD (Figure IV.21a), the MAPD conversion increases by 20% and 10% for 100 and 900 h⁻¹, respectively. Comparing 100 with 900 h⁻¹, the conversion is logically higher for 100 h⁻¹, independently of the H₂/MAPD ratio studied.

Propane: Regarding Figure IV.21b, for a 1 H₂/MAPD ratio, the propane conversion is similar for both WHSV. About propylene conversion, there is higher production at 100 h⁻¹. Looking at the 2 H₂/MAPD ratio, the propane is more produced at 100 h⁻¹ than at 900 h⁻¹, having a difference of 40%. Due to this, the propylene has a higher consumption at 100 h⁻¹ (unwanted effect).

Hydrogen: For the H₂/MAPD range studied (Figure IV.21c), the hydrogen is entirely converted for 100 h⁻¹ (WHSV). However, for 900 h⁻¹, aH₂ is not fully converted, being around ~80% (stable). This explains the difference observed for propane.

The liquid-solid mass transfer coefficients (Figure IV.22a) are constant between the H₂/MAPD studied at each WHSV. Comparing the WHSV studied, 900 h⁻¹ has twice the liquid-solid mass transfer coefficients than 100 h⁻¹. Consequently, the H₂ molar conc. flow (Figure IV.22b) is also twice higher between 900 h⁻¹ and 100 h⁻¹. Figure IV.22c has the ψ_{LS} zones defined, being superior to 1 for all the H₂/MAPD ratio and WHSV range studied. Therefore, there is sufficient time to perform full liquid-solid mass transfer (no problems in liquid-solid mass transfer).

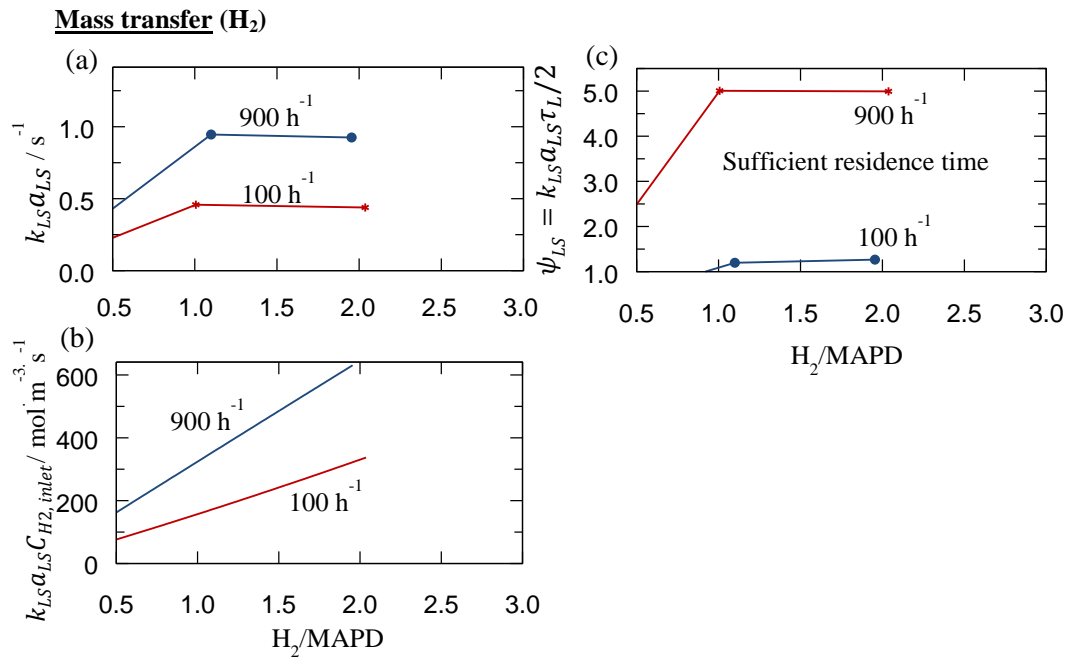


Figure IV.22: Selective hydrogenation at 120bar and 303 K. (a) H₂ mass transfer coefficients (liquid-solid), (b) H₂ molar conc. flow and (c) ψ_{LS} values. The values were calculated based on the developed correlation (Eq. III.36) for $k_{LS} a_{LS}$ (H₂).

Results discussion

According to the experimental results (Figure IV.21b), there should be enough time to perform full H₂ mass transfer between liquid and solid (catalyst) ($\psi_{LS} > 1$). Therefore, if H₂

is still not fully converted, the system might have lower reaction rate than expected (reaction time is lower than residence time). To understand this effect, the Damköhler number can be used.

$$Da = \text{residence time (s)}/\text{reaction time}_{\text{initial}} \text{ (s)} \quad \text{Eq. IV.7}$$

The original Da number tells us if a reaction is controlled by the residence time, based on the initial reaction time (maximum for a $A \rightarrow B$ reaction). Instead of the original Damköhler number, a modified Damköhler number ($Da^{mod.}$) was proposed to incorporate the total reaction time.

$$Da^{mod.} = \frac{\text{residence time (s)}}{\text{reaction time}_{i,\text{total}} \text{ (s)}} = \frac{[\text{pseudo}] \text{ reaction rate}_{i,\text{total}} \text{ (s}^{-1}\text{)}}{\text{space velocity (s}^{-1}\text{)}} = \frac{\int R_i d(1/C_i)}{\tau_L^{-1}} \quad \text{Eq. IV.8}$$

where R_i is the concentration reaction rate ($\text{mol.m}^{-3}.\text{s}^{-1}$) for the i species, C_i (mol.m^{-3}) is the molar concentration for the species i and τ_L (s) is the residence time (it also can be τ_{SC}). A pseudo reaction rate is used (in s^{-1}), since it is not possible to access the reaction rate without modeling the pilot plant.

Similar to the ψ_{LS} dimensionless number, the $Da^{mod.}$ number has similar interpretation. On one hand, if $Da^{mod.} < 1$, the reaction does not have sufficient residence time to fully perform (space velocity is higher than total reaction rate). On the other hand, if $Da^{mod.} > 1$, the reaction rate is faster than the residence time available (total reaction rate is higher than space velocity). This number will be used to enhance result interpretation.

When increasing H_2/MAPD , it is possible to have a higher H_2 molar concentration flow rate between the liquid and the catalyst (Figure IV.22b). Also, when increasing the WHSV from 100 h^{-1} to 900 h^{-1} , the H_2 molar concentration flow rate doubles (also the $k_{LS}a_{LS}$). Despite this duplication, there is a lower conversion at 900 h^{-1} for all the H_2/MAPD range studied. This happens not only for one species, but for all the species. Consequently, we might say that $Da^{mod.} < 1$ for 900 h^{-1} . In other words, the reaction has not sufficient residence time (high space velocity) to fully perform, although the catalyst has access to the reactants ($\psi_{LS} > 1$). To know whether $Da^{mod.} < 1$ or $Da^{mod.} > 1$ for 100 h^{-1} , more WHSV experiments with H_2/MAPD variation are required. For this reason, intermediate WHSV values were evaluated (Figure IV.23).

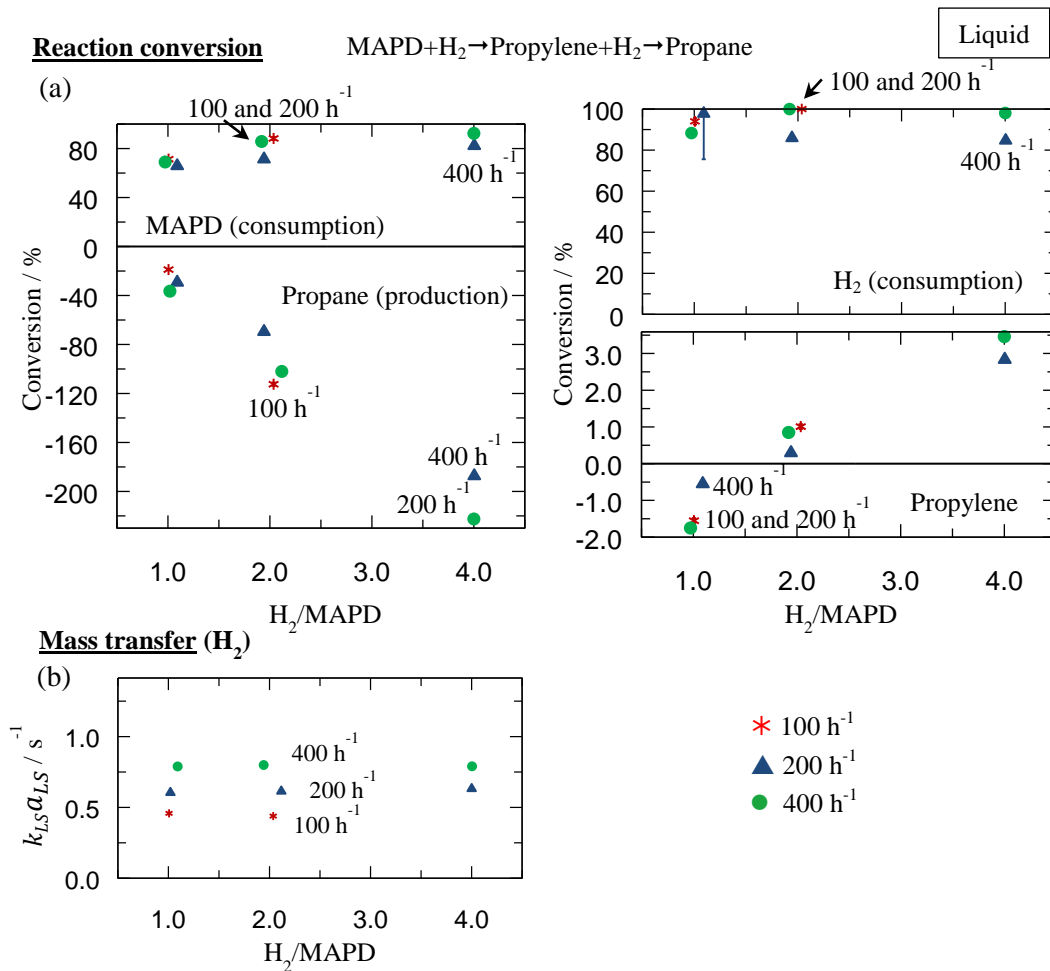


Figure IV.23: Selective hydrogenation at 120bar and 303 K. The plots are related to the H₂/MAPD ratio and WHSV (100, 200 and 400 h⁻¹). (a) Conversions of MAPD, Propane, Hydrogen and Propylene. (b) H₂ mass transfer coefficients (liquid-solid).

Regarding Figure IV.23a, 100 and 200 h⁻¹ have similar conversions for all the reactants in the H₂/MAPD ratio studied range, despite the different hydrogen mass transfer rates (Figure IV.23b). Consequently, we might say that the reaction depends on the reaction rate ($Da^{mod.} > 1$) for 100 and 200 h⁻¹, rather than being controlled by the mass transfer limitations.

Comparing 400 h⁻¹ to 200 and 100 h⁻¹, the points at 400 h⁻¹ have the highest liquid-solid mass transfer rates (Figure IV.23b), but the conversions are lower. This indicates that the reaction rate has not sufficient residence time (reaction rate_{total} < space velocity), therefore $Da^{mod.} < 1$.

With the previous information, it is interesting to create a map for the $Da^{mod.}$ number (Figure IV.24).

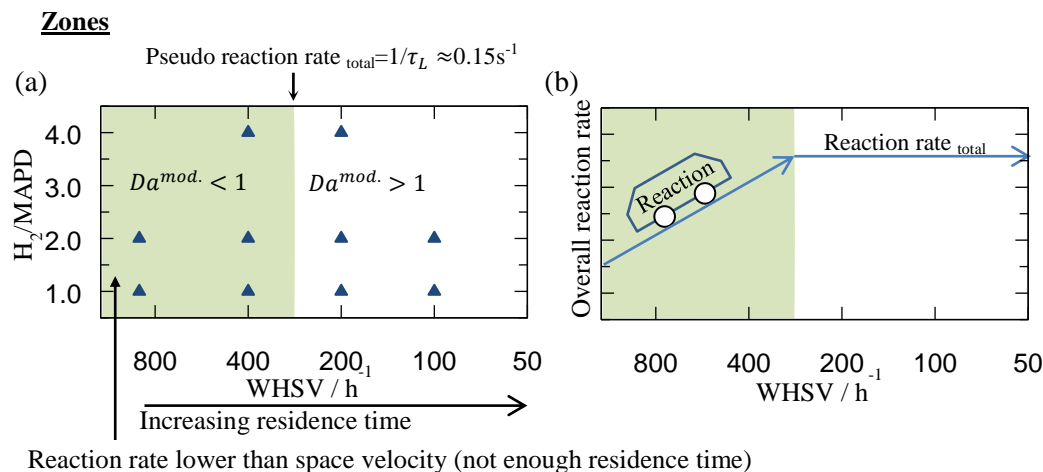


Figure IV.24: (a) Zone for $Da^{mod.} < 1$ (303 K and 120 bar). For all the points evaluated, there is enough time to have full liquid-solid mass transfer ($\psi_{LS} > 1$). (b) Schematic of the overall reaction rate. (▲) Points experimentally evaluated.

When $Da^{mod.} = 1$, it is possible to have a first estimate (order of magnitude) of the MAPD reaction rate $_{\text{total}}$. The value obtained can be later used to help explaining the results. With Figure IV.24a, our goal is not to give an exact value of the reaction rate, but rather to know where the reaction starts losing speed (Figure IV.24b).

Summary

1. As expected, increasing the H_2/MAPD ratio changes the reaction rate;
2. From 400 to 900 h^{-1} , there is the impact of the residence time ($Da^{mod.} < 1$);
3. From 200 to 100 h^{-1} , there is practically no impact of the residence time ($Da^{mod.} > 1$). This is normal since the H_2 is fully converted.

IV.4.4 MAPD concentration effect

Changing MAPD concentration helps clarifying the hypothesis of competition between species for the catalyst active sites. The MAPD concentration was diluted by two means:

1. From 2.8 to 1.6 mol% MAPD, the propylene was used as solvent (conventional procedure);
2. From 2.8 to 0.9 mol% MAPD, the heptane was used as a solvent to avoid changing the equilibria.

Main properties changed: concentration ($\text{mol} \cdot \text{m}^{-3}$) and reaction rate ($\text{mol} \cdot \text{m}^{-3} \cdot \text{s}^{-1}$).

Observations

Figure IV.25 shows the reactant conversions as a function of the MAPD concentration (inlet) at 900 h^{-1} and 1 H_2/MAPD ratio. This WHSV was chosen because the reaction is controlled by the space velocity, *i.e.*, the effects spotted on conversion are linked to the reaction kinetics.

MAPD: The MAPD increases almost linearly from 0.9 to 2.8 mol% of MAPD (inlet), having a conversion variation of 20% (Figure IV.25). From these results, the reaction order for

MAPD concentration might be close to zero. The MAPD conversion decreases since the H₂ concentration also decreases (to maintain 1.0 H₂/MAPD ratio).

Propane: From 0.9 to 2.8 mol% of MAPD (inlet) the propane production has a small increase (8%) (Figure IV.25). These results can be well explained by a power law (kinetic model) in relation to propane ($R_{PR} = k \cdot C_{H_2} C_{PR} \approx k' \cdot C_{H_2}$. If the H₂ concentration increases (more % mol of MAPD → more % mol of MAPD to keep a 1 H₂/MAPD ratio), the propane conversion will also increase.

Hydrogen: The hydrogen is not entirely converted (Figure IV.25), having conversions from ~43 to 80% for 0.9 to 2.8% mol of MAPD (inlet).

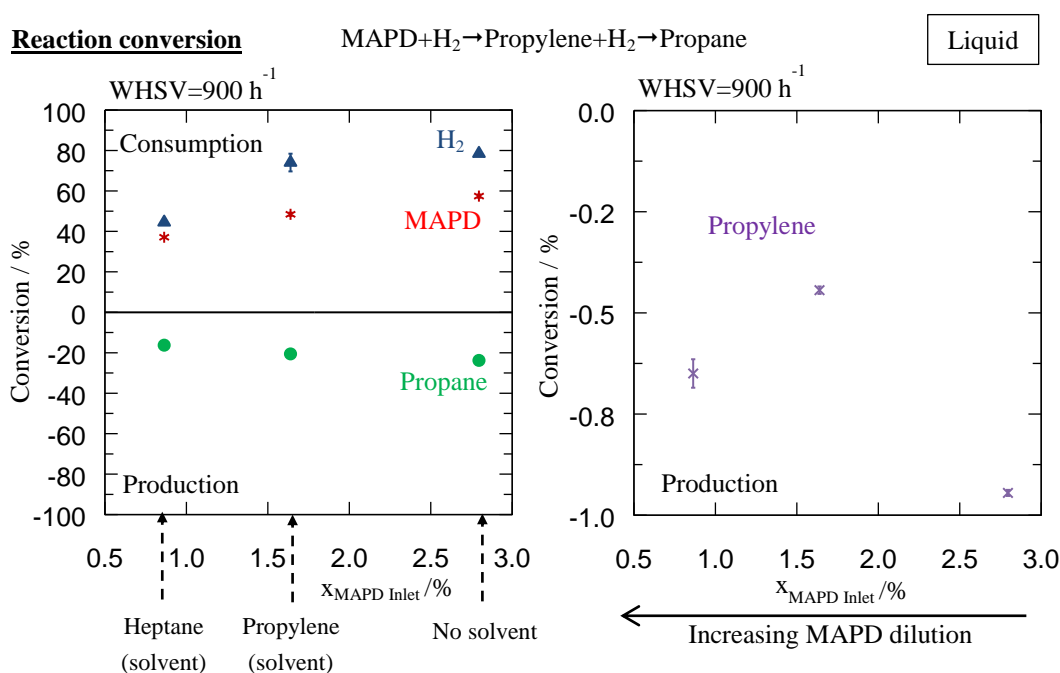


Figure IV.25: Selective hydrogenation at 1 H₂/MAPD ratio, 303K and 120 bar. Conversion of MAPD (*), Propane (●), Hydrogen (▲) and Propylene (×) in function of the MAPD molar percentage.

Mass transfer: The liquid-solid mass transfer coefficients (Figure IV.26a) are constant for the points with propylene and no solvent (2.8 mol% MAPD). For the point with heptane (solvent), due to different physical properties (Re_L), the mass transfer coefficient is lower. This seems not to affect the MAPD molar concentration flow (Figure IV.26b) trend, which is increasing linearly from 0.9 to 2.8 mol% MAPD (inlet). At WHSV=900 h⁻¹ (Figure IV.26c), all the points seems to have enough time to perform full MAPD liquid-solid mass transfer ($\psi_{LS} > 1$).

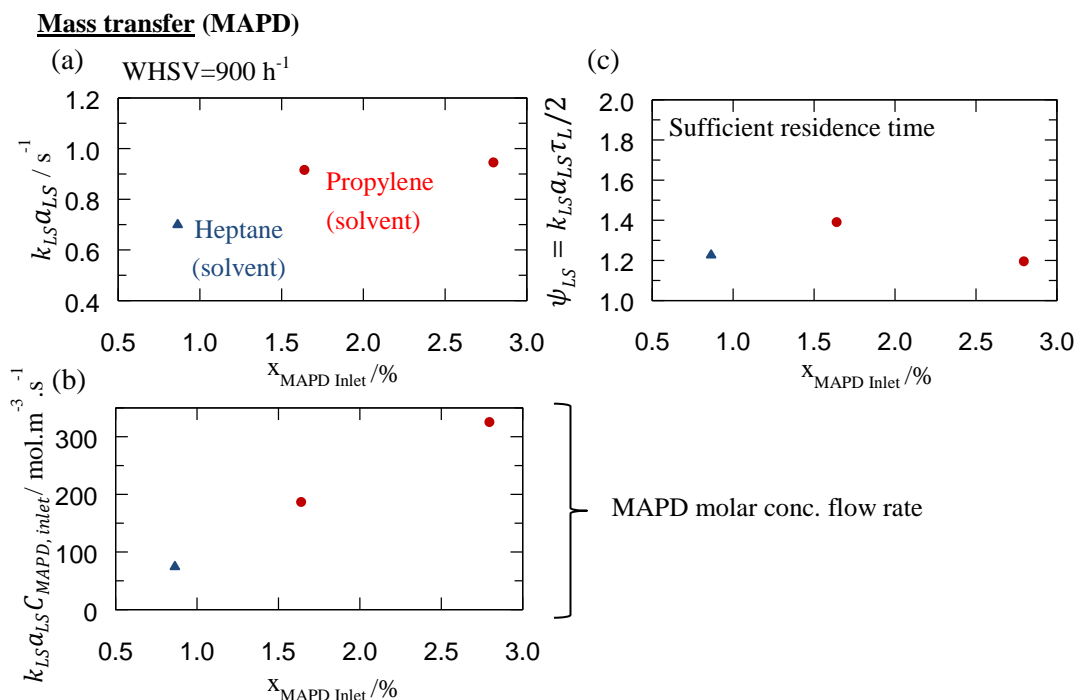


Figure IV.26: Selective hydrogenation at a 1 H₂/MAPD ratio, 303K and 120 bar. The (a) MAPD mass transfer coefficient (liquid-solid), (b) MAPD molar conc. flow rate and (c) ψ_{LS} are presented as a function of MAPD molar percentage. ψ_{LS} were calculated based on the developed correlation (Eq. III.36) for $k_{LS}a_{LS}$ (MAPD). The heptane was used as a solvent at low MAPD concentration.

Results discussion

Regarding Figure IV.25b, between 0.9 and 2.8 mol% of MAPD (inlet), the C₃ cut feedstock is 3 times diluted, and the conversion varies only by 20% and 8% for MAPD and propylene, respectively. The results trend might be explained by a power law (kinetic model: $R_{PR} = k \cdot C_{H_2} C_{PR} \approx k' \cdot C_{H_2}$) [PR is propylene]. This might suggest that the propylene is not competing with MAPD on the same catalytic sites. This explanation will be later checked in chapter V (modeling).

To endorse this explanation, the propane production was checked for a different H₂/MAPD ratio (§IV.3).

Summary

As conclusion, it is suggested that there might be no competition between MAPD and propylene for the active sites.

IV.4.5 Temperature effect

It is interesting to understand the impact of temperature on high-pressure conditions. The reaction was performed for 303 (conventional temperature) and 353 K (temperature to achieve supercritical conditions with all the solvents [§IV.2.1]). At 353 K and 120 bar, the fluid has a single-phase behavior [high MAPD conversion at high WHSV, which is not possible for gas-liquid mixtures; presented in the Sousa (2015) internal report].

Main properties changed: Density ($\text{kg}\cdot\text{m}^{-3}$), viscosity ($\text{Pa}\cdot\text{s}$), diffusivity ($\text{m}^2\cdot\text{s}^{-1}$), mass transfer ($k_{LS}a_{LS}$) and reaction kinetics.

Property variation

When increasing the temperature, the physical properties changed are: density, viscosity and diffusivity (this information will enrich the result discussion). Regarding Figure IV.27, from 303 to 353 K the density and viscosity decreases, 0.85 and 0.67 times, respectively. However, the MAPD diffusivity (infinite diluted) increases 1.67 times, which has an impact on mass transfer (higher) and reaction performance (higher).

C₃ cut properties (120 bar):

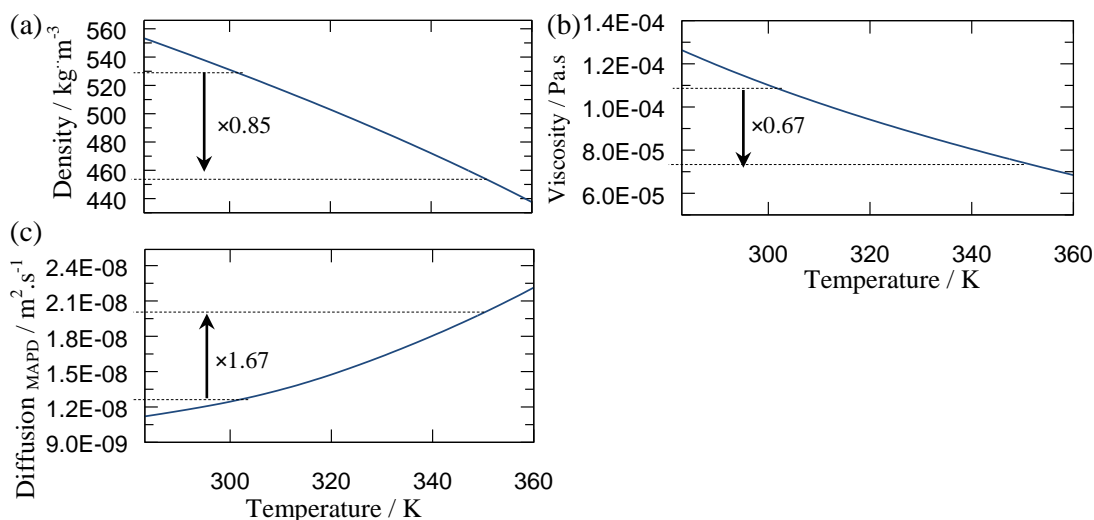


Figure IV.27: C₃ cut physical properties estimated as a function of temperature (at 120 bar). (a) density, (b) viscosity and (c) MAPD diffusion in C₃ cut (infinite dilution). The density and viscosity were obtained with PPR78 EOS, using PROII[®]. The diffusivities were calculated based on the Liu et al. (1997) correlation.

Observations

Figure IV.28 shows the reactant conversions as a function of the temperature at $\sim 900 \text{ h}^{-1}$ and different H₂/MAPD ratios.

As in the previous study, 900 h^{-1} (WHSV) was chosen because of the higher mass transfer (\Rightarrow higher Reynolds number). It was also chosen because it is a zone controlled by space velocity. Therefore, it is interesting to compare the performance obtained in high-pressure conditions with supercritical ones.

For other WHSV at 353K, the plots can be found in the Sousa (2015) internal report.

The industrial feedstock used for this study is more diluted (problematic when working with industrial feedstock): MAPD (1.62 mol% [$200 \text{ mol}\cdot\text{m}^{-3}$]) and propane (0.99 mol% [$275 \text{ mol}\cdot\text{m}^{-3}$]).

MAPD: The MAPD conversion increases from 12 to 16% from 303 to 353 K (Figure IV.28a), depending on the H₂/MAPD ratio.

Propane: From 303 to 353 K the propane conversion is similar to each H₂/MAPD ratio (1 and 2) (Figure IV.28b). The variation (mol) of the MAPD converted goes to propylene (and to oligomerization, which is not quantified). For the 4 H₂/MAPD, the propane is more produced at 353 K.

Hydrogen: The hydrogen is not entirely converted (Figure IV.28c), having conversions of ~75 and 90% for 303 and 353 K, respectively.

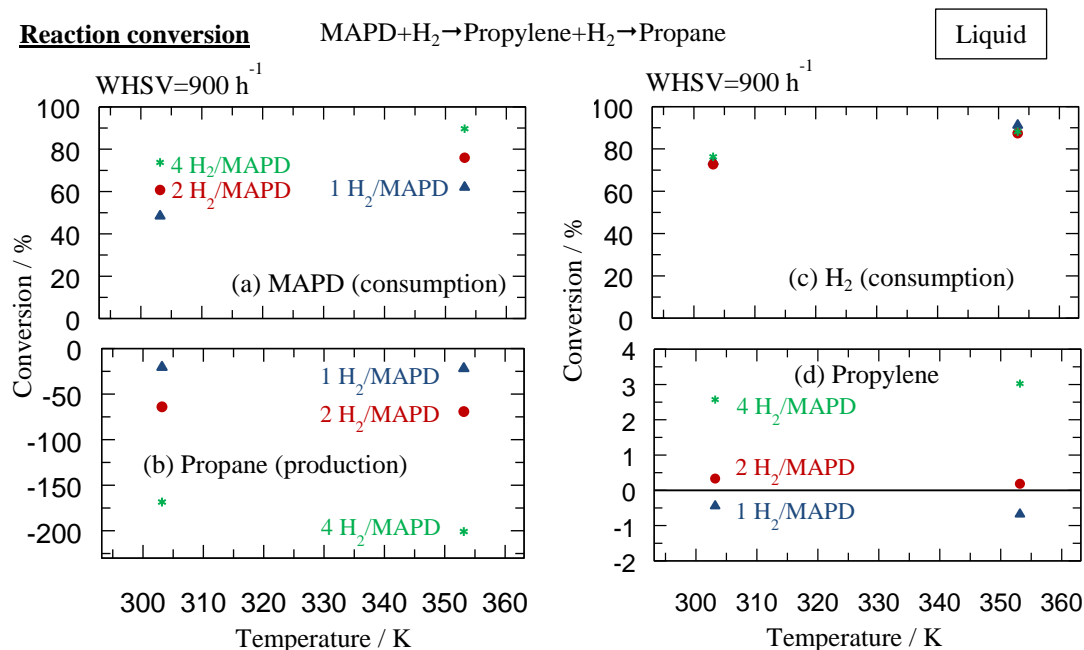


Figure IV.28: Selective hydrogenation at 120 bar for different H₂/MAPD ratios and temperatures. Conversion of MAPD (a), Propane (b), Hydrogen (c) and Propylene (d) as a function of the temperature.

The liquid-solid mass transfer coefficients (Figure IV.29) increase $\times 1.44$ when increasing the temperature from 303 to 353 K at 900 h⁻¹ (WHSV).

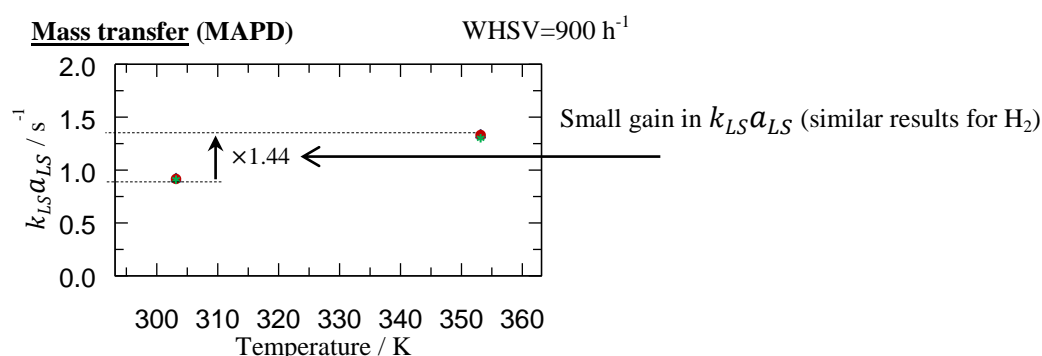


Figure IV.29: Selective hydrogenation at 120 bar for different H₂/MAPD ratios and temperatures. MAPD mass transfer coefficient (liquid-solid), based on the developed correlation (Eq. III.36) for $k_{LS}a_{LS}$ (MAPD).

Summary

As expected, when increasing the temperature the conversion also increases. This happens meaningfully for MAPD and H_2 . At high 900 h^{-1} (WHSV), it is possible to see the impact of the temperature. The results may be used to determine the activation energy.

IV.4.6 Conclusion (high-pressure conditions)

Analysis of pilot results

Figure IV.30 and Figure IV.31 summarizes the results acquired in this subchapter by comparing conventional (303 K; 20 bar) and high-pressure conditions (303 K; 60 and 120 bar).

Conventional conditions (20 bar): Regarding Figure IV.30, three different zones can be noticed: (i) $\psi_{GL} < 1$, (ii) $Da^{mod.} < 1$ and (iii) sufficient H_2 zone. (i) In $\psi_{GL} < 1$, there is not enough residence time to have full gas-liquid mass transfer and the amount of H_2 transferred limits the reaction. (ii) In $Da^{mod.} < 1$, residence time limits the reaction. (iii) Below 200 h^{-1} , the reaction selectivity is controlled by the amount of H_2 transferred to the catalyst (checked at high-pressure conditions). With the previous defined zones, it is now possible to identify and explain the different selectivity obtained (Figure IV.30).

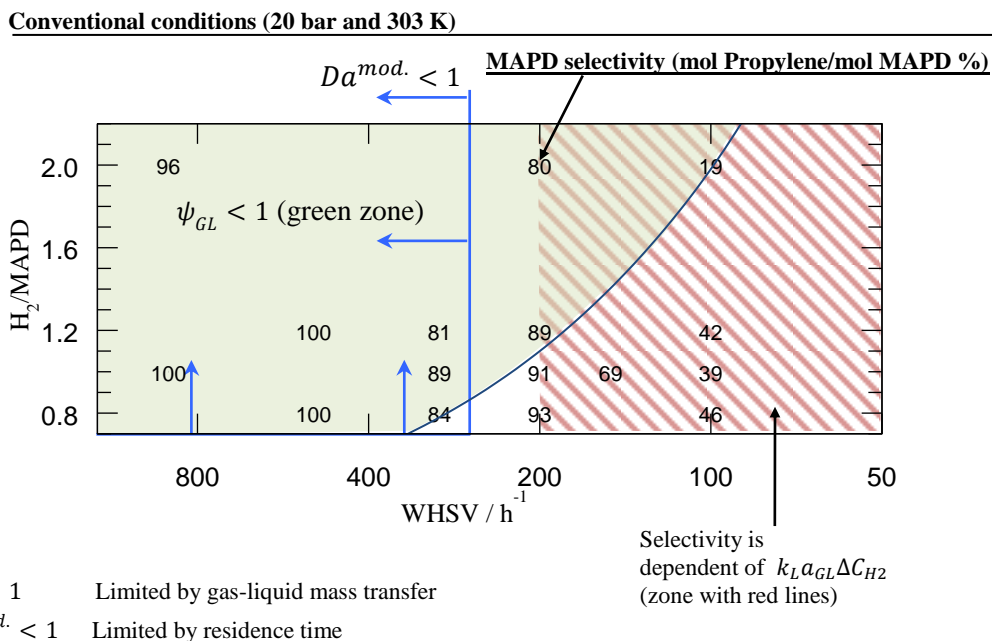


Figure IV.30: Reaction zones for the selected reactor at conventional conditions (303 K and 20 bar).

Unconventional conditions (120 bar): Regarding Figure IV.31, a zone was defined for $Da^{mod.} < 1$ (above 300 h^{-1}). In relation to conventional conditions, the selectivity is lower for 2 $H_2/MAPD$, since the H_2 is available for propane formation (Figure IV.31). Also there is a higher H_2 global mass transfer (less limitations).

For high-pressure conditions, it was shown that the liquid-solid external limitations do not exist. However, it is still possible to have internal mass transfer limitations. Since one of the goals is to develop a pilot plant to measure intrinsic kinetics, supercritical conditions should be used. They may reduce internal limitations.

Unconventional conditions (high-pressure: 120 bar and 303 K)

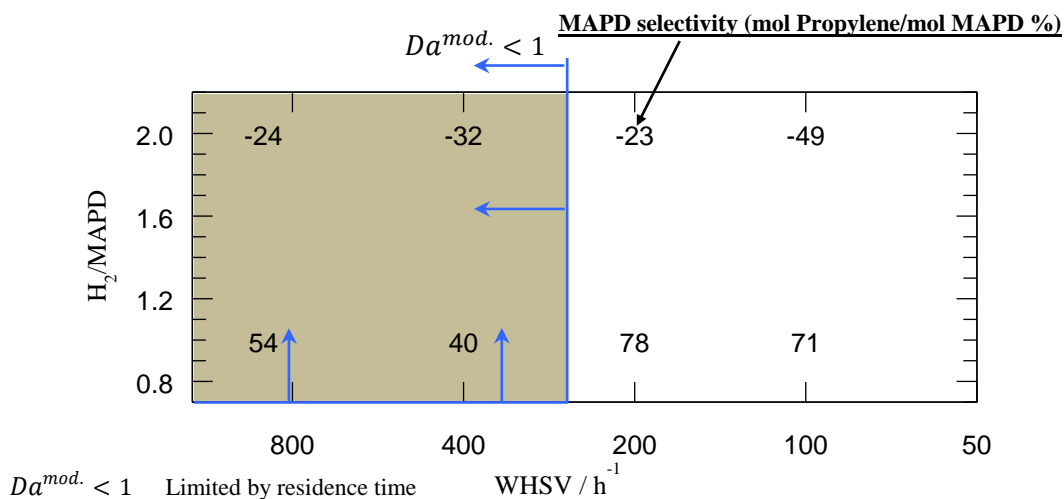


Figure IV.31: Reaction zones for the selected reactor at high-pressure conditions (303 K and 120 bar).

The thesis main goal is to determine the best conditions to compare catalysts. This can be achieved at high-pressure conditions (120 bar). The thesis second goal is to study intrinsic kinetics. This will be achieved using supercritical fluids.

Comparison with industrial reactors

Figure IV.32 compares the selected reactor (pilot scale; 0.6 g catalyst) with three hypothetical industrial reactors [different regimes at 35 h⁻¹ (WHSV); see §III.3.6]. The selected reactor at high-pressure conditions (120 bar) allows us to be closer to the bubble regime (higher interaction), which we think is the most present in the industry.

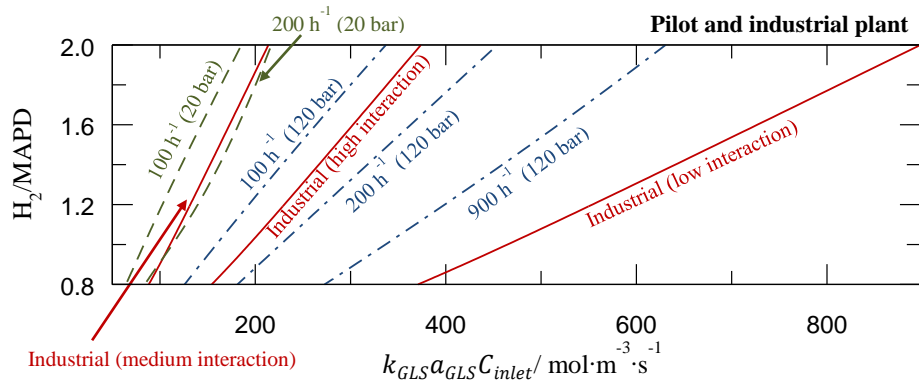


Figure IV.32: H_2 (for 20 bar) or MAPD (for 120 bar) molar conc. flow as a function of the H_2 /MAPD ratio and WHSV (h^{-1}). It was applied for the selected reactor (green and blue lines) and industrial reactors (red lines).

For the selected reactor, the molar conc. flow was estimated using Eq. IV.6 and the Hipolito et al. (2010) correlation for liquid-solid mass transfer. For the industrial reactor, the molar conc. flow was estimated using the Wild G et al. (1992) correlations (§III.3.6).

At the selected pilot reactor, there are no liquid-solid mass transfer limitations. There will be “even less” at the industrial level.

The selected reactor at 120 bar has higher molar conc. flow conditions ($WHSV > 200 h^{-1}$) than industrial reactors: pulse flow regime (medium interaction) and bubble regime (higher interaction).

IV.5 Supercritical conditions

The previous experiments were done at conventional and high-pressure (HP) conditions. Going to supercritical (SC) conditions should give additional information about the catalyst because higher mass transfer rates can be achieved (external and internal). This should give a different catalytic performance (conversion and selectivity). With this new information, it should be possible to understand better the reactive system (estimate the intrinsic kinetics by crossing data at HP and SC). Moreover, the internal mass transfer cannot be easily quantified by other means.

To better illustrate the consequences of changing the operating conditions in the reaction performance, the Thiele modulus was introduced.

The Thiele modulus is a dimensionless number dependent of the resistance inside the grain. The modulus (modified) was defined as:

$$\phi = \text{reaction rate}_{\text{total}} (s^{-1}) / \text{diffusion rate} (s^{-1}) \quad \text{Eq. IV.9}$$

$$\eta \propto f(\phi) \quad \text{Eq. IV.10}$$

$$R_{i,observed} = \eta R_{i,real} \quad \text{Eq. IV.11}$$

where η is the effectiveness number, which defines how far the observed reaction rate ($R_{i,observed}$) is from the real one ($R_{i,real}$). It is defined as a function of the Thiele modulus (ϕ). The diffusion rate is related to the effective diffusion coefficient inside the solid.

Shifting to supercritical conditions, it should be possible to suppress/reduce mass transfer resistances by taking advantage of the fluid properties, such as higher diffusivity ($D_{gas} > D_{supercritical} > D_{liquid}$) and higher Reynolds number, without losing the single-phase characteristics.

$$D_i \uparrow \uparrow Re \uparrow \uparrow \Rightarrow k_l a_{LS} \uparrow \uparrow \eta \uparrow \uparrow$$

Feedstock: MAPD (3.02 mol% [375 mol.m⁻³]) and Propane (3.29 mol% [408 mol.m⁻³]).

Studies performed: (i) Solvent, (ii) H₂/MAPD ratio and (iii) temperature.

Conditions: 303-353 K, 120 bar and catalyst mass of 0.6 g (catalyst W).

IV.5.1 Diffusion in supercritical fluids

The diffusion coefficients in supercritical fluids were obtained through the use of the Liu-Silva-Macedo (1997) correlation (3.6% AARD; §I.5.3). This option was selected since the experimental data for MAPD and H₂ are not available in the literature (see Magalhães et al., 2013; Zhu et al., 2002). The correlation was applied to the MAPD only, because it has the lowest diffusion.

Even knowing that the Liu-Silva-Macedo (1997) correlation has small deviation for hydrocarbon mixtures, its validity needs to be checked for the MAPD diffusion in different mixtures. For that reason, the strategy adopted was:

1. To compare correlations to a close experimental case (literature);
2. To compare correlations for the MAPD in the solvents considered (CH₄, ethane, CO₂ and propylene).

The results of this strategy are presented in Appendix §IV.5 [see also internal report from Sousa (2015)]. It was validated, and it will be used for the C₃ cut.

Note: This correlation is maybe not adapted for H₂ mixtures (only for hydrocarbons). So, the diffusivity ratio between hydrocarbons and H₂ was obtained from the Wilke and Chang (1955) correlation [normally used at conventional conditions (Samimi et al., 2015)].

Results: the Liu-Silva-Macedo (LSM) (1997) correlation

To illustrate the diffusion coefficients obtained with LSM (1997) correlation, Figure IV.33 was plotted for different temperatures (303 to 553 K) and pressures (20 to 150 bar). The figure shows the MAPD diffusion coefficients at infinite dilution in CH₄, ethane, CO₂ and propylene.

As expected, the diffusivity changes with the physical state ($D_{gas} > D_{supercritical} > D_{liquid}$). For the working pressure (Figure IV.33a) at 303 and 353 K, $D_{CH_4} (\sim 10^{-7} \text{ m}^2 \cdot \text{s}^{-1}) > D_{Ethane} \vee D_{CO_2} >$

$D_{Propylene}$ ($\sim 10^{-8} \text{ m}^2 \cdot \text{s}^{-1}$). The gains obtained for each solvent in relation to the propylene (high-pressure: 120 bar) are presented in Table IV.3.

A figure was added for other temperatures at the working pressure (Figure IV.33b). Regarding this figure, small increases in the MAPD diffusion with propylene (as a solvent) are noticed when changing the temperature. For other solvents, in all the temperature range studied the MAPD diffusion coefficients are higher than when using propylene as a solvent.

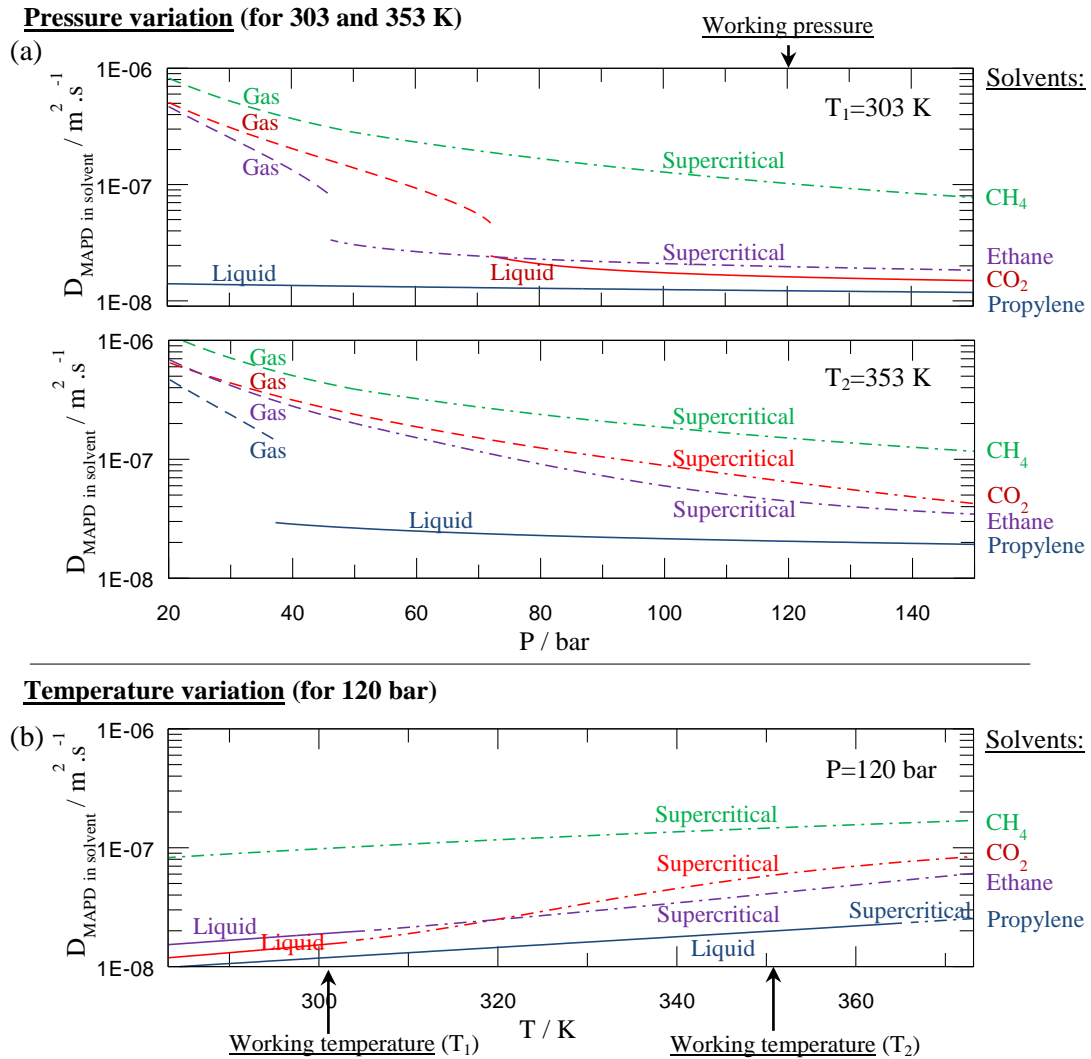


Figure IV.33: Estimated MAPD diffusion coefficients at infinite dilution in different solvents. (a) Pressure variation; (b) Temperature variation. The phase change is related to the pure solvent.

From Table IV.3, the CH_4 (solvent) has higher diffusivity in relation to the propylene solvent (>7) for 303 and 353 K. The other solvents, ethane and CO_2 , have higher diffusivity than propylene, going from 1.3 to 3.1.

Table IV.3: MAPD diffusion coefficients at infinite dilution at working pressure (120 bar) and temperature (303 and 353 K). The gain is related to propylene at the working conditions.

	$D_{in\ Propylene} / m^2 \cdot s^{-1}$	$D_{in\ CO2} / m^2 \cdot s^{-1}$	$D_{in\ Ethane} / m^2 \cdot s^{-1}$	$D_{in\ CH4} / m^2 \cdot s^{-1}$
$T=303\ K$	1.22×10^{-8} (relative gain=1.0)	1.60×10^{-8} (relative gain =1.3)	1.96×10^{-8} (relative gain =1.6)	1.01×10^{-7} (relative gain =8.3)
$T=353\ K$	2.04×10^{-8} (relative gain =1.0)	6.42×10^{-8} (relative gain =3.1)	4.31×10^{-8} (relative gain =2.1)	1.49×10^{-7} (relative gain =7.3)

In conclusion, CH₄ seems to have higher gain in diffusivity (>7) in relation to propylene (solvent present in the C₃ cut feedstock). This was an expected result, since CH₄ is a smaller molecule than propylene. Therefore, CH₄ will suffer fewer interactions with MAPD.

IV.5.2 Solvents

To perform supercritical MAPD hydrogenation with softer operating conditions (lower temperature and pressure), a solvent has to be added to the C₃ cut (§IV.2.1). Adding a solvent also enhances liquid-solid ($k_{LS}a_{LS}$) (even if it is not limited) and intragranular mass transfer, due to the increase of the mixture diffusivity, leading to an increase of the effectiveness factor (η).

In the present study, two solvents will be tested: CH₄ and ethane. The CO₂ will not be tested because CO may be produced, having unwanted effects on the catalytic sites (Burgener et al., 2005b).

Main properties changed: density (kg.m⁻³), viscosity (Pa.s), diffusivity (m².s⁻¹), mass transfer ($k_{LS}a_{LS}$), residence time (h) and adsorption equilibrium.

Conditions: 303 K, 120 bar and 0.6 g of catalyst W. The WHSV was calculated based on the C₃ cut mass flow rate ($WHSV = W_{C3\ cut}/m_{cat.}$), without including the solvent. In all the experiments, the WHSV was maintained at 200 h⁻¹ for C₃. Indeed, when increasing the molar % of solvent, the overall volumetric flow rates increase inside the reactor.

Observations

The following figures are as a function of the mole fraction of solvent (ethane and methane). The physical states of the fluid mixture are shown in the graphic above the points (L – liquid; L/V – liquid/vapor; SC – supercritical). Briefly the physical states are:

- Adding CH₄ (60 bar): L to L/V
- Adding CH₄ (120 bar): L to SC
- Adding ethane (60 and 120 bar): L

MAPD: Higher fractions of solvent have only a slight effect on the MAPD conversion (Figure IV.34). At 120 bar, the MAPD conversion increases of 5% (CH₄) and decreases of 15% (ethane) with the molar fraction of solvent. For 60 bar, the MAPD conversion decreases for CH₄ (~50%; due to liquid-vapor) and ethane (15%).

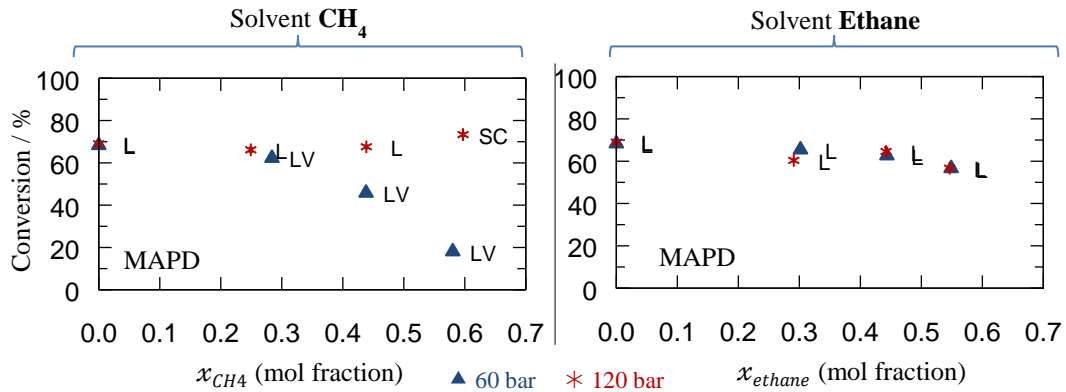


Figure IV.34: Selective hydrogenation at 303 K, 1 H₂/MAPD, 120 and 60 bar. Iso WHSV for the C₃ cut. Solvent effect on MAPD conversion as a function of the molar dilution (CH₄ and ethane).

From Figure IV.34, it appears that the supercritical conditions with CH₄ do not enhance the reaction rate significantly. Other properties need to be studied to understand this result.

Concentration definition

To compare biphasic and monophasic mixtures, the concentration of the reactive medium (at the reactor inlet) was defined. The reactive medium is a concept that varies between single and dual phase systems.

- In a single-phase system (L or V or SC), the reactive medium is the fluid mixture.
- In a dual-phase system (LV), the reactive medium is the liquid phase. Normally, the liquid phase forms a film around the catalyst (total wetting), preventing direct contact of the vapor phase with the catalyst surface.

The expression is:

$$C_{i\,reactive} = \frac{W_{i\,reactive}}{M_i Q_{reactive}} \quad \text{Eq. IV.12}$$

where $C_{i\,reactive}$ (mol.m⁻³) is the concentration, $W_{i\,reactive}$ (kg.h⁻¹) is the mass flow rate, M_i (kg.mol⁻¹) is the molecular weight and $Q_{reactive}$ (m³.h⁻¹) is the total volumetric flow rate.

The values of $W_{i\,reactive}$ and $Q_{reactive}$ were calculated using PPR78, because it gives accurate results for light hydrocarbons at high-pressures (§II.3).

MAPD concentration: When adding a solvent, the concentration in the liquid or the supercritical phase decreases for CH₄ and ethane (Figure IV.35). This is particularly noticed for the supercritical conditions, which have 3 times less concentration than the high-pressure conditions (without solvent). For LV, the concentration is constant.

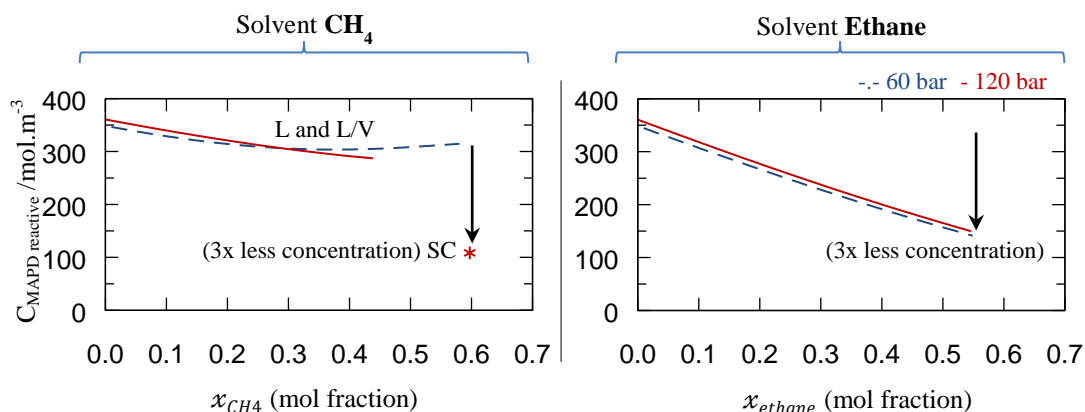


Figure IV.35: Selective hydrogenation at 303 K, 1 H₂/MAPD, 120 and 60 bar. Iso WHSV for the C₃ cut. MAPD reactive concentration (reactor inlet) as a function of the molar dilution (CH₄ and ethane).

Space velocity (inverse of the residence time): Regarding Figure IV.36, it is possible to notice that the space velocity changes when adding solvent (60% solvent has > 3 times less residence time). The most interesting observation is the SC point (for methane solvent). It has 3 times less residence time (300 h⁻¹ against 900 h⁻¹).

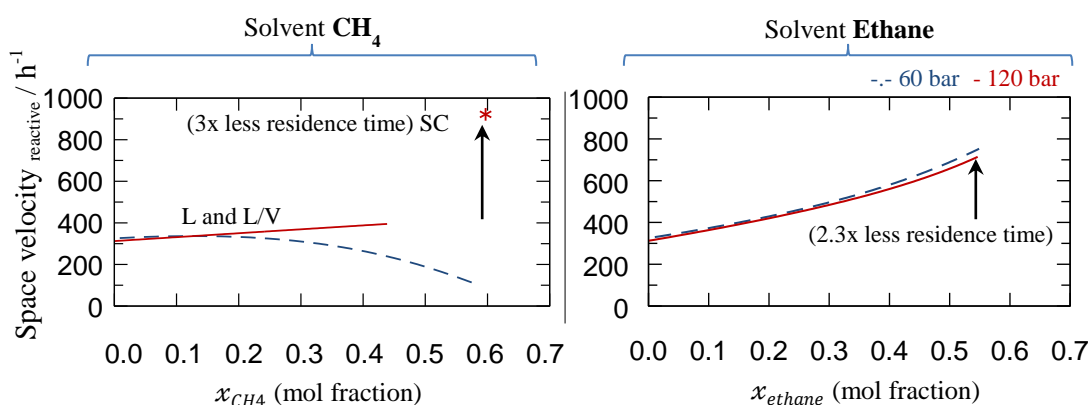


Figure IV.36: Selective hydrogenation at 303 K, 1 H₂/MAPD, 120 and 60 bar. Iso WHSV for the C₃ cut. Space velocity_{reactive} (inverse of the residence time) as a function of the molar dilution (CH₄ and ethane).

Summary

From Figure IV.34, it appears that supercritical fluids do not enhance the reaction rate significantly. However, when analyzing the conversion as a function of the solvent fraction, different important properties are changed, such as space velocity (inverse of residence time) and reactant concentration (Table IV.4). Therefore taking conclusions from Figure IV.34 is difficult.

Table IV.4: Different conditions when comparing fluid at high-pressure and supercritical conditions with iso WHSV_{C₃cut}. ($W_{C_3\text{ cut}}/m_{\text{cat.}} = 200 \text{ h}^{-1}$ → without including the solvent).

Conditions	Type of fluid	solvent%	MAPD concentration	Space velocity
High-pressure	L (no solvent)	0 mol%	375 mol.m ⁻³	300 h ⁻¹ (residence time: 12 s)
Supercritical	SC (with methane)	60 mol%	~100 mol.m ⁻³	900 h ⁻¹ (residence time: 4s)

Comparing both conditions with iso WHSV for the C₃ cut was not the better strategy. To have a fair comparison between high-pressure and supercritical conditions, it was decided to perform the reaction with similar:

1. C_{MAPD reactive};
2. Space velocity_{reactive}.

IV.5.3 Planning of experiments

After defining the strategy to understand the reaction performance with solvents and supercritical fluids, it is interesting to reconstruct the zones ($Da^{mod.} < 1$) formerly detected for high-pressure conditions (Figure IV.37a). Based on this new diagram, the planning of experiments was defined (Figure IV.37b):

Table IV.5: Tests performed to mass transfer limitations and supercritical fluids.

Test	Goal
1. Solvent	Study the impact of the solvent in $Da^{mod.} > 1$ (adsorption, diffusion and mass transfer).
2. SC (303 K)	Study the impact of SC in $Da^{mod.} < 1$ (zone where the reaction rate is slower than space velocity).
3. SC at high temperature (353 K)	Increase reaction rate (by increasing temperature) and study the impact of SC at high space velocity 1800 h ⁻¹ (diffusion and mass transfer). [It is required to increase the temperature to study all the solvents in supercritical conditions]

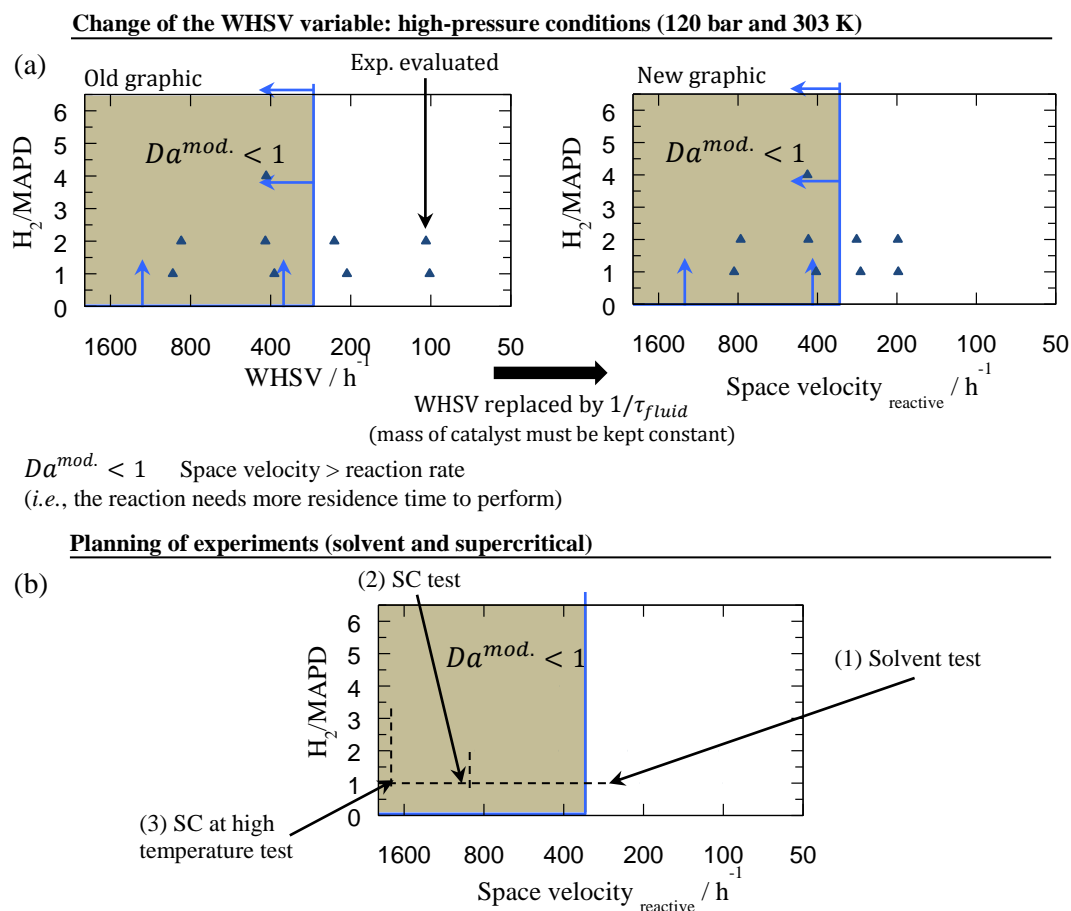


Figure IV.37: (a) High-pressure conditions change of WHSV to space velocity (high-pressure conditions: 303K and 120 bar). (b) Schematic of the zones to be studied with solvent and in supercritical conditions.

IV.5.4 Solvent effect (iso: space velocity and MAPD concentration)

Adding a solvent may enhance liquid-solid transfers ($k_{LS}a_{LS}$) and, in particular, intragranular mass transfers, due to the increase of the mixture diffusivity. It may help reducing the Thiele modulus (ϕ), leading to an increase of the effectiveness factor (η).

To study the solvent effect, only the points with solvent at liquid-phase were used.

Main properties changed: concentration (mol.m^{-3}), density (kg.m^{-3}), viscosity (Pa.s), diffusivity ($\text{m}^2.\text{s}^{-1}$), mass transfer ($k_{LS}a_{LS}$) and adsorption equilibrium.

Conditions: 303 K, 120 bar, 1 H_2/MAPD ratio, space velocity of 900 h^{-1} and 0.6 g of catalyst W.

Observations

Figure IV.38 shows the species conversions as a function of the MAPD molar concentration. There are points with different solvents (ethane and CH_4) and points with “no solvent” (propylene as solvent \rightarrow main species of the C_3 cut). For the conditions used (303 K and 120

bar), the mixtures are in a liquid state. The points were evaluated in a zone where $Da^{mod.} > 1$ (conversion depends on the space velocity [inverse of residence time]).

MAPD: There is slight changes in the MAPD conversion as a function of the MAPD molar concentration (~11 %) (Figure IV.38a). Similar results are obtained for the MAPD conversion when different solvents are used (ethane and CH₄).

Propane: The propane has the same behavior as the MAPD, more precisely; the propane produced varies softly for the points obtained (Figure IV.38b). The propane conversion average value is around -30%.

Hydrogen: For CH₄ and propylene (~no solvent), the hydrogen is fully converted (Figure IV.38c). For ethane, there is still hydrogen available at the end of the reactor. This may be related to a low MAPD molar concentration (lower than the other points).

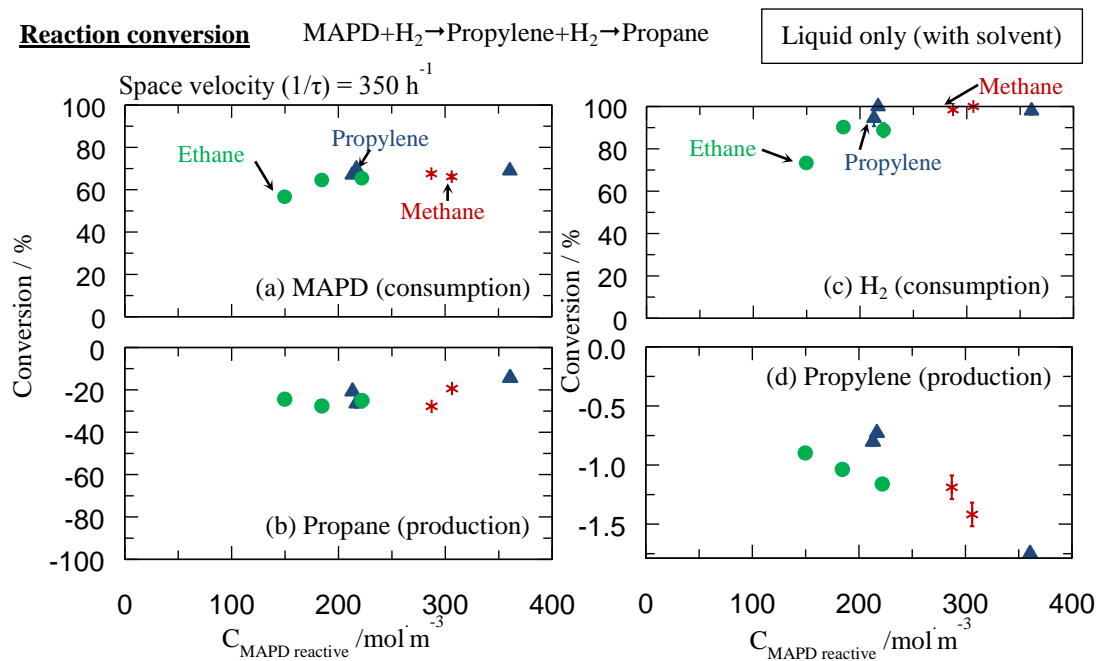


Figure IV.38: Selective hydrogenation at 303 K, 1 H₂/MAPD ratio and 120 bar. Solvent effect (CH₄, ethane and propylene) in the conversion of MAPD (a), propane (b), H₂ (c) and propylene (d).

The MAPD diffusivity in the studied mixtures (Figure IV.39a) is higher in CH₄ (as solvent) than in ethane and in propylene ($D_{MAPD\ in\ CH_4} > D_{MAPD\ in\ ethane} \approx D_{MAPD\ in\ propylene}$). The MAPD mass transfer coefficients (Figure IV.39a) are also higher for CH₄ (as solvent) than for ethane and propylene.

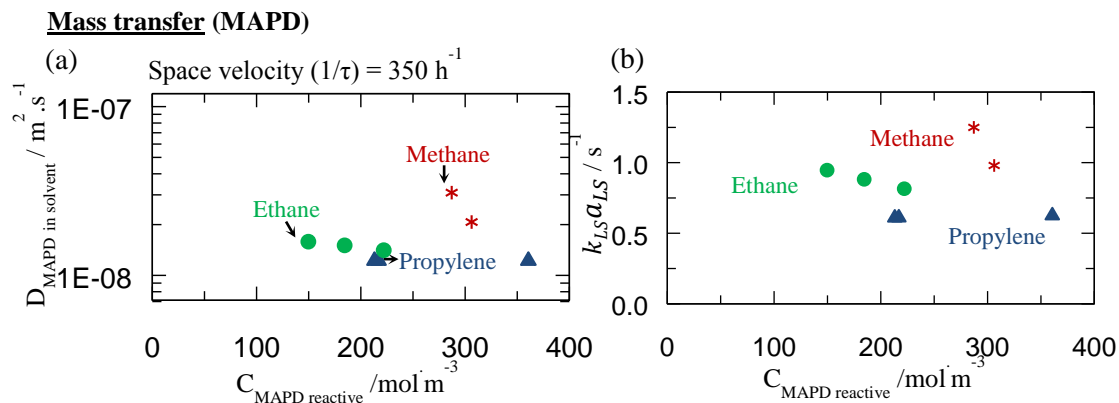


Figure IV.39: Selective hydrogenation at 303 K, 1 H₂/MAPD ratio and 120 bar. (a) MAPD diffusivity coefficients for the mixture composition [Vignes mixing rules (Magalhães et al., 2013)] as a function of the MAPD concentration. (b) MAPD mass transfer coefficient as a function of the MAPD concentration.

Result discussion

From the experimental points (liquid points only), the MAPD and propane conversions are practically constant, since the H₂ is (nearly) fully converted and $Da^{mod.} > 1$. More importantly, the selectivity seems not to change with the diffusivity coefficients for a 1 H₂/MAPD ratio. The selectivity might change when increasing the H₂/MAPD ratio (no more lack of H₂).

For the points with or without solvents, there are virtually no differences in the MAPD conversion at a 1 H₂/MAPD ratio. This happens even if the MAPD diffusion coefficients (until 3 times higher in CH₄ than in propylene; Figure IV.39a) are enhanced. This might be related to an increase of the reaction rates without affecting the propane and the MAPD conversion. In other words, the reaction rates are higher (due to $\eta \uparrow$), but conversions are the same since the ratio between the MAPD and propylene reaction is kept constant. This assumption will be later checked using supercritical fluids. Moreover, at a 1 H₂/MAPD ratio, the H₂ is practically fully converted. It may be expected that at a higher H₂/MAPD ratio, the differences on MAPD diffusion coefficients will be noticed (η difference is easier to observe).

Adding solvent at a space velocity of 350 h^{-1} , the $k_{LS} a_{LS}$ increases, but the conversion stays constant. Therefore, the liquid-solid mass transfer seems not to influence in the reaction. This confirms the explanation obtained at high-pressure (§IV.4.2).

Another conclusion is that solvents do not affect the adsorption equilibrium of the MAPD hydrogenation, since the propane produced, and the MAPD converted have similar values.

Summary

1. Effectiveness factor may increase ($\eta \uparrow$), but reaction rate between MAPD and propylene is kept constant;
2. The addition of a solvent seems to not affect the adsorption constants.

IV.5.5 Supercritical vs high-pressure conditions

In order to check the previous conclusion ($\eta \uparrow\uparrow$, same selectivity), it is interesting to test supercritical fluids in a zone where kinetics are limited by space velocity (inverse of residence time) ($Da^{mod.} < 1$).

Eq. IV.13 resumes what is expected when using supercritical fluids.

$$\left\{ \begin{array}{l} \phi_{SC} < \phi_{HP} \Rightarrow \eta_{SC} > \eta_{HP} \\ \overbrace{R_{i,observed\ SC} = \eta_{SC} R_{i,real}}^{\text{Supercritical conditions}} > \overbrace{R_{i,observed\ HP} = \eta_{HP} R_{i,real}}^{\text{High-pressure conditions (total } \sim 0.15 \text{ s}^{-1})}} \\ Da_{SC}^{mod.} = \frac{\int R_{i,observed\ SC} d(1/C_i)}{\underbrace{\tau_{SC}^{-1}}_{*equal}} < Da_{HP}^{mod.} = \frac{\int R_{i,observed\ HP} d(1/C_i)}{\underbrace{\tau_L^{-1}}_{*equal}} \end{array} \right. \quad \text{Eq. IV.13}$$

If $Da_{SC}^{mod.} > Da_{HP}^{mod.}$ for the same space velocity ($\tau_{SC}^{-1} = \tau_L^{-1}$), it is expected to be more limited by space velocity.

Main properties changed: density (kg.m^{-3}), viscosity (Pa.s), diffusivity ($\text{m}^2.\text{s}^{-1}$) and mass transfer ($k_{LS}a_{LS}$).

Conditions: 303 K, 120 bar, 1 H_2 /MAPD ratio, space velocity of 900 h^{-1} and 0.6 g of catalyst W.

Observations

Figure IV.40a shows the conversion as a function of the MAPD molar concentration for supercritical conditions (with solvent CH_4) and high-pressure conditions. The points were evaluated in a zone where $Da^{mod.} < 1$ (the space velocity is superior to the reaction rate).

MAPD: Although the solution is diluted, the supercritical conditions have higher MAPD conversion (73%) (Figure IV.40a). For the same inlet dilution (100 mol.m^{-3}), the MAPD conversion is around 38% for high-pressure conditions. Another interesting result is that supercritical fluid conditions exhibit higher conversion when compared to concentrated mixtures without solvent (high-pressure).

Propane: The propane is more produced at supercritical conditions than at high-pressure conditions (Figure IV.40b). The propane conversion has similar value to the one obtained in high-pressure conditions at $Da^{mod.} > 1$ (IV.5.4), being around -30%.

Hydrogen: The H_2 conversion (Figure IV.40c) has the same behavior as the MAPD. Regarding the points at 100 mol.m^{-3} (MAPD molar concentration), for supercritical fluid (C_3 cut mixed with CH_4) the hydrogen is fully converted. Oppositely, for high-pressure conditions (without solvent) there is hydrogen available at the end of the reactor (H_2 conversion of 45 % mol [at 100 mol.m^{-3}]).

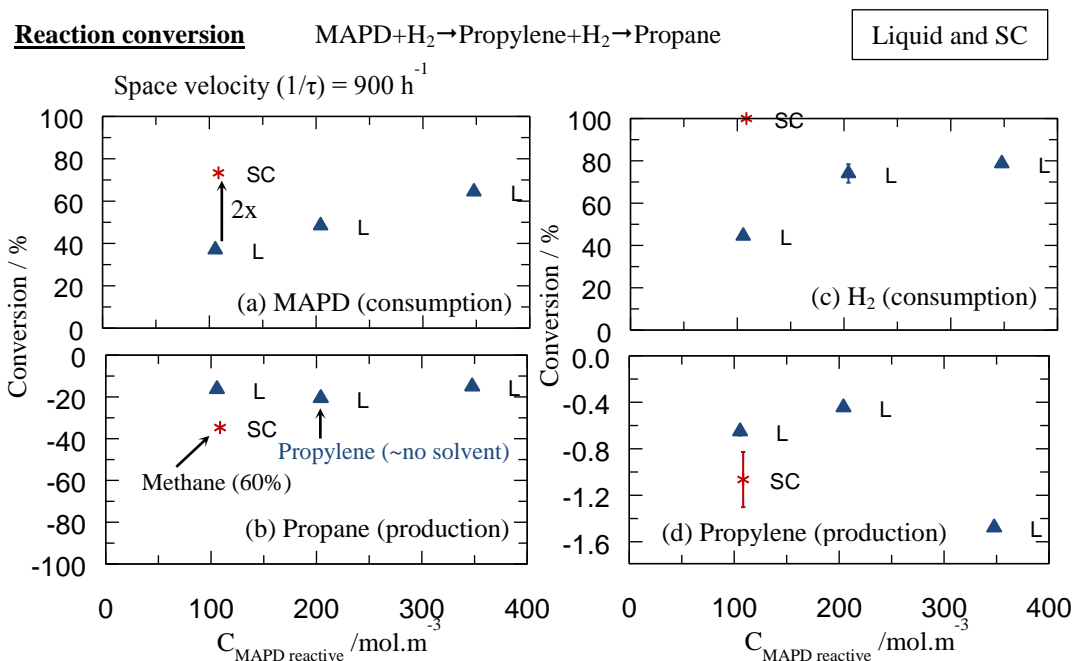


Figure IV.40: Selective hydrogenation at 303 K, 1 H₂/MAPD ratio and 120 bar; supercritical (60% CH₄) vs high-pressure conditions. Conversion of MAPD (a), propane (b), H₂ (c) and propylene (d).

The MAPD diffusivity in the mixtures studied (Figure IV.41a) is higher for SC than HP conditions. The mass transfer coefficients (Figure IV.41b) are also higher for SC than HP conditions.

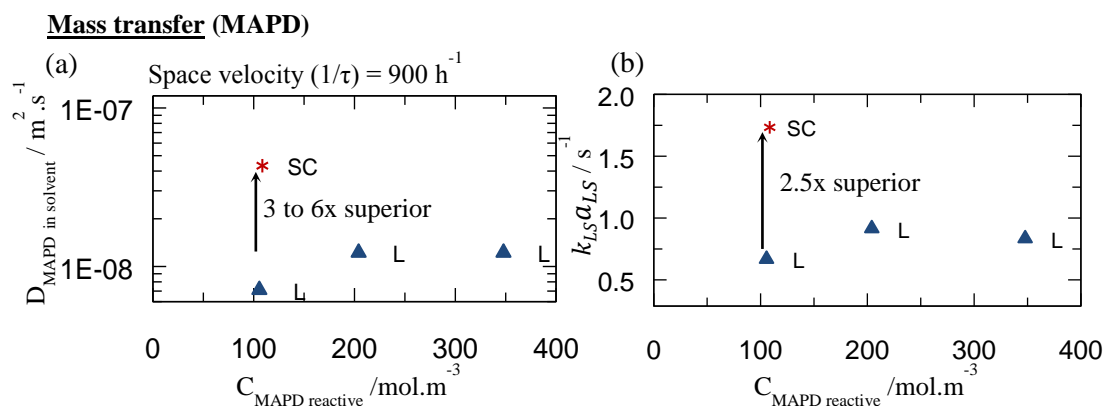


Figure IV.41: Selective hydrogenation at 303 K, 1 H₂/MAPD ratio and 120 bar. (a) MAPD diffusion as a function of the mixture composition [Vignes mixing rules (Magalhães et al., 2013)]. (b) MAPD mass transfer coefficient.

Summary

At these experimental conditions (900 h^{-1}), the MAPD conversion is higher at supercritical conditions. This is primarily due to a higher diffusivity (6x HP [Figure IV.40b]), leading to a higher effectiveness factor ($\eta_{\text{SC}} > \eta_{\text{HP}}$).

At this point (Figure IV.42), $\eta_{SC} > 2.25 \eta_{HP}$. This value was estimated dividing the space velocities near $Da^{mod.} = 1$ for HP and SC. The η_{SC} can even be higher, since we are still far from $Da^{mod.} = 1$ for supercritical conditions.

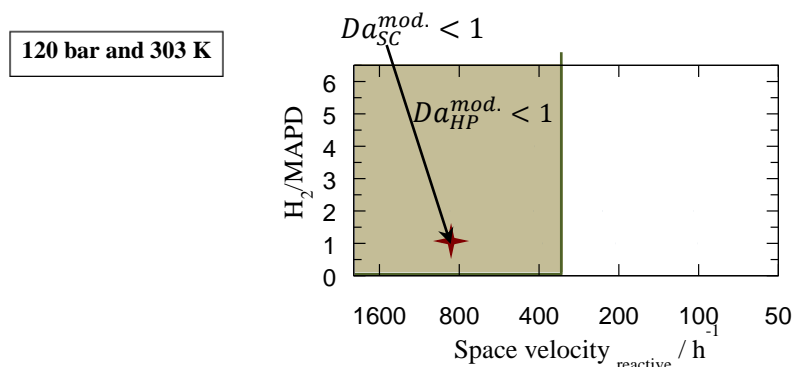


Figure IV.42: Different zones in HP and SC conditions (HP: high-pressure conditions; SC: supercritical conditions).

In this case study, only the 1 H_2 /MAPD ratio was shown. For a H_2 /MAPD ratio of 2, the experimental data are available in Appendix IV.4. These results confirm the gain on effectiveness factor.

IV.5.6 Space velocity effect

The next step is to study higher space velocities (lower residence times) and to define when $Da^{mod.} = 1$ for supercritical conditions. Unfortunately, 900 h^{-1} is the maximum space velocity achievable with the experimental set-up at 303 K, 120 bar and 0.6 g of catalyst. The solution adopted was to reduce the mass of catalyst to 0.3 g (35 spheres instead of 70). Moreover the feedstock (industrial) was changed. After dilution (60 mol%), we have now $60 \text{ mol}_{\text{MAPD}} \cdot \text{m}^{-3}$ instead of $100 \text{ mol}_{\text{MAPD}} \cdot \text{m}^{-3}$.

With this new feed, the direct comparison between previous conversions results is not possible (*e.g.* comparison with Figure IV.40). Even so, it should be possible to study the impact of the space velocity and define the zone where $Da^{mod.} = 1$.

Objective: Quantify the effectiveness of SC at $Da^{mod.} = 1$.

Main properties changed: reaction time (h).

Conditions: 303 K, 120 bar, 1 H_2 /MAPD ratio, 0.3 g of catalyst W and inlet concentration: $60 \text{ mol}_{\text{MAPD}} \cdot \text{m}^{-3}$, $112 \text{ mol}_{\text{Propane}} \cdot \text{m}^{-3}$ and $4861 \text{ mol}_{\text{Propylene}} \cdot \text{m}^{-3}$.

Observations

Figure IV.43 shows the conversion as a function of the space velocity for supercritical conditions (with solvent CH_4).

MAPD: From 1800 to 400 h^{-1} , the MAPD conversion remains constant (Figure IV.43a). However from 3200 to 1800 h^{-1} , the MAPD decreases. The constant conversion at 40% was not expected.

From 1800 to 400 h⁻¹, it was expected a constant conversion at a higher value > 65%. This might be related to the low MAPD concentration and the number of pellets tested (35 spheres).

Propane: From 1800 to 400 h⁻¹, the propane and propylene conversion remains virtually constant (Figure IV.43 b,d). However from 3200 to 1800 h⁻¹, the propylene is consumed, and the propane is less produced.

Hydrogen: The hydrogen seems to be not fully converted (Figure IV.43c). The hydrogen conversion remains constant from 1800 to 400 h⁻¹.

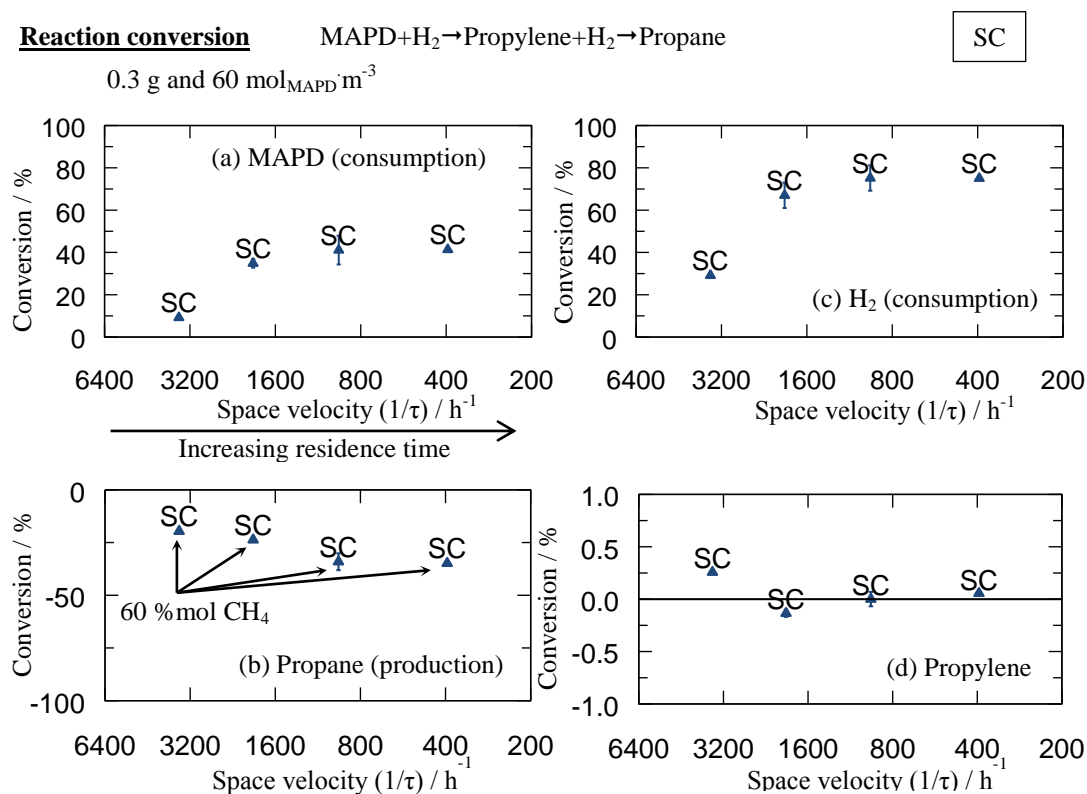


Figure IV.43: Selective hydrogenation at 303 K, 1 H₂/MAPD ratio and 120 bar (with 35 catalyst spheres); supercritical conditions versus space velocity (h⁻¹), having 60% of CH₄. Conversion of MAPD (a), propane (b), H₂ (c) and propylene (d).

Summary

For the conditions studied, the reactants have a constant conversion from 400 to 1800 h⁻¹. Consequently, we might say that the reaction rate is superior to the space velocity (inverse of residence time) ($Da^{mod.} > 1$).

Above 1800 h⁻¹ the conversion decreases. Consequently, the reaction rate is inferior to the space velocity, therefore $Da^{mod.} < 1$. The value of $Da^{mod.} = 1$ should near 1800 h⁻¹.

Based on the results (Figure IV.43), $\eta_{SC} > 4.8 \eta_{HP}$ (estimated based on the space velocity at $Da^{mod.} = 1$).

IV.5.7 H₂/MAPD ratio effect

After estimating the total reaction rate at supercritical conditions, it is interesting to compare SC with HP (high-pressure) in a zone where $Da^{mod.} > 1$ and for different H₂/MAPD ratios (H₂ in excess).

Conditions: 303 K, 120 bar and 0.6 g of catalyst W.

Table IV.6: Comparison of conditions for SC and HP experiments.

Conditions	Mixture characteristics		Working zone		Reaction
	Solvent / % mol	$C_{MAPD, reactive} /$ $mol.m^{-3}$	τ^{-1} / h^{-1}	$Da^{mod.}$	$\int R_{i,observed} d(1/C_i)$
Supercritical (*)	60 % CH ₄	~100	900	>1	~0.50 s ⁻¹
High-pressure (▲)	No solvent	~350	160	>1	0.15 s ⁻¹

Although the experimental conditions are different, both cases can be compared because there are in a zone where $Da^{mod.} > 1$ (no impact of the reaction time).

Observations

Figure IV.44 shows the species conversion as a function of the H₂/MAPD ratio.

MAPD: Similar conversions are obtained for the supercritical and the high-pressure conditions (Figure IV.44a), although the fluid mixture is more diluted at supercritical conditions (3 times more diluted).

Propane: At 1 H₂/MAPD ratio, the propane is more produced at supercritical conditions (Figure IV.44b). However for a 2 H₂/MAPD ratio, the propane is more produced for high-pressure conditions. This might be related to different propane and propylene (reactant) concentrations in the reaction medium (60 mol% diluted in SC) and the H₂ consumption.

Hydrogen: The H₂ is fully converted for 1 and 2 H₂/MAPD ratio at high-pressure conditions (space velocity of 100 h⁻¹). For the supercritical conditions (space velocity of 100 h⁻¹), the H₂ is fully converted at a 1 H₂/MAPD ratio, but it seems to be not fully converted above a 1 H₂/MAPD ratio. This might be related to the uncertainty in the hydrogen estimation.

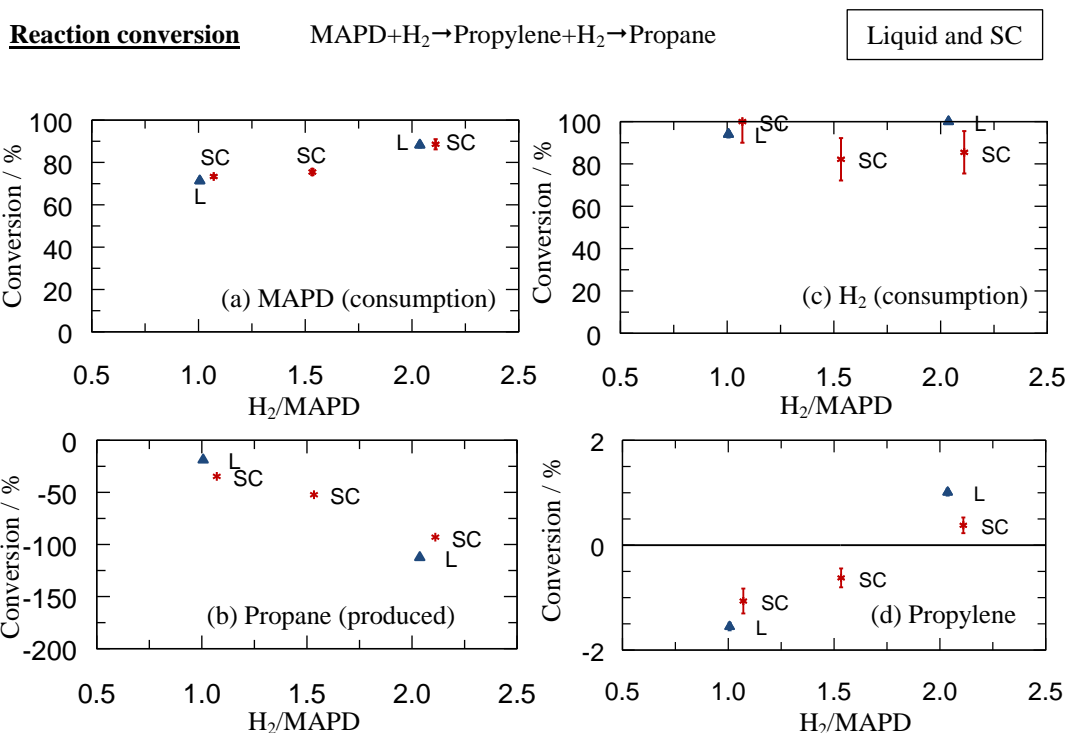


Figure IV.44: Selective hydrogenation at 303K and 120 bar; supercritical (60% CH₄) vs high-pressure conditions for different H₂/MAPD ratios. Conversion of MAPD (a), propane (b), H₂ (c) and propylene (d).

The MAPD diffusivity coefficients (Figure IV.45a) are higher for SC than HP conditions (> 3 times). The mass transfer coefficients (Figure IV.45b) are also higher for SC than HP conditions (> 3 times).

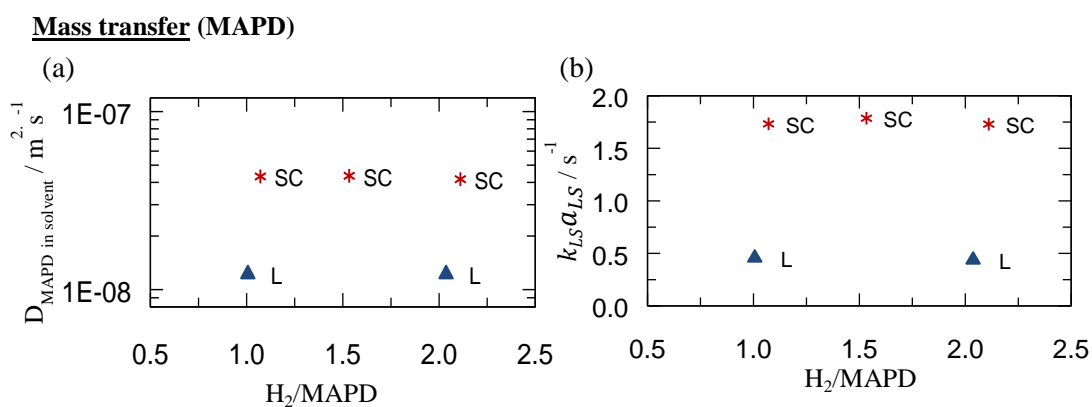


Figure IV.45: Selective hydrogenation at 303K and 120 bar. (a) Supercritical (60% CH₄) vs high-pressure conditions for different H₂/MAPD ratios. (b) Mixture and liquid-solid mass transfer coefficients as a function of H₂/MAPD.

Summary

Despite the difference in diffusivity coefficients and mass transfer (SC > liquid at high-pressure) (Figure IV.45b), the MAPD and propane conversions are similar for the same operating conditions and the H₂/MAPD ratio studied.

It is also possible to notice that supercritical fluids do not change meaningfully the MAPD and propane conversion (iso selectivity), although $\eta_{SC} > 4.8 \eta_{HP}$. It confirms the hypothesis noticed at IV.5.4. This proves that the reaction is in a strong diffusional regime, even when working at SC conditions. This will be later discussed in §V.

IV.5.8 Supercritical conditions with different solvents

Until this point, only the supercritical mixture with CH₄ was studied. Other mixtures are also interesting to be evaluated due to their different properties. To evaluate other supercritical mixtures, the temperature must be increased from 303 to 353 K. The results were compared with two solvents (CH₄ and C₂H₆) with HP results at 353K for a 2 H₂/MAPD ratio (to have excess of H₂). The points presented have 30 mol% CH₄ and 60 mol% C₂H₆.

In this chapter, the temperature study is not presented [it was studied by Sousa (2015)], but the CH₄ (SC), ethane (SC) and C₃ cut (L) are compared.

Main properties changed: density (kg.m⁻³), viscosity (Pa.s), diffusivity (m².s⁻¹), mass transfer ($k_{LS}a_{LS}$) and reaction kinetics.

Conditions: 353 K, 120 bar, 2 H₂/MAPD ratio, space velocity of 900 h⁻¹ and 0.6 g of catalyst W.

Observations

Figure IV.46 shows the MAPD and propane conversion as a function of the MAPD concentration (inlet).

MAPD: From 40 to 170 mol.m⁻³ (no solvent), the MAPD conversion increases of 55% (Figure IV.46a). Taking into account the concentration at the point without solvent (40 mol.m⁻³), it seems that the conversion might be higher for mixtures with solvent than without solvent. When comparing supercritical mixtures, the MAPD conversion is similar for CH₄ and ethane (30 mol% CH₄ and 60 mol% C₂H₆).

Propane: Propane conversions are similar for the points evaluated without solvent (Figure IV.46b). In relation to supercritical mixtures, the propane conversion is similar for CH₄ and ethane.

Hydrogen: The hydrogen conversion follows the same behavior as the MAPD (Figure IV.46c). When comparing supercritical mixtures, the H₂ conversion is higher for CH₄ than for ethane (30 mol% CH₄ and 60 mol% C₂H₆).

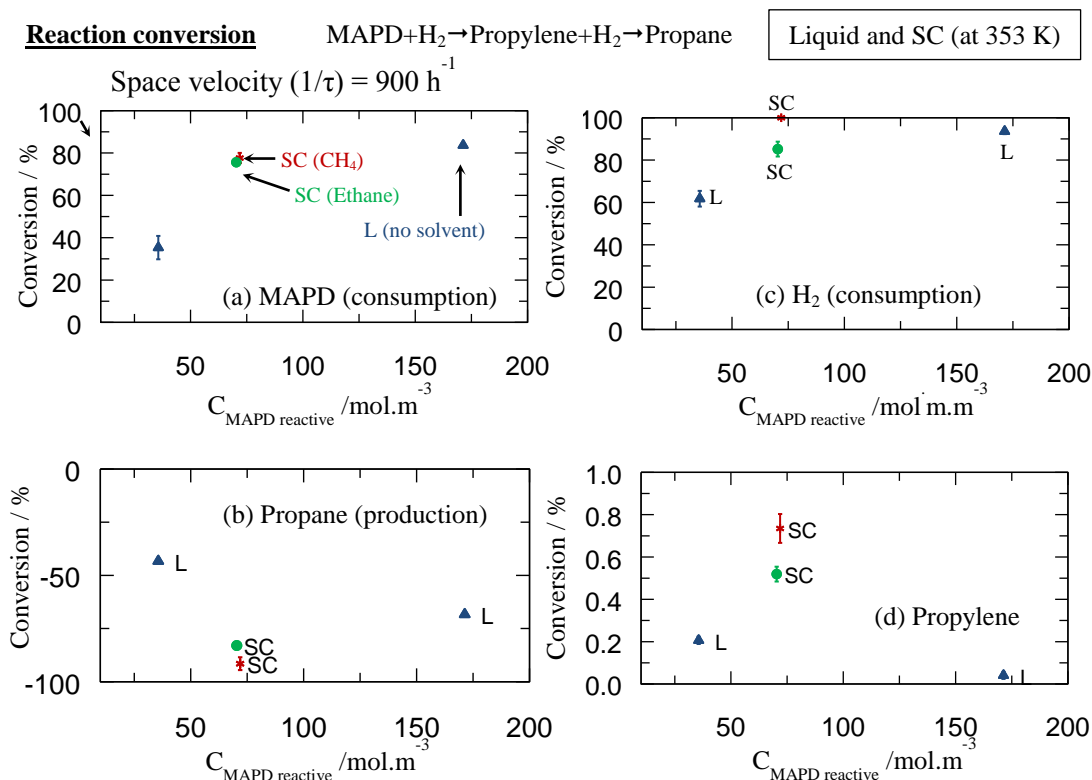


Figure IV.46: Selective hydrogenation at 353 K, 120 bar and a 2 H_2 /MAPD ratio; supercritical (30% CH_4 and 60% ethane) vs high-pressure conditions for different MAPD concentrations. Conversion for MAPD (a), propane (b), H_2 (c) and propylene (d).

The MAPD diffusivity and liquid-solid mass transfer coefficients (Figure IV.47) are higher for SC than HP conditions. When comparing the supercritical mixtures, the diffusivity and mass transfer coefficients are higher for CH_4 than for ethane.

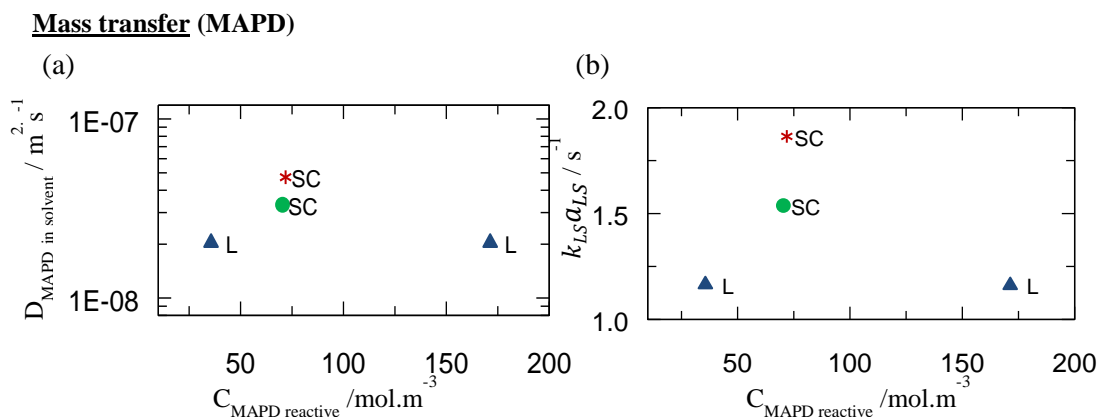


Figure IV.47: (a) Mixture diffusion coefficients. (b) Liquid-solid mass transfer coefficients as a function of the MAPD concentration.

Summary

Despite the difference noticed in diffusivity and mass transfer (Figure IV.46b), the supercritical mixtures analyzed (CH_4 and ethane) have similar MAPD conversions. Thus,

since different solvents were used, and no significant difference was noticed in the MAPD conversion, we might say that the adsorption equilibrium is not affected by the solvent used (CH₄ or ethane).

In summary:

1. For the supercritical mixtures used (CH₄ and ethane) at 900 h⁻¹ and 353 K there are no limitations in the liquid-solid mass transfer;
2. The adsorption equilibrium (or other interactions) is not affected by the supercritical mixture used (CH₄ or ethane as a solvent).

IV.5.9 Conclusion (supercritical conditions)

Figure IV.48(a,b) summarizes the results acquired for high-pressure conditions (303 K and 120 bar) and supercritical conditions (353 K, 120 bar and 60 mol% CH₄).

High-pressure conditions: Regarding Figure IV.48b, a zone was defined for $Da^{mod.} < 1$ (above 375 h⁻¹ [space velocity]). From 375 to 200 h⁻¹, there are no liquid-solid (external) mass transfer limitations, but there are still intragranular (or internal) transfer limitations. When these limitations are reduced, the conversion obtained is practically the same (for $Da^{mod.} > 1$).

Supercritical conditions: Regarding Figure IV.48b, a zone was defined for $Da^{mod.} < 1$ (above 1800 h⁻¹ [space velocity]). These conditions help us accessing an apparent kinetics closer to the intrinsic kinetic ($\eta_{SC} > 4.8 \eta_{HP}$), without changing the MAPD conversion and selectivity [in relation to liquid (high-pressure)], since the reactions rate are increased in the same way.

Between HP and SC, there is a change of the “measuring zone”, due to changes in reaction effectiveness ($\eta_{SC} > 4.8 \eta_{HP}$). It was proven that the reaction is still in a diffusional regime (§IV.5.7).

Thesis main goal: catalyst screening. The catalysts can be compared in HP, but also in SC conditions. When comparing catalyst with iso selectivity and higher MAPD activity, the space velocity should be adapted to the zone where $Da^{mod.} < 1$.

Thesis second goal: study intrinsic kinetics. SC conditions gives further information about the system. To evaluate intrinsic kinetics, HP and SC points will be used in modeling (see §V). For the thesis second goal, HP and SC experimental data are necessary.

These technologies (HP + SC) can help to better understand and evaluate systems with high reactivity.

In conclusion, supercritical conditions are interesting to better understand reaction kinetics and to evaluate the impact of internal mass transfer resistance. With these conditions, it will be possible:

1. To understand the impact of different metal crusts;
2. To understand the impact of metal crust's thickness (catalyst);
3. To construct better kinetic models.

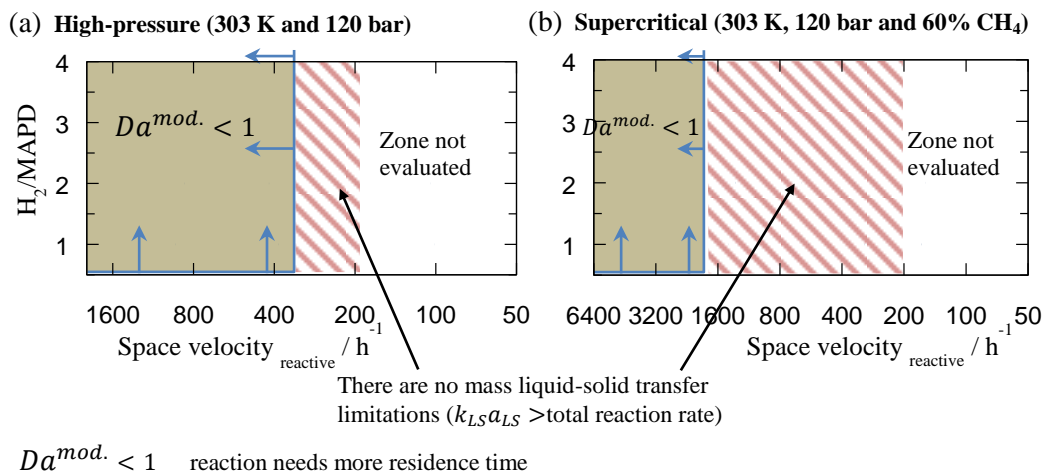
Pilot reactor zones


Figure IV.48: (a) Zones defined for high-pressure conditions (H_2/MAPD ratio vs space velocity). (b) Zones defined for supercritical conditions (H_2/MAPD ratio vs space velocity).

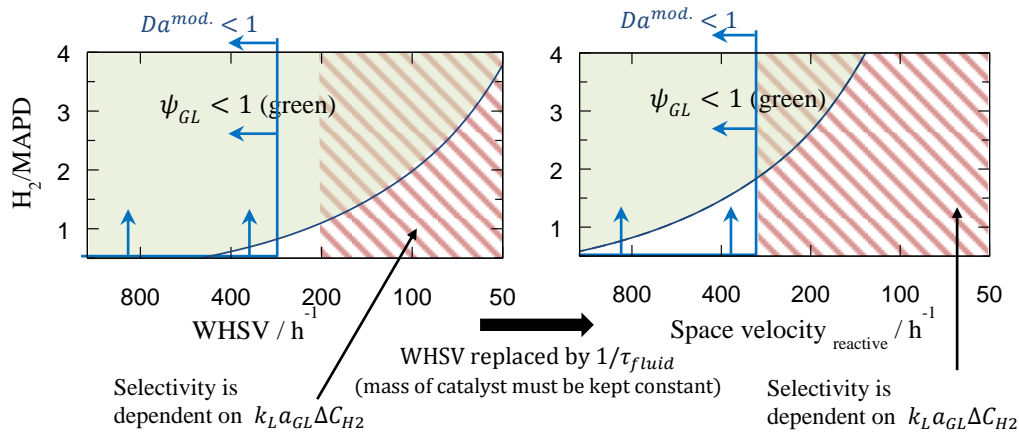
IV.6 Conclusions

The MAPD hydrogenation was investigated in conventional (gas-liquid-solid) and unconventional conditions (high-pressure and supercritical). For each condition several parameters were studied, such as the space velocity (inverse of residence time) and the H_2/MAPD ratio. Based on the parameters and conditions evaluated, a map of the space velocity vs the H_2/MAPD ratio was built (Figure IV.49). It was shown that the reactor can achieve higher conversions at low residence times working in unconventional conditions than in conventional ones.

Conventional conditions: Regarding Figure IV.49, the conventional conditions have three defined zones: $\psi_{GL} < 1$ (not enough time to achieve full gas-liquid mass transfer \rightarrow the reaction is slowdown), $Da^{mod.} < 1$ (not enough residence time \rightarrow the reaction is slowdown) and zone where the selectivity is controlled by the H_2 molar conc. flow rate.

It was suggested that the H_2 molar concentration flow was inferior to an industrial reactor, working in high and low interaction regimes (bubble and trickle flow, respectively) (Figure IV.32). However, conventional conditions are close to an industrial reactor in medium interaction regime (pulse flow) when working at WHSV of 200 h^{-1} .

- These conditions are not adapted to perform catalyst screening, since the selectivity can be easily changed with the gas-liquid (H_2) molar concentration flow.

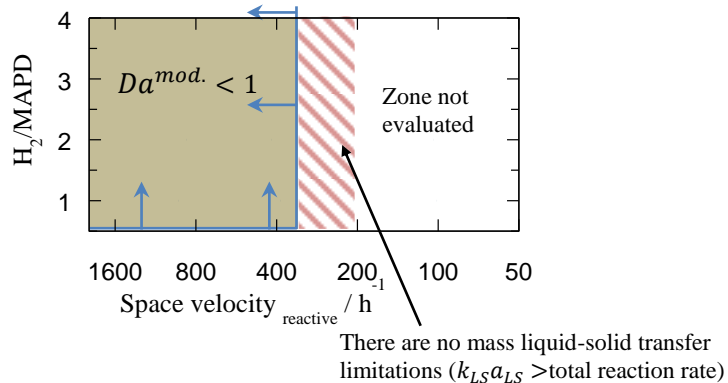


$\psi_{GL} < 1$ not enough time to have full gas-liquid mass transfer
 $Da^{mod.} < 1$ reaction needs more residence time

Figure IV.49: Schematic of different zones for conventional conditions (303K and 20 bar) with WHSV and space velocity.

High-pressure conditions: Regarding Figure IV.50, there are two defined zones: $Da^{mod.} < 1$ (not enough residence time \rightarrow the reaction is slowdown) and $Da^{mod.} > 1$. For these conditions, the MAPD molar concentration flow is close to the industrial reactor with medium (pulse flow) and high (bubble flow) interactions, depending of the WHSV (or space velocity) used. For bubble flow, a WHSV of 150 h^{-1} (or space velocity of 230 h^{-1}) should be used. At HP conditions, there are no gas-liquid (by definition) and liquid-solid mass transfer limitations.

- These conditions are adapted to perform catalyst screening, because the selectivity does not change with the space velocity and since there are no external mass transfer limitations.

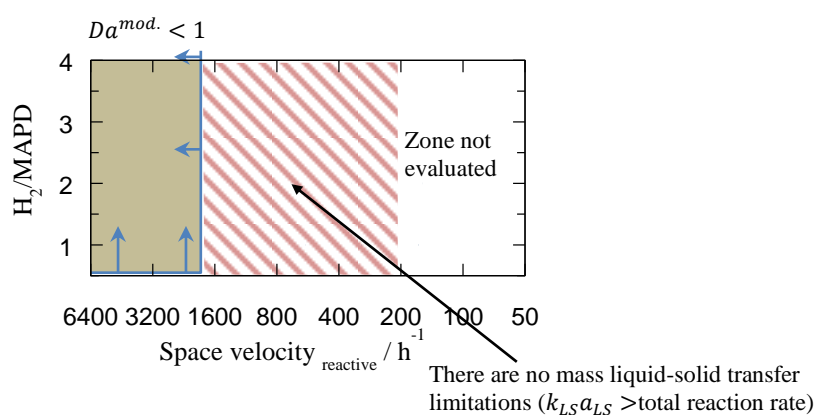


$Da^{mod.} < 1$ reaction needs more residence time

Figure IV.50: Schematic of different zones for high-pressure conditions (303K and 120 bar) with space velocity.

Supercritical conditions: Regarding Figure IV.51, the supercritical conditions have two zones: one with $Da^{mod.} < 1$ and one zone with no liquid-solid mass transfer limitations. For these conditions, the reaction rate is higher (4.8 times) than high-pressure conditions, without having changes in the MAPD and propane conversions. This happens due to higher diffusivity in supercritical medium.

- These conditions are adapted to perform catalyst screening and intragranular studies (thanks to higher diffusivity). Also, it allows having experimental data closer to the intrinsic kinetics ($\eta_{SC} > 4.8 \eta_{HP}$).
- The supercritical data coupled with high-pressure data can give further information about the system. This helps to evaluating intrinsic kinetics by modeling means (see §V).



$Da^{mod.} < 1$ reaction needs more residence time

Figure IV.51: Schematic of different zones for supercritical conditions (303K, 120 bar and 60%mol CH₄) with space velocity.

The main conclusions are summarized in Table IV.7.

Table IV.7: Table of conclusions for the different reaction media tested. * depends on the liquid hold-up expression.

	Conventional	High-pressure	Supercritical
Pressure / bar	20	120	120
Temperature / K	303	303	[303 to 353]
Physical state	liquid-gas	liquid	supercritical
Solvent / % mol	0	0	~60
$C_{\text{MAPD reactive}} / \text{mol m}^{-3}$	~350	~350	~100 (diluted mixture)
Space velocity tested / h^{-1}	$270 > \tau_L^{-1} > 2000^*$	$90 > \tau_L^{-1} > 900$	$400 > \tau_{SC}^{-1} > 3200$
Mass transfer rate / s^{-1}	$0.2 < k_L a_{GL} < 0.8$	$0.5 < k_{LS} a_{LS} < 1.0$	$1.0 < k_{LS} a_{LS} < 3.0$
Pseudo total reaction rate / s^{-1} ($Da^{mod.}=1$)	~0.15 (uncovered)	~0.15	~0.5
Main characteristics	<ol style="list-style-type: none"> 1. Controlled by $k_L a_{GL}$ (zones with $\psi_{GL} > 1$); 2. Conversion and selectivity depend on H_2 molar conc. flow. 	<ol style="list-style-type: none"> 1. No mass liquid-solid mass transfer limitations for $Da^{mod.} > 1$; 2. Virtually no impact of pressure in single-phase mixtures. 	<ol style="list-style-type: none"> 1. Improved effectiveness factor ($\eta_{SC} > 4.8 \eta_{HP}$); 2. No changes in adsorption equilibrium; 3. No changes in MAPD conversion and selectivity in relation to HP; 4. No mass liquid-solid mass transfer limitations for $Da^{mod.} > 1$.
Application	Not convenient for catalyst screening, since selectivity depends on H_2 molar conc. flow	<ol style="list-style-type: none"> 1. Catalyst screening; 2. Kinetics studies; 	<ol style="list-style-type: none"> 1. Catalyst screening; 2. Kinetics studies; 3. Intragranular resistance studies; 4. Catalyst crust thickness studies.

Chapter V

Modeling MAPD hydrogenation

Abstract

Assessing intrinsic kinetics can help better classifying the (MAPD) hydrogenation catalysts according to their performance. The kinetics was studied over a fresh palladium catalyst (symbolically named W) under isothermal conditions (303 K). The dataset used came from the high-pressure and the supercritical experimental results. Several kinetic models were evaluated, such as power law and Langmuir-Hinshelwood-Hougen-Watson (LH-HW), in high pressure and supercritical conditions. To estimate the reaction parameters, the absolute deviation between the experimental and the estimated data were minimized using the MatLab[®] optimization toolbox (function `fminsearch`). The reactor and mass transfer (external and internal) were simulated using Comsol[®] Multiphysics V5.

It was shown that a dataset with high-pressure and supercritical experimental points is an interesting solution to model intrinsic kinetics. The model confirms the results previously obtained for HP and SC conditions (§IV). For instance, there are no liquid-solid mass transfer limitations (for the reactor length used) and the conversion for MAPD and propane at low residence time.

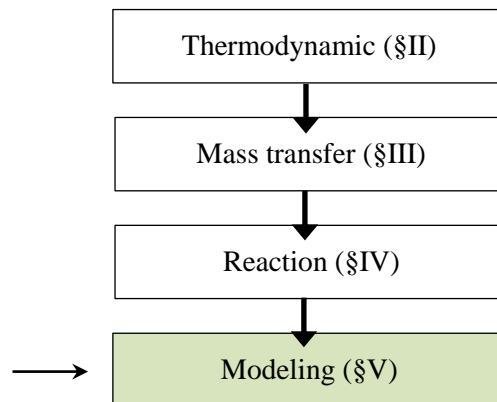


Figure V.1: Manuscript's guideline.

V.1 Introduction

After analyzing the experimental results, a model is required to check the conclusions previously obtained (§IV).

The kinetics for MAPD selective hydrogenation has been a topic studied over the past years (Brandao et al., 2007; Wang and Froment, 2005). **In the literature, the majority of the studies are performed in gas-solid phase** (until max. pressure of 10 bar) [process typically used before 1970-1980]. Therefore, the kinetic parameters evaluated should be only applied for the range and conditions considered (§IV.2). **In industry, the gas-liquid-solid phase is the most established route** to convert MAPD to propylene (Samimi et al., 2015). However, **at these conditions, the intrinsic kinetics cannot be properly evaluated due to the mass transfer limitations**: external (gas-liquid and liquid-solid) and intragranular. For this reason, **high-pressure and supercritical conditions are an interesting solution** (Table V.1) because the fluid is in a **single-phase and higher diffusion coefficients can be achieved** (for supercritical conditions).

Table V.1: Main characteristics of the mass transfer and main properties for HP and SC conditions.

Conditions	Mass transfer limitations		Main properties	
	Gas-liquid	Liquid-solid	$D_{MAPD} / \text{m}^2 \cdot \text{s}^{-1}$	η_{SC} / η_{HP}
High-pressure (HP)	No	Negligible	1.22×10^{-8}	1.0
Supercritical (SC)	No	Negligible	5.49×10^{-8}	>4.8

Indeed, as we have seen in §IV, the diffusivity coefficients and effectiveness factors are different between HP and SC conditions. Therefore, the concentration inside the particle pellet will be higher for SC conditions (Figure V.2). If the reaction is modeled in high-pressure and supercritical conditions, it should be possible to estimate better intrinsic kinetics than in a single-phase dataset. Thus, by using both conditions, the model parameter sensitivity is improved.

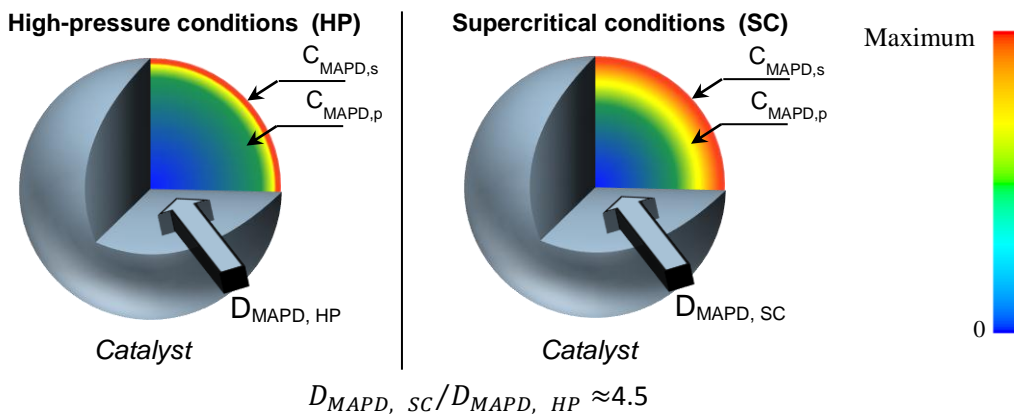


Figure V.2: Possible impact of MAPD diffusivity inside a catalyst pellet. $C_{MAPD,s}$ is the MAPD concentration at the pellet surface and $C_{MAPD,p}$ is the MAPD concentration inside the particle.

V.2 Model

To study the different reaction mechanisms, the methodology adopted was based on the evaluation of intrinsic kinetics. The catalyst pellets were modeled with intragranular diffusion along the reactor, using a numerical solver (Comsol® V5). By modeling the intrinsic kinetics, the aim is to represent experimental data with different diffusivities, namely liquid (high-pressure) and supercritical conditions. The objective function was minimized using Matlab® V2014a *fminsearch* function (optimization). Figure V.3 briefly describes the optimization methodology. Each point of the methodology will be later detailed.

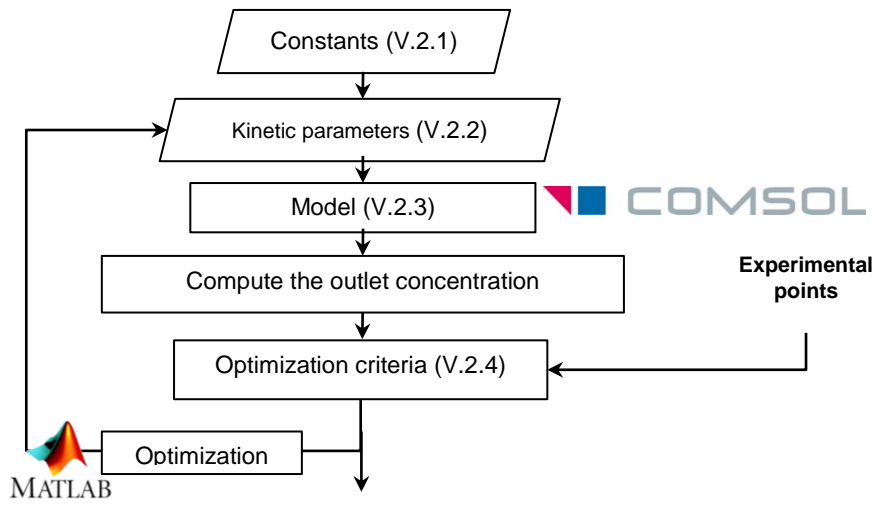


Figure V.3: Methodology adopted to study the MAPD and propylene hydrogenation kinetics.

V.2.1 Constants

The formulated reactor model uses a set of constants, which are related to the reactor, the catalyst packing and the fluid. These constants are defined and presented in Table V.2.

Table V.2: Geometrical and fluid constants. * confidential

Constants			Definitions		
$r_{reactor}$	1.5	mm	$\bar{u}_{int.}$	\bar{u}_L/ε_L	$m.s^{-1}$
$r_{cat.}$	1.22	mm	Sc_i	$\mu/(\rho \times D_{i,b})$	
$L_{reactor}$	20	cm	Re_L	$\bar{u}_L \rho d_{cat.}/\mu$	
$L_{reactor \ 70 \ spheres}$	16.10	cm	ρ_B	$\rho_{cat.}(1 - \varepsilon_L)$	$kg.m^{-3}$
$L_{reactor \ 35 \ spheres}$	8.05	cm			
a_s	$3/r_p$	m^{-1}			
δ_{metal}^*	$\sim [100 - 900]$	μm			
ε_L	0.55				
$\rho_{cat.}$	1001.73	$kg.m^{-3}$			

where $r_{reactor}$ (mm) and r_{cat} (mm) are the reactor and the catalyst radius, respectively. $L_{reactor}$ (cm) is the reactor length, a_s (m^{-1}) is the specific surface area, δ_{metal} (μm) is the thickness of the metallic crust, ε_L is the porosity of the catalyst bed, \bar{u}_L ($m.s^{-1}$) is the superficial velocity at the reactor inlet, \bar{u}_{int} ($m.s^{-1}$) is the interstitial velocity, Sc is the Schmidt number, Re_p is the Reynolds number at the pellet level and ρ_B ($kg.m^{-3}$) is the catalyst density in the reactor volume.

To simulate the reactor, a range of experimental points in high-pressure and supercritical conditions was considered. The operating conditions are presented in Table V.3. For supercritical conditions, only the points with CH_4 solvent are used. They were chosen because: (i) they have the highest diffusivity, (ii) they are at supercritical conditions at 303 K (conventional temperature of the reaction), (iii) the physical properties are the most distant to the C_3 cut feedstock and (iv) the experimental data obtained are larger than for other solvents.

Table V.3: Data range of experimental properties studied at high-pressure and supercritical conditions.

Variables	High-pressure (HP)		Supercritical (SC)	
T	303	K	303	K
P	120	bar	120	bar
Solvent CH_4	0	% mol	60	% mol
μ	$\sim 8.487 \times 10^{-5}$	Pa.s	$\sim 9.9 \times 10^{-5}$	Pa.s
ρ	~ 520	$kg.m^{-3}$	~ 260	$kg.m^{-3}$
$D_{i,m} = D_{i,e}$	$\sim 1.22 \times 10^{-8}$	$m^2.s^{-1}$	$\sim 5.49 \times 10^{-8}$	$m^2.s^{-1}$
$\tau_{L \text{ or } SC}^{-1}$	150 to 1400	h^{-1}	400 to 1900	h^{-1}
Reactor inlet concentration studied:				
$C_{MAPD,0}$	100 to 350	$mol.m^{-3}$	~ 100	$mol.m^{-3}$
$C_{Propane,0}$	120 to 400	$mol.m^{-3}$	~ 120	$mol.m^{-3}$
$C_{Propylene,0}$	3600 to 11600	$mol.m^{-3}$	~ 3600	$mol.m^{-3}$
Points evaluated				
Number	20		9	

In total, there are 20 points at HP and 9 points at SC, which will be used to estimate the kinetics parameters. Only the 303 K points were considered to simplify the model optimization. For modeling the temperature effect, more points are necessary between 303 and 353 K.

V.2.2 Kinetic parameters and reaction mechanisms

As mentioned (§IV.2), the oligomers produced cannot be quantified with the GC methodology used. However, it was shown that their production is low (§IV.2). The reaction conversion was only evaluated for a fresh catalyst (*i.e.*, the deactivation was closely monitored for a defined point) (§III.2.2). Therefore, in the present study, only MAPD and propylene hydrogenation are evaluated. The reaction scheme is detailed in Figure V.4

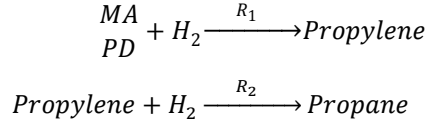


Figure V.4: Simplified reaction scheme proposed (§I.4.4).

In this study, the power law and the Langmuir-Hinshelwood/Hougen-Watson (LH-HW) models were proposed to describe the hydrogenation kinetics (Table I.9). These kinetic models were chosen because they are widely used in literature (Brandao et al., 2007; Samimi et al., 2015; Wu et al., 2011). The kinetic models presented were deduced from separated MAPD and propylene hydrogenation.

Table V.4: Kinetic models for the MAPD and the propylene hydrogenation. More mechanisms can be found in §I.4.4.

Type of model	Mechanistic scheme	Controlling step	Rate expression	Adapted from	Kinetic parameters
Power-law 1	<u>Main reaction:</u> A: $C_3H_4 + H_2 \rightarrow C_3H_6$ <u>Secondary reaction:</u> B: $C_3H_6 + H_2 \rightarrow C_3H_8$	--	$R_{MAPD} = k_1^* C_H^{n_1} C_{MAPD}^{n_2}$ $R_{PR} = k_2^* C_H^{n_3} C_{PR}^{n_4}$	(Fajardo 1996)	$k_1^*; k_2^*$ $n_1; n_2$ $n_3; n_4$
LH-HW 2	A: $H_2 + 2Z \rightleftharpoons 2HZ$ <u>Main reaction:</u> B: $C_3H_4 + Z \rightleftharpoons C_3H_4Z$ C: $C_3H_4Z + 2HZ \rightarrow C_3H_6Z + 2Z$ D: $C_3H_6Z \rightarrow C_3H_6 + Z$ <u>Secondary reaction:</u> E: $C_3H_6Z + 2HZ \rightarrow C_3H_8Z + 2Z$ F: $C_3H_8Z \rightarrow C_3H_8 + Z$	<u>Main reaction:</u> Surface reaction (C) <u>Secondary reaction:</u> Surface reaction (E)	$R_{MAPD} = \frac{k_1^* K_A C_H K_B C_{MAPD}}{(A)^3}$ $R_{PR} = \frac{k_2^* K_A C_H K_D C_{PR}}{(A)^3}$ $A = 1 + \sqrt{K_A C_H} + K_B C_{MAPD} + K_D C_{PR} + K_F C_{PA}$	(Brandao 2007)	$k_1^*; k_2^*$ $K_A; K_B$ $K_D; K_F$
LH-HW 3	A: $H_2 + 2Z \rightleftharpoons 2HZ$ <u>Main reaction:</u> B: $C_3H_4 + S \rightleftharpoons C_3H_4S$ C: $C_3H_4S + HZ \rightarrow C_3H_5S + Z$ D: $C_3H_5S + HZ \rightarrow C_3H_6S + Z$ E: $C_3H_6S \rightleftharpoons C_3H_6 + S$ <u>Secondary reaction:</u> F: $C_3H_6 + 2HZ \rightleftharpoons C_3H_8 + 2Z$	<u>Main reaction:</u> Surface reaction (C) <u>Secondary reaction:</u> Surface reaction (F)	$R_{MAPD} = \frac{k_1^* K_A K_B \sqrt{C_H} C_{MAPD}}{A}$ $R_{PR} = \frac{k_2^* K_A C_{PR} C_H}{A}$ $A = (1 + K_B C_{MAPD}) \times (1 + \sqrt{K_A C_H})^2$	(Brandao 2007)	$k_1^*; k_2^*$ $K_A; K_B$

For the kinetics models presented in Table I.9, the kinetic parameters (k_1^* and k_2^*), the reaction rate powers (n_1, \dots) and the adsorption constants (K_A, \dots) can be considered as decision variables. The total number of decision variables (or estimated parameters) is between 4 and 6.

V.2.3 Model the pilot reactor

Assumptions

The following assumptions were considered for the model construction:

Assumptions	Motivation
(1) Reactions occur on the catalyst surface or inside the metallic crust and not in the bulk phase.	The reaction does not occur without a catalyst.
(2) Temperature gradients inside the catalyst grains are not considered.	Helps simplifying the model, since temperature effect is not modeled.
(3) Radial dispersion is ignored.	There is no presence of radial dispersion in CFD simulations (§III.3.4).
(4) Catalyst deactivation is ignored.	A fresh catalyst is used during experiments (§III.2.2).
(5) The bulk has isothermal conditions.	The millifluidic reactor (1.4 mL) is inside an agitated thermal bath (15 L) (§III.2.2).
(6) The reactor operates at steady state.	Isothermal bath conditions (§III.2.2).
(7) The effective diffusion within the catalyst is equal to the diffusion in the bulk.	Experimental results obtained from DOSY-RMN (§III.2.3).
(8) The diffusion coefficients obtained by correlations and mixture roles are reliable.	Study performed by Sousa (2015) [internal report].

Mass balances and mass transfer

Mass balance for components in the bulk phase (1D model)

The reactor may be interpreted as a plug flow model with axial dispersion ($Pe_{ax} > 50$) (§III.3.4). Therefore, the mass balance for the components in the liquid or supercritical medium can be written as:

$$-D_{i,b} \frac{d^2(C_{i,b})}{dz^2} + \frac{d(C_{i,b}u_s)}{dz} = \underbrace{k_{i,ls}a_{ls}(C_{i,b} - C_{i,s})}_{\text{fluid-solid mass transfer}} \quad \text{Eq. V.1}$$

$$z = 0 \rightarrow C_{i,b} = C_{i,b}^0 \quad \text{Eq. V.2}$$

$$z = L_{\text{reactor (with catalyst)}} \rightarrow \left. \frac{dC_{i,b}}{dz} \right|_{\text{out}} = 0 \quad \text{Eq. V.3}$$

where i represents MAPD, propane, H_2 and propylene. D ($m^2 \cdot s^{-1}$) is the diffusivity coefficient, C ($\text{mol} \cdot m^{-3}$) is the concentration, $L_{\text{reactor (with catalyst)}}$ (m) is the length of the reactor filled with catalyst pellets, $k_{i,LS}$ ($m \cdot s^{-1}$) is the liquid-solid mass transfer coefficient. The subscripts b and s means bulk and solid surface, respectively.

Mass balance at the catalyst surface (1D model)

The fluid mass transport is related to the chemical reaction. It can be represented as:

$$\underbrace{k_{i,LS}a_{LS}(C_{i,b} - C_{i,s})}_{\text{fluid-solid mass transfer}} = m_{cat}.R_{i,s}^* \quad \text{Eq. V.4}$$

$$R_{i,s}^* = f(C_{i,s}; \text{kinetic parameters}) \quad \text{Eq. V.5}$$

$$z = 0 \rightarrow C_{i,s} = 0 \quad \text{Eq. V.6}$$

where $R_{i,s}^*$ (mol.kg⁻¹.m⁻³.s⁻¹) is the molar reaction rate for the heterogeneous catalysis in the particle, being related with the concentration inside the catalyst pellet ($C_{i,p}$).

To estimate $k_{i,LS}$, the correlation developed for the selected reactor at §III.3.5 was used.

Mass balance inside a catalyst spherical pellet (1D model)

For a spherical pellet the mass balance can be written as:

$$\frac{d\left(-r^2 D_{i,e} \frac{dC_{i,p}}{dr}\right)}{dr} + \alpha r^2 m_{cat}.R_{i,p}^* = 0 \quad \begin{cases} 0 < r < r_p \\ \alpha = 1 \forall r > \delta_{metal} \\ \alpha = 0 \forall < \delta_{metal} \end{cases} \quad \text{Eq. V.7}$$

$$r = 0 \rightarrow \frac{dC_i}{dr} = 0 \quad \text{Eq. V.8}$$

The r can change into a dimensionless variable ($\chi = r/r_p$). So, the equation can be reformulated to (at steady-state):

$$\frac{d\left(-\frac{\chi^2}{r_p^2} D_{i,e} \frac{dC_{i,p}}{d\chi}\right)}{d\chi} + \chi^2 m_{cat}.R_{i,p}^* = 0 \quad \begin{cases} 0 < \chi = r/r_p < 1 \\ \alpha = 1 \forall \chi > 1 - \delta_{metal}/r_p \\ \alpha = 0 \forall < 1 - \delta_{metal}/r_p \end{cases} \quad \text{Eq. V.9}$$

$$\chi = 0 \rightarrow \frac{dC_i}{d\chi} = 0 \quad \text{Eq. V.10}$$

where r (m) is radial position of the spherical pellet, r_p (m) is the particle radius and χ is the dimensionless variable for the position along the particle radius. Eq. V.9 (reformulated) will be used in Comsol[®].

Because the pellets are spherical, it is convenient to express the mass balance by Eq. V.9 rather than by Eq. V.7. These equations make it possible to represent a sphere by a 1D model and its evolution along the reactor (Figure V.5). They imply symmetry at the center of the pellet and only normal diffusion to the catalyst surface.

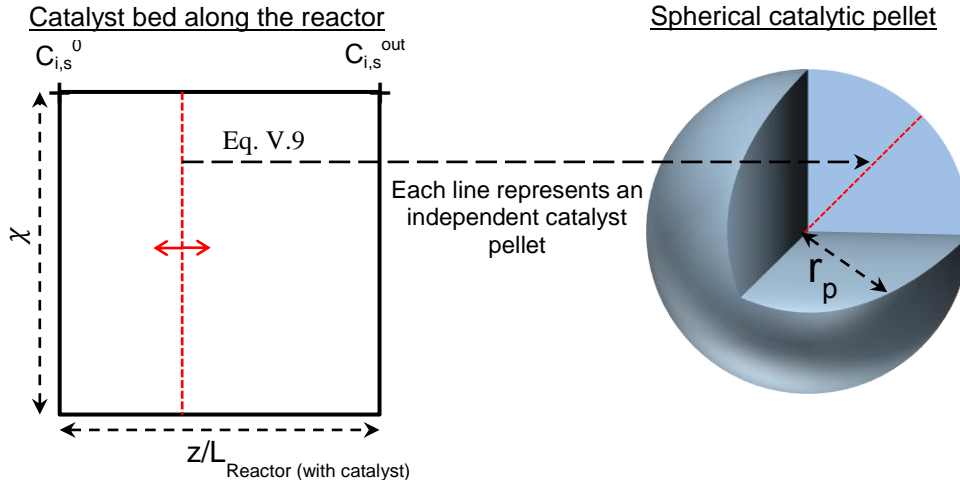


Figure V.5: Schematic of the 1D particle model along the reactor (2D geometry).

Numerical solver

The model's differential and algebraic equations were constructed using Comsol[®] multiphysics V5 environment. This software was chosen, because it can easily handle complex problems and the solution algorithms are time efficient and reliable.

The model was numerically solved at steady state using PARDISO and Newton nonlinear methods. Both methods are applied simultaneously because the model is defined in 1D (reactor) + 1D (spherical pellet). The Newton method is used to compute directly each solution individually in the reactor and in the catalyst bed. The PARDISO method is used to couple both solutions.

Although the model is fully defined (Eq. V.1 to Eq. V.9, boundary conditions and constants), the Comsol[®] can have problems achieving convergence. This is mainly related to high correlated parameters, such as $C_{i,b}$ and $C_{i,s}$. To avoid this problem the Eq. V.4 was replaced by Eq. V.11.

$$\underbrace{k_{i,LS} a_{LS} (C_{i,b} - C_{i,s})}_{\text{applied at 1D reactor}} = \underbrace{-\frac{D_{i,e}}{r_p} \frac{dC_{i,p}}{d\chi} \Big|_{\chi=1}}_{\text{applied at 1D pellet (surface)}} \quad \text{Eq. V.11}$$

Since Eq. V.11 is applied to the pellet surface, the mesh should be finely refined to ensure convergence. The pellet was divided in 500 (χ direction) and 120 (z direction) elements, having a dimensionless χ minimum element size of 4×10^{-7} at the layer near the catalyst surface. In dimensional units ($r = \chi \times r_p$), the minimum element size is $4 \times 10^{-7} r_p = 0.50$ nm. Moreover the mesh is more refined on the first 300 μm , which is the zone where the reaction occurs (thickness of the metallic crust) [element ratio: 0.5×10^{-5} ; distribution method: geometrical sequence].

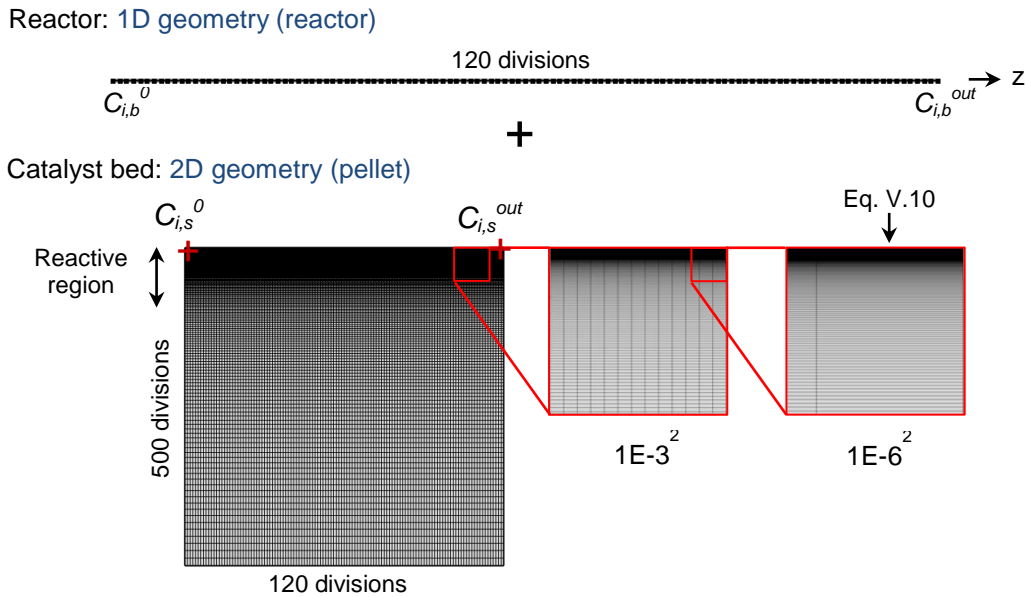


Figure V.6: Mesh for 1D geometry (reactor) and 2D geometry (pellet).

The refinement at the nanometer scale was required to calculate properly Eq. V.11 and avoid problems with convergence. If the reaction occurs at $10\ \mu\text{m}$, to correctly evaluate $\left. \frac{dc_{i,p}}{d\chi} \right|_{\chi=1}$, a minimum element size of $10\ \mu\text{m} / 1000 = 0.01\ \mu\text{m}$ (empirical role) will be necessary. As another example, if the reaction occurs below $0.5\ \mu\text{m}$, the minimum element size will be $0.0005\ \mu\text{m} = 0.5\ \text{nm}$. The minimum element size will be later discussed by studying (reactants) the concentrations gradients near the catalyst surface.

V.2.4 Optimization criteria

To estimate the optimal parameters, a simple and faster numerical method should be used. These methods can be found in Matlab[®] 2014a. To couple Matlab[®] 2014a and Comsol[®] 5, the LiveLink[®] software (incorporated with Comsol[®]) was used. For more information about it, please see “LiveLink for MatLab user guide” (2012) [example of the code: §V.1].

The optimization function selected was the `fminsearch`, which is generally referred as an unconstrained nonlinear optimization. The main advantage of `fminsearch` is the velocity when using a small number of variables (<5). The unconstrained limitation was bypassed by using a constrained objective goal function (later explained). Other limitations are that `fminsearch` gives many local minimums; therefore the initial guesses have to be carefully chosen. Figure V.7 shows the strategy followed to obtain good initials guesses. Kinetic parameters, reaction rate powers and adsorption constants are considered as decision variables.

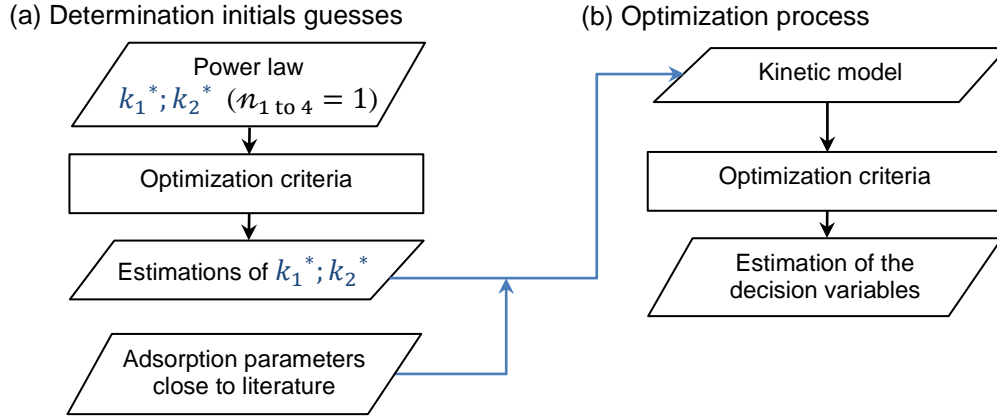


Figure V.7: Strategy developed to optimize the kinetic and adsorption parameters. (a) Determination of initial estimations. (b) Optimization process.

The objective function is defined as:

$$F_{obj} = \min \sum_{j=1}^{N_p} \underbrace{|C_j^{model} - C_j^{exp.}|}_{MAPD} + \underbrace{|C_j^{model} - C_j^{exp.}|}_{Propane} + \underbrace{|C_j^{model} - C_j^{exp.}|}_{Propene} + \underbrace{|C_j^{model} - C_j^{exp.}|}_{H_2} \quad \cap \text{restriction} \quad \text{Eq. V.12}$$

where N_p is the number of experimental points analyzed. The restriction is defined to avoid having negative or high values.

The objective function does not incorporate a penalty weight to be more representative of the experimental results for all the species. A similar expression was used by (Samimi et al., 2015).

V.3 Results

V.3.1 Interest of supercritical fluids in modeling

Objective: Check the fit sensibility for each dataset: high-pressure and supercritical.

Since supercritical fluids has different physical properties compared to high-pressure conditions (liquid only), such as diffusivity and density, it should be possible to reduce the confidence interval for the estimations obtained (more information on the system accessible). Two data series (high-pressure [liquid at 120 bar] and supercritical) were optimized independently to prove the approach. The kinetic method used was the power law with $n_{1\ to\ 4} = 1$ (§IV – experimental results seem to have linear behavior). Assuming these power rate values, there are only two decision variables to be evaluated (k_1^* and k_2^*), which make it easier to compare the values obtained for both data sets.

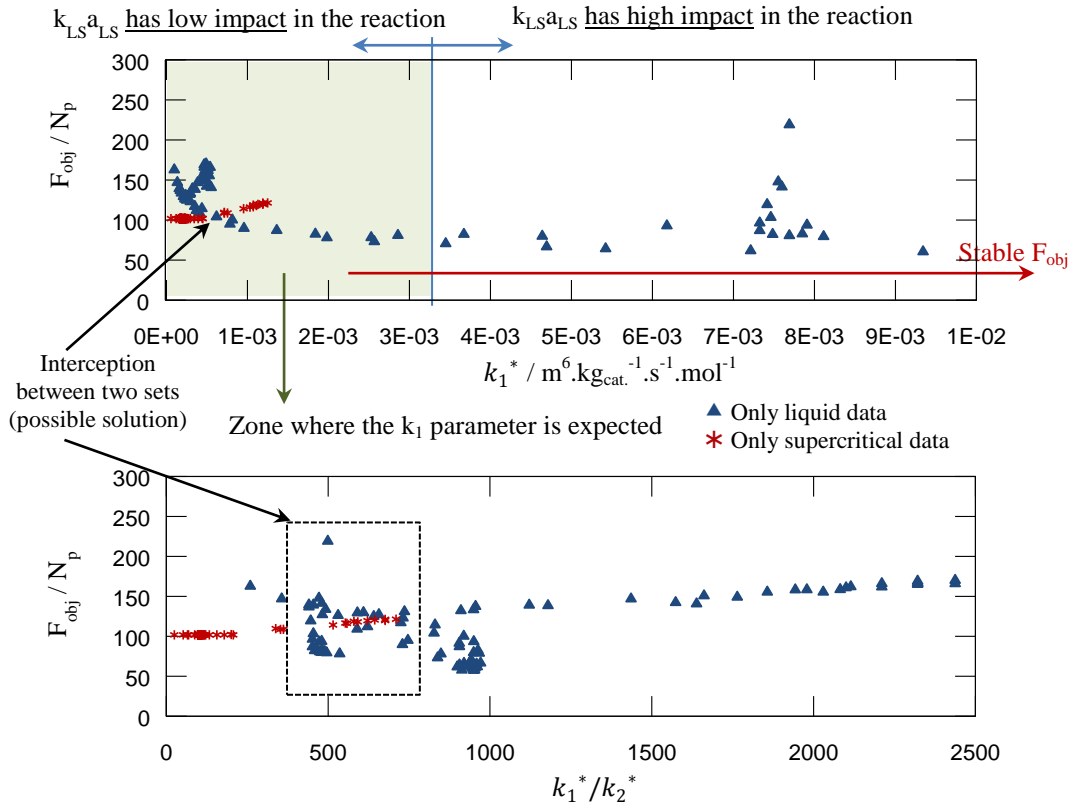


Figure V.8: Objective function values for the decision variables k_1^* and k_2^* . Kinetic model: power law (n_1 to $n_4=1$).

Through the experimental means (§IV), it is known that at high-pressure and supercritical conditions the reaction (at the reactor outlet) is not controlled by liquid-solid mass transfer for the points studied (*e.g.*, similar conversions for different residence times). Therefore, the optimization solutions in the zone where $k_{LS}a_{LS}$ impacts the reaction should be ignored (Figure V.8) [Eq. V.13 to Eq. V.15].

To define the zone where the $k_L a_{LS}$ should impact (high) the reaction, the following equation was used.

$$m_{cat}.R_{MAPD,s}^* = \underbrace{k_{MAPD,LS}a_{LS}(C_{i,b} - C_{i,s})}_{\text{applied at 1D reactor}} \approx \underbrace{k_{MAPD,LS}a_{LS}(C_{MAPD,b}^0 - 0)}_{\text{max. liquid-solid molar flow}} \quad \text{Eq. V.13}$$

where $R_{MAPD,p}$ is related with the kinetic model.

$$k_1^{*max} \approx \frac{\overbrace{k_{MAPD,LS}a_{LS}(C_{i,b}^0 - 0)}^{\text{max. liquid-solid molar flow}}}{\underbrace{C_{MAPD,b}^{out} C_{H2,b}^{out} \rho_B}_{\text{min. reaction}}} \quad \text{Eq. V.14}$$

The “minimum reaction” was considered to be a 98% conversion of MAPD and H₂ (no propane production). Eq. V.14 gives a guess of the maximum value of k_1^* that can be obtained. So, the following expression can be written as:

$$k_1^{*max} \approx \frac{k_{MAPD,L}a_{LS}(C_{MAPD,b}^0 - 0)}{C_{MAPD,b}^0 C_{H2,b}^0 \rho_B (1 - 0.98)^2} \approx 3.2 \times 10^{-3} \text{ m}^6 \cdot \text{kg}_{cat}^{-1} \cdot \text{s}^{-1} \cdot \text{mol}^{-1} \quad \text{Eq. V.15}$$

For a single optimization, such as the high-pressure (liquid state), the global minimum is difficult to evaluate (graphic with a U form) (Figure V.8), because the objective function crosses a zone where the $k_L a_{LS}$ has a high impact on the reaction. In other words, changes in kinetics do not affect the outlet conversion.

Regarding high-pressure and supercritical optimizations (Figure V.8), it can be noticed that the objective functions intercept each other for k_1^* and k_1^*/k_2^* out of the $k_L a_{LS}$ zone. The values obtained at the interception are $k_1^* = 4.08 \times 10^{-4} \text{ m}^6 \cdot \text{kg}_{\text{cat.}}^{-1} \cdot \text{s}^{-1} \cdot \text{mol}^{-1}$ and $k_1^*/k_2^* = 590$. These values are still not the global minimum, since the optimization function should be applied to a data set containing both experimental results (liquid and supercritical).

V.3.2 Liquid-solid mass transfer correlation verification (in the zone of low impact)

Before optimizing the different kinetic models, a study is performed to check the zone with low liquid-solid mass transfer impact.

Objective: Check the zone with low liquid-solid mass transfer impact.

In §III.3, a correlation was obtained for liquid-solid mass transfer by CFD means. In §IV.4.2 and §IV.5, it was seen that the $k_{LS} a_{LS}$ seems not to control the reaction for high-pressure and supercritical conditions (in the studied range). Even so, $k_{LS} a_{LS}$ must be carefully modeled, since the optimization function can give values to $k_{LS} a_{LS}$ that may have an impact on kinetics (k_1^* and k_2^*). Therefore, it should be possible to estimate the liquid-solid mass transfer by optimization.

The kinetic method used was the power law with $n_{1 \text{ to } 4}=1$, having two decision variables: k_1^* and k_2^* . The hydrodynamic correlation used was a general one, having two decision variables: c and n (Eq. V.15). In total four decision variables were optimized. For the optimization process, the experimental points used were at high-pressure (120 bar; liquid-phase) to analyze $Re_L < 200$. The results are shown in Table V.5 and in Figure V.9.

$$Sh = \frac{k_{LS} d_{\text{cat.}}}{D_{i,L}} = 2 + c \left(\frac{d_{\text{cat.}} \bar{u}_L \rho_L}{\mu_L} \right)^n \left(\frac{\mu_L}{\rho_L D_{i,L}} \right)^{1/3} \quad 0 < Re_L < 200 \quad \text{Eq. V.16}$$

Table V.5: Initial guesses and optimal results using only the liquid data set.

Initial guesses	Optimization results
$k_1^* = 1.00 \times 10^{-3}$ $\text{m}^6 \cdot \text{kg}_{\text{cat.}}^{-1} \cdot \text{s}^{-1} \cdot \text{mol}^{-1}$	$k_1^* = 1.12 \times 10^{-3}$ $\text{m}^6 \cdot \text{kg}_{\text{cat.}}^{-1} \cdot \text{s}^{-1} \cdot \text{mol}^{-1}$
$k_2^* = 1.00 \times 10^{-6}$ $\text{m}^6 \cdot \text{kg}_{\text{cat.}}^{-1} \cdot \text{s}^{-1} \cdot \text{mol}^{-1}$	$k_2^* = 1.77 \times 10^{-7}$ $\text{m}^6 \cdot \text{kg}_{\text{cat.}}^{-1} \cdot \text{s}^{-1} \cdot \text{mol}^{-1}$
$n = 0.50$	$n = 0.507$
$c = 1.80$	$c = 1.70$

Table V.5 shows that the c and n optimized are close to the initial guesses, which proves that $k_{LS} a_{LS}$ has low impact in the region defined (see Figure V.8a).

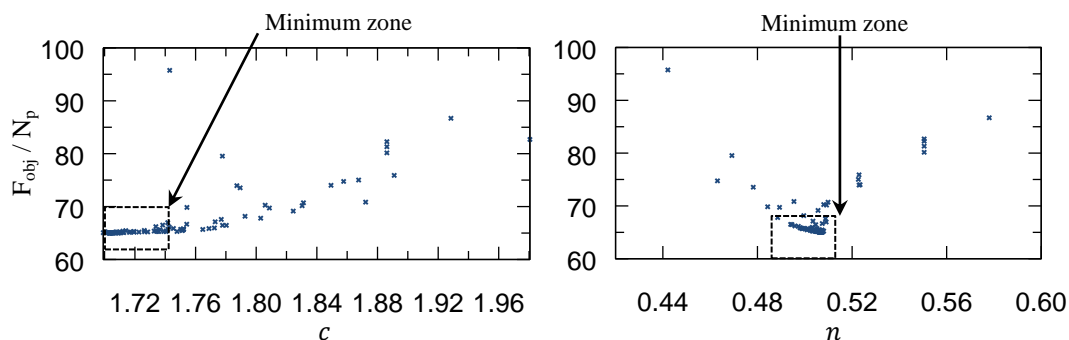


Figure V.9: Optimization of liquid-solid mass transfer parameters. k_1^* and k_2^* vary with n and c .

The kinetics parameters obtained (Table V.5) are not acquired with data at supercritical conditions. Therefore, they should not be used to simulate the reaction.

Regarding Figure V.10, the optimized correlation is close to the one obtained in CFD (§III.3.5). Since the $k_{LS}a_{LS}$ has low impact, the CFD correlation can be used with confidence for liquids and even for supercritical fluids.

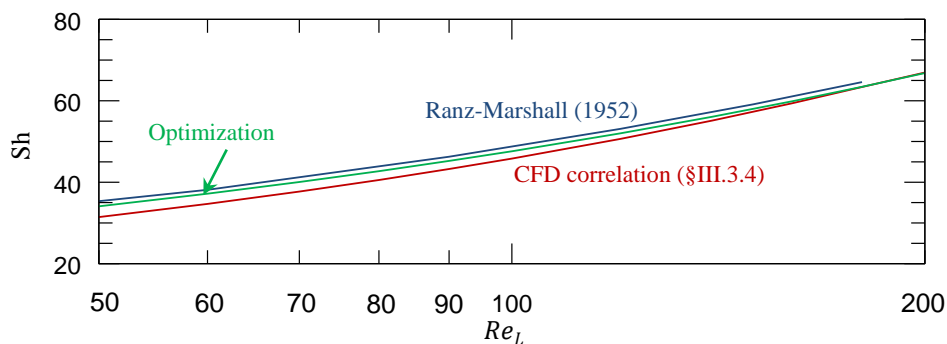


Figure V.10: Comparison of the Sh numbers obtained by different means.

V.3.3 Determination of the initial guesses

Objective: Estimate the kinetic parameters (k_1^* and k_2^*) from a simple kinetic model in order to apply it as first guesses on more complex kinetic models. This helps being closer to the global minimum.

Liquid and supercritical experimental data were optimized (together in one data set) with a power law kinetic model ($n_{1 \text{ to } 4}=1$ as constants) to obtain the initial guesses. The decision variables are k_1^* and k_2^* . Figure V.11 shows the intermediate optimization results obtained using the `fminsearch` function and two different initial guesses. For the initial guesses used (randomly), the minimization trend to the same minimum global point.

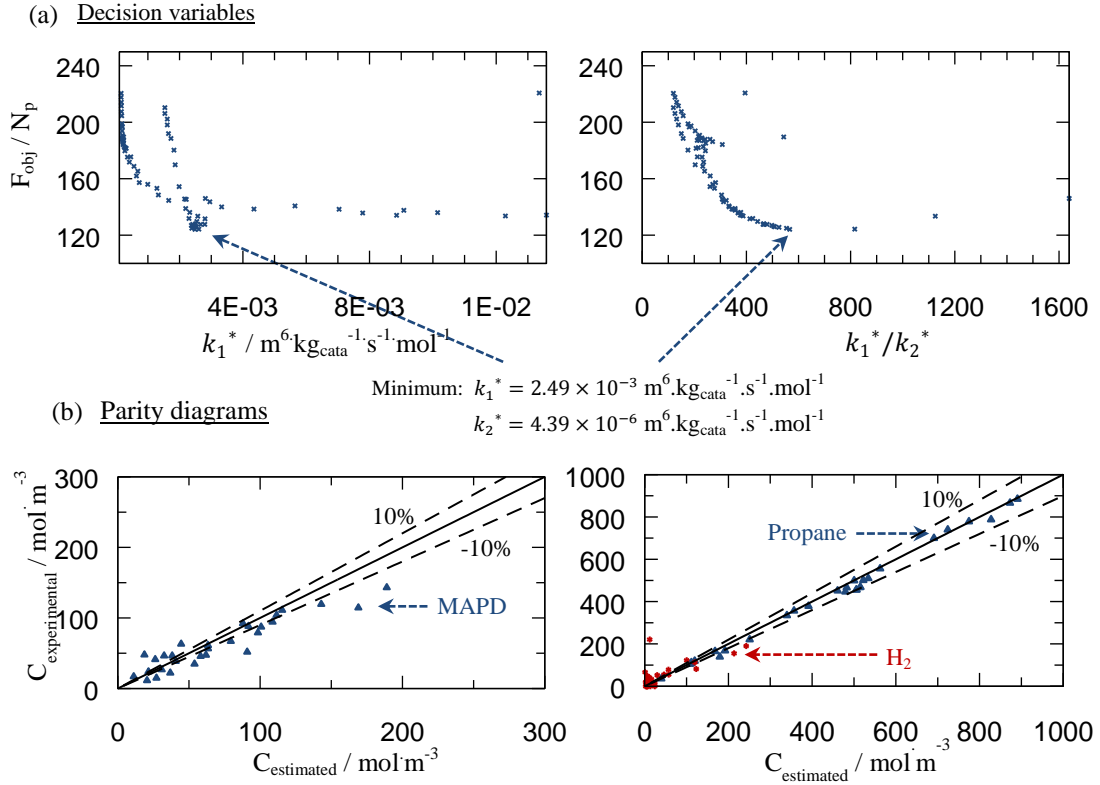


Figure V.11: (a) Objective function values for the decision variables k_1 and k_2 [data supercritical and liquid (120 bar)]. Kinetic model: power law (n_1 to $n_4=1$). (b) Parity diagrams for MAPD, propane and hydrogen.

The initial guesses (optimized values) to other kinetic models are:

$$k_1^* = 2.49 \times 10^{-3} \text{ m}^6 \cdot \text{kg}_{\text{cat.}}^{-1} \cdot \text{s}^{-1} \cdot \text{mol}^{-1} \text{ and } k_2^* = 4.39 \times 10^{-6} \text{ m}^6 \cdot \text{kg}_{\text{cat.}}^{-1} \cdot \text{s}^{-1} \cdot \text{mol}^{-1}$$

V.3.4 Optimization of kinetic models

In our approach, the power-law and the LH-HW kinetic models were studied. Regarding Table V.5, similar results for $F_{obj.}/N_p$ were obtained. The LH-HW kinetic models have proper $F_{obj.}/N_p$ results, but they are non-linear and they depend massively of the kinetic parameters used. To use the LH-HW models with confidence, it would have been necessary to experimentally obtain the adsorption parameters. Since we did not have access to the adsorption values, for simplicity reasons, the power-law kinetic model was selected. Similar model was suggested by Fajardo et al. (1996) after comparing different kinetic models. The power-law 2 model has similar results to power-law 1, therefore power-law 1 will be used, since it needs less computing time.

Table V.6: Kinetic models, objective function and optimization results for a data set with liquid (120 bar) and supercritical conditions (experiments). The green is the chosen kinetic model.

Kinetic model	Kinetic parameters	Fobj/N _p	Optimization results
Power-law 1	k_1^* ; k_2^* ; $n_{1\text{ to }4} = 1$	120	$k_1^* = 2.49 \times 10^{-3}$ $k_2^* = 4.39 \times 10^{-6}$
Power-law 2	k_1^* ; k_2^* ; n_1 ; n_2 ; n_3 ; n_4	110	$k_1^* = 1.84 \times 10^{-3}$ $k_2^* = 2.13 \times 10^{-6}$ $n_1 = 1.85$ $n_2 = 1.42$ $n_3 = 1.36$ $n_4 = 1.09$
LH-HW 2	k_1^* ; k_2^* ; K_A ; K_B ; K_D ; K_F	192	$k_1^* = 2.11 \times 10^{-3}$ $k_2^* = 6.18 \times 10^{-6}$ $K_A = 1.02 \times 10^{-3}$ $K_B = 1.11 \times 10^{-3}$ $K_D = 1.31 \times 10^{-3}$ $K_F = 2.54 \times 10^{-6}$
LH-HW 3	k_1^* ; k_2^* ; K_A ; K_D	619	$k_1^* = 3.44 \times 10^{-3}$ $k_2^* = 6.08 \times 10^{-6}$ $K_A = 9.85 \times 10^{-2}$ $K_B = 1.09 \times 10^{-1}$

V.3.5 Model vs experiments: space velocity and H₂/MAPD ratio (HP)

For the experimental studies carried out at high-pressure conditions, the dimensionless number $Da^{mod.}$ was proposed to define where the reaction reaches its maximal conversion. In other words, if $Da^{mod.} < 1$, the reaction does not have sufficient residence time (\rightarrow needs lower space velocity). By experimental means, a zone was defined for $Da^{mod.} < 1$ (§IV.4.6). In this subsection, points in each side of the zone will be checked and detailed by modeling results.

Conditions: 303 K, 120 bar (no solvent) and catalyst mass of 0.6 g (catalyst W).

Feedstock: MAPD (3.02 mol% [375 mol·m⁻³]) and Propane (3.29 mol% [408 mol·m⁻³]).

Observations

Figure IV.23 shows the influence of the space velocity (h⁻¹) coupled with two H₂/MAPD ratios (1 and 2). The lines represent the model and the points represent the experiments.

MAPD: There is a slight deviation between model (lines) and the experimental points, being higher for high space velocities. Nevertheless, the results clearly follow the same trend. Regarding the model, from 400 to 15 h⁻¹, the MAPD conversion is stable. From 12800 to 400 h⁻¹, there is the impact of the high space velocity (low residence time).

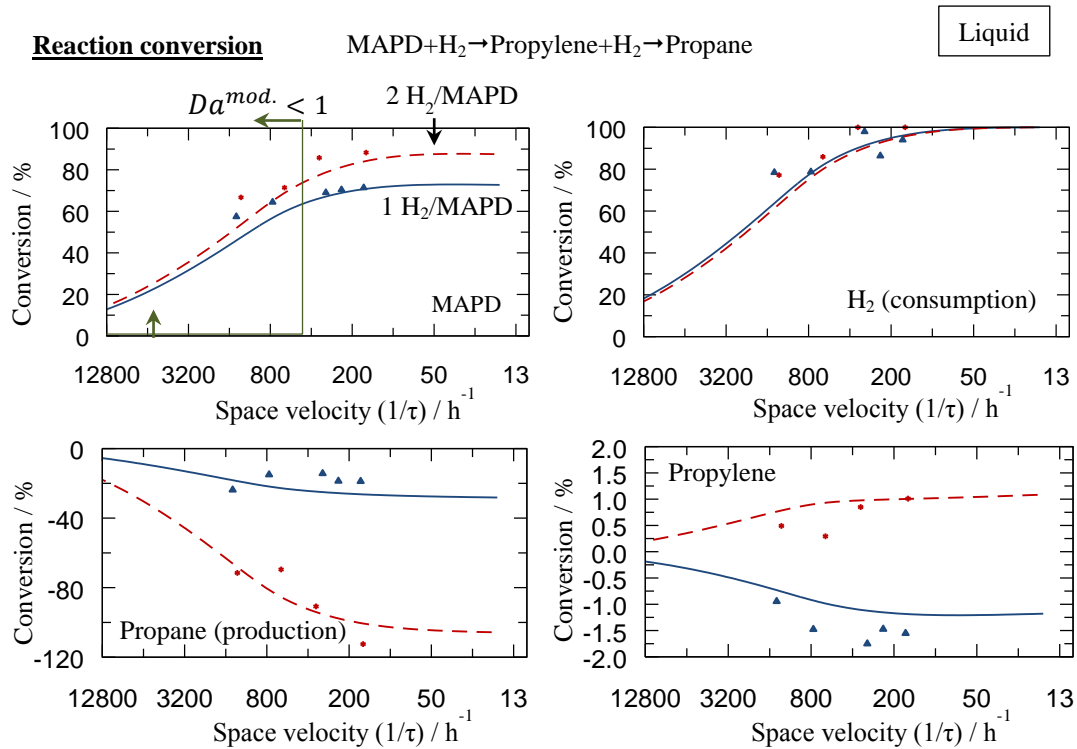


Figure V-12: Selective hydrogenation at 120bar, 303 K and 70 spheres. The plots are as a function of the space velocity and the H₂/MAPD ratio. Lines: model results; Points: experimental results. **Blue: 1 H₂/MAPD ratio. **Red**: 2 H₂/MAPD ratio.**

Propane and propylene: The conversions (propane and propylene) obtained by model and experimental means are close for both species. The model seems to follow the same trend as the experimental points.

Hydrogen: There is a small deviation between the model and the experimental points, due to the deviation in MAPD. But even so, the results seem to follow the same trend. From 100 to 10 h⁻¹ the H₂ is totally converted.

Result discussion

From 12800 to 400 h⁻¹ the zone $Da^{mod.} < 1$ can be defined, since the conversion varies with the space velocity. The model results are according to the ones obtained experimentally, since $Da^{mod.} = 1$ is defined in the same location ($1/\tau \approx 400$ h⁻¹ [space velocity]: 4.3% deviation to the maximum conversion) (§IV.4.3).

From 400 to 15 h⁻¹, the conversion of all species is constant ($Da^{mod.} > 1$). To explain it, the evolutions of the calculated bulk conversions were studied for a 1 H₂/MAPD ratio. By analyzing Figure V-13, the conversion on the bulk reaches the maximum before the reactor outlet (full lines).

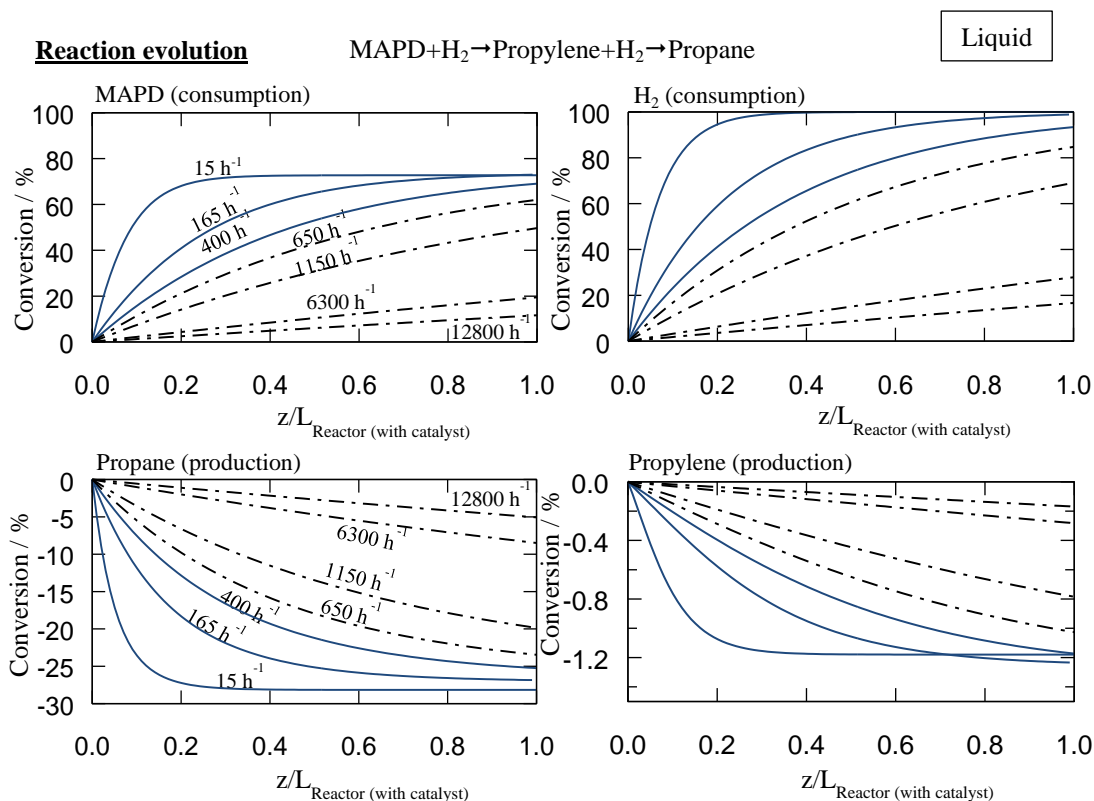


Figure V-13: Evolution of the selective hydrogenation conversion with the length (dimensionless) of the reactor. The model results were obtained at 120bar, 303 K, 1 H₂/MAPD ratio and 70 spheres. Full lines: model with $Da^{mod.} < 1$; Dotted lines: model with $Da^{mod.} > 1$.

Reactive region

In our approach, it is also possible to analyze the hydrogen concentration inside the catalyst pellet in the reactive crust (25% of the catalyst volume covered with metal). For this study, the conditions used were 165 h⁻¹ (space velocity) and a 1 H₂/MAPD ratio (120 bar without solvent). This condition was chosen because it was the smallest space velocity obtained experimentally.

Figure V-14a shows the contours of the H₂ concentration inside a fraction of the catalyst. It can be noticed that only a small percentage of the reactive surface is used. If we considered that only the metal surface with 95% of the H₂ initial concentration is indispensable, only 12 and 15% of the total thickness are being used at the beginning of the reactor (Figure V-14b), for 1 and 2 H₂/MAPD ratio. After it, even less percentage of the metal crust is used.

The results seem to show a very low catalyst efficiency (diffusional regime), which confirms the results obtained experimentally (§IV.6). It will be interesting to optimize (reduction) the thickness of the metal crust.

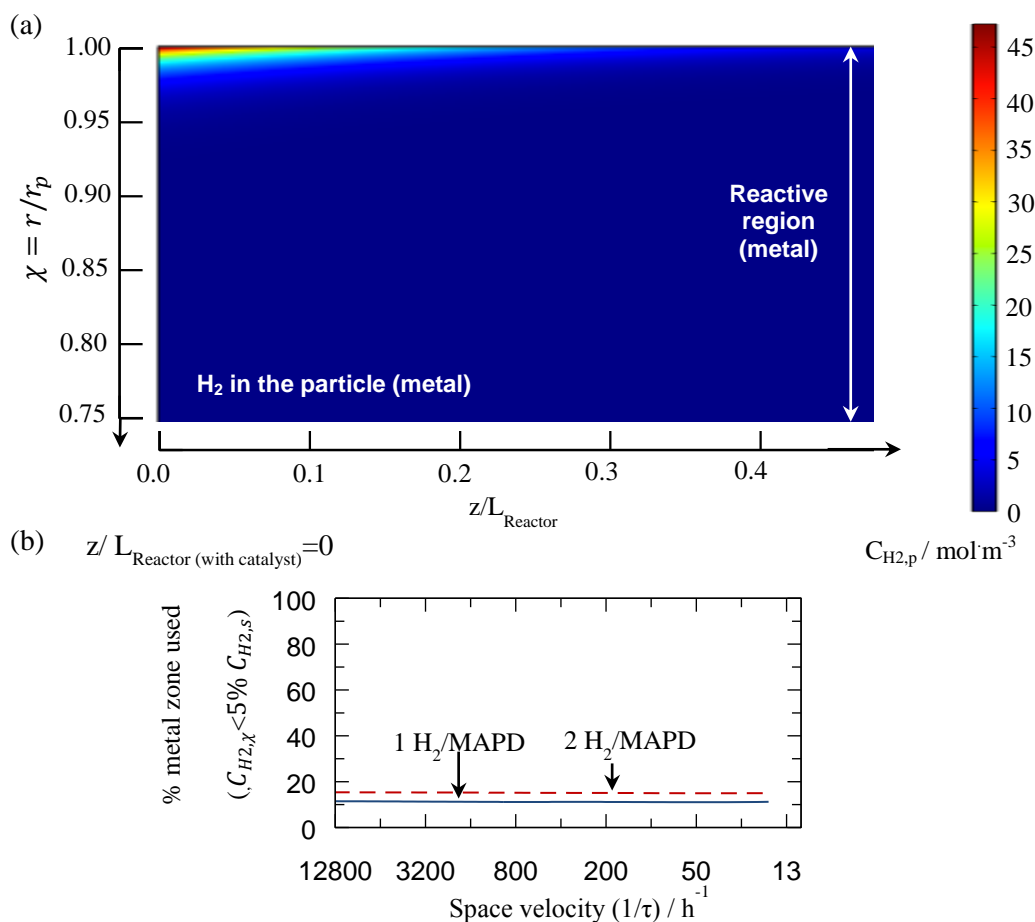
Intragranular analysis


Figure V-14: Selective hydrogenation at 165 h^{-1} (space velocity), 120bar, 303 K and 1 H_2/MAPD ratio. (a) Modeled evolution of H_2 concentration inside the particle. (b) % of the reactive zone used to perform the conversion of 95% of the H_2 initial concentration.

Conclusions

It is possible to conclude that:

4. The simplified model power-law 1 has acceptable deviations to the experimental results. Above all, despite these deviations, it has the same trend behavior as the experimental points;
5. The zone experimentally defined for $Da^{mod.} < 1$ is also spotted using the model;
6. Only a small part of the reactive catalyst crust is used at the beginning of the reactor (10 to 15% at 120 bar and 303 K). After it, even less.

V.3.6 Model vs experiments: high-pressure and supercritical conditions

In the previous chapter (§IV), it was proposed an estimation of the gain in the effectiveness factor between supercritical fluids and liquids at high-pressure ($\eta_{SC} > 4.8 \eta_{HP}$). In this subsection, this value will be confronted with the one estimated by the model (Table V.7). Moreover, the model results will be compared to the experimental ones at supercritical conditions.

Conditions: 303 K, 120 bar and 0.6 g of catalyst W.

Table V.7: Comparison of conditions for SC and HP.

Conditions	Mixture characteristics		Working zone	
	Solvent / mol%	$C_{MAPD, reactive} / mol.m^{-3}$	τ^{-1} / h^{-1}	$Da^{mod.}$
Supercritical (✱)	60 % CH ₄	~100	900	>1
High-pressure (▲)	No solvent	~350	160	>1

Although the experimental conditions are different, both cases can be compared because there are in a zone where $Da^{mod.} > 1$ (no impact of the reaction time).

Objective: The conditions between supercritical and high-pressure are different (space velocity and concentration). However, the model should provide a reliable (low uncertainty) fit of the experimental data.

Observations

Figure V-15 shows the influence of the H₂/MAPD ratio applied with different conditions (Table V.7) for liquid (HP) and supercritical (SC) conditions. The lines represent the model and the points represent the experiments.

MAPD: There is a small deviation between the model (lines) and the experimental points (Figure V-15a). For liquid and supercritical conditions, from a 0.5 to 3.0 H₂/MAPD ratio the MAPD conversion slightly increases.

Propane and propylene: The propane and propylene conversions obtained with the model and the experimental means are close for both species for liquid (Figure V-15 b,d). For supercritical conditions at a 1 H₂/MAPD ratio, the model is close to the experimental results (Figure V-15 b,d). However, when increasing the H₂/MAPD ratio in SC, small deviations appears. This might be related to the kinetic model used (power-law 1) and the uncertainty (~3%) in the diffusivity coefficients for supercritical conditions.

Hydrogen: For SC and HP, the hydrogen is almost fully converted (experimentally), which occurs in the model at the same location.

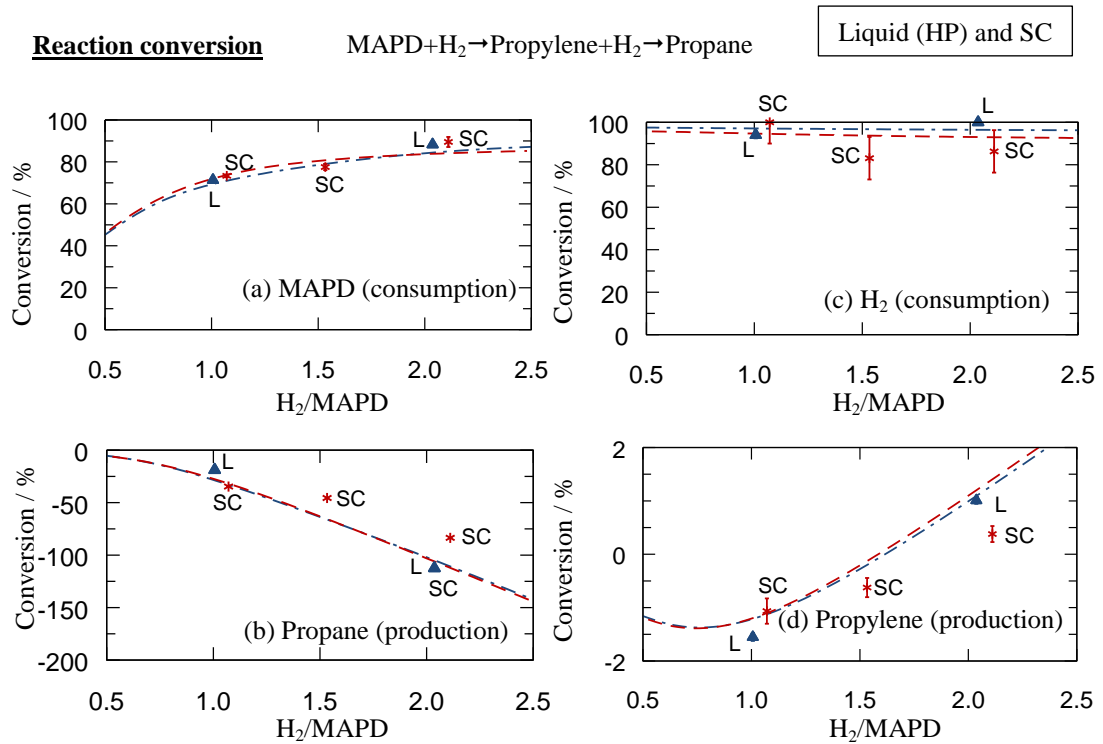


Figure V-15: Selective hydrogenation at 120bar, 303 K and 70 spheres. Species conversion as a function of the H₂/MAPD ratio. Lines: model results (-.- liquid --supercritical); Points: experimental results.

Effectiveness factor: Supercritical fluids have higher effectiveness factor than high-pressure for MAPD and H₂ (Figure V-16 a,b), being 3 to 6 times higher.

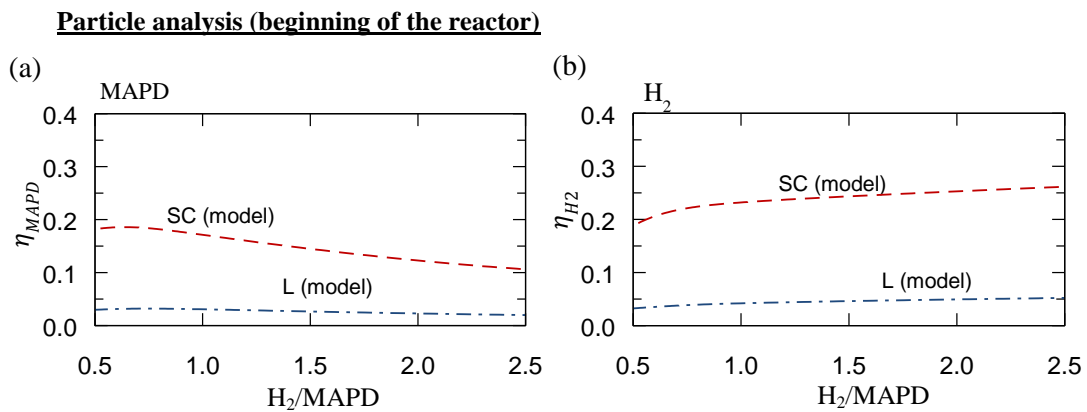


Figure V-16: Selective hydrogenation at 120bar, 303 K and 70 spheres. Effectiveness factors for MAPD (a) and H₂ (b) as a function of the H₂/MAPD ratio. Lines: model results (-.- liquid --supercritical).

Determination of the effectiveness factor

For the model, the effectiveness factor is defined as:

$$\eta_i = \frac{\text{global rate}}{\text{intrinsic rate}} = \frac{1}{V_p} \frac{\iiint_{V_p} R(C_{i,p}, T) dV_p}{R(C_{i,s}, T_S)} \quad \text{Eq. V.17}$$

where V_p (m^3) is the particle volume, $C_{i,s}$ ($\text{mol}\cdot\text{m}^{-3}$) is the concentration of a i species on the catalyst surface and η is the effectiveness factor.

By transforming the integral coordinates to spherical and applying $\chi = r/R_p$, it is possible to write the effectiveness factor for the reactive zone (metal) [$0.75 < \chi < 1$] as:

$$\eta_i = \frac{1}{\int_{0.75}^1 \chi^2 d(\chi)} \frac{\int_{0.75}^1 R(C_{i,p}, T) \chi^2 d(\chi)}{R(C_{i,s}, T_S)} \quad \text{Eq. V.18}$$

The model was applied to a diluted C_3 cut mixture ($100 \text{ mol}_{\text{MAPD}}\cdot\text{m}^{-3}$) [3 times diluted] at a space velocity of 900 h^{-1} .

Conclusions

Regarding Figure V-15, the model and the experimental data for high-pressure (liquid) and supercritical conditions seem to be close. Therefore, the model can be considered as reliable. This happens even though the points have different conditions, such as concentration, diffusivity and space velocity. According to the model, there is an increase of the effectiveness factor up to 6 times higher than liquid (HP) [similar to the results experimentally obtained in §IV.6].

V.4 Conclusions

The MAPD hydrogenation was modeled using a plug flow reactor with axial dispersion and intragranular diffusion. The model was constructed using unconventional conditions (high-pressure and supercritical) to approach the catalyst intrinsic kinetics parameters. Different kinetic mechanisms were tested, such as power law and LH-HW. **The power law with only two decision variables has “good” fitting results.** It was chosen to simulate the MAPD hydrogenation due to its parametric simplicity (only two decision variables).

The results obtained with the model corroborate the conclusions obtained in the previous chapter for high-pressure (liquid at 120 bar) and supercritical fluids (§IV).

It was shown that supercritical and high-pressure data combined are an interesting tool to study kinetics (liquid at 120 bar). **Having two fluids with different effectiveness factors helps increasing the sensitivity of the intrinsic kinetics parameters, giving reliable estimates, which otherwise will not be possible.** If classical (20 bar) and/or high-pressure (120 bar: liquid) conditions were used, the diffusivity of the mixture would be similar. In that case, effectiveness factor will remain similar and the intrinsic kinetics will not be possible to

be determined. For this reason supercritical conditions could be used to explore and understand kinetics in fast reactive systems.

For the first time it was possible to access the intrinsic kinetics parameters with dense fluid studies. With the estimation of the intrinsic parameters, the second objective of this thesis was achieved.

General conclusion and perspectives

The goal of this thesis was to develop an innovative approach to perform catalyst screening for fast multiphase heterogeneous reactions at pilot-scale. To minimize the influence of mass transfer rates over the apparent reaction kinetics, high pressure and supercritical conditions were applied in a single pellet string reactor, making it possible to operate with a homogeneous phase and to improve the reactants diffusion. The methodologies studied should be applied when the reaction occurs in a matter of seconds, and when the overall reaction rate depends on the mass transfer rate.

The experimental evaluation and understanding of a catalyst is a complex procedure. In the recent years, IFP Energies Nouvelles has developed single string pellet reactors to better understand the behavior of catalysts for fast reactions and to improve them. This pilot reactor technology helps reducing the variability of the results, due to the reduction of the random packing of the catalyst. Despite these improvements, the reaction kinetics are often limited by interphase (gas-liquid), external and/or internal mass-transfer rates. They may lead to an inaccurate comparison between catalysts. Therefore, new approaches are required. This is the reason why this PhD thesis was mainly devoted to the study of the MAPD hydrogenation under high pressure and supercritical conditions.

To reach supercritical conditions, the **operating parameters were studied and optimized**, particularly the choice of the solvent, the temperature and the pressure adapted to the C₃ cut hydrogenation. The goal was to locate and to determine the critical coordinates (pressure and temperature) for multicomponent mixtures. The strategy adopted was to develop an innovative tool based on “**design of experiments**” (**using a ternary diagram**) and **microfluidics approaches**. The construction and validation of the **ternary tool** were based on the PPR78 equation of state. To prove its accuracy, this equation was tested for 255 hydrocarbon multicomponent mixtures, providing more reliable results than other EOS. By applying the **ternary diagram tool**, it was possible to determine the optimal number of experimental points required (“design of experiments”). To acquire experimental data, a **microfluidic-based approach** was constructed and validated to determine the P–T phase diagrams of multicomponent mixtures. This method couples an on-chip optical detection of both bubble and dew points with a so-called dynamic stop-flow mode, for fast screening of the operating parameters (temperature, pressure and composition). We demonstrate that this strategy can provide accurate experimental thermodynamic data for multicomponent mixtures, which were successfully compared to model and literature data (e.g. CO₂+cyclohexane, ...). Additionally, this **microfluidic approach** can work very efficiently (typically 5 times faster than conventional HPOC methods).

After the construction and validation of the tools (“design of experiments”+ microfluidics), the critical coordinates and the “design of experiments” were evaluated for the mixture of interest: C₃ cut + H₂ + solvent (CO₂, CH₄ and ethane). The experimental and predicted points

for the C₃ cut were obtained with excellent agreement between both approaches for CO₂ and ethane. The CH₄ proves to be the best solvent to achieve supercritical conditions with C₃ cut, since it has larger working range inside the process restrictions conditions (maximum temperature).

Afterward, the reactor was characterized for **random particle packing (experimental)**, **hydrodynamic** and **liquid-solid mass transfer (simulation)**. The **particle packing characterization** shows that with the reactor designed and the catalyst distribution, it is possible to have small random packing, since 72% of the particle follows 70° and 80° arrangements (organization inside the reactor), which is enough to know how to construct the numerical geometry. A **CFD hydrodynamic** study was performed to investigate the flow inside the reactor. The influence of the Reynolds number was tested for the residence time distribution. It was shown that the fluid has a serpentine flow pattern for the zigzag particle arrangement used. For the residence time distribution studied, it was considered acceptable to model the reactor as a plug flow with low axial dispersion ($Re_L=20$; $Pe_{ax}\approx 70$). This model will allow building a reactor model. A numerical study was performed to investigate the **liquid-solid mass transfer** in the single pellet reactor used. It was shown that the film theory might be assumed, and an average mass transfer coefficient could be used. A mass transfer correlation was proposed for the working zone. The results are close to the Ranz and Marshall (1952) correlation.

After this characterization of the pilot, the MAPD hydrogenation was investigated in conventional (gas-liquid-solid) and unconventional conditions (high-pressure and supercritical). For each condition, the influence (in conversion) of several parameters were studied, such as the space velocity (inverse of residence time) and the H₂/MAPD ratio. Based on the parameters and conditions evaluated, **a map of the space velocity vs the H₂/MAPD ratio was built** for conventional, high-pressure and supercritical conditions. In these maps, the information about selectivity was analyzed.

The conventional conditions have several defined zones: (i) $\psi_{GL} < 1$ (not enough time to achieve full gas-liquid mass transfer → the reaction is slowdown), (ii) $Da^{mod.} < 1$ (not enough residence time → the reaction is slowdown) and (iii) zone where the selectivity is controlled by the H₂ molar concentration flow rate. It was suggested that the H₂ molar concentration flow was inferior to an industrial reactor, working in high and low interaction regimes (bubble and trickle flow, respectively). However, conventional conditions are close to an industrial reactor in medium interaction regime (pulse flow) when working at WHSV of 200 h⁻¹ (at pilot scale).

The high-pressure conditions have two defined zones: (i) $Da^{mod.} < 1$ (not enough residence time → the reaction is slowdown) and (ii) $Da^{mod.} > 1$. For these conditions, the MAPD molar conc. flow is close to the industrial reactor with medium (pulse flow) and high (bubble flow) interactions, depending of the WHSV (or space velocity) used. For bubble flow, a WHSV of 150 h⁻¹ (or space velocity of 230 h⁻¹) should be used. At HP conditions, there are no gas-liquid (by definition) and liquid-solid mass transfer is negligible. These

conditions can be adapted to perform catalyst screening, because the selectivity does not change with the space velocity and there are no external mass transfer limitations.

The supercritical conditions also have two defined zones: (i) $Da^{mod.} < 1$ (not enough residence time \rightarrow the reaction is slowdown) and (ii) $Da^{mod.} > 1$. For SC conditions, the reaction rate is higher (4.8 times) than in high-pressure conditions, without changes in the MAPD and propane conversions. This happens due to higher diffusivity in supercritical medium (up to 5 times higher than HP conditions). Thanks to this higher diffusivity, these conditions are also adapted to perform catalyst screening and intragranular studies. Moreover, it allows having experimental data closer to the intrinsic kinetics ($\eta_{SC} > 4.8 \eta_{HP}$).

With the experimental results at high-pressure and supercritical conditions, the external mass transfer limitations are negligible. In other words, the catalyst has only intragranular mass transfer limitations. Therefore, the primary objective of this thesis was achieved, which was to “define the best conditions to perform catalyst screening”.

Finally, the experiments at high-pressure and supercritical conditions were modeled together to **estimate the intrinsic kinetics parameters**. The MAPD hydrogenation was modeled using a plug flow reactor with axial dispersion and intragranular diffusion. Different kinetic mechanisms were tested, such as power law and LH-HW. The power law with only two decision variables has the best fitting results. The results obtained with the model corroborate the conclusions obtained in the previous chapter for high-pressure (liquid at 120 bar) and supercritical conditions (conversions zones, ratio of η_{SC}/η_{HP} , ...). It was shown that the combination of supercritical and high-pressure data is an interesting tool to study kinetics (liquid at 120 bar). Indeed, having two fluids with different effectiveness factors helps increasing the sensitivity of the intrinsic kinetics parameters, giving reliable estimations, which otherwise will not be accessible. For the first time (at IFPEN) it was possible to have intrinsic kinetics parameters with dense fluid studies for the C₃ cut hydrogenation.

With the estimation of the intrinsic kinetic parameters, the second objective of this thesis was achieved. By achieving the first and second objectives, the future comparison between catalysts will be improved and it will be possible to estimate intrinsic kinetics parameters.

To complete the study started with this thesis, several perspectives can be suggested. To improve the kinetic model proposed, it will be interesting to obtain the adsorption parameters (reactant species and products) by experimental means, which are present in the Langmuir-based **kinetic** models. Also, to improve the model, it will be interesting to study **diffusivity** for high-pressure and supercritical conditions using an experimental set-up based on microfluidics.

This thesis also opens space to other studies. The methodology developed should be applied to other catalysts, allowing to study the intrinsic catalyst performance (chemical level) in relation to the catalyst composition and preparation. As an example, with the methodology proposed, it should be possible to study the effect of the metal thickness (active phase),

particularly the thickness of the catalyst crust and the Pd concentration profile inside the grain. Finally, the methodology (high-pressure and supercritical) proposed in this thesis should be applied to other reactions systems, such as hydrogenation of C₂ and C₄. For fast reactions where the supercritical fluids cannot be used (high critical temperature), the use of HP conditions and HP with a solvent (to improve diffusivity) is suggested.

Notation and glossary

Acronym list

AARD	average absolute relative deviation
C	critical
CCM	constant capacitance
CFD	computational fluid dynamics
CL	critical line
CP	critical point
CYC	cyclohexane
DLM	diffuse layer
EOS	equation of state
FID	flame ionization detector
FSCC	fused silica capillary capsule
GC	gas chromatography
HP	high-pressure
HPOC	high-pressure optical cell
HS	hard sphere
HSDM	homogeneous surface diffusion model
HSDM	homogeneous surface diffusion model
L	liquid phase
LCEP	lower critical end point
LH	Langmuir-Hinshelwood
LH-HW	Langmuir-Hinshelwood-Hougen-Watson
LSM	Liu-Silva-Macedo
LV	liquid vapor
MA	methyl-acetylene
MAPD	methyl-acetylene and propadiene
MCB	maxcondenbar
MCT	maxcondentherm
PA	propane
PD	propadiene
Pe	Peclet number
PIV	particle image velocimetry
PPR78	predictive Peng-Robinson 78
PR	propylene
PR78	Peng-Robinson 78

Notation and glossary

PRSV-2	Peng-Robinson- Stryjek-Vera 2
PVT	pressure volume temperature
RK	Redlich-Kwong
RTD	residence time distribution
SAFT	statistical associating fluid theory
SC	supercritical (condition)
SCF	supercritical fluid
SPHCT	simplified perturbed hard chain theory
SRK	Soave-Redlich- Kwong
TLM	triple layer
TP	triple point
UCEP	upper critical end point
V	vapor phase
VLE	vapor liquid equilibrium
VTPR	volume-translated-peng-robinson

Latin letters

a	effective parameter (EOS)	$\text{bar}\cdot\text{m}^6\cdot\text{mol}^{-2}$
a_{GL}	gas-liquid specific area	$\text{m}^2\cdot\text{m}^{-3}_{\text{gas}}$
a_{GLS}	global (gas-liquid-solid) specific area	$\text{m}^2\cdot\text{m}^{-3}_{\text{gas}}$
a_{GS}	gas-solid specific area	$\text{m}^2\cdot\text{m}^{-3}$
a_{LS}	liquid-solid specific area	$\text{m}^2\cdot\text{m}^{-3}$
a_s	specific surface area of the catalyst	m^{-1}
a_T	adsorptive potential constant	$\text{mol}\cdot\text{m}^{-3}$
A	Helmholtz energy	$\text{J}\cdot\text{mol}^{-1}$
A_p	particle superficial area	m^2
A_z	particle superficial area varying with z	m^2
A_{peaks}	Area of the chromatogram's peaks	u.
$A_{reactor}$	reactor circular section area	m^2 or mm^2
$A_{relative}$	relative area (applied to chromatogram's peaks)	-
b	effective parameter	$\text{mol}\cdot\text{m}^{-3}$
c	parameter to be optimized	-
C_p	molar concentration inside the particle	$\text{mol}\cdot\text{m}^{-3}$
C_s	molar concentration at the catalyst surface	$\text{mol}\cdot\text{m}^{-3}$
C	molar concentration on the fluid analyzed	$\text{mol}\cdot\text{m}^{-3}$
C_{total}	fluid total molar concentration	$\text{mol}\cdot\text{m}^{-3}$

Notation and glossary

C_b^*	bulk (flux) concentration (i.e. bulk concentration based on the molar flux equation)	$\text{mol}\cdot\text{m}^{-3}$
C_s^*	particle surface (flux) concentration	$\text{mol}\cdot\text{m}^{-3}$
$C_{\theta,b}^*$	bulk (flux) concentration at the angle range investigated	$\text{mol}\cdot\text{m}^{-3}$
$C_{\theta,s}^*$	particle (flux) concentration at the angle range investigated	$\text{mol}\cdot\text{m}^{-3}$
C^*	local (flux) concentration	$\text{mol}\cdot\text{m}^{-3}$
\mathbf{d}	matrix of the distance between points in ternary diagram	-
d_h	hydraulic diameter	m
d_p	particle diameter	m
d_{porous}	mean porous diameter	m
$d_{reactor}$	reactor diameter	m or mm
\tilde{D}	time derivative	s^{-1}
D_{ax}	axial dispersion	$\text{m}^2\cdot\text{s}^{-1}$
D (or D_b)	diffusion coefficient in the fluid (or in the bulk)	$\text{m}^2\cdot\text{s}^{-1}$
D_e (or D_{be})	effective diffusion coefficient in the fluid (or in the bulk)	$\text{m}^2\cdot\text{s}^{-1}$
D_k (or D_{ke})	Knudsen effective diffusion coefficient in the fluid (or in the bulk)	$\text{m}^2\cdot\text{s}^{-1}$
D_s	surface diffusion coefficient	$\text{m}^2\cdot\text{s}^{-1}$
D_T	thermal diffusivity	$\text{m}^2\cdot\text{s}$
$D_{Tol.}$	diffusion coefficient of toluene	$\text{m}^2\cdot\text{s}^{-1}$
$d_{cat.}$	catalyst diameter	m or mm
Da	Damkhöler dimensionless number	-
$Da^{mod.}$	dimensionless number to define if the reaction rate is influenced by the residence time	-
E_D	activation energy of the diffusion process	$\text{J}\cdot\text{mol}^{-1}$
$E()$	probability function distribution	-
$E_A^\#$	activation energy (of the transitory state)	$\text{J}\cdot\text{mol}^{-1}$
f	fugacity of the gaseous phase	bar
F_{AB}	correction factor applied to the hard sphere diffusivity equation	-
F_{obj}	objective function (optimization)	-
g_{AB}	contact factor (diffusivity correlation)	-
Ga	Galileo dimensionless number	-
h	Planck's constant	J·s
h	mol increment	mol

Notation and glossary

H	Henry's constant	bar
K	equilibrium adsorption constant	-
K'	linear equilibrium adsorption constant at the solid surface	-
$K^\#$	equilibrium constant of the transitory state	-
$k_{\theta,LS}$	liquid-solid mass transfer coefficient for the angle range investigated	$\text{m}\cdot\text{s}^{-1}$
k^*	kinetic constant for MAPD hydrogenation	vary with the kinetic model
k_{ads}	adsorption rate	s^{-1}
κ_B	Boltzmann's constant	$\text{J}\cdot\text{K}^{-1}$
k_{des}	desorption rate	s^{-1}
k_{GL}	gas-liquid mass transfer coefficient	$\text{m}\cdot\text{s}^{-1}$
k_{GLS}	global (gas-liquid-solid) mass transfer coefficient	$\text{m}\cdot\text{s}^{-1}$
k_{GS}	gas-solid mass transfer coefficient	$\text{m}\cdot\text{s}^{-1}$
k_{ij}	interaction parameters between fluids	-
k_L	liquid side mass transfer coefficient	$\text{m}\cdot\text{s}^{-1}$
k_{LS}	Liquid-solid mass transfer coefficient	$\text{m}\cdot\text{s}^{-1}$
k_r^*	reaction kinetics for a n^{th} order reaction	$\text{m}^{3(n-3)}\text{mol}^{-n+1}\cdot\text{s}^{-1}$ (can have other units)
\mathcal{L}	characteristic length dimension	m
L	length of the channel	m
$L_{reactor}$	length of the reactor	m
$LHSV$	liquid hourly space velocity	h^{-1}
M	molar mass	$\text{g}\cdot\text{mol}^{-1}$
m_{AB}	reduced molar weight	-
m_T	Toth's heterogeneity factor	-
\mathcal{M}	number of points compared	-
$m_{cat.}$	mass of the catalytic bed	kg or g
$n_{cat.}$	number of catalytic pellets	-
n	number of divisions of the binary combination line	-
n	moles	
n	power-law kinetic model exponentials	-
n^*	density number	-
\mathcal{N}	molar conc. flow rate	$\text{mol}\cdot\text{m}^{-3}\cdot\text{s}^{-1}$
N	number of compounds evaluated	-
N_A	Avogadro's number	mol^{-1}
N^{opt}	optimal number of points	-
P	pressure	bar

Notation and glossary

P_C	critical pressure	bar
P_{MCB}	maxcondentherm pressure	bar
P_{MCT}	maxcondenbar pressure	bar
P_R	reduced pressure	-
p^{sat}	vapor pressure in the equilibrium state	bar
Pe	Peclet number	-
q	amount of solute adsorbed per unit weight of adsorbent	mg·g ⁻¹
q_{ij}	Matrix of derivatives of fugacity in function of the number of moles	mol ⁻¹
Q	liquid volumetric flow-rate	m ³ ·h ⁻¹
r	radius	m
r_B	radius of one solute molecule	m
r_p	particle radius	m or mm
$r_{reactor}$	reactor radius	m or mm
R	reaction rate	mol·m ⁻³ ·s
R'	reaction rate per surface area	mol·m ⁻² ·s
R^*	reaction rate per mass of catalyst	mol·m ⁻³ ·s·kg ⁻¹
\mathcal{R}	fluidic resistance	
R_{ads}	adsorption rate	mol·m ⁻³ ·s
Re	Reynolds number	-
Re_{int}	interstitial Reynolds number	-
S	sphericity factor	-
Sc	Schmidt number	-
S_{PR}	selectivity of propylene	-
Sh	Sherwood number	-
t	time	s
$\overline{t_{red}}$	average residence time	s or h
t_r	retention time	s
T	Temperature	K
T_B	boiling temperature	K
T_C	critical temperature	K
T_w	surface temperature	Kelvin
T^*	reduced temperature	-
T_R	reduced temperature	-
u	superficial velocity	m·s ⁻¹
\overline{u}	average superficial velocity	m·s ⁻¹
$\overline{u_{int}}$	average interstitial velocity	m·s ⁻¹

Notation and glossary

\bar{u}_0	average velocity at the inlet	$\text{m}\cdot\text{s}^{-1}$
$u_{mag.}$	velocity magnitude	$\text{m}\cdot\text{s}^{-1}$
\bar{v}	average molar volume	$\text{m}^3\cdot\text{mol}^{-1}$
v	molar volume	$\text{m}^3\cdot\text{mol}^{-1}$
v_b	molar volume at the boiling temperature (1 atm)	$\text{m}^3\cdot\text{mol}^{-1}$ or $\text{cm}^3\cdot\text{mol}^{-1}$
v_c	molar critical volume	$\text{m}^3\cdot\text{mol}^{-1}$ or $\text{cm}^3\cdot\text{mol}^{-1}$
v_t	molar volume translated	$\text{m}^3\cdot\text{mol}^{-1}$ or $\text{cm}^3\cdot\text{mol}^{-1}$
V	volume	m^3
V_p	Volume of a particle	m^3
$V_{reactor}$	reactor bed volume	m^3
W	liquid mass flow-rate	$\text{kg}\cdot\text{h}^{-1}$
w	acentric factor	-
We	Weber number	-
$WHSV$	weight hourly space velocity	h^{-1}
x	molar fraction in the liquid phase	-
x	Position x-axis	m
x^*	molar fraction in the liquid phase at the saturation	-
X	reaction conversion	-
$X^\#$	transitory species	-
y	molar fractions in gas phase	-
y	Position y-axis	m
z	position coordinate	m
Z	compressibility factor	-

Greek letters

α, β and θ	constants, depending on the equation used	-
δ	thickness	μm
δ_{film}	liquid-solid film layer thickness	μm
δ_{metal}	thickness of the metal crust	μm
$\Delta v_{app}^\#$	apparent activation volume	$\text{m}^3\cdot\text{mol}^{-1}$
$\Delta v^\#$	activation volume	$\text{m}^3\cdot\text{mol}^{-1}$
ΔH	enthalpy energy	$\text{J}\cdot\text{mol}^{-1}$
ΔP	pressure drop	Pa or bar
G	Gibbs free energy	$\text{J}\cdot\text{mol}^{-1}$

Notation and glossary

\mathfrak{R}	the ideal gas constant	$\text{m}^3\text{bar mol}^{-1}\text{K}^{-1}$
ρ_A	solvent density	kg mol^{-1}
ρ (or ρ_b)	fluid density (or bulk density)	kg m^{-3}
ρ_s	solid density	kg m^{-3}
α	correction factor	-
Γ	Parachor parameter	$\text{g}^{0.25}\text{cm}^3\text{mol}^{-1}\text{s}^{-0.5}$
γ^{inf}	infinite-dilution activity coefficient	-
ε	reactor porosity	-
$\varepsilon_{G,EC}$	gas hold-up inside an empty channel	-
ε_L	liquid hold-up	-
$\varepsilon_{L,EC}$	liquid hold-up inside an empty channel	-
η	catalyst effectiveness factor	-
$\theta_{cat.}$	fraction of occupied sites at the catalyst surface	-
θ	angle	rad or $^\circ$
κ_T	isothermal compressibility	-
μ	dynamic fluid viscosity	Pa.s
μ^{pot}	chemical potential	
σ	surface tension	N m^{-1}
σ_{AB}^*	characteristic length of intermolecular force law	m
σ^{*eff}	effective size parameter between solute and solvent (from attractive forces)	m or cm
σ^{*LJ}	Lennard-Jones size parameter	m or cm
$1/\tau$	space velocity	h^{-1}
τ^*	tortuosity factor of the material	-
τ_G	gas hold-up	s or h
$\tau_{reactor}$	(volumetric) residence time	s or h
φ	molar flux	$\text{mol m}^{-2}\text{s}^{-1}$
ϕ	Thiele modulus	-
χ	dimensionless position along the particle radius	-
χ^*	transmission coefficient	-
χ	Lockhart-Martinelli Number	-
ψ	dimensionless number to define is there is sufficient time to have full (>90%) mass transfer between phases	-

References

- Abu-Eishah, S., 1999. Prediction of critical properties of mixtures from the PRSV-2 equation of state: A correction for predicted critical volumes. *Int. J. Thermophys.* 20, 1557–1574.
- Adagiri, G.A., Babagana, G., Susu, A.A., State, B., 2012. Effectiveness Factor for Porous Catalysts With Specific Exothermic and Endothermic Reactions Under Langmuir-Hinshelwood Kinetics 13.
- Agbor, V.B., Cicek, N., Sparling, R., Berlin, A., Levin, D.B., 2011. Biomass pretreatment: fundamentals toward application. *Biotechnol. Adv.* 29, 675–85.
- Al-Dahhan, M.H., Duduković, M.P., 1995. Catalyst wetting efficiency in trickle-bed reactors at high pressure. *Chem. Eng. Sci.* 50, 2377–2389.
- Al-Dahhan, M.H., Duduković, M.P., 1995. Catalyst wetting efficiency in trickle-bed reactors at high pressure. *Chem. Eng. Sci.* 50, 2377–2389.
- Ancheyta, J., Marroquín, G., Angeles, M.J., Macías, M.J., Pitault, I., Forissier, M., Morales, R.D., 2002. Some experimental observations of mass transfer limitations in a trickle-bed hydrotreating pilot reactor. *Energy and Fuels* 16, 1059–1067.
- Anikeev, V.I., Yermakova, a., Manion, J., Huie, R., 2004. Kinetics and thermodynamics of 2-propanol dehydration in supercritical water. *J. Supercrit. Fluids* 32, 123–135.
- Aris, R., 1957. On shape factors for irregular particles—I: The steady state problem. *Diffusion and reaction. Chem. Eng. Sci.* 6, 262–268.
- Arunajatesan, V., Subramaniam, B., Hutchenson, K.W., Herkes, F.E., 2001. Fixed-bed hydrogenation of organic compounds in supercritical carbon dioxide. *Chem. Eng. Sci.* 56, 1363–1369.
- Asano, T., Le Noble, W.J., 1978. Activation and reaction volumes in solution. *Chem. Rev.* 78, 407–489.
- Avrami, M., 1939. Kinetics of Phase Change. I General Theory. *J. Chem. Phys.* 7, 1103.
- Benham, A., Katz, D., Williams, R., 1957. Phase behavior of hydrogen–light-hydrocarbon systems. *AIChE J.* 3, 236–241.
- Bertucco, A., Vetter, G., 2001. *High Pressure Process Technology: Fundamentals and Applications* (Vol. 9). Elsevier.
- Blasius, H., 1908. Grenzschichten in Flüssigkeiten mit Kleiner Reibung. *Zeitschrift für Angew. Math. und Phys.* 56, 1–37.
- Bogdan, V.I., Klimenko, T.A., Kustov, L.M., Kazansky, V.B., 2004. Supercritical n-butane isomerization on solid acid catalysts. *Appl. Catal. A Gen.* 267, 175–179.
- Boitiaux, J., Cosyns, J., Derrien, M., Leger, G., 1985. Newest hydrogenation catalysts. *Hydrocarb. Process.*
- Bol'shakov, P.E., Linshits, L.R., 1953. Phase equilibria in liquid-gas systems at high pressure. *Tr. GIAP* 3 18–27.
- Bouaifi, M., Hebrard, G., Bastoul, D., Roustan, M., 2001. A comparative study of gas hold-up, bubble size, interfacial area and mass transfer coefficients in stirred gas-liquid reactors and bubble columns. *Chem. Eng. Process.* 40, 97–111.
- Braga, M., 2014. Etude des phénomènes de transfert et de l'hydrodynamique dans des réacteurs agités à panier catalytique. Université Claude Bernard Lyon 1.
- Brandao, L., Fritsch, D., Mendes, A.M., Madeira, L.M., 2007. Propyne hydrogenation kinetics over surfactant-stabilized palladium nanoclusters. *Ind. Eng.* 46, 377–384.
- Brent, R., 1973. Algorithms for minimization without derivatives. In: *Algorithms for Minimization without Derivatives*. Prentice-Hall, Inc., Englewood Cliffs, New Jersey.
- Bridier, B., 2012. Selective hydrogenation of alkynes Catalyst design aided by molecular understanding. ESCPE Lyon.
- Buffham, B. a., 2000. Size and compactness of particles of arbitrary shape: Application to catalyst effectiveness factors. *Chem. Eng. Sci.* 55, 5803–5811.

References

- Burgener, M., Ferri, D., Grunwaldt, J.-D.D., Mallat, T., Baiker, A., 2005a. Supercritical carbon dioxide: an inert solvent for catalytic hydrogenation? *J. Phys. Chem. B* 109, 16794–800.
- Burgener, M., Ferri, D., Grunwaldt, J.D., Mallat, T., Baiker, A., 2005b. Supercritical carbon dioxide: An inert solvent for catalytic hydrogenation? *J. Phys. Chem. B* 109, 16794–16800.
- Burghardt, A., Bartelmus, G., Jaroszyński, M., Kołodziej, A., 1995. Hydrodynamics and mass transfer in a three-phase fixed-bed reactor with cocurrent gas—liquid downflow. *Chem. Eng. J. Biochem. Eng. J.* 58, 83–99.
- Burghardt, A., Kubaczka, A., 1996. Generalization of the effectiveness factor for any shape of a catalyst pellet. *Chem. Eng. Process. Process Intensif.* 35, 65–74.
- Burriss, W.L., Hsu, N.T., Reamer, H.H., Sage, B.H., 1953a. Phase Behavior of the Hydrogen-Propane System. *Ind. Eng. Chem.* 45, 210–213.
- Burriss, W.L., Hsu, N.T., Reamer, H.H., Sage, B.H., 1953b. Phase Behavior of the Hydrogen-Propane System. *Ind. Eng. Chem.* 45, 210–213.
- Cabiac, A., ZOZAYA, V., Chambard, A., Thomazeau, C., 2013. Catalyseur comprenant du palladium et de l'argent et son application en hydrogenation selective.
- Carlès, P., 2010a. A brief review of the thermophysical properties of supercritical fluids. *J. Supercrit. Fluids* 53, 2–11.
- Carlès, P., 2010b. A brief review of the thermophysical properties of supercritical fluids. *J. Supercrit. Fluids* 53, 2–11.
- Castier, M., Sandler, S., 1997. Critical points with the Wong-Sandler mixing rule—II. Calculations with a modified Peng-Robinson equation of state. *Chem. Eng. Sci.* 5.
- Catchpole, O., King, M., 1994. Measurement and correlation of binary diffusion coefficients in near critical fluids. *Ind. Eng. Chem. ...* 33, 1828–1837.
- Chen, S.S., Kreglewski, A., 1977. Applications of the Augmented van der Waals Theory of Fluids I. Pure Fluids. *Berichte der Bunsengesellschaft für Phys. Chemie* 81, 1048–1052.
- Cheng, H., Fernandez, M.E.P. de, Zollweg, J.A., Streett, W.B., 1989. Vapor-liquid equilibrium in the system carbon dioxide+ n-pentane from 252 to 458 K at pressures to 10 MPa. *J. Chem. Eng. Data* 319–323.
- Cherayil, B.J., 2002. Anomalies in the self-diffusion coefficient near the critical point. *J. Chem. Phys.* 116, 8455.
- Claus, P., Hönicke, D., Zech, T., 2001. Miniaturization of screening devices for the combinatorial development of heterogeneous catalysts. *Catal. Today* 67, 319–339.
- Cornelissen, J.T., Taghipour, F., Escudie, R., Ellis, N., Grace, J.R., 2007. CFD modelling of a liquid-solid fluidized bed. *Chem. Eng. Sci.* 62, 6334–6348.
- Dabrowski, a, 2001. Adsorption—from theory to practice. *Adv. Colloid Interface Sci.* 93, 135–224.
- Dandeu, A., Bazer-Bachi, F., 2012. Process for selective hydrogenation of olefinic feedstocks with switchable reactors including at least one stage for short-circuiting a reactor. *Pub. No. US 2013/0165711 A1* 1.
- Datta, R., Vilekar, S. a., 2010. The continuum mechanical theory of multicomponent diffusion in fluid mixtures. *Chem. Eng. Sci.* 65, 5976–5989.
- Davis, J. a., Leckie, J.O., 1978. Surface Ionization and Complexation at the Oxide / Water Interface II. Surface Properties of Amorphous Iron Oxyhydroxide and Adsorption of Metal Ions. *J. Colloid Interface Sci.* 67, 90–107.
- Derrien, M.L., 1986. Chapter 18 Selective Hydrogenation Applied to the Refining of Petrochemical Raw Materials Produced by Steam Cracking. In: *Catalysis, L.C.B.T.-S. in S.S. and (Ed.), Catalytic Hydrogenation.* Elsevier, pp. 613–666.
- Dessimoz, A.L., Cavin, L., Renken, A., Kiwi-Minsker, L., 2008. Liquid-liquid two-phase flow patterns and mass transfer characteristics in rectangular glass microreactors. *Chem. Eng. Sci.* 63, 4035–4044.
- Devetta, L., Giovanzana, a, Canu, P., Bertucco, a, Minder, B., 1999. Kinetic experiments and modeling of a three-phase catalytic hydrogenation reaction in supercritical CO₂. *Catal. Today* 48, 337–345.
- Dixon, A.G., 2014. COMSOL Multiphysics Š Simulation of 3D Single-phase Transport in a Random Packed Bed of Spheres. *Proc. COMSOL Conf. Bost.*

References

- Dixon, A.G., Nijemeisland, M., 2001. CFD as a Design Tool for Fixed-Bed Reactors. *Ind. Eng. Chem. Res.* 40, 5246–5254.
- Dixon, A.G., Walls, G., Stanness, H., Nijemeisland, M., Stitt, E.H., 2012. Experimental validation of high Reynolds number CFD simulations of heat transfer in a pilot-scale fixed bed tube. *Chem. Eng. J.* 200–202, 344–356.
- Dorai, F., 2012. Étude numérique des chargements, de l'hydrodynamique et de la réactivité dans des réacteurs pilotes à lits fixes.
- Dorai, F., Rolland, M., Wachs, A., Marcoux, M., Climent, E., 2012. Packing Fixed Bed Reactors with Cylinders: Influence of Particle Length Distribution. *Procedia Eng.* 42, 1335–1345.
- Doraiswamy, L.K., Tajbl, D.G., 1974. LABORATORY CATALYTIC REACTORS. *Catal. Rev.* 10, 177–219.
- Drljaca, a., Hubbard, C.D., van Eldik, R., Asano, T., Basilevsky, M. V., le Noble, W.J., 1998. Activation and Reaction Volumes in Solution. 3. *Chem. Rev.* 98, 2167–2290.
- Drozdov, A.N., Tucker, S.C., 2001. Self-diffusion near the liquid–vapor critical point. *J. Chem. Phys.* 114, 4912.
- Durand, E., Clemancey, M., Quoineaud, A.-A., Verstraete, J., Espinat, D., Lancelin, J.-M., 2008. 1H Diffusion-Ordered Spectroscopy (DOSY) Nuclear Magnetic Resonance (NMR) as a Powerful Tool for the Analysis of Hydrocarbon Mixtures and Asphaltenes. *Energy & Fuels* 22, 2604–2610.
- Eaton, A.P., Akgerman, A., 1997. Infinite-Dilution Diffusion Coefficients in Supercritical Fluids. *Ind. Eng. Chem. Res.* 36, 923–931.
- Eberl, H., Picioreanu, C., Heijnen, J., van Loosdrecht, M.C., 2000. A three-dimensional numerical study on the correlation of spatial structure, hydrodynamic conditions, and mass transfer and conversion in biofilms. *Chem. Eng. Sci.* 55, 6209–6222.
- Edgar, T., Himmelblau, D., Lasdon, L., 2001. Optimization of chemical processes, New York.
- Eldik, R. Van, Asano, T., Noble, W.J. LE, 1989. Activation and Reaction Volumes in Solution. 2. *Chem. Rev.* 89, 549–688.
- Elliott, J.R., Daubert, T.E., 1987a. Evaluation of an equation of state method for calculating the critical properties of mixtures. *Ind. Eng. Chem. Res.* 26, 1686–1691.
- Elliott, J.R., Daubert, T.E., 1987b. Evaluation of an equation of state method for calculating the critical properties of mixtures. *Ind. Eng. Chem. Res.* 26, 1686–1691.
- Fajardo, J.C., Godinez, C., Cabanes, a L., Villora, G., 1996. Kinetic analysis of rate data for propylene hydrogenation. *Chem. Eng. Process.* 35, 203–211.
- Fall, D.J., Fall, J.L., Luks, K.D., 1985. Liquid-Liquid-Vapor Immiscibility Limits in Carbon Dioxide + n-Paraffin Mixtures. *J. Chem. Eng. Data* 30, 82–88.
- Fan, L., Yokota, K., Fujimoto, K., 1992. Supercritical phase fischer-tropsch synthesis: Catalyst pore-size effect. *AIChE J.* 38, 1639–1648.
- Fecant, A., Fischer, L., Rebours, B., 2009. Selective hydrogenation catalyst and process for its preparat. *US Pat. App.* 8586808 B2.
- Fisher, R., Shah, M.K., Eskin, D., Schmidt, K., Singh, A., Molla, S., Mostowfi, F., 2013. Equilibrium gas-oil ratio measurements using a microfluidic technique. *Lab Chip.*
- Flores, R., Lopez-Castillo, Z.K., Kani, I., Fackler, J.P., Akgerman, A., 2003. Kinetics of the Homogeneous Catalytic Hydrogenation of Olefins in Supercritical Carbon Dioxide Using a Fluoroacrylate Copolymer Grafted Rhodium Catalyst. *Ind. Eng. Chem. Res.* 42, 6720–6729.
- Fogler, H.S., Gurmen, M.N., 2008. Diffusion and Reaction. *Essentials Chem. React. Eng.* 813–866.
- Fonte, C.P., Pinho, B.S., Santos-Moreau, V., Lopes, J.C.B., 2014. Prediction of the Induced Gas Flow Rate from a Self-Inducing Impeller with CFD. *Chem. Eng. Technol.* 37, 571–579.
- Frouws, M.J., Vellenga, K., De Wilt, H.G., 1976. Combined external and internal mass transfer effects in heterogeneous (enzyme) catalysis. *Biotechnol. Bioeng.* 18, 53–62.
- García-Sánchez, F., Ruiz-Cortina, J., 1992. Critical point calculations for oil reservoir fluid systems using the SPHCT equation of state. *Fluid Phase Equilib.* 81, 39–84.
- Gendrineau, T., Marre, S., Vaultier, M., Pucheault, M., Aymonier, C., 2012. Microfluidic synthesis of palladium nanocrystals assisted by supercritical CO₂: tailored surface properties for applications in boron chemistry. *Angew. Chem. Int. Ed. Engl.* 51, 8525–8.

References

- Gervais, T., El-Ali, J., Günther, A., Jensen, K.F., 2006. Flow-induced deformation of shallow microfluidic channels. *Lab Chip* 6, 500–7.
- Gervais, T., Jensen, K.F., 2006. Mass transport and surface reactions in microfluidic systems. *Chem. Eng. Sci.* 61, 1102–1121.
- Gianetto, A., Specchia, V., 1992. Trickle-bed reactors: state of art and perspectives. *Chem. Eng. Sci.* 47, 3197–3213.
- Giese, M., Rottschäfer, K., Vortmeyer, D., 1998. Measured and modeled superficial flow profiles in packed beds with liquid flow. *AIChE J.* 44, 484–490.
- Giovangigli, V., Matuszewski, L., 2012. Supercritical fluid thermodynamics from equations of state. *Phys. D Nonlinear Phenom.* 241, 649–670.
- Girgis, M.J., Gates, B.C., 1991. Reactivities, reaction networks, and kinetics in high-pressure catalytic hydroprocessing. *Ind. Eng. Chem. Res.* 30, 2021–2058.
- Gnielinski, V., 1975. New equations for heat and mass transfer in the turbulent flow in pipes and channels. *NASA STI/Recon Tech. Rep. A* 75, 22028.
- Godinez, C., Cabanes, A.L., Villora, G., 1996. Experimental study of the tail end selective hydrogenation of steam cracking C2-C3 mixture. *Can. J. Chem. Eng.* 74, 225–247.
- Goto, S., Smith, J.M., 1975. Trickle-bed reactor performance Part I. Holdup and mass transfer effects. *AIChE J.* 21, 706–713.
- Gourgouillon, D., Avelino, H.M.N.T., Fareleira, J.M.N. a, Nunes da Ponte, M., 1998. Simultaneous viscosity and density measurement of supercritical CO₂-saturated PEG 400. *J. Supercrit. Fluids* 13, 177–185.
- Grunwaldt, J.D., Wandeler, R., Baiker, a, 2003a. Supercritical fluids in catalysis: Opportunities of in situ spectroscopic studies and monitoring phase behavior. *Catal. Rev. Eng.* 45, 1–96.
- Grunwaldt, J.D., Wandeler, R., Baiker, a, 2003b. Supercritical fluids in catalysis: Opportunities of in situ spectroscopic studies and monitoring phase behavior. *Catal. Rev. Eng.* 45, 1–96.
- Guedes De Carvalho, J.R.F., Delgado, J.M.P.Q., Alves, M. a., 2004. Mass Transfer between Flowing Fluid and Sphere Buried in Packed Bed of Inerts. *AIChE J.* 50, 65–74.
- Guo Jun-Wang, Niu Yu-Qin, Z.B.-J., 1998. Effects of the temperature and space velocity on catalytic performance in liquid phase dimethyl ether synthesis from syngas. *J. Nat. Gas Chem.* 7, 259–265.
- Gut, G., Kut, O.M., Yucelen, F., Wagner, D., 1986. Chapter 15 Liquid-Phase Hydrogenation: The Role of Mass and Heat Transfer in Slurry Reactors. In: *Catalysis, L.C.B.T.-S. in S.S. and (Ed.), Catalytic Hydrogenation*. Elsevier, pp. 517–545.
- Haase, S., Weiss, M., Langsch, R., Bauer, T., Lange, R., 2013. Hydrodynamics and mass transfer in three-phase composite minichannel fixed-bed reactors. *Chem. Eng. Sci.* 94, 224–236.
- Hageman, M., Van, D.W.H., 2005. Method for partially and selectively hydrogenating polymers made of conjugated dienes.
- Hamilton, C. a., Jackson, S.D., Kelly, G.J., Spence, R., De Bruin, D., 2002. Competitive reactions in alkyne hydrogenation. *Appl. Catal. A Gen.* 237, 201–209.
- Hanika, J., Staněk, V., 1986. Chapter 16 Application of Fixed-Bed Reactors to Liquid-Phase Hydrogenation. In: *Catalysis, L.C.B.T.-S. in S.S. and (Ed.), Catalytic Hydrogenation*. Elsevier, pp. 547–577.
- Härröd, M., Macher, M.B., van den Hark, S., Møller, P., 2001. 9.3 Hydrogenation under supercritical single-phase conditions. *Ind. Chem. Libr.* 9, 496–508.
- Hassan, F., 2011. Heterogeneous catalysis in supercritical fluids: the enhancement of catalytic stability to coking.
- Hassan, F., Al-Duri, B., Wood, J., 2012. Effect of Supercritical Conditions Upon Catalyst Deactivation in the Hydrogenation of Naphthalene. *Chem. Eng. J.* 207-208, 133–141.
- He, C., Yu, Y., 1998. New equation for infinite-dilution diffusion coefficients in supercritical and high-temperature liquid solvents. *Ind. Eng. Chem. Res.* 3, 3793–3798.
- Heidemann, R., Khalil, A., 1980. The calculation of critical points. *AIChE J.* 26, 769.
- Henderson, N., Sacco, W.F., Baruffati, N.E., Ali, M.M., 2010. Calculation of Critical Points of Thermodynamic Mixtures with Differential Evolution Algorithms. *Ind. Eng. Chem. Res.* 49, 1872–1882.

References

- Highfill, W., Al-Dahhan, M., 2001. Liquid-solid mass transfer coefficient in high pressure trickle bed reactors. *Chem. Eng. Res. Des.* 79.
- Hill, C.G.J., 2014. *Introduction to Chemical Engineering Kinetics and Reactor Design*. John Wiley & Sons.
- Hipolito, A.I., Rolland, M., Boyer, C., de Bellefon, C., 2010. Single Pellet String Reactor for Intensification of Catalyst Testing in Gas/Liquid/Solid Configuration. *Oil Gas Sci. Technol. – Rev. d'IFP Energies Nouv.* 65, 689–701.
- Hipolito, A.I.F., 2010. Étude Des Phenomenes De Transport Dans Un Réacteur Catalytique Pilote De Type “ Filaire ” 264.
- Hitzler, M.G., Poliakoff, M., 1997. Continuous hydrogenation of organic compounds in supercritical fluids. *Chem. Commun.* 1667–1668.
- Hitzler, M.G., Smail, F.R., Ross, S.K., Martyn Poliakoff, 1998. Selective Catalytic Hydrogenation of Organic Compounds in Supercritical Fluids as a Continuous Process. *Org. Process Res. Dev.* 6160, 137–146.
- Hodnett, B.K., Delmon, B., 1986. Chapter 2 Synergy in Catalytic Reactions Involving Hydrogen : Possible Role of Surface-Mobile Species. In: *Catalysis, L.C.B.T.-S. in S.S. and (Ed.), Catalytic Hydrogenation*. Elsevier, pp. 53–78.
- Horstmann, S., 1999. Experimental determination of critical points of pure components and binary mixtures using a flow apparatus. *Chem. Eng. ...* 22, 839–842.
- Horstmann, S., Fischer, K., Gmehling, J., 2001. Experimental determination of critical data of mixtures and their relevance for the development of thermodynamic models. *Chem. Eng. Sci.* 56, 6905–6913.
- Hoteit, H., Santiso, E., Firoozabadi, A., 2006. An efficient and robust algorithm for the calculation of gas–liquid critical point of multicomponent petroleum fluids. *Fluid Phase Equilib.* 241, 186–195.
- Hou, S.-X., Maitland, G.C., Trusler, J.P.M., 2013. Measurement and modeling of the phase behavior of the (carbon dioxide+water) mixture at temperatures from 298.15K to 448.15K. *J. Supercrit. Fluids* 73, 87–96.
- Hwang, S., Linke, P., Smith, R., 2004. Heterogeneous catalytic reactor design with optimum temperature profile II: Application of non-uniform catalyst. *Chem. Eng. Sci.* 59, 4245–4260.
- Hyde, J., Licence, P., Carter, D., Poliakoff, M., 2001. Continuous catalytic reactions in supercritical fluids. *Appl. Catal. A Gen.* 222, 119–131.
- Iliuta, I., Larachi, F., Grandjean, B.P. a., Wild, G., 1999. Gas–liquid interfacial mass transfer in trickle-bed reactors: state-of-the-art correlations. *Chem. Eng. Sci.* 54, 5633–5645.
- Jadhav, S.V., Pangarkar, V.G., 1990. Solid–liquid mass transfer in packed bubble columns. *Chem. Eng. Sci.* 45, 1139–1143.
- James F. Epperson, 2007. *An introduction to numerical methods and analysis*. Wiley-Interscience.
- Jandeleit, B., Schaefer, D.J., Powers, T.S., Turner, H.W., Weinberg, W.H., 1999. Combinatorial Materials Science and Catalysis. *Angew. Chemie Int. Ed.* 38, 2494–2532.
- Jaubert, J.-N., Mutelet, F., 2004. VLE predictions with the Peng–Robinson equation of state and temperature dependent kij calculated through a group contribution method. *Fluid Phase Equilib.* 224, 285–304.
- Jaubert, J.-N., Privat, R., Qian, J., 2011. Pénéloux’s mixing rules: 25 years ago and now. *Fluid Phase Equilib.* 308, 164–167.
- Jaubert, J.-N., Vitu, S., Mutelet, F., Corriou, J.-P., 2005. Extension of the PPR78 model (predictive 1978, Peng–Robinson EOS with temperature dependent kij calculated through a group contribution method) to systems containing aromatic compounds. *Fluid Phase Equilib.* 237, 193–211.
- Jensen, K.F., 2001. Microreaction engineering — is small better? *Chem. Eng. Sci.* 56, 293–303.
- Jenzer, G., 2001. Palladium-Catalyzed Oxidation of Octyl Alcohols in “Supercritical” Carbon Dioxide. *J. Catal.* 199, 141–148.
- Junmei, Z., Chunjian, X., Ming, Z., 2006. The mechanism model of gas-liquid mass transfer enhancement by fine catalyst particles. *Chem. Eng. J.* 120, 149–156.

References

- Juntarachat, N., Bello, S., Privat, R., Jaubert, J.-N., 2013. Validation of a New Apparatus Using the Dynamic Method for Determining the Critical Properties of Binary Gas/Gas Mixtures. *J. Chem. Eng. Data* 58, 671–676.
- Juntarachat, N., Beltran Moreno, P.D., Bello, S., Privat, R., Jaubert, J.-N., 2012. Validation of a new apparatus using the dynamic and static methods for determining the critical properties of pure components and mixtures. *J. Supercrit. Fluids* 68, 25–30.
- Justo-García, D.N., García-Sánchez, F., Díaz-Ramírez, N.L., Romero-Martínez, A., 2008. Calculation of critical points for multicomponent mixtures containing hydrocarbon and nonhydrocarbon components with the PC-SAFT equation of state. *Fluid Phase Equilib.* 265, 192–204.
- Kashid, M.N., Renken, A., Kiwi-Minsker, L., 2014. *Microstructured Devices for Chemical Processing*. John Wiley & Sons.
- Ke, J., Buxing, H., George, M.W., Yan, H., Poliakoff, M., 2001. How does the critical point change during a chemical reaction in supercritical fluids? A study of the hydroformylation of propene in supercritical CO₂. *J. Am. Chem. Soc.* 123, 3661–3670.
- Ke, J., Sanchez-Vicente, Y., Akien, G.R., Novitskiy, a. a., Comak, G., Bagratashvili, V.N., George, M.W., Poliakoff, M., 2010. Detecting phase transitions in supercritical mixtures: an enabling tool for greener chemical reactions. *Proc. R. Soc. A Math. Phys. Eng. Sci.* 466, 2799–2818.
- Kennedy, D.R., Webb, G., Jackson, S.D., Lennon, D., 2004. Propyne hydrogenation over alumina-supported palladium and platinum catalysts. *Appl. Catal. A Gen.* 259, 109–120.
- Keybl, J., 2011. A microreactor system for high-pressure, multiphase homogeneous and heterogeneous catalyst measurements under continuous flow.
- Khammar, M., Shaw, J.M., 2011. Phase behaviour and phase separation kinetics measurement using acoustic arrays. *Rev. Sci. Instrum.* 82, 104902.
- Kim, S.D., Kang, Y., 1997. Heat and mass transfer in three-phase fluidized-bed reactors—an overview. *Chem. Eng. Sci.* 52, 3639–3660.
- Koning, B., 2002. *Heat and Mass Transport in Tubular Packed Bed Reactors at Reacting and Non-Reacting Conditions*. University of Twente.
- Konynenburg, P.H. V., Scott, R.L., 1980. Critical Lines and Phase Equilibria in Binary Van Der Waals Mixtures. *Philos. Trans. R. Soc. A Math. Phys. Eng. Sci.*
- Krishna, R., Wesselingh, J.A., 1997. The Maxwell-Stefan approach to mass transfer. *Chem. Eng. Sci.* 52, 861–911.
- Kumar, K.V., Porkodi, K., Rocha, F., 2008. Langmuir-Hinshelwood kinetics - A theoretical study. *Catal. Commun.* 9, 82–84.
- Laidler, K.J., King, M.C., 1983. The Development of Transition-State Theory. *J. Phys. Chem.* 87, 2657–2664.
- Lakota, A., Levec, J., 1990a. Solid-liquid mass transfer in packed beds with cocurrent downward two-phase flow. *AIChE J.* 36, 1444–1448.
- Lakota, A., Levec, J., 1990b. Solid-liquid mass transfer in packed beds with cocurrent downward two-phase flow. *AIChE J.* 36, 1444–1448.
- Lane, G.L., Schwarz, M.P., Evans, G.M., 2002. Predicting gas-liquid flow in a mechanically stirred tank. *Appl. Math. Model.* 26, 223–235.
- Larachi, F., Larachi, F., Belfares, L., Belfares, L., Iliuta, I., Iliuta, I., Grandjean, B.P. a, Grandjean, B.P. a, 2003. Heat and Mass Transfer in Cocurrent Gas-Liquid Packed Beds. Analysis, Recommendations, and New Correlations. *Ind. Eng. Chem. Res.* 42, 222–242.
- Laranjeira, P.E., Martins, A.A., Lopes, J.C.B., Dias, M.M., 2009. NETmix®, a new type of static mixer: Modeling, simulation, macromixing, and micromixing characterization. *AIChE J.* 55, 2226–2243.
- Lee, J.K., Ko, J.B., Kim, D.H., 2004. Methanol steam reforming over Cu/ZnO/Al₂O₃ catalyst: kinetics and effectiveness factor. *Appl. Catal. A Gen.* 278, 25–35.
- Lemmon, E.W., McLinden, M.O., Friend, D.G., 2015. “Thermophysical Properties of Fluid Systems” in NIST Chemistry WebBook, NIST Standard Reference Database Number 69.
- Liong, K.K., Wells, P. a., Foster, N.R., 1991. Diffusion in supercritical fluids. *J. Supercrit. Fluids* 4, 91–108.

References

- Lito, P.F., Magalhães, A.L., Gomes, J.R.B., Silva, C.M., 2013. Universal model for accurate calculation of tracer diffusion coefficients in gas, liquid and supercritical systems. *J. Chromatogr. A* 1290, 1–26.
- Lito, P.F., Magalhães, A.L., Gomes, J.R.B., Silva, C.M., 2013. Universal model for accurate calculation of tracer diffusion coefficients in gas, liquid and supercritical systems. *J. Chromatogr. A* 1290, 1–26.
- Liu, H., Silva, C.M., Macedo, E. a., 1997a. New Equations for Tracer Diffusion Coefficients of Solutes in Supercritical and Liquid Solvents Based on the Lennard-Jones Fluid Model. *Ind. Eng. Chem. Res.* 36, 246–252.
- Liu, H., Silva, C.M., Macedo, E. a., 1997b. New Equations for Tracer Diffusion Coefficients of Solutes in Supercritical and Liquid Solvents Based on the Lennard-Jones Fluid Model. *Ind. Eng. Chem. Res.* 36, 246–252.
- Liu, X., Vlught, T.J.H., Bardow, A., 2011. Predictive Darken equation for Maxwell-Stefan diffusivities in multicomponent mixtures. *Ind. Eng. Chem. Res.* 50, 10350–10358.
- Logtenberg, S. a., Nijemeisland, M., Dixon, a. G., 1999. Computational fluid dynamics simulations of fluid flow and heat transfer at the wall–particle contact points in a fixed-bed reactor. *Chem. Eng. Sci.* 54, 2433–2439.
- Losey, M.M.W., Schmidt, M. a., Jensen, K.K.F., 2001. Microfabricated multiphase packed-bed reactors: characterization of mass transfer and reactions. *Ind. Eng. Chem.* 40, 2555–2562.
- Maćkowiak, J., 2011. Model for the prediction of liquid phase mass transfer of random packed columns for gas-liquid systems. *Chem. Eng. Res. Des.* 89, 1308–1320.
- Magalhães, A.L., Lito, P.F., Da Silva, F. a., Silva, C.M., 2013. Simple and accurate correlations for diffusion coefficients of solutes in liquids and supercritical fluids over wide ranges of temperature and density. *J. Supercrit. Fluids* 76, 94–114.
- Magnico, P., Fongarland, P., 2006. CFD simulations of two stirred tank reactors with stationary catalytic basket. *Chem. Eng. Sci.* 61, 1217–1236.
- Malek Abbaslou, R.M., Soltan Mohammadzadeh, J.S., Dalai, A.K., 2009. Review on Fischer–Tropsch synthesis in supercritical media. *Fuel Process. Technol.* 90, 849–856.
- Mangers, R.J., Ponter, A.B., 1980. Effect of Viscosity on Liquid Film Resistance to Mass Transfer in a Packed Column. *Ind. Eng. Chem. Process Des. Dev.* 19, 530–537.
- Maniquet, A., Girardon, S., 2012. Quantification de l'hydrogène dissout dans les coupes pétrolières C 3. *IFP Intern. Note* 1–29.
- Mariani, N.J., Mocciano, C., Martínez, O.M., Barreto, G.F., 2009. Estimation of Effectiveness Factor for Arbitrary Particle Shape and Non-Linear Kinetics. *Ind. Eng. Chem. Res.* 48, 1172–1177.
- Marre, S., Adamo, A., Basak, S., Aymonier, C., Jensen, K.F., 2010. Design and Packaging of Microreactors for High Pressure and High Temperature Applications. *Ind. Eng. Chem. Res.* 49, 11310–11320.
- Marre, S., Roig, Y., Aymonier, C., 2012. Supercritical microfluidics: Opportunities in flow-through chemistry and materials science. *J. Supercrit. Fluids* 66, 251–264.
- Marshall, R., Webb, G., Jackson, S.D., Lennon, D., 2005. Propyne hydrogenation: Characteristics of a carbon-supported palladium catalyst that exhibits a kinetic discontinuity effect. *J. Mol. Catal. A Chem.* 226, 227–230.
- Martins, E., Aranda, D., 2000. Hydrogenation of diesel aromatic compounds in supercritical solvent environment. *Brazilian J. Chem. Eng.* 1–9.
- Mears, D.E., 1971. Tests for Transport Limitations in Experimental Catalytic Reactors. *Ind. Eng. Chem. Process Des. Dev.* 10, 541–547.
- Mederos, F.S., Ancheyta, J., Chen, J., 2009. Review on criteria to ensure ideal behaviors in trickle-bed reactors. *Appl. Catal. A Gen.* 355, 1–19.
- Medina, I., 2012. Determination of diffusion coefficients for supercritical fluids. *J. Chromatogr. A* 1250, 124–40.
- Meille, V., de Bellefon, C., Schweich, D., 2002. Kinetics of α -Methylstyrene Hydrogenation on Pd/Al₂O₃. *Ind. Eng. Chem. Res.* 41, 1711–1715.
- Mena, P., Ferreira, a., Teixeira, J. a., Rocha, F., 2011. Effect of some solid properties on gas-liquid mass transfer in a bubble column. *Chem. Eng. Process. Process Intensif.* 50, 181–188.

References

- Moffat, R.J., 1988. Describing the uncertainties in experimental results. *Exp. Therm. Fluid Sci.* 1, 3–17.
- Mostowfi, F., Molla, S., Tabeling, P., 2012. Determining phase diagrams of gas-liquid systems using a microfluidic PVT. *Lab Chip* 12, 4381–7.
- Mulder, A., van de Graaf, A. a., Robertson, L. a., Kuenen, J.G., 1995. Anaerobic ammonium oxidation discovered in a denitrifying fluidized bed reactor. *FEMS Microbiol. Ecol.* 16, 177–184.
- Müller, A., Ludwig, M., Arlit, M., Lange, R., 2015. Evaluation of reactor concepts for the continuous production of fine chemicals using the selective hydrogenation of cinnamaldehyde over palladium catalysts. *Catal. Today* 241, 214–220.
- Müller, A., Petschick, J., Lange, R., 2012. Model-based investigation of a Pellet String Reactor. *Procedia Eng.* 42, 1189–1201.
- Musko, N.E., Jensen, A.D., Baiker, A., Kontogeorgis, G.M., Grunwaldt, J.D., 2012. Fluid phase equilibria of the reaction mixture during the selective hydrogenation of 2-butenal in dense carbon dioxide. *Appl. Catal. A Gen.* 443-444, 67–75.
- Mutelet, F., Vitu, S., Privat, R., Jaubert, J.-N., 2005. Solubility of CO₂ in branched alkanes in order to extend the PPR78 model (predictive 1978, Peng–Robinson EOS with temperature-dependent kij calculated through a group contribution method) to such systems. *Fluid Phase Equilib.* 238, 157–168.
- Nasa, 2013. Nasa Mars photos [WWW Document].
- Neurock, M., Nigam, A., Trauth, D., Klein, M., 1994. Molecular representation of complex hydrocarbon feedstocks through efficient characterization and stochastic algorithms. *Chem. Eng. Sci.* 49.
- Nilsson, M., 2009. The DOSY Toolbox: A new tool for processing PFG NMR diffusion data. *J. Magn. Reson.* 200, 296–302.
- Nilsson, M., Morris, G. a., 2008. Speedy component resolution: An improved tool for processing diffusion-ordered spectroscopy data. *Anal. Chem.* 80, 3777–3782.
- Nishiumi, H., Gotoh, H., 1990. Generalization of binary interaction parameters of Peng-Robinson equation of state for systems containing hydrogen. *Fluid Phase Equilib.* 56.
- Oh, K.W., Lee, K., Ahn, B., Furlani, E.P., 2012. Design of pressure-driven microfluidic networks using electric circuit analogy. *Lab Chip* 12, 515–45.
- Ortiz, A., 2001. Prediction of critical properties for mixtures of carbon dioxide and reservoir fluids. Faculty of Texas Tech University.
- Pan, T., Zhu, B., 1998. Study on diffusion-reaction process inside a cylindrical catalyst pellet. *Chem. Eng. Sci.*
- Pereda, S., Bottini, S., Brignole, E., 2002. Phase equilibrium engineering of supercritical hydrogenation reactors. *AIChE J.* 48, 2635–2645.
- Pereda, S., Bottini, S.B., Brignole, E. a., 2002. Gas–liquid reactions under supercritical conditions—phase equilibria and thermodynamic modeling. *Fluid Phase Equilib.* 194-197, 493–499.
- Perego, C., Peratello, S., 1999. Experimental methods in catalytic kinetics. *Catal. Today* 52, 133–145.
- Pérez-Ramírez, J., Berger, R.J., Mul, G., Kapteijn, F., Moulijn, J. a., 2000. Six-flow reactor technology a review on fast catalyst screening and kinetic studies. *Catal. Today* 60, 93–109.
- Perez-Tello, M., Hong, Y.S., Rajamani, R.K., 1999. The effect of bulk concentration gradient on fluid-solid reaction rate. *Chem. Eng. Sci.* 54, 803–806.
- Perrut, M., 2000. *Supercritical Fluid Applications : Industrial Development and Economic Issues*. *Ind. Eng. Chem. Res.* 39, 4531–4535.
- Petersen, E.E., 1965. *Chemical reaction analysis*. Prentice-Hall, Inc., New Jersey.
- Phiong, H.-S., Lucien, F.P., Adesina, A. a, 2003. Three-phase catalytic hydrogenation of α -methylstyrene in supercritical carbon dioxide. *J. Supercrit. Fluids* 25, 155–164.
- Pillai, U., Sahle-Demessie, E., 2003a. Hydrogenation of 4-oxoisophorone over a Pd/Al₂O₃ catalyst under supercritical CO₂ medium. *Ind. Eng. Chem. ...* 6688–6696.
- Pillai, U., Sahle-Demessie, E., 2003b. Hydrogenation of 4-oxoisophorone over a Pd/Al₂O₃ catalyst under supercritical CO₂ medium. *Ind. Eng. Chem. Res.* 6688–6696.
- Pinho, B., 2012. Analysis, Validation and Optimization of a Three-Phase Catalytic Basket Reactor using CFD. Engineering Faculty of the University of Porto (FEUP).

References

- Pitault, I., Fongarland, P., Koepke, D., Mitrovic, M., Ronze, D., Forissier, M., 2005. Gas-liquid and liquid-solid mass transfers in two types of stationary catalytic basket laboratory reactor. *Chem. Eng. Sci.* 60, 6240–6253.
- Pitault, I., Fongarland, P., Mitrovic, M., Ronze, D., Forissier, M., 2004. Choice of laboratory scale reactors for HDT kinetic studies or catalyst tests. *Catal. Today* 98, 31–42.
- Pitla, S.S., Groll, E.A., Ramadhyani, S., 2002. New correlation to predict the heat transfer coefficient during in-tube cooling of turbulent supercritical CO₂. *Int. J. Refrig.* 25, 887–895.
- Privat, R., 2008. Développement du modèle PPR78 pour décrire, comprendre et prédire les diagrammes de phases hautes et basses pressions des systèmes binaires et des fluides pétroliers 1–451.
- Privat, R., Jaubert, J.-N., 2013. Classification of global fluid-phase equilibrium behaviors in binary systems. *Chem. Eng. Res. Des.* 91, 1807–1839.
- Qian, J.-W., Jaubert, J.-N., Privat, R., 2012. Phase equilibria in hydrogen-containing binary systems modeled with the Peng–Robinson equation of state and temperature-dependent binary interaction parameters calculated through a group–contribution method. *J. Supercrit. Fluids* 75, 58–71.
- Qian, J.-W., Jaubert, J.-N., Privat, R., 2013. Prediction of the phase behavior of alkene-containing binary systems with the PPR78 model. *Fluid Phase Equilib.* 354, 212–235.
- Qian, J.-W.W., Jaubert, J.-N.N., Privat, R., 2013. Phase equilibria in hydrogen-containing binary systems modeled with the Peng-Robinson equation of state and temperature-dependent binary interaction parameters calculated through a group-contribution method. *J. Supercrit. Fluids* 75, 58–71.
- Quiñones-Cisneros, S., 1997. Phase and critical behavior in type III phase diagrams. *Fluid Phase Equilib.* 134.
- Ranz, W.E., Marshall, W.R., 1952. Evaporation from drops - Part 1. *Chem. Eng. Prog.*
- Robinson, D.B., Peng, D.-Y., Ng, H.-J., 1977. Applications of the Peng-Robinson equation of state. *ACS Symp. Ser.* 60, 200–220.
- Rolland, M., 2014. Des limites à la réduction d'échelle en réacteur de test catalytique en lit fixe? Claude Bernard Lyon 1 University.
- Romkes, S.J.P., Dautzenberg, F.M., van den Bleek, C.M., Calis, H.P. a, 2003. CFD modelling and experimental validation of particle-to-fluid mass and heat transfer in a packed bed at very low channel to particle diameter ratio. *Chem. Eng. J.* 96, 3–13.
- Ronze, D., Fongarland, P., Pitault, I., Forissier, M., 2002. Hydrogen solubility in straight run gasoil. *Chem. Eng. Sci.* 57, 547–553.
- Rovetto, L.J.L., Bottini, S.B., Brignole, E. a. E., Peters, C.J.C., 2003. Supercritical hydrogenation processes experimental results on the fluid phase behavior of binary and ternary mixtures of hydrogen, propane and tripalmitin. *J. Supercrit. Fluids* 25, 165–176.
- Sáez, a. E., Carbonell, R.G., 1985. Hydrodynamic Parameters for Gas-Liquid Cocurrent Flow in Packed Beds. *AIChE J.* 31, 52–62.
- Samanta, S., Richert, R., 2014. Limitations of heterogeneous models of liquid dynamics: Very slow rate exchange in the excess wing. *J. Chem. Phys.* 140, 054503.
- Samimi, F., Ahmadi, a. R., Dehghani, O., Rahimpour, M.R., 2015. DE Approach in Development of a Detailed Reaction Network for Liquid Phase Selective Hydrogenation of Methylacetylene and Propadiene in a Trickle Bed Reactor. *Ind. Eng. Chem. Res.* 54, 117–129.
- Satterfield, C.N., 1970. Mass transfer in heterogeneous catalysis. Massachusetts Institute of Technology Press, Cambridge.
- Satterfield, C.N., 1975. Trickle-Bed Reactors. *AIChE J.* 21, 209–228.
- Satterfield, C.N., Pelossof, A.A., Sherwood, T.K., 1969. Mass transfer limitations in a trickle-bed reactor. *AIChE J.* 15, 226–234.
- Savage, P.E., Gopalan, S., Mizan, T.I., Martino, C.J., Brock, E.E., 1995a. Reactions at supercritical conditions: Applications and fundamentals. *AIChE J.* 41, 1723–1778.
- Savage, P.E., Gopalan, S., Mizan, T.I.T.I., Martino, C.J., Brock, E.E., 1995b. Reactions at supercritical conditions: Applications and fundamentals. *AIChE J.* 41, 1723–1778.

References

- Schindler, P.W., Fürst, B., Dick, R., Wolf, P.U., 1976. Ligand properties of surface silanol groups. I. surface complex formation with Fe³⁺, Cu²⁺, Cd²⁺, and Pb²⁺. *J. Colloid Interface Sci.* 55, 469–475.
- Schneider, M.S., 2004. In situ Phase Behaviour and Infrared Studies of Catalytic Reactions in “Supercritical” Fluids. Swiss Federal Institute of Technology Zurich.
- Schweitzer, J.M., Dandeu, A., Hipolito, A.I.F., 2010. Modeling of three-phase single pellet string reactor. Application to the selective hydrogenation. *ISCRE 21* 2.
- Seki, T., Grunwaldt, J.-D., Baiker, A., 2008. Heterogeneous Catalytic Hydrogenation in Supercritical Fluids: Potential and Limitations. *Ind. Eng. Chem. Res.* 47, 4561–4585.
- Shah, U., Mahajani, S.M., Sharma, M.M., Sridhar, T., 2000. Effect of supercritical conditions on the oxidation of isobutane. *Chem. Eng. Sci.* 55.
- Sharma, R., 1991. Effective diffusion coefficients and tortuosity factors for commercial catalysts. *Ind. Eng. Chem. Res.* 30, 1428–1433.
- Sherwood, T.K., Holloway, F.A.L., 1940. Performance of Packed Towers — Liquid Film Data for several Packings. *Trans. Am. Inst. Chem. Eng.* 36, 39–70.
- Shi, Y., Zhang, Y., 2008. Simulation of random packing of spherical particles with different size distributions. *Appl. Phys. A* 92, 621–626.
- Shinohara, K., Sugii, Y., Aota, A., Hibara, A., Tokeshi, M., Kitamori, T., Okamoto, K., 2004. High-speed micro-PIV measurements of transient flow in microfluidic devices. *Meas. Sci. Technol.* 15, 1965–1970.
- Singh, U.K., Vannice, M.A., 2001. Kinetics of liquid-phase hydrogenation reactions over supported metal catalysts — a review. *Appl. Catal. A Gen.* 213, 1–24.
- Smith, F.L., Harvey, A.H., 2007. Avoid common pitfalls when using Henry ’s law. *Chem. Eng. Prog.* 33–39.
- Smith, J.M., 1970. *Chemical Engineering Kinetics*. Appl. Catal.
- Smith, P.G., 2007. Applications of Fluidization to Food Processing. In: *Applications of Fluidization to Food Processing*. pp. 1–244.
- Song, D., Seibert, a. F., Rochelle, G.T., 2014. Effect of Liquid Viscosity on the Liquid Phase Mass Transfer Coefficient of Packing. *Energy Procedia* 63, 1268–1286.
- Soo, C.-B., Théveneau, P., Coquelet, C., Ramjugernath, D., Richon, D., 2010. Determination of critical properties of pure and multi-component mixtures using a “dynamic–synthetic” apparatus. *J. Supercrit. Fluids* 55, 545–553.
- Sousa, B., 2015. Impact of supercritical reaction medium with different types of solvents. FEUP and IFPEN.
- Speccia, V., Baldi, G., Gianetto, A., 1978. Solid-Liquid Mass Transfer in Concurrent Two-Phase Flow through Packed Beds. *Ind. Eng. Chem. Process Des. Dev.* 17, 362–367.
- Stockfleth, R., Dohrn, R., 1998. An algorithm for calculating critical points in multicomponent mixtures which can easily be implemented in existing programs to calculate phase equilibria. *Fluid Phase Equilib.* 145, 43–52.
- Stradi, B., Brennecke, J., Kohn, P., Stadtherr, M., 2004. Reliable computation of mixture critical points. *AIChE J.* 1999.
- Stradi, B.A., Stadtherr, M.A., Brennecke, J.F., 2001. Multicomponent phase equilibrium measurements and modeling for the allylic epoxidation of trans-2-hexen-1-ol to carbon dioxide. *J. Supercrit. Fluids* 20, 1–13.
- Stumm, W., Kummert, R., Sigg, L., 1980. A ligand exchange model for the adsorption of inorganic and organic ligands at hydrous oxide interfaces. *Croat. Chem. acta* 53, 291–312.
- Theysen, N., Hou, Z., Leitner, W., 2006. Selective oxidation of alkanes with molecular oxygen and acetaldehyde in compressed (supercritical) carbon dioxide as reaction medium. *Chemistry* 12, 3401–9.
- Thiele, E.W., 1939. Relation between Catalytic Activity and Size of Particle. *Ind. Eng. Chem.* 31, 916–920.
- Thomazeau, C., Boyer, C., 2004. Hydrogénation des hydrocarbures. *Tech. du Eng. J* 5 500v2.

References

- Thomson, S., Hoffmann, C., Ruthe, S., Schmidt, H.-W., Schüth, F., 2001. The development of a high throughput reactor for the catalytic screening of three phase reactions. *Appl. Catal. A Gen.* 220, 253–264.
- Toda, M., Fujii, T., Yoshida, A., Hashida, T., Ono, T., 2011. Measurements of the phase transition and the average length of the density fluctuation under supercritical fluid using micromechanical resonators. *Appl. Phys. Lett.* 99, 074101.
- Torab-Mostaedi, M., Safdari, J., 2009. Mass transfer coefficients in a pulsed packed extraction column. *Chem. Eng. Process. Process Intensif.* 48, 1321–1326.
- Trust, D.B., Kurata, F., 1971. Vapor-Liquid Phase Behavior of the Hydrogen-Propane and Hydrogen-Carbon Monoxide-Propane Systems. *AIChE J.* 17, 86–91.
- Tsai, J., Chen, Y., 1998. Application of a volume-translated Peng-Robinson equation of state on vapor-liquid equilibrium calculations. *Fluid Phase Equilib.* 145, 193–215.
- Tyn, M.T., Calus, W.F., 1975. Diffusion coefficients in dilute binary liquid mixtures. *J. Chem. Eng. Data* 20, 106–109.
- Urakawa, A., Trachsel, F., von Rohr, P.R., Baiker, A., 2008. On-chip Raman analysis of heterogeneous catalytic reaction in supercritical CO₂: phase behaviour monitoring and activity profiling. *Analyst* 133, 1352–1354.
- Valderrama, J.O., 2003. The State of the Cubic Equations of State. *Ind. Eng. Chem. Res.* 42, 1603–1618.
- Valyashko, V.M., 2002. Fluid phase diagrams of ternary systems with one volatile component and immiscibility in two of the constituent binary mixtures Presented at the International Bunsen Discussion Meeting of the Deutsche Bunsen-Gesellschaft für Physikalische Chemie, Walberber. *Phys. Chem. Chem. Phys.* 4, 1178–1189.
- Van Krevelen, D.W., Krekels, J.T.C., 1948. Rate of dissolution of solid substances. *Rec. Trav. Chim. Pays Bas* 67, 512–520.
- Van Pelt, A., Peters, C.J., De Swaan Arons, J., 1991. Liquid–liquid immiscibility loops predicted with the simplified-perturbed-hard-chain theory. *J. Chem. Phys.* 95, 7569.
- Vayenas, C., Pavlou, S., 1987. Optimal catalyst activity distribution and generalized effectiveness factors in pellets: single reactions with arbitrary kinetics. *Chem. Eng.* 42, 2633–2645.
- Vesovic, V., Assael, M.J., Gallis, Z.A., 1998. Prediction of the Viscosity of Supercritical Fluid Mixtures. *Int. J. Thermophys.* 19, 1297–1313.
- Vesovic, V., Wakeham, W. a., 1989. Prediction of the viscosity of fluid mixtures over wide ranges of temperature and pressure. *Chem. Eng. Sci.* 44, 2181–2189.
- Vitu, S., Privat, R., Jaubert, J.-N., Mutelet, F., 2008. Predicting the phase equilibria of CO₂+hydrocarbon systems with the PPR78 model (PR EOS and kij calculated through a group contribution method). *J. Supercrit. Fluids* 45, 1–26.
- Wandeler, R., 2001. Continuous Enantioselective Hydrogenation of Ethyl Pyruvate in “Supercritical” Ethane: Relation between Phase Behavior and Catalytic Performance. *J. Catal.* 200, 377–388.
- Wang, B., Froment, G.F., 2005. Kinetic Modeling and Simulation of the Selective Hydrogenation of the C 3 -Cut of a Thermal Cracking Unit. *Ind. Eng. Chem. Res.* 44, 9860–9867.
- Wang, X., Chou, I.-M., Hu, W., Burruss, R.C., Sun, Q., Song, Y., 2011. Raman spectroscopic measurements of CO₂ density: Experimental calibration with high-pressure optical cell (HPOC) and fused silica capillary capsule (FSCC) with application to fluid inclusion observations. *Geochim. Cosmochim. Acta* 75, 4080–4093.
- Weisz, P.B., Hicks, J.S., 1962. The behaviour of porous catalyst particles in view of internal mass and heat diffusion effects. *Chem. Eng. Sci.* 265–275.
- Wernert, V., Bouchet, R., Denoyel, R., 2010. Influence of Molecule Size on Its Transport Properties through a Porous Medium. *Anal. Chem.* 82, 2668–2679.
- Wild G, Larachi F, C.J., 1992. Heat and Mass Transfer in Gas-Liquid-Solid Fixed Bed Reactors. *Heat and Mass Transfer in Porous Media.* Elsevier, Amsterdam 616–632.
- Wilke, C.R., Chang, P., 1955a. Correlation of diffusion coefficients in dilute solutions. *AIChE J.* 1, 264–270.
- Wilke, C.R., Chang, P., 1955b. Correlation of diffusion coefficients in dilute solutions. *AIChE J.* 1, 264–270.

References

- Williams, R.B., Katz, D.L., 1954a. Vapor-Liquid Equilibria in Binary Systems. Hydrogen with Ethylene, Ethane, Propylene, and Propane. *Ind. Eng. Chem.* 46, 2512–2520.
- Williams, R.B., Katz, D.L., 1954b. Vapor-Liquid Equilibria in Binary Systems. Hydrogen with Ethylene, Ethane, Propylene, and Propane. *Ind. Eng. Chem.* 46, 2512–2520.
- Wu, B., Klein, M., Sandler, S., 1991. Solvent effects on reactions in supercritical fluids. *Ind. Eng. Chem. Res.* 30, 822–828.
- Wu, W., Li, Y.-L., 2011. Selective Hydrogenation of Methylacetylene and Propadiene in an Industrial Process: A Multiobjective Optimization Approach. *Ind. Eng. Chem. Res.* 50, 1453–1459.
- Wu, W., Li, Y.L., 2010. Kinetic modeling of selective hydrogenation of methylacetylene and propadiene in an industrial process. *Ind. Eng. Chem. Res.* 50, 1453–1459.
- Wu, W., Li, Y.L., Chen, W.S., Lai, C.C., 2011. Kinetic studies and operating strategies for an industrial selective hydrogenation process. *Ind. Eng. Chem. Res.* 50, 1264–1271.
- Yang, H.-J., Chu, G.-W., Zhang, J.-W., Shen, Z.-G., Chen, J.-F., 2005. Micromixing Efficiency in a Rotating Packed Bed: Experiments and Simulation. *Ind. Eng. Chem. Res.* 44, 7730–7737.
- Yermakov, Y.I., Arzamaskova, L.N., 1986. Chapter 13 Supported Metal Complexes as Hydrogenation Catalysts. In: *Catalysis*, L.C.B.T.-S. in S.S. and (Ed.), *Catalytic Hydrogenation*. Elsevier, pp. 459–495.
- Yin, J.-Z., Tan, C.-S., 2006. Solubility of hydrogen in toluene for the ternary system H₂+CO₂+toluene from 305 to 343K and 1.2 to 10.5MPa. *Fluid Phase Equilib.* 242, 111–117.
- Yiotis, A.G., Tsimpanogiannis, I.N., Stubos, A.K., Yortsos, Y.C., 2007. Coupling between external and internal mass transfer during drying of a porous medium. *Water Resour. Res.* 43, 1–12.
- Zabaleta, A.G., 2007. *Computational Fluid Dynamics Studies in Heat and Mass Transfer Phenomena in Packed Bed Extraction and Reaction Equipment: Special Attention to Supercritical Fluids Technology*.
- Zamostny, P., Belohlav, Z., 2002. Identification of kinetic models of heterogeneously catalyzed reactions. *Appl. Catal. A Gen.* 225, 291–299.
- Zappoli, B., Beysens, D., Garrabos, Y., 2014. *Heat Transfers and Related Effects in Supercritical Fluids. Technology & Engineering*.
- Zhang, R., Qin, Z., Wang, G., Dong, M., 2005. Critical properties of the reacting mixture in the selective oxidation of cyclohexane by oxygen in the presence of carbon dioxide. *J. Chem. Eng. Data* 50, 1414–1418.
- Zhang, Z., 2011. An Improvement to the Brent's Method. *Int. J. Exp. Algorithms* 2, 21–26.
- Zhao, F., Ikushima, Y., Arai, M., 2003. Hydrogenation of 2-butyne-1,4-diol to butane-1,4-diol in supercritical carbon dioxide. *Green Chem.* 5, 656.
- Zhu, Y., Lu, X., Zhou, J., Wang, Y., Shi, J., 2002. Prediction of diffusion coefficients for gas, liquid and supercritical fluid: application to pure real fluids and infinite dilute binary solutions based on the simulation of Lennard-Jones fluid. *Fluid Phase Equilib.* 194-197, 1141–1159.
- Zimmermann, S., Taghipour, F., 2005. CFD Modeling of the Hydrodynamics and Reaction Kinetics of FCC Fluidized-Bed Reactors. *Ind. Eng. Chem. Res.* 44, 9818–9827.
- Zimm, B.H., 1950. The Opalescence of a Two-Component Liquid System near the Critical Mixing Point. *J. Phys. Chem.* 54, 1306–1317.

Appendix

I. Chapter I

I.1 Catalysis in stationary catalytic basket reactors

The catalyst screening can be studied in a stationary catalytic basket reactor (Doraiswamy and Tajbl, 1974; Perego and Peratello, 1999). In this type of reactors, the catalyst pellets are immobilized in a basket container and flow is forced to pass through it with the help of a stirrer. Its operation principle is based on the pressure gradient generated due to rotation of the hollow self-inducing impeller, which drives the gas into the liquid. This technology has a better performance than a slurry reactor, because the mixture can be highly agitated, ensuring homogeneous gas-liquid concentrations at the catalyst's surface and higher mass transfer coefficients. Also, there are virtually no preferential paths, the fluid always wets the catalyst and there is also homogeneity in temperature.

Besides the previous positives aspects, the performance of these reactors is easily affected by the stirring rate, the gas flow-rate and the type of stirrer. To overview the role of each parameter, Braga 2014 carried out an exhaustive experimental study for hydrodynamic and mass transfer with a standard Rushton impeller. This work has identified the mass transfer correlation for different stirring rates and the velocity vectors in the reactor and catalytic basket, contributing to a better knowledge of the reactor performance.

In comparison to packed bed reactors, the performance in stationary catalytic basket reactors is less affected by the catalyst pellet size distribution. Indeed, for larger ranges of solid distributions, the overall hydrodynamics of the reactor will only be softly altered (Braga, 2014; Pitault et al., 2005). By its turn, since the hydrodynamic and mass transfer rates are mostly depend on the stirring velocity, the impeller and the reactor working conditions should be carefully designed (Fonte et al., 2014; Pinho, 2012; Pitault et al., 2005). The velocity fields for liquid-gas flows in the catalytic bed are poorly understood, because of the technical difficulty to apply the measuring method inside the catalytic basket (Braga, 2014). So the correlations used cannot be easily generalized or used in other cases.

Hydrodynamics and transport phenomena in stirred reactors at lab-scale can be quite different from the industrial-scale stirred reactors. Since it is very complex to have experimental measurements of velocity fields in the catalytic basket, an alternative can be to use computational fluid dynamics (CFD). It allows to study different configuration and scale and for any fluid, without the need to build prototypes and experiments (Magnico and Fongarland, 2006). The CFD gives empirical lines of action and error-prone approaches to reactor design.

I.2 Interphase mass transfer: boundary conditions and equations

Initially, there is no mass transfer between phases in a continuous reactor:

$$x_i(z, t = 0) = x_{i,0} = 0 \quad \text{Eq. 19}$$

The secondary boundary condition can be written according to the Henry's law, which states that the gas fugacity is directly proportional to the gas fraction in the liquid phase for infinite-diluted systems:

$$H_i = \lim_{x_i \rightarrow 0} \frac{f_i}{x_i} \quad \text{Eq. 20}$$

where H_i (bar) is the Henry's constant for solute i and f_i (bar) is the fugacity in the gaseous phase.

In the case of gas-liquid diffusion, if we consider that the diffusion transfer is slow, the concentration of gas species i near the catalyst surface will be low but not zero (Smith and Harvey, 2007). Since real systems never reach the limit of infinite dilution, it is reasonable to assume that the f_i/x_i remains constant for non-zero values of x_i . According to the system used, the previous equation needs to be changed by incorporating corrections to non-ideality and to improve f_i value (Smith and Harvey, 2007). Also, the Henry's constant typically increases at low temperature and decreases with higher temperatures. As a consequence, the following expression can be used:

$$\frac{H_i(T_1)}{H_i(T_0)} \approx \frac{\gamma_i^{inf}(T_1)}{\gamma_i^{inf}(T_0)} \times \frac{P_i^{sat}(T_1)}{P_i^{sat}(T_0)} \quad \text{Eq. 21}$$

where the γ_i^{inf} is the infinite-dilution activity coefficient, P_i^{sat} is the vapor pressure in the equilibrium state and T is temperature.

If the interface between two phases can be interpreted as an infinitely thin plane, where the phases are in equilibrium. If we are in the presence of a real gas, the molar flux of the gas [φ_i (mol.m⁻².s⁻¹)] can be written as:

$$\varphi_i = \frac{V}{A_{GL}} \frac{d(x_i C_{total})}{dt} \Big|_{z=0} = \frac{V}{A_{GL} Z \mathfrak{R} T} \frac{dP_i}{dt} \Big|_{z=0} = -D_i \frac{d(x_i C_{total})}{dz} \Big|_{z=0} \quad \text{Eq. 22}$$

where V (m³) is the volume, Z is the compressibility factor, \mathfrak{R} (m³.bar.mol⁻¹.K⁻¹) is the ideal gas constant and A_{GL} (m²) is the interface area. Joining all the previous equations, we obtain:

$$\left\{ \begin{array}{l} \frac{\partial(x_i C_{total})}{\partial t} = D_i \frac{\partial^2(x_i C_{total})}{\partial z^2} \\ \frac{V}{A_{GL} Z \mathfrak{R} T} \frac{dP_i}{dt} \Big|_{z=0} = -D_i \frac{d(x_i C_{total})}{dz} \Big|_{z=0} \\ f_i = f(P_i, V, T) \\ A_{GL} = f(Re, We) \\ x_i = \frac{f_i}{H_i(t)} \\ \frac{H_i(T_1)}{H_i(T_0)} \approx \frac{\gamma_i^{inf}(T_1)}{\gamma_i^{inf}(T_0)} \times \frac{P_i^{sat}(T_1)}{P_i^{sat}(T_0)} \end{array} \right. \quad \text{Eq. 23}$$

To know the composition profile in the liquid, it is necessary to solve the previous system, by using the following sequence (until convergence):

$$T \rightarrow f_i \rightarrow P_i \rightarrow H_i \rightarrow x_i \leftarrow \quad \text{Eq. 24}$$

Although there are not many equations, the solution is not easily obtained.

1.3 Empirical isotherm adsorption models

Table 1: Characterization of empirical isotherm adsorption models. In these models, $K_{F,i}$, $K_{E,i}$, $K_{T,i}$ and K_i are equilibrium constants for a i species (according to each author). The a_T is adsorptive potential constant and m_T is the Toth's heterogeneity factor. In gray is the adsorption model that we are interested in.

Adsorption model	Equation	Characteristics
Freundlich	$\theta_{i,cat.} = \frac{K_{F,i} C_i^{1/n}}{q_m}$	Can be applied to heterogeneous surfaces and for multilayer adsorption. Fails at high pressures.
Elovich	$\theta_{i,cat.} = K_{E,i} C_i e^{\frac{q_i}{q_m}}$	The adsorption sites increase exponentially with adsorption, implying multilayer adsorption.
Temkin	$\theta_{i,cat.} = \frac{\mathfrak{R}T}{-\Delta H} \ln(K_{T,i} C_i)$	Takes into account the interactions between adsorbent and adsorbate.
Langmuir	$\theta_{i,cat.} = \frac{K_i C_i}{1 + \sum_i K_i C_i}$	Monolayer adsorption without interaction between molecules.
Toth	$\theta_{i,cat.} = \frac{C_i}{(a_T - C_i^{m_T})^{\frac{1}{m_T}}}$	Derived to improve the Langmuir model at both low and high concentration limits.

1.4 Pilot scale uncertainties

Our goal is to estimate how much the conversion in pilot scale (controlled by mass transfer) can be affected by uncertainties. After estimating the uncertainties, an experimental diagnosis test to check if the system is diffusion-controlled will be discussed.

In the uncertainty function ("F" function), the variable uncertainties ($\delta\gamma_i$) are combined by a root-sum-square method and the overall uncertainty (δF) can be expressed by:

$$\delta F^2 = \sum_{i=1}^N \left(\frac{\partial F}{\partial \gamma_i} \delta \gamma_i \right)^2 \quad \text{Eq. 1}$$

This equation can be used as long as:

1. All the uncertainties are independent of each other;

2. Repeated observations of each measurement display Gaussian distribution (Moffat, 1988).

The main uncertainties are related to the feedstock, hydrodynamic and catalyst packing (Figure 1). Thus, if the conversion (X_i) can be expressed as a function of the main uncertainties, a pseudo equation can be written as:

$$\delta X_i^{max} = \left[\left(\frac{\partial X_i}{\partial Feed} \delta Feed \right)^2 + \left(\frac{\partial X_i}{\partial Packing} \delta Packing \right)^2 + \left(\frac{\partial X_i}{\partial Hydro} \delta Hydro \right)^2 \right]^{1/2} \quad \text{Eq. 2}$$

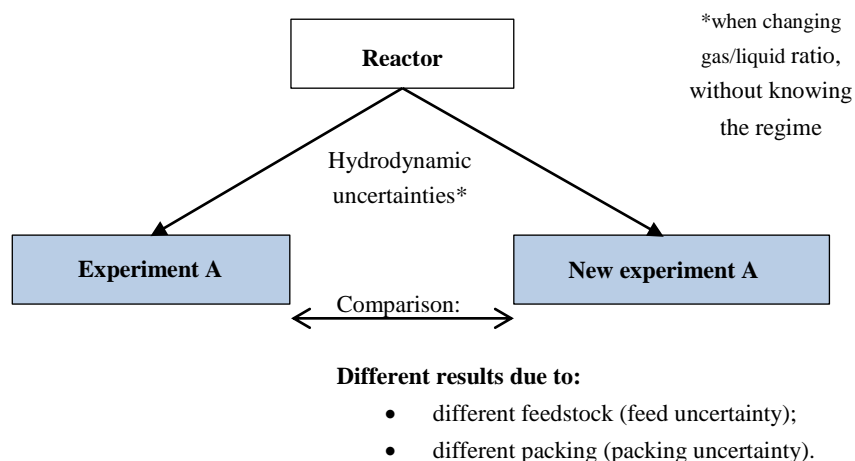


Figure 1: Major uncertainties presented when using the same reactor for the same experiment (same operating conditions).

Feedstock uncertainty

The feedstock comes from refineries because the desired feedstock is usually unavailable in the market (Agbor et al., 2011; Dandeu and Bazer-Bachi, 2012; Wu and Li, 2011). These industrial cuts have a high level of complexity and, apart from the light cuts (less than six carbon atoms), it is very difficult to obtain a detailed chemical analysis of the feed. The reasons are due to the number of isomers or to the resolution of analytical techniques, which cannot always discriminate between molecules with too close signatures (Neurock et al., 1994; Rolland, 2014). This means that chemical process would be, of course, harder to develop, but closer to reality. Indeed, the feedstock from refineries has specific species that can poison the catalyst and lead to quite different catalytic behavior, depending on their concentration.

If it is considered that there are only variations in the reactant concentration and no inhibition of the catalyst between feedstocks, the maximum uncertainty attended is (for the C_3 process → data from a case with inhibition during experiments):

$$\frac{\partial X_i}{\partial Feed} \delta Feed \approx 10\% \quad \text{Eq. 3}$$

Packing uncertainty

For pilot plants with random packing beds, the available surface depends on the orientation, the roughness and the surface deformation of the catalyst particles. According to Giese et al. (1998), the bed porosity is higher near the wall than in the center of the reactor, causing mass dispersion and an increase of the axial fluid velocity. These three parameters can induce preferential paths, which may change the hydrodynamic of the reactor. For diffusion-controlled reactions if the hydrodynamic inside is less favorable, there will be variations in the external mass transfer, leading to a lower effectiveness factor.

Giese et al. (1998) evaluated interstitial flow velocity profiles inside a packed bed with different monodisperse shapes (spheres, cylinders and Raschig-rings). They conclude that the void fraction is influenced by the ratio of the tube and the particle diameters. In another work, Dorai et al. (2012) used computational physical models (solid and fluid) to evaluate the random packing effect on monodisperse and polydisperse shapes, in order to obtain the porosity and velocity distributions. The authors concluded that liquid velocities are not very different between random packing beds. So, based on their results, we expect that the maximum uncertainty related to the different random packing beds is less than 5%.

$$\frac{\partial X_i}{\partial Packing} \delta Packing \approx 5\% \quad \text{Eq. 4}$$

Hydrodynamic uncertainty

Knowing the quantity of liquid and gas reactants supplied to the catalyst is important to identify the effectiveness factor. The prediction of the flow regime and liquid holdup^b in multiphase reactions is quite complex, involving a balance between different physical forces: gravity, inertia, viscosity and capillarity. According to Sáez and Carbonell (1985), a downflow packed bed reactor has four types of regimes. The trickle flow or low interaction regime (low gas and liquid flux) is described by a continuous stratified flow between gas-liquid phases. The spray flow regime (high gas and low liquid flux) is described by the appearance of small bubbles in the liquid medium. The dispersed bubble flow regime (low gas and high liquid flux) is characterized by having big dispersed bubbles in the center of the channel. Finally, the pulsing flow regime (high gas and liquid flux) is described by having periodically liquid or gas zones. This last regime is often called high interaction regime. Each regime affects the thickness of the liquid-film around the solid (capillary number^c) and the dispersion of flow (Peclet number^d) inside the reactor.

As previously discussed (§I.3.2 and §I.3.3), the most widely used models for mass transfer are semi-empirical. In literature, Wild G. et al. (1992) pointed to three different gas-liquid Sh correlations for different regimes. To the best of our knowledge, there is no universal

^b liquid holdup: amount of liquid retained in the catalytic bed after it has been drained;

^c capillary number: ratio of viscous forces to surface tension acting across an interface between a liquid and solid;

^d Peclet number: ratio of advection of a flow to its diffusion.

correlation to account Sh (Sherwood number) for different regimes. So, if the correlations proposed by Wild G. et al. (1992) are compared between flow-regimes with equal dimensionless numbers, the $k_L a_{GL}$ uncertainty is estimated to be around 15%. For the $k_{LS} a_{LS}$, the main uncertainty is related with the surface area. Since $k_{LS} a_{LS}$ is difficult to evaluate due to its connection to $k_L a_{GL}$, we consider that the maximum uncertainty attended is only related with $k_L a_{GL}$:

$$\frac{\partial X_i}{\partial Hydro} \delta Hydro \approx 15\% \quad \text{Eq. 5}$$

This values only accounts uncertainties for $k_L a_{GL}$ when choosing a wrong correlation and not the global impact of $k_L a_{GL}$ in the reaction.

We estimate that δX_i^{max} is around 19% (Eq. 2) for external diffusion-controlled reactive systems. In order to check if the system is limited by diffusion, two types of experimental diagnoses can be done to verify external and internal mass transfer limitations.

Experimental verification of external mass transfer limitations

According to literature (Perego and Peratello, 1999), two different approaches can be followed to check for external mass transfer limitations: (i) change the catalytic bed volume at iso LHSV or (ii) change the LHSV at iso catalytic bed volume. When changing the catalytic bed volume at iso LHSV, the liquid velocity also changes. This impacts the external transfer coefficients: $k_L a_{GL}$ and $k_{LS} a_{LS}$. The same happens when changing the LHSV at iso catalytic bed volume. If the catalytic conversion is dependent at LHSV or with catalytic bed volume, the system has external diffusional limitations.

Experimental verification of internal mass transfer limitations

After checking for external mass transfer limitations, the next step is to know if there are internal limitations. A useful diagnosis test to check for their presence is to evaluate the apparent activation energy (Mears, 1971). This diagnosis should be done in a system that does not have external mass limitations. The goal is to compare theoretical with experimental values for the apparent activation energy (Perego and Peratello, 1999). When the activity of a catalyst increases (or the temperature increases), the internal transfer becomes more important. For instance, the activation energy for petrochemical refining around 50-100 kJ mol^{-1} , but in the presence of internal limitations, the apparent activation energy is around of 25-50 kJ mol^{-1} . Since the apparent activation energy is lower than expected, there might be diffusional limitations (internal transfer).

For a system in external diffusional controlled regime, δX_i^{max} is estimated to be 18% ($= \sqrt{10^2 + 5^2 + 15^2}$). If a reactive system is in a chemical regime, the hydrodynamic uncertainty is negligible, so the δX_i^{max} will be reduced to 11% ($= \sqrt{10^2 + 5^2 + 0^2}$).

1.5 Reaction rates (schemes)

Following I.4.4, the reaction net rate for each compound can be defined per scheme (Wang and Froment, 2005). In scheme 1, the reaction rate can be defined as:

$$\left\{ \begin{array}{l} R_{MA} = R_1 + 2R_4 + R_5 \\ R_{PD} = R_2 + 2R_6 + R_7 \\ R_{PR} = R_1 + R_2 - R_3 \\ R_{PN} = R_3 \\ R_{C6} = R_4 - R_5 \\ R_{C9} = R_5 + R_7 \end{array} \right. \quad \text{Eq. 6}$$

In scheme 2, the reaction rate can be defined as:

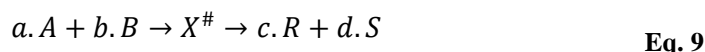
$$\left\{ \begin{array}{l} R_{MA} = R_1 \\ R_{PD} = R_2 \\ R_{PR} = R_1 + R_2 - R_3 - 2R_4 - R_5 \\ R_{PN} = R_3 \\ R_{C6} = R_4 - R_5 \\ R_{C9} = R_5 \end{array} \right. \quad \text{Eq. 7}$$

In scheme 3, the reaction rate can be defined as:

$$\left\{ \begin{array}{l} R_{MA} = R_1 + 2R_6 + R_7 \\ R_{PD} = R_2 + 2R_8 + R_9 \\ R_{PR} = R_1 + R_2 - R_3 - 2R_4 - R_5 \\ R_{PN} = R_3 \\ R_{C6} = R_4 + R_6 + R_8 - R_5 - R_7 - R_9 \\ R_{C9} = R_5 + R_7 + R_9 \end{array} \right. \quad \text{Eq. 8}$$

1.6 Activation volume (pressure effect)

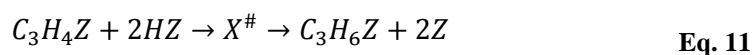
Asano and Le Noble (1978) stated that the molar volume is one of the very few properties of the transition state that can be accurately and easily determined. An elegant entry to understand the reaction rate at high pressure goes back to Eyring-Evans-Polanyi studies for the transition state theory (Laidler and King, 1983), which describes a hypothetical transition between reactants and products. This theory tries to explain how the chemical reaction takes place by determining standard Gibbs free energy, enthalpy, and entropy of the reaction. The concept can be defined as a generic bimolecular reaction as:



The bimolecular reaction starts with an initial free Gibbs energy, then the reaction occurs and the maximum state energy (transition state) is reached, forming an activated complex defined as $X^\#$. After the transition state, the energy decreases as the products separate. The complex is in equilibrium state with the reactants (Bertuccio and Vetter, 2001), and an equilibrium constant can be written as:

$$K^\# = \frac{C_{X^\#}^{eq.}}{(C_A^{eq.})(C_B^{eq.})} \quad \text{Eq. 10}$$

For the C_3 cut hydrogenation, if we look at the $MAPD + H_2 \xrightarrow{R_1} Propylene (PR)$ reaction, we can write as



for the surface reaction of the adsorbed species. Depending on the catalyst material for the active sites and support surface, the transition-state can be stable or rather unstable. A studied related to transition-state was done by Bridier (2012). In their study, the energy profiles were obtained during the adsorption, desorption and transition-state for hydrogenation of methylacetylene to propylene. This was achieved on (111) surfaces of different metal sites: Cu, Pd, Pd-CO and Ni with Cu.

According to the transition theory, the reaction rate k_i^* can be expressed as a function of $K^\#$ as:

$$k_i^* = \chi^* \frac{\kappa_B T}{h} K^\# \quad \text{Eq. 12}$$

where χ^* is the transmission coefficient, which defines the probability that the activated complex decomposes into the wanted products, κ_B (J.K^{-1}) is the Boltzmann's constant, h (J.s) is the Planck's constant and T (K) is the temperature. The previous expression can be derivate for pressure as:

$$\ln k_i^* = \ln K^\# + \ln T + \text{const.} \Rightarrow \left. \frac{\partial \ln k_i^*}{\partial P} \right|_T = \left. \frac{\partial \ln K^\#}{\partial P} \right|_T \quad \text{Eq. 13}$$

The equilibrium can be related to Gibbs free energy (G) as:

$$\left. \frac{\partial \ln k_i}{\partial P} \right|_T = \left. \frac{\partial \ln K^\#}{\partial P} \right|_T = -\frac{1}{\mathfrak{R}T} \frac{\partial \Delta G^\#}{\partial P} = -\frac{\Delta v^\#}{\mathfrak{R}T} \Leftrightarrow \left. \frac{\partial \ln k_i^*}{\partial P} \right|_T = -\frac{\Delta v^\#}{\mathfrak{R}T} \quad \text{Eq. 14}$$

The $\Delta v^\#$ ($\text{m}^3 \cdot \text{mol}^{-1}$) is called the activation volume, and it represents the excess of molar volume in relation to the initial reactants. The $\Delta v^\#$ stands for the pressure changes, as the activation energy [$E_A^\#$ ($\text{J} \cdot \text{mol}^{-1}$)] stands for the temperature variations.

$$\left. \frac{\partial \ln k_i^*}{\partial T} \right|_P = -\frac{E_A^\#}{\mathfrak{R}T} \quad \text{Eq. 15}$$

In terms of applications, the activation energy and the molar volume have different goals. The activation energy is used to investigate mass transfer limitations (Meille et al., 2002). The activation volume is used to acquire information about the bond formation and the stretching in transitory-state (Asano and Le Noble, 1978). This means that the reaction mechanism can be identified by comparing the $\Delta v^\#$ experimentally obtained with databases presented in literature for different bonds (Bertuccio and Vetter, 2001), such as unimolecular dissociation, association, simultaneous bond-formation and -breaking, radical polymerizations, etc. The typical values found in literature for the activation volumes are presented in Table 2.

Table 2: Typical values of activation volume of different reactions. Adapted from Girgis and Gates (1991).

Reaction	Range $\Delta v^\#$ (cm^3/mol)
Unimolecular dissociation $AB \rightarrow A \dots B \rightarrow A + B$	0 to +15

Molecular association $A + B \rightarrow A \dots B \rightarrow AB$	0 to -15
Rearrangement reactions $C - C - C \rightarrow C - C - C$ $R \qquad \qquad R$	-8 to -20
Radical polymerization $A + A + A \rightarrow AAA$	-10 to -25

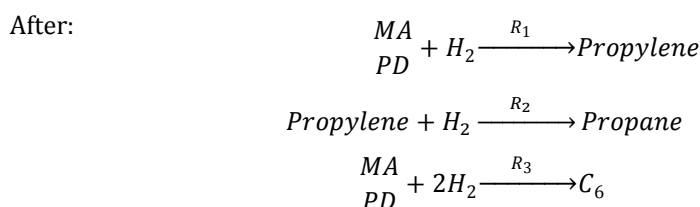
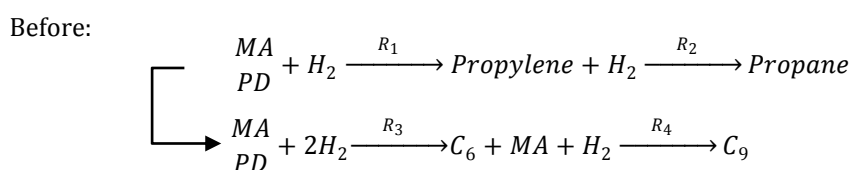
Although, the previous table is small, it can already give us some information about the reaction mechanism. Indeed, bigger databases can be found in the literature. Since 1978, several databases for activation molar volume have been published (Asano and Le Noble, 1978; Drljaca et al., 1998; Eldik et al., 1989).

As previously mentioned, the overall reaction rate in heterogeneous catalysis depends on species transportation, adsorption, chemical reaction and desorption. To evaluate the activation volume in the wanted reaction, the main approach is to model the key stages of reaction system and fit values for k_i^* and K_A, K_B, \dots for each pressure, using the least mean squares method (Bertucco and Vetter, 2001). After this step, evaluate $\left. \frac{\partial \ln k_i^*}{\partial P} \right|_T$ to determine the activation volume, Eq. 14.

To easily understand parameters that are influenced by pressure in C_3 cut hydrogenation, we can simplify the reaction scheme (Figure I.9). So, several hypotheses have to be considered:

1. The concentration of propylene is so high, and the production of new propylene is so small, that the R_2 reaction can be considered in parallel with the MAPD hydrogenation;
2. The concentration of C_9 is negligible.

Therefore, the main reaction scheme is:



According to Bertucco and Vetter (2001), parallel reactions are easier to express: selectivity variations as a function of pressure variations. Before obtaining the general expression, some

derivations have to be done. So, starting with the ratio between reaction rates for C₃ cut hydrogenation:

$$\begin{cases} \frac{R_1}{R_2} = \frac{k_C^* K_B P_{MAPD}}{k_G^* K_F P_{PR}} \\ \frac{R_1}{R_3} \approx \frac{k_C^* K_A K_B}{k_{MAPD-C_6}^* P_H P_{MAPD}} \end{cases} \Rightarrow \begin{cases} \ln\left(\frac{R_1}{R_2}\right) = \ln\left(\frac{k_C^*}{k_G^*}\right) + \ln\left(\frac{K_B P_{MAPD}}{K_F P_{PR}}\right) \\ \ln\left(\frac{R_1}{R_3}\right) \approx \ln\left(\frac{k_C^*}{k_{MAPD-C_6}^*}\right) + \ln\left(\frac{K_A K_B}{P_H P_{MAPD}}\right) \end{cases} \quad \text{Eq. 16}$$

Deriving the previous expressions for pressure at constant temperature, we will obtain:

$$\begin{cases} \left. \frac{\partial \ln(R_1/R_2)}{\partial P} \right|_T = \left. \frac{\partial \ln(k_C^*/k_G^*)}{\partial P} \right|_T + \left. \frac{\partial \ln(K_B P_{MAPD}/[K_F P_{PR}])}{\partial P} \right|_T \\ \left. \frac{\partial \ln(R_1/R_3)}{\partial P} \right|_T \approx \left. \frac{\partial \ln(k_C^*/k_{MAPD-C_6}^*)}{\partial P} \right|_T + \left. \frac{\partial \ln(K_A K_B/[P_H P_{MAPD}])}{\partial P} \right|_T \end{cases} \quad \text{Eq. 17}$$

The previous expressions detail the increase or decrease of the selectivity with the pressure. It also gives information about the dependence of selectivity with other variations, such as species amount, kinetics and adsorption equilibrium. If we look closely, the activation volumes are also presented. We can express:

$$\begin{cases} \left. \frac{\partial \ln(k_C^*/k_G^*)}{\partial P} \right|_T = -\frac{\Delta v_1^\# - \Delta v_2^\#}{\mathfrak{R}T} \\ \left. \frac{\partial \ln(k_C^*/k_{MAPD-C_6}^*)}{\partial P} \right|_T \approx -\frac{\Delta v_1^\# - \Delta v_3^\#}{\mathfrak{R}T} \end{cases} \quad \text{Eq. 18}$$

where $\Delta v_i^\#$ is the activation volume for each reaction.

Although the previous expressions came from the presumption of a reaction model, it can still give acceptable clues about the reaction mechanism. Furthermore, the ratio between reaction models, R_1/R_2 and R_1/R_3 , are less sensitive to the adsorption parameter (denominator in LH-HW reaction models).

For the C₃ cut hydrogenation, the Eq. 18 may allow us to quantify the impact of the pressure and obtain additional clues about the reaction mechanism.

II. Chapter II

II.1 Algorithm formulation

Critical formulation

Heidemann and Khalil (1980) based their algorithm formulation on the limit of stability for homogeneous phases, which corresponds to the critical point. This limit can be expressed by

different forms, depending on the dependent and independent variables chosen. The authors chose the temperature, volume and composition as independent variables and Helmholtz energy as a dependent variable.

$$\begin{aligned} & \left[A - A_0 - \sum_{i=1}^N \mu_{i,0}^{pot} \Delta n_i \right]_{T_0, P_0} = \\ & = \frac{1}{2!} \sum \sum \frac{\partial^2 A}{\partial n_i \partial n_j} \Delta n_i \Delta n_j + \frac{1}{3!} \sum \sum \sum \frac{\partial^3 A}{\partial n_i \partial n_j \partial n_k} \Delta n_i \Delta n_j \Delta n_k + 0(\Delta n)^4 \end{aligned} \quad \text{Eq. 19}$$

where A (J) is the Helmholtz energy, μ^{pot} (J.mol⁻¹) the chemical potential, N the number of components in the mixture, n (mol) the mole number, 0 and i the points where the properties are evaluated, P (Pa) the pressure and T (K) the temperature. To reach the limit of stability (critical point), the Taylor series must be superior to zero. For more information about the critical formulation see Heidemann and Khalil (1980). At the end of the deduction, two restrictions for the critical point were proposed:

$$\frac{1}{2} \sum \sum \frac{\partial^2 A}{\partial n_i \partial n_j} \Delta n_i \Delta n_j = \frac{1}{2} \sum \sum \frac{\partial \ln(f_i)}{\partial n_j} \Delta n_i \Delta n_j = 0 \quad \text{Eq. 20}$$

$$\begin{aligned} \frac{1}{6} \sum \sum \sum \frac{\partial^3 A}{\partial n_i \partial n_j \partial n_k} \Delta n_i \Delta n_j \Delta n_k &= \frac{1}{6} \Re T \sum \sum \frac{\partial^2 \ln(f_i)}{\partial n_j \partial n_k} \Delta n_i \Delta n_j \Delta n_k \\ &= 0 \end{aligned} \quad \text{Eq. 21}$$

These expressions can be simplified by applying matrices and algebra.

$$\frac{1}{2} \Delta n^T \mathbf{Q} \Delta n = 0 \Rightarrow \det(\mathbf{Q}) = 0 \Leftrightarrow \mathbf{Q} \Delta n = 0 \quad \text{Eq. V.22}$$

$$\frac{1}{6} \Re T \sum \sum \mathbf{q}_{ij}^* \Delta n_i \Delta n_j = 0 \quad \text{Eq. 23}$$

where $\mathbf{q}_{ij}^* = \sum \left(\frac{\partial^2 \ln(f_i)}{\partial n_j \partial n_k} \right)_{T, V, n_{l \neq j}} \Delta n_k$ and \mathbf{Q} is the matrix of \mathbf{q}_{ij} , which is defined as

$$\mathbf{q}_{ij} = \left(\frac{\partial \ln(f_i)}{\partial n_j} \right)_{T, V, n_{l \neq j}}.$$

The authors have created an algorithm to solve these two restrictions, having the goal to solve Eq. 23. The algorithm is composed by:

1. Initial guess of critical temperature and critical molar volume;
2. A loop to create the matrix of \mathbf{Q} and converge critical temperature;
3. A loop to determine the \mathbf{q}_{ij}^* and converge the critical volume;
4. A loop until the values of critical pressure and critical temperature do not change between interactions for the steps 2 and 3.

Numerical formulation

The authors applied the numerical derivatives in the steps 2 and 3 in the algorithm presented in the critical formulation. For more details, see Stockfleth & Dohrn (1998).

When the critical formulation was firstly reported, the authors used analytical derivatives of the PR78 equation of state. In terms of computational time-consuming, the analytical

derivatives are an excellent option, but their use is limited. In general, it is not possible to implement other EOS without making huge changes in the resolution code. Due to the time-consuming of deriving and coding the analytical derivatives, the numerical derivation is preferred. Furthermore, the numerical derivatives can be used even when there are no analytical derivatives. Stockfleth & Dohrn (1998) proposed a four-point numerical derivative scheme:

$$q_{ij} \approx \frac{\ln(f_i[-2h]) - 8\ln(f_i[h]) + 8\ln(f_i[h]) - \ln(f_i[2h])}{12h} \quad \text{Eq. 24}$$

$$q_{ij}^* \approx \frac{q_{ij}[-2h] - 8q_{ij}[-h] + 8q_{ij}[h] - q_{ij}[2h]}{12h} \quad \text{Eq. 25}$$

The numerical derivatives were computed by small variations of a finite increment of the number of moles (h), usually around 0.001 mol. Each fugacity is a temperature, molecular volume and composition dependent function, so when making an increment of moles it becomes:

$$f_i(T, v, x) \xrightarrow{h \text{ increment}} f_i(T, \tilde{v}, \tilde{x}) \quad \text{Eq. 26}$$

$$\tilde{x}_i = \frac{\tilde{n}_i}{n_{total} + h} \quad \text{Eq. 27}$$

$$\tilde{v} = \frac{n_{total}}{n_{total} + h} \quad \text{Eq. 28}$$

Convergence formulation

In parallel to the calculations made, a careful attention has to be done to the convergence method used (in each loop of the algorithm proposed in the critical formulation). To assure the system convergence and the minimum loops, Hoteit et al. (2006) discussed the use of Brent's method (one-dimensional search method) in detriment of 1D Newton-Raphson method. Contrary to this method, Brent's method does not need to evaluate the function derivatives to find the zero(s) of non-linear functions. In an algorithm with numerical formulation (higher tendency to diverge), Brent's method assures convergence. To achieve the convergence, it takes advantage of the reliability of the bisection method and the speed of secant and inverse quadratic methods. The Brent method, which was used in the algorithm, can be generically written as:

- A. Have an interval $[T_A; T_B]$;
- B. Evaluate the value function in the extremes of the interval (f_{T_A} and f_{T_B}):
 - i. If $f_{T_A} f_{T_B} > 0$ there is no root in the function;
 - ii. Otherwise, find the root T_i using:
 - Inverse quadratic method (James F. Epperson, 2007);
 - Secant method;
 - Bisection method.
- C. Evaluate the f_{T_i} :
 - i. If $f_{T_i} < Error$, the value of T_i was found;
 - ii. Otherwise, change the interval evaluated and repeat B.

Algorithm construction

The proposed algorithm is based on the three formulations previously presented, and it is divided into two different loops, as suggested in the critical formulation. The first loop of the algorithm allows to calculate an iterative critical temperature. The second loop allows to calculate an iterative critical volume. As the critical volume is necessary to calculate the critical temperature and vice versa, the algorithm final solution is the results of the successive iterative solution.

To calculate the critical point of binary and multicomponent mixtures, an EOS and a mixing rule (which allow to extend the EOS from pure fluids to mixtures) are required. In literature, the majority of the critical points calculated were obtained by using the Peng-Robinson EOS and Van der Waals mixing rules (Henderson et al., 2010; Ke et al., 2001; Konynenburg and Scott, 1980; Stradi et al., 2004). The reasons are the small input information required (EOS: T_c , P_c and acentric factor $[w]$; Van der Waals: α and k_{ij}), the lower complexity and the low time consumption.

Considering all the methodologies developed in this subchapter, the sum-up of the overall algorithm can be written as:

- A. Initial guess of the mixture critical point (T_c and v_c):
 - i. Calculate $T_{c,0} = \sum_{i=1}^{n_c} T_{c \text{ pure } i} x_i$;
 - ii. Calculate $v_{c,0} = \sum_{i=1}^{n_c} v_{c \text{ pure } i} x_i$;
 - iii. Create an interval to be analyzed with Brent's method:
 - $T_c \in [0.5 T_{c,0}; 2 T_{c,0}]$
 - $v_c \in [v_{c,0}; 4 v_{c,0}]$
- B. Critical temperature calculation loop (constant v_c):
 - i. Determine the matrix \mathbf{Q} for $T_{c,i}$ and $v_{c,i}$;
 - ii. Determine $\det(\mathbf{Q})$;
 - iii. If $\det(\mathbf{Q}) > Error$, calculate $T_{c,i+1}$ with Brent's method and restart B step;
 - iv. If $\det(\mathbf{Q}) < Error$, then go to C.
- C. Critical volume calculation loop (constant T_c):
 - i. Determine Δn using the equation $\mathbf{Q}\Delta n = 0$;
 - ii. Normalize $\Delta n \Rightarrow \Delta n^T \Delta n = 1$;
 - iii. Determine each q_{ij}^* ;
 - iv. If $\frac{1}{6} \Re T \sum \sum q_{ij}^* \Delta n_i \Delta n_j > Error$, calculate $v_{c,i+1}$ with Brent's method and restart C step;
 - v. If $\frac{1}{6} \Re T \sum \sum q_{ij}^* \Delta n_i \Delta n_j < Error$, then go to C;
- D. Re-do the step B and C until the critical temperature and critical volume converges, i.e., $v_{c,i+1} \approx v_{c,i}$ and $T_{c,i+1} \approx T_{c,i}$.

For more information, a more detailed explanation of the algorithm is presented on the Appendix §II.2.

II.2 Algorithm detailed

Step 1. Inputs:

Compositions: $x_1, \dots, x_n \in [0; 1]$; Compounds pure critical points: T_c (K) P_c (Pa);

Equation of state parameters



Step 2. Estimation of the mixture critical temperature (T) and molar volume (v) →

$$T_0 = \sum_{i=1}^n T_{c_i} x_i ; v_0 = \sum_{i=1}^n b_i x_i$$



Step 3. Determine the critical temperature of the mixture

Heidemann et al. 1980 proposed:

$$\frac{1}{2} \sum_{i=1}^n \sum_{j=1}^n \frac{\partial^2 A}{\partial n_i \partial n_j} \Delta n_i \Delta n_j = \frac{1}{2} RT \sum_{i=1}^n \sum_{j=1}^n \frac{\partial \ln f_i}{\partial n_j} \Delta n_i \Delta n_j = \frac{1}{2} RT \Delta n^T Q \Delta n = 0 \rightarrow \det(Q) = 0 \text{ to } \Delta n \neq 0$$

Loop 1: While $\det(Q) > error = 10^{-5}$

Based in Stockfleth et al. 1998 proposed a numerical approach to Heidemann et al. 1980 algorithm:

For i=1 to n (number of compounds in the mixture)

For k=-2 to 2

$$x_i = \frac{x_{total} + hk}{n_{total} + hk}$$

$$x_{\neq i} = \frac{x_{total}}{n_{total} + hk}$$

$$v = \frac{v_0}{(1 + hk)}$$

f_i → Fugacity calculated using an EOS

End

End

Create the matrix Q where

$$Q_{i,j} = \frac{\partial \ln f_i}{\partial n_j} = \frac{f_i(\bar{x}; \bar{v}; k = 2) - 8f_i(\bar{x}; \bar{v}; k = 1) + f_i(\bar{x}; \bar{v}; k = -1) - 8f_i(\bar{x}; \bar{v}; k = -2)}{12h}$$

If $\det(Q) < 10^{-5}$

Exit while

Else

Calculate the new T_c with Brent's method until the superior condition is satisfied, based in Hoteit et al. 2006 algorithm.

End

Step 4. Determine the critical molar volume

Heidemann et al. 1980 proposed:

$$\frac{1}{6} \sum_{i=1}^n \sum_{j=1}^n \sum_{k=1}^n \frac{\partial^3 A}{\partial n_i \partial n_j \partial n_k} \Delta n_i \Delta n_j \Delta n_k = \frac{1}{6} RT \sum_{i=1}^n \sum_{j=1}^n \sum_{k=1}^n \frac{\partial^2 \ln f_i}{\partial n_j \partial n_k} \Delta n_i \Delta n_j \Delta n_k = C = 0$$

Loop 2: While $C > error = 10^{-5}$

Based in Stockfleth et al. 1998:

Determine Δ_n $Q\Delta_n = 0$

Normalize Δ_n $\Delta n^T \Delta n = 1$

For $i=1$ to n (number of compounds in the mixture)

For $k=-2$ to 2

$$\tilde{n}_i = n_{total} x_i + k \varepsilon \Delta n_i$$

$$\tilde{n}_{\neq i} = n_{total} x_i$$

$$\tilde{n}_{total} = n_{total} + k \varepsilon \Delta n_i$$

Calculate $x_{i,1}$

For $j=1$ to n

For $l=-2$ to 2

$$x_{i,2} = (x_i + lh)/(1 + lh)$$

$$x_{\neq i,2} = x_i/(1 + lh)$$

$$v_2 = v_1 / (n_{total} + lk)$$

$f_j \rightarrow$ Fugacity calculated using an EOS

End

End

Create the matrix

$$\frac{\partial \ln f_i}{\partial n_j} = \frac{f_i(\tilde{x}_2; \tilde{v}_2; k=2) - 8f_i(\tilde{x}_2; \tilde{v}_2; k=1) + f_i(\tilde{x}_2; \tilde{v}_2; k=-1) - 8f_i(\tilde{x}_2; \tilde{v}_2; k=-2)}{12h}$$

End

End

Create the matrix

$$\frac{\partial \ln^2 f_i}{\partial n_j \partial n_k} = \frac{\partial \ln f_i}{\partial n_j}(\tilde{x}_1; \tilde{v}_1; k=2) - 8 \frac{\partial \ln f_i}{\partial n_j}(\tilde{x}_1; \tilde{v}_1; k=1) + \frac{\partial \ln f_i}{\partial n_j}(\tilde{x}_1; \tilde{v}_1; k=-1) - 8 \frac{\partial \ln f_i}{\partial n_j}(\tilde{x}_1; \tilde{v}_1; k=-2)}{12h}$$

If $C < 10^{-5}$

Exit while

Else

Calculate the new molar volume based in Brent's method until the superior condition is satisfied. Based in Hoteit et al. 2006 algorithm.

End

Step 5. Repeat Loop 1 and Loop 2 until the critical pressure and molar volume don't vary between iterations. For instance, the critical temperature and molar volume should be the same at the beginning of the algorithm and at the end.

$$Error = |Value_{Actual\ iteration} - Value_{Previous\ iteration}|$$

Step 6. Convert the critical molar volume to pressure.

II.3 Interaction parameters

Table 3 shows the interactions parameters used in algorithm validation [§II.3.4].

Table 3: Upper triangular matrix from a symmetric matrix of the interaction parameters (k_{ij}) for the components (for PR78 EOS). The gray zone is the same as the upper part ($k_{1,2} = k_{2,1}$). Values obtained from Henderson et al. (2010) and Pro/II® database.

	1	2	3	4	5	6	7	8	9	10	11	12
1	0	0	0.0140	0	0	0.0422	0	0.0311	0.0919	0.016	-	0.085
2		0	0	0.096	0.0078	-0.01	0.067	0	0.1322	-0.067	-	0.085
3			0	0	0	0	0	0.0852	0.124	0.148	-	0.075
4				0	0	-0.005	0.033	0	0.1333	-0.397	-	0.06
5					0	0	0.0074	0	0.122	0.269	-	0.06
6						0	0	0.1	0.11	-0.03	-	0.06
7							0	0	0.1	-0.117	-	0.06
8								0	-0.017	-0.03	-	0.18
9									0	0.154	-0.05	0.1
10										0	0.17	0.1
11											0	
12												0

II.4 From binary to quaternary diagrams

We later introduce H_2 into the mixture to investigate the quaternary phase diagram (CO_2 + propylene + propane + H_2). Using the same microfluidic approach, the P–T phase diagrams were plotted and the critical locus was determined as a function of the molar fraction of CO_2 (Figure 2).

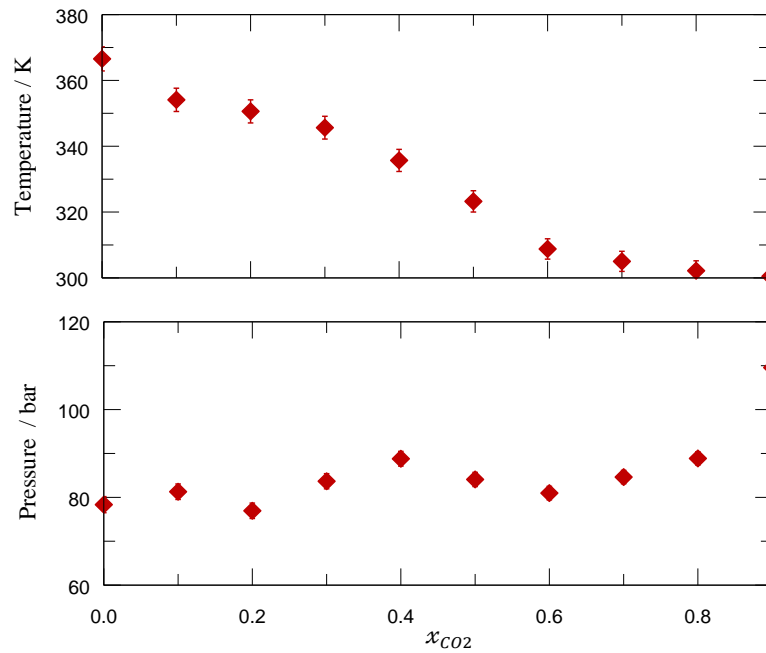


Figure 2: Critical points for the quaternary CO_2 + propylene + propane + H_2 mixture with a constant 10% molar composition of hydrogen and constant propylene to propane molar ratio of 93:7. ♦ On-chip experimental results.

II.5 C₃ cut - ternary combination (direct interpretation)

Here it is presented the direct interpretation (without interpolation) of the experimental results for ternary and quaternary mixtures: C₃ cut + solvent (CO₂, Ethane and CH₄) + H₂.

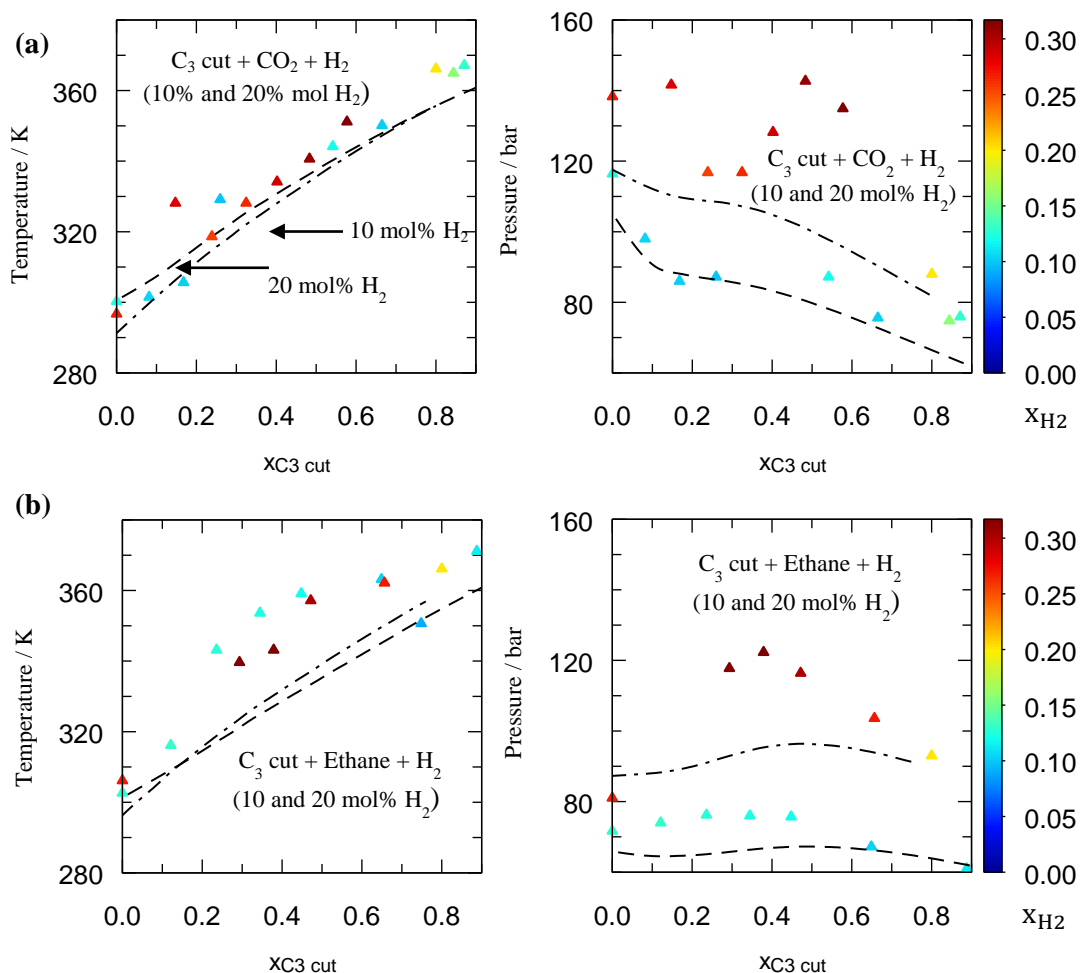


Figure 3: Critical data (pressure and temperature) for ternary combinations of C₃ cut (2.8 mol% MAPD) + solvent (CO₂ and Ethane) + H₂. (a) Solvent: CO₂ (b) Solvent: ethane. The dots are values experimentally obtained with on-chip technology, and the lines were estimated with PPR78 EOS. Normal dashed-lines are 10 mol% H₂ and the others are 20 mol% H₂.

For ternary combinations, in one hand the results are close to the ones estimated for C₃ cut + CO₂ + H₂ with ~10% H₂ (Figure 3a). In the other hand, the experimental results seem higher than predicted ones for C₃ cut + CO₂ + H₂ with ~20% H₂ (pressure) and for C₃ cut + ethane + H₂ (temperature and pressure). Unfortunately in Figure 3, the comparison between experiments and model is not clear (points with different hydrogen composition lead to difficult interpretation). The experimental points have higher hydrogen content than model lines (10 and 20%). To make a fair interpretation of the experimental results with the model, a ternary diagram with interpolation is necessary.

For the ternary combination with methane, it was experimentally impossible to obtain the critical data for critical temperatures below 300 K (impossible to perform experiments below

atmospheric temperature with the current set-up). Even so, several dew points were experimentally obtained (Figure 4), which means that at the conditions taken, the fluid is completely miscible.

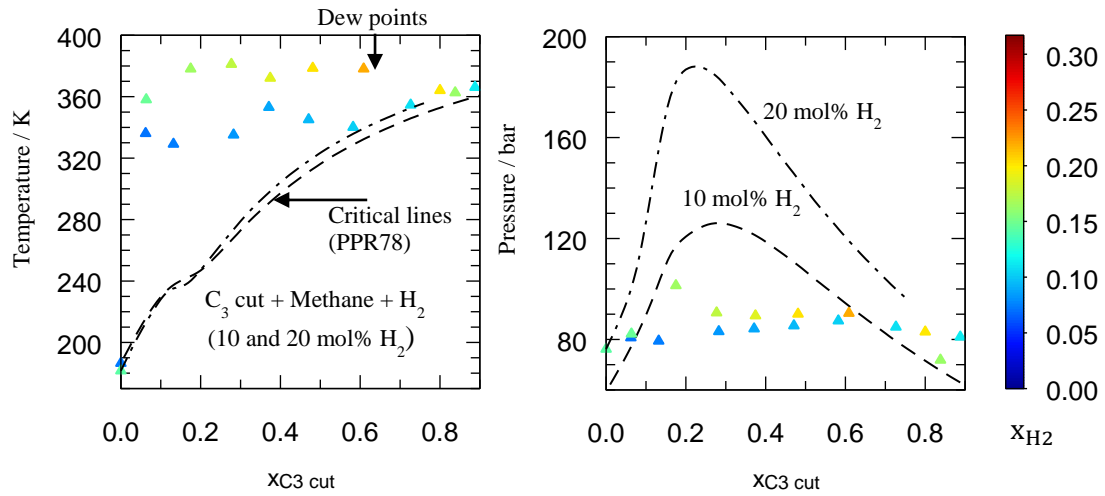


Figure 4: Dew points for C₃ cut (2.8 mol% MAPD) + solvent (CH₄) + H₂. The dots are values experimentally obtained. The lines were estimated with PPR78 EOS for critical coordinates. Normal dashed-lines are 10% mol H₂ and the others are 20 mol% H₂.

The results cannot be easily interpreted; therefore, a ternary representation should be used.

The next step is to use the ternary representation with interpolation of experimental points, which was presented in §II.3.5.

III. Chapter III

III.1 Intragranular diffusion

In this technique, the liquid toluene self-diffusion, also known as Brownian molecular movement, is evaluated in a free zone (free self-diffusion) and in a confined zone (confined self-diffusion ~ particle diffusion) (Durand et al., 2008; Nilsson and Morris, 2008; Nilsson, 2009). The values obtained for free self-diffusion ($D_{Tol,b}$) and particle diffusion (or effective diffusion) ($D_{Tol,e}$) can be written as:

$$D_{Tol,e} = \frac{D_{Tol,b}\varepsilon + \rho_s K'_{Tol,s} D_{Tol,s}}{\tau^*} \quad \text{Eq. 29}$$

where ρ_s (kg.m⁻³) is the solid density, $K'_{Tol,s}$ (m³.kg⁻¹) is the linear equilibrium adsorption constant at the solid surface and $D_{Tol,s}$ (m².s⁻¹) is the surface diffusion (more details about this equation on §I.3.3). The τ^* is the tortuosity factor.

The Eq. 29 can be written in a more intuitive form (Eq. 30), allowing to detail the relation between both diffusions.

$$\frac{D_{Tol,e}}{D_{Tol,b}} = \frac{\varepsilon + \rho_s K'_{Tol,s} \frac{D_{Tol,s}}{D_{Tol,b}}}{\tau^*} = \beta \quad \text{Eq. 30}$$

where β is a function depending on fluid physical parameters (ε , ρ_s , τ^* and $D_{Tol,b}$) and chemical interaction parameters ($D_{Tol,s}$ and $K'_{Tol,s}$).

Using the DOSY-RMN methodology, the toluene particle diffusion was evaluated in four different particles (Table 4): the catalyst W and three $\alpha - Al_2O_3$ supports were obtained from different industrial batches. In this study, a tube with an inner diameter of ~ 3 mm was filled with 2 cm of particles (~ 10 particles) with similar diameter range (from 2.38 to 2.50 mm).

Table 4: Toluene diffusivities DOSY-RMN for free and confined zones.

		D_{Tol} (m ² s) at 295K	Standard deviation (m ² s)	β
Catalyst W	Free toluene	2.22×10^{-9}	6.99×10^{-11}	
	Confined toluene	2.26×10^{-9}	5.70×10^{-11}	1.02
Support batch 1	Free toluene	2.37×10^{-9}	4.95×10^{-11}	
	Confined toluene	2.30×10^{-9}	7.69×10^{-11}	1.03
Support batch 2	Free toluene	2.17×10^{-9}	5.83×10^{-11}	
	Confined toluene	2.29×10^{-9}	1.41×10^{-10}	0.94
Support batch 3	Free toluene	2.33×10^{-9}	3.32×10^{-11}	
	Confined toluene	2.26×10^{-9}	5.96×10^{-11}	1.03

Regarding Table 4, the toluene diffusion in the four particles has identical values to the toluene in the free zone ($\beta \approx 1$), which is a typical value for gases. These results are unexpected, since in the majority of cases the confined self-diffusion (in a particle) for liquids is 10 times less than the free self-diffusion ($\beta \approx 0.1$) (Sharma, 1991). To better understand why $\beta \approx 1$, the Eq. 30 can be used as simplified model to understand the physical phenomena. To have a more complex approach, see Yiotis et al. (2007) and Pan and Zhu (1998).

$$\beta = 1 = \frac{\varepsilon + \rho_s K'_{Tol,s} \frac{D_{Tol,s}}{D_{Tol,b}}}{\tau} \Rightarrow \overset{=1}{\beta} \frac{\tau - \varepsilon}{\rho_s} D_{Tol,b} = \underbrace{\frac{K'_{Tol,s} D_{Tol,s}}{\text{chemical interaction par.}}}_{\text{fluid physical par.}} \quad \text{Eq. 31}$$

where $D_{Tol,s}$ should be equal or lower than $D_{Tol,b}$.

If we assume $\tau=1.4$ (usual value), the previous expression can be written as:

$$\underbrace{1 \times (1.4 - 0.65) \times 2.30 \times 10^{-9}}_{\text{fluid physical par.}} = 1.72 \times 10^{-9} \text{ m}^2\text{s}^{-1} = \underbrace{\rho_s K'_{Tol,s} D_{Tol,s}}_{\text{solid characteristic diffusion}} \quad \text{Eq. 32}$$

The previous equation (Eq. 32) suggests that for $\beta = 1$, the $\rho_s K'_{Tol,s} D_{Tol,s}$ should be compensated. The value $1.72 \times 10^{-9} \text{ m}^2\text{s}^{-1}$ is a curious result, because it has the same

dimensions as diffusion ($\text{m}^2 \cdot \text{s}^{-1}$). This value can be seen as a solid characteristic diffusion, since it takes into account surface diffusion and wall adsorption.

The results show that the free self-diffusion ($D_{Tol,b}$) and particle diffusion ($D_{Tol,e}$) are identical ($\beta = 1$) only because the value of solid characteristic diffusion is close the free self-diffusion ($1.72 \times 10^{-9} \text{ m}^2 \cdot \text{s}^{-1}$ is close to $2.30 \times 10^{-9} \text{ m}^2 \cdot \text{s}^{-1}$). Even with limited knowledge about diffusion in a solid particle, which is a complex phenomenon, it is possible to propose the following conclusions:

1. $D_{Tol,s}$ may lose 25% of free self-diffusion (in relation to the free zone), but the $D_{Tol,e}$ has the same value as the free self-diffusion;
2. toluene should suffer interaction with the catalyst walls to explain the high fluid effective diffusion ($D_{Tol,e}$).

To fully understand the DOSY-RMN results, more studies, and an enhanced model might be required. Our goal was to draft some guidelines to analyze the obtained data, in order to have hints about the diffusion of species presented in C_3 cut hydrogenation. Concerning the effective diffusion of MA, PD, and other species in C_3 cut, it is assumed that their value might be equal to their diffusion in the bulk.

III.2 Catalyst reduction

The catalyst active phase is reduced under H_2 flow-rate of $40 \text{ L} \cdot \text{h}^{-1}$ (normal PT conditions). The operating conditions are atmospheric pressure and 423 K (Figure 5), being maintained for 2 hours before descending to room temperature.

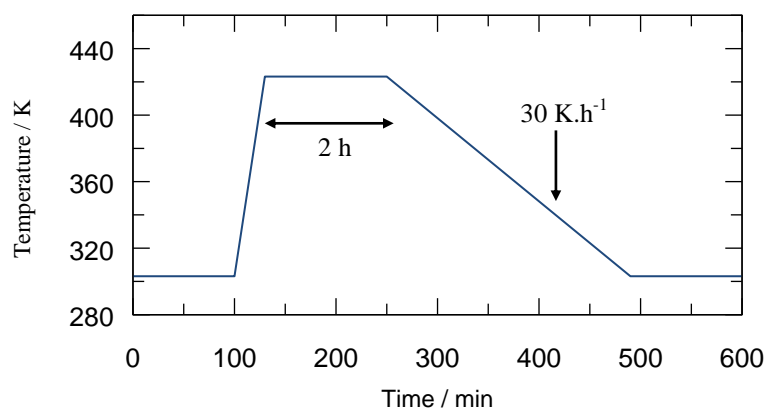


Figure 5: Temperature profiles during the catalyst reduction.

III.3 Packing characterization

3D particle arrangements: concept and application

For a single pellet string reactor, the use of a 2D projection to describe particle arrangements can lead to a false hypothesis. A simple example is when a particle is above another in a yz projection (Figure 6a). If the channel is rotated, we cannot be sure of the particle new position, since a 2D projection of a 3D arrangement has one degree of freedom. Another projection is required to have more information about the particle position, such as a xz

projection (Figure 6b). With two axis projections, the particle arrangement can be defined in the 3D view.

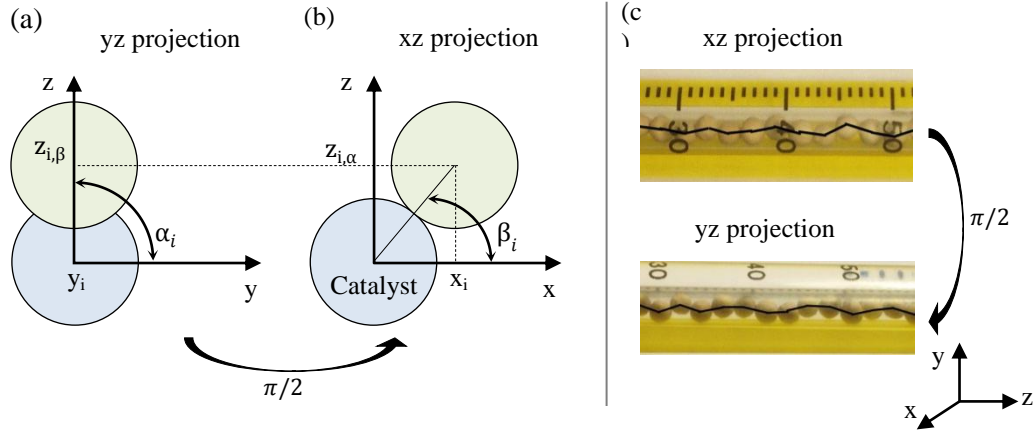


Figure 6: Scheme of the methodology used to obtain the relative angle between catalyst pellets (α_i and β_i). The angle is acquired from the center of one particle to another. (a) yz axis projection; (b) xz axis projection; (c) photos of the portion of particle arrangement for xz and yz axis projection. The angle of each line-segment was determined using ImageJ (open source software).

To obtain data about the particle arrangement, two photos were taken with different angles (0 and $\pi/2$) of a graduated tube filled with catalyst pellets (Figure 6c). The graduated tube has the same inner diameter as the single pellet reactor selected (3 mm). To locate the particles, two options can be adopted: locate each particle position (x_i, y_i, z_i) or obtain the angle between adjoin particles (α_i and β_i) and, by using trigonometric equations, calculate the particle positions. Locate the particle position in a photo is not the best choice, because a referential distance has to be defined and the values are subject to optical and perspective distortion. On the other hand, locate the angles between particles (Figure 6c line) does not require a defined referential distance and the data is not subjected to optical and perspective distortion.

After acquiring α and β , with trigonometry, it is possible to obtain each particle position by:

$$x_i = \cos(\alpha_i) (r_{cat. i-1} + r_{cat. i}) + x_{i-1} \quad \text{Eq. 33}$$

$$z_{i,\alpha} = \sin(\alpha_i) (r_{cat. i-1} + r_{cat. i}) + z_{i-1} \quad \text{Eq. 34}$$

$$y_i = \cos(\beta_i) (r_{cat. i-1} + r_{cat. i}) + y_{i-1} \quad \text{Eq. 35}$$

$$z_{i,\beta} = \cos(\beta_i) (r_{cat. i-1} + r_{cat. i}) + z_{i-1} \quad \text{Eq. 36}$$

where $x_i, y_i, z_{i,\alpha}$ and $z_{i,\beta}$ are relative positions of each particle center. The reference point is in the center of the previous particle (see Figure 6). Two values of z were proposed for the system, $z_{i,\alpha}$ and $z_{i,\beta}$. These values should match, but since particles can have an oval geometry, sometimes they do not match at 100%. For example, there was a deviation of 0.001 mm for $d_{cat.} \approx 2.45$ mm. Therefore, the following equation should be adopted:

$$z_i = (z_{i,\alpha} + z_{i,\beta})/2 \quad \text{Eq. 37}$$

where z_i is the value that should be used for the z axis.

Since the catalyst pellets have a small standard deviation in size distribution, $r_{cat. i-1} + r_{cat. i}$ can be approximate to $d_{cat. i}$. A prominent example of a 3D reconstruction data (using the previous equations) is shown in Figure 7.

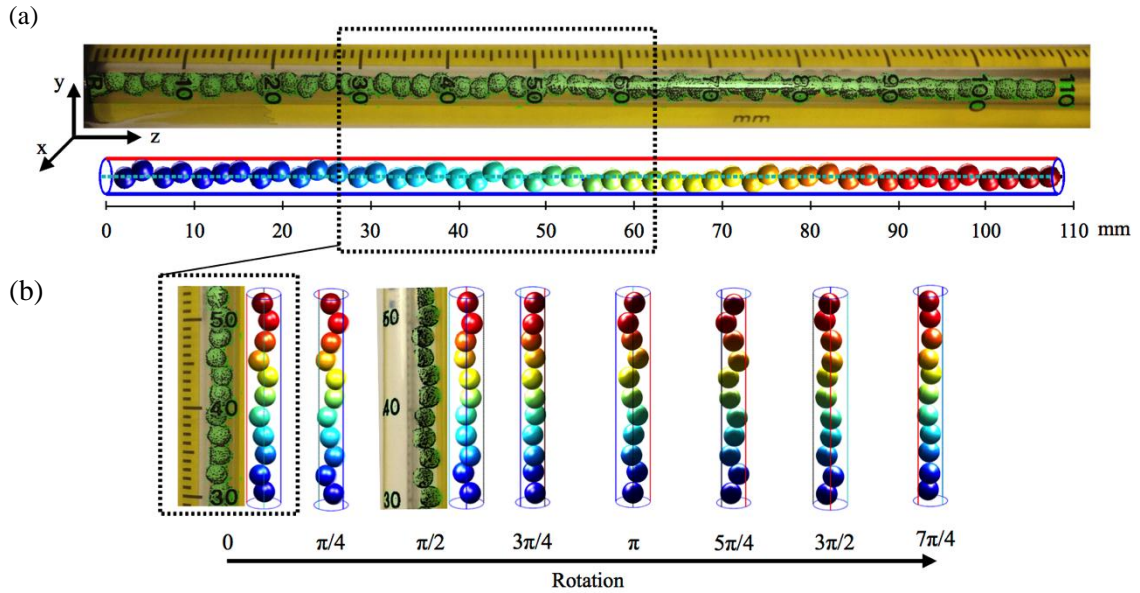


Figure 7: (a) Comparison between the real and calculated catalyst packing ($d_{cata} = 2.45$ mm) for a vertical channel ($d_{reactor} = 3.00$ mm) (48 particles). (b) Reconstruction of the catalyst packing during a 2π rotation (11 catalyst pellets are presented).

Regarding Figure 7, the calculated particle positions obtained by angles measurements (in ImageJ) are close to the real case. Another relevant information (Figure 7b) is that each catalyst pellet is in contact with the wall. If the contact points between adjoining particles are connected by lines, a near-net helical shape seems to be formed. This shape can be interesting in hydrodynamic point of view.

The next step is to quantify packing distribution and check if the particle arrangement is not exclusive of the sample analyzed.

Particle arrangement

To study particle arrangement, a channel was trunked with 50 catalyst pellets (total length of 110 mm) (see Figure 7a). Several measurements were done with the same the tube and particles, which means that no additional effects were introduced. Between measurements, the tube was agitated to compact the catalyst bed. The goal is to find the angle distribution inside the channel.

It was previously discussed that two angles are required to access the particle location. These angles can be applied to construct a distribution of the particle arrangement. Therefore, three distributions were created: front view (0 rad), right view ($\pi/2$ rad) and a characteristic view (γ_i rad). For the characteristic view, the γ_i was defined as the most distant angle (α_i or β_i)

from $\frac{\pi}{2}$ rad (particle be perfectly above another [Figure 6]). This guarantees that the most pronounced angle is clearly defined.

$$\gamma_i = \begin{cases} \alpha_i & \text{if } \left(\alpha_i - \frac{\pi}{2}\right)^2 > \left(\beta_i - \frac{\pi}{2}\right)^2 \\ \beta_i & \text{if } \left(\alpha_i - \frac{\pi}{2}\right)^2 < \left(\beta_i - \frac{\pi}{2}\right)^2 \end{cases} \quad \text{Eq. 38}$$

In this study, a total of 8 particle arrangements (composed by 50 particles) were tested by shaking the trunked channel. In total, 384 particles and 768 angles were analyzed.

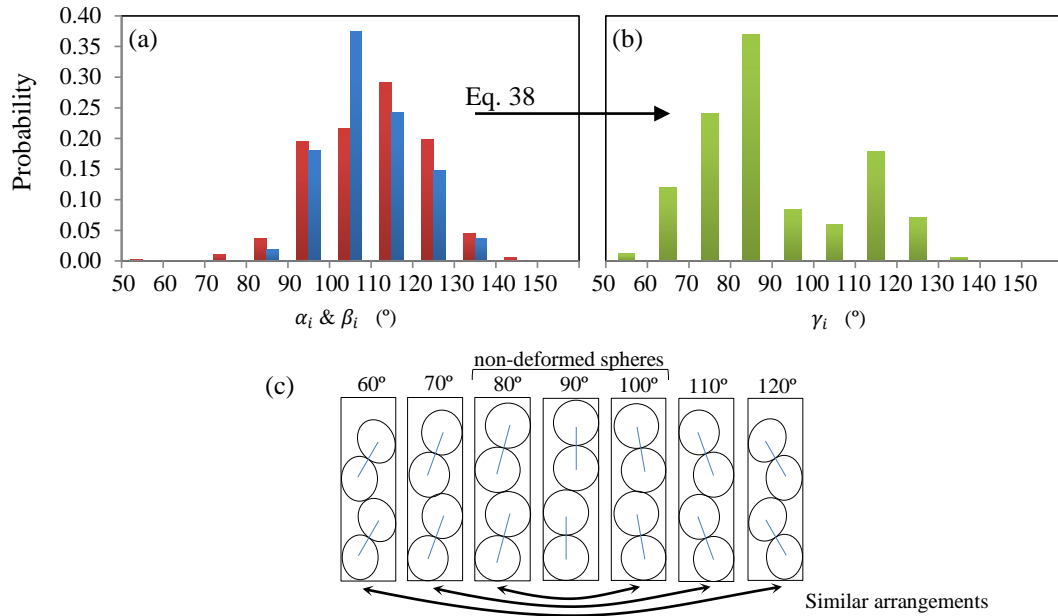


Figure 8: Particle angle distributions for random particle packing ($d_{cata} \approx 2.45$ mm) inside the reactor channel ($d_{reactor} = 3.00$ mm). (a) Front (blue; α_i) and right view (red; β_i); (b) Characteristic view (green; γ_i); (c) Typical arrangements based on the angle. The angle is expressed in degrees to simplify histogram construction.

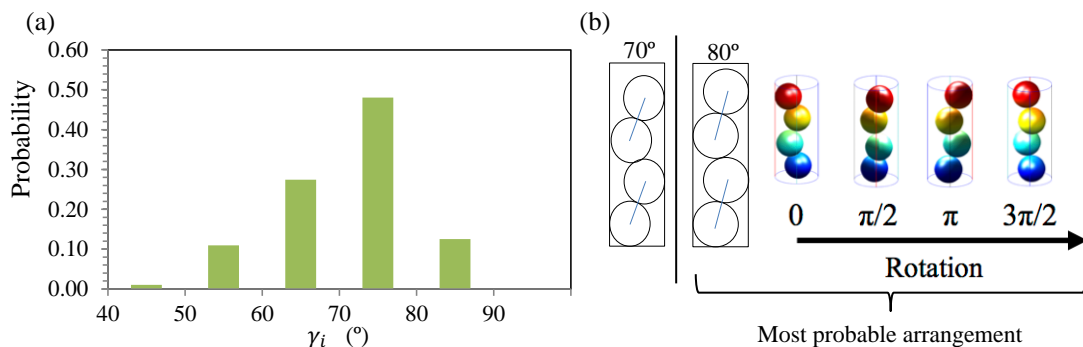


Figure 9: Particle angle distributions for random particle packing with similar arrangements joined. (a) Characteristic view (green; γ_i); (b) Most probable particle arrangements and 3D view of a 80° particle arrangement reconstruction.

Regarding the front and right view angle distributions (Figure 8a), the majority of particles (20 to 35%) have a 90° arrangement (i.e., 80° to 90° bin) (Figure 8c). As previously discussed,

this may mislead us to wrong hypothesis (2D versus 3D). So, when applying the equation Eq. 38, the majority of 90° arrangements is suppressed, being now predominant 80° and 70° arrangements (Figure 8 and Figure 9), representing 72% of the total particles analyzed. The preferential particle disposition is at 80°, having a probability of 48%. This disposition is characterized to have smooth spherical particles. For the other dispositions, from 40° to 70°, these arrangements are possible mainly because the spherical shaped particles are deformed.

In this section, it was presented a fast way to acquire data from catalyst packing in single pellet string reactors. The methodology proposed takes advantage of two-axis projection to reconstruct the particle location by a 3D view. The particles diameter used was restricted to a small range, which improve the results acquired. The application of the methodology requires two photos of the packing and trigonometric equations, which are easy to apply.

III.4 Single string pellet reactor: hydrodynamic regime

Some trials were already done in literature to describe flow dynamics in a single pellet string reactor (velocity fields and residence times). Müller et al. (2012) constructed a 2D simulation of 30 particles in a cylindrical pellet string reactor (channel and particle diameter of 4 mm and 3.3 mm, respectively), having a mesh with a total of 38 000 elements. In their CFD model, the fluid was in liquid-phase and a turbulent model was assumed (k- ϵ). They considered that a single pellet string reactor should pass to turbulent flow above Reynolds of 10, which correspond to the transition regime for a single pellet surrounded by flow. For single pellet string reactors, there are no clear guidelines to delimit the Reynolds in transition regime. To have an idea of this Reynolds, we first looked at the one for fixed bed reactors. Logtenberg et al. (1999) studied numerically heat transfer for 10 solid spheres (tube-to-particle ratio of 2.43). The authors found that there were not eddy turbulence spotted until Reynolds of 184. Dixon (2014) simulated a 400-sphere random packing fixed bed reactor (tube-to-particle ratio of 5.96) using both laminar ($50 < Re_L < 400$) and turbulent regimes ($400 < Re_L < 5000$) (k- ϵ model).

For single pellet reactor, Romkes et al. (2003) simulated a structured monolith with different tube-to-particle ratio (in a square channel), from 1 to 5, using laminar ($1.27 \times 10^{-4} < Re_L < 127$) and turbulent regimes ($127 < Re_L < 1.27 \times 10^5$) (k- ϵ model). Satterfield et al. (1969) investigated experimentally the dynamic hold up and mass transfer in a single pellet string reactor for a total of 75 experimental points ($d_p=8.25$ mm and tube-to-particle ratio around 2). The experimental data was consistent with the theoretical line (correlation based on laminar regime) for Reynolds superior to 10 and inferior to 600. For Reynolds above 600, the authors explained that inertia effects start to be more significant. This can be interpreted as a transition regime.

IV. Chapter IV

IV.1 Derivation of ψ

The ψ appears in the mass transfer between phases. It can be easily derive for a system without reaction and for a system with infinite reaction (extreme cases). The actual system should be between both cases.

Without reaction:

The ψ appears when deriving the mass transfer between phases in a close system without reaction. A title of example the derivation was done for gas-phase, but the results are the same for other phases.

The equations of depart are:

$$\begin{cases} \frac{dC_{i,G}}{dt} = -k_L a_{GL} (C_{i,G} - C_{i,L}) & \text{gas - phase} \\ \frac{dC_{i,L}}{dt} = k_L a_{GL} (C_{i,G} - C_{i,L}) & \text{liquid - phase} \end{cases} \quad \text{Eq. 39}$$

This system can be simplified by defining $\dot{D} \equiv \frac{d}{dt}$,

$$\begin{cases} \dot{D}C_{i,G} = -k_L a_{GL} (C_{i,G} - C_{i,L}) \\ \dot{D}C_{i,L} = k_L a_{GL} (C_{i,G} - C_{i,L}) \end{cases} \Leftrightarrow \begin{cases} C_{i,G}(\dot{D} + k_L a_{GL}) = k_L a_{GL} C_{i,L} \\ C_{i,L}(\dot{D} + k_L a_{GL}) = k_L a_{GL} C_{i,G} \end{cases} \quad \text{Eq. 40}$$

by multiplying the first equation of the system by $\left(\frac{\dot{D}}{k_L a_{GL}} + 1\right)$ and summing both equations.

$$\frac{\dot{D}^2 C_{i,G}}{k_L a_{GL}} + 2\dot{D}C_{i,G} = 0 \Rightarrow \frac{d^2 C_{i,G}}{k_L a_{GL} dt^2} + 2 \frac{dC_{i,G}}{dt} = 0 \quad \text{Eq. 41}$$

To determine $C_{i,L}$, the liquid-phase balance in Eq. 39 should be used. The Eq. III.25 is a second order ordinary equation. By applying the generic solution ($C_{i,G} = c_1 e^{y_1 t} + c_2 e^{y_2 t}$), it is possible to obtain:

$$C_{i,G} = \frac{C_{i,G,t=0} + C_{i,L,t=0}}{2} + \frac{C_{i,G,t=0} - C_{i,L,t=0}}{2} e^{-2k_L a_{GL} t} \quad \text{Eq. 42}$$

$$C_{i,L} = \frac{C_{i,G,t=0} + C_{i,L,t=0}}{2} - \frac{C_{i,G,t=0} - C_{i,L,t=0}}{2} e^{-2k_L a_{GL} t} \quad \text{Eq. 43}$$

Regarding both equations, the $k_L a_{GL} t$ appears (in the exponential term). It can be defined as:

$$\psi_{GL}^* = k_L a_{GL} t = \frac{\text{flow time}}{\text{transfer time}} \quad \text{Eq. 44}$$

For $\psi_{GL}^* = 1$, 86% of the initial concentration in the gas phase (Eq. 42 and Eq. 43) has already been transfer between phases (gas to liquid). For $\psi_{GL}^* = 2$, 98% of the initial concentration (gas) has been transferred to liquid. For a system in equilibrium without reaction, the minimum time needed to have more than 98% mass transfer of the gas phase is ($\psi_{GL}^* \geq 2 \Rightarrow t \geq 2/(k_L a_{GL})$).

Infinite reaction:

The ψ also appears when deriving the mass transfer between phases in a close system with infinite reaction (the transferred species reacts immediately after being transferred).

A title of example the derivation was done for gas-phase. The equations of depart are:

$$\begin{cases} \frac{dC_{i,G}}{dt} = -k_L a_{GL} (C_{i,G} - C_{i,L}) & \text{gas - phase} \\ \frac{dC_{i,L}}{dt} = 0 & \text{liquid - phase} \end{cases} \quad \text{Eq. 45}$$

By solving these equations, the solution is:

$$C_{i,G} = C_{i,G t=0} e^{-k_L a_{GL} t} \quad \text{Eq. 46}$$

$$C_{i,L} = 0 \quad \text{Eq. 47}$$

Regarding both equations, the $\psi_{GL}^* = k_L a_{GL} t$ is present. Between Eq. 46 and Eq. 42, the main different is at the exponential. In Eq. 46, ψ_{GL}^* is multiplied by -1. In Eq. 42, ψ_{GL}^* is multiplied by -2. This will give different results for the minimum time needed to have more than 98% initial concentration transferred to liquid.

For $\psi_{GL}^* = 1$, the 63% of the initial concentration presented in the gas phase (Eq. 46) has already been transfer between phases. For $\psi_{GL}^* = \{2, 3 \text{ and } 4\}$, 86, 95 and 98% of the initial concentration (gas) has been transferred to liquid. For a system in equilibrium with infinite reaction, the minimum time needed to have more than 98% mass transfer of the gas phase is ($\psi_{GL}^* \geq 4 \Rightarrow t \geq 4/(k_L a_{GL})$). This time is twice the time for the case without reaction.

Considerations to use ψ :

- a) The mass transfer coefficients are constant during the reaction;
- b) The experimental results should be between the case with and without reaction. It was considered that $\psi_{GL}^* = 2$ [$t \geq 2/(k_L a_{GL})$] is sufficient to considered that there is fully mass transfer between the gas and liquid phase (more than 86% of the initial

concentration was transferred between phases). This concept will be used for the liquid-solid mass transfer;

- c) To simplify the interpretation $\psi = \psi^*/2$. Therefore if $\psi > 1$, the system has time to achieve full mass transfer between phases. If $\psi < 1$, the system has no sufficient residence time to achieve full mass transfer.

IV.2 Choice of liquid hold-up correlation (Eq. IV.5)

For single pellet string reactors with spherical pellets, there are only a few studies available to evaluate the liquid hold-up, such as Hipolito et al. (2010) and Müller et al. (2015).

The Hipolito's correlation for liquid hold-up ($\epsilon_L = \epsilon \frac{\bar{u}_L}{\bar{u}_G + \bar{u}_L}^{0.16}$) is not entirely adapted for the reactor selected, because it has a square section instead of a circular one, leading to a different flow pattern (stratified slow pattern). Figure 10 shows the comparison of the gas-liquid flow pattern between a square and a circular section reactor (helical flow pattern).

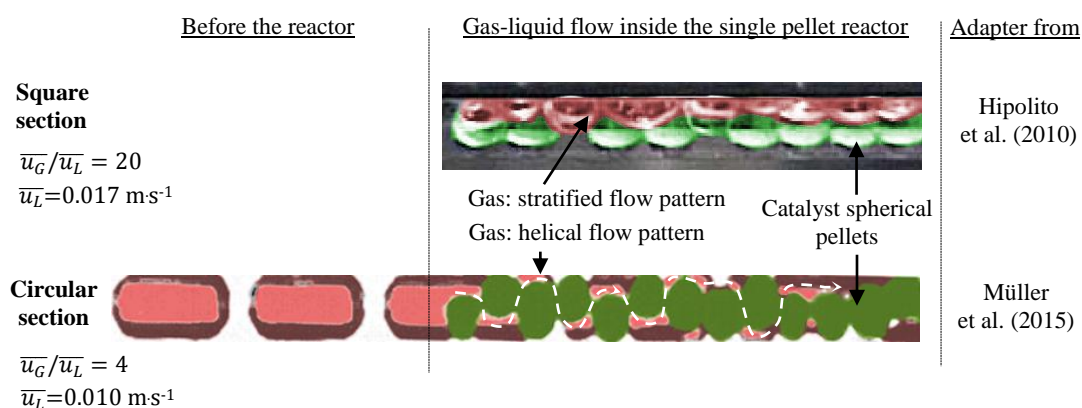


Figure 10: Observations of the flow regime (gas-liquid) for two different pellet string reactors (square and circular section). The square reactor has a $d_h = 4$ mm and $d_p = 3$ mm. The circular reactor has a $d_h = 2.4$ mm and $d_p = 1.9$ mm.

The Müller et al. (2015) flow observations (Figure 10) seems closer to the reactor selected, since the reactor has the same $d_r/d_p = 1.22$. The authors perform a reaction and compared its conversion with the gas hold-up in an empty channel (before contacting the spheres) ($\epsilon_{L,EC} = 1 - \epsilon_{G,EC} = \epsilon \frac{\bar{u}_L}{\bar{u}_G + \bar{u}_L}$). The conversion obtained had a linear behavior with the liquid hold-up. This may mean that the liquid hold-up in the reactor can be expressed as $\epsilon_L = 1 - \epsilon_{G,EC} = c \frac{\bar{u}_L}{\bar{u}_G + \bar{u}_L}$. As far as we know, there are no data available in literature to determine c for the reactor selected. Therefore, the c was considered 1 (Eq. IV.5).

IV.3 High-pressure: MAPD concentration effect and H₂/MAPD ratio

Feedstock: MAPD (3.02 mol% [375 mol.m⁻³]) and Propane (3.29% mol [408 mol.m⁻³]).

Conditions: 303 K, 120 bar and catalyst mass of 0.6 g (catalyst W).

Main properties changed: molar conc. flow ($k_{LS}a_{LS}\Delta C_{MAPD}$ and $k_{LS}a_{LS}\Delta C_{H_2}$) and reaction kinetics.

Figure 11 shows the reactant conversions in function of MAPD concentration (inlet) at 900 h^{-1} for 1 and 2 H_2 /MAPD ratio.

Hydrogen and MAPD: The H_2 is not entirely converted for 2 H_2 /MAPD ratio (Figure 11), having similar conversions ($\sim 70\%$) for the MAPD molar range studied. This trend is different for 1 H_2 /MAPD ratio, since the H_2 conversion increases from 0.9 to 2.8 mol% of MAPD (inlet). Moreover, the H_2 conversion is lower at 1 H_2 /MAPD ratio than at 2. About MAPD conversion (Figure 11), similar observations can be noticed.

Propane and propylene: For 2 H_2 /MAPD ratio, the propane production has a variation of 10% for the MAPD molar range studied. This variation is similar to one with 1 H_2 /MAPD ratio. Between 1 and 2 H_2 /MAPD ratio, the propane produced triples. For propylene, for 2 H_2 /MAPD there is consumption of propylene rather than production, which is noticed at 1 H_2 /MAPD.

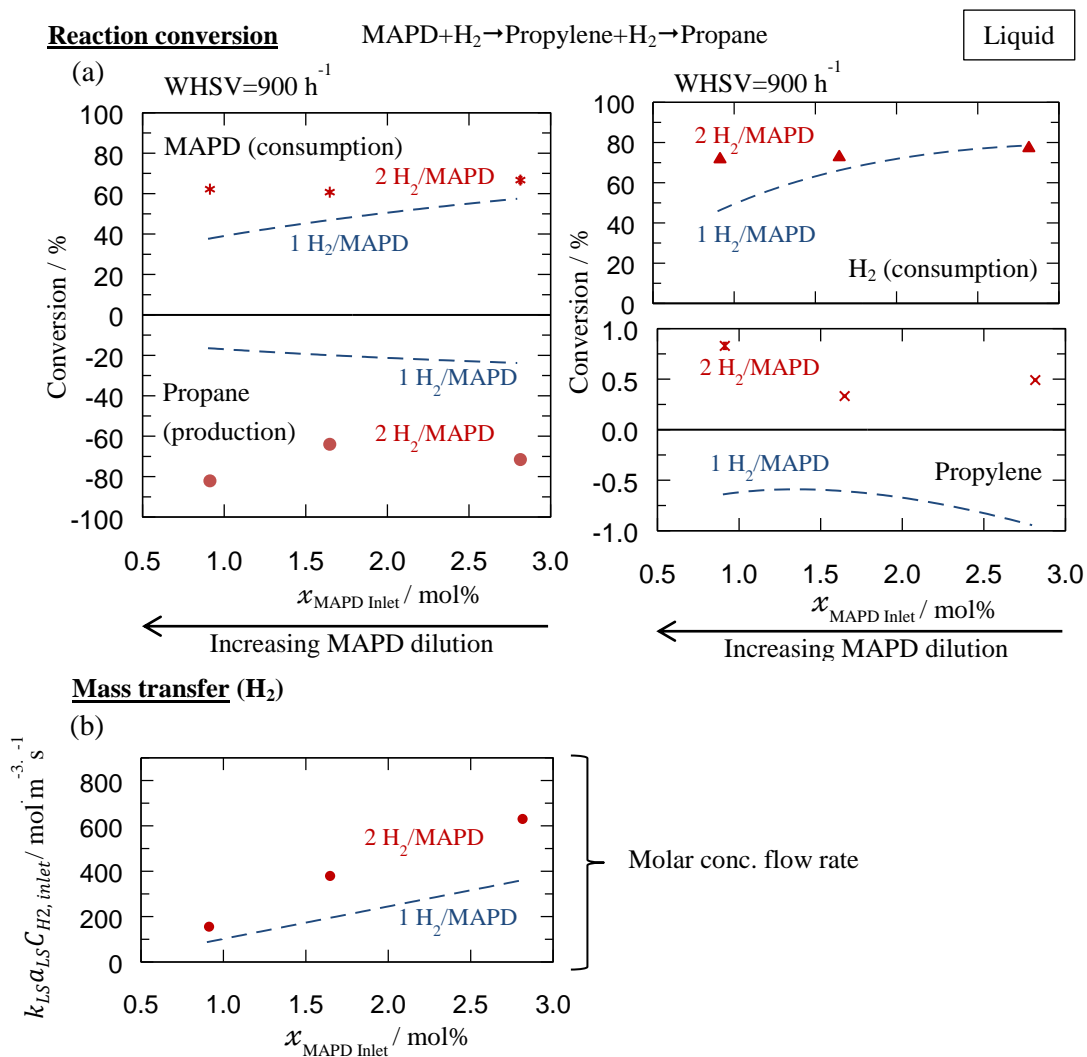


Figure 11: Selective hydrogenation at 303 K, 900 h⁻¹ and 120 bar for 1 and 2 H₂/MAPD ratio. (a) Conversions of MAPD (*), Propane (•), Hydrogen (▲) and Propylene (×) in function of the MAPD molar percentage. (b) H₂ molar conc. flow rate (liquid-solid). The lines are fitted curves of the experimental results for 1 H₂/MAPD ratio. The heptane was used as a solvent at the lowest MAPD concentration.

Conclusions

Due to the double hydrogen molar conc. flow (liquid to solid), it was anticipated superior propane production (lower reaction selectivity) when increasing H₂/MAPD ratio from 1 to 2. Regarding Figure 11b, between 0.9 and 2.8 mol% of MAPD, the H₂ molar conc. flow increase ~3 times. Since the MAPD decreases and the propane has the same conversions, it endorses that there is no competition between MAPD and propylene for the active sites (see §IV.4.4).

IV.4 Supercritical vs high-pressure: 2 H₂/MAPD ratio

Main properties changed: density (kg.m⁻³), viscosity (Pa.s), diffusivity (m².s⁻¹) and mass transfer ($k_{LS}a_{LS}$).

Conditions: 303 K, 120 bar, 2 H₂/MAPD ratio, space velocity of 900 h⁻¹ and 0.6 g of catalyst.

Figure 12 shows the conversion in function of MAPD molar concentration for supercritical fluids (with solvent CH₄) and high-pressure conditions. The points were evaluated in a zone where $Da^{mod.} < 1$ (space velocity is superior to the reaction rate).

Hydrogen: Regarding the points at 100 mol.m⁻³ (MAPD molar concentration). For supercritical fluid (C₃ cut mixed with CH₄), the hydrogen is not fully converted. At high-pressure conditions [propylene (~no solvent)], there is also hydrogen available at the end of the reactor (H₂ conversion of 70 %).

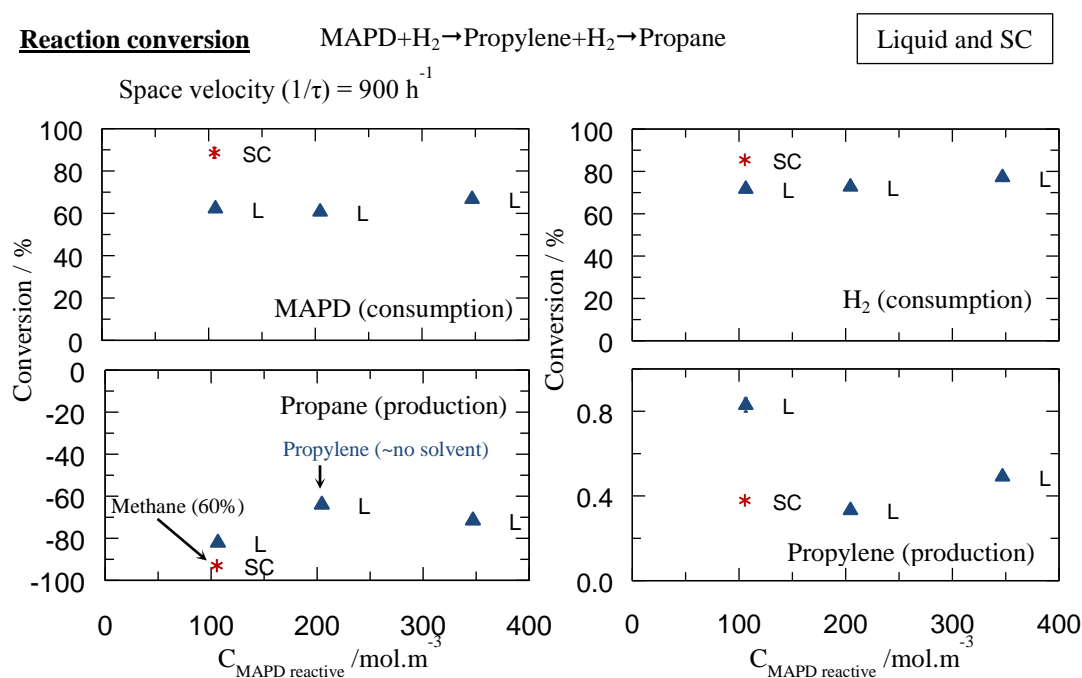


Figure 12: Selective hydrogenation at 303 K, 2 H₂/MAPD ratio and 120 bar. Supercritical (60% CH₄) vs high-pressure conditions.

MAPD: The supercritical fluid has higher MAPD conversion (90%). For the same inlet dilution (100 mol.m⁻³), the MAPD conversion is around 60% for high-pressure conditions. Another interesting result is that supercritical fluid has higher conversion when compared to concentrated mixtures (high-pressure).

Propane: The propane is more produced in supercritical conditions than in high-pressure conditions.

Propylene: The propylene consumed lower in supercritical conditions.

Conclusions

The MAPD conversion is favored at 2 H₂/MAPD ratio in supercritical conditions than in high-pressure conditions. This is due to higher effectiveness factor in supercritical fluids ($\eta_{SC} > \eta_{HP}$).

IV.5 Diffusion correlations

The correlations were selected since diffusion data for MAPD are not available in literature (Zhu et al., 2002; Medvedev and Shapiro, 2004; Magalhães et al., 2013). They were only applied to the MAPD, because it is a bigger molecule than hydrogen, being the most interesting molecule to study. Four correlations were chosen to predict diffusion coefficients: He-Yu, Fuller, Wilke-Chang and Liu-Silva-Macedo (LSM)

Fuller and Wilke-Chang correlations are only adapted to predict tracer diffusion coefficients in gas and liquid phases, respectively. The He-Yu correlation is similar to Wilke-Chang in the working range, meaning that it can only be used in liquid phase. Even knowing that they are not suitable to the supercritical region, they will still be used to set the boundaries (max. and min.) of the diffusion coefficients.

Liu-Silva-Macedo (LSM) correlation is able to predict tracer diffusion coefficients in gas, supercritical and liquid media ($D_{\text{gas}} > D_{\text{supercritical}} > D_{\text{liquid}}$).

The strategy followed was to check the correlations reliability and chose the most reliable.

Verification of LSM correlation

Since, Fuller et al., Wilke-Chang and He-Yu correlations have a straightforward formulation. On the other hand, the LSM equation involves a several amount of parameters and should be carefully analyzed. A mixture of tetrahydrofuran (THF) in supercritical carbon dioxide was chosen to verify the LSM correlation application (Silva and Macedo, 1998). In their work, a comparison was made between experimental data and estimated data using LSM. The Lennard-Jones parameters and mixing rules proposed by the authors were used. According to

authors, the AARD (%) is close to 14.87 %. An equal AARD was obtained (14.78 %). This give us confidence about the application of LSM.

In Figure 13, the difference between experimental and predicted data values is shown for illustrative purposes.

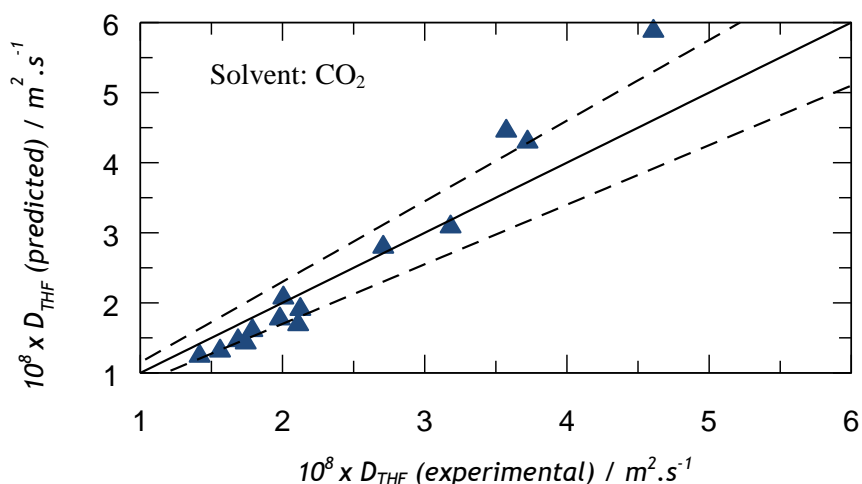


Figure 13: Deviation between experimental data and estimated values for the diffusion of THF in supercritical CO₂. The dashed line represents a deviation of 15 %.

The next step is to compare the different correlations and select the best suitable one.

Comparison between different correlations

To compare the four correlations (He-Yu, Fuller, Wilke-Chang and Liu-Silva-Macedo), similar conditions and fluid properties were used. In Table 5, all data necessary for prediction calculations are listed, except for viscosity and density. Those were retrieved from National Institute of Standards and Technology (2011). The values were obtained from the authors publications, whenever possible. For the present correlations, methylacetylene and propadiene were considered as a single fluid, having average properties. It should be a fair assumption, since both species have very close physical properties.

Table 5: Fluid data to be used in the chosen correlations. Information gather in ¹National Institute of Standards and Technology (2011); ²database of Pro II V9.2 software; ³Sastri et al. (1996); ⁴Fuller et al. (1966); ⁵Liu et al. (1996). *Properties V_d and V are both the molar volume, but the tables used for their estimation were not the same.

Property	MAPD	Propylene	Methane	Ethane	CO ₂
¹ M , g/mol	40.07	42.08	16.04	30.07	44.01
¹ T_c , K	398.12	365.57	190.56	305.33	304.13
¹ P_c , bar	53.87	46.65	45.99	48.72	73.77
² V_c , cm ³	163.00	188.40	99.00	145.50	94.00
³ V^* , cm ³ /mol	59.32	63.00	---	---	---

Appendix

${}^4 V_d^*$, cm ³ /mol	57.42	61.38	---	---	---
${}^5 \sigma_{LJ}$, Å	4.391**	4.473**	3.585	4.176	3.262
${}^5 \epsilon_{LJ}/k_B$, K	316.10***	290.26***	167.15	213.08	500.71

The correlations were compared for four solvents: methane, ethane, carbon dioxide and propylene. The strategy is to find the one that has the most reliable diffusional behavior.

Figure 14 (a-d) illustrate the diffusion coefficients of MAPD for each solvent as a function of temperature. The results are presented at constant pressure of 120 bar. For the four correlations used, the diffusion is slower for propylene as solvent (bigger molecule). The propylene and MAPD have both 3 carbon molecules, therefore no substantial differences in diffusion are expected. In contrast, when using methane as solvent, it is more likely to achieve higher diffusion. Diffusion coefficients for CO₂ and ethane are similar.

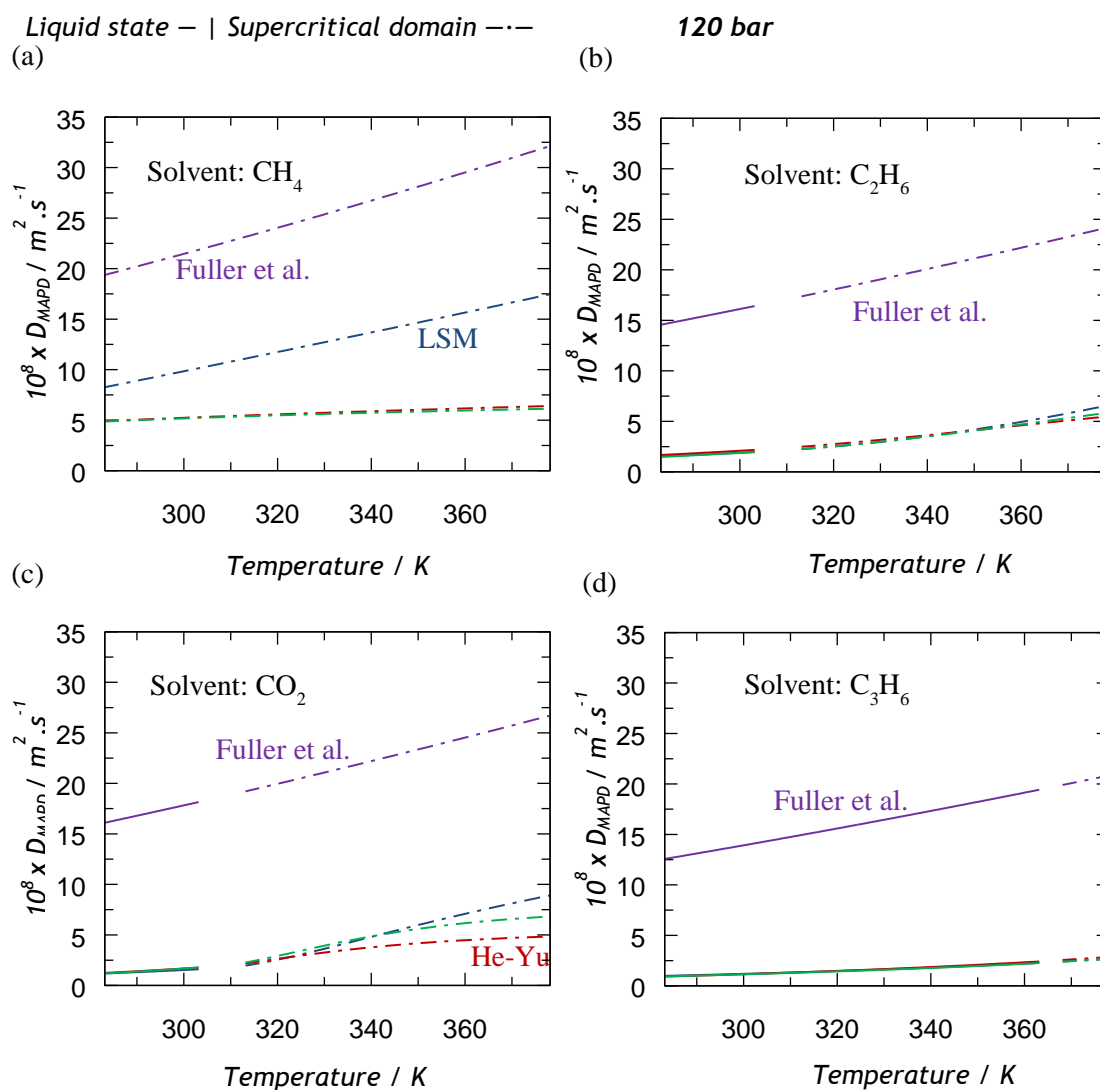


Figure 14: Diffusivity of MAPD in (a) methane, (b) ethane, (c) carbon dioxide, and (d) propylene at constant pressure of 120 bar. Range of temperatures between 283.15 and 373.15 K. (blue) Liu-

Silva-Macedo (1997); (red) He-Yu (1998); (green) Wilke-Chang (1955); (purple) Fuller et al. (1966).

Fuller et al. correlation overestimates the diffusion coefficients of MAPD for all solvents. This result was expected, because the correlation is meant to be used with gases, which has a higher diffusional than liquids. Since the other correlations have lower values, we could assume that that correlation would be unrealistic for our case. Wilke-Chang's obtains similar results to those of LSM, except for methane. The values obtained from He-Yu correlation are also similar to those of Wilke-Chang correlation (in the considered range). The only exception occurs for CO₂, where the estimates are lower than those of other correlations.

Considering these results, the decisions can be summarized as:

- Fuller et al. can be discarded because it can only be applied for the gas phase;
- Wilke-Chang and He-Yu will be not used since it is not adapted to the supercritical conditions, more particularly for the case of methane. In literature, these correlations have higher desviations (see §I.5.3 and §I.6.2);
- Liu-Silva-Macedo correlation will ne used because the diffusivity is well estimated for the liquid state and it takes into account the change of physical state. Also, its paremeters have physical meaning (e.g. distance between solute and solvent).

Therefore, the diffusion coefficient will be determined through Liu-Silva-Macedo correlation.

V. Chapter V

V.1 Main function (Matlab+Comsol)

%The following Matlab code is for the power-law 2 model.

```
clear;
clc;
global Values
global iter
global concentration
global model
iter=0;
Values=0;
concentration=0;
%Ea1=7000;
%Ea2=7000;
%k1_0=5.13E-3/(exp(-Ea1/(8.314472*(273.15+30))));
%k2_0=2.21E-6/(exp(-Ea2/(8.314472*(273.15+30))));

x0(1)=2.488e-03;
```

```
x0(2)=4.3929e-06;
x0(3)=1;
x0(4)=1;
x0(5)=1;
x0(6)=1;

model=mphload('Reactor_C3v4_with_my_correlation_diff4.mph');

% myfun4 - for pressure at 120bar and 30 degrees (liquid)
% myfun6 - for pressure at 60 bar and 30 degrees (liquid)
% myfun7 - for pressure at 120 bar and 30 degrees (liquid) - another
% kinetic
% myfun8 - for pressure at 120bar and 30 degrees (liquid) - Another charge
% myfun9 - for pressure at 120bar and 30 degrees (liquid) - All the charge
% results with langmuir LHHW
x=fminsearch(@myfunMin,x0);
disp(x);
```

V.2 Minimization function (Matlab+Comsol)

```
function [f]=myfunMin(x)
global Values
global iter
global concentration
model=mphload('Reactor_C3v4_with_my_correlation_diff4.mph');

% Experiments values
% -----Inlet-----
% 28_07_2014 10 00
u_feed(1)=0.010680389;
CMAPD_feed(1)=348.879;
CPropene_feed(1)=11627.96;
CPropane_feed(1)=407.92;
CH2_feed(1)=671.72566;
rho_fluid(1)=522.8521;
visco_fluid(1)=7.843E-5;
CMAPD_out(1)=47.54;
CPropene_out(1)=11558.63;
CPropane_out(1)=778.31;
CH2_out(1)=0.00;
L_reactor(1)=70*0.244*0.94;
T(1)=273.15+30;
```

```
Dif(1)=1.17024E-08;

%22_05_2014 13 51
u_feed(2)=0.0067495;
CMAPD_feed(2)=369.76;
CPropene_feed(2)=11667.05;
CPropane_feed(2)=412.09;
CH2_feed(2)=364.33;
rho_fluid(2)=524.6725;
visco_fluid(2)=8.487E-05;
CMAPD_out(2)=94.33;
CPropene_out(2)=11847.84;
CPropane_out(2)=500.98;
CH2_out(2)=0.00;
L_reactor(2)=70*0.244*0.94;
T(2)=273.15+30;
Dif(2)=1.17024E-08;

...

iter=1+iter;
disp('k10:');
disp(x(1));
disp('k20:');
disp(x(2));

disp('n1:');
disp(x(3));
disp('n2:');
disp(x(4));
disp('n3:');
disp(x(5));
disp('n4:');
disp(x(6));

Values(iter,1)=x(1);
Values(iter,2)=x(2);
Values(iter,3)=x(3);
Values(iter,4)=x(4);
Values(iter,5)=x(5);
Values(iter,6)=x(6);
```

```

if x(1)>5E-7 & x(2)>8E-10 & x(1)<12E-2 & x(2)<8E-3 & x(3)>1E-6 & x(4)>1E-6 &
x(5)>1E-6 & x(6)>1E-6 & x(3)<200 & x(4)<200 & x(5)<200 & x(6)<200
ftemp=0;
for j=1:29
%%%%%%
%Load of initial variables
temp=strcat(",num2str(u_feed(j)), ' [m/s]');
model.param.set('u_feed',temp);
temp=strcat(",num2str(CMAPD_feed(j)), ' [mol/m^3]');
model.param.set('CMAPD_feed',temp);
temp=strcat(",num2str(CPropane_feed(j)), ' [mol/m^3]');
model.param.set('CPropane_feed',temp);
temp=strcat(",num2str(CPropene_feed(j)), ' [mol/m^3]');
model.param.set('CPropene_feed',temp);
temp=strcat(",num2str(CH2_feed(j)), ' [mol/m^3]');
model.param.set('CH2_feed',temp);
temp=strcat(",num2str(rho_fluid(j)), ' [kg/m^3]');
model.param.set('rho_fluid',temp);
temp=strcat(",num2str(visco_fluid(j)), ' [Pa*s]');
model.param.set('m_fluid',temp);
temp=strcat(",num2str(L_reactor(j)), ' [cm]');
model.param.set('L_reactor',temp);
temp=strcat(",num2str(T(j)), ' [K]');
model.param.set('T',temp);
%%%%%%%%

temp=strcat(",num2str(x(1)), ' [m^6/(kg*s*mol)]');
model.param.set('k1_0',temp);
temp=strcat(num2str(x(2)), ' [m^6/(kg*s*mol)]');
model.param.set('k2_0',temp);

temp=strcat(num2str(Dif(j)/Dif(1)), ' ');
model.param.set('Dm_parameter',temp);

temp=strcat(",num2str(x(3)), ' ');
model.param.set('n1',temp);
temp=strcat(num2str(x(4)), ' ');
model.param.set('n2',temp);
temp=strcat(",num2str(x(5)), ' ');
model.param.set('n3',temp);

```

```
temp=strcat(num2str(x(6)), ' ');
model.param.set('n4',temp);

temp=strcat("",num2str(0), ' [J/(mol)]');
model.param.set('Ea1',temp);
temp=strcat(num2str(0), ' [J/(mol)]');
model.param.set('Ea2',temp);
model.sol('sol1').runAll;

temp=struct2cell(mpheval(model,'CMAPD','edim','boundary','selection',2));
CMAPD_out_comsol(j)=cell2mat(temp(2));
temp=struct2cell(mpheval(model,'CH2','edim','boundary','selection',2));
CH2_out_comsol(j)=cell2mat(temp(2));
temp=struct2cell(mpheval(model,'CPropene','edim','boundary','selection',2));
CPropene_out_comsol(j)=cell2mat(temp(2));
temp=struct2cell(mpheval(model,'CPropane','edim','boundary','selection',2));
CPropane_out_comsol(j)=cell2mat(temp(2));

concentration(1,iter,j)=CMAPD_out_comsol(j);
concentration(2,iter,j)=CH2_out_comsol(j);
concentration(3,iter,j)=CPropene_out_comsol(j);
concentration(4,iter,j)=CPropane_out_comsol(j);

ftemp=abs(CMAPD_out_comsol(j)-CMAPD_out(j))^2+abs(CPropene_out_comsol(j)-
CPropene_out(j))^2+abs(CPropane_out_comsol(j)-
CPropane_out(j))^2+abs(CH2_out_comsol(j)-CH2_out(j))^2+ftemp;
disp('F_temp_individual');
disp(abs(CMAPD_out_comsol(j)-CMAPD_out(j))+abs(CPropene_out_comsol(j)-
CPropene_out(j))+abs(CPropane_out_comsol(j)-CPropane_out(j))+abs(CH2_out_comsol(j)-
CH2_out(j)));
disp('F_temp_individual^2');
disp(abs(CMAPD_out_comsol(j)-CMAPD_out(j))^2+abs(CPropene_out_comsol(j)-
CPropene_out(j))^2+abs(CPropane_out_comsol(j)-
CPropane_out(j))^2+abs(CH2_out_comsol(j)-CH2_out(j))^2);

end
f=ftemp;

else
    f=1000000000;
end
disp('F_objective:');
```

```
disp(f);  
Values(iter,7)=f;  
save('Global_vars.mat','Values','concentration');  
end
```


Titre : Les propriétés spécifiques des fluides supercritiques au service des systèmes réactifs contraignants

Resumé : Le développement de nouveaux catalyseurs pour l'hydrogénation sélective du propyne et du propadiène (MAPD) est un processus complexe, puisqu'il s'agit d'une réaction rapide effectuée en gaz-liquide-solide. Dans ces conditions, le flux d'hydrogène transporté aux sites actifs du catalyseur contrôle la vitesse de la réaction, particulièrement à l'échelle pilote. Cela rend difficile la comparaison des performances des différents catalyseurs (conversion et sélectivité). Afin d'améliorer la discrimination des solides, l'hydrogénation sélective du MAPD a été étudiée en monophasique (fluide/solide) dans un réacteur filaire à haute pression et en supercritique.

La première partie de la thèse a eu pour objectif de déterminer les conditions de fonctionnement adéquates : un dispositif expérimental microfluidique et une méthodologie associée ont été développés et validés pour obtenir les diagrammes P-T de miscibilité et les coordonnées critiques des systèmes réactionnels mis en jeu. En parallèle, le réacteur a été caractérisé en utilisant des outils numériques (CFD) appliqués à l'hydrodynamique et au transfert de masse. Les tests expérimentaux ont alors pu être menés, dans la seconde partie de la thèse, afin d'étudier l'hydrogénation du MAPD à 303 K entre 20 et 120 bar. Dans ces conditions, plusieurs paramètres ont été étudiés, tels que la PPH (vitesse spatiale horaire, ou WHSV en anglais), la pression et la fraction de solvant. Les résultats montrent un gain important de conversion du MAPD à haute pression et en conditions supercritiques par rapport aux conditions classiques (>5 fois plus). Cela peut s'expliquer par la suppression de l'interface gaz-liquide et l'amélioration des diffusivités. Les variations de sélectivité observées en parallèle montre sa dépendance au flux d'hydrogène amené. Ces résultats prometteurs permettent une meilleure discrimination des catalyseurs ainsi qu'une meilleure compréhension du système réactif. Ainsi, pour la première fois, en utilisant ces données non classiques, il a au final été possible d'estimer des paramètres cinétiques intrinsèques pour l'hydrogénation sélective des coupes C₃.

Mots clés: fluides supercritiques, hydrogénation sélective, CFD, réacteur filaire, MAPD.

Title : Specific properties of supercritical fluids for fast and exothermic reactive systems

Abstract : The development of new catalysts for propyne and propadiene (MAPD) hydrogenation is a complex process, because it is a fast reaction performed in gas-liquid-solid. Indeed, in these conditions, the hydrogen flux (G/L and L/S) transported to the reaction sites controls the overall reaction rate, particularly at pilot scale. To avoid this limitation, the MAPD selective hydrogenation was performed in single-phase, using a single pellet string reactor (SPSR) at high-pressure and supercritical conditions. For both conditions, the literature is scarce. Thus, the first step was to develop and validate a microfluidic experimental apparatus and a methodology based on "design of experiments", in order to obtain PT miscibility diagrams and critical coordinates. These methods combined allowed a fast PT screening compared to conventional phase behavior cells, being around 5 times higher. In parallel, the SPSR was characterized by computational fluid dynamics (CFD) for flow and mass transfer. It was shown that the hydrodynamic inside the reactor can be modeled as a plug flow reactor with low axial dispersion, and a LS mass transfer correlation was proposed. After the fluid and reactor characterization, the MAPD hydrogenation was performed at 303 K and from 20 to 120 bar. At these conditions, several parameters were tested, such as *WHSV* (weight hourly space velocity), pressure and solvent fraction. The results showed that high-pressure and supercritical conditions offer better reaction performance, which is due to the suppression of the gas-liquid limitation and to the diffusivity enhancements (more than 5 times faster than conventional conditions). With this thesis, it was possible, for the first time, to estimate the intrinsic kinetics parameters of a dense C₃ cut mixture hydrogenation, allowing a deeper understanding of the involved mechanism. Thus, the use of unconventional conditions has opened a door to new forms of catalyst screening and new ways to study kinetics.

Keywords: supercritical fluids, microfluidics, hydrogenation, CFD, single pellet reactor, MAPD.

Unité de Recherche: ICMCB, UPR9048, 87 Avenue du docteur Albert Schweitzer, 33608, Pessac, France